

THIS WEEK

EDITORIALS

TABLET The international weekly journal of science — on the iPad **p.154**

WORLD VIEW Everything science tells us about obesity is wrong **p.155**

FAG END Finches and sparrows nest with used cigarette butts **p.156**



Words are not enough

The political inertia that characterizes the world's response to global warming cannot continue. Politicians and policy-makers must follow the climate's lead — and change.

The past week saw a number of pronouncements on the subject of climate change. Not surprising given that, in Doha, the United Nations was wrapping up the latest round of its annual political negotiations on a global agreement to regulate greenhouse-gas emissions. But the words, and the bundle of small practical actions, that emerged from the meeting had a familiar ring.

"There has been, yet again, a very big mismatch between the scale and urgency of action required to effectively manage the huge risks of climate change, and the political will and ambition that has been displayed," said Nicholas Stern, chair of the Grantham Research Institute on Climate Change and the Environment at the London School of Economics.

"This package offers improved continuity from existing carbon markets to the new markets of the future. But it still won't inspire action at the scale commensurate with the Copenhagen objective of limiting warming to 2°C," said Dirk Forrister, president of the International Emissions Trading Association.

Both statements tell you that the Doha talks followed the recent trend: warm political words but little sign of serious action. There was some minor progress on secondary issues, just enough to keep the show on the road, but little to address the core problem of soaring emissions.

There were some familiar problems as well. Here's Oleg Shamanov, Russian negotiator at Doha, grumbling at the way his objection to the final Doha text was overruled: "It has to be clearly stated that this is an outrageous violation and absolutely unacceptable conduct of business. The way those decisions were adopted extremely seriously undermines the legitimacy of the regime." And Christiana Figueres, executive secretary of the UN's Framework Convention on Climate Change: "What we understand is that what Russia wants and needs is actually in those texts so my recommendation to our good Russian colleague is to take the time to read these texts."

Once again, the climate talks dragged on into the small hours, way past their scheduled finish time, and descended into acrimony — even with so little of substance on the negotiating table. A late and messy end is becoming as much a pre-Christmas tradition as the trees erected in the airports that the delegates pass through on their way home. "In the 16 years we have been coming to these conferences, there has been no global warming at all." That statement came from the British climate sceptic Christopher Monckton, who impersonated a delegate from Myanmar to address the conference floor, and did at least offer some light relief. "Can we have your conference pass back, please?" was pretty much the UN response. "Oh, and don't come back."

Bona fide attendees at Doha together produced a plan and timetable of sorts towards establishing a new agreement in 2015. In the meantime, a weakened Kyoto Protocol was extended to 2020, minus the signatures of Russia, Canada and Japan. Talks on how the rich world

will finance efforts to cut emissions and adapt to changed weather patterns in the poor world ran into the desert sand and will be taken up again at the end of 2013 in Warsaw.

Away from Doha, here is another statement on climate change: average global temperature will rise by 0.7–1.5°C between 1990 and 2030,

"The global atmosphere, the planet itself, has shifted while the politics has stood still."

with a best estimate of 1.1°C. That is derived from the very first report of the Intergovernmental Panel on Climate Change in 1990. In many ways it is the first consensus prediction of climate change. We're now more than half way through the period covered by that prediction and so far, at least, it is bang on.

In a paper published this month, climate researchers David Frame and Dáithí Stone analyse that original prediction — and its success (D. J. Frame and D. A. Stone *Nature Clim. Change* <http://doi.org/jx6>; 2012). "It seems highly likely that even in 1990 we understood the climate system well enough to make credible statements about how its aggregate properties would change on timescales out to a couple of decades," they write.

And, from the same paper, here's a line on climate that deserves to roll around the world. "The scientific community has now been working on the climate change topic for a period comparable to the prediction and the timescales over which the climate is expected to respond." The global atmosphere, the planet itself, has shifted while the politics has stood still. What more is there to say? ■

Life on land

Evidence for the first land life is controversial, but the fossil record has a tendency to surprise.

When did life first appear on land? The answer to this question — one of the most fundamental in science — rather depends on the values you choose for 'life' and 'land'.

There is certainly evidence for freshwater life — pond life, essentially — a billion years ago or so (P. K. Strother *et al. Nature* **473**, 505–509; 2011). Apart from that, the evidence is indirect and inferred from signs of weathering of non-marine rocks and the presence of apparent palaeosols — sediments indicative of fossilized soil that, by definition, were exposed to the air. Actual fossils that might be signs of land life in the Precambrian eon (before 542 million years ago) are exceedingly rare — or, some say, mythical.

It is a highly controversial subject, and one scientist who didn't shy away from controversy was the late palaeobotanist Jane Gray. Starting in the 1950s, Gray argued, often vociferously, for the presence of

life on land at an early date. Being female, ferocious and an advocate of an unpopular view, she didn't get many grants. But as biologist William Shear wrote in her obituary, she "was as astute at playing the stock market as she was at interpreting fossil spores, and used her independent wealth to fund her own research" (see *Nature* 405, 34; 2000).

Gregory Retallack of the University of Oregon in Eugene, like Jane Gray, is unafraid to plough a contrarian furrow in this much-debated area. For many years now, he has worked on palaeosols from the Precambrian. The problem with fossil soils is that they are conventionally recognized by traces of the organisms that lived in them, especially plant roots. There lies a conundrum — how do you recognize a palaeosol in sediment that lacks plant roots? The answer comes through careful geological work, to show that the palaeosol is associated with rock formed under non-marine conditions, together with work on geochemistry and data from stable isotopes. But there might also be direct evidence in the fossil soil, in the form of carbonate nodules, sand crystals and cracks caused by desiccation or the presence of ice.

Evidence of this sort has now led Retallack to infer the presence of palaeosols among rocks from the Ediacaran period (635 million to 542 million years ago) of South Australia. One might think that soils from the latest Precambrian are hardly controversial, even by the standards of a highly charged field. But these rocks contain fairly abundant evidence for the first macroscopic life — which, until now, was widely assumed to have been marine.

Ediacaran rocks feature a wide range of large, distinctive and yet enigmatic structures, usually thought to be fossils of living creatures. Originally found in South Australia, Ediacaran fossils have since been discovered in localities as far-flung as Newfoundland in Canada, Arctic Russia and the English Midlands.

The Ediacarans, however, were a rum lot. Although clearly highly organized, their precise nature has been elusive. If they were animals, they bore little or no resemblance to any other creatures, either fossil or extant. This has led to suggestions that they were giant protists, fungi,

algae, lichens or even a kind of life entirely different from anything else known and now wholly extinct.

Perhaps the only point of agreement is that, whatever else they were, the Ediacarans lived on the sandy beds of shallow, sunlit seas. This is where Retallack parts company with just about everyone else, because some of his Ediacaran palaeosols are associated with Ediacaran fossils. This would mean that at least some Ediacarans lived on land,

"The stately progression of life from water to land was not necessarily a single, simple narrative."

under the sky, perhaps in the manner of lichens, or microbial colonies that form soil crusts. The Ediacarans, then, would be the now-not-so-rare (and not at all mythical) creatures that first colonized the land — not just in puddles, but in soils indicative of a dry, cold desert. This is as far away as imaginable from the oceanic idyll that many have assumed for Ediacaran organisms, and have

reconstructed as such in a million coffee-table books.

These conclusions are published in a paper on *Nature's* website this week (G. J. Retallack *Nature* <http://dx.doi.org/10.1038/nature11777>; 2012) and will cause sharp intakes of breath in the palaeontological community; so much so that we have commissioned a News and Views Forum to air the arguments (S. Xiao & L. P. Knauth *Nature* <http://dx.doi.org/10.1038/nature11765>; 2012).

More work — and more science — will be the only way to validate this challenging and exciting work. But the lesson from the past is clear. Jane Gray's advocacy of land life in the relatively recent Ordovician period (485 million to 443 million years ago), once seen as off-the-wall, is now orthodoxy. There is nothing outré in principle in the supposition that life of some sort, however humble, lived on land from a very early date: the stately progression of life from water to land was not necessarily the single, simple narrative that seems so cut and dried in retrospect. The fossil record has this irritating habit: just when everyone thinks that the narrative has been sorted out, something comes along to force the story in a new, unexpected and breathtaking direction. ■

ANNOUNCEMENT

A new iPad app for *Nature* readers

Many publishers hope that tablet renditions of newspapers and magazines will revive the fortunes of once-mighty but now financially stressed publications founded in print. *Nature's* fortunes over the years have been relatively positive. Its print circulation has declined since its peak in 2002, but not as markedly as those of many other publications. Meanwhile, the online readership of *Nature* is more than 3 million unique users every month, and growing significantly year on year.

However, there is a world of difference in user experience between *Nature* on a desktop computer or laptop and a digital rendition that captures the feel and easy portability of the weekly print issue with the added features that an online platform allows. Although *Nature* has had an iPad version since January 2011, a version is now being released that includes the weekly edition in its traditionally structured form. Existing personal subscribers to *Nature* have full access to the tablet edition. New subscribers can choose to buy only the iPad version at a comparatively low price (see go.nature.com/pvfvqy).

Nine journals from the Nature Publishing Group are included in this app: *Nature*, *Nature Biotechnology*, *Nature Medicine*, *Nature*

Physics, *Nature Genetics*, *Nature Reviews Genetics*, *Nature Reviews Microbiology*, *Nature Communications* and *Scientific Reports*. Also included are News articles and papers published online but not yet available in print. More journals will follow next year.

At present, the accessibility of these diverse strands of content varies. Access for much of it is unrestricted. All of *Nature's* journalistic output is freely available. *Scientific Reports* is a 'gold' open-access journal — in other words, its papers are freely available, in their final published form, to anybody from the moment of publication. *Nature Communications* has about half of its content openly accessible. All of the rest is from now on available in the new iPad app, although so far only to personal print and iPad subscribers. We aim to provide access arrangements for readers who work at institutions with an online-only site licence by the middle of 2013.

The journals iPad app has been designed to deliver a reading experience that has all the clarity and convenience of print while surpassing print in its various functions. Alongside the issue-based navigation and tables of content, the new version allows the following: sharing; accessible bookmarks; saved searches (synced with nature.com); downloading of PDF files of articles; variable font sizes; figures at a glance in a figure-viewing panel; downloading and offline access to the journals; active links for references; and enhanced navigation from within the article.

We hope that those who value *Nature* will find its tablet edition even more stimulating and useful than the more traditional renditions. ■

KIRSTEN LARA GETCHELL



Treat obesity as physiology, not physics

The energy in–energy out hypothesis is not set in stone, argues Gary Taubes. It is time to test hormonal theories about why we get fat.

“It is better to know nothing,” wrote French physiologist Claude Bernard in *An Introduction to the Study of Experimental Medicine* (1865), “than to keep in mind fixed ideas based on theories whose confirmation we constantly seek.”

Embracing a fixed idea is one of the main dangers in the evolution of any scientific discipline. Ideally, errors will be uncovered in the trial-by-fire of rigorous testing and the science will right itself. In rare cases, however, an entire discipline can be based on a fundamental flaw.

As a science journalist turned science historian, I have written at length about how and why this may have happened in obesity research. I have suggested that the discipline may be a house of cards — as, by extension, may much research into the chronic diseases associated with obesity, such as diabetes.

Before the Second World War, European investigators believed that obesity was a hormonal or regulatory disorder. Gustav von Bergmann, a German authority on internal medicine, proposed this hypothesis in the early 1900s.

The theory evaporated with the war. After the lingua franca of science switched from German to English, the German-language literature on obesity was rarely cited. (Imagine the world today if physicists had chosen to ignore the thinking that emerged from Germany and Austria before the war.)

Instead, physicians embraced the ideas of the University of Michigan physician Louis Newburgh, who argued that obese individuals had a “perverted appetite” that failed to match the calories that they consumed with their bodies’ metabolic needs. “All obese persons are alike in one fundamental respect,” Newburgh insisted, “they literally overeat.” This paradigm of energy balance/overeating/gluttony/sloth became the conventional, unquestioned explanation for why we get fat. It is, as Bernard would say, the fixed idea.

This history would be no more than an interesting footnote in obesity science if there were not compelling reason to believe that the overeating hypothesis has failed. In the United States, and elsewhere, obesity and diabetes rates have climbed to crisis levels in the time that Newburgh’s energy-balance idea has held sway, despite the ubiquity of the advice based on it: if we want to lose fat, we have to eat less and/or move more. Yet rather than blame the advice, we have taken to blaming individuals for not following it ‘properly’.

The alternative hypothesis — that obesity is a hormonal, regulatory defect — leads to a different prescription. In this paradigm, it is not excess calories that cause obesity, but the quantity and quality of carbohydrates consumed. The carbohydrate content of the diet must be rectified to restore health.

This conclusion is based on endocrinology that has been understood for 50 years: insulin regulates fat accumulation, and blood levels of insulin are effectively determined by carbohydrate intake. The more easily digestible are the carbohydrates we eat (the higher their glycaemic index) and the sweeter they are (the higher their fructose content) the higher are our blood insulin levels, and the more fat accumulates.

If this is true, it suggests that the obesity epidemic was caused at least in part by the research community’s failure to understand the nature of the disease, and by the food industry’s exploitation of that failure.

But is it true? Or is it the case, as conventional wisdom has it, that these competing hypotheses of obesity have been rigorously tested, and the energy-balance hypothesis has simply won out?

Over the past year, with physician Peter Attia and support from the Laura and John Arnold Foundation of Houston, Texas, I have co-founded the non-profit Nutrition Science Initiative (NuSI) in San Diego, California, with the goal of resolving this controversy.

Among our first tasks was to comb the medical literature back to the 1930s, identifying all studies relevant to the question of whether carbohydrates or excess calories cause obesity. We found much ambiguous smoke, but none of the fire of rigorous experimental evidence necessary to establish definitively the truth or falsehood of either hypothesis. This is unacceptable, considering the critical public-health problem presented by obesity and diabetes. (The studies and our conclusions are available at <http://nusi.org>.)

The trials share many shortcomings. One common flaw is true of all free-living diet trials: the investigators simply fail to control what the

participants actually eat. The evidence suggests that few participants comply with the dietary advice, yet the researchers interpret the results as somehow speaking to the fundamental cause of obesity. It is as if we drew conclusions about whether smoking causes lung cancer on the basis of trials (poorly controlled ones, at that) of the efficacy of different methods of smoking cessation — nicotine patches, say, versus nicotine gum. This problem must be solved to establish reliable knowledge.

NuSI aims to fund and facilitate the trials necessary to rigorously test the competing hypotheses, beginning with inpatient feeding studies that will rigidly control dietary interventions for participants so that we know unambiguously the effects of macronutrients — protein, fat and carbohydrates — on weight and body fat. These studies will be done by independent, sceptical researchers. This may be an idealistic dream, but we have committed ourselves to the effort. ■

Gary Taubes is a science writer, author of *Why We Get Fat* and founder of the Nutrition Science Initiative in San Diego, California. e-mail: taubes@gmail.com

THERE IS
**COMPELLING
REASON**
TO BELIEVE THAT
THE OVEREATING
HYPOTHESIS HAS
FAILED.

➔ **NATURE.COM**
Discuss this article
online at:
go.nature.com/3rt7vo

RESEARCH HIGHLIGHTS

Selections from the
scientific literature

CHEMISTRY

Greenhouse gas finds a use

A potent greenhouse gas that is a by-product of refrigerant production can be used to add a fluorine-based group to molecules — a desirable reaction in the manufacture of drugs and agrochemicals.

G. K. Surya Prakash and his colleagues at the University of Southern California in Los Angeles report that the gas — which has the formula CF_3H and is known as fluoroform or HFC-23 — can be reacted with other molecules, resulting in the addition of CF_3 to carbon, silicon, boron or sulphur atoms. The reaction occurs under simple conditions and provides a rare use for a chemical with a global-warming potential 11,700 times greater than that of carbon dioxide.

Science 338, 1324–1327 (2012)

ANTHROPOLOGY

Romani have Indian ancestry

The 11 million members of Europe's largest minority group, the Romani (pictured), are descended from a single population that left India some 1,500 years ago and dispersed across Europe through the Balkans.



David Comas at Pompeu Fabra University in Barcelona, Spain, Manfred Kayser at Erasmus University in Rotterdam, the Netherlands, and their colleagues analysed

the genomes of 152 Romani individuals from across Europe and compared them with those of populations worldwide. European Romani probably originated from northern and northwestern India.

Genetic analysis suggests that, after leaving India, Romani ancestors interbred with local populations on the way to the Balkans before beginning to spread throughout Europe around 900 years ago. Since then, Romani have interbred with local populations in Europe. *Curr. Biol.* <http://dx.doi.org/10.1016/j.cub.2012.10.039> (2012)



URBAN ECOLOGY

Cigarette butts repel nest pests

City-dwelling sparrows and finches incorporate the butts of smoked cigarettes into their nests, seemingly to ward off parasitic mites.

Isabel López-Rull and her colleagues at the National Autonomous University of Mexico in Mexico City found that nests of house sparrows (*Passer domesticus*) and house finches (*Carpodacus mexicanus*; pictured) with higher levels of cellulose acetate, a component of cigarette butts, had fewer mites. The researchers attached fibres from either smoked or unsmoked cigarette filters to parasite-attracting heat traps and placed them in 27 sparrow and 28 finch

nests. Traps bearing fibres from smoked filters, which contain more nicotine than those of unsmoked ones, captured fewer mites, suggesting that nicotine — and perhaps other compounds in cigarettes — repel the parasites.

Birds have long been known to line their nests with vegetation that deters parasites, and the authors suggest that the use of cigarette butts is an urbanized form of this earlier adaptation.

Biol. Lett. <http://dx.doi.org/10.1098/rsbl.2012.0931> (2012)

For a longer story on this research, see go.nature.com/ygvtvn

DEVELOPMENT

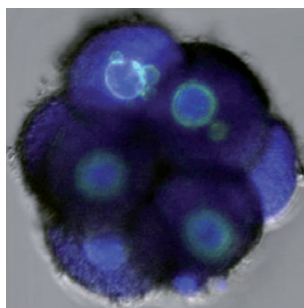
Early signs of embryo trouble

Human embryos with genetic defects may exhibit unusual cellular behaviour by the time they reach the four-cell stage, about 48 hours after fertilization.

Renee Reijo Pera at Stanford University in California and her colleagues analysed the genetics of 45 single-celled embryos left over from *in vitro* fertilization procedures. About 75% of the embryos contained an abnormal number of chromosomes, with two carrying three copies of

VICTOR ARGAEZ/R. SOC.

TIM GRAHAM/GETTY



chromosome 21, which leads to Down syndrome. Time-lapse imaging revealed that normal embryos underwent precisely timed cell divisions, whereas 70% of embryos with abnormal chromosome counts did not. The researchers also observed that cells in abnormal embryos often fragmented into tiny pieces containing chromosomes (**pictured**).

Automated image tracking of cell division and fragmentation could provide a non-invasive tool to screen embryos for healthy *in vitro* fertilization candidates, the authors say. *Nature Commun.* 3, 1251 (2012)

QUANTUM PHYSICS

Atom cooled to ground state

Using a tightly focused beam of light as optical tweezers, researchers have confined a single neutral atom for long enough to cool it to its lowest-energy quantum state, a requirement for many quantum-computing applications.

Researchers have previously cooled charged atoms in a similar way, but uncharged atoms may be more appealing for use in quantum devices because they do not interact with electric fields. Cindy Regal and her collaborators at JILA, a joint research institute of the US National Institute of Standards and Technology and the University of Colorado at Boulder, first used optical tweezers to trap an individual rubidium atom. Then, using a laser-based technique called Raman sideband cooling, they cooled the atom to its near-motionless ground state. *Phys. Rev. X* 2, 041014 (2012)

CLIMATE CHANGE

Rain shifts bear human fingerprint

Summer rainfall patterns in the Southern Hemisphere have changed markedly in response to rising greenhouse-gas concentrations and ozone-layer depletion, both caused by human activity.

Since the 1960s, southern regions at mid-latitudes have become drier whereas a zone around Antarctica has grown wetter. John Fyfe at the Canadian Centre for Climate Modelling and Analysis in Victoria, British Columbia, and his colleagues found that the observed trends agree with predicted precipitation patterns obtained from a set of 29 climate models.

They found that greenhouse gases and ozone changes were primarily responsible for the shifts in precipitation levels. Moreover, natural climate variability cannot explain the observed and modelled trends, the team found.

Geophys. Res. Lett. <http://dx.doi.org/10.1029/2012GL054199> (2012)

PLANETARY SCIENCE

Surprises beneath Moon's surface

The crust beneath the Moon's heavily battered surface is almost entirely pulverized, indicating that it took an even greater beating from space debris during the Solar System's first billion years than planetary scientists suspected.

Maria Zuber at the Massachusetts Institute of Technology in Cambridge and her colleagues report these and other findings from NASA's twin lunar-orbiting spacecraft, known as GRAIL, in a trio of articles. The twin craft probe the Moon's interior by mapping the lunar gravitational field. GRAIL data have also revealed that the Moon's average crust is considerably thinner than previously

COMMUNITY CHOICE

The most viewed papers in science

BEHAVIOUR

Hormone may aid monogamy

HIGHLY READ
on jneurosci.org
in November

Men in monogamous relationships keep their distance from good-looking women after receiving nasal puffs of oxytocin — the human hormone that has been linked to romantic attraction — whereas single men do not.

René Hurlemann at the University of Bonn, Germany, and his colleagues recruited 86 heterosexual men who were either single or in stable monogamous relationships. The volunteers were asked to choose how close to stand to female or male experimenters, or to perform a similar task using photographs. Compared with single men and partnered men who had received a placebo, partnered men given oxytocin stood 10–15 centimetres farther away from women they deemed attractive, and approached pictures of attractive women more slowly. No effect was seen with the male experimenters.

The authors suggest that oxytocin could help to maintain fidelity in romantic relationships.

J. Neurosci. 32, 16074–16079 (2012)

estimated — measuring between 34 and 43 kilometres — suggesting that some of the fracturing caused by space debris could have penetrated the full depth of the crust and into the mantle. Such deep fracturing, which would also be expected on Earth and Mars, could have created porous structures that held hot groundwater for long periods, providing possible niches for life in the early Solar System.

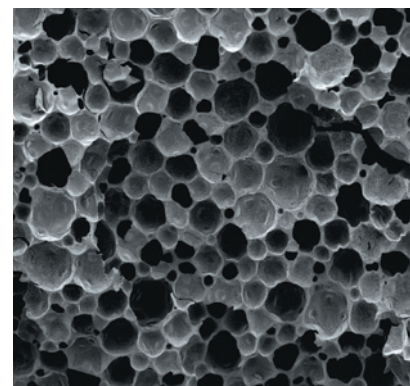
Science <http://dx.doi.org/10.1126/science.1231507>; <http://dx.doi.org/10.1126/science.1231530>; <http://dx.doi.org/10.1126/science.1231753> (2012)

MATERIALS

Foams for cell-friendly scaffolds

Porous foams with nanometre-scale patches to which cells and proteins can adhere could one day be used in tissue engineering.

A group led by Giuseppe Battaglia at the University of Sheffield, UK, and Adam Engler at the University of California, San Diego, used an established technique to



create porous polystyrene-based foams (**pictured**). By incorporating various other polymers into their foams, the researchers controlled the surface topology of the pores and thus the distribution and size of the places where cells and proteins could attach over three dimensions.

The technique could allow bioengineers to create self-assembling scaffolds that control, for example, where stem cells adhere.

J. Am. Chem. Soc. <http://dx.doi.org/10.1021/ja308523f> (2012)

NATURE.COM

For the latest research published by Nature visit:

www.nature.com/latestresearch

SEVEN DAYS

The news in brief

POLICY

Next US Mars rover

NASA will land another rover on Mars in 2020 at a cost of US\$1.5 billion, said John Grunsfeld, the agency's science chief, on 4 December. Earlier this year, NASA pulled out of the European Space Agency's 2016–18 ExoMars mission, which included a NASA rover intended to cache rocks before their eventual return to Earth, alongside a European life-detection rover. See go.nature.com/k4cm8b for more.

Facilities cash

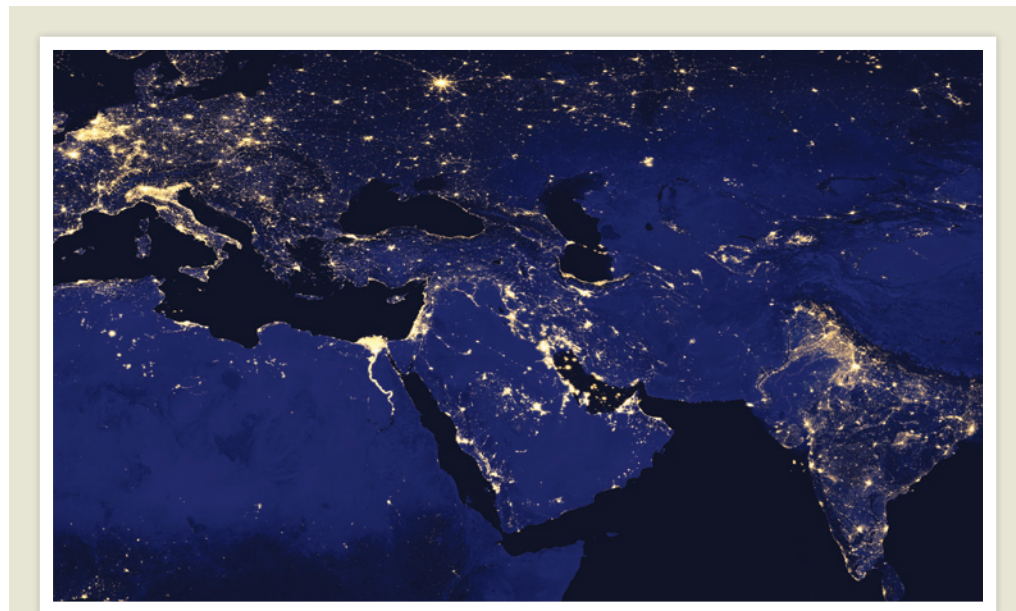
UK chancellor George Osborne is investing an extra £600 million (US\$967 million) in UK science. The cash, announced on 5 December, will go partly to academic researchers for infrastructure projects, and partly to industrial research facilities. The UK government has now announced more than £1.5 billion of new science funding over the past two years, but the money has yet to fully make up for drastic infrastructure funding cuts made in 2010. See go.nature.com/dw9kqn for more.

Arctic report card

An annual environmental assessment of the far north has revealed that the Arctic broke a string of environmental records in 2012, including the lowest summer extent of sea ice. The warming of the Arctic will have global repercussions, says the US National Oceanic and Atmospheric Administration, which released the report on 5 December. See go.nature.com/kyxdxd for more.

Embryo research

A government-backed bill to relax rules on research using embryonic stem cells and embryos was passed by the



NASA EARTH OBSERVATORY/NOAA NGDC

NASA snaps Earth at night

Almost exactly 40 years after *Apollo 17* astronauts took the iconic Blue Marble photograph of Earth, NASA has released a spectacular view of the planet at night, appropriately named Black Marble. The views, unveiled on 5 December, were stitched together

from images taken by a high-resolution sensor aboard the Suomi National Polar-orbiting Partnership weather satellite. Data from the new sensor could be used as a proxy for factors such as population distribution and carbon emissions. See go.nature.com/jfv8ql for more.

French Senate last week. Such research is currently banned in France, although a 2004 law giving scientists dispensation for research that promises “major therapeutic progress” against serious diseases has allowed some work. The bill, supported by President François Hollande (see *Nature* **484**, 298–299; 2012), will go to a vote in the national assembly next year, before returning for a second reading in both chambers.

Stem-cell drive

A coalition of 10 drug companies and 23 academic institutions announced a plan on 5 December to create 1,500 new induced pluripotent stem-cell lines. With €26 million (US\$34 million) from the European Union

and €21 million of ‘in-kind’ contributions from the private sector, the StemBANCC project will derive cell lines from 500 patients and make them available to other researchers. See go.nature.com/ohez8u for more.

PEOPLE

Physics awards

Seven scientists will share a US\$3-million prize for their key roles at the Large Hadron Collider at CERN, Europe's particle-physics lab near Geneva, Switzerland, and UK theoretical physicist Stephen Hawking will receive the same amount for his insight that black holes should emit Hawking radiation. The awards were made on 11 December by the Fundamental Physics

Prize Foundation, a non-profit organization founded by Internet investor Yuri Milner. They follow nine \$3-million awards to physicists made by the foundation in August. See go.nature.com/jzkdcj for more.

RESEARCH

Cancer sequencing

Up to 100,000 patients with cancer and rare diseases in England will have their DNA mapped under plans to integrate whole-genome sequencing into the United Kingdom's National Health Service. In an announcement on Monday, Prime Minister David Cameron said that £100 million (US\$160 million) had been earmarked for the project, which includes wider plans to boost genetic science

and build an infrastructure to feed data back to researchers. See go.nature.com/myvpxs for more.

Big-data bonanza

The US National Institutes of Health will spend about US\$125 million a year for up to seven years on training and on upgrading its ability to analyse, optimize and share the gigantic data sets being generated in biomedicine, the agency announced on 7 December. From 2014, such 'big data' awards will be available mostly to grant applicants, but also to the agency's staff.

Desert science

Qatar has announced plans to set up a climate-research institute in Doha. A key focus of the institute will be the effects of climate change on dry regions around the world, officials from the Qatar Foundation said on 5 December, at the sidelines of international climate talks in the capital. A research plan and budget figures are to be announced once a founding committee has been established.

Robot sailor

A wave-powered robot named Papa Mau has broken the record for the longest distance travelled by an autonomous vehicle, its maker announced on 6 December.



The robot is one of four 'Wave Gliders' (pictured) launched by Liquid Robotics in Sunnyvale, California, to gather oceanographic data. It took over a year to cover the more than 16,000 kilometres between California and Australia. See go.nature.com/jo8jsz for more.

BUSINESS

Drug sales concern

On 3 December, a US federal appeals court overthrew the conviction of a pharmaceutical salesman who had promoted drugs for uses that had not been approved by the Food and Drug Administration, ruling that a long-standing ban on drug marketing violated free speech. The pharmaceutical industry has already paid billions of dollars in penalties for marketing drugs this way. If upheld by higher courts, the ruling could make it more difficult for the US

government to prosecute those who promote such 'off-label' uses of drugs.

Genetics buyout

Biotechnology giant Amgen has announced plans to acquire deCODE Genetics for US\$415 million. deCODE, based in Reykjavik, struggled through bankruptcy in 2009. However, it has identified a wealth of genetic variants associated with conditions from Alzheimer's disease to schizophrenia. Amgen chief executive Robert Bradway said that the acquisition would allow his company, based in Thousand Oaks, California, to produce more-innovative drugs.

Whistleblower deal

A US scientific-integrity official who says he was fired for raising scientific concerns about a dam project (see *Nature* **484**, 15; 2012) has reached a settlement with the government, a watchdog group representing him announced on 4 December. Paul Houser, a hydrologist at George Mason University in Fairfax, Virginia, was employed by the US Department of the Interior's Bureau of Reclamation but lost his government job in February. He launched a complaint under the Whistleblower Protection Act, a rare example of a scientist appealing to the act to protect

COMING UP

15–19 DECEMBER

The American Society for Cell Biology meets in San Francisco — with an address from US energy secretary Steven Chu on how physical scientists are changing biomedical science (see *Nature* **474**, 20–22; 2011).

go.nature.com/xkzgw8

17–18 DECEMBER

With research on modifying avian H5N1 flu viruses still under a moratorium, scientists and policy-makers meet at the US National Institutes of Health in Bethesda, Maryland, to discuss conditions under which experiments might restart.

go.nature.com/5bvzvz

his scientific disclosures. In a joint statement, both sides said they had reached agreement through mediation and would not be disclosing details of the settlement.

Vaccine landmark

A cheap vaccine against meningitis A last week reached the landmark of immunizing more than 100 million people in Africa's 'meningitis belt' — a region in the north of the continent where the bacterial disease periodically kills thousands in intense epidemics. In Burkina Faso, Mali and Niger, where MenAfriVac was first rolled out in 2010 (see *Nature* **468**, 143; 2010), no cases of meningitis A had been detected up to October this year. The vaccine has now been launched in seven other countries. The project is led by the World Health Organization and PATH, a non-profit body based in Seattle, Washington.

➔ NATURE.COM

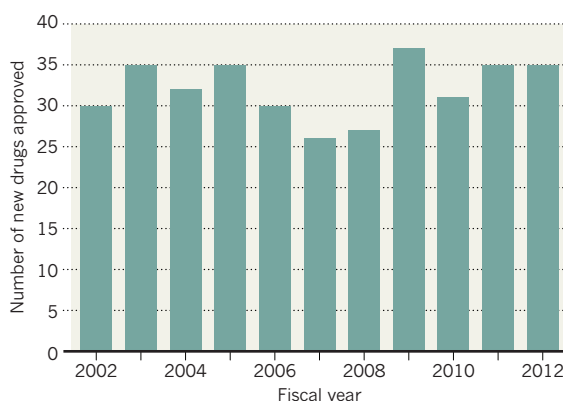
For daily news updates see:
www.nature.com/news

TREND WATCH

The US Food and Drug Administration (FDA) approved 35 new drugs in the fiscal year 2012, the same number as in 2011 (see chart). Half of the drugs were authorized through programmes designed to accelerate the process — for example, in cases of serious unmet medical need involving life-threatening diseases. The class of 2012 includes nine cancer drugs, nine treatments for rare, or 'orphan', diseases and the first approved drug made from human umbilical-cord blood.

US DRUG APPROVALS HOLD STEADY

The US Food and Drug Agency approved 35 new drugs in fiscal year 2012.

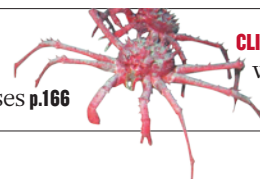


NEWS IN FOCUS

MARINE BIOLOGY It's alive!
Fungus found in deep
muck **p.163**

PHYSICS Long-sought
quantum material was
hiding in plain sight **p.165**

EPIDEMIOLOGY
Alarm over new
coronavirus increases **p.166**



CLIMATE Invaders ride
warming Antarctic
seas **p.170**

EUGENE CERNAN/NASA



Forty years after Apollo 17, the last mission to send astronauts to the lunar surface, the Moon still beckons the US space agency.

SPACE EXPLORATION

Duelling visions stall NASA

A US plan to send humans to explore an asteroid is losing momentum.

BY ERIC HAND

Once again, NASA's human space-flight programme is looking for a destination. It happened in the early 1970s, after US astronauts had left the Moon for the last time; then in the 1990s, after the collapse of a costly vision of sending astronauts to Mars; and again in 2010, when US President Barack Obama abandoned a plan to return humans to the Moon because he did not consider it ambitious enough. He suggested visiting a near-Earth asteroid

instead, but a report released on 5 December by the National Academies says that this plan, too, has misfired.

"There is no broad acceptance of the asteroid as the next principal destination for space flight, despite the fact that the president has indeed said so several times," says

➔ NATURE.COM
Read more about the
impact of the Apollo
programme:
go.nature.com/8gd5ru

Albert Carnesale, chairman of the committee behind the report and a former chancellor of the University of California, Los Angeles.

For its part, NASA — whether through inertia or out of practicality — seems unwilling to shift the focus of its human space-flight efforts away from the Moon.

Part of the tug of war over destinations is political. The administration's choice of an asteroid is a volte-face from the 'Moon-first' doctrine espoused during the presidency of George W. Bush. By many accounts, Obama had not garnered much support for the new policy before springing it on NASA and Congress nearly three years ago. NASA's administrator, Charles Bolden, has been left to ▶

MOONSTRUCK

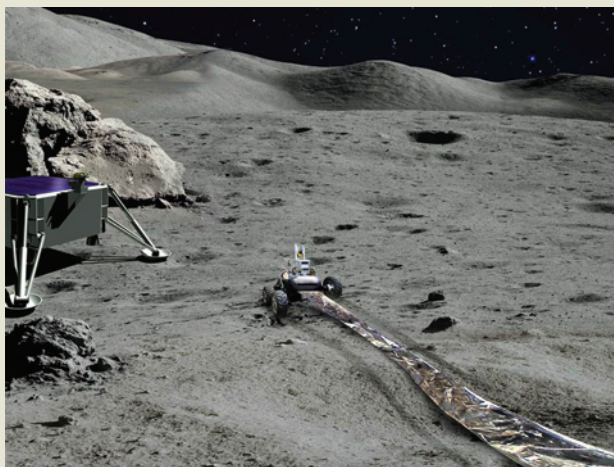
Why scientists yearn for the far side

Some 60,000 kilometres beyond the far side of the Moon lies a spot known as 'L2', a Lagrangian point at which gravitational forces are balanced, so that a spacecraft could sit there without expending much fuel. The next time US astronauts leave low Earth orbit, L2 might just be their next destination.

On 28 November, William Gerstenmaier, associate administrator for NASA's human-exploration division, told the NASA Advisory Council that a mission to L2 or another Lagrangian point could be an early test for NASA's planned crewed rockets. Such locations could serve as staging grounds for other missions, he says: "They're nice places to put cargo or samples from the Moon or Mars." Gerstenmaier reckons that an uncrewed mission could get to L2 by 2017, to be followed by a crewed mission in 2021, but he is careful not to specify what activities the astronauts would pursue.

David Kring wants those activities to include lunar science. Kring, a geologist at the Lunar and Planetary Institute in Houston, Texas, has for years been among the chorus of lunar scientists calling for a sample to be retrieved from the vast South Pole–Aitken basin, one of the largest impact craters in the Solar System (see *Nature* **453**, 1160–1163; 2008). Getting a firm date for this far-side

adventure would help to set the time for a barrage of asteroids that theorists believe pummelled the inner Solar System about 3.9 billion years ago. Although Kring does



A foil-like antenna could detect radio waves from the distant Universe.

not expect funding for a human landing, he thinks that it could be possible for the 2021 mission to fly a small robotic lander carrying a rover capable of collecting samples for later retrieval. Astronauts circling overhead at the L2 point could tele-robotically operate the rover with a joystick — an activity that many think will be necessary practice for any future operations at Mars. "The lunar far side is *terra incognita*," says Kring. "We've never been there."

Jack Burns, an astrophysicist at the University of Colorado at Boulder, wants to use the same rover to lay down a thin, foil-like antenna that would receive low-frequency

radio waves from the distant Universe. He says that the lunar far side, shielded from Earth noise, is the ideal site for an array of such antennas, which could search for radio signals from the hydrogen atoms that formed soon after the Big Bang. The signals would be similar to the ubiquitous 21-centimetre emission that originates from hydrogen in the Milky Way, but shifted to much longer wavelengths by the expansion of the Universe. Burns would look for a change in the hydrogen signals that would mark the moment the first stars turned on, and indicate how quickly their ultraviolet light ionized the hydrogen that makes up the

bulk of intergalactic space today. "We're reaching into territory that will be difficult, if not impossible, for James Webb," he says, referring to NASA's 6.5-metre infrared space telescope, which is scheduled to launch in 2018.

Stephen Mackwell, director of the Lunar and Planetary Institute, says that such ideas show how the Moon is still relevant for scientific inquiry. "I get ticked off when people say, 'Been there, done that'." **E.H.**

► negotiate the rocky ground between a suspicious Congress and an administration that has largely neglected the space agency. Some say that Bolden — who was not the administration's first choice when he was appointed in 2009 — may face replacement as Obama heads into his second term. "It's not a happy situation," says a senior astrophysicist. "Names are being discussed."

Politics aside, the asteroid proposal remains short on details and long on technical challenges, including the problem of which asteroid to visit. Few asteroids would be close enough in the mid-2020s for a crew to reach them within a year-long round trip, the longest that many experts think practical, and NASA has not yet made a serious effort to prioritize possible targets. If the administration is serious about a rendezvous with an asteroid, Carnesale says, then "which asteroid do you have in mind, and when?"

Even if one is selected, some scientists are worried about the hazards of approaching an object that may be no more than a loosely

bound pile of rubble — that could also be spinning dangerously fast. And how would astronauts anchor themselves to the potentially friable surface without kicking up dust? asks Stephen Mackwell, director of the Lunar and Planetary Institute in Houston, Texas. "We have problems enough at the Moon with dust."

Then there is the problem of just getting there. NASA is increasingly concerned about the radiation exposure and bone loss that astronauts might face during a long voyage outside Earth's protective magnetosphere. "You get a bad solar storm and you're toast," says Mackwell.

Meanwhile, Carnesale notes that private companies and other nations are mobilizing to visit the Moon. And NASA itself has not written off the Moon either. On 28 November, William Gerstenmaier, associate administrator for NASA's human-exploration division, presented plans to test the agency's next generation of heavy-lift rockets with trips to the vicinity of the Moon in 2017 and 2021.

Although those missions could be seen as stepping stones to a later asteroid mission, many lunar scientists view the region as a destination in its own right (see 'Moonstruck').

But Mark Sykes, president of the Planetary Science Institute in Tucson, Arizona, and chair of NASA's Small Bodies Assessment Group, remains a big fan of asteroids. He notes that human explorers could search for resources such as water. Scientists could seek to understand the subtle pressure of light that causes asteroids to change their spin, and could retrieve samples for dating and chemical analysis that would offer a clearer picture of Solar System material than do meteorites, which, although they are pieces of asteroids, are altered during their fall through Earth's atmosphere.

But all this could be done more cheaply with a robotic mission, says Sykes. Without a sustained drive towards something bigger — such as a human presence on Mars — even Sykes isn't terribly excited. "You go to an asteroid, then what?" he says. "If it's all performance art, that's not much of a mission." ■

OCEAN SCIENCE

Ancient fungi found in deep-sea mud

Discovery raises hopes that sea floor could yield previously unknown antibiotics.

BY RICHARD MONASTERSKY

Researchers have found evidence of fungi thriving far below the floor of the Pacific Ocean, in nutrient-starved sediments more than 100 million years old. The discovery has the potential to turn the brown muck of the sea floor into pure gold for biologists looking for alternative forms of life — and possibly for pharmaceutical companies seeking antibiotics to combat the growing problem of drug-resistant bacteria.

“This is adding a new family of potential drugs,” says Brandi Reese, a biogeochemist at the University of Southern California in Los Angeles who studied the fungi, some of which belong to the genus *Penicillium*, the source of penicillin. Finding multicellular organisms in such a deprived environment “extends what we understand about the limits of life on the planet,” says Heath Mills, a molecular geomicrobiologist at Texas A&M University in College Station, who collaborated with Reese. They reported their results on 6 December at a meeting of the American Geophysical Union (AGU) in San Francisco, California.

To follow up on earlier reports of deep-sea fungi, Reese and her colleagues studied sediments pulled up from as deep as 127 metres below the sea floor during an expedition of the Integrated Ocean Drilling Program in the South Pacific in 2010. They searched the samples for fungal genetic material and found sequences from at least eight groups. The team succeeded in growing cultures of four of the fungi.

A decade ago, the only organisms known to live in deep layers of sediment were single-celled — bacteria and archaea. Hints of fungi in sediments started emerging in 2005, but just a handful of researchers are studying those sediment dwellers and the other fungi living

in ocean water. “These things are ubiquitous and they’re largely ignored,” says Jennifer Biddle, a microbial ecologist at the University of Delaware in Lewes, who was among the first to culture fungi from sea-floor sediments (J. F. Biddle *et al. Geobiology* 3, 287–295; 2005).

Some biologists have been sceptical about



Penicillium fungi have been grown from sediments.

such reports, suggesting that the material might be the result of contamination — or inactive spores of surface fungi that became trapped in the muck. But Reese and her colleagues say that they took several steps to rule out contamination. Steven D’Hondt, who studies microbes in sediments at the University of Rhode Island in Narragansett, says that Reese’s group and others are “accumulating a lot of evidence that there are fungi in the deep sediments”.

And the material seems to be more than spores, says William Orsi, a molecular

ecologist at the Woods Hole Oceanographic Institution in Massachusetts. Working with Biddle and Virginia Edgcomb, a microbiologist at Woods Hole, Orsi has studied deep-sea sediments from off the coast of Peru and detected bits of fungal messenger RNA that code for several proteins, including those involved in transporting ions and metals across membranes. This shows that the subsurface fungi are metabolically active, says Orsi, who presented the work at the AGU meeting.

Now that the evidence in favour of fungi in deep sediments is accumulating, “the pressing question is: what are they doing?” says Orsi. The sediments studied by Reese and her colleagues underlie the South Pacific Gyre — “One of the most dead places on the planet,” says Mills. The gyre is far from land, so few nutrients get there. Marine life is scarce and microbes in the surface sediments devour the scant organic matter that sinks to the bottom.

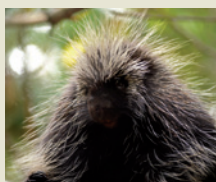
Mills thinks that the fungi might have a key role in the nutrient-starved deep ecosystem. Researchers have previously presumed that the organic matter left in sediments after millions of years is too difficult for most single-celled organisms to consume. But fungi are masters at breaking down tough organic molecules, says Mills, so they could be providing sources of food for microbes far below the sea floor.

The team says that it is not clear whether the fungi in the deepest sediments are more than 100 million years old; they might have colonized those layers by moving in from younger deposits. But if the fungi have been isolated for a long time, they may have evolved unusual biological defences against bacteria and could provide a source of useful antibiotics. “What if this is a new version of penicillin?” asks Mills. “That’s one of the benefits of going to the deep biosphere.” ■



**MORE
ONLINE**

SLIDESHOW

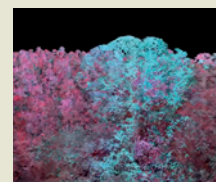


Porcupine quills’ vicious secret revealed
go.nature.com/tq6d4f

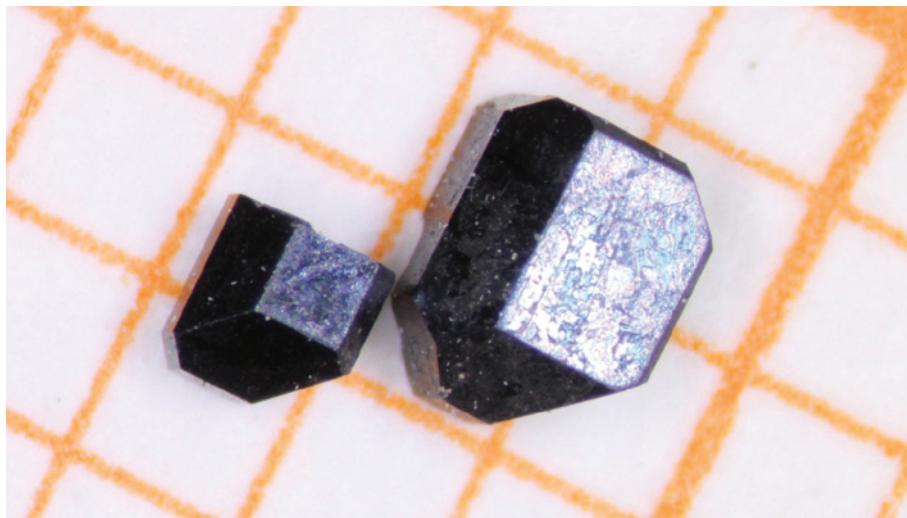
MORE NEWS

- Brain cells made from urine go.nature.com/de36vx
- James Cameron reveals some of the results from his deep dive go.nature.com/aihhdy
- Pharmaceutical lab loses valuable gold stash go.nature.com/hycw7l

VIDEO



Airborne observatory reveals drought damage
go.nature.com/hbfgno



Despite being insulators inside, samarium hexaboride crystals can conduct electricity on their surface.

CONDENSED-MATTER PHYSICS

Hopes surface for exotic insulator

Findings by three teams may solve a 40-year-old mystery.

BY EUGENIE SAMUEL REICH

A compound whose odd electrical behaviour has puzzled physicists for decades could turn out to be a boon for quantum physics and electronic-device makers.

When theorists proposed in 2005 that it should be possible to find materials that conduct electricity at the surface while the rest of the sample behaves as an insulator, physicists were intrigued. They wanted to study the quantum effects that should emerge in such materials, and to explore applications in low-power electronics and quantum computing. But topological insulators, as the materials were called, proved fiendishly difficult to make. Some researchers have slaved to produce thin films using complex techniques that are unlikely ever to scale up to the levels needed for industrial purposes. Others have contented themselves with compounds that approximate topological insulators but still have a degree of internal conductivity.

Now, three papers^{1–3} suggest that samarium hexaboride, a poorly understood compound that was first found to gain conducting properties at very low temperatures⁴ in 1969 by researchers at Bell Labs in New Jersey, may in fact be a topological insulator in its bulk form.

In the most recent paper¹ in the trend, posted online on 28 November, researchers

at the University of California, Irvine, report seeing remarkably fast-moving electrons on the surface of SmB₆ crystals, which they take as a sign of a superb surface conductor. Five days earlier, researchers at the University of Maryland in College Park had reported measurements tracing the path of electrons injected into SmB₆ samples as they were cooled². Those results suggest that the material is insulating in its interior at temperatures below around 30 kelvin. And, in a paper posted on 21 November³, scientists from the University of Michigan in Ann Arbor and University of California, Irvine, describe their measurements of conductivity through the surface and bulk of the material, and find evidence that the

surface conducting behaviour persists despite imperfections and impurities, as would be expected from a true topological insulator.

A spurt of interest in topological insulators over the past few years (see ‘Charging up’) led to a 2010 prediction that SmB₆ would be such a material⁵. “I’d say we’ve been tentatively vindicated,” says Piers Coleman of Rutgers University in Piscataway, New Jersey, one of the four theoretical physicists who made the prediction. “We’re thrilled by these new results.”

COOL CHARACTERISTICS

The prediction grew, in part, from studies of materials known as Kondo insulators, which, unlike ordinary insulators, retain some of the small amount of conductivity they do have when they are cooled to a few degrees above absolute zero. SmB₆, which is often categorized as a Kondo insulator, fits this description.

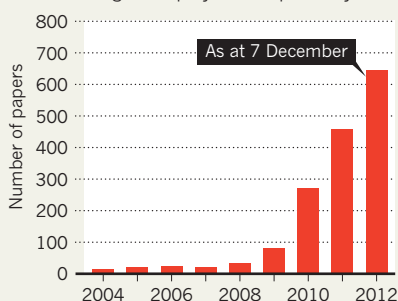
Coleman and other theorists realized that the material’s behaviour would make sense if it were a topological insulator. That would mean that the quantum properties of the material would be such that electrons cannot flow through it freely, as they would in an ordinary conductor, except at the material’s surface. If this proves correct, Coleman thinks that insights gleaned from SmB₆ and other Kondo insulators could carry over to all topological insulators.

SmB₆ is an unusual topological insulator because the electrons in the outer shells of the samarium atoms interact with one another strongly, such that a coordinated motion emerges. This could make the material useful for creating some exotic quantum effects, including magnetic monopoles, or Majorana fermions — quasiparticles that might be useful for quantum computing, says Shoucheng Zhang, who has pioneered work on topological insulators at Stanford University in California. Zhang adds that the rush of interest in SmB₆ is part of a trend to study materials with electrons that interact strongly with each other. “Now we’re looking at a number of systems. It’s a very exciting development,” he says.

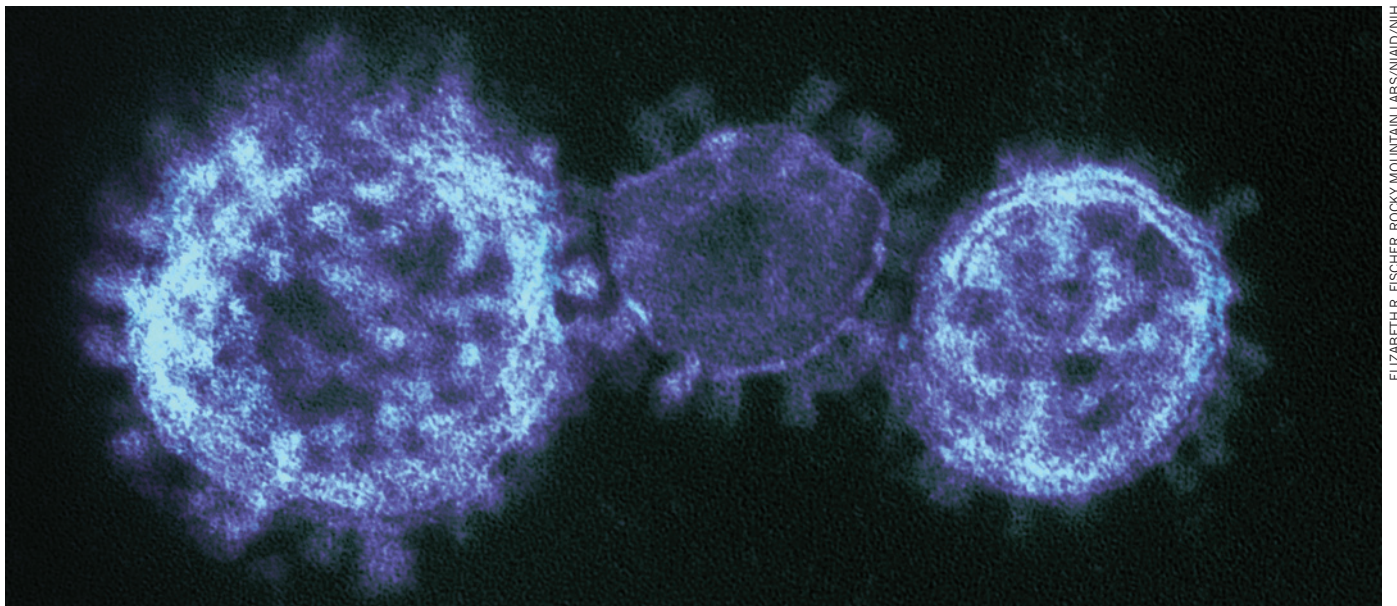
Peter Armitage, who has been working on topological insulating behaviour in bismuth-based compounds at John Hopkins University in Baltimore, Maryland, says that in the field of condensed-matter physics, experiment usually leads theory, but this is a remarkable example of the opposite. He is now hoping to start experiments on SmB₆ in the next week or two to confirm and study the surface states. “These are beautiful effects that were hiding under our noses,” he says. “This is a very big advance.” ■

CHARGING UP

The number of papers published on topological insulators has grown rapidly over the past few years.



1. Botimer, J. *et al.* Preprint at <http://arxiv.org/abs/1211.6769> (2012).
2. Zhang, X. *et al.* Preprint at <http://arxiv.org/abs/1211.5532> (2012).
3. Wolgast, S. *et al.* Preprint at <http://arxiv.org/abs/1211.5104> (2012).
4. Menth, A., Buehler, E. & Geballe, T. H. *Phys. Rev. Lett.* **22**, 295–297 (1969).
5. Dzero, M., Sun, K., Galitski, V. & Coleman, P. *Phys. Rev. Lett.* **104**, 106408 (2010).



ELIZABETH R. FISCHER, ROCKY MOUNTAIN LABS/NIH

A new coronavirus found in the Middle East is one of a family of viruses named after the corona-like appearance of their surface spikes.

VIROLOGY

Clusters of coronavirus cases put scientists on alert

Surveillance ramped up after novel virus is identified in three Middle Eastern countries.

BY DECLAN BUTLER

Is the coronavirus that has appeared in the Middle East a simmering threat to global public health or a viral footnote that will end up being of interest only to academics? That is the key question that researchers and public-health officials are now struggling to resolve. Two unsettling developments have fed their concerns: fresh hints that the virus might show at least limited spread from person to person, and signs that it has extended its geographical range.

Last week, the World Health Organization (WHO) urged that surveillance for the virus, called human betacoronavirus 2c EMC/2012, should be extended to all countries worldwide, with a special focus on all clusters of severe pneumonia, particularly in health workers. Epidemiologists say that the nebulous threat requires close monitoring, by investigating and controlling any new clusters of human cases that could signal that the virus has adapted to spread between people more easily.

The coronavirus, first reported on 20 September, causes severe pneumonia and often kidney failure. In the nine cases confirmed so far, it has had a death rate of more than 50%. “It’s an extremely serious disease;

it’s very much in the category of H5N1 [avian influenza],” says David Heymann, chairman of the UK Health Protection Agency and former head of the communicable-diseases programme at the WHO during the 2003 SARS epidemic, caused by a different coronavirus. Yet this latest coronavirus is still limited to the Middle East and shows no sign of spreading easily between people, Heymann emphasizes.

“It’s an extremely serious disease; it’s very much in the category of H5N1.”

In late November, however, the WHO reported a household cluster of four cases in Saudi Arabia, in which two people died. Retrospective tests looking for the coronavirus in samples from a cluster of 11 people who were admitted with serious respiratory symptoms to a hospital in Jordan in April have revealed the virus in another two fatal cases. This pushes back the first known date of its emergence by several months and marks the first evidence for infection outside Saudi Arabia and Qatar.

Although independent infections from the same animal or environmental source might explain these outbreaks, such clusters always raise the possibility of transmission between humans. Because the disease did not spread

any further, however, person-to-person transmission of the virus — if it occurred at all — would have had to have been through close contact. Still, the extension of the disease to Jordan, and the identification of these earlier cases, marks a significant epidemiological development and suggests that infections may have gone undetected in other countries.

What is needed now, says Heymann, is “good old shoe-leather epidemiology; that’s what worked in SARS”. Epidemiologists need to talk to the families and neighbours of any infected people; try to track down everyone who has come into contact with them to look for symptoms and test for the virus; and isolate infected people to try to stop any spread.

Researchers including Christian Drosten, director of the Institute of Virology at the University of Bonn Medical Centre in Germany, have moved quickly to develop diagnostic tests to determine whether people or samples are infected with the coronavirus^{1,2}. These tests are now being rolled out by many national health authorities, and Drosten says that a survey in

Europe is showing a particularly quick response.

Teams from the WHO and the US Centers for Disease Control and

NATURE.COM
For a coronavirus case timeline, see:
go.nature.com/xtr5wj

Prevention in Atlanta, Georgia, have been helping countries in the Middle East to boost surveillance. During the annual hajj religious pilgrimage in Saudi Arabia in late October, when millions of people visited the country before returning home — a potential recipe for global virus spread — both Saudi Arabia and return countries were on high alert.

Beyond immediate surveillance efforts, increased monitoring for coronavirus antibodies in the wider population should help to pin down the true death rate. The current high death rate would fall, for example, if many people in the vicinity of cases turn out to have antibodies to the virus but have not developed serious disease.

Meanwhile, laboratory studies are shedding light on the virus itself. This week, a team including Drosten has shown that this coronavirus seems to differ from the SARS virus in some important ways³. Because the SARS virus binds to the ACE-2 receptor on human cells deep in the lungs, it causes serious disease in the lower respiratory tract but is relatively difficult to contract and is not easily spread by coughing or sneezing. The researchers have determined that the new coronavirus does not bind to the ACE-2 receptor, but declined to elaborate on which receptor it does use, pending a separate publication. But ruling out the ACE-2 receptor has immediate practical implications — all the reagents and therapeutic strategies developed for the SARS virus will be of little use with this latest virus, says Drosten.

The same team also found that cells from bats, pigs and humans can all be infected in the lab with the coronavirus. This suggests that it is “promiscuous among mammals”, says Drosten, and that it might jump readily between mammal species, although he cautions against extrapolating such *in vitro* studies to the real world.

More clues have come from Ian Lipkin, a renowned ‘virus hunter’ from Columbia University in New York, who was invited by the Saudi government in October to study the first cases there. He told *Nature* that he has discovered that partial genetic sequences of a virus isolated from bats match the coronavirus found in humans. “The finding gives insight into the original source of the virus,” he says.

The route taken by this coronavirus to infect humans is still not clear. It could, for example, be carried by intermediate animal hosts, or in foodstuffs contaminated by the faeces of bats or other infected animals. To answer that, says Lipkin, “one would need to work for months”. He hopes to send in another team to work alongside his Saudi colleagues in the near future. ■

1. Corman, V. M. *et al.* *Euro Surveill.* **17**, 39 (2012).
2. Corman, V. M. *et al.* *Euro Surveill.* **17**, 49 (2012).
3. Müller, M. A. *et al.* *mBio* **3**, e00515-12 (2012).

COMMUNITY

NIH tackles major workforce issues

US agency aims to expand training options for graduate students and to increase demographic diversity.

BY MEREDITH WADMAN

The world’s largest biomedical research funding agency last week announced a programme of nudges, incentives and requirements intended to respond to two thorny workforce-related problems: the over-supply of young scientists who face diminishing prospects of landing academic jobs, and the lack of demographic diversity in the US biomedical workforce.

Two reports issued in June challenged the US National Institutes of Health (NIH) to better prepare young biologists for an evolving and increasingly competitive job market, and to boost diversity (see *Nature* **486**, 304; 2012). In response, the agency, based in Bethesda, Maryland, will spend an average of US\$50 million a year for 10 years on a grant programme designed to provide financial support and mentoring to undergraduates at less-research-intensive institutions, which tend to have more diverse student populations. Another set of up to 50 grants, each worth about \$250,000, will entice institutions to launch innovative training programmes that prepare students for careers outside academia, in everything from science policy to industry and research administration. The agency will also encourage universities and other institutions to limit NIH-supported doctoral studies to five years.

To measure the success of the new initiatives, the NIH will require universities and academic medical centres to track the careers of all of their NIH-funded graduate students and postdocs for 15 years after they are trained. “The challenges facing the biomedical workforce are complex and these proposed initiatives are designed to effect real change,” says Francis Collins, director of the NIH. “I’m optimistic that the entire scientific-research community will come together to help implement them.”

The National Medical Association (NMA) in Silver Spring, Maryland, the main group representing black medical scientists, praised the agency’s diversity plans, which also include a nationwide mentoring consortium, training on diversity issues for NIH review staff and members of peer-review panels, and a pilot scheme to assess anonymized grant applications. These initiatives were spurred by a study showing that, when other factors such as education are

controlled for, black applicants are 10% less likely than whites to win NIH grant funding (D. K. Ginther *et al.* *Science* **333**, 1015–1019; 2011). Rahn Bailey, president of the NMA, called the plans “a move in the right direction”.

But Shirley Tilghman, who co-chaired the working group that wrote the June workforce report, said that simply encouraging institutions to limit the length of doctoral studies

isn’t enough. Tilghman, a molecular biologist and the president of Princeton University in New Jersey, told Collins’s advisory committee on 6 December that “unless you get a stick, this won’t happen”. Her group’s report noted that the number of US PhD biomedical graduates who secure tenure-track or tenured jobs has fallen from 34% in 1993 to 26% today. She said that unless the NIH



“These proposed initiatives are designed to effect real change.”

Francis Collins

takes tougher steps, “we will be looking at data that look just like this ten more years from now”.

Neither the June report nor the NIH response answer one key question — how many biomedical PhDs the United States should be training — because the necessary data and workforce-modelling expertise were not available either to the report’s authors or to NIH staff. Indeed, the NIH also plans to hire at least one labour economist, to work as part of a new unit devoted to modelling biomedical-workforce needs.

As part of its workforce initiative, the NIH will increase yearly stipends for the 35,000 postdocs it supports from \$39,000 to \$42,000, a 7.7% rise, in an effort to reflect postdocs’ extensive training and to discourage lab heads from prolonging the postdoctoral training period. The National Postdoctoral Association in Washington DC applauded the NIH’s plans. “The NIH has really stepped up to the plate in regard to early-career scientists,” says Cathée Johnson Phillips, the group’s executive director. The last time NIH-funded postdocs got a significant pay rise was in 2003. ■

NIH

Prevention in Atlanta, Georgia, have been helping countries in the Middle East to boost surveillance. During the annual hajj religious pilgrimage in Saudi Arabia in late October, when millions of people visited the country before returning home — a potential recipe for global virus spread — both Saudi Arabia and return countries were on high alert.

Beyond immediate surveillance efforts, increased monitoring for coronavirus antibodies in the wider population should help to pin down the true death rate. The current high death rate would fall, for example, if many people in the vicinity of cases turn out to have antibodies to the virus but have not developed serious disease.

Meanwhile, laboratory studies are shedding light on the virus itself. This week, a team including Drosten has shown that this coronavirus seems to differ from the SARS virus in some important ways³. Because the SARS virus binds to the ACE-2 receptor on human cells deep in the lungs, it causes serious disease in the lower respiratory tract but is relatively difficult to contract and is not easily spread by coughing or sneezing. The researchers have determined that the new coronavirus does not bind to the ACE-2 receptor, but declined to elaborate on which receptor it does use, pending a separate publication. But ruling out the ACE-2 receptor has immediate practical implications — all the reagents and therapeutic strategies developed for the SARS virus will be of little use with this latest virus, says Drosten.

The same team also found that cells from bats, pigs and humans can all be infected in the lab with the coronavirus. This suggests that it is “promiscuous among mammals”, says Drosten, and that it might jump readily between mammal species, although he cautions against extrapolating such *in vitro* studies to the real world.

More clues have come from Ian Lipkin, a renowned ‘virus hunter’ from Columbia University in New York, who was invited by the Saudi government in October to study the first cases there. He told *Nature* that he has discovered that partial genetic sequences of a virus isolated from bats match the coronavirus found in humans. “The finding gives insight into the original source of the virus,” he says.

The route taken by this coronavirus to infect humans is still not clear. It could, for example, be carried by intermediate animal hosts, or in foodstuffs contaminated by the faeces of bats or other infected animals. To answer that, says Lipkin, “one would need to work for months”. He hopes to send in another team to work alongside his Saudi colleagues in the near future. ■

1. Corman, V. M. *et al.* *Euro Surveill.* **17**, 39 (2012).
2. Corman, V. M. *et al.* *Euro Surveill.* **17**, 49 (2012).
3. Müller, M. A. *et al.* *mBio* **3**, e00515-12 (2012).

COMMUNITY

NIH tackles major workforce issues

US agency aims to expand training options for graduate students and to increase demographic diversity.

BY MEREDITH WADMAN

The world’s largest biomedical research funding agency last week announced a programme of nudges, incentives and requirements intended to respond to two thorny workforce-related problems: the over-supply of young scientists who face diminishing prospects of landing academic jobs, and the lack of demographic diversity in the US biomedical workforce.

Two reports issued in June challenged the US National Institutes of Health (NIH) to better prepare young biologists for an evolving and increasingly competitive job market, and to boost diversity (see *Nature* **486**, 304; 2012). In response, the agency, based in Bethesda, Maryland, will spend an average of US\$50 million a year for 10 years on a grant programme designed to provide financial support and mentoring to undergraduates at less-research-intensive institutions, which tend to have more diverse student populations. Another set of up to 50 grants, each worth about \$250,000, will entice institutions to launch innovative training programmes that prepare students for careers outside academia, in everything from science policy to industry and research administration. The agency will also encourage universities and other institutions to limit NIH-supported doctoral studies to five years.

To measure the success of the new initiatives, the NIH will require universities and academic medical centres to track the careers of all of their NIH-funded graduate students and postdocs for 15 years after they are trained. “The challenges facing the biomedical workforce are complex and these proposed initiatives are designed to effect real change,” says Francis Collins, director of the NIH. “I’m optimistic that the entire scientific-research community will come together to help implement them.”

The National Medical Association (NMA) in Silver Spring, Maryland, the main group representing black medical scientists, praised the agency’s diversity plans, which also include a nationwide mentoring consortium, training on diversity issues for NIH review staff and members of peer-review panels, and a pilot scheme to assess anonymized grant applications. These initiatives were spurred by a study showing that, when other factors such as education are

controlled for, black applicants are 10% less likely than whites to win NIH grant funding (D. K. Ginther *et al.* *Science* **333**, 1015–1019; 2011). Rahn Bailey, president of the NMA, called the plans “a move in the right direction”.

But Shirley Tilghman, who co-chaired the working group that wrote the June workforce report, said that simply encouraging institutions to limit the length of doctoral studies

isn’t enough. Tilghman, a molecular biologist and the president of Princeton University in New Jersey, told Collins’s advisory committee on 6 December that “unless you get a stick, this won’t happen”. Her group’s report noted that the number of US PhD biomedical graduates who secure tenure-track or tenured jobs has fallen from 34% in 1993 to 26% today. She said that unless the NIH



“These proposed initiatives are designed to effect real change.”

Francis Collins

takes tougher steps, “we will be looking at data that look just like this ten more years from now”.

Neither the June report nor the NIH response answer one key question — how many biomedical PhDs the United States should be training — because the necessary data and workforce-modelling expertise were not available either to the report’s authors or to NIH staff. Indeed, the NIH also plans to hire at least one labour economist, to work as part of a new unit devoted to modelling biomedical-workforce needs.

As part of its workforce initiative, the NIH will increase yearly stipends for the 35,000 postdocs it supports from \$39,000 to \$42,000, a 7.7% rise, in an effort to reflect postdocs’ extensive training and to discourage lab heads from prolonging the postdoctoral training period. The National Postdoctoral Association in Washington DC applauded the NIH’s plans. “The NIH has really stepped up to the plate in regard to early-career scientists,” says Cathée Johnson Phillips, the group’s executive director. The last time NIH-funded postdocs got a significant pay rise was in 2003. ■

NIH

FUNDING

Cash injection set to revive Swiss drug site

Merck Serono facility could become biotech research hub.

BY DANIEL CRESSEY

One of the largest philanthropic donations in European research history could give some former pharmaceutical-company laboratories fresh life as a centre for bioengineering.

In April, German pharmaceutical company Merck KGaA announced that it was closing the headquarters of Merck Serono, its drug-development unit based in Geneva, Switzerland, as part of a restructuring effort that cut about 500 jobs.

But last week, Swiss billionaire businessmen Hansjörg Wyss and Ernesto Bertarelli rode to the rescue with an undisclosed offer to buy the 45,000-square-metre site close to the shores of Lake Geneva. They plan to give the laboratory facilities to the University of Geneva and the Swiss Federal Institute of Technology in Lausanne (EPFL), under the umbrella of a new Wyss Institute, and would fund research at the institute with a donation of 125 million Swiss francs (US\$133.9 million) over six years.

"We've seen a lot of these gifts going to the United States," says Patrick Aebischer, president of the EPFL, but donations of this size are vanishingly rare in Europe. A 2011 report from the European Commission, for example, noted that "philanthropic fundraising is not, on the whole, taken seriously in European universities" (B. Breeze *et al.* *Giving In Evidence* European Commission; 2011).

The Swiss Wyss Institute would house about ten life-science laboratories, led by new research chairs affiliated to the universities, and would provide jobs for up to 150 people. Merck Serono's state-of-the-art laboratories would not need to be refitted, says Jean-Dominique Vassalli, rector of the University of Geneva, so "I would guess within six months or a year we can have people moving in and working there. That's an extraordinary opportunity." The labs would focus on areas of overlap between medical research and engineering, such as tissue regeneration, implants and transplants.

Start-ups and other biotechnology businesses could also be hosted on the site, which is close to many existing companies. Wyss and

Bertarelli were unavailable for interviews, but a spokeswoman for the project says that they have not finalized their plans for the remainder of the site. A property consultancy is reviewing the proposal on Merck KGaA's behalf.

The move is the latest in a string of projects to transform former pharmaceutical-company sites into academic-industrial research hubs. In 2007, Yale University in New Haven, Connecticut, paid \$109 million for a local site vacated by Bayer. Two years later, the University of Michigan in Ann Arbor handed over \$108 million for a 28-building former Pfizer site, which the university turned into the North Campus Research Complex. And since Pfizer announced that it was pulling out of a large site in Sandwich, UK, last year (see *Nature* **470**, 154; 2011), the British government has been trying to foster a science park there.

"Within a year we can have people moving in and working there. That's an extraordinary opportunity."

Both of the Swiss philanthropists certainly have the experience and the resources to make their plan work. Bertarelli's grandfather founded Serono, and Bertarelli was chief executive of the com-

pany before selling it to Merck KGaA in 2007. And in 2009, Wyss made a similar endowment to create the Wyss Institute for Biologically Inspired Engineering at Harvard University in Boston, Massachusetts.

Donald Ingber, director of the Harvard institute, says that it brings together former industry researchers, who have product-development experience, with scientists working in basic biology. "What we've created is a start-up culture within an academic environment," he says. Although it is not yet clear whether a future Swiss Wyss centre would follow the same model, Ingber says, "I could see potentially great things coming out of that place". ■

➔ NATURE.COM

Read more about philanthropy and science:
go.nature.com/biq27t

CORRECTION

The source for the graphic 'Urban emitters' in the News story 'Megacities move to track emissions' (*Nature* **492**, 20–21; 2012) should have been P. Romero Lankao *et al.* *Clim. Res.* **38**, 17–29 (2008).



Submersible pilots from the University of Ghent in Belgium find invading crustaceans at Antarctica's Palmer Deep in 2010.

TROUBLE BARES ITS CLAWS

Crabs invading the Antarctic continental shelf could deal a crushing blow to a rare ecosystem.

BY DOUGLAS FOX

On a dim February evening, seven people crowded around a row of television monitors in a shack on the rear deck of the RV *Nathaniel B. Palmer*. The research icebreaker was idling 30 kilometres off the coast of Antarctica with a cable as thick as an adult's wrist dangling over the stern. At the end of that cable, on the continental shelf 1,400 metres down, a remote-operated vehicle (ROV) skimmed across the sea floor, surveying a barren, grey mudscape. The eerie picture of desolation, piped back to the television monitors, was the precursor to an unwelcome discovery.

The ROV had visited 11 different sea-floor locations during this 57-day research cruise along the Antarctic Peninsula in 2010. Each time, it had found plenty of life, mostly

invertebrates: sea lilies waving in the currents; brittlestars with their skinny, sawtoothed arms; and sea pigs, a type of sea cucumber that lumbers along the sea floor on water-inflated legs. But at this spot, they were all absent. After 15 minutes, the reason became clear: a red-shelled crab, spidery and with a leg-span as wide as a chessboard, scuttled into view of the ROV's cameras. It probed the mud methodically — right claw, left claw, right claw — looking for worms or shellfish. Another crab soon appeared, followed by another and another. The crowded shack erupted into chatter. "They're natural invaders," murmured Craig Smith, a marine ecologist from the University of Hawaii at Manoa. "They're coming in with the warmer water."

Cold temperatures have kept crabs out of

Antarctic seas for 30 million years. But warm water from the ocean depths is now intruding onto the continental shelf, and seems to be changing the delicate ecological balance. An analysis¹ by Smith and his colleagues suggests that 1.5 million crabs already inhabit Palmer Deep, the sea-floor valley that the ROV was exploring that night (see 'A warming welcome'). And native organisms have few ways of defending themselves. "There are no hard-shell-crushing predators in Antarctica," says Smith. "When these come in they're going to wipe out a whole bunch of endemic species."

Researchers are worried that rising crab populations and other effects of the warming waters could irrevocably change a sea-floor ecosystem that resembles no other on Earth. Scientists are racing to document these effects, even as they continue to explore this little-understood region. "This could have a really major reorganizing impact on these unique and endemic marine communities," says Richard Aronson, a marine biologist at the Florida Institute of Technology in Melbourne, who was part of a team that found crabs on another part of Antarctica's continental shelf in December 2010 (ref. 2). "It's a fascinating thing," he says. "A little scary, because it's a very obvious footprint of climate change."

CUT OFF BY COLD

Aronson has worried about the fragility of life on the Antarctic shelf for more than a decade. He spent December 1994 collecting fossils from Seymour Island, on the northeast fringe of the Antarctic Peninsula. The island's bare, crumbling hills contain the remnants of an ancient sea floor. In 200 metres of layered rock and fossils exposed by wind erosion, Aronson saw evidence of the most pivotal event in Antarctica's history: the continent's final separation from South America, starting around 40 million years ago. This event allowed the emergence of the circumpolar ocean current, which isolated Antarctica from warmer air and water masses farther north, and plunged it into perpetual winter. Aronson and his students analysed 10,000 fossils from before and after that sudden cooling, and a striking pattern emerged.

As temperatures fell, the sea floor bloomed with soft-bodied echinoderms — invertebrates including starfish, brittlestars, sea lilies and sea cucumbers. At the same time, crush wounds caused by crabs or sharks on the arms of fossil starfish and sea lilies became rare — evidence that these predators were declining³.

Crabs and lobsters were probably excluded by a physiological quirk. At temperatures below about 1 °C, they become unable to regulate magnesium in body fluids, leading to narcosis, clumsiness and paralysis of breathing. Most of the 100 or so fish species currently found on the Antarctic shelf belong to a single sub-order, whose members evolved antifreeze proteins to keep their blood flowing at

subzero temperatures and then diversified to fill most niches in the frigid seas. They lack powerful jaws⁴.

The result is an ecosystem reminiscent of that 350 million years ago, in which the top predators are slow-moving invertebrates such as starfish, sea spiders and ribbon worms⁴. "All of this stuff has got a very Palaeozoic flavour to it," says Aronson. The relaxation of natural selection allowed species to lose their natural armour, says James McClintock, a marine biologist at the University of Alabama at Birmingham. Animals on the Antarctic sea floor "are very weakly skeletonized," he says. "You can pick up an Antarctic clam and crush it in your hand."

By the mid 2000s, Aronson began to believe that if Antarctica's oceans warmed up, the ecological cascade that caused this blast-from-the-past ecosystem to flourish would run in reverse: crushing predators would return and wreak havoc⁴. That prediction is now being tested.

Westerly winds are strengthening and the circumpolar current is intensifying, driven by atmospheric warming and a hole in the ozone layer over Antarctica. These changes are lifting warm, dense, salty water from 4,000 metres down in the Southern Ocean up over the lip of the continental shelf.

Douglas Martinson, an oceanographer at the Lamont-Doherty Earth Observatory in Palisades, New York, has documented this process on the western side of the Antarctic Peninsula, where crabs are invading. Martinson installed five temperature and current sensors around Marguerite Trough — a deep canyon carved

into the sea floor by glaciers advancing to the edge of the continental shelf in past ice ages. The moorings captured an insidious process: as the circumpolar current skirts Antarctica's continental shelf, it runs head-on into the steep wall of the trough. About once a week, a swirling eddy containing 100 cubic kilometres of warm water wafts up from that collision, spilling onto the continental shelf^{5,6}. The same thing happens elsewhere, says Martinson: "It looks like this is what happens at all of the canyons that cut across the shelf."

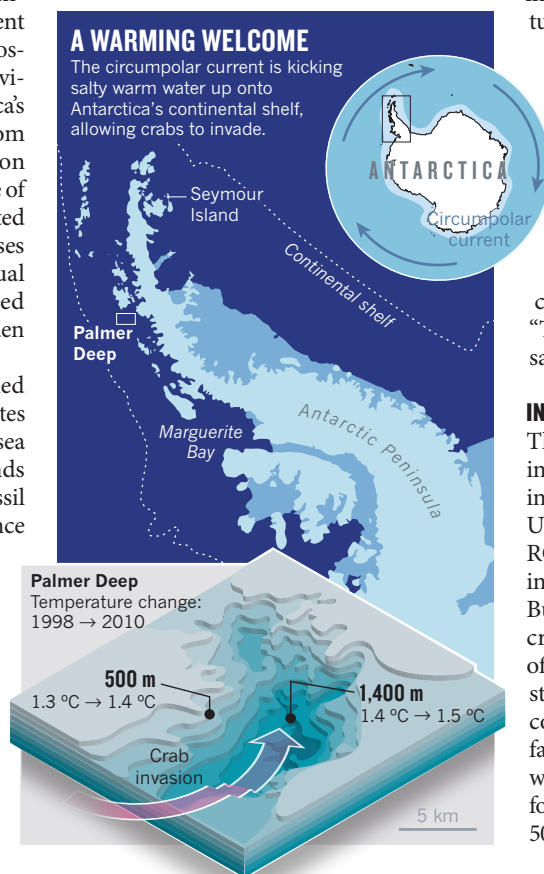
The temperature of this intruding water is only about 1.8 °C — but for an ocean region generally between 1 and –2 °C, the impact is substantial. And the incursion seems to have begun only recently, says Eugene Domack, a marine geologist at Hamilton College in Clinton, New York, who led the 2010 cruise to Palmer Deep.

Domack has managed to date⁷ the onset by measuring the amount of radioactive carbon-14 in deep-sea corals collected from the continental shelf — a process similar to reading tree rings. The corals had grown for 400 years before being dredged up. The carbon-14 content increased smoothly along the coral's growth axis for the first 350 years, and then dropped suddenly — indicating that the coral was being bathed in water with a reduced carbon-14 content. The water from the depths of the circumpolar current would fit the bill: it has been isolated from the carbon in the atmosphere for centuries. On the basis of these measurements, Domack has deduced that the warm-water incursion "kicked in somewhere around the turn of the last century, 1920 or 1930".

According to Domack's results, the incursion seems to have started following the end of the Little Ice Age — a period of relative cold that began in the Middle Ages — but it has intensified as anthropogenic warming and southern ozone depletion have taken hold. Average water temperatures west of the Antarctic Peninsula have risen by 1 °C in the past 50 years, and continue to rise by 0.01–0.02 °C per year^{1,6}. "The heat injection is going through the roof," says Martinson. "It's going up exponentially."

INVASIVE SPECIES

The first evidence that crabs were poised to invade along with the warm water came early in 2007. Sven Thatje, a marine ecologist at the University of Southampton, UK, launched an ROV to the outer slope of the Antarctic Peninsula to map glacial grooves on the sea floor. But its cameras also caught sight of 13 king crabs (*Paralomis birsteini*) between depths of 1,300 and 1,100 metres (ref. 8). Thatje had studied the cold tolerance of these crabs and concluded that they could probably survive farther north at 2,000–4,000 metres, where the water is a degree or two warmer — "but then we found them even on the continental slope" only 500 metres below the shelf itself, he says. "These





King crabs (*Neolithodes yaldwyni*) are invading Antarctic seas, where they prey on local species.

crabs were thriving at 1 °C. They were basically at the physiological limit that I had anticipated.”

But it was Smith's discovery of *Neolithodes yaldwyni* king crabs in Palmer Deep, 120 kilometres in from the edge of the continental shelf, that demonstrated a true invasion. West of the Antarctic Peninsula, cold water sits on top of warmer water. To reach Palmer Deep from the outer ocean, crabs or larvae must have crossed what amounts to a cold, high mountain pass only 450 metres below sea level before settling into Palmer Deep, at depths of 800–1,400 metres (ref. 1).

In December 2010, Thatje, working with Aronson and McClintock, returned to Antarctica and towed a submersible up and down the continental slope near the mouth of Marguerite Trough. The ROV traced 100 kilometres of sea floor, capturing 150,000 photographs that revealed hundreds of *P. birsteinii* crabs between 2,300 and 830 metres down². “If you extrapolate,” says McClintock, “we’re talking about millions of crabs.”

The crab invasion could have started a decade or two ago. When Smith re-examined photographs taken at the bottom of Palmer Deep in 1998, he saw telltale claw marks in the mud — indicating that at least some crabs were already present, even if none had been caught on camera¹. Domack looked at 30 years of water-temperature data measured at Palmer Deep during earlier cruises, and found that the sea-floor valley had gradually warmed¹ — becoming ever-more hospitable to the crabs. Smith is now comparing gene sequences from crabs sampled in Palmer Deep with ones collected

from deeper, warmer waters farther north in the Southern Ocean. The data from these experiments should help him to zero in on the crabs’ origins and the date of their arrival.

But even without knowing the exact history of the invasion, the implications seem clear. Animals living on the edge of their physiological limits often struggle to survive and reproduce, but 19 out of 27 crabs that Smith collected during a cruise in 2011 turned out to be females carrying larvae or eggs. “This population is reproducing like crazy,” he says. “It’s probably here to stay and expand.” As the ceiling of cold water continues to lift over the next 10 or 20 years, crabs could spill out of Palmer Deep and Marguerite Trough — and colonize the broader continental shelf at depths of 400–600 metres, devastating the endemic sea life.

STIFLING HEAT

The warm waters will also bring other perils for Antarctica’s sea-floor gardens. Many of the species here are exquisitely sensitive to increases in temperature. The brittlestars and other invertebrates have extremely slow metabolisms — an adaptation to the cold water — and only meagre ability to absorb and transport oxygen. “So what do those guys do if it warms up and their metabolic rate speeds up?” asks Lloyd Peck, a biologist at the British Antarctic Survey in Cambridge, who has monitored these creatures in aquarium warming experiments. Their oxygen demand revs beyond what their gills can supply — and they slowly suffocate^{9,10}.

About half of the two dozen Antarctic species that Peck has studied seem to do fine in water 2 °C warmer than current maximum summer temperatures — but the rest seem to suffer.

“At least two of the species that we think are going to be the first [to disappear] could give problems for the balance of the ecosystem,” he says. Those are the Antarctic clam (*Laternula elliptica*)⁹ and the shallow-water brittlestar (*Ophionotus victoriae*)¹⁰, both mainstay species that eat dead plankton and other organic trash that falls from above, and turn it into the biomass that feeds everything else on the sea floor. But these species either die or become dangerously sluggish at even 1 °C above current summer highs — temperatures that could become widespread in 50–100 years.

If rising temperatures cause brittlestars and clams to disappear, then more falling detritus might be consumed by microbes instead of being converted into edible biomass — meaning that it would sustain fewer animals, overall, on the sea floor. Alternatively, filter-feeding sponges might multiply to fill the niche. Either way, the mix of species supported further up the food chain might no longer include large numbers of archaic predators such as starfish, ribbon worms and sea spiders.

Julian Gutt, a marine ecologist at the Alfred Wegener Institute for Polar and Marine Research in Bremerhaven, Germany, admires Smith’s work with the crabs, but withholds final judgement on whether the crustaceans are a new piece of this destructive puzzle, or a long-present fixture. Repeat surveys showing that the crabs are expanding their foothold over time would confirm an invasion, he says. But “if they move into new habitat, some serious impact is quite likely”.

Aronson, for one, will be watching closely for signs that this is happening. And in his experience, optimism is not warranted. “Every time we make a prediction of what we think will happen in the next 50 years, then poof, 10 years later, there it is,” he says. “So I think this is going to be happening more rapidly than, as conservative scientists, we’re used to predicting.” ■

Douglas Fox is a freelance writer in the San Francisco Bay area, California.

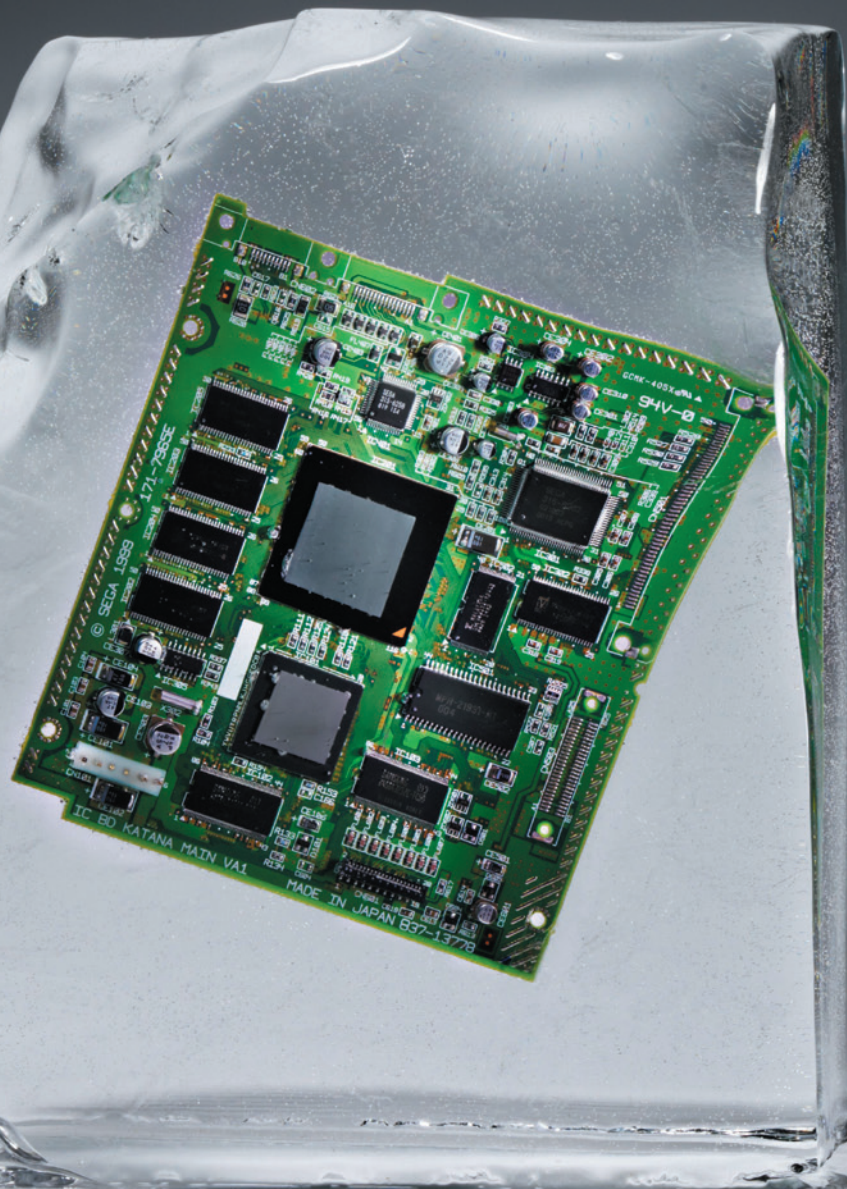
1. Smith, C. R. *et al.* *Proc. R. Soc. B* **279**, 1017–1026 (2012).
2. Aronson, R. B., Vos, S., Thatje, S., McClintock, J. & Amsler, M. *Climate Change and the King Crab Invasion of Antarctica* Presented at the SCAR Annual Meeting, Portland, Oregon, 13–25 July 2012.
3. Aronson, R. B., Blake, D. B. & Oji, T. *Geology* **25**, 903–906 (1997).
4. Aronson, R. B. *et al.* *Annu. Rev. Ecol. Evol. Syst.* **38**, 129–154 (2007).
5. Martinson, D. G. & McKee, D. C. *Ocean Sci.* **8**, 433–442 (2012).
6. Martinson, D. G., Stammerjohn, S. E., Iannuzzi, R. A., Smith, R. C. & Vernet, M. *Deep Sea Res II* **55**, 1964–1987 (2008).
7. Allinger, T., Burt, T. & Domack, E. W. *et al.* Abstract A41D-0135. Presented at the 2010 Fall Meeting, AGU, San Francisco, California, 13–17 December.
8. Thatje, S., Hall, S., Hauton, C., Held, C. & Tyler, P. *Polar Biol.* **31**, 1143–1148 (2008).
9. Peck, L. S., Morley, S. A., Pörtner, H.-O. & Clark, M. S. *Oecologia* **154**, 479–484 (2007).
10. Peck, L. S., Massey, A., Thorne, M. A. S. & Clark, M. S. *Polar Biol.* **32**, 399–402 (2009).

➔ **NATURE.COM**
For a slideshow of crabs and the species they threaten, see: go.nature.com/xbbdml

Feeling the heat

The more that microcircuits are shrunk, the hotter they get. Engineers are on the hunt for ways to cool off computing.

BY PHILIP BALL



D. SAELINGER/CORBIS

A laptop computer can double as an effective portable knee-warmer — pleasant in a cold office. But a bigger desktop machine needs a fan. A data centre as large as those used by Google needs a high-volume flow of cooling water. And with cutting-edge supercomputers, the trick is to keep them from melting. A world-class machine at the Leibniz Supercomputing Centre in Munich, for example, operates at 3 petaflops (3×10^{15} operations per second), and the heat it produces warms some of the centre's buildings. Current trends suggest that the next milestone in computing — an exaflop machine performing at 10^{18} flops — would consume hundreds of megawatts of power (equivalent to the output of a small nuclear plant) and turn virtually all of that energy into heat.

Increasingly, heat looms as the single largest obstacle to computing's continued advancement¹. The problem is fundamental: the smaller and more densely packed circuits become, the hotter they get. "The heat flux generated by today's microprocessors is loosely comparable to that on the Sun's surface," says Suresh Garimella, a specialist in computer-energy management at Purdue University in West Lafayette, Indiana. "But unlike the Sun, the devices must be cooled to temperatures lower than 100 °C" to function properly, he says.

To achieve that ever more difficult goal, engineers are exploring new ways of cooling — by pumping liquid coolants directly on to chips, for example, rather than circulating air around them. In a more radical vein, researchers are also seeking to reduce heat flux by exploring ways to package the circuitry. Instead of being confined to two-dimensional (2D) slabs, for example, circuits might be arrayed in 3D grids and networks inspired by the architecture of the brain, which manages to carry out massive computations without any special cooling gear. Perhaps future supercomputers will not even be powered by electrical currents borne along metal wires, but driven electrochemically by ions in the coolant flow.

This is not the most glamorous work in computing — certainly not compared to much-publicized efforts to make electronic devices ever smaller and faster. But those high-profile innovations will count for little unless engineers crack the problem of heat.

GO WITH THE FLOW

The problem is as old as computers. The first modern electronic computer — a 30-tonne machine called ENIAC that was built at the University of Pennsylvania in Philadelphia at the end of the Second World War — used 18,000 vacuum tubes, which had to be cooled by an array of fans. The transition to solid-state silicon devices in the 1960s offered some respite, but the need for cooling returned as device densities climbed. In the early 1990s, a shift from earlier 'bipolar' transistor technology to complementary metal oxide semiconductor (CMOS) devices offered another respite by greatly reducing the power dissipation per device. But chip-level computing power doubles roughly every 18 months, as famously described by Moore's Law, and this exponential growth has brought the problem to the fore yet again² (see 'Rising temperatures'). Some of today's microprocessors pump out heat from more than one billion transistors. If a typical desktop machine let its chips simply radiate their heat into a vacuum, its interior would reach several thousand degrees Celsius.

That is why desktop computers (and some laptops) have fans. Air that has been warmed by the chips carries some heat away by convection, but not enough: the fan circulates enough air to keep temperatures at a workable 75 °C or so.

But a fan also consumes power — for a laptop, that is an extra drain on

the battery. And fans alone are not always sufficient to cool the computer arrays used in data centres, many of which rely on heat exchangers that use liquid to cool the air flowing over the hot chips.

Still larger machines demand more drastic measures. As Bruno Michel, manager of the advanced thermal packaging group at IBM in Rüschlikon, Switzerland, explains: "An advanced supercomputer would need a few cubic kilometres of air for cooling per day." That simply is not practical, so computer engineers must resort to liquid cooling instead³.

Water-cooled computers were commercially available as early as 1964, and several generations of mainframe computers built in the 1980s and 1990s were cooled by water. Today, non-aqueous, non-reactive liquid coolants such as fluorocarbons are sometimes used, often coming into direct contact with the chips. These substances generally cool by boiling — they absorb heat and the vapour carries it away. Other systems involve liquid sprays or refrigeration of the circuitry.

SuperMUC, an IBM-built supercomputer housed at the Leibniz centre, became operational in 2012. The 3-petaflop machine is one of the world's most powerful supercomputers. It has a water-based cooling system, but the water is warm — around 45 °C. The water is pumped through microchannels carved into a customized copper heat sink above the central processing unit, which concentrates cooling in the parts of the system where it is most needed. The use of warm water may seem odd, but it consumes less energy than other cooling methods, because the hot water that emerges from the system requires less chilling before it is reintroduced. And the use of hot-water outflow for heating nearby office buildings results in further energy savings.

Michel and his colleagues at IBM believe that flowing water could

be used not just to extract heat, but also to provide power for the circuitry in the first place, by carrying dissolved ions that engage in electrochemical reactions at energy-harvesting electrodes. In effect, the coolant doubles as an electrolyte 'fuel'. The idea is not entirely new, says Yogendra Joshi, a mechanical engineer at the Georgia Institute of Technology in Atlanta. "It has been used for many years in thermal management of aircraft electronics", which are cooled by jet fuel, he says.

Delivering electrical power with an electrolyte flow is already a burgeoning technology. In a type of fuel cell known as a redox flow battery, for example, two electrolyte solutions are pumped into an electrochemical cell, where they are kept separate by a membrane that ions can flow through. Electrons travel between ions in the solutions in a process known as a reduction-oxidation (redox) reaction — but they are forced to do so through an external circuit, generating energy that can be tapped to

provide electrical power.

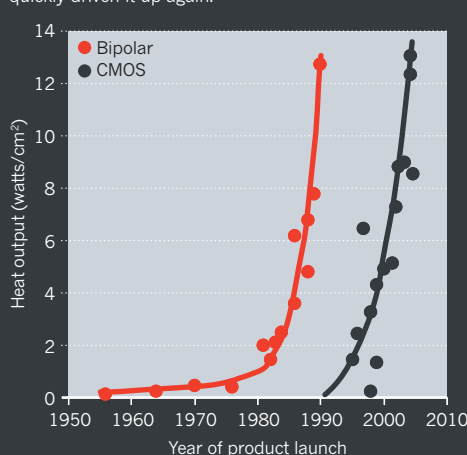
SALTY LOGIC

Redox-flow cells can be miniaturized using microfluidic technology, in which the fluid flows are confined to microscopic channels etched into a substrate such as silicon⁴. At such small scales, the liquids can flow past each other without mixing, so there is no need for a membrane to separate them. With this simplification, the devices are easier and cheaper to make, and they are compatible with silicon-chip technology.

Michel and his colleagues have begun to develop microfluidic cells for powering microprocessors, using a redox process based on vanadium ions. The electrolyte is pumped along microchannels that are 100–200 micrometres wide and similar to those used to carry coolant flows around some chips. Power is harvested at electrodes spaced along the channel, then distributed to individual devices by conventional

RIISING TEMPERATURES

The switch from bipolar to complementary metal oxide semiconductor (CMOS) transistors lowered microchips' heat output — but increasing device densities have quickly driven it up again.





Steam carries heat away from Google's data centre in The Dalles, Oregon.

metal wiring. The researchers unveiled their preliminary results in August, at a meeting of the International Society of Electrochemistry in Prague⁵.

But they remain some way from actually powering circuits this way. At present, the power density of microfluidic redox-flow cells is less than 1 watt per square centimetre at 1 volt — two or three orders of magnitude too low to drive today's microprocessors. However, Michel believes that future processors will have significantly lower power requirements. And, he says, delivering power with microfluidic electrochemical cells should at least halve the power losses that occur with conventional metal wiring, which squanders around 50% of the electrical energy it carries as resistive heating.

BECOMING BRAINIER

Electrochemical powering could help to reduce processors' heat dissipation, but there is a way to make a much bigger difference. Most of the heat from a chip is generated not by the switching of transistors, but by resistance in the wires that carry signals between them. The problem is not the logic, then, but the legwork. During the late 1990s, when transistors were about 250 nanometres across, 'logic' and 'legwork' accounted for roughly equal amounts of dissipation. But today, says Michel, "wire energy losses are now more than ten times larger than the transistor-switching energy losses". In fact, he says, "because all components have to stay active while waiting for information to arrive, transport-induced power loss accounts for as much as 99% of the total".

This is why "the industry is moving away from traditional chip architectures, where communication losses drastically hinder performance and efficiency", says Garimella. The solution seems obvious: reduce the distance over which information-carrying pulses of electricity must travel between logic operations. Transistors are already packed onto 2D chips about as densely as they can be. If they were stacked in 3D arrays instead, the energy lost in data transport could be cut drastically. The transport would also be faster. "If you reduce the linear dimension by a factor of ten, you save that much in wire-related energy, and your

information arrives almost ten times faster," says Michel. He foresees 3D supercomputers as small as sugar lumps.

What might 3D packaging look like? "We have to look for examples with better communication architecture," Michel says. "The human brain is such an example." The brain's task is demanding: on average, neural tissue consumes roughly ten times more power per unit volume than other human tissues — an energy appetite unmatched even in an Olympic runner's quadriceps. The brain accounts for just 2% of the body's volume, but 20% of its total energy demand.

Yet the brain is fantastically efficient compared to electronic computers. It can achieve five or six orders of magnitude more computation for each joule of energy consumed. Michel is convinced that the brain's efficiency is partly due to its architecture: it is a 3D, hierarchical network of interconnections, not a grid-like arrangement of circuits.

SMART BUILD

This helps the brain to make much more efficient use of space. In a computer, as much as 96% of the machine's volume is used to transport heat, 1% is used for communication (transporting information) and just one-millionth of one per cent is used for transistors and other logic devices. By contrast, the brain uses only 10% of its volume for energy supply and thermal transport, 70% for communication and 20% for computation. Moreover, the brain's memory and computational modules are positioned close together, so that data stored long ago can be recalled in an instant. In computers, by contrast, the two elements are usually separate. "Computers will continue to be poor at fast recall unless architectures become more memory-centric", says Michel. Three-dimensional packaging would bring the respective elements into much closer proximity.

All of this suggests to Michel that, if computers are going to be packaged three-dimensionally, it would be worthwhile to try to emulate the brain's hierarchical architecture⁶. Such a hierarchy is already implicit in some proposed 3D designs: stacks of individual microprocessor chips (on which the transistors themselves could be wired in a branching network) are stacked into towers and interconnected on circuit boards, and these, in turn, are stacked together, enabling vertical communication between them. The result is a kind of 'orderly fractal' structure, a regular subdivision of space that looks the same at every scale.

Michel estimates that 3D packaging could, in principle, reduce computer volume by a factor of 1,000, and power consumption by a factor of 100, compared to current 2D architectures. But the introduction of brain-like, 'bionic' packaging structures, he says, could cut power needs by another factor of 30 or so, and volumes by another factor of 1,000. The heat output would also drop: 1-petaflop computers, which are now large enough to occupy a small warehouse, could be shrunk to a volume of 10 litres.

If computer engineers aspire to the awesome heights of zetaflop computing (10^{21} flops), a brain-like structure will be necessary: with today's architectures, such a device would be larger than Mount Everest and consume more power than the current total global demand. Only with a method such as bionic packaging does zetaflop computing seem remotely feasible. Michel and his colleagues believe that such innovations should enable computers to reach the efficiency — if not necessarily the capability — of the human brain by around 2060. That is something to think about. ■

Philip Ball is a writer based in London.

1. Garimella, S. V. et al. *IEEE Trans. Components Packaging Technol.* **31**, 801–815 (2008).
2. Chu, R. C., Simons, R. E., Ellsworth, M. J., Schmidt, R. R. & Cozzolino, V. *IEEE Trans. Device Mater. Reliability* **4**, 568–585 (2004).
3. Ellsworth, M. J. et al. *ITHERM* 266–274 (2008).
4. Shaegh, S. A. M., Nguyen, N.-T. & Chan, S. H. *Int. J. Hydrogen Energ.* **36**, 5675–5694 (2011).
5. Ruch, P. W., Rapp, T., Schmidt, T. J. & Michel, B. Studies of power density in microfluidic redox flow cells. Abstract presented at the 63rd Annual Meeting of the International Society of Electrochemistry (2012).
6. Ruch, P., Brunschweiler, T., Escher, W., Paredes, S. & Michel, B. *IBM J. Res. & Dev.* **55**, 593–605 (2011).

COMMENT

MATHEMATICS Reviewer begs biologists to sort out their shoddy statistics **p.180**

HEALTH Life outpaces a programme of newborn genetic screening **p.182**

CULTURE Why is so much science on US television bad? **p.184**

BIOLOGY A call to end the costly scandal of misidentified cell lines **p.186**



GEOLOGICAL SOCIETY OF LONDON



In John Cooke's painting *Discussion on the Piltdown Skull* (1915), scientists examine a human-like cranium found in Piltdown, England, in 1912.

The 100-year mystery of Piltdown Man

Chris Stringer explains why the longest-running whodunnit in palaeontology is still worth solving.

Nine years ago, the Natural History Museum in London, where I work, celebrated the 50th anniversary of the disclosure of one of the most successful scientific hoaxes in history. In 1953, scientists from the museum and the University of Oxford, UK, showed that specimens unearthed in the early twentieth century from the village of Piltdown in Sussex, UK, were an elaborate forgery — not evidence of a primitive human, as their discoverers had

claimed in December 1912.

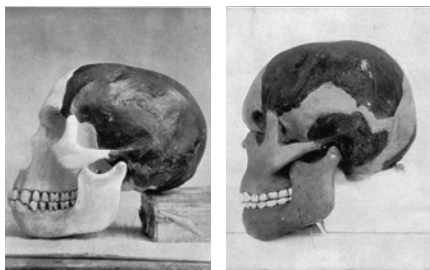
During our celebrations, a jaded colleague said: “I’d like to see the anniversary commemorated by the crushing of all the material and the burning of the Piltdown archive!” Yet, almost a decade later, I find myself part of a growing team of investigators hoping to reveal how the forgery was accomplished, and so to work out, finally, who did it and what drove them.

Why — 100 years after ‘Piltdown Man’

was presented to the Geological Society of London — does it matter?

Personally, I am intrigued by the question of whether the hoax was driven by scientific ambition or by more jocular or vindictive motives. Also, the story has continuing relevance beyond its allure as a whodunnit: it is a warning to scientists to keep their critical guard up, and an example of the (eventual) triumph of the scientific method.

In 1891, a Dutch palaeoanthropologist ►



Clockwise from top: Charles Dawson (sitting) and Arthur Smith Woodward (right) at the Piltdown site around 1913; a local pub's homage to Piltown Man; the forgery's extent is revealed in London, 1954; Kenneth Oakley (left) and L. E. Parsons examine Piltdown jaw, 1949; *Eoanthropus* skull models, 1913.

► described the first known specimens of *Homo erectus* ('Java Man'), which he had discovered in Indonesia. Sixteen years later, a workman in Germany unearthed the jaw of 'Heidelberg Man', a possible descendant of *H. erectus*. Thus it was with great pride that Arthur Smith Woodward and Charles Dawson announced on 18 December 1912 that they had found an even more remarkable fossil human at Piltdown¹.

Woodward was a distinguished British palaeontologist and 'Keeper of Geology' at what was then the British Museum of Natural History; Dawson was an amateur antiquarian. What Woodward called *Eoanthropus dawsoni* ('Dawson's dawn man') consisted of an ape-like mandible containing two molar teeth and parts of a human-like cranium. Woodward and Dawson had also unearthed primitive stone tools and fragments of fossilized mammals, including a hippopotamus and an elephant-like creature — all stained the same dark brown as the gravels in the pit where they were found. The finds led Woodward and Dawson to assert that *Eoanthropus* was potentially as ancient as Java Man — now known to be about one million years old.

Excavations led by the pair over the next two years recovered more artefacts and fauna from the Piltdown site, including a canine tooth. Even a slab of elephant bone was dug up which, because of its shape, became known as the 'cricket bat'. Further work was disrupted by the onset of the First World War and Dawson's declining health. But before Dawson died in 1916, he wrote to Woodward saying that he had found further remains of fauna and *Eoanthropus* at a second site, a few kilometres from the original gravel pit.

A COMPLEX FORGERY

The discoveries made headlines throughout the world. But in palaeontological circles, reactions were mixed from the beginning. Several prominent British scientists fully accepted the existence of *Eoanthropus*. A minority joined some US and German researchers in questioning the association of the jaw and skull parts. They believed that an ancient ape fossil could have become mixed into deposits containing fragments of a more recent human skull. Some dissenters were won over by the tooth and skull fragments Dawson found at the second Piltdown location, which matched those from the first site.

Through the 1920s and 1930s, *Eoanthropus* was increasingly marginalized as other ancient humans were discovered in Africa, China and Indonesia. None of these fossils showed *Eoanthropus*' strange combination of ape-like jaw and human-like braincase.

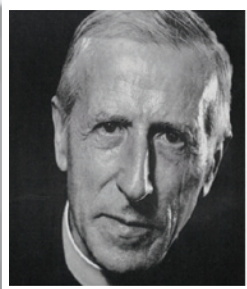
By 1950, things had become even worse for *Eoanthropus*. Kenneth Oakley, a geo-archaeologist at the museum, applied chemical tests to the relics and determined

C. MYDANS/TIME LIFE/GETTY (PUB SIGN); MARY EVANS PICTURE LIBRARY (SKULL MODELS); NATURAL HISTORY MUSEUM, LONDON (ALL OTHERS)

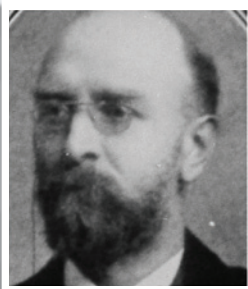
WHO DID IT?

Four main suspects in the Piltdown case

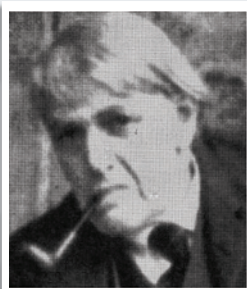
Teilhard de Chardin
Priest who discovered canine tooth at Piltdown.



Arthur Smith Woodward
Museum head of geology and co-leader of Piltdown finds.



Martin Hinton
Woodward's subordinate; later, 'Keeper of Zoology'.



Charles Dawson
Ambitious fossil collector and co-leader of Piltdown finds.



that the jaw could not be more than 50,000 years old, even though some of the Piltdown fauna was clearly much older. More comprehensive studies by Oakley and his colleagues, published in 1953 and 1955, revealed the full extent of the forgery^{2,3}.

A jaw and canine, probably from a modern orangutan, had been manipulated and stained, along with parts of a modern human skull. The fossil fauna had been gathered from many different places before being planted in the Piltdown gravels, and the stone tools had been similarly introduced after being stained to match the colour of the deposits. As for the 'cricket bat' — it had been carved with a steel knife from a fossilized elephant femur.

Once the truth was out and national embarrassment overcame, the hunt was on for the culprit(s) in a palaeontological mystery that persists to this day (see 'Who did it?'). Dawson was and is a prime suspect⁴⁻⁶. Woodward and at least 12 others have also been accused, singly or in combination (see go.nature.com/x8ub0q).

My colleagues and I (at present, we are a team of 15 researchers from the Natural History Museum and several British universities) are now examining the finds at a microscopic level. Using techniques such as radiocarbon dating and DNA and isotope studies, we hope to pin down the taxonomic identities and geographical origins of the specimens. We are also using spectroscopy to establish how many different staining methods were applied to the Piltdown assemblages of bones, teeth and tools.

If the materials collected from the two sites

match up, the culprit was likely to have been Dawson, as he was the sole 'discoverer' of the remains from the second site. If the canine turns out to have a different origin (and to have been stained differently) from the other samples, then its discoverer, Teilhard de Chardin, may have been involved in the scam⁷. De Chardin, then a novice Jesuit priest (later, a famous thinker and palaeontologist), helped Dawson in his work at the site.

Alternatively, our results could strengthen or refute another recently proposed scenario involving zoologist Martin Hinton⁸. At the time of the Piltdown discoveries, Hinton was a volunteer in Woodward's department at the museum. During the 1970s, more than a dozen modified and stained bones and teeth were found among Hinton's personal possessions (he died in 1961).

MIXED BLESSING

Identifying who doctored and planted the Piltdown assemblage is the key to understanding why they did so. If it turns out that Dawson was to blame, for instance, scientific recognition was almost certainly the driving force. Dawson had ambitions to become a Fellow of the Royal Society, and he clearly liked to cultivate relationships with important people.

It is unclear why Hinton would have played trickster. One possibility is that he surmised that something was amiss with the Piltdown findings but felt unable to raise his concerns to his department head (Woodward). Or perhaps he planted the 'cricket bat' (seemingly a far less sophisticated forgery than the other artefacts) as a

way to alert his colleagues⁹.

Regardless of who was responsible, the Piltdown hoax is a stark reminder to scientists that if something seems too good to be true, then perhaps it is. The hoax is unprecedented in its complexity (some of the Piltdown finds were more expertly modified than others, and the skill of the forger(s) is one of the aspects we are examining). But it is not the only example of trickery within palaeontological and archaeological circles. Indeed, what happened at Piltdown may well have sped the revelation, in 2000, that the famous Japanese archaeologist Shinichi Fujimura was burying stone tools he had collected in previous digs to later unearth them as fresh finds.

Piltdown Man's temporary ascendancy undoubtedly cost the field. For instance, it delayed widespread acceptance of *Australopithecus africanus*, an early hominin found in South Africa in the mid-1920s, as a genuinely ancient relic of human evolution.

Less obviously, Piltdown Man demonstrates the power of the scientific method to expose the truth, eventually (see go.nature.com/tbb9ma). The discoveries at Piltdown were steadily undermined by finds made elsewhere, even though the reasons for the specimens' failure to withstand scrutiny were not

"It shows how far the field of palaeo-anthropology has come in the past 100 years."

fully articulated until 1953. Indeed, Piltdown Man's days were numbered once radiocarbon dating began to be routinely applied to the fossil record, from about 1959.

That the story of Piltdown Man still resonates today is understandable: as a 'real-life' whodunnit, it is hard to beat. Ultimately, however, it shows how far the field of palaeoanthropology has come in the past 100 years. ■

Chris Stringer is Research Leader in Human Origins in the Department of Earth Sciences, Natural History Museum, London SW7 5BD, UK.

e-mail: c.stringer@nhm.ac.uk

1. Dawson, C., Woodward, A. S. & Smith, G. E. *Q. J. Geol. Soc. Lond.* **69**, 117–152 (1913).
2. Weiner, J. S., Oakley, K. P. & Le Gros Clark, W. E. *Bull. Br. Mus. Nat. Hist.* **2**, 139–146 (1953).
3. Weiner, J. S. et al. *Bull. Br. Mus. Nat. Hist.* **2**, 225–287 (1955).
4. Weiner, J. S. & Stringer, C. *The Piltdown Forgery* (Oxford Univ. Press, 2003).
5. Russell, M. *Piltdown Man: The Secret Life of Charles Dawson and the World's Greatest Archaeological Hoax* (Tempus, 2003).
6. McNabb, J. *Archaeol. J.* **163**, 1–41 (2006).
7. Thackeray, J. F. *Trans. R. Soc. S. Afr.* **66**, 9–13 (2011).
8. Gardiner, B. G. *Zool. J. Linn. Soc.* **139**, 315–335 (2003).
9. Stringer, C. *Homo Britannicus* (Penguin, 2007).



ILLUSTRATION BY PETE ELLIS/DRAWGOOD.COM

Know when your numbers are significant

Experimental biologists, their reviewers and their publishers must grasp basic statistics, urges **David L. Vaux**, or sloppy science will continue to grow.

The incidence of papers in cell and molecular biology that have basic statistical mistakes is alarming. I see figures with error bars that do not say what they describe, and error bars and *P* values for single, 'representative' experiments. So, as an increasingly weary reviewer of many a biology publication, I'm going to spell out again¹ the basics that every experimental biologist should know.

Simply put, statistics and error bars should be used only for independent data, and not for identical replicates within a single experiment. Because science represents the knowledge gained from repeated observations or experiments, these have to be performed more than once — or must use multiple independent samples — for us to have confidence that the results are not just a fluke, a coincidence or a mistake. To show only the result of a single experiment, even if it is a representative one, and then misuse statistics

to justify that decision, erodes the integrity of the scientific literature.

It is eight years since *Nature* adopted a policy of insisting that papers containing figures with error bars describe what the error bars represent². Nevertheless, it is still common to find papers in most biology journals — *Nature* included — that contain this and other basic statistical errors. In my opinion, the fact that these scientifically sloppy papers continue to be published means that the authors, reviewers and editors cannot comprehend the statistics, that they have not read the paper carefully, or both.

Why does this happen? Most cell and molecular biologists are taught some statistics during their high-school or undergraduate years, but the principles seem to be forgotten somewhere between graduation and starting in the lab. Often, the type of statistics they learnt is not relevant to the kinds of experiment they are now doing.

And, once in the lab, people generally just do what everyone else does, without always understanding why.

Even if experimental biologists do not need to use statistical evidence for their own experiments, they should have an understanding of the basics so that they can interpret others' work critically. They don't all need to understand complex statistics, or to hire professional statisticians, but there would be fewer sloppy papers if every author, reviewer and editor understood statistical concepts such as standard deviation, standard error of the mean (s.e.m.), sampling error and the difference between replicate and independent data (see 'Statistics glossary').

BACK TO BASICS

In the life sciences there are typically two types of publication: those that use large data sets and rely mostly or wholly on statistical

evidence (for example, epidemiology, psychology, clinical trials and genome-wide association studies), and those that do not — such as much cell and molecular biology, biochemistry and classical genetics.

For papers with large data sets that rely purely on statistical evidence, recommendations exist for computing sample size, reporting on outlying results and other issues^{3,4}. But these guidelines do not serve authors of the other category of papers. Cell and molecular biologists have the luxury of being able to probe their experimental systems in multiple, independent ways and can therefore often get by with *N*s of three, without the need for sophisticated statistics.

The first figure in a typical paper in cell or molecular biology, for example, might show the difference in phenotype between three wild-type and three gene-deleted mice. The second figure might compare the levels of proteins in cells derived from the mice, looking at both the deleted protein and one of its substrates, or the effects of treating wild-type cells with an inhibitor of the protein encoded by the deleted gene. If the evidence from these experiments is consistent, and gives support to a coherent model, it would be unnecessary to analyse 30 mice of each type, or to repeat the Western blots of protein levels 30 independent times. Watson and Crick's paper on the structure of DNA⁵ does not contain statistics, graphs with error bars or large *N*s.

Understanding the rudiments of statistics would stop experimental biologists from calculating a *P* value and a s.e.m. from triplicates from one representative experiment, and might stop the reviewers and editors from letting these pass unquestioned. If the results from one representative experiment are shown, then *N* = 1 and statistics do not apply. Besides, it is always better to include a full data set, rather than withholding results that are not representative. When *N* is only 2 or 3, it would be more transparent to just plot the independent data points, and let the readers interpret the data for themselves, rather than showing possibly misleading *P* values or error bars and drawing statistical inferences.

If the data in an experiment are equivocal, or the effect size is small, it is much better to come up with an extra, mechanistically different, experiment to test the hypothesis, than to repeat the same experiment until *P* is less than 0.05.

If statistics are shown, it should be for a good reason. Descriptive statistics, such as range or standard deviations, are only necessary when there are too many data points to visualize easily. Inferential statistics (an s.e.m., confidence interval or *P* value) should be shown only if they make it easier to interpret the results, and they should not detract from other key considerations such as the magnitude of

STATISTICS GLOSSARY

Some common statistical concepts and their uses in analysing experimental results.

Term	Meaning	Common uses
Standard deviation (s.d.)	The typical difference between each value and the mean value.	Describing how broadly the sample values are distributed. $s.d. = \sqrt{\sum (x - \text{mean})^2 / (N - 1)}$
Standard error of the mean (s.e.m.)	An estimate of how variable the means will be if the experiment is repeated multiple times.	Inferring where the population mean is likely to lie, or whether sets of samples are likely to come from the same population. $s.e.m. = s.d. / \sqrt{N}$
Confidence interval (CI; 95%)	With 95% confidence, the population mean will lie in this interval.	To infer where the population mean lies, and to compare two populations. $CI = \text{mean} \pm s.e.m. \times t_{(N-1)}$
Independent data	Values from separate experiments of the same type that are not linked.	Testing hypotheses about the population.
Replicate data	Values from experiments where everything is linked as much as possible.	Serves as an internal check on performance of an experiment.
Sampling error	Variation caused by sampling part of a population rather than measuring the whole population.	Can reveal bias in the data (if it is too small) or problems with conduct of the experiment (if it is too big). In binomial distributions (such as live and dead cell counts) the expected s.d. is $\sqrt{N \times p \times (1 - p)}$; in Poisson distributions (for example, cells per field) the expected s.d. is $\sqrt{\text{mean}}$.

N, number of independent samples; *t*, the *t*-statistic; *p*, probability.

the effects or their biological significance.

Figure legends should state the number of independent data points and, for experiments in which replicates were performed, only the mean of the replicates should be shown as a single independent data point. For replicates, no statistics should be shown, because they give only an indication of the fidelity with which the replicates were created: they might indicate how good the pipetting was, but they have no bearing on

“Experimental biologists should know what sort of sampling errors are to be expected.”

the hypothesis being tested.

All experimental biologists and all those who review their papers should know what sort of sampling errors are to be expected in common experiments, such as determining the percentages of live and dead cells or counting the number of colonies on a plate or cells in a microscope field. Otherwise, they will not be able to judge their own data critically, or anyone else's.

REPEAT AFTER ME

How can the understanding and use of elementary statistics be improved? Young researchers need to be taught the practicalities of using statistics at the point at which they obtain the results of their very first experiments.

To encourage established researchers to use statistics properly, journals should publish guidelines for authors, reviewers and editors on the use and presentation of data and statistics that are relevant to

the fields they cover. All journals should follow the lead of the *Journal of Cell Biology*⁷ and make a final check of all figures in accepted papers before publication. They should refuse to publish papers that contain fundamental errors, and readily publish corrections for published papers that fall short. This requires engaging reviewers who are statistically literate and editors who can verify the process. Numerical data should be made available either as part of the paper or as linked, computer-interpretable files so that readers can perform or confirm statistical analyses themselves.

When William Strunk Jr, a professor of English, was faced with a flood of errors in spelling, grammar and English usage, he wrote a short, practical guide that became *The Elements of Style* (also known as Strunk and White)⁸. Perhaps experimental biologists need a similar booklet on statistics. ■

David L. Vaux is professor of cell biology at the Walter and Eliza Hall Institute of Medical Research and at the University of Melbourne, Parkville, Victoria 3052, Australia.
e-mail: vaux@wehi.edu.au

- Cumming, G., Fidler, F. & Vaux, D. L. *J. Cell Biol.* **177**, 7–11 (2007).
- Vaux, D. L. *Nature* **428**, 799 (2004).
- Landis, S. C. et al. *Nature* **490**, 187–191 (2012).
- Nakagawa, S. & Cuthill, I. C. *Biol. Rev. Camb. Philos. Soc.* **82**, 591–605 (2007).
- Watson, J. D. & Crick, F. H. *Nature* **171**, 737–738 (1953).
- Vaux, D. L., Fidler, F. & Cumming, G. *EMBO Rep.* **13**, 291–296 (2012).
- Rosner, M. *The Scientist* **20**, 24–25 (2006).
- Strunk, W. Jr & White, E. B. *The Elements of Style* (5th edn) (Allyn & Bacon, 2009).



A nurse takes blood from the heel of a newborn baby to screen for the amino-acid disorder phenylketonuria.

GENETICS

Testing infant destinies

Henry Greely hails a study examining California's experience of mandatory newborn genetic screening.

At the heart of *Saving Babies?* are the tiny consultation rooms in a Southern California academic medical centre, crowded with families, genetics staff, medical students and “nosy ethnographers, who did their best to take up as little space, and air, as possible”. Medical sociologist Stefan Timmermans and medical anthropologist Mara Buchbinder may have been holding their breath, but their observations provide a fascinating portrait of the state's expanded newborn-genetic-screening programme, and of the lives it has changed.

In 2005, California became one of the first US states to adopt recommendations to expand its mandatory newborn genetic screening to more than 50 conditions, adding rarer, less well-understood ones like the organic acid oxidation disorder 3-MCC to those such as phenylketonuria (PKU) and sickle-cell disease. *Saving Babies?* covers the history of newborn genetic testing, but is



Saving Babies?
The Consequences of Newborn Genetic Screening
STEFAN TIMMERMANS
AND MARA
BUCHBINDER
Univ. Chicago Press:
2012. 320 pp. \$30,
£19.50

it is not clear how many babies received effective treatment as a result of the testing programme, nor how many lives were

based on a three-year study of 75 families who were referred, after screening, to an academic clinic for children's metabolic disorders. The picture it paints is not one of unalloyed success.

Timmermans and Buchbinder argue that the Californian system was adopted too hastily and without sufficient concern for consequences. They find that unexpected results were common in the study, but that

saved. Quite clear, however, are the difficulties of plugging a universal “entitlement” to a screening test into the complex and often irrational US health-care system.

The book begins with Scott and Renee Baio, a US celebrity couple whose daughter Bailey tested positive for glutaric aciduria type 1 (GA1), a condition involving an inability to process certain amino acids. Her test turned out to be a false positive, but during the harrowing wait to find out, her father pledged that if Bailey did not have the disease he would support children who did. Surprisingly, in light of the distress that accompanied the testing process, the Baioes became strong advocates for newborn testing. Their experience of the uncertainties of genetic testing sets the stage for the rest of the book.

The historical overview of newborn screening is excellent, covering both its 1960s origins with PKU screening and the programme's expansion throughout the United States, starting in 2005. At least three factors drove the expansion. One was the discovery that an existing technology, tandem mass spectroscopy, could be used to gauge the levels of many different proteins simultaneously, and hence cheaply. Another was pressure from organizations focusing on genetic diseases, such as the March of Dimes. And a third was an influential set of recommendations from the American College of Medical Genetics (ACMG), supporting expanded screening.

Timmermans and Buchbinder powerfully convey how the screening programme converted some children into “patients-in-waiting”. One child in their study underwent repeated rounds of GA1 testing while his parents remained uncertain whether their child was actually a ‘patient’. This uncertainty, in part a function of the tests but also of our limited knowledge about many of the newly added conditions, can affect the lives of children and parents profoundly.

The authors show how new evidence from the screening programme changed medical understanding of some of the conditions tested for, and how clinicians used shifting definitions of ‘normal’ to lead parents through various stages of their children's conditions. The authors examine the Californian programme's record in disease prevention and saving lives, goals that they show were inevitably compromised by flaws in the health-care system. They conclude that, at least for the metabolic diseases added into expanded screening, the results are not clear.

Saving Babies? isn't perfect. I would have liked some exploration of why, in its 2005 report, the ACMG moved from being cautious about neonatal screening to enthusiastic about its expansion.

➔ **NATURE.COM**
For fetal
diagnostics, see:
go.nature.com/1xwdzu

The book may also suffer from a kind of sampling bias. The families the authors saw most were those trapped in the most difficult situations — of either medical uncertainty or medical danger. They saw less of families for whom the screening was beneficial, particularly those whose children were diagnosed with a condition already in the screening programme before 2005. So the picture may be unduly gloomy. Finally, more discussion of how newborn screening is (or is not) done outside the United States would have contextualized this California-based study.

The book does highlight some broader problems about scholarly work in this area. The first is its audience. Although, happily, the book is largely jargon-free, readers without much genetic knowledge may struggle to follow the valuable information for shaping screening policy, or be frustrated by the medical-sociology focus on observation rather than an assessment of alternative policies. Good policy will require input from many disciplines. All of us, from whatever discipline, need to work hard to make our findings useful to others.

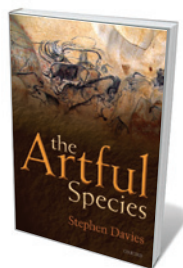
The second problem is time. After the 2005 adoption of expanded screening in California, the authors studied families from November 2007 through to July 2010. The book will be read in 2013. That time lag was largely unavoidable, but by the time the programme can be assessed, it and its settings are no longer the same. The screening programme itself has already changed our understanding of some of the conditions in ways that undercut some of the authors' findings. Meanwhile, the US health-care system is in the process of transformation.

And newer challenges are at hand. Today, whole-exome and whole-genome sequencing are being used clinically, often for children with conditions as poorly understood as those described here. With the plunging cost of sequencing, I think newborn sequence screening will not be far behind. And the challenges will not wait for a baby's birth. In the United States and elsewhere, several companies are already using sequencing technologies for prenatal testing for aneuploidies (disorders in which the fetus has the wrong number of chromosomes) using a simple maternal blood draw within the first trimester; wider applications are surely coming.

How can we implement and assess new technologies competently when the world is changing too fast for the assessors? That, to me, is the most disturbing question raised by this excellent book. ■

Henry T. Greely is the Deane F. and Kate Edelman Professor of Law; professor (by courtesy) of genetics; and director of the Center for Law and the Biosciences at Stanford University, California.
e-mail: hgreely@stanford.edu

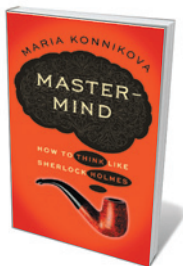
Books in brief



The Artful Species: Aesthetics, Art, and Evolution

Stephen Davies OXFORD UNIV. PRESS 320 pp. £25 (2012)

This spare and elegant treatise by philosopher of aesthetics Stephen Davies posits that art is part of human nature, and is tied in a number of ways to human evolution. Moreover, he argues, the evidence could stretch back at least 400,000 years — to a blood-red quartzite hand axe dubbed Excalibur by the archaeologists who dug it up. Davies marshals findings in disciplines ranging from neuroscience, ethology and evolutionary biology to the arts, musicology and literature. Ultimately, he says, our artistic behaviour is both “puzzling and magnificent”, as we shoulder the heavy costs with perennial zeal.



Mastermind: How to Think Like Sherlock Holmes

Maria Konnikova VIKING 288 pp. \$26.95 (2013)

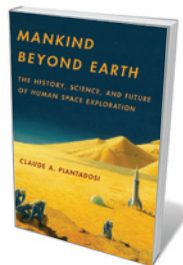
Devotees of Arthur Conan Doyle's conundrum-cracker will be thrilled by this portmanteau of strategies for sharpening cognitive ability. *Scientific American* columnist Maria Konnikova mixes psychology and neuroscience with Holmesian technique and insights on everything from information storage (Holmes's 'brain attic') to observation, awareness and razor-sharp deduction. A few hours in Konnikova's company and, along with Holmes, you might intone, “give me the most abstruse cryptogram or the most intricate analysis, and I am in my own proper atmosphere” (*The Sign of Four*, 1890).



The Fragile Wisdom: An Evolutionary View on Women's Biology and Health

Grazyna Jasienska HARVARD UNIV. PRESS 298 pp. £25.95 (2013)

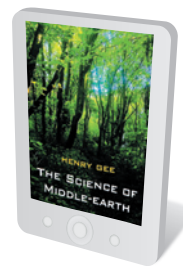
Women may aim for perfect health through diet, exercise and close attention to medical advice, but still develop breast cancer or osteoporosis. Reproductive fitness often wars with general physical fitness over a woman's lifetime, argues public-health specialist Grazyna Jasienska. Drawing on a raft of research in evolutionary biology and beyond, she points to factors such as the disjunction between 'palaeo' and current lifestyles, hormonal disparities and longer lifespans as key to informing disease-prevention strategies.



Mankind Beyond Earth: The History, Science, and Future of Human Space Exploration

Claude A. Piantadosi COLUMBIA UNIV. PRESS 336 pp. \$35 (2013)

Despite difficulties such as cosmic radiation, huge distances, near-vacuum conditions and zero gravity, manned space flight still ignites the imaginations of millions. Medical doctor Claude Piantadosi fans the flames by boldly going into the past and possible future of US space exploration. This is a chronicle at warp speed, covering the science of space exploration; robots, spacecraft and the International Space Station; NASA's glory years; and the constraints on kick-starting 'cheap' space transportation.



The Science of Middle-earth

Henry Gee JILL GRINBERG LITERARY MANAGEMENT Available for Kindle only \$4.99 (2012)

Repeat immersions in Middle-earth beckon again as Peter Jackson's first instalment of *The Hobbit* trilogy, *An Unexpected Journey*, opens in cinemas. *Nature* senior editor Henry Gee offers a revised and reissued guide to the science in J. R. R. Tolkien's fictional world. This is a completist's feast, from the glow of Bilbo's Elvish blade Sting (possibly the result of a chemical sensor “specifically tuned to Orkish exhalations”) to the aerodynamic unfeasibility of a Balrog's wings.

The book may also suffer from a kind of sampling bias. The families the authors saw most were those trapped in the most difficult situations — of either medical uncertainty or medical danger. They saw less of families for whom the screening was beneficial, particularly those whose children were diagnosed with a condition already in the screening programme before 2005. So the picture may be unduly gloomy. Finally, more discussion of how newborn screening is (or is not) done outside the United States would have contextualized this California-based study.

The book does highlight some broader problems about scholarly work in this area. The first is its audience. Although, happily, the book is largely jargon-free, readers without much genetic knowledge may struggle to follow the valuable information for shaping screening policy, or be frustrated by the medical-sociology focus on observation rather than an assessment of alternative policies. Good policy will require input from many disciplines. All of us, from whatever discipline, need to work hard to make our findings useful to others.

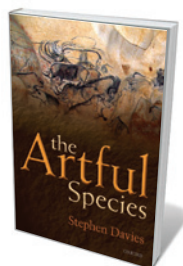
The second problem is time. After the 2005 adoption of expanded screening in California, the authors studied families from November 2007 through to July 2010. The book will be read in 2013. That time lag was largely unavoidable, but by the time the programme can be assessed, it and its settings are no longer the same. The screening programme itself has already changed our understanding of some of the conditions in ways that undercut some of the authors' findings. Meanwhile, the US health-care system is in the process of transformation.

And newer challenges are at hand. Today, whole-exome and whole-genome sequencing are being used clinically, often for children with conditions as poorly understood as those described here. With the plunging cost of sequencing, I think newborn sequence screening will not be far behind. And the challenges will not wait for a baby's birth. In the United States and elsewhere, several companies are already using sequencing technologies for prenatal testing for aneuploidies (disorders in which the fetus has the wrong number of chromosomes) using a simple maternal blood draw within the first trimester; wider applications are surely coming.

How can we implement and assess new technologies competently when the world is changing too fast for the assessors? That, to me, is the most disturbing question raised by this excellent book. ■

Henry T. Greely is the Deane F. and Kate Edelman Professor of Law; professor (by courtesy) of genetics; and director of the Center for Law and the Biosciences at Stanford University, California.
e-mail: hgreely@stanford.edu

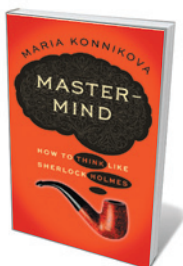
Books in brief



The Artful Species: Aesthetics, Art, and Evolution

Stephen Davies OXFORD UNIV. PRESS 320 pp. £25 (2012)

This spare and elegant treatise by philosopher of aesthetics Stephen Davies posits that art is part of human nature, and is tied in a number of ways to human evolution. Moreover, he argues, the evidence could stretch back at least 400,000 years — to a blood-red quartzite hand axe dubbed Excalibur by the archaeologists who dug it up. Davies marshals findings in disciplines ranging from neuroscience, ethology and evolutionary biology to the arts, musicology and literature. Ultimately, he says, our artistic behaviour is both “puzzling and magnificent”, as we shoulder the heavy costs with perennial zeal.



Mastermind: How to Think Like Sherlock Holmes

Maria Konnikova VIKING 288 pp. \$26.95 (2013)

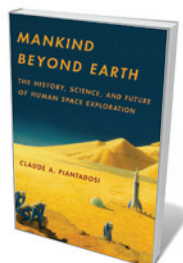
Devotees of Arthur Conan Doyle's conundrum-cracker will be thrilled by this portmanteau of strategies for sharpening cognitive ability. *Scientific American* columnist Maria Konnikova mixes psychology and neuroscience with Holmesian technique and insights on everything from information storage (Holmes's 'brain attic') to observation, awareness and razor-sharp deduction. A few hours in Konnikova's company and, along with Holmes, you might intone, “give me the most abstruse cryptogram or the most intricate analysis, and I am in my own proper atmosphere” (*The Sign of Four*, 1890).



The Fragile Wisdom: An Evolutionary View on Women's Biology and Health

Grazyna Jasienska HARVARD UNIV. PRESS 298 pp. £25.95 (2013)

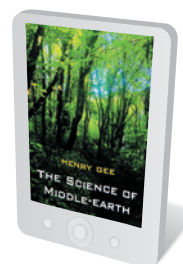
Women may aim for perfect health through diet, exercise and close attention to medical advice, but still develop breast cancer or osteoporosis. Reproductive fitness often wars with general physical fitness over a woman's lifetime, argues public-health specialist Grazyna Jasienska. Drawing on a raft of research in evolutionary biology and beyond, she points to factors such as the disjunction between 'palaeo' and current lifestyles, hormonal disparities and longer lifespans as key to informing disease-prevention strategies.



Mankind Beyond Earth: The History, Science, and Future of Human Space Exploration

Claude A. Piantadosi COLUMBIA UNIV. PRESS 336 pp. \$35 (2013)

Despite difficulties such as cosmic radiation, huge distances, near-vacuum conditions and zero gravity, manned space flight still ignites the imaginations of millions. Medical doctor Claude Piantadosi fans the flames by boldly going into the past and possible future of US space exploration. This is a chronicle at warp speed, covering the science of space exploration; robots, spacecraft and the International Space Station; NASA's glory years; and the constraints on kick-starting 'cheap' space transportation.



The Science of Middle-earth

Henry Gee JILL GRINBERG LITERARY MANAGEMENT Available for Kindle only \$4.99 (2012)

Repeat immersions in Middle-earth beckon again as Peter Jackson's first instalment of *The Hobbit* trilogy, *An Unexpected Journey*, opens in cinemas. *Nature* senior editor Henry Gee offers a revised and reissued guide to the science in J. R. R. Tolkien's fictional world. This is a completist's feast, from the glow of Bilbo's Elvish blade Sting (possibly the result of a chemical sensor “specifically tuned to Orkish exhalations”) to the aerodynamic unfeasibility of a Balrog's wings.



NECU PHOTO BANK/GETTY

In the hit US television show *Watch Mr. Wizard*, actor Don Herbert (right) presented a weekly experiment to teach children about aspects of science.

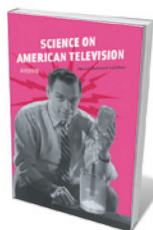
SCIENCE COMMUNICATION

Science fresh from the box

Eugenie Scott relishes a history of science programming on US television that reveals an often intrusive emphasis on thrills and chills.

Between the start of the Second World War and the 1990s, US television evolved from a novel box with a handful of network channels in flickering black and white to a cultural necessity: all flat screens in brilliant colour with hundreds of broadcast, satellite and cable channel choices. In *Science on American Television*, historian Marcel Chotkowski LaFollette tracks and analyses how television treated science over those crucial 50 years — a follow-up to her 2008 analysis of science programmes on radio and early television, *Science on the Air* (University of Chicago Press).

Entertainment is the key to understanding the relationship between science and



Science on American Television: A History

MARCEL CHOTKOWSKI
LAFOLLETTE

University of Chicago
Press: 2012. 296 pp.
\$45

television. Towards the end of her well-researched, thought-provoking book, LaFollette explains, "The need to attract the largest possible audiences pushed television's version of science, whether intended as education or fiction, ever more toward sensationalization, politics, celebrities,

and representation and away from ... the thought and reasoning behind scientific conclusions and recommendations."

When the medium first emerged in the United States in the 1930s and 1940s, it followed a path already blazed by radio. The government licensed frequencies to commercial entities that paid a fee for broadcast rights, but also sold advertising and provided entertaining content in which to intersperse it. Under this commercial model, governmental efforts to increase the quality of broadcasts were sporadic and mostly anaemic. Attracting listeners and viewers became paramount. LaFollette notes that British radio and television, by contrast,

were supported and supervised by the government, which established standards for quality and diversity of programming.

Early on, says LaFollette, US networks experimented, mixing news and entertainment with science programmes and other cultural and educational fare. By modern standards, much of the science would be considered dry, wordy and stiff, as earnest scientists and science teachers declaimed while tapping blackboards with pointers.

Jazzier representations were on offer, however. The sitcom *Mister Peepers* (1952–55) starred Wally Cox as a science teacher peering through thick glasses — stereotypically smart but nerdy, and falling into absurd fixes. In the hit show *Watch Mr. Wizard* (1951–65), science-obsessed actor Don Herbert, with the help of a shifting coterie of child actors, tackled a weekly experiment, often of considerable sophistication.

A standout mixture of science, animation and live actors was the *Bell Laboratory Science Series*. It began in 1956 with the Frank Capra-directed *Our Mr. Sun*, a conversation among a scientist, a writer, the Sun and other characters, many of them animated. (Capra, who shot classics such as *It's a Wonderful Life* (1946), had a degree in chemical engineering from the California Institute of Technology.) The most popular of these films were seen by an estimated one-third of the television audience — about 24 million North Americans. But they were, first and foremost, entertainment.

In search of entertainment, the presentation of science on television grew increasingly artificial. Disney's *True-Life Adventures* nature films, recut for television, engaged young people with exotic species and regions. But the films anthropomorphized the animals and overshadowed the facts. One, *In Beaver Valley* (1950), shows beavers labouring with “stubborn resolve”, while “carefree” otters slide down snowy hills to zany music. Fictional medical doctors from Marcus Welby to Dr Kildare were heavy on charisma and light on science. LaFollette shows how even news reportage on the AIDS epidemic in the 1980s changed perspective, from scientific accuracy and searches for a cure to human interest, as homophobia and political debate took their toll.

Not all is bleak in LaFollette's history. The Public Broadcasting Service (PBS), a non-commercial network partly supported by the government and founded in 1969, is the natural home of art, opera, ballet, classical music — and science. Several series have given brilliant science communicators their say, such as Carl Sagan in the 1980 *Cosmos*, on the nature and history of the Universe and life, and Philip Morrison in the 1987 *The Ring of Truth*, on the process (and excitement) of scientific discovery. *Bill Nye the Science Guy* (1993–98) is a model of



Fictional forensics on the job in *CSI: Crime Scene Investigation*.

outreach to young people.

Meanwhile, imported programmes such as *The Nature of Things*, starring Canadian David Suzuki, and many from the BBC have been beacons in the gloom. Also strong are the *Nova* documentaries produced by Boston PBS station WGBH since 1974 and featuring compelling presenters such as astronomer Neil deGrasse Tyson or biologist Sean B. Carroll. Even the commercial series *CSI* models scientific reasoning as actors hypothesize, eliminate alternatives and finally settle on the most probable explanation.

When cable stations underwent their primary adaptive radiation in the 1980s and 1990s, science fans hoped that the ‘long tail’ of specialized programming would produce networks serving their interests. But even the National Geographic and Discovery channels have proved disappointing — presenting a mishmash of actual science and breathless forays into cryptozoology, crank medicine and paranormal phenomena. The network TLC's similar transition in focus from quality history, science, news, and technology to fluffier reality-based

programming is disheartening, given that it was set up by NASA and the US Department of Health, Education, and Welfare, and was once known as The Learning Channel.

If television is a vast wasteland, as the chair of the Federal Communications Commission famously said in 1961, it is especially inhospitable to science. LaFollette analyses attempts by the Smithsonian Institution, the American Association for the Advancement of Science and other scientific bodies to engage with television. These have often failed. The culture of professional scientists and the culture of an entertainment medium are destined to clash. However, we must find a way to improve the situation while working within commercial constraints. Americans spend about half of their leisure time in front of the descendants of those flickering boxes of the 1940s. Wasteland or not, television is simply too important to ignore. ■

Eugenie Scott is the executive director of the National Center for Science Education in Oakland, California, USA.
e-mail: scott@ncse.com

Correspondence

End the scandal of false cell lines

Cell-line misidentification is a continuing problem (see, for example, *Nature* **457**, 935–936; 2009), with an estimated 15% or more of human cell lines not being derived from the claimed source. This means that billions of dollars have been wasted over the past 45 years on producing misleading or false data. Although a few progressive journals and funding bodies demand that cell lines be authenticated, this practice needs to become standard and universal.

Cross-contamination between human cell lines was first described in 1967, yet these same cell lines continue to be used in published studies under their false names and tissue attributions (see *Nature Rev. Cancer* **10**, 441–448; 2010).

The method used to authenticate human cell lines is called short-tandem-repeat (STR) profiling, and a standard released by the American National Standards Institute provides protocols (see go.nature.com/cijups). The International Cell Line Authentication Committee (ICLAC) has produced helpful hints for testing authenticity (see go.nature.com/utig5g) and for incorporating authentication into good tissue-culture practice (see go.nature.com/jgip8v).

A rapidly expanding list that already contains more than 400 misidentified cell lines is freely accessible (see go.nature.com/soppaj) so that anyone can check whether a cell line has already been identified as false. Also, the US National Center for Biotechnology Information is developing a database of reference STR profiles of human cell lines (see go.nature.com/edfmcj).

Given that these resources are now available to the scientific community, and once all journals and funding bodies make authentication testing compulsory, the scandalous use of misidentified human cells should finally become a thing of the past.

John R. Masters* *University College London, UK.*

j.masters@ucl.ac.uk

**On behalf of the ICLAC. For a full list of signatories and competing financial interests, see go.nature.com/7vadcc.*

Settle discord over the Southern Ocean

It is alarming that the Commission for the Conservation of Antarctic Marine Living Resources (CCAMLR) failed to reach consensus over proposals to establish any new large-scale marine protected areas (MPAs) in the Southern Ocean this year (*Nature* <http://doi.org/jxb>; 2012). Some members set a worrying precedent by trying to dismiss advice previously agreed by the commission's scientific committee and working groups. The CCAMLR must deliver on its commitments, to uphold its reputation and convince the world that protecting the Antarctic marine ecosystem remains paramount.

The CCAMLR was committed to establishing MPAs by 2012, having designated its first MPA in 2009. Since then, the viewpoints of CCAMLR member states have polarized (see CCAMLR report XXXI; go.nature.com/fqqpdh). These fishing nations may fear that new MPAs could deny them future economic opportunities.

Food security is a vital global issue, and the Southern Ocean, home to one of the last underdeveloped sources of marine protein, Antarctic krill, could be critical. Governments need to recognize that conservation must go hand in hand with sustainable harvesting.

To ensure that their history of cooperation continues, all CCAMLR members should engage in the development process for MPA proposals, evaluating threats to biodiversity and identifying mutually

desirable outcomes. Joint MPA proposals are needed that incorporate data and analyses from as many members as possible. Input from non-governmental organizations that focus on development, as well as from conservationists, would help.

Philip N. Trathan *British Antarctic Survey, Natural Environment Research Council, Cambridge, UK.*
pnt@bas.ac.uk

Romania needs overseas reviewers

International review has had a positive influence on funding decisions in Romanian universities. As members of the first overseas grant-review panel to operate in the country, we are therefore concerned to learn that the research minister intends to discontinue the use of international referees (*Nature* <http://doi.org/jwn>; 2012) in a scheme originally drawn up to improve the country's scientific and ethical standing.

Every proposal we adjudicated — for postdoctoral fellowships or grants for early-stage researchers and senior principal investigators — was evaluated by at least three anonymous international experts and by external rapporteurs. These panels each examined about 100 applications, with particular emphasis on the merit of proposals and on the integrity of CVs. We were impressed by the overall quality of this innovative system.

Young Romanian scientists will be heartened to learn that this round of grant funding met all international standards of scrutiny and peer review. It will be most unfortunate for Romania to thwart this progress towards improving its international research status.

Illimar Altosaar* *University of Ottawa, Canada.*

altosaar@uottawa.ca

**On behalf of 9 co-authors (see go.nature.com/m7rdby).*

Put soil security on the global agenda

An international coalition of scientists has launched the Soil Carbon Initiative (see go.nature.com/onhgcv), convened by the United States Studies Centre and the Faculty of Agriculture at the University of Sydney in Australia, to bring policy on soil security in line with that on food and water security.

Soil security refers to the maintenance and improvement of soils worldwide so that they can continue to provide food, fibre and fresh water, contribute to energy and climate sustainability and help to maintain biodiversity and protect ecosystem goods and services.

Soil carbon needs to be monitored and managed — as was discussed during Global Soil Week in Berlin last month, at a meeting organized by the Institute for Advanced Sustainability Studies in Potsdam, Germany, and its international partners (see www.globalsoilweek.org). Also on the agenda were topics such as carbon trading and 'zero net land degradation' (see go.nature.com/d1y4g3).

Although scientists have made significant inroads into understanding soil function, international policy must keep pace with these advances.

Andrea Koch, Alex McBratney *University of Sydney, Australia.*
andrea.koch@sydney.edu.au
Rattan Lal *Ohio State University, Columbus, Ohio, USA.*

CONTRIBUTIONS

Correspondence may be submitted to **correspondence@nature.com** after consulting the author guidelines at **<http://go.nature.com/cmchno>**. Alternatively, readers may comment online: **www.nature.com/nature**.

FORUM Synthesis

A constructive debate

Synthetic chemistry has long been used to prepare useful compounds — especially those that are hard to obtain from natural sources. But synthetic biology is coming of age as an alternative strategy. A biologist and two chemists debate the merits of their fields' synthetic prowess.

Building with biology

JAY D. KEASLING

Synthetic biology is essentially the assembly of well-characterized biological components into a system that performs a function, such as synthesizing a chemical. The field has advanced to the point that one can imagine producing nearly any organic molecule — even those that are not produced naturally — in an engineered microorganism. This has enormous implications for the production of speciality and bulk chemicals, drugs and fuels.

Structurally complex pharmaceutical ingredients based on natural products are particularly good targets for microbial production (Fig. 1a), because they can be difficult to produce by conventional chemical synthesis. Even when chemical syntheses for natural products are available, the routes used are often too long and/or low-yielding for large-scale preparation. For commercial production, such molecules are therefore typically harvested from organisms that produce them naturally, or from a mutant that generates higher yields. Alternatively, a semi-synthesis can be used in which a precursor to a desired compound is obtained from an organism and then converted to the final product using organic synthesis. However, these approaches tend to be time-consuming and expensive.

Naturally occurring compounds can be produced in microorganisms by transferring product-specific enzymes, or even whole metabolic pathways, from rare and/or genetically intractable organisms to those that can be readily engineered¹. Similarly, fuels, bulk chemicals and speciality chemicals that are not produced naturally can be obtained by combining enzymes or metabolic pathways from different hosts into a single microorganism, or by engineering enzyme functions².

Synthetic biology has also been used for the large-scale semi-synthesis of natural products. For example, the antimalarial drug artemisinin is extracted from the plant *Artemisia annua*,



Figure 1 | Reaction vessels. **a**, Some biologists have argued that structurally complex molecules are best prepared in genetically engineered organisms, such as the bacterium *Escherichia coli* (pictured). **b**, Others think that chemical methods will endure as the most general option for synthesizing any desired compound.

but it is in short supply and is too expensive for most people with malaria³. By combining genes from *A. annua* and other organisms into a single strain of the yeast *Saccharomyces cerevisiae*, we have produced a fermentation process⁴ to make artemisinic acid — which can easily be converted to artemisinin using chemical methods⁵ — from simple sugars. The process is cost-effective, environmentally friendly and reliable, and is being developed for commercial production of the drug.

Synthetic biology has many advantages over chemical synthesis. First, the intermediates in a biosynthesis do not need to be purified before being used as substrates in the next reaction. Second, the many 'protection' and 'de-protection' steps typical of chemical synthesis — steps in which chemical groups are temporarily modified to stop them taking part in unwanted side reactions — can be avoided, because biosynthetic enzymes catalyse reactions only at the required positions in a substrate, avoiding side reactions at other groups. Third, most products of enzymatic reactions are racemically pure (the products form as just one of two possible mirror-image isomers), which is important for biologically active molecules. Fourth, cells can be engineered to secrete the final product, making it easier to purify. Finally, synthetic biology can use simple starting materials from renewable

sources, helping to reduce our dependence on oil-derived feedstocks.

Even so, if synthetic biology is to match the power of synthetic chemistry, several problems must be addressed. For example, the biosynthetic enzymes responsible for producing important natural products need to be identified, so that they can be used in syntheses. We must also improve our ability to design enzymes that catalyse reactions not found in nature⁶ if we are to expand the types of chemistry that can be engineered into cells. And we must learn how to reliably engineer biosynthetic pathways to achieve desired outcomes.

I envisage a day when customized cells will be built as catalysts for the biosynthesis of natural products, by designing chromosomes that harbour genes encoding the necessary biosynthetic pathways and also the minimal set of genes needed to construct the host organism from minimal nutrients. That day is fast approaching.

Jay D. Keasling is in the Department of Chemical and Biomolecular Engineering, and the Department of Bioengineering, University of California, Berkeley, Berkeley, California 94720, USA. He is also at the Lawrence Berkeley National Laboratory and at the Joint BioEnergy Institute in California.
e-mail: keasling@berkeley.edu

Practical chemistry

ABRAHAM MENDOZA & PHIL S. BARAN

Since the birth of synthetic chemistry about 180 years ago, society has loved the wonders bestowed by the field, such as life-saving medicines, pest control and molecules that light up telephone displays, yet has harshly criticized it as being solely responsible for pollution and environmental harm. Synthetic biology emerged as an alternative for constructing molecules only about ten years ago, but some have already proclaimed⁷ that it will supplant chemical synthesis. No one should doubt the usefulness of synthetic biology, or its potential to shorten synthetic routes and reduce waste in chemical production. But we are convinced that synthetic chemistry will continue to dominate for the foreseeable future (Fig. 1b), for three main reasons.

The first reason is that chemical synthesis is the best way to solve supply problems. For decades, synthetic chemistry has provided sufficient quantities of agrochemicals, medicines, perfumes and materials for society's needs. The pharmaceutical industry in particular relies on chemical methods for the large-scale production of most small-molecule drugs. The majority of these compounds are based on molecular structures not found in nature, which means that they cannot be prepared through enzymatic processes and are likely to be toxic to the host organisms used in synthetic biology. Synthetic biology has had a crucial impact on the commercial production of some medicines derived from complex natural products, such as artemisinin² and the anticancer drug paclitaxel (Taxol)⁸. But natural products are essentially the only compounds for which biological syntheses can compete with chemical ones, because evolution has optimized the biosynthesis of those products over time.

So the supply of chemicals is best addressed by synthetic chemistry, unless a specific natural product is required in large quantities — and even then, semi-synthetic strategies involving a few chemical steps are often required. In fact, total chemical syntheses of natural products are becoming increasingly efficient and scalable, as demonstrated by the impressive routes used to make tetracycline antibiotics⁹ and the anticancer agent eribulin¹⁰. A practical chemical synthesis of artemisinin has also now emerged¹¹ that could form the basis of an industrial-scale process for making the drug, and a large-scale synthesis of Taxol is being developed¹².

Optimizing the properties of useful compounds, or adapting their functions to new applications, often requires modification of their molecular structures. The second reason that synthetic chemistry will endure is that chemical methods provide a reliable

set of tools to do this in many fundamentally different cases. Moreover, unlike biological syntheses, chemical syntheses can often be developed and implemented rapidly, which is a great advantage.

The third reason is that chemistry excels in the invention of unnatural molecules that have desirable physical properties — such as dyes for printable organic solar cells, fluorescent probes for biological research or radiolabelled drugs used in medicine. The molecular needs of vibrant modern fields such as supramolecular chemistry, chemical biology and nanotechnology can be addressed only by synthetic chemistry. This is partly because the required molecules contain motifs that nature cannot assemble or that would be toxic to host organisms when biosynthesized at the concentrations required for a practical production process. The exponential pace of development of these fields also means that the compounds needed are continuously changing, limiting the time available to synthesize and evaluate them. General chemical methods that can be applied quickly are therefore much more suitable for making such compounds than bioengineering.

Over the years, many people have advocated alternatives to synthetic chemistry or expressed the opinion that it is already a mature field and

that all future advances will be incremental at best. But the field is as lively as ever: a seemingly infinite number of problems are waiting to be solved, and legions of talented students are eager to solve them. Synthetic biology surely has a bright future, but no approach to making molecules is more generally useful and has such seemingly limitless potential than synthetic chemistry. It is here to stay. ■

Abraham Mendoza and Phil S. Baran are in the Department of Chemistry, The Scripps Research Institute, La Jolla, California 92037, USA.

e-mail: pbaran@scripps.edu

1. Malpartida, F. & Hopwood, D. A. *Nature* **309**, 462–464 (1984).
2. Steen, E. J. *et al.* *Nature* **463**, 559–562 (2010).
3. Enserink, M. *Science* **307**, 33 (2005).
4. Ro, D. K. *et al.* *Nature* **440**, 940–943 (2006).
5. Acton, N. & Roth, R. J. *J. Org. Chem.* **57**, 3610–3614 (1992).
6. Siegel, J. B. *et al.* *Science* **329**, 309–313 (2010).
7. McDaniel, R. & Weiss, R. *Curr. Opin. Biotechnol.* **16**, 476–483 (2005).
8. Bringi, V., Kadkade, P. G., Prince, C. L. & Roach, B. L. US patent 7264951 (2007).
9. Charest, M. G., Lerner, C. D., Brubaker, J. D., Siegel, D. R. & Myers, A. G. *Science* **308**, 395–398 (2005).
10. Ledford, H. *Nature* **468**, 608–609 (2010).
11. Zhu, C. & Cook, S. P. *J. Am. Chem. Soc.* **134**, 13577–13579 (2012).
12. Mendoza, A., Ishihara, Y. & Baran, P. S. *Nature Chem.* **4**, 21–25 (2012).

CELL BIOLOGY

All clear for ribosome landing

The discovery of a dramatic structural rearrangement that is stabilized by an RNA scaffold helps to explain how nascent proteins are delivered for export from the cell cytoplasm. SEE LETTER P.271

HARRIS D. BERNSTEIN

Protein sorting within a cell is not an easy undertaking. The synthesis of many proteins destined to leave the cell or to become part of a cellular membrane must be coupled with their transport across or into the appropriate membrane. A universal RNA–protein complex called the signal recognition particle (SRP) plays an essential role in this process by interacting with ribosomes, the cell's protein-synthesizing factories, while they are engaged in protein translation. SRP then escorts the translating ribosomes to a cellular organelle known as the endoplasmic reticulum or, in bacteria, to the cytoplasmic membrane, where they dock onto a transport channel called the Sec complex, or SecYEG in bacteria. SRP must presumably be displaced from the ribosome for docking to happen, but

the mechanism of this molecular exchange has been an enigma. On page 271 of this issue, Shen *et al.*¹ provide compelling evidence that a remarkable conformational change driven by the RNA component of SRP enables the ribosome to deliver its protein cargo efficiently.

Most membrane and secreted proteins that emerge from translating ribosomes carry a signal peptide — a sequence at their amino terminus that earmarks them for export from the cytoplasm. SRP recognizes and binds to this peptide and then interacts with a membrane receptor (FtsY) before releasing its nascent-protein cargo and transferring the ribosome to SecYEG (Fig. 1). This co-translational mode of protein targeting ensures that proteins destined to leave the cytoplasm begin their journey before they aggregate or fold into a structure that cannot fit through the SecYEG channel.

Although SRP has undergone dramatic

Practical chemistry

ABRAHAM MENDOZA & PHIL S. BARAN

Since the birth of synthetic chemistry about 180 years ago, society has loved the wonders bestowed by the field, such as life-saving medicines, pest control and molecules that light up telephone displays, yet has harshly criticized it as being solely responsible for pollution and environmental harm. Synthetic biology emerged as an alternative for constructing molecules only about ten years ago, but some have already proclaimed⁷ that it will supplant chemical synthesis. No one should doubt the usefulness of synthetic biology, or its potential to shorten synthetic routes and reduce waste in chemical production. But we are convinced that synthetic chemistry will continue to dominate for the foreseeable future (Fig. 1b), for three main reasons.

The first reason is that chemical synthesis is the best way to solve supply problems. For decades, synthetic chemistry has provided sufficient quantities of agrochemicals, medicines, perfumes and materials for society's needs. The pharmaceutical industry in particular relies on chemical methods for the large-scale production of most small-molecule drugs. The majority of these compounds are based on molecular structures not found in nature, which means that they cannot be prepared through enzymatic processes and are likely to be toxic to the host organisms used in synthetic biology. Synthetic biology has had a crucial impact on the commercial production of some medicines derived from complex natural products, such as artemisinin² and the anticancer drug paclitaxel (Taxol)⁸. But natural products are essentially the only compounds for which biological syntheses can compete with chemical ones, because evolution has optimized the biosynthesis of those products over time.

So the supply of chemicals is best addressed by synthetic chemistry, unless a specific natural product is required in large quantities — and even then, semi-synthetic strategies involving a few chemical steps are often required. In fact, total chemical syntheses of natural products are becoming increasingly efficient and scalable, as demonstrated by the impressive routes used to make tetracycline antibiotics⁹ and the anticancer agent eribulin¹⁰. A practical chemical synthesis of artemisinin has also now emerged¹¹ that could form the basis of an industrial-scale process for making the drug, and a large-scale synthesis of Taxol is being developed¹².

Optimizing the properties of useful compounds, or adapting their functions to new applications, often requires modification of their molecular structures. The second reason that synthetic chemistry will endure is that chemical methods provide a reliable

set of tools to do this in many fundamentally different cases. Moreover, unlike biological syntheses, chemical syntheses can often be developed and implemented rapidly, which is a great advantage.

The third reason is that chemistry excels in the invention of unnatural molecules that have desirable physical properties — such as dyes for printable organic solar cells, fluorescent probes for biological research or radiolabelled drugs used in medicine. The molecular needs of vibrant modern fields such as supramolecular chemistry, chemical biology and nanotechnology can be addressed only by synthetic chemistry. This is partly because the required molecules contain motifs that nature cannot assemble or that would be toxic to host organisms when biosynthesized at the concentrations required for a practical production process. The exponential pace of development of these fields also means that the compounds needed are continuously changing, limiting the time available to synthesize and evaluate them. General chemical methods that can be applied quickly are therefore much more suitable for making such compounds than bioengineering.

Over the years, many people have advocated alternatives to synthetic chemistry or expressed the opinion that it is already a mature field and

that all future advances will be incremental at best. But the field is as lively as ever: a seemingly infinite number of problems are waiting to be solved, and legions of talented students are eager to solve them. Synthetic biology surely has a bright future, but no approach to making molecules is more generally useful and has such seemingly limitless potential than synthetic chemistry. It is here to stay. ■

Abraham Mendoza and Phil S. Baran are in the Department of Chemistry, The Scripps Research Institute, La Jolla, California 92037, USA.

e-mail: pbaran@scripps.edu

1. Malpartida, F. & Hopwood, D. A. *Nature* **309**, 462–464 (1984).
2. Steen, E. J. *et al.* *Nature* **463**, 559–562 (2010).
3. Enserink, M. *Science* **307**, 33 (2005).
4. Ro, D. K. *et al.* *Nature* **440**, 940–943 (2006).
5. Acton, N. & Roth, R. J. *J. Org. Chem.* **57**, 3610–3614 (1992).
6. Siegel, J. B. *et al.* *Science* **329**, 309–313 (2010).
7. McDaniel, R. & Weiss, R. *Curr. Opin. Biotechnol.* **16**, 476–483 (2005).
8. Bringi, V., Kadkade, P. G., Prince, C. L. & Roach, B. L. US patent 7264951 (2007).
9. Charest, M. G., Lerner, C. D., Brubaker, J. D., Siegel, D. R. & Myers, A. G. *Science* **308**, 395–398 (2005).
10. Ledford, H. *Nature* **468**, 608–609 (2010).
11. Zhu, C. & Cook, S. P. *J. Am. Chem. Soc.* **134**, 13577–13579 (2012).
12. Mendoza, A., Ishihara, Y. & Baran, P. S. *Nature Chem.* **4**, 21–25 (2012).

CELL BIOLOGY

All clear for ribosome landing

The discovery of a dramatic structural rearrangement that is stabilized by an RNA scaffold helps to explain how nascent proteins are delivered for export from the cell cytoplasm. SEE LETTER P.271

HARRIS D. BERNSTEIN

Protein sorting within a cell is not an easy undertaking. The synthesis of many proteins destined to leave the cell or to become part of a cellular membrane must be coupled with their transport across or into the appropriate membrane. A universal RNA–protein complex called the signal recognition particle (SRP) plays an essential role in this process by interacting with ribosomes, the cell's protein-synthesizing factories, while they are engaged in protein translation. SRP then escorts the translating ribosomes to a cellular organelle known as the endoplasmic reticulum or, in bacteria, to the cytoplasmic membrane, where they dock onto a transport channel called the Sec complex, or SecYEG in bacteria. SRP must presumably be displaced from the ribosome for docking to happen, but

the mechanism of this molecular exchange has been an enigma. On page 271 of this issue, Shen *et al.*¹ provide compelling evidence that a remarkable conformational change driven by the RNA component of SRP enables the ribosome to deliver its protein cargo efficiently.

Most membrane and secreted proteins that emerge from translating ribosomes carry a signal peptide — a sequence at their amino terminus that earmarks them for export from the cytoplasm. SRP recognizes and binds to this peptide and then interacts with a membrane receptor (FtsY) before releasing its nascent-protein cargo and transferring the ribosome to SecYEG (Fig. 1). This co-translational mode of protein targeting ensures that proteins destined to leave the cytoplasm begin their journey before they aggregate or fold into a structure that cannot fit through the SecYEG channel.

Although SRP has undergone dramatic

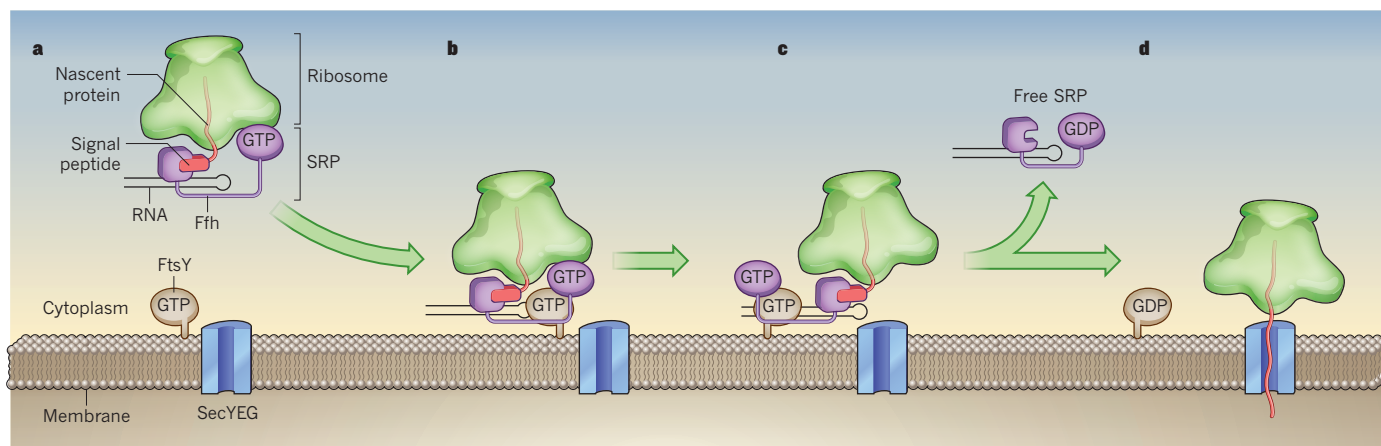


Figure 1 | Handover of translating ribosomes. **a**, The signal recognition particle (SRP) has a protein (Ffh) component and an RNA component that forms a hairpin structure. Ffh recognizes and binds to signal peptides on nascent proteins during protein translation. **b**, The GTPase domain of Ffh (labelled GTP) subsequently interacts with the GTPase domain of FtsY — a receptor that resides in the endoplasmic reticulum or the bacterial cytoplasmic membrane. In bacteria, FtsY recruits the SecYEG

protein-translocation channel. **c**, Shen *et al.*¹ report that SecYEG stimulates a dramatic relocalization of the two interacting GTPases from the tetraloop region of SRP RNA to an evolutionarily conserved distal sequence. **d**, Reorientation of the GTPase complex facilitates both the docking of the translating ribosome onto SecYEG and hydrolysis of the two GTP nucleotides to GDP. GTP hydrolysis stimulates the recycling of SRP and FtsY.

expansions and contractions during evolution, even the simplest bacterial SRPs contain two highly conserved core elements — a protein (Ffh) that binds to the signal peptide and an elongated, roughly 100-nucleotide RNA that forms a 'hairpin'. Despite this relative simplicity, SRP must not only distinguish signal peptides from the bulk of nascent polypeptides, but also release them at the right place and time.

Many aspects of the protein-targeting cycle mediated by SRP are well understood. For instance, it is known that the signal-peptide-recognition and RNA-binding activities of Ffh both reside in a single domain, called the M domain. Also, both Ffh and FtsY contain a GTPase domain that hydrolyses the nucleotide GTP to GDP and thereby acts as a regulatory switch. In the presence of a signal peptide, SRP RNA catalyses an interaction between the GTPase domains of Ffh and FtsY, and the binding of GTP brings the two domains into close proximity^{2,3}. Subsequently, structural rearrangements in the GTPase domains promote GTP hydrolysis, disassembly of the SRP-FtsY complex and dissociation of SRP from the ribosome⁴. Moreover, in the bacterium *Escherichia coli*, FtsY seems to recruit SecYEG to ensure that nascent polypeptides are released at the correct location⁵.

Despite much progress, however, it has remained unclear how the transfer of ribosome-nascent-protein complexes to SecYEG is coordinated with the enzymatic activity of the GTPase domain and the recycling of the SRP-FtsY complex. To complicate matters, SRP and SecYEG bind to overlapping sites on L23, a ribosomal protein located at the point where nascent polypeptides emerge from a tunnel in the large subunit of the ribosome⁶. SRP must therefore be reoriented without prematurely releasing its ribosome-nascent-protein cargo.

A clue as to how the transfer might occur

emerged from a crystal structure of the SRP-FtsY complex⁷ that captured the interacting GTPase domains bound to a sequence near the distal end of the SRP RNA hairpin. This configuration was unexpected, because previous work⁸ had shown that the complex is stabilized by bonds between the FtsY GTPase and a 4-nucleotide turn (a tetraloop) at the top of the hairpin. The structure⁷ suggested that the two domains might travel together to a remote 'landing pad' more than 100 Å away after first interacting at the tetraloop. Such spectacular molecular gymnastics would be possible only because the two domains of Ffh are connected by a flexible linker.

To obtain direct evidence for this putative large-scale movement and to glean its functional significance, Shen *et al.* attached a dye to the FtsY GTPase domain and a different dye to the distal end of SRP RNA. They then measured the distance between the dyes throughout the SRP cycle using an innovative method called single-molecule fluorescence resonance energy transfer (smFRET). In this way, they could obtain precise positional information about individual Ffh-FtsY GTPase complexes.

The authors made several intriguing observations. They not only showed that the Ffh-FtsY GTPase complex relocates to the far end of the SRP RNA hairpin, but also obtained evidence that the complex undergoes a lengthy 'search process' before landing at its new destination. This migration is stimulated by SecYEG and requires a conformational change within the GTPase complex that primes it for GTP hydrolysis. The relocation of the complex is also required for both GTP hydrolysis and effective delivery of the nascent protein to SecYEG. Taken together, these results suggest that the GTPase complex is brought to the brink of activation, whereupon its relocation to the distal end of the RNA exposes the nascent

protein's exit site on the ribosome and allows the ribosome to dock onto SecYEG (Fig. 1c, d). The relocation also stimulates GTP hydrolysis by the complex and SRP recycling.

Although Shen and colleagues' work provides notable mechanistic insights, it also raises several questions. For one, how does SecYEG trigger the reorientation of the Ffh-FtsY GTPase complex and the subsequent hydrolysis of GTP? Also, in the likely event that the signal peptide remains bound to the M domain of Ffh upon relocalization of the GTPase complex, what catalyses cargo release? One possibility is that the movement of the complex reduces the affinity of Ffh for the signal peptide by repositioning another segment of Ffh that has been proposed⁹ to participate in substrate recognition. Finally, how can these results be reconciled with the observation¹⁰ that the distal end of SRP RNA is not required for a cell to survive? It is conceivable that, even in the absence of a distal binding site, transient displacement of the GTPase complex from the tetraloop allows the translating ribosomes to be transferred to SecYEG, albeit with reduced efficiency.

Perhaps the most striking implication of Shen and co-workers' study is that the two ends of the SRP RNA hairpin have distinct functions at different stages of the targeting cycle (Fig. 1). We take it for granted that proteins can be multifunctional, but much less is known about the capabilities of the many RNAs found in nature. As the characterization of RNA proceeds, the message that even a small nucleic-acid sequence can encode considerable functional information is certainly worth bearing in mind. ■

Harris D. Bernstein is in the Genetics and Biochemistry Branch, National Institute of Diabetes and Digestive and Kidney Diseases,

National Institutes of Health, Bethesda,
Maryland 20892-0538, USA.
e-mail: harris_bernstein@nih.gov

- Shen, K., Arslan, S., Akopian, D., Ha, T. & Shan, S. O. *Nature* **492**, 271–275 (2012).
- Bradshaw, N., Neher, S. B., Booth, D. S. & Walter, P. *Science* **323**, 127–130 (2009).
- Shan, S., Stroud, R. M. & Walter, P. *PLoS Biol.* **2**, e320 (2004).
- Zhang, X., Schaffitzel, C., Ban, N. & Shan, S.

- Proc. Natl Acad. Sci. USA* **106**, 1754–1759 (2009).
- Angelini, S., Deitermann, S. & Koch, H. G. *EMBO Rep.* **6**, 476–481 (2005).
- Gu, S.-Q., Peske, F., Wieden, H.-J., Rodnina, M. V. & Wintermeyer, W. *RNA* **9**, 566–573 (2003).
- Ataide, S. F. et al. *Science* **331**, 881–886 (2011).
- Shen, K. & Shan, S. *Proc. Natl Acad. Sci. USA* **107**, 7698–7703 (2010).
- Newitt, J. A. & Bernstein, H. D. *Eur. J. Biochem.* **245**, 720–729 (1997).
- Batey, R. T., Rambo, R. P., Lucast, L., Rha, B. & Doudna, J. A. *Science* **287**, 1232–1239 (2000).

ASTROPHYSICS

A pas de trois birth for wide binary stars

The widest binary star systems pose a challenge to theory: true stellar twins could not form so far apart. Simulations suggest these twins are in fact triplets, two of which masquerade as one star and cast out the third. [SEE LETTER P.221](#)

KEIVAN GUADALUPE STASSUN

About half of all stars are found in pairs, presumably because they were born as twins. Although there is no consensus theory for exactly how binary stars form, it is gratifying that most cases satisfy a basic check on the twin-birth hypothesis: that binary-star orbits be small enough to fit within the proto-stellar ‘cloud cores’ in which stars form. Most cases, that is, but not all. Some binary stars have orbits comparable in size to entire star clusters. In this issue (page 221), Reipurth and Mikkola¹ describe simulations showing that such ultra-wide binary systems may be explained if they are born not as twins, but rather as triplets that undergo an intricate dance — a dance that at first protects but later expels one of the three siblings*.

The existence of wide binary star systems has been known about for a long time², and some of the best examples are very familiar. Our nearest stellar neighbour, Proxima Centauri, is a gravitationally bound³ companion of our next-nearest, α Centauri, even though the two are physically separated by about 0.1 parsecs (about 15,000 times the Earth–Sun separation, or about 500 times the size of the Solar System). In the past few years, large astronomical surveys have discovered^{4,5} thousands of such systems (Fig. 1), comprising a few per cent of all binary star systems.

One explanation is that the stars in these ultra-wide systems were not born together, but were brought together after birth. Indeed, simulations have shown^{6–8} that two stars can be paired through a mutual, ‘soft’ gravitational capture when a cluster of hundreds of stars slowly disperses after formation. This

mechanism is appealing for at least three reasons. First, it explains why the widest binary systems have separations comparable to the sizes of star clusters. Second, it explains how such wide binaries survive the harsh, crowded environments of star clusters: they do not have to, because they come together only on leaving the cluster. Third, observations of wide binary systems show⁴ a strikingly bimodal distribution of separations, which seems to be reproduced in cluster-dispersal simulations.

The simulations by Reipurth and Mikkola represent a fresh take on the problem. They

follow the dynamical gravitational interaction of each of 180,000 stellar triplets, from their birth in cloud cores up to an age of 100 million years, when star clusters such as the Pleiades complete their formation and begin to disperse. These simulations mimic the variety of perturbations, collisions, flybys and slingshots that three gravitationally interacting bodies will exert on one another.

In the authors’ simulations, 90% of the triplets disrupt themselves — but about 10% persist. Seen from a distance, these survivors do not resemble triplets so much as wide pairs: two of the three stars form a tight pair. The simulations show that these triplets survive because they initially have a compact configuration — necessary to fit within their natal clouds — that permits them to withstand the jostling of a thousand stellar neighbours in the birth cluster. But over time, the three siblings develop a rivalry that brings two of them tightly together at the expense of the third, which is cast out to an increasingly distant orbit about the tight pair. These ‘hierarchical’ triplets, the authors argue, are what observers see as wide binaries: the tight pair masquerades as a single star owing to the limited imaging resolution of our telescopes.

It remains to be determined whether this hypothesis is consistent with all of the observational data on ultra-wide binaries. One high-resolution imaging study showed⁹ that as many as 30% of such binaries were indeed triplets. By contrast, an analysis of the radial velocities of ultra-wide binary systems found only about 10% to be triplets¹⁰. To ascertain whether all apparently wide binaries are in fact triplets, both types of measurement must be applied to a large sample of systems. Furthermore, certain

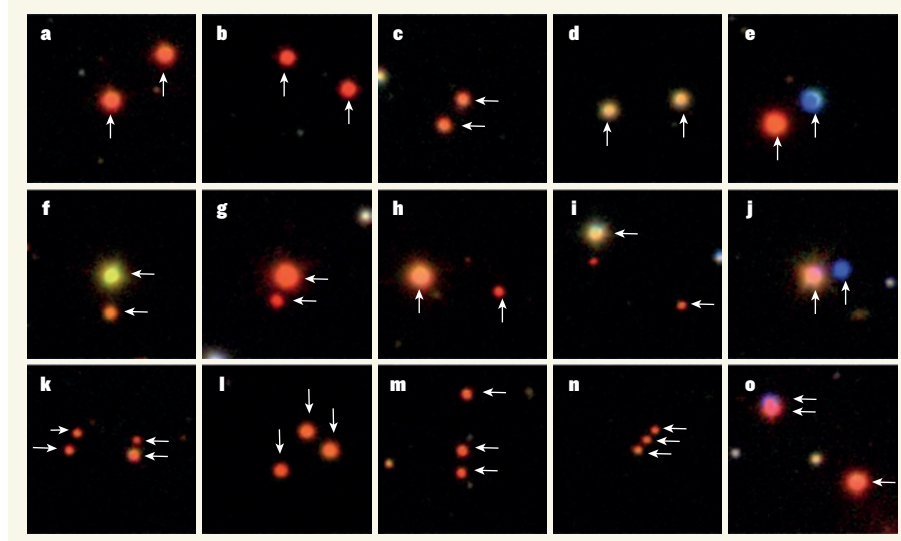


Figure 1 | Wide binary star systems. Three-colour composite images of a sample of ultra-wide binary star systems, out of more than 1,300 such systems identified in the Sloan Digital Sky Survey⁴. Each image is 50 arcseconds on a side, corresponding to physical separations of the binary systems of up to 1 parsec. The systems include ‘identical twins’ (a–d) and non-identical twins (e–j). In some cases, the systems are found to be triplets (l–o) or even quadruplets (k). Reipurth and Mikkola show¹ that one explanation for ultra-wide binary systems is that they are born as triplets.

S. DHITAL (VANDERBILT UNIV., BOSTON UNIV.)

*This article and the paper under discussion¹ were published online on 5 December 2012.

National Institutes of Health, Bethesda, Maryland 20892-0538, USA.
e-mail: harris_bernstein@nih.gov

- Shen, K., Arslan, S., Akopian, D., Ha, T. & Shan, S. O. *Nature* **492**, 271–275 (2012).
- Bradshaw, N., Neher, S. B., Booth, D. S. & Walter, P. *Science* **323**, 127–130 (2009).
- Shan, S., Stroud, R. M. & Walter, P. *PLoS Biol.* **2**, e320 (2004).
- Zhang, X., Schaffitzel, C., Ban, N. & Shan, S.

- Proc. Natl Acad. Sci. USA* **106**, 1754–1759 (2009).
- Angelini, S., Deitermann, S. & Koch, H. G. *EMBO Rep.* **6**, 476–481 (2005).
- Gu, S.-Q., Peske, F., Wieden, H.-J., Rodnina, M. V. & Wintermeyer, W. *RNA* **9**, 566–573 (2003).
- Ataide, S. F. et al. *Science* **331**, 881–886 (2011).
- Shen, K. & Shan, S. *Proc. Natl Acad. Sci. USA* **107**, 7698–7703 (2010).
- Newitt, J. A. & Bernstein, H. D. *Eur. J. Biochem.* **245**, 720–729 (1997).
- Batey, R. T., Rambo, R. P., Lucast, L., Rha, B. & Doudna, J. A. *Science* **287**, 1232–1239 (2000).

ASTROPHYSICS

A pas de trois birth for wide binary stars

The widest binary star systems pose a challenge to theory: true stellar twins could not form so far apart. Simulations suggest these twins are in fact triplets, two of which masquerade as one star and cast out the third. [SEE LETTER P.221](#)

KEIVAN GUADALUPE STASSUN

About half of all stars are found in pairs, presumably because they were born as twins. Although there is no consensus theory for exactly how binary stars form, it is gratifying that most cases satisfy a basic check on the twin-birth hypothesis: that binary-star orbits be small enough to fit within the proto-stellar ‘cloud cores’ in which stars form. Most cases, that is, but not all. Some binary stars have orbits comparable in size to entire star clusters. In this issue (page 221), Reipurth and Mikkola¹ describe simulations showing that such ultra-wide binary systems may be explained if they are born not as twins, but rather as triplets that undergo an intricate dance — a dance that at first protects but later expels one of the three siblings*.

The existence of wide binary star systems has been known about for a long time², and some of the best examples are very familiar. Our nearest stellar neighbour, Proxima Centauri, is a gravitationally bound³ companion of our next-nearest, α Centauri, even though the two are physically separated by about 0.1 parsecs (about 15,000 times the Earth–Sun separation, or about 500 times the size of the Solar System). In the past few years, large astronomical surveys have discovered^{4,5} thousands of such systems (Fig. 1), comprising a few per cent of all binary star systems.

One explanation is that the stars in these ultra-wide systems were not born together, but were brought together after birth. Indeed, simulations have shown^{6–8} that two stars can be paired through a mutual, ‘soft’ gravitational capture when a cluster of hundreds of stars slowly disperses after formation. This

mechanism is appealing for at least three reasons. First, it explains why the widest binary systems have separations comparable to the sizes of star clusters. Second, it explains how such wide binaries survive the harsh, crowded environments of star clusters: they do not have to, because they come together only on leaving the cluster. Third, observations of wide binary systems show⁴ a strikingly bimodal distribution of separations, which seems to be reproduced in cluster-dispersal simulations.

The simulations by Reipurth and Mikkola represent a fresh take on the problem. They

follow the dynamical gravitational interaction of each of 180,000 stellar triplets, from their birth in cloud cores up to an age of 100 million years, when star clusters such as the Pleiades complete their formation and begin to disperse. These simulations mimic the variety of perturbations, collisions, flybys and slingshots that three gravitationally interacting bodies will exert on one another.

In the authors’ simulations, 90% of the triplets disrupt themselves — but about 10% persist. Seen from a distance, these survivors do not resemble triplets so much as wide pairs: two of the three stars form a tight pair. The simulations show that these triplets survive because they initially have a compact configuration — necessary to fit within their natal clouds — that permits them to withstand the jostling of a thousand stellar neighbours in the birth cluster. But over time, the three siblings develop a rivalry that brings two of them tightly together at the expense of the third, which is cast out to an increasingly distant orbit about the tight pair. These ‘hierarchical’ triplets, the authors argue, are what observers see as wide binaries: the tight pair masquerades as a single star owing to the limited imaging resolution of our telescopes.

It remains to be determined whether this hypothesis is consistent with all of the observational data on ultra-wide binaries. One high-resolution imaging study showed⁹ that as many as 30% of such binaries were indeed triplets. By contrast, an analysis of the radial velocities of ultra-wide binary systems found only about 10% to be triplets¹⁰. To ascertain whether all apparently wide binaries are in fact triplets, both types of measurement must be applied to a large sample of systems. Furthermore, certain

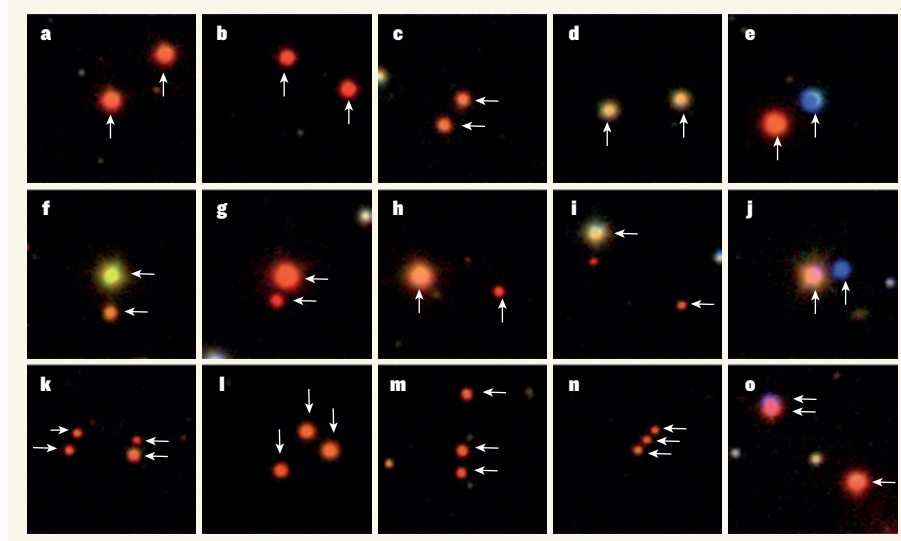


Figure 1 | Wide binary star systems. Three-colour composite images of a sample of ultra-wide binary star systems, out of more than 1,300 such systems identified in the Sloan Digital Sky Survey⁴. Each image is 50 arcseconds on a side, corresponding to physical separations of the binary systems of up to 1 parsec. The systems include ‘identical twins’ (a–d) and non-identical twins (e–j). In some cases, the systems are found to be triplets (l–o) or even quadruplets (k). Reipurth and Mikkola show¹ that one explanation for ultra-wide binary systems is that they are born as triplets.

S. DHITAL (VANDERBILT UNIV., BOSTON UNIV.)

*This article and the paper under discussion¹ were published online on 5 December 2012.

assumptions of Reipurth and Mikkola's simulations will need to be checked — such as that the three stars in a triplet begin their lives with equal masses. It will be necessary to assess how important these assumptions are to the study's main conclusions.

Ongoing surveys should be able to test some of Reipurth and Mikkola's predictions, including the proportion of triplets in stellar populations of different ages and the number of triplets that are dominated by the mass in the tight binary as opposed to the mass of the third star. The work also presents speculations that may be testable by other means, such as the possibility that some tight pairs within triplets spiral towards one another and merge, creating a true wide binary. Moreover, as extrasolar planets continue to be found in various types of stellar family, it would be valuable to have quantitative predictions for the survivability of planets from both the triplets-as-twins and cluster-dispersal mechanisms. As for our neighbouring wide binary, Proxima Centauri and α Centauri, it is in fact a triplet: α Centauri

is a tight pair, with a planet to boot¹¹. ■

Keivan Guadalupe Stassun is in the *Department of Physics and Astronomy, Vanderbilt University, Nashville, Tennessee 37235, USA, and the Department of Physics, Fisk University, Nashville.*
e-mail: keivan.stassun@vanderbilt.edu

1. Reipurth, B. & Mikkola, S. *Nature* **492**, 221–224 (2012).
2. Innes, R. T. A. *Union Obs. Circ.* **30**, 235–236 (1915).
3. Wertheimer, J. G. & Laughlin, G. *Astron. J.* **132**, 1995–1997 (2006).
4. Dhital, S., West, A. A., Stassun, K. G. & Bochanski, J. J. *Astron. J.* **139**, 2566–2586 (2010).
5. Sesar, B., Ivezić, Ž. & Jurić, M. *Astrophys. J.* **689**, 1244–1273 (2008).
6. Bate, M. R. & Bonnell, I. A. *Mon. Not. R. Astron. Soc.* **356**, 1201–1221 (2005).
7. Kouwenhoven, M. B. N. *et al. Mon. Not. R. Astron. Soc.* **404**, 1835–1848 (2010).
8. Moeckel, N. & Clarke, C. J. *Mon. Not. R. Astron. Soc.* **415**, 1179–1187 (2011).
9. Law, N. M., Dhital, S., Kraus, A., Stassun, K. G. & West, A. A. *Astrophys. J.* **720**, 1727–1737 (2010).
10. Dhital, S. *et al. Astron. J.* **143**, 67 (2012).
11. Dumusque, X. *et al. Nature* **491**, 207–211 (2012).

made it possible to study dust absorption at high redshift. Buat *et al.* used all of these data to study the dependence of dust absorption on a variety of global galaxy properties, such as observed luminosity, stellar mass and the slope of the spectrum in the ultraviolet, for a large sample of galaxies with redshifts in the range 0.95–2.2. At these redshifts, optical observations sample the stars' emission of ultraviolet light — the wavelength regime at which massive stars emit most of their light and suffer the most absorption by dust.

Buat and colleagues used a detailed computer code⁸ that derives properties of galaxies by fitting the light emission predicted from the computations to observations made across the wavelength spectrum. They concluded that the inclusion of infrared data improved the determination of dust-absorption parameters. Interestingly, they found a wide range of values for these parameters, which they postulate could be due to the large variations in the extinction curves for galaxies. They infer that a constant extinction curve for all galaxies at all redshifts cannot be assumed, and that variations should be allowed for when computing the amount of reprocessed ultraviolet light.

The authors' finding that infrared data are crucial for studies of the effects of absorption by dust in individual galaxies makes sense — previous work has shown how notoriously difficult it is to predict far-infrared emission from observed ultraviolet emission⁹. The study's goal was to find dependences of the dust-absorption parameters on global galaxy properties, which Buat *et al.* hoped to use to correct large samples of galaxies in a statistical way. Although they did identify some trends, there is large scatter about the averages of the parameters that needs to be further understood. This serves as a reminder that if the galaxy property one is trying to calculate is strongly dependent on an assumed dust extinction curve, then one should be cautious about the result. Studies such as this are essential for determining the reliability of dust-absorption corrections. These corrections are pivotal in determining the extent to which massive star formation in galaxies is hidden from optical view. ■

Amy Barger is in the *Department of Astronomy, University of Wisconsin-Madison, Madison, Wisconsin 53706, USA.*
e-mail: barger@astro.wisc.edu

1. Buat, V. *et al. Astron. Astrophys.* **545**, A141 (2012).
2. Wijesinghe, D. B. *et al. Mon. Not. R. Astron. Soc.* **410**, 2291–2301 (2011).
3. Wild, V. *et al. Mon. Not. R. Astron. Soc.* **417**, 1760–1786 (2011).
4. Conroy, C., Schiminovich, D. & Blanton, M. R. *Astrophys. J.* **718**, 184–198 (2010).
5. Noll, S. & Pierini, D. *Astron. Astrophys.* **444**, 137–155 (2005).
6. Buat, V. *et al. Astron. Astrophys.* **533**, A93 (2011).
7. Calzetti, D. *et al. Astrophys. J.* **533**, 682–695 (2000).
8. Noll, S. *et al. Astron. Astrophys.* **507**, 1793–1813 (2009).
9. Chapman, S. C. *et al. Mon. Not. R. Astron. Soc.* **319**, 318–330 (2000).

ASTRONOMY

Clearing up the dust

Constructing the history of star formation over cosmic time requires an understanding of how starlight is absorbed by dust in galaxies. It now seems that there is less universality in such absorption across galaxies than expected.

AMY BARGER

One of the main tools for studying how galaxies form and evolve is to measure the rate at which massive stars are born in galaxies per unit volume of the Universe. However, some of the light emitted by stars in galaxies, especially light at ultraviolet and visible wavelengths, can be absorbed by dust (grains of silicon and carbon up to a few hundred micrometres in size) that is present in the galaxies. This absorption means that the rate at which massive stars are forming cannot be measured accurately. One way to solve this problem is to observe galaxies at longer wavelengths — the infrared regime — where the dust grains re-radiate the light. The ultraviolet and infrared data can then be combined for each galaxy to account completely for the emission produced by the stars. However, infrared data are not usually available for large samples of distant galaxies. Thus, a second approach is to try to apply a dust correction to the data. Writing in *Astronomy & Astrophysics*, Buat *et al.*¹ have attempted to determine how best to do this for a large sample of distant galaxies, at least in a statistical way.

Deciding what wavelength-dependent dust corrections to apply to galaxies is a classic

problem. Even for nearby galaxies, it is uncertain^{2–4} whether there is a 'bump' in the dust extinction curve at 217.5 nanometres, which may relate to the grain size distribution or composition; an extinction curve describes how the dust absorption changes with wavelength. Extinction curves along sight lines towards stars in the Milky Way show a strong bump at this wavelength. However, the bump is weaker towards stars in galaxies of the neighbouring Large and Small Magellanic Clouds. At higher redshifts, there is evidence^{5,6} for the presence of such a bump in at least some galaxies, but the extinction curve of a local 'starburst' galaxy⁷, which does not display a bump, is usually adopted in correcting for dust absorption in distant galaxies. (Redshift is what is measured directly by spectroscopy. Because of the Universe's expansion, the light from distant sources has been stretched, shifting the wavelengths towards the red end of the spectrum. The more the light is shifted to the red, the farther away, and thus the older, the source is.)

Fortunately, the many new observations obtained for the distant Universe — including far-infrared data from the Herschel Space Telescope, mid-infrared data from the Spitzer Space Telescope and optical-to-near-infrared data from ground-based telescopes — have

assumptions of Reipurth and Mikkola's simulations will need to be checked — such as that the three stars in a triplet begin their lives with equal masses. It will be necessary to assess how important these assumptions are to the study's main conclusions.

Ongoing surveys should be able to test some of Reipurth and Mikkola's predictions, including the proportion of triplets in stellar populations of different ages and the number of triplets that are dominated by the mass in the tight binary as opposed to the mass of the third star. The work also presents speculations that may be testable by other means, such as the possibility that some tight pairs within triplets spiral towards one another and merge, creating a true wide binary. Moreover, as extrasolar planets continue to be found in various types of stellar family, it would be valuable to have quantitative predictions for the survivability of planets from both the triplets-as-twins and cluster-dispersal mechanisms. As for our neighbouring wide binary, Proxima Centauri and α Centauri, it is in fact a triplet: α Centauri

is a tight pair, with a planet to boot¹¹. ■

Keivan Guadalupe Stassun is in the *Department of Physics and Astronomy, Vanderbilt University, Nashville, Tennessee 37235, USA, and the Department of Physics, Fisk University, Nashville.*
e-mail: keivan.stassun@vanderbilt.edu

1. Reipurth, B. & Mikkola, S. *Nature* **492**, 221–224 (2012).
2. Innes, R. T. A. *Union Obs. Circ.* **30**, 235–236 (1915).
3. Wertheimer, J. G. & Laughlin, G. *Astron. J.* **132**, 1995–1997 (2006).
4. Dhital, S., West, A. A., Stassun, K. G. & Bochanski, J. J. *Astron. J.* **139**, 2566–2586 (2010).
5. Sesar, B., Ivezić, Ž. & Jurić, M. *Astrophys. J.* **689**, 1244–1273 (2008).
6. Bate, M. R. & Bonnell, I. A. *Mon. Not. R. Astron. Soc.* **356**, 1201–1221 (2005).
7. Kouwenhoven, M. B. N. *et al. Mon. Not. R. Astron. Soc.* **404**, 1835–1848 (2010).
8. Moeckel, N. & Clarke, C. J. *Mon. Not. R. Astron. Soc.* **415**, 1179–1187 (2011).
9. Law, N. M., Dhital, S., Kraus, A., Stassun, K. G. & West, A. A. *Astrophys. J.* **720**, 1727–1737 (2010).
10. Dhital, S. *et al. Astron. J.* **143**, 67 (2012).
11. Dumusque, X. *et al. Nature* **491**, 207–211 (2012).

made it possible to study dust absorption at high redshift. Buat *et al.* used all of these data to study the dependence of dust absorption on a variety of global galaxy properties, such as observed luminosity, stellar mass and the slope of the spectrum in the ultraviolet, for a large sample of galaxies with redshifts in the range 0.95–2.2. At these redshifts, optical observations sample the stars' emission of ultraviolet light — the wavelength regime at which massive stars emit most of their light and suffer the most absorption by dust.

Buat and colleagues used a detailed computer code⁸ that derives properties of galaxies by fitting the light emission predicted from the computations to observations made across the wavelength spectrum. They concluded that the inclusion of infrared data improved the determination of dust-absorption parameters. Interestingly, they found a wide range of values for these parameters, which they postulate could be due to the large variations in the extinction curves for galaxies. They infer that a constant extinction curve for all galaxies at all redshifts cannot be assumed, and that variations should be allowed for when computing the amount of reprocessed ultraviolet light.

The authors' finding that infrared data are crucial for studies of the effects of absorption by dust in individual galaxies makes sense — previous work has shown how notoriously difficult it is to predict far-infrared emission from observed ultraviolet emission⁹. The study's goal was to find dependences of the dust-absorption parameters on global galaxy properties, which Buat *et al.* hoped to use to correct large samples of galaxies in a statistical way. Although they did identify some trends, there is large scatter about the averages of the parameters that needs to be further understood. This serves as a reminder that if the galaxy property one is trying to calculate is strongly dependent on an assumed dust extinction curve, then one should be cautious about the result. Studies such as this are essential for determining the reliability of dust-absorption corrections. These corrections are pivotal in determining the extent to which massive star formation in galaxies is hidden from optical view. ■

Amy Barger is in the *Department of Astronomy, University of Wisconsin-Madison, Madison, Wisconsin 53706, USA.*
e-mail: barger@astro.wisc.edu

1. Buat, V. *et al. Astron. Astrophys.* **545**, A141 (2012).
2. Wijesinghe, D. B. *et al. Mon. Not. R. Astron. Soc.* **410**, 2291–2301 (2011).
3. Wild, V. *et al. Mon. Not. R. Astron. Soc.* **417**, 1760–1786 (2011).
4. Conroy, C., Schiminovich, D. & Blanton, M. R. *Astrophys. J.* **718**, 184–198 (2010).
5. Noll, S. & Pierini, D. *Astron. Astrophys.* **444**, 137–155 (2005).
6. Buat, V. *et al. Astron. Astrophys.* **533**, A93 (2011).
7. Calzetti, D. *et al. Astrophys. J.* **533**, 682–695 (2000).
8. Noll, S. *et al. Astron. Astrophys.* **507**, 1793–1813 (2009).
9. Chapman, S. C. *et al. Mon. Not. R. Astron. Soc.* **319**, 318–330 (2000).

ASTRONOMY

Clearing up the dust

Constructing the history of star formation over cosmic time requires an understanding of how starlight is absorbed by dust in galaxies. It now seems that there is less universality in such absorption across galaxies than expected.

AMY BARGER

One of the main tools for studying how galaxies form and evolve is to measure the rate at which massive stars are born in galaxies per unit volume of the Universe. However, some of the light emitted by stars in galaxies, especially light at ultraviolet and visible wavelengths, can be absorbed by dust (grains of silicon and carbon up to a few hundred micrometres in size) that is present in the galaxies. This absorption means that the rate at which massive stars are forming cannot be measured accurately. One way to solve this problem is to observe galaxies at longer wavelengths — the infrared regime — where the dust grains re-radiate the light. The ultraviolet and infrared data can then be combined for each galaxy to account completely for the emission produced by the stars. However, infrared data are not usually available for large samples of distant galaxies. Thus, a second approach is to try to apply a dust correction to the data. Writing in *Astronomy & Astrophysics*, Buat *et al.*¹ have attempted to determine how best to do this for a large sample of distant galaxies, at least in a statistical way.

Deciding what wavelength-dependent dust corrections to apply to galaxies is a classic

problem. Even for nearby galaxies, it is uncertain^{2–4} whether there is a 'bump' in the dust extinction curve at 217.5 nanometres, which may relate to the grain size distribution or composition; an extinction curve describes how the dust absorption changes with wavelength. Extinction curves along sight lines towards stars in the Milky Way show a strong bump at this wavelength. However, the bump is weaker towards stars in galaxies of the neighbouring Large and Small Magellanic Clouds. At higher redshifts, there is evidence^{5,6} for the presence of such a bump in at least some galaxies, but the extinction curve of a local 'starburst' galaxy⁷, which does not display a bump, is usually adopted in correcting for dust absorption in distant galaxies. (Redshift is what is measured directly by spectroscopy. Because of the Universe's expansion, the light from distant sources has been stretched, shifting the wavelengths towards the red end of the spectrum. The more the light is shifted to the red, the farther away, and thus the older, the source is.)

Fortunately, the many new observations obtained for the distant Universe — including far-infrared data from the Herschel Space Telescope, mid-infrared data from the Spitzer Space Telescope and optical-to-near-infrared data from ground-based telescopes — have

ECONOMICS

Conservation in the red

The Convention on Biological Diversity has pledged to reduce species-extinction threats around the globe by 2020. Analysis shows that this goal is achievable but requires a significant increase in the current rate of investment.

STEPHEN POLASKY

International environmental agreements often contain lofty goals, but gathering the necessary resources and commitment to implement such agreements has proven far more difficult than signing them. Over recent decades, numerous target dates have passed with little or no progress made. Writing in *Science*, McCarthy *et al.*¹ provide a financial assessment of the prospects for meeting the targets of the international Convention on Biological Diversity. The good news is that meeting the convention's goals for 2020 is achievable without breaking the bank — the authors' estimated costs to reduce the extinction risk for all globally threatened species is only about 0.1% of global gross domestic product. The bad news, however, is that this level of spending far outstrips the amount currently spent. If this financing gap continues, then these conservation targets will also remain unmet.

The Convention on Biological Diversity (CBD) was signed at the United Nations Conference on Environment and Development (also known as the Earth Summit) in Rio de Janeiro in 1992. After a decade of little progress, the CBD member states agreed to set a target of achieving a significant reduction in the rate of biodiversity loss by 2010. But 2010 came and went and biodiversity loss continued unabated. Towards the end of 2010, the member states agreed to a new strategic plan, which included targets to prevent the extinction of all threatened species and to improve their conservation status, as well as protect 17% of terrestrial ecosystems, by 2020. McCarthy and colleagues sought to assess what these goals mean in dollar terms, and how likely it is that they will be achieved from a financial perspective.

The evidence base from which one can estimate the cost of reducing extinction risk is relatively poor, and the methods McCarthy *et al.* used are 'back-of-the-envelope' calculations. The authors surveyed 236 experts in bird conservation, who supplied estimates of the cost of improving the conservation status of a species about which they were knowledgeable. The survey covered 211 globally threatened bird species, and McCarthy and collaborators extrapolated these per-species estimates to cover all 1,115 threatened bird species. They then determined an upper-bound

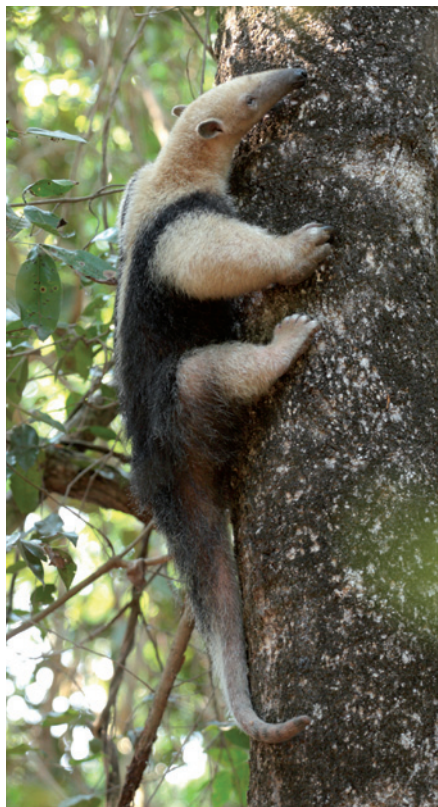


Figure 1 | Dollars for diversity. McCarthy *et al.*¹ have estimated that the international community will have to spend US\$76.1 billion each year to protect and manage all terrestrial sites of global conservation significance, such as regions of the Mato Grosso state of Brazil, home to this collared anteater (*Tamandua tetradactyla*).

cost estimate, based on the assumption that expenditure for each species is independent (in other words, that expenditure on one species would not help any other species), and a lower-bound estimate determined from a degree of shared expenditure. To further extrapolate these estimates to costs for non-bird species, the authors used data from New Zealand showing that birds are on average 4.2 times more expensive to conserve per species, and they factored in that there are approximately 12 times more threatened non-bird species than threatened bird species.

There is somewhat more evidence on which to base estimates for the costs of protecting terrestrial sites of biodiversity significance. We have global maps for 'Important Bird Areas' that are thought to contain habitat for

threatened, restricted-range or migratory birds², and maps of areas that are already protected³. McCarthy *et al.* combined these maps with information on management costs and rough estimates of land-purchase costs⁴ to work out the money required to protect important bird habitat. They then used these values, together with estimates of the land needed for habitat to conserve non-bird threatened species, to derive a total amount.

The authors' final estimates are that between US\$3.41 billion and \$4.76 billion would need to be spent annually to reduce the threat of species extinctions, and that the cost of protecting and managing all terrestrial sites of global conservation significance would be \$76.1 billion annually (Fig. 1). This might sound like a lot of money, until one considers that the value of the global economy is roughly \$70 trillion per year. But, according to the present paper, the estimates are still ten times larger than the amount currently being invested in conservation.

The actual costs of protecting biodiversity could easily be higher (or lower) than these values. For example, the recent rise in food and commodity prices has increased land prices around the globe; in the United States, the average price of farmland in real terms roughly doubled between 1990 and 2010 (ref. 5). Furthermore, many additional threats that will variably affect species, including climate change, introduced pests and pathogens, pollution, poaching, or many of these combined, could make it much harder and more costly to conserve species. On the other hand, species protection will bring with it other ecosystem services that could significantly reduce the net cost of conservation. For example, some areas that are targeted for protection also supply drinking water for major cities — here, the benefits of improved ecosystem-service provision alone are surely enough to justify conservation.

Although the data and methods used in this paper are simple and subject to potentially significant error, they still probably get the big picture right. McCarthy and colleagues show that the costs of providing adequate protection for biodiversity are substantial yet clearly affordable, but that they are much larger than the sums currently being devoted to conservation. Obtaining more refined estimates might be desirable, but will require better data and more detailed methods — and more exact numbers are unlikely to alter either of these two main conclusions.

In the end, whether or not the 2020 CBD targets will be met rests primarily on making the political and economic argument that the benefits of conserving biodiversity outweigh the costs. This point may be self-evident to most biologists, but it is not to many politicians. McCarthy *et al.* have supplied a piece of useful evidence on the costs of conserving biodiversity and have shown that they are

JAMES LOWEN/FLPA

affordable. What is needed now is compelling evidence that conserving biodiversity is essential for human well-being⁶, in the hope that this will convince decision-makers that conservation is well worth the investment. ■

Stephen Polasky is in the Departments of Applied Economics and of Ecology, Evolution and Behavior, University of Minnesota, St Paul, Minnesota 55108, USA.

e-mail: polasky@unm.edu

1. McCarthy, D. P. *et al.* *Science* **338**, 946–949 (2012).
2. www.birdlife.org
3. Butchart, S. H. M. *et al.* *PLoS ONE* **7**, e32529 (2012).
4. Naidoo, R. & Iwamura, T. *Biol. Conserv.* **140**, 40–49 (2007).
5. Nickerson, C. *et al.* *Trends in US Farmland Values and Ownership* (US Dept Agric., 2012).
6. Millennium Ecosystem Assessment: *Ecosystems and Human Well-Being* (Island Press, 2005).

CELL BIOLOGY

Death by deacetylation

Necrosis is associated with various diseases, yet it is arguably the least-understood form of programmed cell death. It emerges that a sirtuin protein regulates one form of necrosis through a deacetylation reaction. SEE ARTICLE P.199

WEN ZHOU & JUNYING YUAN

It has long been thought that necrotic cell death is simply a passive process resulting from severe stress on a cell, due to infection or trauma, rather than a regulated mechanism. But there is increasing evidence that at least one form of necrosis is mediated by a cellular program called necroptosis¹. In this issue (page 199), Narayan *et al.*² add to this body of evidence by showing that necroptosis is regulated by the deacetylase enzyme sirtuin-2. Deciphering the molecular basis of this process is an exciting prospect, not least because dying cells showing characteristics of necrosis are found in various diseases. Mechanistic insight into necroptosis might therefore provide opportunities for developing inhibitors that block disease-related cell death*.

Necroptosis is activated by TNF- α , an immune-mediator protein that is associated with diseases such as rheumatoid arthritis³ and inflammatory bowel disease⁴. When this protein interacts with its receptor TNFR1 on the cell membrane, a cytoplasmic complex called complex I rapidly forms, binding to the receptor's intracellular domain. Among the proteins that make up complex I, RIP1 is involved in activating the transcription factor NF- κ B and thereby counteracting another form of programmed cell death called apoptosis (Fig. 1a).

RIP1 is a kinase enzyme, which modifies the activity of its substrates by adding phosphate groups to them. Its amino-terminal domain is essential for mediating necroptosis. If caspase-8, a key enzyme in apoptosis, is inhibited, RIP1 leaves complex I. It then interacts with RIP3 — another member of the RIP enzyme family — to form complex IIb. The formation of complex IIb is essential for necroptosis^{5–7}, and so the biochemical mechanisms that

regulate it are under intense investigation.

Narayan *et al.* present intriguing data that implicate sirtuin-2 in mediating the formation of complex IIb. Sirtuin-2 belongs to the sirtuin family of enzymes, which are deacetylases, removing acetyl groups from their substrates. Notably, deacetylases have been linked to the regulation of transcription, apoptosis, stress resistance and ageing⁸. While searching for binding partners of sirtuin-2, the authors came upon RIP3. They also found that, in cells lacking sirtuin-2 or in the presence of pharmacological inhibitors of this protein, TNF- α -mediated necroptosis is blocked. This finding suggests that sirtuin-2-mediated protein deacetylation is involved in controlling necrosis.

Indeed, Narayan and colleagues show that, as well as binding to RIP3, sirtuin-2 deacetylates RIP1 at a specific lysine amino-acid residue; this deacetylation seems to be required for the direct interaction between RIP1 and RIP3. Moreover, in the absence of sirtuin-2, the formation of complex IIb — defined as the interaction between RIP1 and RIP3 following TNF- α stimulation — does not occur (Fig. 1b).

Consistent with the importance of RIP1 deacetylation in necrosis, the researchers show that, on activation of necroptosis in cultured mouse cells, RIP1 acetylation markedly declines. This was also observed in a mouse model of a disorder known as heart ischaemia reperfusion, in which the heart tissue is damaged when the blood supply to it is re-established after a period of limited supply. Inhibition of sirtuin-2 activity prevented RIP1 deacetylation and protected the heart from injury. Because necroptosis also mediates ischaemic brain injury¹, and given that sirtuin-2 is abundantly present in the central nervous system, it is possible that this protein also contributes to necroptosis in neurodegenerative diseases by deacetylating RIP1.

Deacetylation of RIP1 by RIP3-bound

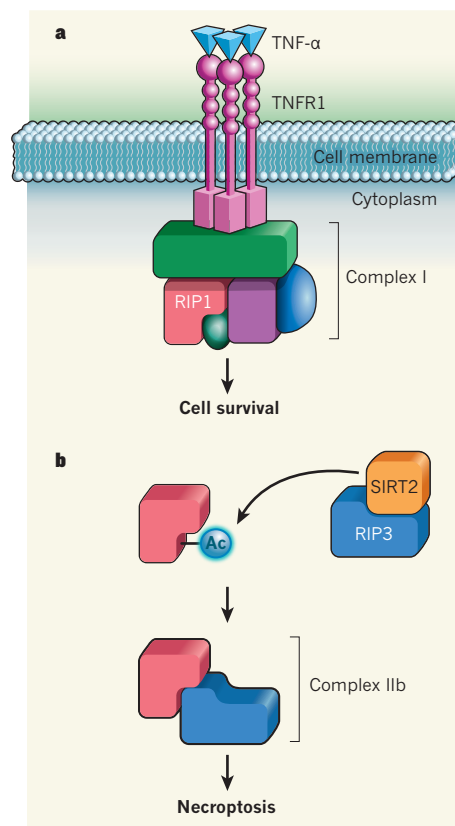


Figure 1 | Evolution of a death complex. **a**, When TNF- α binds to its receptor TNFR1, which is a protein that straddles the cell membrane, the receptor is activated and a group of proteins — collectively known as complex I — assembles on its cytoplasmic side. As part of complex I, RIP1 mediates NF- κ B activation and so promotes cell survival. **b**, RIP1 that dissociates from complex I is in the acetylated form, and this prevents a stable interaction between RIP1 and RIP3. Narayan *et al.*² show that the deacetylase enzyme sirtuin-2 (SIRT2) interacts with RIP3 and is required to deacetylate RIP1. Deacetylated RIP1 forms another stable complex with RIP (complex IIb), leading to necroptosis.

sirtuin-2 suggests that at least one reason for the formation of RIP1–RIP3 in complex IIb is to allow this deacetylation. A recent study⁹ suggests that RIP1–RIP3, as part of complex IIb, might be present in insoluble filamentous protein clusters called amyloid structures, which are linked to various neurodegenerative disorders. It is possible, therefore, that protein deacetylation is involved in amyloid formation — and thus in these diseases — where it serves as a platform to maintain a stable RIP1–RIP3 complex in the amyloid state.

The enzymatic activity of sirtuin-2 depends on the level of its cofactor NAD⁺, a metabolic intermediate. Reduced activity of NAD⁺ is associated with energy deficiency and oxidative stress in cells. This indicates that deacetylation — and, by inference, necroptosis — is subject to metabolic regulation. Although NAD⁺ levels and sirtuin-2 activity are not altered during necroptosis, NAD⁺ depletion

*This article and the paper under discussion² were published online on 28 November 2012.

affordable. What is needed now is compelling evidence that conserving biodiversity is essential for human well-being⁶, in the hope that this will convince decision-makers that conservation is well worth the investment. ■

Stephen Polasky is in the Departments of Applied Economics and of Ecology, Evolution and Behavior, University of Minnesota, St Paul, Minnesota 55108, USA.

e-mail: polasky@unm.edu

1. McCarthy, D. P. *et al.* *Science* **338**, 946–949 (2012).
2. www.birdlife.org
3. Butchart, S. H. M. *et al.* *PLoS ONE* **7**, e32529 (2012).
4. Naidoo, R. & Iwamura, T. *Biol. Conserv.* **140**, 40–49 (2007).
5. Nickerson, C. *et al.* *Trends in US Farmland Values and Ownership* (US Dept Agric., 2012).
6. Millennium Ecosystem Assessment: *Ecosystems and Human Well-Being* (Island Press, 2005).

CELL BIOLOGY

Death by deacetylation

Necrosis is associated with various diseases, yet it is arguably the least-understood form of programmed cell death. It emerges that a sirtuin protein regulates one form of necrosis through a deacetylation reaction. SEE ARTICLE P.199

WEN ZHOU & JUNYING YUAN

It has long been thought that necrotic cell death is simply a passive process resulting from severe stress on a cell, due to infection or trauma, rather than a regulated mechanism. But there is increasing evidence that at least one form of necrosis is mediated by a cellular program called necroptosis¹. In this issue (page 199), Narayan *et al.*² add to this body of evidence by showing that necroptosis is regulated by the deacetylase enzyme sirtuin-2. Deciphering the molecular basis of this process is an exciting prospect, not least because dying cells showing characteristics of necrosis are found in various diseases. Mechanistic insight into necroptosis might therefore provide opportunities for developing inhibitors that block disease-related cell death*.

Necroptosis is activated by TNF- α , an immune-mediator protein that is associated with diseases such as rheumatoid arthritis³ and inflammatory bowel disease⁴. When this protein interacts with its receptor TNFR1 on the cell membrane, a cytoplasmic complex called complex I rapidly forms, binding to the receptor's intracellular domain. Among the proteins that make up complex I, RIP1 is involved in activating the transcription factor NF- κ B and thereby counteracting another form of programmed cell death called apoptosis (Fig. 1a).

RIP1 is a kinase enzyme, which modifies the activity of its substrates by adding phosphate groups to them. Its amino-terminal domain is essential for mediating necroptosis. If caspase-8, a key enzyme in apoptosis, is inhibited, RIP1 leaves complex I. It then interacts with RIP3 — another member of the RIP enzyme family — to form complex IIb. The formation of complex IIb is essential for necroptosis^{5–7}, and so the biochemical mechanisms that

regulate it are under intense investigation.

Narayan *et al.* present intriguing data that implicate sirtuin-2 in mediating the formation of complex IIb. Sirtuin-2 belongs to the sirtuin family of enzymes, which are deacetylases, removing acetyl groups from their substrates. Notably, deacetylases have been linked to the regulation of transcription, apoptosis, stress resistance and ageing⁸. While searching for binding partners of sirtuin-2, the authors came upon RIP3. They also found that, in cells lacking sirtuin-2 or in the presence of pharmacological inhibitors of this protein, TNF- α -mediated necroptosis is blocked. This finding suggests that sirtuin-2-mediated protein deacetylation is involved in controlling necrosis.

Indeed, Narayan and colleagues show that, as well as binding to RIP3, sirtuin-2 deacetylates RIP1 at a specific lysine amino-acid residue; this deacetylation seems to be required for the direct interaction between RIP1 and RIP3. Moreover, in the absence of sirtuin-2, the formation of complex IIb — defined as the interaction between RIP1 and RIP3 following TNF- α stimulation — does not occur (Fig. 1b).

Consistent with the importance of RIP1 deacetylation in necrosis, the researchers show that, on activation of necroptosis in cultured mouse cells, RIP1 acetylation markedly declines. This was also observed in a mouse model of a disorder known as heart ischaemia reperfusion, in which the heart tissue is damaged when the blood supply to it is re-established after a period of limited supply. Inhibition of sirtuin-2 activity prevented RIP1 deacetylation and protected the heart from injury. Because necroptosis also mediates ischaemic brain injury¹, and given that sirtuin-2 is abundantly present in the central nervous system, it is possible that this protein also contributes to necroptosis in neurodegenerative diseases by deacetylating RIP1.

Deacetylation of RIP1 by RIP3-bound

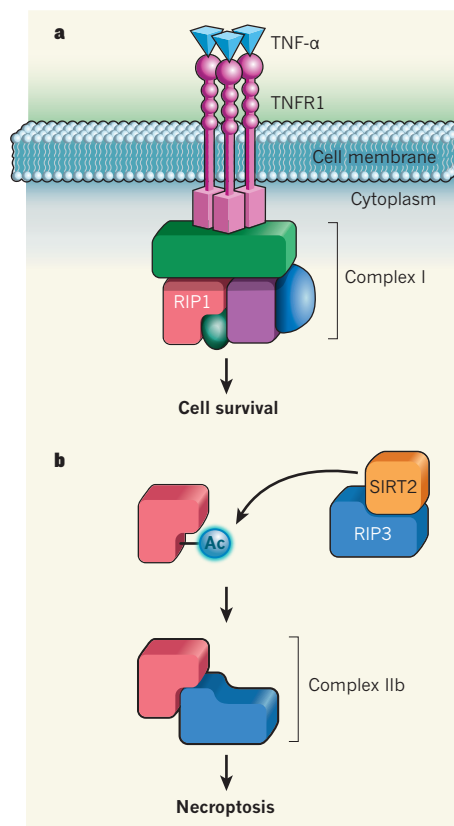


Figure 1 | Evolution of a death complex. **a**, When TNF- α binds to its receptor TNFR1, which is a protein that straddles the cell membrane, the receptor is activated and a group of proteins — collectively known as complex I — assembles on its cytoplasmic side. As part of complex I, RIP1 mediates NF- κ B activation and so promotes cell survival. **b**, RIP1 that dissociates from complex I is in the acetylated form, and this prevents a stable interaction between RIP1 and RIP3. Narayan *et al.*² show that the deacetylase enzyme sirtuin-2 (SIRT2) interacts with RIP3 and is required to deacetylate RIP1. Deacetylated RIP1 forms another stable complex with RIP (complex IIb), leading to necroptosis.

sirtuin-2 suggests that at least one reason for the formation of RIP1–RIP3 in complex IIb is to allow this deacetylation. A recent study⁹ suggests that RIP1–RIP3, as part of complex IIb, might be present in insoluble filamentous protein clusters called amyloid structures, which are linked to various neurodegenerative disorders. It is possible, therefore, that protein deacetylation is involved in amyloid formation — and thus in these diseases — where it serves as a platform to maintain a stable RIP1–RIP3 complex in the amyloid state.

The enzymatic activity of sirtuin-2 depends on the level of its cofactor NAD⁺, a metabolic intermediate. Reduced activity of NAD⁺ is associated with energy deficiency and oxidative stress in cells. This indicates that deacetylation — and, by inference, necroptosis — is subject to metabolic regulation. Although NAD⁺ levels and sirtuin-2 activity are not altered during necroptosis, NAD⁺ depletion

*This article and the paper under discussion² were published online on 28 November 2012.

occurs during the acute phase of ischaemia, owing to lack of oxygen. This might explain why there is initially no extensive cell death during ischaemia, but that it instead occurs after reperfusion, when NAD^+ levels are once again replenished. There could therefore be a window of opportunity for inhibiting ischaemic injury by blocking necroptosis before reperfusion occurs.

Little is known about the composition of complex IIb and how it is regulated. The present study reveals one aspect of this complex, together with a new layer in the regulation of necroptosis. But there is still much to be learnt. For instance, given that acetylated RIP1 does not interact with RIP3, how does RIP3 bring sir-tuin-2 to RIP1? It could be that RIP1 and RIP3 form a transient interaction complex that must be stabilized by RIP1 deacetylation. It is equally likely that there are other scaffold proteins that bring RIP1 and RIP3 together. Also, the kinase activity of RIP1 and RIP3 is essential for their

interaction: the two proteins both phosphorylate themselves and each other. But it is unclear how phosphorylation and deacetylation are coordinated to achieve the active state of complex IIb. Finding answers to these questions will be a major goal, especially given the relevance of necroptosis to human disease. ■

Wen Zhou and Junying Yuan are in the Department of Cell Biology, Harvard Medical School, Boston, Massachusetts 02115, USA. e-mail: junying_yuan@hms.harvard.edu

1. Degterev, A. *et al.* *Nature Chem. Biol.* **1**, 112–119 (2005).
2. Narayan, N. *et al.* *Nature* **492**, 199–204 (2012).
3. Taylor, P. C. & Feldmann, M. *Nature Rev. Rheumatol.* **5**, 578–582 (2009).
4. Chowdhury, Y. & Allez, M. *Curr. Drug Targets* **11**, 138–142 (2010).
5. He, S. *et al.* *Cell* **137**, 1100–1111 (2009).
6. Cho, Y. S. *et al.* *Cell* **137**, 1112–1123 (2009).
7. Zhang, D. *et al.* *Science* **325**, 332–336 (2009).
8. Milne, J. C. & Denu, J. M. *Curr. Opin. Chem. Biol.* **12**, 11–17 (2008).
9. Li, J. *et al.* *Cell* **150**, 339–350 (2012).

BIOCHEMISTRY

Molecular hurdles cleared with ease

Single-molecule studies reveal that a ring-like enzyme that encircles and 'slides' along one strand of duplex DNA, separating it from the other strand, overcomes molecular barriers in its path by transiently opening its ring. [SEE ARTICLE P.205](#)

MICHAEL A. TRAKSELIS & BRIAN W. GRAHAM

For all the benefits that are gained by encoding genetic information in double-stranded DNA, the long, linear, anti-parallel arrangement of complementary strands in DNA duplexes provides challenges for enzymes that replicate genomes. Many proteins involved in replication have therefore adopted oligomeric, toroidal conformations that allow them to remain bound to, and to act on, DNA over long distances. One such protein complex is the DNA helicase, which regulates the initiation of replication, separates duplex strands and can traverse many obstacles in its path.

Most organisms have a circular DNA-replication helicase consisting of six subunits. The large T antigen of simian virus 40 is a well-characterized example, and serves as a model for deciphering the mechanism of DNA unwinding in eukaryotes (organisms that include plants, animals and fungi). Conflicting evidence has fuelled a debate about whether a single or a double hexamer of large T antigen encircles and acts on single-stranded DNA

(ssDNA) or double-stranded DNA (dsDNA) during unwinding. On page 205 of this issue, Yardimci *et al.*¹ convincingly show that a double hexamer of large T antigen assembles at replication origins, and then separates into two single hexamers, which unwind dsDNA by encircling and translocating along each ssDNA in the 3'-to-5' direction*.

In addition to its hexameric unwinding ability, the authors describe the surprising ability of large T antigen to bypass large objects that are covalently attached to the encircled translocating strand, highlighting the hexameric structure's remarkable plasticity. Although other hexameric helicases have been observed to have similar translocating and unwinding abilities in single-molecule studies^{2–5}, this is the first report of a helicase overcoming a covalent block to unwinding.

Replication helicases face three main challenges. First, the enzymes must intimately associate with the DNA, but at the same time be able to slide efficiently along it over great (molecular) distances. Second, separation of the stable duplex into single strands is required before each of the strands can be replicated. And third, genomes are huge, and the strands of duplex DNA are bound by an array of

*This article and the paper under discussion¹ were published online on 28 November 2012.

occurs during the acute phase of ischaemia, owing to lack of oxygen. This might explain why there is initially no extensive cell death during ischaemia, but that it instead occurs after reperfusion, when NAD⁺ levels are once again replenished. There could therefore be a window of opportunity for inhibiting ischaemic injury by blocking necroptosis before reperfusion occurs.

Little is known about the composition of complex IIb and how it is regulated. The present study reveals one aspect of this complex, together with a new layer in the regulation of necroptosis. But there is still much to be learnt. For instance, given that acetylated RIP1 does not interact with RIP3, how does RIP3 bring sir-tuin-2 to RIP1? It could be that RIP1 and RIP3 form a transient interaction complex that must be stabilized by RIP1 deacetylation. It is equally likely that there are other scaffold proteins that bring RIP1 and RIP3 together. Also, the kinase activity of RIP1 and RIP3 is essential for their

interaction: the two proteins both phosphorylate themselves and each other. But it is unclear how phosphorylation and deacetylation are coordinated to achieve the active state of complex IIb. Finding answers to these questions will be a major goal, especially given the relevance of necroptosis to human disease. ■

Wen Zhou and Junying Yuan are in the Department of Cell Biology, Harvard Medical School, Boston, Massachusetts 02115, USA. e-mail: junying_yuan@hms.harvard.edu

1. Degterev, A. *et al.* *Nature Chem. Biol.* **1**, 112–119 (2005).
2. Narayan, N. *et al.* *Nature* **492**, 199–204 (2012).
3. Taylor, P. C. & Feldmann, M. *Nature Rev. Rheumatol.* **5**, 578–582 (2009).
4. Chowers, Y. & Allez, M. *Curr. Drug Targets* **11**, 138–142 (2010).
5. He, S. *et al.* *Cell* **137**, 1100–1111 (2009).
6. Cho, Y. S. *et al.* *Cell* **137**, 1112–1123 (2009).
7. Zhang, D. *et al.* *Science* **325**, 332–336 (2009).
8. Milne, J. C. & Denu, J. M. *Curr. Opin. Chem. Biol.* **12**, 11–17 (2008).
9. Li, J. *et al.* *Cell* **150**, 339–350 (2012).

BIOCHEMISTRY

Molecular hurdles cleared with ease

Single-molecule studies reveal that a ring-like enzyme that encircles and 'slides' along one strand of duplex DNA, separating it from the other strand, overcomes molecular barriers in its path by transiently opening its ring. [SEE ARTICLE P.205](#)

MICHAEL A. TRAKSELIS & BRIAN W. GRAHAM

For all the benefits that are gained by encoding genetic information in double-stranded DNA, the long, linear, anti-parallel arrangement of complementary strands in DNA duplexes provides challenges for enzymes that replicate genomes. Many proteins involved in replication have therefore adopted oligomeric, toroidal conformations that allow them to remain bound to, and to act on, DNA over long distances. One such protein complex is the DNA helicase, which regulates the initiation of replication, separates duplex strands and can traverse many obstacles in its path.

Most organisms have a circular DNA-replication helicase consisting of six subunits. The large T antigen of simian virus 40 is a well-characterized example, and serves as a model for deciphering the mechanism of DNA unwinding in eukaryotes (organisms that include plants, animals and fungi). Conflicting evidence has fuelled a debate about whether a single or a double hexamer of large T antigen encircles and acts on single-stranded DNA

(ssDNA) or double-stranded DNA (dsDNA) during unwinding. On page 205 of this issue, Yardimci *et al.*¹ convincingly show that a double hexamer of large T antigen assembles at replication origins, and then separates into two single hexamers, which unwind dsDNA by encircling and translocating along each ssDNA in the 3'-to-5' direction*.

In addition to its hexameric unwinding ability, the authors describe the surprising ability of large T antigen to bypass large objects that are covalently attached to the encircled translocating strand, highlighting the hexameric structure's remarkable plasticity. Although other hexameric helicases have been observed to have similar translocating and unwinding abilities in single-molecule studies^{2–5}, this is the first report of a helicase overcoming a covalent block to unwinding.

Replication helicases face three main challenges. First, the enzymes must intimately associate with the DNA, but at the same time be able to slide efficiently along it over great (molecular) distances. Second, separation of the stable duplex into single strands is required before each of the strands can be replicated. And third, genomes are huge, and the strands of duplex DNA are bound by an array of

*This article and the paper under discussion¹ were published online on 28 November 2012.

different proteins along its length, which may interfere with replication.

Previous structural studies^{6–8} have indicated that a double hexamer of large T antigen pumps dsDNA into the protein's central channel (Fig. 1a), where it separates into two ssDNA sequences that are extruded out of side channels to form rabbit-ear-like loops. This double-hexamer structure was predicted to remain intact during the entire course of unwinding. Large T antigen also initiates DNA replication by binding specifically to replication origins as a double hexamer. The assembly of a double hexamer is an intriguing initiation activity, but it is inconsistent with nearly every other unwinding mechanism identified for replication helicases, in which single hexamers act through a steric exclusion mode: they encircle one strand while excluding the other.

To address this inconsistency, Yardimci *et al.* performed single-molecule studies of large T antigen in the process of unwinding origin-containing dsDNA. They tethered dsDNA to a surface in a microfluidic flow chamber and added large T antigen so that it bound to the DNA. They then added a cell extract containing replication proteins, to initiate DNA replication, followed by a type of nucleotide that, when incorporated into replicated dsDNA, could be tagged with a fluorescent label. By monitoring the growth of newly replicated, fluorescently labelled DNA, Yardimci *et al.* calculated the fork rate (the rate of bidirectional replication). They observed that when both ends of the original DNA were tethered to the surface such that it was stretched to prevent rabbit-ear ssDNA from forming, the fork rate was the same as that of DNA tethered at just one end. This is a telling result — if large T antigen unwinds DNA as a double hexamer, then its ability to unwind the doubly tethered DNA should be reduced, because it cannot pump such dsDNA into its central channel. The authors' results therefore show that the large T antigen double hexamer separates into single hexamers, which each unwind DNA in opposite directions from the origin (Fig. 1b).

To further distinguish whether ssDNA or dsDNA passes through large T antigen's central channel, Yardimci *et al.* tested the helicase's ability to unwind dsDNA in which the protein streptavidin was non-covalently attached to the leading and/or lagging strands. If dsDNA is encircled by large T antigen, streptavidin would be removed if it is on either of the single strands, or on both strands; but if ssDNA alone is encircled by the helicase, streptavidin would be removed only from the translocating strand. Consistent with a single hexamer encircling only one strand, the authors observed streptavidin displacement from the leading strand but not from the lagging strand. The researchers also performed single-molecule experiments in which dsDNA was non-covalently tagged with large fluorescent labels called quantum

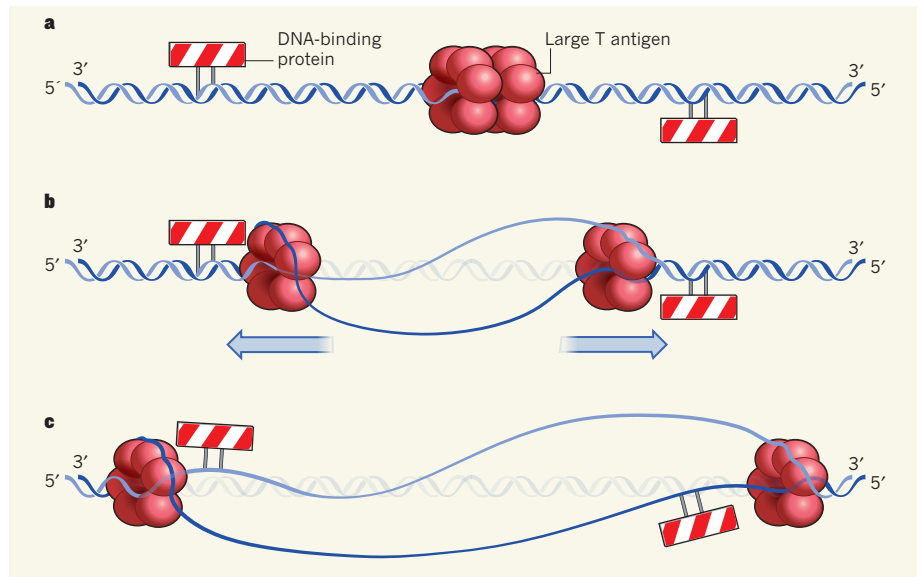


Figure 1 | Mechanism of DNA unwinding by the large T antigen of simian virus 40. Hexameric DNA-replication helicase enzymes, such as large T antigen, bind to double-stranded DNA (dsDNA) at sites known as replication origins before separating the duplex into single strands. **a**, Yardimci *et al.*¹ report that large T antigen binds dsDNA as a double hexamer. **b**, The double hexamer then splits into two single hexamers that each track along a 'leading' strand in the 3'-to-5' direction while excluding the other, 'lagging' strand, unwinding dsDNA as they go. **c**, If the hexamers encounter a 'roadblock', such as a protein covalently attached to the leading strand, they can bypass it efficiently without dissociating from the DNA.

dots, instead of streptavidin. These experiments confirmed that unwinding occurs in the 3'-to-5' direction, with the helicase travelling along the leading strand.

Surprisingly, Yardimci *et al.* found that many of the bulky quantum dots on the leading strand were bypassed by large T antigen, without affecting the unwinding rate. To provide a more natural block to unwinding, the authors covalently attached a protein called HpaII methyltransferase (M.HpaII) to either the leading or the lagging strand. Amazingly, in both cases, unwinding occurred with equal efficiency in spite of the covalent block.

To test whether the helicase remains attached to DNA on encountering a covalently attached blockage, or whether a new helicase is recruited instead, the authors assembled large T antigen on DNA, washed away any unbound protein and then mixed the large T antigen–DNA assembly with replication protein A to initiate unwinding. Once again, they observed that the unwinding ability of large T antigen was not significantly different when M.HpaII was covalently attached to either the leading or the lagging strands, which suggests that a preassembled helicase is able to bypass the 'roadblock' (Fig. 1c). When the researchers attached two M.HpaII proteins to DNA 60 bases apart on the leading strand, the unwinding rate of the DNA by large T antigen was again similar to that of unadulterated DNA. However, when Yardimci *et al.* tested DNA labelled with proteins attached just 14 bases apart, unwinding was strongly inhibited. It will be interesting to determine whether the second block limits

large T antigen's ability to remain bound to the DNA in this case, or whether the proximity of the blocks prevents large T antigen from reassembling around ssDNA.

The authors suggest that plasticity within the hexamer ring is responsible for the transient opening of translocating large T antigen, and that this opening overcomes natural barriers to unwinding. They also argue that multiple blocks located close together prevent the reclosing of large T antigen, or stimulate the protein's dissociation from DNA. It is known that the asymmetrical hexameric arrangement of subunits in the eukaryotic replication helicase MCM2–7 — which is thought to have an analogous structure and unwinding mode to large T antigen — results in a labile interface between this helicase's MCM2 and MCM5 subunits⁹. This is thought to facilitate the opening and loading of MCM2–7 at replication origins, but might also allow the helicase to open transiently, to bypass protein roadblocks as it unwinds DNA.

It is now important to reconcile exactly how large T antigen bypasses impediments. For example, how are the molecular interactions with DNA in the central channel of the antigen disrupted by a roadblock? If the hexamer opens transiently, how does it remain associated with the DNA? Does the degree of opening depend on the size of the roadblock, and what is the mechanism for reclosure around ssDNA afterwards? Perhaps, after opening of a hexamer, large T antigen jumps or rotates over a roadblock before reassociating with the DNA, akin to a molecular hurdler. Or perhaps interactions with the lagging strand on

the external surface of the large T antigen are required to keep it from fully dissociating from DNA, similarly to what has been observed for an archaeal hexameric helicase¹⁰.

Large T antigen, despite having served as a model for studies of the unwinding mechanisms of hexameric helicases for years, continues to surprise scientists with its abilities. It will be interesting to see whether other hexameric helicases share these abilities, or if there are specific differences between them. In the meantime, Yardimci *et al.* have greatly advanced our understanding of how helicases unwind long stretches of DNA in the presence of competing cellular processes. ■

Michael A. Trakselis and Brian W. Graham
are in the Department of Chemistry,
University of Pittsburgh, Pittsburgh,

Pennsylvania 15260, USA.
e-mail: mtraksel@pitt.edu

1. Yardimci, H. *et al.* *Nature* **492**, 205–209 (2012).
2. Fu, Y. V. *et al.* *Cell* **146**, 931–941 (2011).
3. Tanner, N. A. *et al.* *Nature Struct. Mol. Biol.* **15**, 170–176 (2008).
4. Manos, M., Spiering, M. M., Zhuang, Z., Benkovic, S. J. & Croquette, V. *Nature Chem. Biol.* **5**, 904–912 (2009).
5. Hamdan, S. M., Loparo, J. J., Takahashi, M., Richardson, C. C. & van Oijen, A. M. *Nature* **457**, 336–339 (2009).
6. Gai, D., Zhao, R., Li, D., Finkelstein, C. V. & Chen, X. S. *Cell* **119**, 47–60 (2004).
7. Gomez-Lorenzo, M. G. *et al.* *EMBO J.* **22**, 6205–6213 (2003).
8. Wessel, R., Schweizer, J. & Stahl, H. J. *Virology* **66**, 804–815 (1992).
9. Bochman, M. L. & Schwacha, A. *Nucleic Acids Res.* **38**, 6078–6088 (2010).
10. Graham, B. W., Schauer, G. D., Leuba, S. H. & Trakselis, M. A. *Nucleic Acids Res.* **39**, 6585–6595 (2011).

APPLIED PHYSICS

Molecules that convert heat into light

A class of fluorescent organic molecule has been designed that enables highly efficient light-emitting diodes to be made. The devices may turn out to be competitors to their conventional analogues. SEE LETTER P.234

BRIAN D'ANDRADE

Electronic displays are almost ubiquitous, not least because they are the means by which people interact with the Internet. The mobile display market has seen tremendous growth¹, for example, with more than 1 billion mobile phones being sold in 2006. Liquid-crystal displays are a dominant technology for display applications, but organic light-emitting diodes (OLEDs) have steadily been incorporated into mobile devices and are increasingly being used in televisions. On page 234 of this issue, Uoyama *et al.*² report a type of OLED that may offer an alternative to its conventional equivalents.

One of the unique features of an OLED display is that every pixel has an OLED, which is essentially a micrometre-sized light source. The millions of red, green and blue OLEDs in a display all have to be efficient, manufacturable with good yields and capable of providing a highly consistent light output. These requirements have been achieved by improving the organic materials used in OLEDs.

One of the key drivers of OLED technology is novel chemistry. New molecules constantly offer surprises that challenge conventional wisdom and offer alternative solutions. Tang and colleagues³ introduced the world to modern OLED designs 25 years ago. However, the

devices were poor at converting input electric current to light because they incorporated inefficient fluorescent organic materials. Then, in 1998, a team led by Forrest (a physicist) and Thompson (a chemist) introduced⁴ devices with phosphorescent molecules that enabled almost 100% efficient conversion. Phosphorescent molecules differ from their fluorescent analogues in that they contain a heavy metal atom such as iridium.

This work led to an explosion of phosphorescent materials that enabled many desirable characteristics, such as a variety of colours, long operational lifetimes and high efficiencies. However, it remains difficult to produce a single display that uses blue, green and red phosphorescent devices, because the operational lifetimes and colour characteristics of some phosphorescent devices do not meet the strict performance requirements for display applications. It is important to solve these problems because phosphorescent materials are the most promising materials for displays, with the potential to deliver nearly 100% efficiency. Now, Uoyama *et al.* describe how they have made efficient OLEDs that use a special type of fluorescent material.

When an organic molecule absorbs electrical energy, it moves from its original state to a higher-energy (excited) state. For high-efficiency devices, the excited molecule preferably

sheds the extra energy by producing a photon of light when it returns to its original, unexcited state. The molecular transition from excited to unexcited states has a few strict rules related to quantum-mechanical conditions that must be satisfied. These rules prevent every excited molecule from emitting a photon and returning to an unexcited state. As a result, fluorescent materials used in OLEDs often generate heat instead of light. Phosphorescent materials break those rules by using a heavy metal atom, such as iridium, bonded to the organic materials (typically comprising carbon, nitrogen and hydrogen) in an individual molecule. This makes it significantly more likely that after absorbing electrical energy, a phosphorescent molecule can efficiently transition from a high energy state to a low one by emitting a photon.

Uoyama and colleagues developed fluorescent molecules that can achieve high efficiency by using heat instead of a heavy metal atom. They convincingly demonstrated the molecules' potential by making highly efficient fluorescent OLEDs with a performance comparable to that of phosphorescent OLEDs. Their fluorescent molecules are based on carbazoyl dicyanobenzene and as such have the potential to be synthesized at low cost, Uoyama *et al.* believe, because the synthetic process does not require rare metal catalysts or rare heavy metal atoms. Furthermore, the OLEDs can emit multiple colours, from sky-blue (with a peak wavelength at 473 nanometres) to orange (577 nm).

There are many challenges ahead before these molecules can be fully accepted into production. The emissive colours have to be developed for display applications; the operational lifetime of devices that incorporate the molecules needs to be comparable to, or preferably better than, state-of-the-art devices (possibly the hardest challenge); and the ability to manufacture products based on the new OLEDs must be proven. The molecules are not certain to replace existing ones, but they may be shaped into contenders in terms of the cost and quality of desirable performance characteristics. Indeed, perfecting the new molecules will take time and effort, but Chihaya Adachi, who leads the work and is a co-author of the study², has the experience needed to help his team to overcome these obstacles. ■

Brian D'Andrade is at Exponent, Inc.,
1150 Connecticut Avenue NW, Suite 1100,
Washington DC 20036, USA.
e-mail: bdandrade@exponent.com

1. Li, Z., Bhowmik, A. K. & Bos, P. J. in *Mobile Displays: Technology and Applications* (eds Bhowmik, A. K., Li, Z. & Bos, P. J.) 2 (Wiley, 2008).
2. Uoyama, H., Goushi, K., Shizu, K., Nomura, H. & Adachi, C. *Nature* **492**, 234–238 (2012).
3. Tang, C. W. & VanSlyke, S. A. *Appl. Phys. Lett.* **51**, 913–915 (1987).
4. Baldo, M. A. *et al.* *Nature* **395**, 151–154 (1998).

the external surface of the large T antigen are required to keep it from fully dissociating from DNA, similarly to what has been observed for an archaeal hexameric helicase¹⁰.

Large T antigen, despite having served as a model for studies of the unwinding mechanisms of hexameric helicases for years, continues to surprise scientists with its abilities. It will be interesting to see whether other hexameric helicases share these abilities, or if there are specific differences between them. In the meantime, Yardimci *et al.* have greatly advanced our understanding of how helicases unwind long stretches of DNA in the presence of competing cellular processes. ■

Michael A. Trakselis and Brian W. Graham
are in the Department of Chemistry,
University of Pittsburgh, Pittsburgh,

Pennsylvania 15260, USA.
e-mail: mtraksel@pitt.edu

1. Yardimci, H. *et al.* *Nature* **492**, 205–209 (2012).
2. Fu, Y. V. *et al.* *Cell* **146**, 931–941 (2011).
3. Tanner, N. A. *et al.* *Nature Struct. Mol. Biol.* **15**, 170–176 (2008).
4. Manos, M., Spiering, M. M., Zhuang, Z., Benkovic, S. J. & Croquette, V. *Nature Chem. Biol.* **5**, 904–912 (2009).
5. Hamdan, S. M., Loparo, J. J., Takahashi, M., Richardson, C. C. & van Oijen, A. M. *Nature* **457**, 336–339 (2009).
6. Gai, D., Zhao, R., Li, D., Finkelstein, C. V. & Chen, X. S. *Cell* **119**, 47–60 (2004).
7. Gomez-Lorenzo, M. G. *et al.* *EMBO J.* **22**, 6205–6213 (2003).
8. Wessel, R., Schweizer, J. & Stahl, H. J. *Virology* **66**, 804–815 (1992).
9. Bochman, M. L. & Schwacha, A. *Nucleic Acids Res.* **38**, 6078–6088 (2010).
10. Graham, B. W., Schauer, G. D., Leuba, S. H. & Trakselis, M. A. *Nucleic Acids Res.* **39**, 6585–6595 (2011).

APPLIED PHYSICS

Molecules that convert heat into light

A class of fluorescent organic molecule has been designed that enables highly efficient light-emitting diodes to be made. The devices may turn out to be competitors to their conventional analogues. SEE LETTER P.234

BRIAN D'ANDRADE

Electronic displays are almost ubiquitous, not least because they are the means by which people interact with the Internet. The mobile display market has seen tremendous growth¹, for example, with more than 1 billion mobile phones being sold in 2006. Liquid-crystal displays are a dominant technology for display applications, but organic light-emitting diodes (OLEDs) have steadily been incorporated into mobile devices and are increasingly being used in televisions. On page 234 of this issue, Uoyama *et al.*² report a type of OLED that may offer an alternative to its conventional equivalents.

One of the unique features of an OLED display is that every pixel has an OLED, which is essentially a micrometre-sized light source. The millions of red, green and blue OLEDs in a display all have to be efficient, manufacturable with good yields and capable of providing a highly consistent light output. These requirements have been achieved by improving the organic materials used in OLEDs.

One of the key drivers of OLED technology is novel chemistry. New molecules constantly offer surprises that challenge conventional wisdom and offer alternative solutions. Tang and colleagues³ introduced the world to modern OLED designs 25 years ago. However, the

devices were poor at converting input electric current to light because they incorporated inefficient fluorescent organic materials. Then, in 1998, a team led by Forrest (a physicist) and Thompson (a chemist) introduced⁴ devices with phosphorescent molecules that enabled almost 100% efficient conversion. Phosphorescent molecules differ from their fluorescent analogues in that they contain a heavy metal atom such as iridium.

This work led to an explosion of phosphorescent materials that enabled many desirable characteristics, such as a variety of colours, long operational lifetimes and high efficiencies. However, it remains difficult to produce a single display that uses blue, green and red phosphorescent devices, because the operational lifetimes and colour characteristics of some phosphorescent devices do not meet the strict performance requirements for display applications. It is important to solve these problems because phosphorescent materials are the most promising materials for displays, with the potential to deliver nearly 100% efficiency. Now, Uoyama *et al.* describe how they have made efficient OLEDs that use a special type of fluorescent material.

When an organic molecule absorbs electrical energy, it moves from its original state to a higher-energy (excited) state. For high-efficiency devices, the excited molecule preferably

sheds the extra energy by producing a photon of light when it returns to its original, unexcited state. The molecular transition from excited to unexcited states has a few strict rules related to quantum-mechanical conditions that must be satisfied. These rules prevent every excited molecule from emitting a photon and returning to an unexcited state. As a result, fluorescent materials used in OLEDs often generate heat instead of light. Phosphorescent materials break those rules by using a heavy metal atom, such as iridium, bonded to the organic materials (typically comprising carbon, nitrogen and hydrogen) in an individual molecule. This makes it significantly more likely that after absorbing electrical energy, a phosphorescent molecule can efficiently transition from a high energy state to a low one by emitting a photon.

Uoyama and colleagues developed fluorescent molecules that can achieve high efficiency by using heat instead of a heavy metal atom. They convincingly demonstrated the molecules' potential by making highly efficient fluorescent OLEDs with a performance comparable to that of phosphorescent OLEDs. Their fluorescent molecules are based on carbazoyl dicyanobenzene and as such have the potential to be synthesized at low cost, Uoyama *et al.* believe, because the synthetic process does not require rare metal catalysts or rare heavy metal atoms. Furthermore, the OLEDs can emit multiple colours, from sky-blue (with a peak wavelength at 473 nanometres) to orange (577 nm).

There are many challenges ahead before these molecules can be fully accepted into production. The emissive colours have to be developed for display applications; the operational lifetime of devices that incorporate the molecules needs to be comparable to, or preferably better than, state-of-the-art devices (possibly the hardest challenge); and the ability to manufacture products based on the new OLEDs must be proven. The molecules are not certain to replace existing ones, but they may be shaped into contenders in terms of the cost and quality of desirable performance characteristics. Indeed, perfecting the new molecules will take time and effort, but Chihaya Adachi, who leads the work and is a co-author of the study², has the experience needed to help his team to overcome these obstacles. ■

Brian D'Andrade is at Exponent, Inc.,
1150 Connecticut Avenue NW, Suite 1100,
Washington DC 20036, USA.
e-mail: bdandrade@exponent.com

1. Li, Z., Bhowmik, A. K. & Bos, P. J. in *Mobile Displays: Technology and Applications* (eds Bhowmik, A. K., Li, Z. & Bos, P. J.) 2 (Wiley, 2008).
2. Uoyama, H., Goushi, K., Shizu, K., Nomura, H. & Adachi, C. *Nature* **492**, 234–238 (2012).
3. Tang, C. W. & VanSlyke, S. A. *Appl. Phys. Lett.* **51**, 913–915 (1987).
4. Baldo, M. A. *et al.* *Nature* **395**, 151–154 (1998).

The NAD-dependent deacetylase SIRT2 is required for programmed necrosis

Nisha Narayan^{1*}, In Hye Lee^{1*}, Ronen Borenstein¹, Junhui Sun², Renee Wong², Guang Tong^{2,3}, Maria M. Fergusson¹, Jie Liu¹, Ilsa I. Rovira¹, Hwei-Ling Cheng⁴, Guanghui Wang⁵, Marjan Gucak⁵, David Lombard⁶, Fredrick W. Alt⁴, Michael N. Sack¹, Elizabeth Murphy², Liu Cao⁷ & Toren Finkel¹

Although initially viewed as unregulated, increasing evidence suggests that cellular necrosis often proceeds through a specific molecular program. In particular, death ligands such as tumour necrosis factor (TNF)- α activate necrosis by stimulating the formation of a complex containing receptor-interacting protein 1 (RIP1) and receptor-interacting protein 3 (RIP3). Relatively little is known regarding how this complex formation is regulated. Here, we show that the NAD-dependent deacetylase SIRT2 binds constitutively to RIP3 and that deletion or knockdown of SIRT2 prevents formation of the RIP1-RIP3 complex in mice. Furthermore, genetic or pharmacological inhibition of SIRT2 blocks cellular necrosis induced by TNF- α . We further demonstrate that RIP1 is a critical target of SIRT2-dependent deacetylation. Using gain- and loss-of-function mutants, we demonstrate that acetylation of RIP1 lysine 530 modulates RIP1-RIP3 complex formation and TNF- α -stimulated necrosis. In the setting of ischaemia-reperfusion injury, RIP1 is deacetylated in a SIRT2-dependent fashion. Furthermore, the hearts of *Sirt2*^{-/-} mice, or wild-type mice treated with a specific pharmacological inhibitor of SIRT2, show marked protection from ischaemic injury. Taken together, these results implicate SIRT2 as an important regulator of programmed necrosis and indicate that inhibitors of this deacetylase may constitute a novel approach to protect against necrotic injuries, including ischaemic stroke and myocardial infarction.

Several forms of cell death exist, each showing distinctive morphological features. The apoptotic program is an energy-dependent method of cell death that results in cytoplasmic shrinking, nuclear condensation, caspase activation and the ultimate fragmentation of the cell. Necrosis, on the other hand, is thought to occur in an energy-depleted setting and involves loss of membrane integrity, subsequent swelling of the cell and eventual cellular lysis. Although initially viewed as a passive or default pathway, accumulating evidence suggests that at least some forms of necrosis are programmed and regulated¹⁻³. This programmed necrosis, also termed necroptosis, may have important implications in the cellular response to a host of insults, including bacterial and viral infection, various neurodegenerative processes, as well as ischaemia-reperfusion injury of the brain and heart¹⁻³.

Ligands such as TNF- α , FASL and TRAIL can induce both apoptotic and necrotic cell death. For instance, the addition of TNF- α results in the activation of the serine/threonine kinase RIP1 that is in turn important for the ligand-stimulated activation of NF- κ B, the execution of apoptosis through its interaction with FADD, as well as the induction of necrosis via its complex formation with the RIP3 kinase^{1,2,4-6}. The interaction of RIP1 and RIP3 seems to be required for necrosis and occurs through a homotypic interaction motif known as the RHIM domain^{4,5}. Necrostatin-1, a pharmacological inhibitor of RIP1 kinase, seems to inhibit RIP1-RIP3 interaction as well as inhibiting necrotic cell death⁷. Nonetheless, the precise molecular mechanisms that regulate the interaction of RIP1 and RIP3 are poorly understood. Here, we demonstrate an obligate role for the NAD-dependent deacetylase SIRT2.

SIRT2 binds to RIP3

Of the seven known mammalian sirtuin isoforms, relatively little is known about the predominantly cytosolic family member SIRT2⁸. In an effort to more fully understand the role of SIRT2, we transfected cells with a Flag-tagged version of SIRT2 to identify interacting proteins. Using a threshold of two or more independent peptide fragments, we identified only a handful of proteins that were specifically immunoprecipitated when the Flag peptide eluant was analysed by mass spectroscopy (Supplementary Fig. 1). Besides SIRT2 itself, this analysis identified heat shock protein 1A as well as β -tubulin, the heterodimeric partner of one of the few known targets of SIRT2-dependent deacetylation⁹. The final SIRT2 candidate interacting protein using this approach was RIP3. On the basis of the novelty and potential biological importance, we sought to pursue the putative interaction of SIRT2 and RIP3.

We first confirmed this protein interaction using epitope-tagged SIRT2. Using this approach, we were able to identify co-immunoprecipitation of SIRT2 and RIP3 (Fig. 1a). In contrast, SIRT2 did not seem to interact with RIP1 (Supplementary Fig. 2). The interaction between SIRT2 and RIP3 was not altered when cells were stimulated to undergo programmed necrosis using the combination of TNF- α along with the caspase inhibitor z-VAD-fmk. We were able to observe a similar interaction with and without necrotic stimulation between endogenous SIRT2 and endogenous RIP3 (Fig. 1b). Using ³⁵S-labelled SIRT2 and either full-length glutathione-S-transferase (GST)-tagged GST-RIP3 or various GST-RIP3 deletion mutants, we could demonstrate that SIRT2 bound the carboxy terminus of RIP3 *in vitro* (Fig. 1c).

¹Center for Molecular Medicine, National Heart, Lung and Blood Institute, NIH Bethesda, Maryland 20892, USA. ²Systems Biology Center, National Heart, Lung and Blood Institute, NIH Bethesda, Maryland 20892, USA. ³Department of Cardiovascular Surgery, Xijing Hospital, Fourth Military Medical University, Xi'an 710032, China. ⁴Howard Hughes Medical Institute, Program in Cellular and Molecular Medicine, Children's Hospital Boston and Departments of Genetics and Pediatrics, Harvard Medical School, Boston, Massachusetts 02115, USA. ⁵Proteomics Core, National Heart, Lung and Blood Institute, NIH Bethesda, Maryland 20892, USA. ⁶Department of Pathology and Institute of Gerontology, University of Michigan, Ann Arbor, Michigan 48109, USA. ⁷Key Laboratory of Medical Cell Biology, China Medical University, Shenyang 110001, China.

*These authors contributed equally to this work.

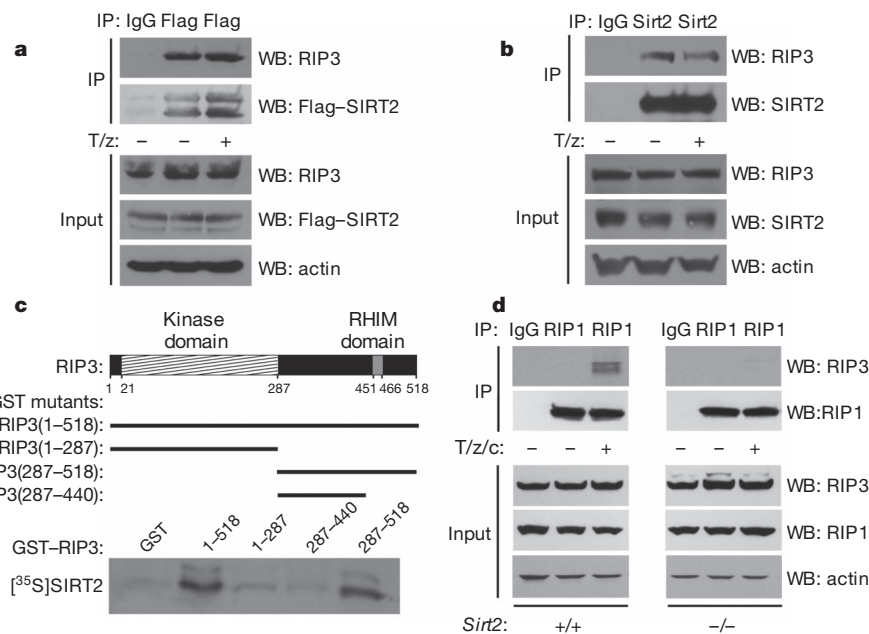


Figure 1 | SIRT2 interacts with RIP3 and regulates RIP1-RIP3 complex formation. **a, b**, In L929 cells epitope-tagged SIRT2 co-immunoprecipitates with endogenous RIP3 (**a**), as does endogenous SIRT2 and RIP3 (**b**). IP, immunoprecipitation; WB, western blot. This interaction was unchanged by the addition of the necrotic stimulus TNF- α and z-VAD-fmk (T/z).

Given the interaction of SIRT2 with RIP3, we next asked whether SIRT2 might modulate the RIP1-RIP3 interaction. Mouse embryonic fibroblasts (MEFs) obtained from wild-type or *Sirt2*^{-/-} mice (Supplementary Fig. 3) were analysed in the presence or absence of the combination of TNF- α , cycloheximide and z-VAD-fmk to induce necrosis. As expected, in wild-type MEFs, the addition of this necrotic stimulus resulted in RIP1-RIP3 complex formation (Fig. 1d). In contrast, in *Sirt2*^{-/-} MEFs formation of this necroptosis complex was not observed.

c, Schematic representation of the functional domains of RIP3 and corresponding GST fusion constructs used to assess *in vitro* binding of [³⁵S]SIRT2. Amino acids 440-518 seem to be required for SIRT2 binding. **d**, Wild-type and *Sirt2*^{-/-} MEFs were stimulated for 2 h with the combination of TNF- α , z-VAD-fmk and cycloheximide (T/z/c) to induce necrosis.

SIRT2 is required for necroptosis

The absence of a RIP1-RIP3 complex indicated that SIRT2 might modulate the overall necrotic response. The mouse L929 cell line is often analysed in this context because it undergoes robust necrosis in response to the combination of TNF- α and z-VAD-fmk⁴⁻⁶. To assess the role of SIRT2 in programmed necrosis, we knocked down the expression of SIRT2 in L929 cells using two separate short hairpin RNAs (shRNAs; Fig. 2a). As we observed in *Sirt2*^{-/-} MEFs, knock-down of SIRT2 in L929 cells blocked RIP1-RIP3 complex formation

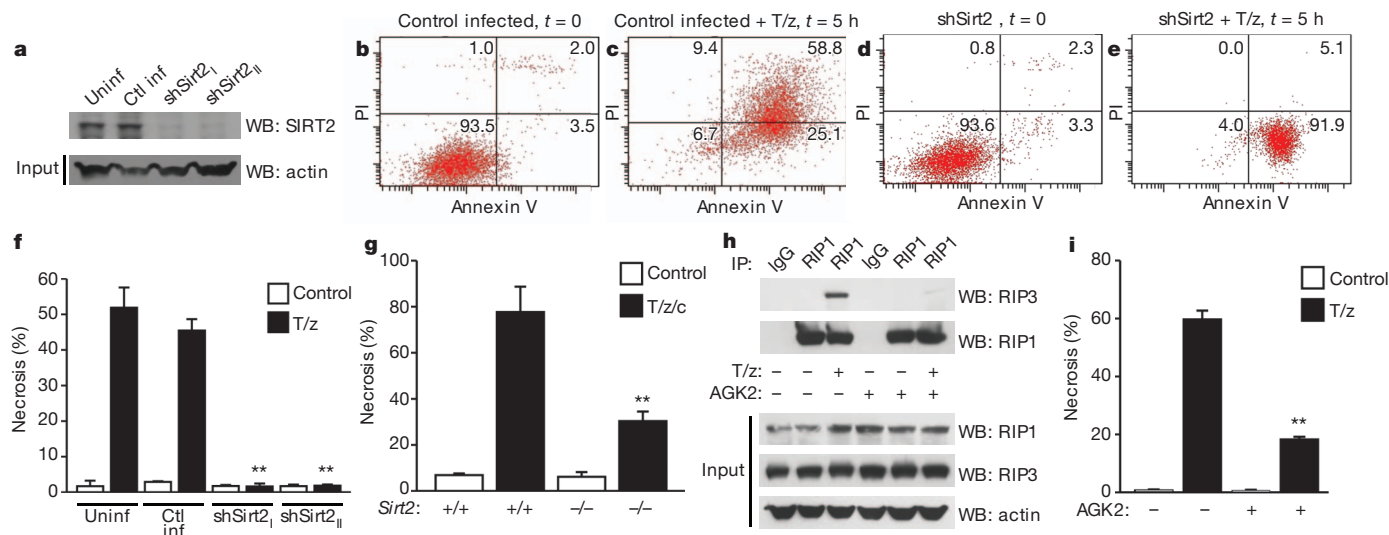


Figure 2 | Inhibition of SIRT2 prevents cellular necrosis. **a**, Expression of SIRT2 in L929 cells in uninfected cells (Uninf), cells infected with a control lentivirus (Ctl inf), or cells infected with one of two independent shRNAs targeting SIRT2 (shSirt2₁ and shSirt2₂). **b-e**, Representative FACS analysis of annexin V and propidium iodide (PI) staining initially (**b, d**) or 5 h after stimulation with TNF- α and z-VAD-fmk (T/z) (**c, e**). **f**, Level of PI-positive necrotic cells in the presence or absence of TNF- α and z-VAD-fmk for control cells or cells with shRNA-mediated knockdown of SIRT2 (mean \pm s.d., $n = 4$

independent experiments). **g**, Necrosis in the presence or absence of TNF- α , z-VAD-fmk and cycloheximide (T/z/c) in wild-type MEFs (+/+) or *Sirt2*^{-/-} MEFs (mean \pm s.d., $n = 3$ independent experiments). **h, i**, Treatment with the SIRT2 inhibitor AGK2 blocks RIP1-RIP3 complex formation (**h**) and TNF- α -induced necrosis (**i**) (mean \pm s.d., $n = 3$ independent experiments). ** $P < 0.01$ by ANOVA followed by Tukey-Kramer multiple comparison for significance.

in the setting of TNF- α stimulation (Supplementary Fig. 4). In control knockdown cells, 5 h after the addition of TNF- α and z-VAD-fmk, a significant fraction of the cells appeared necrotic as evident by showing positive staining for both annexin V and propidium iodide (Fig. 2b, c). In contrast, in cells with stable SIRT2 knockdown, there was a lack of positive propidium iodide staining, indicating a defect in programmed necrosis (Fig. 2d, e). This lack of necrosis was evident in both stable cell lines containing SIRT2 knockdown (Fig. 2f), as it was in *Sirt2*^{-/-} MEFs treated with TNF- α , cycloheximide and z-VAD-fmk (Fig. 2g). Finally, we took advantage of the availability of a previously developed pharmacological inhibitor of SIRT2 deacetylase activity^{10,11}. Treatment of L929 cells with the specific SIRT2 deacetylase inhibitor AGK2 inhibited the formation of the RIP1–RIP3 complex (Fig. 2h). This treatment also effectively inhibited programmed necrosis in these cells (Fig. 2i).

SIRT2 regulates RIP1 acetylation

Taken together, our results demonstrate a requirement for SIRT2 in the formation of the RIP1–RIP3 complex and subsequent programmed necrosis that is observed following stimulation with TNF- α . Given that AGK2 inhibits SIRT2 deacetylase activity¹⁰, the observation that this compound inhibits the RIP1–RIP3 interaction suggests that SIRT2-dependent deacetylation of RIP3 or RIP1 might regulate complex formation. Our analysis revealed that, although RIP3 was acetylated, the level of endogenous RIP3 acetylation was not altered following necrotic stimulation or after knockdown of SIRT2 (Supplementary

Fig. 5). In contrast, transfection of RIP1 into the L929 cell line demonstrated that RIP1 was acetylated under basal conditions and that the level of RIP1 acetylation markedly declined after stimulation with TNF- α and z-VAD-fmk (Fig. 3a and Supplementary Fig. 6). This decline was not observed in L929 cells with stable SIRT2 knockdown (Fig. 3a). A similar TNF- α -induced, SIRT2-dependent deacetylation was also observed with endogenous RIP1 (Supplementary Fig. 7).

These results indicate that RIP1 may be a target for SIRT2-dependent deacetylation. Consistent with this hypothesis, immunopurified RIP1 could be effectively deacetylated *in vitro* by the addition of purified wild-type SIRT2, whereas the addition of a catalytically inactive mutant of SIRT2 (Q130A) had no effect (Fig. 3b). Furthermore, addition of the specific SIRT2 inhibitor AGK2, but not the HDAC6 inhibitor tubacin, blocked RIP1 deacetylation under necrotic conditions (Fig. 3c). We next sought to gain further insight into the relationship between necrosis and RIP1 deacetylation. Our results indicate that the addition of TNF- α and z-VAD-fmk stimulates the SIRT2-dependent deacetylation of RIP1. The two most likely explanations for these observations is either that necrosis directly stimulates SIRT2 activity, or that necrosis brings RIP1 and the RIP3–SIRT2 complex in close proximity, thus facilitating deacetylation of RIP1. When cells were stimulated to undergo necrosis, we observed no significant increase in SIRT2 activity, nor were there measurable changes in cellular NAD levels (Supplementary Fig. 8). In contrast, knockdown of RIP3 inhibited RIP1 deacetylation under necrotic conditions (Fig. 3d and Supplementary Fig. 9). Similarly, addition

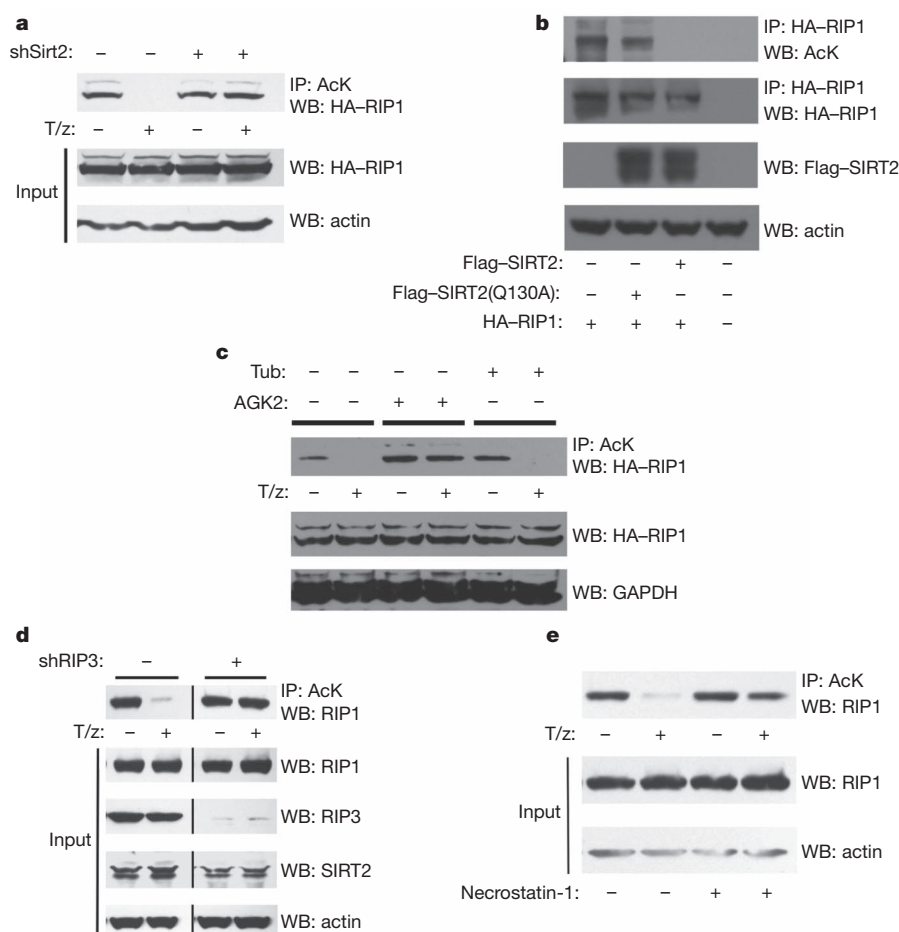


Figure 3 | RIP1 is a target of SIRT2-dependent deacetylation. **a**, Levels of acetylation for epitope-tagged RIP1 in either control L929 cells or L929 cells with stable knockdown of SIRT2 expression. Acetylation was determined in the presence or absence of TNF- α and z-VAD-fmk (T/z) treatment and assessed using an acetyl-lysine (AcK)-specific antibody. HA, haemagglutinin. **b**, RIP1 can be deacetylated *in vitro* by wild-type SIRT2, but not by a deacetylase-

inactive SIRT2 mutant (SIRT2(Q130A)). **c**, Under necrotic conditions, deacetylation of RIP1 is blocked by the SIRT2 inhibitor AGK2, but not by the HDAC6 inhibitor tubacin. **d**, In L929 cells, knockdown of RIP3 inhibits RIP1 deacetylation following the induction of necrosis. **e**, Treatment of L929 cells with necrostatin-1 inhibits the necrosis-induced deacetylation of RIP1.

of necrostatin-1, a small molecule that is thought to lock RIP1 in an inactive configuration and block RIP1–RIP3 interaction¹², also inhibited RIP1 deacetylation (Fig. 3e). Thus, our data are most consistent with TNF- α and z-VAD-fmk bringing RIP1 and the RIP3–SIRT2 complex in close proximity to each other, thereby facilitating SIRT2-dependent deacetylation of RIP1.

We next sought to identify the lysine residues of RIP1 that might be critical targets for SIRT2-dependent deacetylation. Unfortunately, we found it difficult to map *in vivo* acetylation sites, most probably because RIP1 is both toxic and rapidly degraded when overexpressed^{13–16}. We did however note that *in vivo* expression of the p300 acetyltransferase markedly increased the level of basal RIP1 acetylation (Supplementary Fig. 10). We reasoned that lysine acetylation of RIP1 near the RHIM domain of the protein would provide an attractive model to explain the SIRT2-dependent nature of the RIP1–RIP3 interaction. The RHIM domain of human RIP1 encompasses amino acid residues 531–547 (ref. 17). Interestingly, there is a lysine residue immediately adjacent to the RHIM domain (lysine 530) that is predicted to be a site for internal acetylation using a widely available bioinformatic approach (Supplementary Fig. 11; score of 1.17 by the PAIL algorithm on high stringency, predictive power >89%). Using mass spectroscopy, we confirmed that this lysine residue could be acetylated by p300 (Supplementary Fig. 11). Moreover, recombinant SIRT2 efficiently deacetylated lysine 530 when a mixture of acetylated and deacetylated peptides encompassing amino acids 529 to 546 of RIP1 was used as a substrate (Fig. 4a).

We next sought to obtain further evidence that SIRT2-dependent deacetylation regulates RIP1. In cells, expression of wild-type SIRT2 resulted in the deacetylation of co-expressed wild-type RIP1 (Fig. 4b).

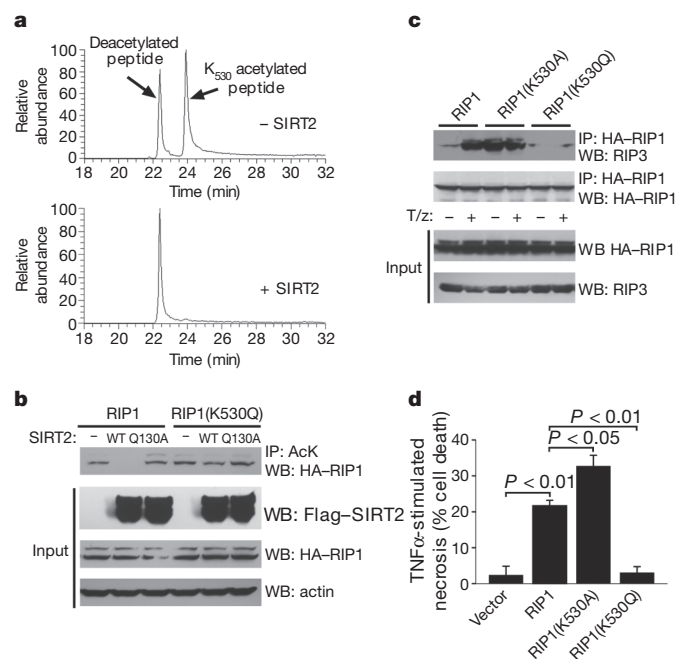


Figure 4 | Acetylation status of RIP1 lysine 530 regulates necrosis.

a, Recombinant SIRT2 can efficiently deacetylate a peptide substrate encompassing amino acids 529 to 546 of RIP1. The substrate contains a mixture of peptides with either acetylated or non-acetylated lysine 530. **b**, Lysine acetylation of wild-type RIP1 and the site directed mutant RIP1(K530Q) in L929 cells following co-transfection of either wild-type SIRT2 or a deacetylase inactive mutant (Q130A). **c**, Comparison of complex formation for wild-type RIP1, a loss of function mutant (RIP1(K530A)) or for a gain of function mutant (RIP1(K530Q)). **d**, Analysis of various RIP1 constructs reconstituted in a Jurkat T cell line that lacks RIP1 expression. Stable cell lines were generated and the level of necrosis was assessed 14 h after TNF- α stimulation. Data were analysed by an ANOVA followed by the Tukey–Kramer multiple comparison method to determine significance ($n = 3$, mean \pm s.d.).

This was not observed when a deacetylase-deficient form of SIRT2 (Q130A) was expressed. Similarly, this deacetylation seemed to be specific, as expression of a related sirtuin family member, SIRT1, did not alter the level of wild-type RIP1 acetylation (Supplementary Fig. 12). In contrast, a site-directed mutant of RIP1 at position 530 that mimics constitutive acetylation (RIP1(K530Q)) was insensitive to further SIRT2-dependent deacetylation (Fig. 4b). Similarly, whereas as previously observed wild-type RIP1 underwent marked deacetylation following TNF- α and z-VAD-fmk treatment, the acetylation of the RIP1(K530Q) mutant was insensitive to ligand addition (Supplementary Fig. 13).

These results are consistent with lysine 530 being a critical target of SIRT2 and that, following deacetylation of this residue, additional RIP1 lysine residues can be deacetylated by SIRT2 in a processive fashion. To further pursue the role of lysine 530, we analysed site-directed mutants of RIP1 that represent potential gain (RIP1(K530Q)) or loss (RIP1(K530A)) of acetylation function. We then evaluated the ability of these various RIP1 mutants to form a complex with RIP3. As expected, using wild-type RIP1, a RIP1–RIP3 complex was induced after stimulation with TNF- α and z-VAD-fmk (Fig. 4c). In contrast, the RIP1(K530A) mutant seemed to form a complex with RIP3 independent of ligand stimulation, whereas the RIP1(K530Q) mutant failed to interact with RIP3 either under basal conditions, or under conditions that stimulate cellular necrosis (Fig. 4c). To further confirm the specific functional importance of lysine 530, we used a previously described Jurkat T cell line that had been engineered to lack RIP1 expression and fails to undergo programmed necrosis with TNF- α and z-VAD-fmk unless RIP1 is reconstituted^{18,19}. Using this RIP1-deficient cell line, we created stable cell lines reconstituted with wild-type RIP1, the various lysine 530 RIP1 mutants, or an empty vector. As expected, expression of wild-type RIP1 restored a necrotic response to cells that were stimulated with TNF- α and z-VAD-fmk (Fig. 4d). Compared to wild-type RIP1, the level of observed necrosis was higher in cells expressing RIP1(K530A), whereas cells expressing the RIP1(K530Q) mutant were unable to undergo TNF- α -induced necrosis. Together, these data support the notion that SIRT2-dependent deacetylation of lysine 530 of RIP1 is required for stable RIP1–RIP3 complex formation and for ligand-dependent programmed necrosis.

Inhibiting SIRT2 reduces ischaemic injury

We next sought to further assess the physiological implications of our observations. Previous data have indicated that inhibition of necrosis by agents such as necrostatin-1 can reduce ischaemia-reperfusion injuries in critical organs such as the brain and heart^{7,20}. We reasoned that genetic or pharmacological inhibition of SIRT2 might provide similar protection. We subjected the hearts of age- and sex-matched littermates of wild-type or *Sirt2*^{-/-} mice to a protocol of ischaemia-reperfusion (Fig. 5a). At the end of reperfusion, the hearts of *Sirt2*^{-/-} mice showed improved function as assessed by their rate pressure product (Fig. 5b). This functional improvement was accompanied by an approximate 50% reduction in the size of myocardial infarcts when *Sirt2*^{-/-} mice were compared to their wild-type littermates (Fig. 5c, d; wild-type mice infarct size $32.3 \pm 4.7\%$ of myocardium, *Sirt2*^{-/-} mice $19.0 \pm 8.8\%$, mean \pm s.d., $n = 11$ per genotype, $P < 0.001$). As we observed following TNF- α and z-VAD-fmk stimulation, ischaemia-reperfusion also resulted in the *in vivo* deacetylation of RIP1 (Fig. 5e). This deacetylation was reduced in *Sirt2*^{-/-} mice, or in wild-type mice treated with the SIRT2 inhibitor AGK2. Similarly, as observed in other cases of stimulated necrosis, ischaemia-reperfusion resulted in an observed increase in RIP1–RIP3 interaction that was also not evident in either *Sirt2*^{-/-} mice or in AGK2-treated wild-type animals (Supplementary Fig. 14). Consistent with these biochemical data, treatment of wild-type mice with AGK2 produced a similar improvement in functional recovery after ischaemia-reperfusion (Fig. 5f) and corresponding reduction in ultimate infarct size (Fig. 5g; wild-type vehicle $29.4 \pm 2.4\%$ of myocardium and AGK2-treated $16.0 \pm 0.4\%$, mean \pm s.d., $n = 5$ per group, $P < 0.001$). When we further assessed

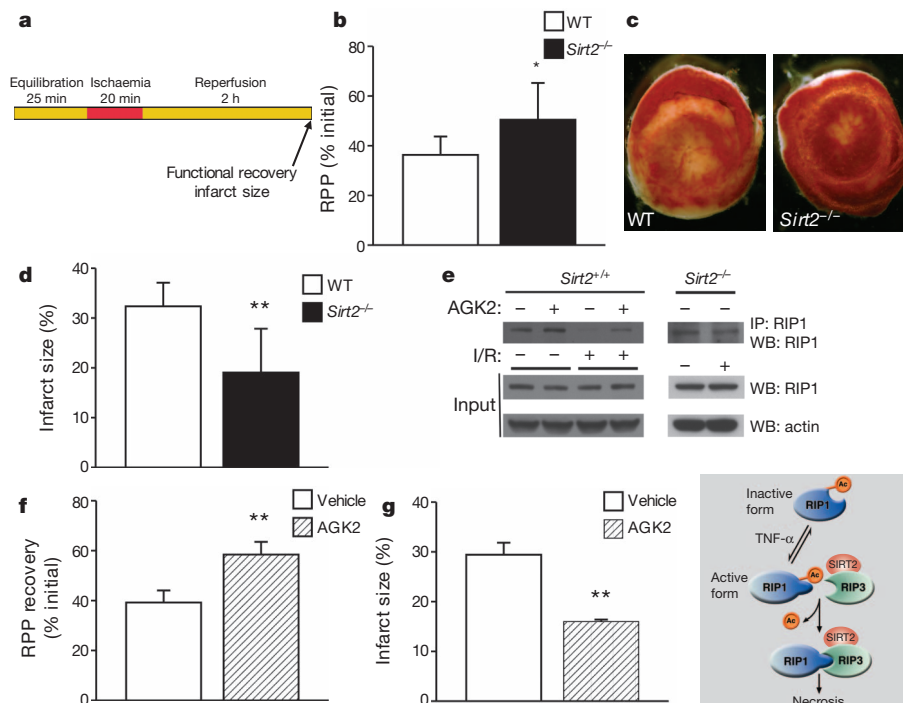


Figure 5 | Inhibition of SIRT2 protects against ischaemia-reperfusion injury. **a**, Protocol for myocardial injury involving 20 min of global ischaemia followed by a 2-h reperfusion period. **b**, Rate pressure product (RPP = heart rate \times left ventricular developed pressure), a measurement of cardiac function demonstrating preserved function in *Sirt2*^{-/-} mice, compared to wild-type (WT) littermates ($n = 11$ mice per group; 6 females and 5 males per group). **c**, Representative histological sections stained with 2,3,5-triphenyltetrazolium chloride (TTC) as a marker of necrotic damage demonstrating less apparent infarct area (pale region/TTC positive) in the hearts of *Sirt2*^{-/-} mice. **d**, Quantification of infarct size in WT and *Sirt2*^{-/-} mice ($n = 11$ per group;

6 females and 5 males per group). **e**, Levels of RIP1 acetylation in hearts under basal conditions or after ischaemia/reperfusion (I/R). RIP1 acetylation decreased in WT heart after I/R. Acetylation of RIP1 was maintained during I/R in wild-type AGK2 treated animals or *Sirt2*^{-/-} hearts. Shown is one of two similar experiments. **f**, **g**, RPP (**f**) and infarct size (**g**) in WT mice treated with vehicle alone or with 15 μ M AGK2, a specific SIRT2 inhibitor. $n = 5$ per group; 3 males and 2 females with all data expressed as mean \pm s.d.; * $P < 0.05$, ** $P < 0.01$ by unpaired Student *t*-test. **h**, A model for SIRT2-dependent regulation of programmed necrosis.

cardiac ischaemia-reperfusion injury using additional *in vivo* models, we noted a similar decrease in infarct size in *Sirt2*^{-/-} mice (Supplementary Fig. 15).

Discussion

Our results establish a role for SIRT2 in regulating necroptosis. In particular, we show that SIRT2-dependent deacetylation of RIP1 serves as an important regulatory mechanism for programmed necrosis. Although no formal structure exists, on the basis of work with related kinases, RIP1 is thought to spontaneously interconvert between two separate conformations, with TNF- α stimulation stabilizing the active state¹². We propose that necrotic stimulation brings this active conformation of RIP1 into close proximity with the pre-formed RIP3-SIRT2 complex, allowing for lysine 530 deacetylation with subsequent stable complex formation (Fig. 5g). This model is supported by our data using necrostatin-1 that indicate that, in the setting of TNF- α stimulation, RIP1 most likely needs to be in an active conformation to undergo deacetylation (Fig. 3e and Supplementary Fig. 16). Similarly, because RIP3 knockdown inhibits RIP1 deacetylation without altering overall SIRT2 levels (Fig. 3d), our data indicate that, under physiological conditions, RIP1 deacetylation occurs in a RIP3-dependent fashion. Finally, our results with the RIP1 gain and loss of function mutants, including the RIP1(K530A) mutant that undergoes ligand-independent interaction, indicate that RIP1 deacetylation precedes RIP1-RIP3 complex formation. Interestingly, although the RIP1(K530A) mutant formed a constitutive complex with RIP1 these cells did not undergo spontaneous necrosis, suggesting that RIP1-RIP3 complex formation is not by itself sufficient for necroptosis. It will be important to further test the *in vivo* correlates of these observations using the appropriate RIP1 K530 knock-in mouse models.

SIRT2 has been previously implicated as a tubulin deacetylase⁹, a potential regulator of cell cycle progression²¹, a determinant of myelination²² and very recently as a tumour suppressor²³. Our data establish another important biological function of SIRT2, namely a regulator of necroptosis. Given that the activities of the sirtuins are thought to be regulated by NAD levels, it is possible that the SIRT2-dependence of the RIP1-RIP3 interaction may provide a mechanism to regulate cellular necrosis based on overall cellular energetics. In this scenario, the balance between apoptosis and necrosis would be potentially regulated by tissue NAD levels²⁴.

Finally, it may also be important to note that the initial description of the specific SIRT2 inhibitor AGK2 showed that this compound was effective in a *Drosophila* model of neurodegeneration¹⁰. The mechanism for this protection was not defined in this initial study. Given the known role of necrosis in neurodegenerative conditions^{1,2}, it is tempting to speculate that our present observations may provide some insight into these previously observed benefits. These past observations, coupled with our own *in vivo* data, suggest that transient inhibition of SIRT2 may have widespread clinical utility for a range of clinically important conditions including ischaemic stroke, myocardial infarction, as well as presumably the growing list of conditions where necrosis is thought to have a significant role^{1,2}.

METHODS SUMMARY

Cells and mice. L929 cells (American Type Culture Collection) were cultured at 37 °C in DMEM (Invitrogen) supplemented with 10% FBS, 100 units ml⁻¹ penicillin, and 100 μ g ml⁻¹ streptomycin. MEFs were prepared in standard fashion and maintained in DMEM supplemented with 15% FBS. To generate SIRT2-deficient mice, we cloned the murine *Sirt2* gene from a 129 mouse genomic DNA library. A 2.7 kb SacI-SacI fragment containing exons 3 and 4 was cloned

into the pLNTK vector as a 5' arm, and a 3.8-kb SacI–SacI fragment was inserted into the opposite side of the pGK-Neo cassette as a 3' arm. By homologous recombination, the resulting targeting construct deleted exons 5, 6 and a part of exon 7 of the *Sirt2* gene. The targeting construct was electroporated into TC1 embryonic stem cells, and correctly targeted clones were isolated via positive and negative selection followed by Southern blotting. The targeted clones were further transiently transfected with pMC Cre recombinase to remove the *Neo* gene and subsequently injected into C57BL/6J blastocysts to obtain chimaeras. The induction of necrosis was in general as previously described⁵. In brief, L929 cells were pre-treated with 50 μ M of zVAD-fmk for 1 h before stimulation with 100 ng ml⁻¹ of recombinant mouse TNF- α (R&D Systems). L929 cells were collected 2 h after stimulation for biochemical assays, including RIP1–RIP3 complex formation and acetylation detection, or 5 h after stimulation to assess necrosis. Induction of necrosis was similar for MEF cells, except that these cells were pre-treated for 1 h with 20 μ M zVAD-fmk and 1 μ g ml⁻¹ cycloheximide followed by 50 ng ml⁻¹ TNF- α stimulation. MEF cells were routinely collected 5 h after TNF- α stimulation for biochemical studies and 18 h after stimulation for determining necrosis. Full methods are available as Supplementary Information.

Full Methods and any associated references are available in the online version of the paper.

Received 14 November 2011; accepted 20 October 2012.

Published online 28 November 2012.

- Vandenabeele, P., Galluzzi, L., Vanden Berghe, T. & Kroemer, G. Molecular mechanisms of necroptosis: an ordered cellular explosion. *Nature Rev. Mol. Cell Biol.* **11**, 700–714 (2010).
- Christofferson, D. E. & Yuan, J. Necroptosis as an alternative form of programmed cell death. *Curr. Opin. Cell Biol.* **22**, 263–268 (2010).
- Yuan, J. & Kroemer, G. Alternative cell death mechanisms in development and beyond. *Genes Dev.* **24**, 2592–2602 (2010).
- He, S. *et al.* Receptor interacting protein kinase-3 determines cellular necrotic response to TNF- α . *Cell* **137**, 1100–1111 (2009).
- Cho, Y. S. *et al.* Phosphorylation-driven assembly of the RIP1–RIP3 complex regulates programmed necrosis and virus-induced inflammation. *Cell* **137**, 1112–1123 (2009).
- Zhang, D. W. *et al.* RIP3, an energy metabolism regulator that switches TNF-induced cell death from apoptosis to necrosis. *Science* **325**, 332–336 (2009).
- Degterev, A. *et al.* Chemical inhibitor of nonapoptotic cell death with therapeutic potential for ischemic brain injury. *Nature Chem. Biol.* **1**, 112–119 (2005).
- Finkel, T., Deng, C. X. & Mostoslavsky, R. Recent progress in the biology and physiology of sirtuins. *Nature* **460**, 587–591 (2009).
- North, B. J., Marshall, B. L., Borra, M. T., Denu, J. M. & Verdin, E. The human Sir2 ortholog, SIRT2, is an NAD⁺-dependent tubulin deacetylase. *Mol. Cell* **11**, 437–444 (2003).
- Outeiro, T. F. *et al.* Sirtuin 2 inhibitors rescue alpha-synuclein-mediated toxicity in models of Parkinson's disease. *Science* **317**, 516–519 (2007).
- Zhao, Y. *et al.* Cytosolic FoxO1 is essential for the induction of autophagy and tumour suppressor activity. *Nature Cell Biol.* **12**, 665–675 (2010).
- Degterev, A. *et al.* Identification of RIP1 kinase as a specific cellular target of necrostatins. *Nature Chem. Biol.* **4**, 313–321 (2008).
- Fearn, C., Pan, Q., Mathison, J. C. & Chuang, T. H. Triad3A regulates ubiquitination and proteasomal degradation of RIP1 following disruption of Hsp90 binding. *J. Biol. Chem.* **281**, 34592–34600 (2006).
- Vucic, D., Dixit, V. M. & Wertz, I. E. Ubiquitylation in apoptosis: a post-translational modification at the edge of life and death. *Nature Rev. Mol. Cell Biol.* **12**, 439–452 (2011).
- McComb, S. *et al.* cIAP1 and cIAP2 limit macrophage necroptosis by inhibiting Rip1 and Rip3 activation. *Cell Death Differ.* **19**, 1791–1801 (2012).
- Mahul-Mellier, A. L. *et al.* De-ubiquitinating proteases USP2a and USP2c cause apoptosis by stabilising RIP1. *Biochim. Biophys. Acta* **1823**, 1353–1365 (2012).
- Sun, X., Yin, J., Starovasnik, M. A., Fairbrother, W. J. & Dixit, V. M. Identification of a novel homotypic interaction motif required for the phosphorylation of receptor-interacting protein (RIP) by RIP3. *J. Biol. Chem.* **277**, 9505–9511 (2002).
- Ting, A. T., Pimentel-Muinos, F. X. & Seed, B. RIP mediates tumor necrosis factor receptor 1 activation of NF- κ B but not Fas/APO-1-initiated apoptosis. *EMBO J.* **15**, 6189–6196 (1996).
- Zheng, L. *et al.* Competitive control of independent programs of tumor necrosis factor receptor-induced cell death by TRADD and RIP1. *Mol. Cell Biol.* **26**, 3505–3513 (2006).
- Lim, S. Y., Davidson, S. M., Mocanu, M. M., Yellon, D. M. & Smith, C. C. The cardioprotective effect of necrostatin requires the cyclophilin-D component of the mitochondrial permeability transition pore. *Cardiovasc. Drugs Ther.* **21**, 467–469 (2007).
- North, B. J. & Verdin, E. Interphase nucleo-cytoplasmic shuttling and localization of SIRT2 during mitosis. *PLoS ONE* **2**, e784 (2007).
- Beirowski, B. *et al.* Sir-two-homolog 2 (Sirt2) modulates peripheral myelination through polarity protein Par-3/atypical protein kinase C (aPKC) signaling. *Proc. Natl Acad. Sci. USA* **108**, E952–E961 (2011).
- Kim, H. S. *et al.* SIRT2 maintains genome integrity and suppresses tumorigenesis through regulating APC/C activity. *Cancer Cell* **20**, 487–499 (2011).
- Houtkooper, R. H., Canto, C., Wanders, R. J. & Auwerx, J. The secret life of NAD⁺: an old metabolite controlling new metabolic signaling pathways. *Endocr. Rev.* **31**, 194–223 (2010).

Supplementary Information is available in the online version of the paper.

Acknowledgements We are grateful to M. Lenardo for providing the RIP1-deficient Jurkat cell line, X. Wang for the Flag-tagged RIP3 plasmid and Y. Zhao for helpful discussions. This work was supported by NIH Intramural funds. F.W.A. is an Investigator of the Howard Hughes Medical Institute.

Author Contributions N.N., I.H.L., R.B., J.S., R.W., G.T., M.M.F., J.L., G.W. and L.C. carried out experimental work and analysed data, H.-L.C., F.W.A., D.L. and M.N.S. provided critical materials and data interpretation, M.G. and E.M. supervised the research, I.I.R. analysed the data, T.F. supervised the research and wrote the manuscript.

Author Information Reprints and permissions information is available at www.nature.com/reprints. The authors declare no competing financial interests. Readers are welcome to comment on the online version of the paper. Correspondence and requests for materials should be addressed to T.F. (finkelt@nih.gov).

METHODS

Cells, immunoprecipitation and protein analysis. HeLa and 293T cells (both obtained from ATCC) were grown in DMEM (Invitrogen) supplemented with 10% FBS, 100 units ml⁻¹ penicillin, and 100 µg ml⁻¹ streptomycin. RIP1-deficient Jurkat T cells (a gift of M. Lenardo) were cultured in RPMI media (ATCC) supplemented with 15% FBS (ATCC), 100 units ml⁻¹ penicillin and 100 µg ml⁻¹ streptomycin.

For immunoprecipitation analysis, L929 or MEF cell lysates (3 mg protein) were mixed with the indicated antibody (2 µg) at 4 °C overnight followed by the addition of 80 µl of protein G-Sepharose (Amersham Biosciences) for 1 h at 4 °C. Immune complexes were washed five times with lysis buffer (Cell Lysis Buffer from Cell Signaling), supplemented with complete mini-protease inhibitor cocktail (Roche Applied Science). After boiling in 5× sample buffer, samples were subjected to SDS/PAGE, transferred to nitrocellulose using the iBlot Dry Blotting System (Invitrogen), and then immunoblotted with the indicated primary antibodies, including anti-haemagglutinin (Roche Applied Science), anti-Flag (Sigma), SIRT2 (SantaCruz Biotechnology), RIP3 (ProSci), actin (Cell Signaling), RIP1 (BD Biosciences) or acetyl-lysine (Cell Signaling), followed by the appropriate horseradish-peroxidase-conjugated secondary antibodies (Santa Cruz Biotechnology). Bands were visualized by enhanced chemiluminescence (Pierce). Where indicated, cells treated with 10 µM AGK2 (Tocris) for 16 h before collection.

For the initial detection of SIRT2-interacting proteins, HCT-116 cells were transfected with either 5 µg of an empty Flag vector or a Flag-SIRT2 plasmid using Effectene transfection reagent (Qiagen). After an overnight incubation, the cells were collected in 1 ml of lysis buffer (50 mM Tris pH 7.4, 1% Triton X-100, 0.5% NP-40, 150 mM NaCl, protease and phosphatase inhibitor cocktail (Sigma) and 10% glycerol) to yield 15–20 mg of protein lysates. These lysates were then incubated with anti-Flag agarose beads (Sigma) overnight at 4 °C. Immunoprecipitates were then washed 3 times in lysis buffer and twice more in elution buffer (50 mM Tris pH 7.4, 150 mM NaCl). Elution was performed at 4 °C in 150 µl of elution buffer, including 3 µl of a 5 mg ml⁻¹ solution of Flag peptide (Sigma). The supernatant was then collected and subjected to in-solution protein digestion and processing by mass spectrometry.

To determine acetylation sites, the RIP1 amino acid sequence was analysed using a widely available bioinformatics tool called PAIL (prediction of acetylation on internal lysines). We used high stringency settings to determine that lysine 530 had a score of 1.17, demonstrating that the residue was likely acetylated (89% confidence). Further details regarding the algorithm can be found from previous studies²⁵ and at <http://bdmpail.biocuckoo.org/>.

To directly measure SIRT2 activity we used the SIRT-Glo Assay (Promega). Briefly, mouse L929 cells were transfected with a plasmid encoding for Flag-SIRT2 or an empty vector. Transfected cells were then either left untreated or stimulated to undergo necrosis with TNF-α (100 ng ml⁻¹ for L929 cells and 20 ng ml⁻¹ for Jurkat T cells) and z-VAD-fmk (40 µM). Cells were collected and immunoprecipitated using the Sigma Flag M2 antibody. The SIRT2 protein was eluted using Flag Peptide and was subsequently used as a source of purified enzyme in the protocol as specified by the manufacturer.

NAD levels were measured in untreated L929 cells and L929 cells treated with TNF/zVAD combination using the EnzyChrom NAD/NADH Assay Kit (BioAssay Systems). The methods followed the manufacturer's protocol. The values obtained were normalized for protein concentration.

GST-tagged fusion proteins were expressed and purified as described previously²⁶. The purity of the fusion proteins was tested by sodium dodecyl sulphate (SDS)-polyacrylamide gel electrophoresis (PAGE) and Coomassie staining. For protein interaction studies, *in vitro* translations were performed with rabbit reticulocyte lysate and the Promega TNT system, and radiolabelling was done with [³⁵S]cysteine (Perkin Elmer). Equal amounts of radiolabelled *in-vitro*-translated SIRT2 proteins was added to GST fusion proteins bound to glutathione resin and incubated for 1 h at 4 °C. After extensive washing with phosphate-buffered saline (PBS) containing 0.25% NP-40, the bound proteins were analysed by SDS-PAGE and autoradiography.

Acetylation and deacetylation measurements. For assessment of RIP1 acetylation, protein lysates from HeLa cells (4 mg), L929 cells (4 mg) or heart tissue (3.5 mg) were mixed with 20 µl of acetyl-lysine or RIP1 antibodies overnight at 4 °C followed by the addition of 60 µl of protein G-Sepharose (Amersham Biosciences) for 2 h at 4 °C. Immunoprecipitates were washed five times with lysis buffer as previously described. After boiling in 2× sample buffer, samples were subjected to SDS/PAGE. After transfer to nitrocellulose, membranes were immunoblotted with the indicated primary antibodies followed by the appropriate horseradish peroxidase-conjugated secondary antibodies (Santa Cruz Biotechnology or Pierce). Bands were visualized by enhanced chemiluminescence (Pierce) as previously described²⁷.

For analysis of *in vivo* RIP1 acetylation, heart tissues with or without ischaemia/reperfusion injury were collected from wild-type untreated mice, wild-type

AGK2-treated mice or *Sirt2*^{-/-} mice. The tissues were incubated in lysis buffer for 30 min at 4 °C followed by sonication (Sonicator XL 2020 Misonix, Inc.) for 15–30 s at 20% amplitude. Lysates were subsequently clarified by centrifugation at 16,000g (30 min at 4 °C) before further processing as described above. RIP acetylation was detected directly by immunoprecipitation with RIP1 antibodies (BD) and subsequent immunoblotting for acetyl-lysine antibody (Cell Signaling Technology). Similarly, we detected RIP1-RIP3 complex formation in myocardial tissues under basal conditions or following ischaemia/reperfusion. Lysate was prepared as above and samples were first immunoprecipitated with a RIP1 antibody followed by western blotting with a RIP3 antibody (Millipore). For endogenous RIP3 acetylation, we analysed L929 cells with or without shRNA-mediated knockdown of SIRT2. Cell lysates were immunoprecipitated with an acetyl-lysine antibody and subsequently analysed by western blotting using a RIP3 antibody as described above.

To assess the effect of p300 expression on RIP1 acetylation, we co-transfected HeLa cells with Flag-tagged RIP1 with or without an expression vector encoding the p300 acetyltransferase as previously described²⁸. Cells were collected 24 h after transfection and RIP1 acetylation assessed as described above.

To assess *in vitro* deacetylation of full-length RIP1, we first prepared acetylated substrate by transfecting 293T cells with an expression construct encoding HA-RIP1. Twenty-four hours after transfection, cells were collected in lysis buffer and 7 mg of transfected protein lysate was incubated with 4 µg of HA antibody and subsequently bound to Protein G Sepharose beads. To increase levels of RIP1 acetylation, 10 µM AGK2 was added for the last 12 h before cell collection. Purified SIRT2 protein was obtained by transfecting a Flag-tagged wild-type or deacetylase-inactive SIRT2 expression construct into 293T cells. The epitope product was purified by using an anti-Flag M2 affinity gel (Sigma) and subsequently eluted competitively with five one-column volumes of a solution containing 100 µg ml⁻¹ Flag peptide (Sigma) in elution buffer.

The deacetylase reaction was performed in the presence or absence of ≈300 ng of purified wild-type or mutant SIRT2 along with NAD (10 mM). Equal amounts of acetylated substrate was prepared and the deacetylation reaction was performed for 2 h at 37 °C in deacetylation assay buffer (50 mM Tris·HCl, 1 mM MgCl₂ and 150 mM NaCl (pH 8.0)) using a total reaction volume of 50 µl. The deacetylation of each protein substrate was subsequently detected after SDS/PAGE, transfer to nitrocellulose, and immunodetection with an anti-acetyl-lysine antibody.

For measurement of deacetylation of a peptide substrate, a RIP1 peptide with the sequence IKYTIYNSTGIQIAYNY was synthesized in the unacetylated and K530 acetylated form by Elim Biopharmaceuticals Inc. *In vitro* deacetylase assays were conducted with 15 µM acetylated/unacetylated RIP1 peptide mixture, 2 µg of human recombinant SIRT2 (Cayman Chemicals), 10 mM NAD, in the deacetylation assay buffer at 37 °C for 2 h.

In vitro acetylation assays were performed with 150 µM RIP1 peptide, 12 µg of the HAT domain of the acetyltransferase p300 (Enzo Life Sciences), 1 mM acetyl CoA, in a buffer containing 150 mM HEPES, 10% glycerol, 3 mM DTT, 30 mM sodium butyrate at 30 °C for one hour.

LCMS analysis was carried out using an Eksigent nanoLC Ultra system connected to an LTQ Orbitrap Velos mass spectrometer (Thermo Scientific). Peptide sample was first loaded on to a trapping cartridge (Agilent) at a flow rate of 6 µl min⁻¹. Separation of the trapped peptides was performed on a reversed-phase PicoFrit column (New Objective) using a linear gradient of acetonitrile (5–45%) in 0.1% formic acid at a flow rate of 250 nl min⁻¹. Eluted peptides were sprayed into the mass spectrometer equipped with a nano-spray ion source.

FACS analysis and necrosis assays. After stimulation with TNF-α (5 h for L929 cells, 14 h for Jurkat T cells and 18 h for MEFs) cells were washed twice with cold PBS and then resuspended in 1× binding buffer (BD Biosciences) at a concentration of ~1 × 10⁶ cells ml⁻¹. Then, 100 µl of the solution (~1 × 10⁵ cells) was transferred to a 5 ml culture tube and stained with 5 µl each of allophycocyanin-annexin V (BD Biosciences) and 50 µg ml⁻¹ propidium iodide (Invitrogen). The cells were gently mixed and incubated at room temperature for 15 min. For assessment of necrosis, 400 µl of 1× binding buffer was then added to each tube and the samples were analysed by flow cytometry using a LSRII instrument (Becton-Dickinson). Where indicated tubacin and necrostatin-1 (Enzo Life Sciences) were used at concentrations of 2 µM for 4 h and 20 µM for 1 h, respectively, before the addition of the necrotic stimuli.

Transfections, plasmids and lentiviral transductions. L929 cells were routinely transfected with GenJet (Signagen) as per the manufacturer's protocol. The Flag-SIRT2 plasmid was obtained from Addgene, and the Q130A deacetylase-inactive mutant was made using the following primers: Forward primer 5'-CTACTCCT GCGCTGCTACACGGCAAACATAGAT; Reverse primer 5'-CGTGGTAGC AGCGCAGGAGTAGCCCCCTTGTC. Glutathione-S-transferase (GST) fusion plasmids were all cloned in pGEX-6T. The RIP3 truncations below were cloned

into pGEX-6T with the following primers: Full length RIP3, forward primer 5'-TCCCCCGGGTATGTCGTCGTCGAAGTTATGGCCC and reverse primer 5'-CCGCTCGAGTTTCCCGCTATGATTATACCAACC; RIP3 with residues spanning positions 1 to 287, forward primer 5'-TCCCCCGGGTATGTCGTCGTCGAAGTTATGGCCC and reverse primer 5'-CCGCTCGAGCTCACTGCTCCAGCAGAGCTGCATT; Residues spanning position 287 to 440 or 518, forward primer 5'-TCCCCCGGGTGAGCCCAAGGACAGACCCTCCTTC, and reverse primers for 440, 5'-CCGCTCGAGTCGGGGTCCAGGACCTGGTGTTC, and 518, 5'-CCGCTCGAGAGGGCCTTCTTGGCAACCTACTGG. The haemagglutinin-tagged RIP1 and the K530 mutants were cloned into pcDNA3.1+ vector using EcoRV and XhoI sites and the following primers: K530Q, forward primer 5'-CCAACAGATGAATCTATACAGTATACCATATACAATAGT and reverse primer 5'-ACTATTGTATATGGTATAGTATAGATTCATCTGTTGG. K530A, forward primer 5'-CCAACAGATGAATCTATAGCATATACCATATACAATAGT and reverse primer 5'-ACTATTGTATATGGTATAGTATAGATTCATCTGTTGG. For the construction of the 3×Flag-RIP1 we inserted the *Rip1* gene into the pCMV-3×Flag vector by cutting both with EcoRI and KpnI. *Rip1* gene products were prepared by PCR with the following primers: Forward primer: 5'-CCGGAATTCATGCAACCAGACATGTCCTT Reverse primer: 5'-CGGGGTACCCTAGTTCTGGTGACGTAAT The HA-tagged wild-type SIRT1 has been described²⁹. The Flag-tagged RIP3 plasmid was a gift from X. Wang. Lentiviral vectors for stable shRNA-mediated knockdown of SIRT2 and RIP3 were purchased from Open Biosystems. We in general screened five shRNA for each gene to be knockdown and confirmed the biochemical and biological endpoints using at least two independent shRNAs. The sequence and clone ID used in this study included: SIRT2: clone ID TRCN0000012121, mature antisense TTCCAGC GTGTCTATGTTCTG. SIRT2: clone ID TRCN0000012119, mature antisense TTCTCCAGGTTTGCATAGAGG. RIP3: clone ID TRCN0000022536, mature antisense AAAGCTGTAGACATCACTCGC. RIP3: clone ID TRCN0000022538, mature antisense AAGGAGTTGTAGTTCCTCAATC.

Amplification was via standard methods in subconfluent 293T cells. Infection of L929 cells was performed in the presence of polybrene (Sigma) at a final concentration of 8 µg ml⁻¹. Cells were incubated with virus mixture for 24 h and medium was changed to fresh growth medium with puromycin (Sigma) for stable knockdown.

For constructing stable Jurkat T cells lines, we used a previously described mutant line of Jurkat cells that had undergone random chemical mutagenesis and was selected on the basis of the absence of detectable RIP1 expression^{18,19}. These cells fail to undergo TNF-α-stimulated necrosis without the re-introduction of RIP1¹⁹. RIP1-deficient Jurkat cells were electroporated with the indicated RIP1 wild-type or mutant construct, or with an empty vector control plasmid. Cells were selected for two weeks using 400 µg ml⁻¹ of geneticin (Invitrogen) before analysis. Pooled colonies expressing wild-type RIP1 or the various RIP1 mutants were analysed for their degree of programmed necrosis stimulated by

addition of TNF-α and z-VAD-fmk. Western blot analysis demonstrated that overall RIP1 expression was similar in all stable pooled clones.

Langendorff perfusion and infarct model. Hearts from young wild-type or *Sirt2*^{-/-} littermates were isolated and Langendorff-perfused with Krebs–Heinseleit (KH) buffer for 25 min (equilibration) before being subjected to 20 min of no-flow ischaemia. Functional recovery of left ventricular developed pressure (LVDP) and rate pressure product (RPP; product of LVDP and heart rate) was measured following 2 h of reflow and expressed as a percentage of the initial RPP before ischaemia as previously described³⁰. For the AGK2 inhibitor experiments, mouse hearts were perfused with 1% BSA in KH buffer containing either the vehicle control (0.1% DMSO) or 15 µM of AGK2 (a specific SIRT2 inhibitor) for 10 min before 20 min of no-flow ischaemia. This was then followed by 120 min of reperfusion with normal KH buffer. At the end of the 2-h reflow, hearts were incubated in KH buffer containing 1% (w/v) 2,3,5-triphenyltetrazolium chloride (TTC) to measure the extent of necrosis³¹. Samples were sliced into cross-sections and area of infarct as a percent of the whole heart was quantified.

For *in vivo* infarction, we used the previously described method of mouse coronary artery ligation that does not require ventilation support³². In brief, the left coronary artery of the mouse was ligated for 30 min with a slipknot suture placed approximately 2 mm from the artery's origin. At the end of the ischaemic period, the slipknot suture is removed and the hearts were reperfused *in vivo* for an additional 4 h. At the end of the reperfusion procedure the animals were euthanized. Quantification was performed in a blinded fashion using the area at risk (determined by perfusing with Evans blue dye) and the area of infarction (TTC staining). These experiments were performed with female mice that were age-matched littermates. All animal experiments were performed in accordance and with approval from the NHLBI Animal Care and Use Committee.

25. Li, A., Xue, Y., Jin, C., Wang, M. & Yao, X. Prediction of N^ε-acetylation on internal lysines implemented in Bayesian discriminant method. *Biochem. Biophys. Res. Commun.* **350**, 818–824 (2006).
26. Thomas, M., Massimi, P. & Banks, L. HPV-18 E6 inhibits p53 DNA binding activity regardless of the oligomeric state of p53 or the exact p53 recognition sequence. *Oncogene* **13**, 471–480 (1996).
27. Lee, I. H. *et al.* A role for the NAD-dependent deacetylase Sirt1 in the regulation of autophagy. *Proc. Natl Acad. Sci. USA* **105**, 3374–3379 (2008).
28. Lee, I. H. & Finkel, T. Regulation of autophagy by the p300 acetyltransferase. *J. Biol. Chem.* **284**, 6322–6328 (2009).
29. Nemoto, S., Fergusson, M. M. & Finkel, T. SIRT1 functionally interacts with the metabolic regulator and transcriptional coactivator PGC-1α. *J. Biol. Chem.* **280**, 16456–16460 (2005).
30. Sun, J., Morgan, M., Shen, R. F., Steenbergen, C. & Murphy, E. Preconditioning results in S-nitrosylation of proteins involved in regulation of mitochondrial energetics and calcium transport. *Circ. Res.* **101**, 1155–1163 (2007).
31. Csonka, C. *et al.* Measurement of myocardial infarct size in preclinical studies. *J. Pharmacol. Toxicol. Methods* **61**, 163–170 (2010).
32. Gao, E. *et al.* A novel and efficient model of coronary artery ligation and myocardial infarction in the mouse. *Circ. Res.* **107**, 1445–1453 (2010).

Bypass of a protein barrier by a replicative DNA helicase

Hasan Yardimci¹, Xindan Wang², Anna B. Loveland¹, Inger Tappin³, David Z. Rudner², Jerard Hurwitz³, Antoine M. van Oijen^{4*} & Johannes C. Walter^{1*}

Replicative DNA helicases generally unwind DNA as a single hexamer that encircles and translocates along one strand of the duplex while excluding the complementary strand (known as steric exclusion). By contrast, large T antigen, the replicative DNA helicase of the simian virus 40 (SV40), is reported to function as a pair of stacked hexamers that pumps double-stranded DNA through its central channel while laterally extruding single-stranded DNA. Here we use single-molecule and ensemble assays to show that large T antigen assembled on the SV40 origin unwinds DNA efficiently as a single hexamer that translocates on single-stranded DNA in the 3'-to-5' direction. Unexpectedly, large T antigen unwinds DNA past a DNA-protein crosslink on the translocation strand, suggesting that the large T antigen ring can open to bypass bulky adducts. Together, our data underscore the profound conservation among replicative helicase mechanisms, and reveal a new level of plasticity in the interactions of replicative helicases with DNA damage.

An essential step in DNA replication is the unwinding of the double helix by a DNA helicase^{1,2}. In general, these enzymes form a hexameric ring that encircles and translocates along one DNA strand in the 3'-to-5' or 5'-to-3' direction while excluding the other strand. This steric exclusion mechanism of DNA unwinding has been demonstrated for gp4 protein in phage T7 (ref. 3), DnaB in bacteria⁴, and MCM2-7 in eukaryotes^{5,6}.

The mammalian DNA tumour virus SV40 encodes a multifunctional protein, large T antigen, which functions as a replicative helicase that cooperates with host cell replication factors to copy the SV40 genome. Although cell-free SV40 replication has served as a model for mammalian DNA replication for several decades⁷, fundamental aspects of how large T antigen unwinds DNA remain controversial⁸. In particular, it is unclear whether large T antigen functions as an obligate double hexamer (Fig. 1A, a and b) or as a single hexamer (Fig. 1A, c and d). In support of the double-hexamer model, large T antigen caught in the act of unwinding displayed 'rabbit ear' structures with two single-stranded DNA (ssDNA) loops emanating from the double hexamer⁹ (Fig. 1A, a and b). In addition, mutations in large T antigen that disrupt double-hexamer formation inhibit origin-dependent DNA unwinding^{10,11}. Finally, purified large T antigen double hexamers exhibit higher unwinding activity than single hexamers on forked DNA substrates^{12,13}. Another long-standing question is whether large T antigen unwinds DNA by means of steric exclusion (Fig. 1A, a and c) or a fundamentally different mechanism in which the translocating helicase encircles duplex DNA while extruding ssDNA from side channels (Fig. 1A, b and d). Large T antigen can translocate on ssDNA in the 3'-to-5' direction when presented with a ssDNA template¹⁴⁻¹⁶, and the closely related E1 helicase encircles ssDNA in its central channel¹⁷, supporting the steric exclusion model. Consistent with the double-stranded DNA (dsDNA) translocation model, structural studies showed that the central channel of large T antigen can expand to accommodate dsDNA and that large T antigen has side channels large enough for extrusion of ssDNA^{18,19}.

Furthermore, several studies suggest that large T antigen assembled on the SV40 origin encircles dsDNA²⁰⁻²². These results raise the possibility that large T antigen activated at an origin uses a dsDNA translocation mode. Inspired in part by large T antigen, both the double-hexamer and dsDNA translocation models were proposed for MCM2-7 (refs 23, 24), but recent evidence indicates that the native MCM2-7 complex unwinds DNA by steric exclusion and can function as a single hexamer^{5,25}.

Uncoupling of large T antigen double hexamers

The double-hexamer model suggests that DNA is pumped towards the interface between two large T antigen hexamers (Fig. 1A, a and b). Therefore, an extended DNA molecule that is attached to a surface at both ends should not be replicated efficiently owing to tension that accumulates at the ends of the DNA (Supplementary Fig. 1c). By contrast, if large T antigen can function as a single hexamer, a stretched DNA molecule should undergo extensive large-T-antigen-dependent replication (Supplementary Fig. 1d). To distinguish between the single- and double-hexamer models, we replicated λ DNA containing the SV40 origin (λ ori) that was attached at one or both ends to the surface of a microfluidic flow cell (Fig. 1B). We first examined replication of singly tethered λ ori DNA. After immobilizing DNA on the surface²⁶, large T antigen was drawn into the flow cell, allowing it to assemble on the origin (Fig. 1B). HeLa cell extract containing replication proteins^{27,28} was then introduced to initiate replication, followed, after 20 min, by a second extract containing digoxigenin-modified dUTP (dig-dUTP) to pulse-label newly replicated DNA. After further incubation, dsDNA was stained with SYTOX Orange (SYTOX), and dig-dUTP-containing regions were labelled with fluorescein-conjugated anti-digoxigenin antibody (anti-dig). On 10–20% of the molecules, the SYTOX signal showed a high intensity tract (Fig. 1C, left, and Supplementary Fig. 2a) corresponding to a replication bubble. Furthermore, two anti-dig tracts were present at the ends of each replication bubble, consistent with bidirectionally

¹Department of Biological Chemistry and Molecular Pharmacology, Harvard Medical School, Boston, Massachusetts 02115, USA. ²Department of Microbiology and Immunobiology, Harvard Medical School, Boston, Massachusetts 02115, USA. ³Program of Molecular Biology, Memorial Sloan-Kettering Cancer Center, New York, New York 10065, USA. ⁴The Zernike Institute for Advanced Materials, University of Groningen, 9747 AG Groningen, The Netherlands.

*These authors contributed equally to this work.

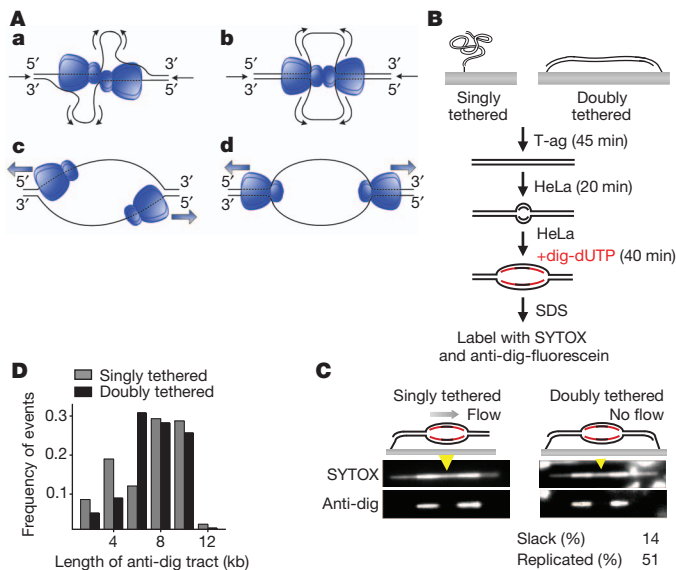


Figure 1 | Large T antigen is not an obligate double hexamer during replication. **A**, Models for DNA unwinding by large T antigen (T-ag). See main text for details. **B**, Experimental procedure for replication of singly and doubly tethered λ ori DNA. **C**, SYTOX and anti-dig images of singly tethered (left) and doubly tethered (right) λ ori DNAs that underwent replication in HeLa cell extracts. Dig-dUTP-incorporated regions occasionally exhibited higher SYTOX intensity owing to nonspecific staining of an anti-dig antibody with SYTOX. Extent of slack and replication on the doubly tethered DNA are indicated. Yellow arrowheads, estimated position of the origin. **D**, Length of anti-dig tracts on singly tethered (grey) and doubly tethered (black) DNA molecules after a 40-min dig-dUTP pulse. To measure the fork rate, the tract length distribution was fit to a Gaussian and the resulting average tract length was divided by the duration of the dig-dUTP pulse (40 min).

growing bubbles (Fig. 1C, left, and Supplementary Fig. 2a). The gap between two anti-dig tracts always coincided with the expected location of the origin (Fig. 1C and Supplementary Fig. 2, yellow arrowheads), and replication bubbles were not observed on λ DNA lacking the SV40 origin (data not shown). The average fork rate measured from the anti-dig tract length was 188 ± 61 base pairs (bp) min^{-1} (mean \pm s.d., $n = 174$, Fig. 1D) in agreement with previous reports^{29,30}. Therefore, this single-molecule approach is well suited to study large-T-antigen-dependent replication.

We repeated the experiment on λ ori DNA that was stretched to 85–90% of its B-form contour length and tethered at both 3' ends. If large T antigen functions as an obligate double hexamer, a doubly tethered DNA will not be replicated to a greater extent than the slack (10–15%) that is initially present in the molecule. In contrast to this prediction, we found that doubly tethered λ ori molecules contained replication bubbles comprising much more than 10–15% of the molecule (Fig. 1C, right, and Supplementary Fig. 2b, c), indicating that individual large T antigen hexamers function efficiently, similar to MCM2–7 (ref. 25). Importantly, the average fork rate on doubly tethered DNA (195 ± 75 bp min^{-1} , $n = 78$, Fig. 1D) was essentially the same as on singly tethered DNA, suggesting that any uncoupling of double hexamers does not impair fork progression. Finally, as expected from independently functioning replisomes, progression of sister forks showed no correlation on singly tethered ($R = 0.17$, $P = 0.11$, $n = 87$, Supplementary Fig. 2d) and doubly tethered ($R = -0.15$, $P = 0.35$, $n = 39$, Supplementary Fig. 2d) λ ori molecules.

To visualize the spatial separation of large T antigen double hexamers in real time, we examined large-T-antigen-mediated DNA unwinding on doubly tethered λ ori (Fig. 2a) using the ssDNA-binding replication protein A (RPA) fused to the green fluorescent protein (GFP)-like protein mKikGR (RPA^{mKikGR}). We detected bidirectionally growing linear tracts of RPA^{mKikGR} (Fig. 2b), demonstrating that large T antigen double

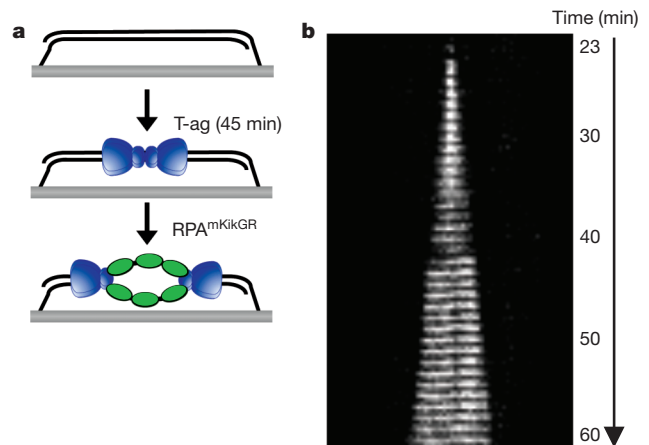


Figure 2 | Real-time visualization of sister fork uncoupling during unwinding of doubly tethered DNA. **a**, Large T antigen was drawn into a flow cell containing doubly tethered λ ori. After 45 min, RPA^{mKikGR} was introduced and mKikGR was imaged for 60 min. **b**, Kymograph of mKikGR fluorescence. Minutes denote time after introduction of RPA^{mKikGR}.

hexamers can uncouple after initiation. The average unwinding rate (215 ± 24 bp $\text{min}^{-1} \pm$ s.d., $n = 16$), determined through the growth rate of RPA^{mKikGR} tracts, was consistent with the unwinding rate of purified large T antigen³⁰ and our analysis of anti-dig tracts (Fig. 1D). The fact that DNA unwinding by large T antigen alone occurs at a similar rate as large-T-antigen-dependent replication indicates that large T antigen does not require coupling with a DNA polymerase to unwind DNA at optimal rates, unlike some prokaryotic helicases^{31,32}.

Large T antigen unwinds DNA by steric exclusion

We next examined whether large T antigen that initiates unwinding from the SV40 origin ultimately translocates on ssDNA or dsDNA. To this end, large T antigen was collided with biotin–streptavidin adducts, which large T antigen is known to disrupt¹⁵. We modified a 518-bp-long linear duplex DNA containing the SV40 origin with a site-specific biotin on the top or bottom strands (Fig. 3A, a). If large T antigen translocates on ssDNA in the 3'-to-5' direction, the hexamer moving to the right from the origin should remove streptavidin from the bottom strand (SA^{bottom}) but not the top strand (SA^{top}) (Fig. 3A, b). By contrast, the dsDNA translocation model predicts that both SA^{bottom} and SA^{top} will be dislodged by large T antigen (Fig. 3A, c). We found that large T antigen displaced SA^{bottom} (Fig. 3B, lane 8, red arrowhead, and Supplementary Fig. 3) but not SA^{top} (Fig. 3B, lane 6, green arrowhead, and Supplementary Fig. 3), indicating that the bottom strand passes through the central chamber of large T antigen while the top strand is excluded (see Fig. 3C for quantification). We conclude that large T antigen that assembles on the origin DNA translocates on the leading strand template in the 3'-to-5' direction.

To examine the translocation mechanism of large T antigen during DNA replication, we attached a quantum dot (Qdot) by a digoxigenin–anti-dig interaction to either the leading (Qdot^{lead}) or lagging (Qdot^{lag}) strand templates to the left of the origin on λ ori (Fig. 3D, cartoons). As in the experiment above, the 3'-to-5' ssDNA translocation model predicts the specific removal of Qdot^{lead}, whereas the dsDNA translocation model predicts the removal of both Qdot^{lead} and Qdot^{lag}. Because most Qdots dissociated from λ ori independently of replication (Supplementary Fig. 4 and data not shown), we could not compare replicated molecules that retained and lost Qdots, respectively, to evaluate Qdot removal by the replisome. Given that large T antigen can displace streptavidin (Fig. 3B), most events in which the edge of an anti-dig tract coincided with a Qdot (Fig. 3D and Supplementary Fig. 4f) are likely to represent spontaneous fork stalling independently of the Qdot (see Supplementary Fig. 2 for examples of spontaneous fork stalling). Because the likelihood of such an

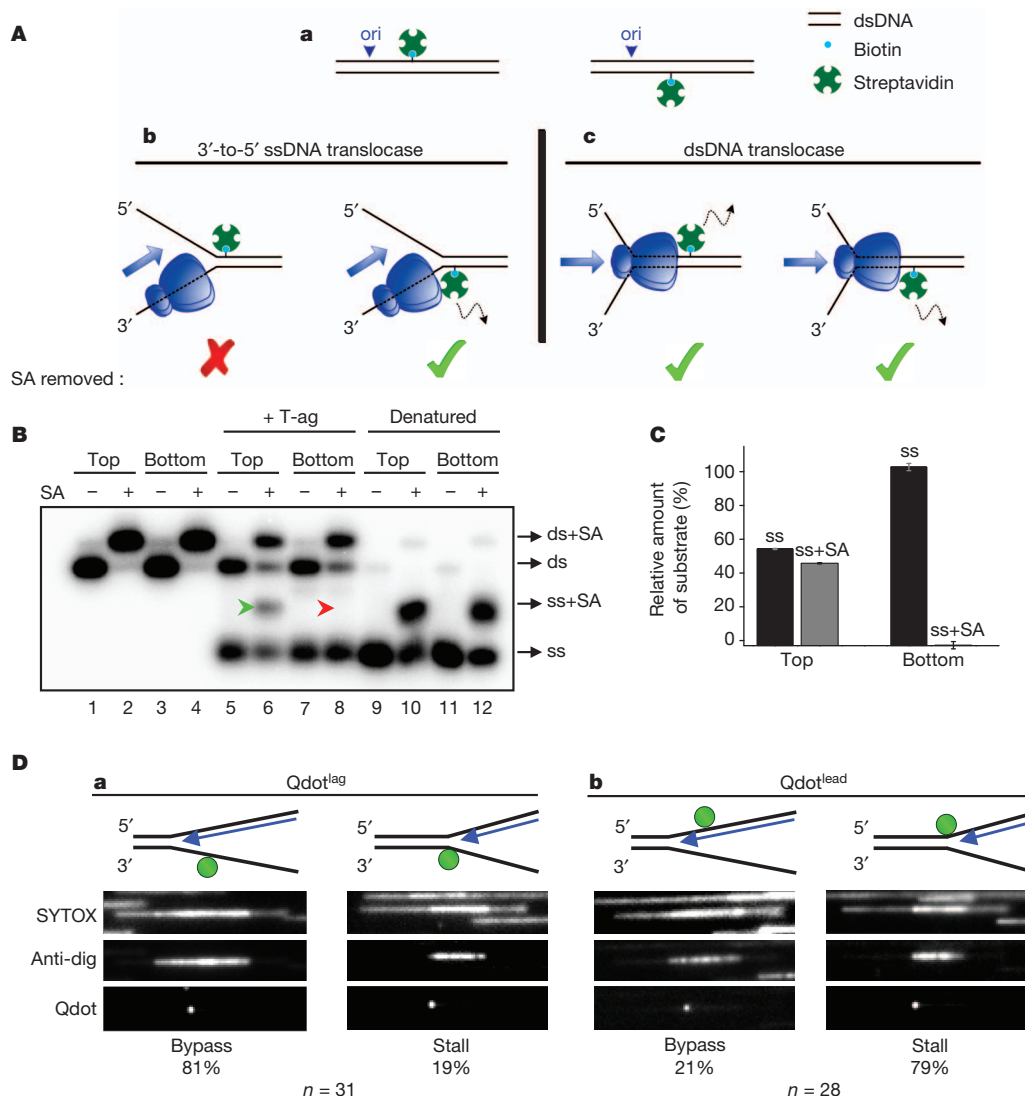


Figure 3 | Large T antigen translocates on ssDNA in the 3'-to-5' direction.

A, a, Cartoon of 518-bp-long 5'-labelled (red stars) DNA templates used for streptavidin displacement assays. **A, b, c**, Predictions of 3'-to-5' ssDNA translocation (**b**) and dsDNA translocation (**c**) models. **B**, DNAs biotinylated on the top or bottom strands (as in **A, a**) undergo complete mobility shift after streptavidin (SA) addition, indicating that all DNA molecules are modified with biotin (lanes 2, 4). DNA was pre-incubated with buffer (lanes 5, 7) or streptavidin (lanes 6, 8), and unwinding was initiated with large T antigen and RPA (lanes 5–8). Excess biotin saturated any displaced streptavidin. To assess the migration of ssDNA with or without streptavidin, DNA was heat denatured, rapidly cooled down and mixed with buffer (lanes 9, 11) or streptavidin (lanes 10, 12). Because both strands are radiolabelled, streptavidin association with one strand shifts only half of the signal (lanes 10, 12). ds, dsDNA; ss, ssDNA. **C**, Quantification of

ssDNA with (grey) and without (black) streptavidin from lanes 6 and 8 of **B**. Error bars indicate s.d. for three independent experiments. Some spontaneous dissociation of streptavidin occurred in the presence of free biotin (**B**, lanes 6 and 8, ds). The extent of large-T-antigen-independent streptavidin dissociation was determined using the relative amounts of dsDNA that lost (ds) and retained SA (ds+SA). This fraction was then used to measure the amount of ssDNA that lost and retained streptavidin, respectively, if no spontaneous streptavidin dissociation had occurred. **D, a, b**, SYTOX, anti-dig and Qdot images of representative molecules after fork collision with Qdot^{lag} (**a**) or Qdot^{lead} (**b**) in HeLa cell extracts (performed as in Fig. 1B). Because dig-dUTP was continuously present during the replication reaction, replication bubbles were fully labelled with anti-dig. The percentage of molecules exhibiting fork bypass and stalling events is indicated (see also Supplementary Fig. 4).

event is the same for Qdot^{lead} and Qdot^{lag}, we determined the ratio of molecules showing fork bypass through a Qdot (Supplementary Fig. 4e) to those exhibiting stalling at the Qdot (Supplementary Fig. 4f) to obtain a relative probability of Qdot removal by the replisome. Importantly, 81% of the molecules exhibited fork bypass through Qdot^{lag} (Fig. 3D, a) whereas only 21% bypass was observed through Qdot^{lead} (Fig. 3D, b), suggesting that Qdot^{lead} is more prone to displacement by the replisome. This result suggests that large T antigen also functions as a 3'-to-5' ssDNA translocase during DNA replication.

Large T antigen can bypass a bulky protein adduct

Given that large T antigen encircles and translocates on the leading strand template, our observation that a considerable number of

anti-dig tracts bypassed Qdot^{lead} was unexpected (Fig. 3D, b, left panel). Bypass through Qdot^{lead} indicates that large T antigen or other helicases in the extract can circumvent a bulky adduct on the leading strand template. To test this idea further, we covalently conjugated HpaII methyltransferase (M.HpaII) to the lagging (MH^{lag}) or leading (MH^{lead}) strand templates of a 518-bp-long linear DNA substrate containing the SV40 origin (Supplementary Fig. 5a). Notably, large T antigen unwound DNA containing MH^{lag} and MH^{lead} equally well (Fig. 4A). MH^{lead} was not removed from DNA by large T antigen during unwinding, as seen by the presence of ssDNA conjugated to M.HpaII (Fig. 4A, b). Uneven labelling of the two strands resulted in the intensity difference of ssDNA with and without M.HpaII (Supplementary Fig. 5b).

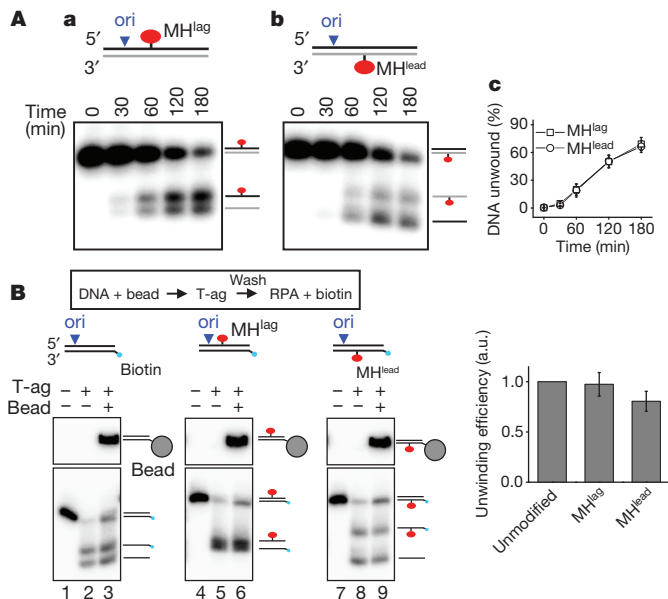


Figure 4 | Large T antigen can bypass a covalent protein barrier on the translocation strand. **A, a, b,** Large-T-antigen-dependent unwinding of DNA containing MH^{lag} (**a**) or MH^{lead} (**b**). The species corresponding to each band are depicted. Heat denaturation caused electrophoretic smearing of M.HpaII-conjugated DNA and therefore was not used for assessment of ssDNA migration (data not shown). **A, c,** Quantification of unwinding in **a** and **b**. **B,** Left, unwinding of unmodified (lane 3), MH^{lag} -modified (lane 6), and MH^{lead} -modified (lane 9) DNA by pre-assembled large T antigen (see text for details). The first two lanes in all samples correspond to 10% of input DNA without bead conjugation in the absence (lanes 1, 4, 7) and presence (lanes 2, 5, 8) of large-T-antigen-mediated unwinding. Right, quantification of unwound DNA by pre-assembled large T antigen (lanes 3, 6, 9). Amount of unwinding was normalized to that of unmodified DNA. a.u., arbitrary units. Error bars indicate s.d. for three independent experiments.

We next addressed whether the same large T antigen that initially collides with MH^{lead} bypasses the protein adduct, or whether a new large T antigen hexamer from solution assembles downstream of the protein adduct. To this end, DNA was immobilized on magnetic beads, incubated with large T antigen to assemble the helicase at the origin, washed to remove free large T antigen, and finally mixed with RPA to initiate unwinding. We confirmed that during this sequence, unwinding initiated from the origin and that most unwinding was carried out by pre-assembled large T antigen (Supplementary Fig. 6). Importantly, large T antigen pre-assembled on the origin was sufficient to unwind the template containing MH^{lead} (Fig. 4B, left, lane 9), and unwinding efficiency was only moderately reduced relative to MH^{lag} (Fig. 4B, right). Thus, the vast majority of large T antigen molecules are able to bypass a bulky adduct on the translocation strand.

Large T antigen collision with two protein barriers

Our results suggest that after collision with a protein adduct, the large T antigen ring either opens to allow bypass (Supplementary Fig. 7a, ii) or denatures the protein adduct and threads the unfolded polypeptide chain through the helicase central channel (Supplementary Fig. 7a, iii). Because M.HpaII interacts with DNA by an internal amino acid³³, the latter model would require large T antigen to accommodate two polypeptide chains and ssDNA in its central channel (Supplementary Fig. 7a, iii), which seems unlikely. To rule out the denaturation model, we repeated the experiment with a DNA template containing two protein adducts spaced 60 nucleotides (~ 200 Å) apart along the duplex (Supplementary Fig. 7b, i). In this way, unwinding the DNA by M.HpaII denaturation would require four polypeptide chains and the translocation strand to be threaded through the central channel of large T antigen (Supplementary Fig. 7b, ii), which is incompatible

with known large T antigen structures^{18,19}. Notably, large T antigen unwound the template with two adducts as efficiently as the unwound template (Fig. 5A, compare lanes 9 and 12, and 5B, b, for quantification), suggesting that bypass must occur by transient opening of the large T antigen ring. We found that two M.HpaII adducts spaced 14 nucleotides apart severely inhibited unwinding by large T antigen (Fig. 5A, lane 18, and 5B, c). Because the longitudinal axis of large T antigen (~ 120 Å) is now greater than the inter-adduct distance (~ 50 Å), this result indicates that to perform effective bypass of the second obstruction, the large T antigen ring must re-close after the first adduct has traversed the entire channel (Supplementary Fig. 7b, iii and iv). Together, the data suggest that the large T antigen ring transiently opens to bypass protein–DNA crosslinks.

Discussion

Here we present single-molecule and ensemble experiments that determine the molecular mechanism by which large T antigen unwinds DNA at the replication fork. In contrast with the prominent double-hexamer model²³, we demonstrate that the large T antigen double hexamers that form at the origin of replication can physically separate and function independently when the DNA template is placed under tension. Together with previous results^{10,11}, our data suggest that interactions between hexamers are required for initiation but dispensable during elongation. The coupling between two hexamers that led to the observation of rabbit ear structures⁹ may be due to direct interactions between hexamers or facilitated by other factors³⁴. Whether such double hexamers are normally retained during replication elongation in the complex environment of the cell is difficult to assess. Importantly, the ability of hexamers to function independently is advantageous because it allows replication to go to completion even if one replisome stalls or collapses. Notably, we found that large T antigen that initiates unwinding from the origin ultimately surrounds ssDNA and moves in the 3'-to-5' direction, as proposed for the related E1 helicase¹⁷. Taken together, our results

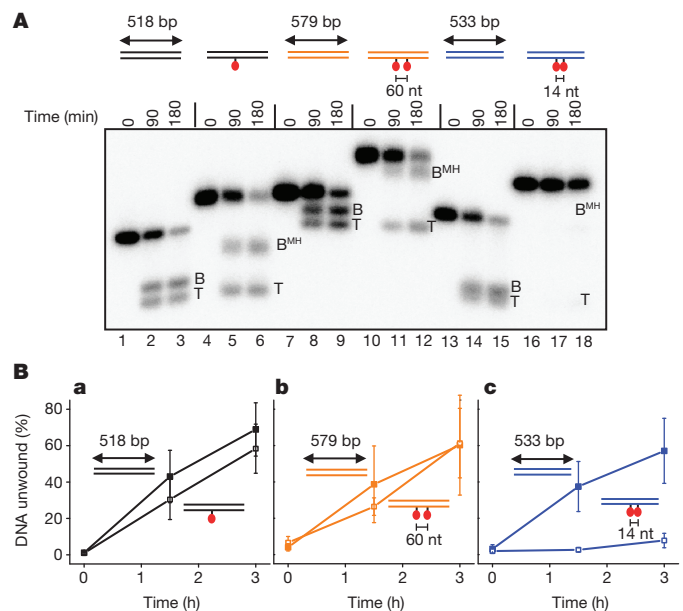


Figure 5 | Bypass of tandem protein adducts by large T antigen depends on the inter-adduct distance. **A,** Unwinding of DNA containing, none, one or two M.HpaII adducts on the translocation strand by large T antigen. The three templates (colour-coded differentially) had slightly different lengths because each template contained 240 bp before the first protein adduct and 277 bp after the last protein adduct but different amounts of DNA between the adducts. DNAs were internally labelled with $[\gamma\text{-}^{32}\text{P}]\text{-dATP}$. **B,** bottom strand; B^{MH} , bottom strand modified with M.HpaII; nt, nucleotide; T, top strand. **B,** Quantification of unwinding from three independent experiments as in **A**. Error bars indicate s.d.

emphasize that replicative helicases in different organisms use a common mechanism to unwind DNA.

Our results also show that large T antigen is able to bypass a protein crosslinked to the translocation strand, and they favour a model in which the bypass occurs by opening of the hexamer. This unprecedented flexibility of large T antigen may allow the SV40 replisome to bypass natural impediments including tightly bound proteins on DNA such as transcription complexes or covalently trapped proteins^{35,36}. If large T antigen initially assembles around dsDNA at the origin^{21,22}, the ability of the large T antigen ring to open on DNA may also facilitate the exclusion of one strand from the central channel during replication initiation as proposed³⁷. In the future, it will be important to confirm by more direct means that the large T antigen ring opens while bypassing a bulky adduct. Furthermore, determining whether other replicative helicases exploit similar plasticity to bypass replication barriers can guide our understanding of how these enzymes interact with DNA damage.

METHODS SUMMARY

For single-molecule experiments, λ ori DNA was annealed to 3'-biotin-modified oligonucleotides at its ssDNA end and attached to the streptavidin-functionalized surface of a microfluidic flow cell. Large T antigen and HeLa cell extracts were diluted in large T antigen binding (TAB) buffer containing 30 mM Hepes, pH 7.5, 7 mM MgCl₂, 0.5 mM dithiothreitol and 50 μ g ml⁻¹ BSA, and introduced into the flow cell. Total internal reflection fluorescence imaging was performed on a custom-built setup. Ensemble DNA unwinding assays were performed on radio-labelled PCR fragments in TAB buffer supplemented with large T antigen and RPA.

Full Methods and any associated references are available in the online version of the paper.

Received 17 August; accepted 31 October 2012.

Published online 28 November 2012.

- Patel, S. S. & Picha, K. M. Structure and function of hexameric helicases. *Annu. Rev. Biochem.* **69**, 651–697 (2000).
- Enemark, E. J. & Joshua-Tor, L. On helicases and other motor proteins. *Curr. Opin. Struct. Biol.* **18**, 243–257 (2008).
- Egelman, E. H., Yu, X., Wild, R., Hingorani, M. M. & Patel, S. S. Bacteriophage T7 helicase/primase proteins form rings around single-stranded DNA that suggest a general structure for hexameric helicases. *Proc. Natl Acad. Sci. USA* **92**, 3869–3873 (1995).
- Kaplan, D. L. & O'Donnell, M. Twin DNA pumps of a hexameric helicase provide power to simultaneously melt two duplexes. *Mol. Cell* **15**, 453–465 (2004).
- Fu, Y. V. *et al.* Selective bypass of a lagging strand roadblock by the eukaryotic replicative DNA helicase. *Cell* **146**, 931–941 (2011).
- Kaplan, D. L., Davey, M. J. & O'Donnell, M. Mcm4,6,7 uses a “pump in ring” mechanism to unwind DNA by steric exclusion and actively translocate along a duplex. *J. Biol. Chem.* **278**, 49171–49182 (2003).
- Fanning, E. & Zhao, K. SV40 DNA replication: from the A gene to a nanomachine. *Virology* **384**, 352–359 (2009).
- Fanning, E., Zhao, X. & Jiang, X. in *DNA Tumor Viruses* (eds Damania, B. & Pipas, J. M.) 1–24 (Springer US, 2009).
- Wessel, R., Schweizer, J. & Stahl, H. Simian virus 40 T-antigen DNA helicase is a hexamer which forms a binary complex during bidirectional unwinding from the viral origin of DNA replication. *J. Virol.* **66**, 804–815 (1992).
- Weissbart, K. *et al.* Two regions of simian virus 40 large T antigen determine cooperativity of double-hexamer assembly on the viral origin of DNA replication and promote hexamer interactions during bidirectional origin DNA unwinding. *J. Virol.* **73**, 2201–2211 (1999).
- Barbaro, B. A., Sreekumar, K. R., Winters, D. R., Prack, A. E. & Bullock, P. A. Phosphorylation of simian virus 40 large T antigen on Thr 124 selectively promotes double-hexamer formation on subfragments of the viral core origin. *J. Virol.* **74**, 8601–8613 (2000).
- Smelkova, N. V. & Borowiec, J. A. Dimerization of simian virus 40 T-antigen hexamers activates T-antigen DNA helicase activity. *J. Virol.* **71**, 8766–8773 (1997).
- Alexandrov, A. I., Botchan, M. R. & Cozzarelli, N. R. Characterization of simian virus 40 T-antigen double hexamers bound to a replication fork. *J. Biol. Chem.* **277**, 44886–44897 (2002).
- SenGupta, D. J. & Borowiec, J. A. Strand-specific recognition of a synthetic DNA replication fork by the SV40 large tumor antigen. *Science* **256**, 1656–1661 (1992).
- Morris, P. D. *et al.* Hepatitis C virus NS3 and simian virus 40 large T antigen helicases displace streptavidin from 5'-biotinylated oligonucleotides but not from 3'-biotinylated oligonucleotides: evidence for directional bias in translocation on single-stranded DNA. *Biochemistry* **41**, 2372–2378 (2002).
- Goetz, G. S., Dean, F. B., Hurwitz, J. & Matsun, S. W. The unwinding of duplex regions in DNA by the simian virus 40 large tumor antigen-associated DNA helicase activity. *J. Biol. Chem.* **263**, 383–392 (1988).
- Enemark, E. J. & Joshua-Tor, L. Mechanism of DNA translocation in a replicative hexameric helicase. *Nature* **442**, 270–275 (2006).
- Li, D. *et al.* Structure of the replicative helicase of the oncoprotein SV40 large tumor antigen. *Nature* **423**, 512–518 (2003).
- Gai, D., Zhao, R., Li, D., Finkelstein, C. V. & Chen, X. S. Mechanisms of conformational change for a replicative hexameric helicase of SV40 large tumor antigen. *Cell* **119**, 47–60 (2004).
- Gomez-Lorenzo, M. G. *et al.* Large large T antigen on the simian virus 40 origin of replication: a 3D snapshot prior to DNA replication. *EMBO J.* **22**, 6205–6213 (2003).
- Cuesta, I. *et al.* Conformational rearrangements of SV40 large large T antigen during early replication events. *J. Mol. Biol.* **397**, 1276–1286 (2010).
- Borowiec, J. A. & Hurwitz, J. ATP stimulates the binding of simian virus 40 (SV40) large tumor antigen to the SV40 origin of replication. *Proc. Natl Acad. Sci. USA* **85**, 64–68 (1988).
- Scalfani, R. A., Fletcher, R. J. & Chen, X. S. Two heads are better than one: regulation of DNA replication by hexameric helicases. *Genes Dev.* **18**, 2039–2045 (2004).
- Takahashi, T. S., Wigley, D. B. & Walter, J. C. Pumps, paradoxes and ploughshares: mechanism of the MCM2–7 DNA helicase. *Trends Biochem. Sci.* **30**, 437–444 (2005).
- Yardimci, H., Loveland, A. B., Habuchi, S., van Oijen, A. M. & Walter, J. C. Uncoupling of sister replisomes during eukaryotic DNA replication. *Mol. Cell* **40**, 834–840 (2010).
- Yardimci, H., Loveland, A. B., van Oijen, A. M. & Walter, J. C. Single-molecule analysis of DNA replication in *Xenopus* egg extracts. *Methods* **57**, 179–186 (2012).
- Stillman, B. W. & Gluzman, Y. Replication and supercoiling of simian virus 40 DNA in cell extracts from human cells. *Mol. Cell. Biol.* **5**, 2051–2060 (1985).
- Wobbe, C. R., Dean, F., Weissbach, L. & Hurwitz, J. *In vitro* replication of duplex circular DNA containing the simian virus 40 DNA origin site. *Proc. Natl Acad. Sci. USA* **82**, 5710–5714 (1985).
- Bullock, P. A., Seo, Y. S. & Hurwitz, J. Initiation of simian virus 40 DNA synthesis *in vitro*. *Mol. Cell. Biol.* **11**, 2350–2361 (1991).
- Murakami, Y. & Hurwitz, J. Functional interactions between SV40 large T antigen and other replication proteins at the replication fork. *J. Biol. Chem.* **268**, 11008–11017 (1993).
- Kim, S., Dallmann, H. G., McHenry, C. S. & Marians, K. J. Coupling of a replicative polymerase and helicase: a τ -DnaB interaction mediates rapid replication fork movement. *Cell* **84**, 643–650 (1996).
- Stano, N. M. *et al.* DNA synthesis provides the driving force to accelerate DNA unwinding by a helicase. *Nature* **435**, 370–373 (2005).
- Chen, L. *et al.* Direct identification of the active-site nucleophile in a DNA (cytosine-5)-methyltransferase. *Biochemistry* **30**, 11018–11025 (1991).
- Seinsoth, S., Uhlmann-Schiffler, H. & Stahl, H. Bidirectional DNA unwinding by a ternary complex of large T antigen, nucleolin and topoisomerase I. *EMBO Rep.* **4**, 263–268 (2003).
- Barker, S., Weinfeld, M. & Murray, D. DNA-protein crosslinks: their induction, repair, and biological consequences. *Mutat. Res.* **589**, 111–135 (2005).
- Anand, R. P. *et al.* Overcoming natural replication barriers: differential helicase requirements. *Nucleic Acids Res.* **40**, 1091–1105 (2011).
- Wu, C., Roy, R. & Simmons, D. T. Role of single-stranded DNA binding activity of large T antigen in simian virus 40 DNA replication. *J. Virol.* **75**, 2839–2847 (2001).

Supplementary Information is available in the online version of the paper.

Acknowledgements We thank C. Richardson for critical reading of the manuscript, and C. Eton for help in the preparation of λ ori DNA. J.C.W. was supported by grants from the National Institutes of Health (NIH) (GM62267 and HL098316) and American Cancer Society (ACS) (RSG0823401GMC). A.M.v.O. was supported by grants from the NIH (GM077248), ACS (RSG0823401GMC), and the Netherlands Organization for Scientific Research (NWO; Vici 680-47-607). J.H. was funded by NIH grant GM5 R01 GM034559. X.W. was a long-term postdoctoral fellow of the Human Frontier Science Program; D.Z.R. was supported by NIH grant GM086466.

Author Contributions H.Y., A.M.v.O. and J.C.W. designed the experiments. H.Y. performed the experiments. X.W. and D.Z.R. supervised and assisted H.Y. for construction of λ ori DNA. A.B.L. made fluorescently tagged RPA. I.T. and J.H. provided RPA and large T antigen. H.Y., A.M.v.O. and J.C.W. interpreted the data and wrote the paper. X.W. and A.B.L. contributed equally.

Author Information Reprints and permissions information is available at www.nature.com/reprints. The authors declare no competing financial interests. Readers are welcome to comment on the online version of the paper. Correspondence and requests for materials should be addressed to A.M.V. (a.m.v.oijen@rug.nl) or J.C.W. (johannes_walter@hms.harvard.edu).

METHODS

Protein expression and purification. SV40 large T antigen³⁸ and RPA³⁹ were expressed and purified as described. Fluorescently tagged RPA was made by cloning mKikGR and a histidine-tag onto the amino terminus of the RPA70 subunit. RPA^{mKikGR} was purified by Ni-NTA chromatography.

Preparation of λ ori. To construct the λ DNA with the SV40 origin (λ ori), we first carried out a series of cloning steps to generate a plasmid that contains a 4.7-kb DNA fragment including the 233 bp SV40 origin region from pUC.HSO⁴⁰ at one end, a 22-bp sequence (5'-CCTCAGCATAGATGTCCTCAGC-3') for Qdot attachment at the other end, and a 4.5-kb DNA spacer in between, which contains a tetracycline-resistance gene, an ampicillin-resistance gene and part of a *Bacillus subtilis* non-essential gene, *yrvN*. This fragment was PCR-amplified using primers flanking with 40-bp sequences homologous to the λ genome (5'-ACAGCCGCCGGAACCGGTGGGCTTTTGTGGGGTGAAT-3' and 5'-CCTGCGGCATATCACAAAACGATTACTCCATAACAGGGACA-3'), and electroporated into a lysogen MC4100 (λ CI857 Sam7)⁴¹ to replace two non-essential genes (*stf* and *tfa*) in the prophage using a recombineering method⁴². The modified λ DNA was purified from the lysogen by Lofstrand Labs Limited.

Labelling λ ori with Qdot. λ ori contains a 22-bp sequence (5'-CCTCAGCATAGATGTCCTCAGC-3') approximately 4 kb away from the SV40 origin. This sequence has two sequential sites (5'-CCTCAGC-3') that are recognized by nicking enzymes Nt.BbvCI and Nb.BbvCI. We used Nt.BbvCI or Nb.BbvCI, respectively, to modify either the top or bottom strands of λ ori with a digoxigenin at a single base according to a previously established protocol^{43,44}. To place a digoxigenin in the top strand, λ ori was treated with Nt.BbvCI, mixed with 100-fold molar excess of oligonucleotide (5'-TCAGCAT^{dig}AGATGTCC-3', Biosynthesis) containing a digoxigenin at T^{dig}, heated to 60 °C, and slowly cooled down to room temperature. This procedure leads to melting of a 15-nucleotide region between the two Nt.BbvCI sites, which is then replaced by the digoxigenin-modified oligonucleotide. The modified oligonucleotide was then ligated to λ ori using T4 DNA Ligase (NEB). The same procedure was performed to modify the bottom strand of λ ori with digoxigenin except that DNA was nicked with Nb.BbvCI and annealed and ligated to 5'-TGAGGACAT^{dig}CTATGC-3'. Attachment of anti-dig-conjugated Qdot605 (Invitrogen) to surface-immobilized λ ori was performed as described⁵.

Preparation of DNA constructs. To produce biotin-modified linear DNA for use in ensemble unwinding assays, we cloned an insert (5'-CCTCAGCAGATATCACCTCAGC-3') between the EcoRI and NdeI sites of the pUC.HSO vector⁴⁰ that places the insert approximately 150 nucleotides away from the SV40 origin. A 518-bp fragment within the resulting vector was PCR-amplified using the following oligonucleotides: forward: 5'-CCTCAAAAAAGCCTCCTACTA-3', reverse: 5'-GTGCCACCTGACGTCTAAGAAACC-3'.

The length of the DNA substrate was chosen such that dsDNA (Fig. 3B, lanes 1 and 3), dsDNA bound to streptavidin (Fig. 3B, lanes 2 and 4), ssDNA (Fig. 3B, lanes 9 and 11), and ssDNA bound to streptavidin (Fig. 3B, lanes 10 and 12) ran at discrete positions on a 3% agarose gel. The PCR fragment contains the origin near one end and the 22-bp insert close to the centre (Fig. 3A). We first inserted an amine residue on the top or bottom strands using the same template exchange strategy as before. DNA was either nicked with Nt.BbvCI and annealed/ligated to 5'-TGAGGTGAT^{amnn}ATCTGC-3' (to modify the top strand), or nicked with Nb.BbvCI and annealed/ligated to 5'-TCAGCAGAT^{amnn}ATCACC-3' (to modify the bottom strand). Modified oligonucleotides were purchased from IDT that contained a C6-amine at T^{amnn}. To attach biotin to the amine-modified thymidine residue, amine-modified DNA (400 ng) was mixed with NHS-PEG4-biotin (2.5 μ l of 100 μ M dissolved in dimethylsulphoxide, Pierce) in PBS buffer (25 μ l final volume), and incubated overnight at room temperature. Excess NHS-PEG4-amine was removed by running DNA on a 1.5% agarose gel and subsequent gel extraction of DNA. This protocol generally resulted in half of the DNA molecules being modified with biotin at the specific site. To purify biotinylated DNA selectively, DNA was mixed with streptavidin (0.6 mg ml⁻¹ final), incubated for at least 2 h and separated on a 1.5% agarose gel. We then excised the band corresponding to the streptavidin-bound DNA that ran slower than free DNA. Purification of DNA from agarose gel was performed using a QIAquick gel extraction kit (Qiagen) unless stated otherwise. We note that streptavidin dissociated from biotin on DNA during the gel purification process, possibly owing to the denaturation of streptavidin by the ethanol wash of the spin column.

To conjugate M.HpaII covalently to DNA, we first cloned 5'-CCTCAGCATCCGGTACCTCAGC-3' between the EcoRI and NdeI sites of the pUC.HSO (in which bold denotes the sequence recognized by M.HpaII). We then used the same primers as before to make a 518-bp PCR fragment containing the origin and the insert. The same nicking strategy described above was used to insert a 5-fluoro-2'-deoxycytidine (C^{flu})-modified oligonucleotide to either the top or bottom strands for subsequent covalent attachment of M.HpaII to DNA^{33,45}. The

PCR fragment was either nicked with Nt.BbvCI and annealed/ligated to 5'-TCAGCATCC^{flu}GGTACC-3' (to modify the top strand), or nicked with Nb.BbvCI and annealed/ligated to 5'-TGAGGTACC^{flu}GGATGC-3' (to modify the bottom strand). Custom-synthesized 5-fluoro-modified oligonucleotides were purchased from Biosynthesis. Modified DNA was gel-purified as described above and mixed with M.HpaII (1,000 U ml⁻¹ final, NEB) in HpaII methylase reaction buffer (50 mM Tris-HCl, pH 7.5, 5 mM 2-mercaptoethanol, 10 mM EDTA) supplemented with 100 μ M S-adenosylmethionine. After 6–9 h of incubation at 37 °C, DNA was separated on a 1.5% agarose gel and the slow migrating band corresponding to M.HpaII-conjugated DNA was excised. To prevent denaturation of M.HpaII, DNA was purified by electroelution. In brief, the gel fragment containing M.HpaII-bound DNA was placed in a dialysis tube (3.5 kilodalton cut-off) filled with TBE buffer, and electrophoresis was used to run the DNA off the gel into the dialysis tube. The gel fragment was then removed from the tube, and DNA was dialysed against 10 mM Tris, pH 8, and concentrated using a spin concentrator (Ultrafree Biomax-10K, ThermoFisher Scientific).

To generate DNA constructs containing two M.HpaII adducts, we first cloned two inserts of the same sequence (5'-CCTCAGCATCCGGTACCTCAGC-3'; in which bold denotes the sequence recognized by M.HpaII) into pUC.HSO that were separated by reported lengths. After making a PCR product of the desired length, the same protocol as above was used for insertion of 5-fluoro-2'-deoxycytidine-modified oligonucleotide and subsequent M.HpaII conjugation.

Single-molecule DNA replication and unwinding assays. A microfluidic flow cell with a streptavidin-functionalized bottom surface was prepared as described⁴⁶. Similar to the wild-type λ DNA, λ ori contains 12-nucleotide ssDNA at both ends. λ ori was biotinylated and singly or doubly tethered to the surface using biotin-modified oligonucleotides complementary to these ends as described²⁶. For large-T-antigen-dependent replication of λ ori in HeLa cell extracts, the flow cell containing surface-immobilized λ ori molecules was placed on a heat block (VWR) set to 37 °C. The flow cell was flushed with 50 μ l large T antigen binding (TAB) buffer containing 30 mM Hepes, pH 7.5, 7 mM MgCl₂, 0.5 mM dithiothreitol (DTT) and 50 μ g ml⁻¹ BSA. Large T antigen (10 μ g ml⁻¹) was introduced into the flow cell in TAB buffer supplemented with an ATP regeneration mixture (4 mM ATP, 50 mM phosphocreatine and 10 ng μ l⁻¹ creatine phosphokinase), and 5 ng μ l⁻¹ competitor DNA (pUC19) for origin-specific assembly of large T antigen¹⁶, and incubated for the indicated times.

For large-T-antigen-dependent replication, a replication mixture was prepared by diluting 15 μ l HeLa cell extract (Chimerx) twofold in buffer containing 30 mM Hepes, pH 7.5, 7 mM MgCl₂, 0.5 mM DTT, 50 μ g ml⁻¹ BSA, 4 mM ATP, 50 mM phosphocreatine, 10 μ g ml⁻¹ creatine phosphokinase, 0.1 mM each of dATP, dGTP, dTTP and dCTP, and 50 μ M each of GTP, TTP and CTP (all concentrations final). The replication mixture was drawn into the flow cell and incubated for the indicated times. To confirm bidirectional replication, a second replication mixture containing 1.7 μ M dig-dUTP was drawn into the flow cell and further incubated. Competitor DNA (pUC19; 5 ng μ l⁻¹) was included to suppress non-specific interaction of proteins in the extract with λ ori that interferes with fork progression (data not shown). To stop the reaction, the flow cell was washed with buffer containing 20 mM Tris, pH 7.5, 50 mM NaCl, 12 mM EDTA and 0.1% SDS.

To visualize unwinding of λ ori by large T antigen in real time, large T antigen was first assembled on doubly tethered λ ori as described above. RPA^{mKikGR} (15 nM) was then drawn into the flow cell in TAB supplemented with the ATP regeneration mixture. The flow cell was heated to 37 °C on a microscope stage with an objective heater (Biopetechs) during large T antigen assembly and subsequent unwinding reactions. Imaging of RPA^{mKikGR} is described below.

Ensemble DNA unwinding assays. PCR fragments were labelled either internally with [α ³²P]-dATP (Perkin Elmer) during the PCR reaction, or at their 5' ends using T4 polynucleotide kinase (NEB) and [γ ³²P]-ATP (Perkin Elmer). Unwinding reactions were performed with 0.3–0.5 ng μ l⁻¹ labelled DNA, 10 μ g ml⁻¹ large T antigen, 40 μ g ml⁻¹ RPA and the ATP regeneration mixture in TAB and incubated for the indicated amount of time at 37 °C. Unlabelled competitor DNA (FspI linearized pUC19; 5 ng μ l⁻¹) was included in unwinding reactions to ensure origin-specific unwinding. The reaction was stopped with 0.5% SDS and 20 mM EDTA, DNA was separated on a 3% agarose gel, and visualized using a phosphorimager. Quantification of band intensities was carried out using Quantity One software.

To prepare 5'-biotin-modified DNA for bead-immobilization, one of the primers used in the PCR reaction contained biotin at the 5' end. Fifteen nanograms of DNA was mixed with streptavidin-coated magnetic beads (Invitrogen) in 10 mM Tris supplemented with 0.2 mg ml⁻¹ BSA. Beads were washed twice using a magnet, resuspended in TAB buffer containing the ATP regeneration mixture and 20 μ g ml⁻¹ large T antigen, and incubated for 2.5 h at 37 °C rotating on a rotisserie. Beads were washed twice with TAB buffer containing 0.6 mM ATP,

resuspended in TAB buffer supplemented with the ATP regeneration mixture, 40 $\mu\text{g ml}^{-1}$ RPA, 50 μM biotin, 15 ng cold DNA containing the origin, and incubated for 30 min at 37 °C before stopping the reaction.

Single-molecule imaging. Total internal reflection fluorescence imaging was carried out on an inverted microscope (Olympus IX-71) using a $\times 60$ oil objective (PlanApo, numerical aperture = 1.45, Olympus). SYTOX and fluorescein-anti-dig images on surface-immobilized DNA after replication in HeLa extracts were recorded as described²⁶. Live monitoring of RPA^{mKikGR} was performed by capturing an image every minute using 488-nm laser light.

38. Eki, T., Matsumoto, T., Murakami, Y. & Hurwitz, J. The replication of DNA containing the simian virus 40 origin by the monopolymerase and dipolymerase systems. *J. Biol. Chem.* **267**, 7284–7294 (1992).
39. Ishimi, Y., Claude, A., Bullock, P. & Hurwitz, J. Complete enzymatic synthesis of DNA containing the SV40 origin of replication. *J. Biol. Chem.* **263**, 19723–19733 (1988).
40. Wold, M. S., Li, J. J. & Kelly, T. J. Initiation of simian virus 40 DNA replication *in vitro*: large-tumor-antigen- and origin-dependent unwinding of the template. *Proc. Natl Acad. Sci. USA* **84**, 3643–3647 (1987).
41. Wang, I.-N. Lysis timing and bacteriophage fitness. *Genetics* **172**, 17–26 (2005).
42. Thomason, L. C., Oppenheim, A. B. & Court, D. L. Modifying bacteriophage lambda with recombineering. *Methods Mol Biol.* **501**, 239–251 (2009).
43. Kuhn, H. & Frank-Kamenetskii, M. D. Labeling of unique sequences in double-stranded DNA at sites of vicinal nicks generated by nicking endonucleases. *Nucleic Acids Res.* **36**, e40 (2008).
44. Loparo, J. J., Kulczyk, A. W., Richardson, C. C. & van Oijen, A. M. Simultaneous single-molecule measurements of phage T7 replisome composition and function reveal the mechanism of polymerase exchange. *Proc. Natl Acad. Sci. USA* **108**, 3584–3589 (2011).
45. MacMillan, A. M., Chen, L. & Verdine, G. L. Synthesis of an oligonucleotide suicide substrate for DNA methyltransferases. *J. Org. Chem.* **57**, 2989–2991 (1992).
46. Tanner, N. A. & van Oijen, A. M. in *Single Molecule Tools, Part B: Super-Resolution, Particle Tracking, Multiparameter, and Force Based Methods* (ed. Walter, N. G.) 259–278 (Academic, 2010).

Structure of the TatC core of the twin-arginine protein transport system

Sarah E. Rollauer^{1,2}, Michael J. Tarry^{3†}, James E. Graham^{1,2†}, Mari Jääskeläinen³, Franziska Jäger⁴, Steven Johnson¹, Martin Krehenbrink², Sai-Man Liu^{1,2}, Michael J. Lukey^{1,2†}, Julien Marcoux⁵, Melanie A. McDowell¹, Fernanda Rodriguez², Pietro Roversi^{1†}, Phillip J. Stansfeld², Carol V. Robinson⁵, Mark S. P. Sansom², Tracy Palmer⁴, Martin Högbom³, Ben C. Berks² & Susan M. Lea¹

The twin-arginine translocation (Tat) pathway is one of two general protein transport systems found in the prokaryotic cytoplasmic membrane and is conserved in the thylakoid membrane of plant chloroplasts. The defining, and highly unusual, property of the Tat pathway is that it transports folded proteins, a task that must be achieved without allowing appreciable ion leakage across the membrane. The integral membrane TatC protein is the central component of the Tat pathway. TatC captures substrate proteins by binding their signal peptides. TatC then recruits TatA family proteins to form the active translocation complex. Here we report the crystal structure of TatC from the hyperthermophilic bacterium *Aquifex aeolicus*. This structure provides a molecular description of the core of the Tat translocation system and a framework for understanding the unique Tat transport mechanism.

The Sec¹ and Tat^{2–4} protein transport pathways are responsible for protein export across the cytoplasmic membrane of bacteria and archaea, and for protein import into the thylakoids of chloroplasts. The Sec system threads unfolded proteins through a membrane-bound channel¹. By contrast, the Tat pathway transports proteins that have already attained a folded state⁵, a more challenging task because folded proteins have a much larger cross-section than an unfolded peptide and so require a larger transport pathway. In addition, folded proteins have a diverse range of shapes and sizes, making it difficult to seal tightly around the protein during transport to preserve the membrane permeability barrier. How the Tat apparatus is able to accomplish this feat is unknown. In bacteria the Tat pathway has an important role in energy metabolism, nutrient acquisition and virulence^{2,5,6}, whereas in plants the Tat pathway is essential for photosynthesis⁷.

Tat transport is carried out by the integral membrane proteins TatA^{8,9}, TatB⁸ and TatC¹⁰. TatA and TatB are structurally related and contain a single transmembrane helix followed by an amphipathic helix^{8,11}, whereas TatC has multiple transmembrane helices⁹. Proteins are targeted to the Tat pathway by amino-terminal signal peptides possessing a twin-arginine-containing sequence motif^{12–14} that is recognized by the TatC protein within a TatBC complex^{15–19}. Binding of substrate proteins to the TatBC complex induces recruitment of TatA to assemble a transient TatABC-containing translocation site^{15,20,21}, which is thought to facilitate transport by perturbing the membrane bilayer^{2,4,22}.

TatC emerges as the core organizing component of the Tat pathway, directly and dynamically binding substrate, TatB and TatA^{23,24}, and maintaining these interactions during the transport step^{16,20}. A molecular-level understanding of TatC, the largest and most conserved element of the Tat translocation machinery, is required to begin to understand the remarkable Tat transport mechanism.

Structure of TatC

We targeted TatC proteins from thermophilic bacteria and archaea for structure determination. *Aquifex aeolicus* TatC solubilized in the detergent lauryl maltose neopentyl glycol (LMNG)²⁵ formed crystals that diffracted to high resolution. LMNG-solubilized *A. aeolicus* TatC was able to bind a synthetic Tat signal peptide (dissociation constant (K_d) = 3 μ M) at an approximately 1:1 protein:peptide ratio (Fig. 1a), but not a functionally inactive variant signal peptide^{15,16,26} (Fig. 1b). Thus, the protein used for crystallization was functional for Tat signal peptide binding. Identical binding affinities were measured for the full-length signal peptide and for a truncated signal peptide comprising only the twin-arginine-containing n-region (Fig. 1c), consistent with crosslinking studies which indicate that TatC contacts the n-region of the signal peptide^{15,16}.

Crystals of selenomethionine-labelled *A. aeolicus* TatC (Supplementary Fig. 1) were produced and the structure of the protein solved at a resolution of 3.5 Å using anomalous dispersion (Supplementary Fig. 2a, b). The first four and last eleven amino acids of *A. aeolicus* TatC are disordered and are not included in the structure (Supplementary Fig. 3). The final refined structure has an R_{free} of 28.8% (Supplementary Table 1). The *A. aeolicus* TatC fold is well-maintained in atomistic molecular dynamics (MD) simulations in a phospholipid bilayer, indicating that the structure would be stable in a membrane environment (Supplementary Fig. 4). *A. aeolicus* TatC shares 40% sequence identity with *Escherichia coli* TatC (Supplementary Fig. 3), allowing functional data from the *E. coli* Tat system to be readily mapped to the *A. aeolicus* TatC structure.

A. aeolicus TatC (Fig. 2a) contains six transmembrane helices (TM1–TM6), as anticipated^{9,27–29}, which experimental evidence shows are oriented with the amino and carboxy termini of the protein at the cytoplasmic side of the membrane^{27–30}. MD simulations of *A. aeolicus* TatC in a phospholipid environment indicate that little of the structure protrudes outside the membrane bilayer (Fig. 2a and Supplementary Fig. 5). Three helices (TM2, TM3 and TM5) are

¹Sir William Dunn School of Pathology, University of Oxford, South Parks Road, Oxford OX1 3RE, UK. ²Department of Biochemistry, University of Oxford, South Parks Road, Oxford OX1 3QU, UK. ³Stockholm Center for Biomembrane Research, Department of Biochemistry and Biophysics, Stockholm University, S-106 91 Stockholm, Sweden. ⁴Division of Molecular Microbiology, College of Life Sciences, University of Dundee, Dundee DD1 5EH, UK. ⁵Physical & Theoretical Chemistry Laboratory, Department of Chemistry, University of Oxford, South Parks Road, Oxford OX1 3QZ, UK. [†]Present addresses: Department of Biochemistry, McGill University Room 457, Bellini Life Science Complex, 3649 Promenade Sir William Osler, Montreal, Quebec H3G 0B1, Canada (M.J.T.); 306 Briggs Hall, Department of Microbiology, University of California Davis, One Shields Avenue, Davis, California 95616-2866, USA (J.E.G.); Department of Molecular Medicine, Cornell University, Ithaca, New York 14853, USA (M.J.L.); CIC bioGUNE, Parque Tecnológico de Bizkaia, 48160 Dorio, Bizkaia, Spain (P.R.).

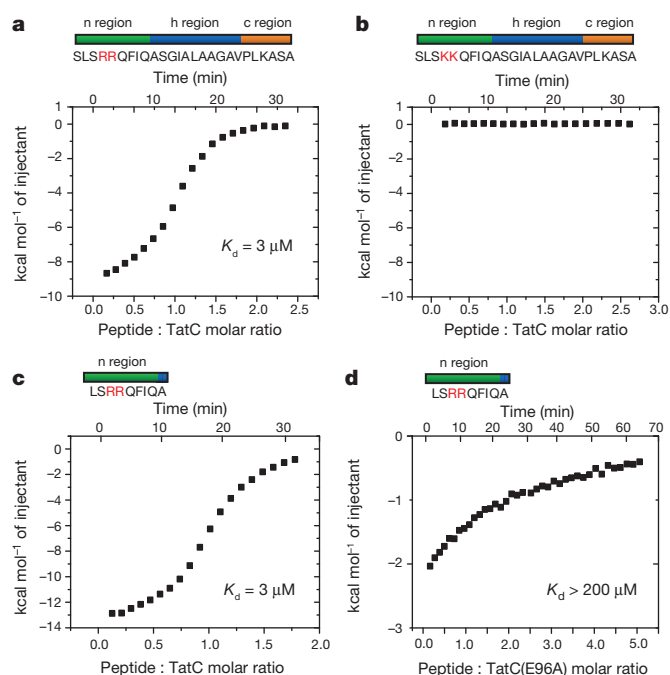


Figure 1 | Purified *A. aeolicus* TatC binds Tat signal peptides.

a–c, Isothermal titration calorimetry was used to assess interactions between *A. aeolicus* TatC and the Tat signal peptide of the *E. coli* protein SufI (**a**), a functionally inactive variant SufI signal peptide in which the twin arginine residues have been substituted with twin lysine residues (**b**) and the n-domain of the SufI signal peptide (**c**). **d**, Interaction between the n-domain peptide and an *A. aeolicus* TatC E96A variant.

strongly kinked within their transmembrane spans, whereas TM1 kinks abruptly towards the periplasmic side of the membrane to form an interfacial helix (helix 1b). The six transmembrane helices, with the exception of the C-terminal half of TM2 following the kink, are tilted at angles between 20° and 40° to the membrane normal. TM5 and TM6 are too short to span the membrane bilayer fully. Indeed, in MD simulations the membrane is distorted inwards at the ends of these helices (Supplementary Fig. 5). The restricted length of these helices is probably required, in part, to accommodate the TatB partner (see below) but it is also possible that the bilayer distortion caused by TM5 and TM6 may assist in forming the protein translocation pathway. The loops joining the transmembrane helices on the cytoplasmic face of *A. aeolicus* TatC are short. However, at the periplasmic face of the membrane the loops are more elaborate, with the interfacial helix 1b and succeeding loop into TM2 making extensive interactions with the TM3–TM4 loop. The result is a structured periplasmic cap that stabilizes the relative positions and tilted orientations of the transmembrane helices. The presence of the cap structure explains why insertions and deletions in this region are not tolerated^{31,32} and why these loops are hotspots for inactivating mutations³² (Fig. 2c).

The overall shape of *A. aeolicus* TatC resembles a cupped hand in which the transmembrane helices form a curved wall overhanging on the concave face by the periplasmic cap (Fig. 2b). The result is a structure with a notably high surface area (~16,500 Å²) for the length of protein. A gap between the short TM5 and TM6 helices and the cap results in a prominent groove leading from the concave face of *A. aeolicus* TatC to the periplasm. The *A. aeolicus* TatC fold shows no similarity to previously described membrane protein structures. Importantly, the structure of TatC is unrelated to that of the Sec translocase even though the two proteins bind signal peptides of similar overall structure¹². Crystallographic *B*-factors suggest that *A. aeolicus* TatC has very restricted structural flexibility (Supplementary Fig. 6a). Similarly, MD simulations of *A. aeolicus* TatC

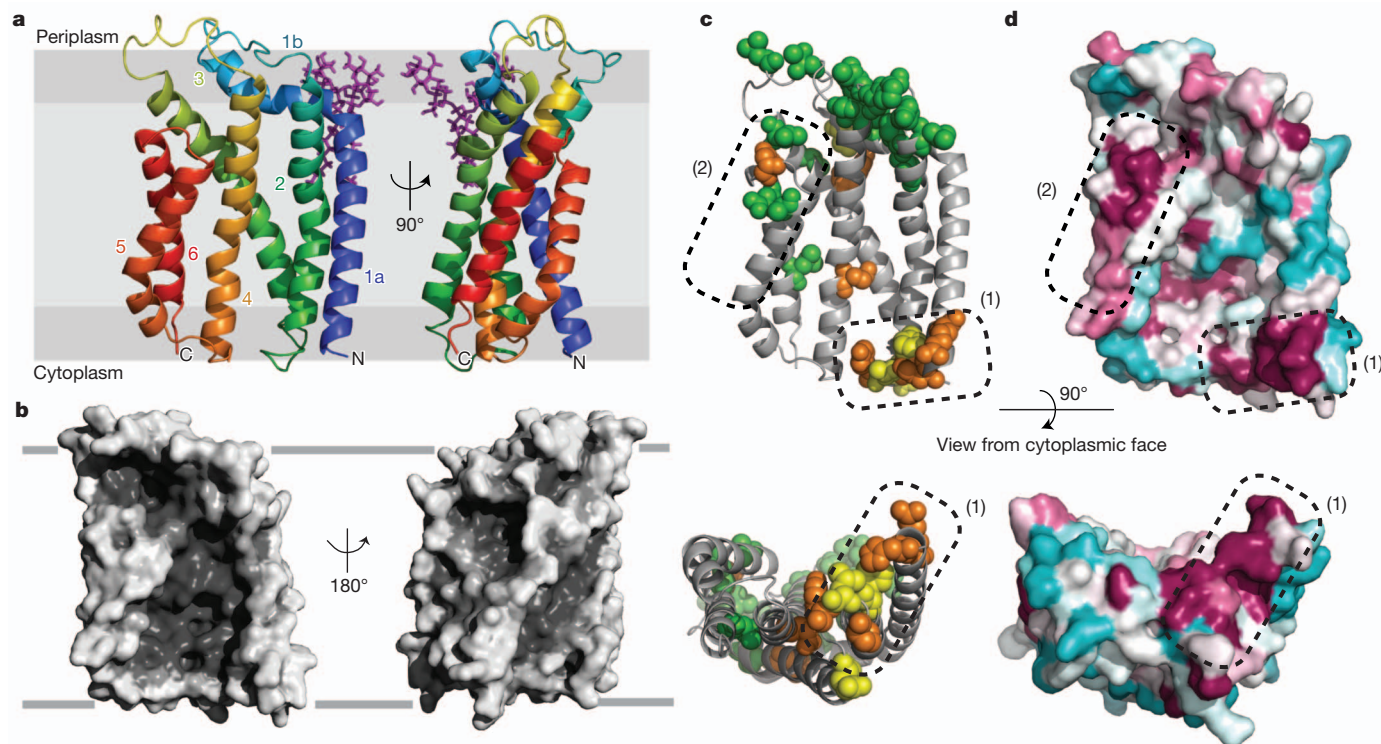


Figure 2 | Structure of *A. aeolicus* TatC. **a**, Cartoon representation of *A. aeolicus* TatC coloured from blue at the N terminus to red at the C terminus. The position within the membrane bilayer is predicted by MD simulations (Supplementary Fig. 5). A semi-ordered molecule of LMNG detergent is present and is shown in purple. **b**, Surface representation of the *A. aeolicus* TatC structure. The left hand views in **a** and **b** are the same orientation. **c**, Positions of

inactivating substitutions in *E. coli* TatC identified by genetic screening³² (green), targeted substitution^{17,34} (orange), or both (yellow), mapped to *A. aeolicus* TatC (full details in Supplementary Table 2). **d**, Sequence conservation at the surface of TatC displayed in the ConSurf³⁶ colouring scheme in which maroon represents high, and cyan low, sequence conservation. **c**, **d**, Dotted regions labelled (1) and (2) highlight conserved functional regions of the structure.

in a phospholipid bilayer show limited deformation modes (Supplementary Fig. 6b). It is, therefore, unlikely that TatC undergoes large conformational changes as typically found in small-molecule transporters³³.

A notable feature of the surface of *A. aeolicus* TatC is that the side chain of Glu 165 is exposed at the centre of the concave face, thereby placing an ionisable group in the hydrophobic interior of the bilayer (Fig. 3a). This residue is highly conserved as glutamate or glutamine. Substitution of the equivalent residue in *E. coli* TatC (Glu 170) with alanine does not affect signal peptide binding¹⁷, but severely compromises overall Tat transport activity^{17,34}. In MD simulations Glu 165 is hydrated and perturbs the local bilayer environment by attracting a lipid head group. This suggests that burying Glu 165 in the membrane is highly unfavourable and that Glu 165 has an interaction partner in the cell.

Tat transport is energized by the proton electrochemical gradient³⁵. However, no membrane surface-linked channels or transmembrane hydrogen bonding networks are apparent within *A. aeolicus* TatC. Glu 165 is part of a short hydrogen-bonding network with Ser 107 and Trp 85 (Supplementary Fig. 7) but this is isolated from the membrane surface. Thus, if TatC participates in coupling transport to transmembrane proton movement, it does so in conjunction with other components.

To highlight functionally important regions of TatC we plotted amino acid substitutions that suppress the transport function of *E. coli* TatC (refs 17, 32, 34) on to the equivalent positions in the *A. aeolicus* TatC structure (Fig. 2c). We also mapped sequence conservation on to the protein surface (Fig. 2d). There are two clusters of conserved and functionally important residues on the surface of TatC (labelled (1) and (2) in Fig. 2c, d). These are located at each end of the TatC molecule, on opposite sides of the membrane, and probably correspond to sites of interactions with partner proteins. A sequence covariance analysis shows that the strongest structural constraints in TatC are within those helix pairs (TM1/TM2 and TM5/TM6) that form the structural framework underlying the two functionally conserved surface sites (Supplementary Fig. 8 and Supplementary Table 3). Functionally important residues in the interior of the TatC molecule have structural roles mediating transmembrane kinks (conserved) or stabilizing the periplasmic cap (weakly conserved).

Signal peptide recognition

Residues in *E. coli* TatC that may be involved in signal peptide binding have been identified by crosslinking and genetic analysis^{17,18,19,36,37}.

The equivalent residues in *A. aeolicus* TatC cluster on the cytoplasmic face of TM1–TM3 within conserved functional surface site (1) (Fig. 3b). Within this site the two negatively charged amino acids Glu 9 and Glu 96 would be appropriately positioned to coordinate the positively charged guanidinium groups of the sequential arginine residues of the signal peptide.

To directly test the involvement of this part of *A. aeolicus* TatC in signal peptide interactions we measured the signal peptide binding affinities of single amino acid substitutions within the site (Figs 1d and 3c, and Supplementary Fig. 9). All the substitutions, including those of Glu 9 and Glu 96, resulted in large reductions in the affinity of *A. aeolicus* TatC for the n-region peptide. By contrast, changing a functionally important³⁴ residue in surface site (2) had no effect on signal peptide binding (Fig. 3c and Supplementary Fig. 9). This analysis confirms that the twin-arginine-containing region of Tat signal peptides bind to surface site (1).

Interactions with Tat components

In *E. coli*, and in plant thylakoids, multiple copies of TatC are present in the TatBC complex^{26,34,38,39} and TatC has been reported to self-interact⁴⁰, possibly as local TatC dimers⁴¹. We considered whether the protomer arrangement in the *A. aeolicus* TatC crystal might reflect such interactions. One of two packing interactions in the crystals (between molecules X and X' in Fig. 4a) forms a topologically reasonable dimer (752 Å² × 2 buried surface area; Supplementary Fig. 10), and biochemical characterization confirms that the LMNG-solubilized protein is a dimer in solution (Supplementary Fig. 11). Nevertheless, the low sequence conservation of the subunit interface (Fig. 2d and Supplementary Fig. 10), the results of sequence covariance analysis (Supplementary Fig. 8 and Supplementary Table 3), and inconsistency with site-specific photocrosslinking results (Fig. 4b)³⁶ all argue against the biological relevance of this dimer. More generally, the lack of plausible inter-subunit contacts in the covariance analysis suggests that interactions between TatC protomers are not subject to specific structural or mechanistic constraints.

In Gram-negative bacteria and plants TatC forms a tight complex with TatB. Known contact information for the two proteins in *E. coli*^{32,34,36} maps to the periplasmic end of conserved functional surface patch (2) in TatC (Fig. 4b) and to the periplasmic⁴² N terminus

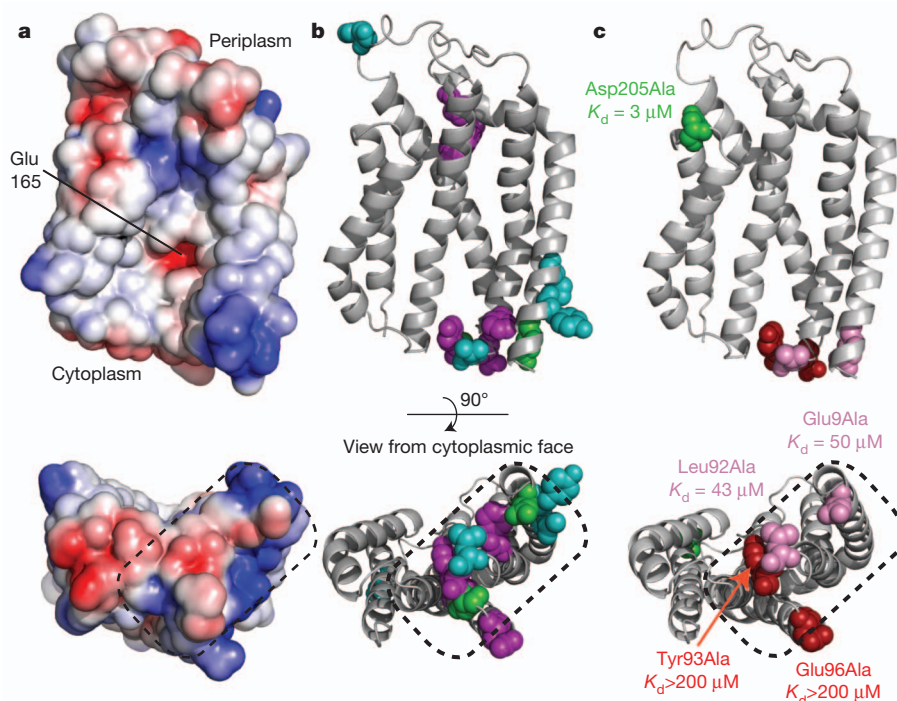


Figure 3 | Identification of the signal peptide binding site on TatC. **a**, The electrostatic surface of TatC showing negatively charged regions as red and positively charged regions as blue. **b**, *E. coli* TatC residues implicated in signal peptide or substrate interactions mapped to *A. aeolicus* TatC (full details in Supplementary Table 4). Substitutions that prevent signal peptide crosslinking to *E. coli* TatC (ref. 17) are shown in purple. Positions that give prominent photo-affinity crosslinks to substrate proteins³⁶ are shown in green. Single amino acid substitutions that enable transport of substrates with defects in the signal peptide twin-arginine motif^{18,19,37} are shown in cyan. **c**, Effects of the indicated amino acid substitutions on the affinity of *A. aeolicus* TatC for the SufI n-region peptide. Substitutions that affect signal peptide binding are coloured red or pink, and those that do not are coloured green. The corresponding experimental data are shown in Fig. 1d and Supplementary Fig. 9. The dotted region in a–c corresponds to region (1) in Fig. 2c, d.

of the TatB transmembrane helix³² (TatB(TM)). To delineate further the proposed TatB–TatC contact site we undertook limited disulphide scanning mutagenesis of the *E. coli* TatB and TatC proteins in these areas (Fig. 4c). In the *A. aeolicus* TatC crystals the contact between molecules X and X' involves packing an inverted TM5 from one TatC molecule against the proposed TatB contact site in the other (Fig. 4a), showing that a transmembrane helix with the same orientation as TatB(TM) (N terminus at the periplasmic side of the membrane) is able to pack at this site. On the basis of this crystallographic contact we produced a model for the TatB(TM)–TatC complex consistent with the experimental interaction data (Fig. 4d). A notable feature of the model is that the C-terminal half of TM5 is well matched in length to the short TatB(TM) to which it binds.

Although our analyses localize the signal peptide and TatB binding sites to opposite ends of the TatC molecule, some evidence exists for functional and structural connections between TatB and signal peptides. First, photocrosslinks to TatB have been reported in the vicinity of the

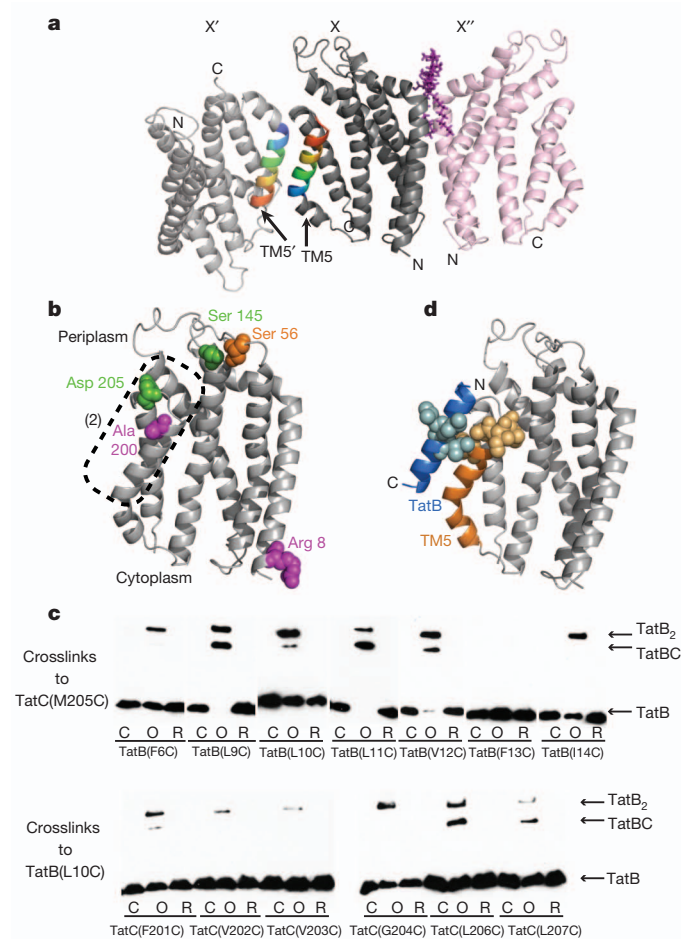


Figure 4 | Sites of interaction with other Tat components. **a**, *A. aeolicus* TatC crystal contacts. The contact between molecules X and X' involves a packing interaction between antiparallel TM5 helices, whereas that between molecules X and X'' involves the semi-ordered LMNG molecule shown in purple. **b**, Positions in *E. coli* TatC that have been reported^{32,34,36} to interact with both TatA and TatB (green), with TatB (magenta), or with TatC (orange) mapped on to *A. aeolicus* TatC (full details in Supplementary Table 5). The dotted region corresponds to region (2) in Fig. 2c, d. **c**, Disulphide crosslinking between *E. coli* TatB and TatC variants detected by immunoblotting with TatB antibodies. Lanes are untreated (C), oxidized with Cu(II)phenanthroline (O), or oxidized and then reduced with DTT (R). **d**, The complex between TatC and the transmembrane helix of TatB modelled on the *A. aeolicus* TatC X–X' crystal contact. Positions in *E. coli* TatC that form a disulphide bond to a *E. coli* TatB L10C variant (yellow), or positions in *E. coli* TatB that form a disulphide bond to a *E. coli* TatC M205C variant (blue), (data from c) are mapped on to the model.

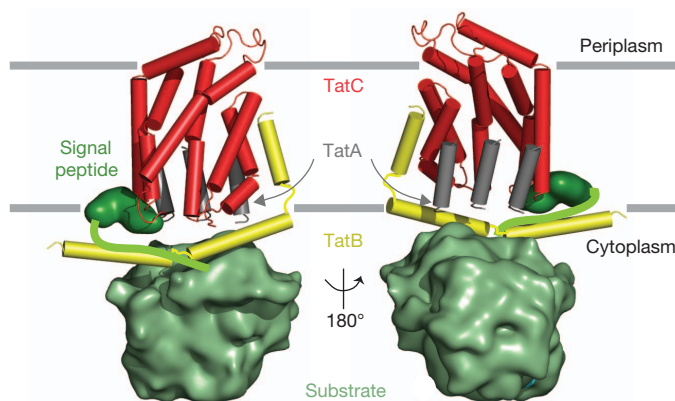


Figure 5 | A conceptual model for the environment of TatC in the substrate-bound translocation site. The model is viewed from the convex (left) and concave (right) sides of TatC. The interaction of TatC with the transmembrane helix of TatB is modelled as in Fig. 4d. The TatB amphipathic helices are positioned to allow TatB to be in the vicinity of the N terminus of TatC as shown by crosslinking³⁶. The TatA transmembrane helix is shown bound to the concave face of TatC based on *in silico* docking experiments (Supplementary Fig. 12). The position of the TatA amphipathic helix is unclear and is omitted from the conceptual model. TatA forms large polymers but only representative TatA molecules directly contacting TatC are shown. For simplicity, the model depicts a single TatC molecule but each TatC protein will be operating in the context of a larger TatBC complex.

signal peptide binding site in TatC³⁶ (Fig. 4b). Second, the signal peptide h-region, which directly follows the n-region, photocrosslinks predominantly to TatB^{15,16}. Third, some substitutions that allow transport of substrates with defective Tat signal peptides map to the N terminus of TatB(TM)^{18,37}. These data suggest that the amphipathic helix of TatB could run across the cytoplasmic face of TatC from the TatB(TM) binding site at TM5 to the signal peptide binding site at TM1 (Fig. 5). Alternatively, some of these interactions may relate to a stage in the transport cycle where the signal peptide is reaching across the membrane from the point of attachment of the twin-arginine motif at region (1) to the TatB(TM)-binding site in region (2). It is also possible that it is a TatB molecule bound to a neighbouring TatC molecule within the TatBC complex that is close to the signal peptide binding site.

The interaction of TatA with TatC is transient and may involve multiple TatA protomers binding to a single TatC protein. The only identified points of interaction between the two proteins are photocrosslinks³⁶ at the periplasmic side of the membrane close to the modelled position of the TatB N terminus (Fig. 4b). This suggests that the periplasmically located N terminus⁴² of TatA can reach this region. In the absence of more detailed experimental information on the TatA binding site(s) we carried out *in silico* docking experiments and MD simulations using a homology model of the *A. aeolicus* TatA transmembrane helix (TatA(TM)). The results suggest that TatA(TM) binds within the concave face of TatC (Supplementary Fig. 12). This location might allow TatA to act as the interaction partner for exposed Glu 165, perhaps via interaction with the functionally essential conserved Gln/Glu in TatA(TM)^{21,43}. The relatively large and concave surface of this region of TatC could promote a binding-induced conformational change in the bound TatA protomers that would allow them to act as the nucleation site for TatA polymerization.

The conceptual model shown in Fig. 5 summarizes the possible arrangement of the components of an active Tat translocation site indicated by the *A. aeolicus* TatC structure.

METHODS SUMMARY

Native and SeMet *A. aeolicus* TatC were heterologously expressed in *E. coli* as GFP fusions⁴⁴ and purified in LMNG. After GFP removal the protein was crystallized by the sitting-drop vapour diffusion method at 21 °C in 0.2 M ammonium sulphate,

0.02 M NaCl, 0.02 M sodium acetate pH 4.0, 33% v/v PEG 200. Diffraction data were collected at the Diamond light source (Beamline I04-1) at 120 K from four SeMet-labelled crystals grown directly in mother liquor ($\lambda = 0.92 \text{ \AA}$). The crystals diffracted to 3.5 \AA and belonged to the space group *H32*. The data were phased using single-wavelength anomalous dispersion. The final structure has a MolProbity⁴⁵ Score of 3.1 (84th percentile for structures $3.5 \text{ \AA} \pm 0.25 \text{ \AA}$).

Full Methods and any associated references are available in the online version of the paper.

Received 31 July; accepted 18 October 2012.

Published online 2 December 2012.

- Park, E. & Rapoport, T. A. Mechanisms of Sec61/SecY-mediated protein translocation across membranes. *Annu. Rev. Biophys.* **41**, 21–40 (2012).
- Palmer, T. & Berks, B. C. The twin-arginine translocation (Tat) protein export pathway. *Nature Rev. Microbiol.* **10**, 483–496 (2012).
- Frobel, J., Rose, P. & Muller, M. Twin-arginine-dependent translocation of folded proteins. *Phil. Trans. R. Soc. Lond. B* **367**, 1029–1046 (2012).
- Celedon, J. M. & Cline, K. Intra-plastid protein trafficking; how plant cells adapted prokaryotic mechanisms to the eukaryotic condition. *Biochim. Biophys. Acta* <http://dx.doi.org/10.1016/j.bbamcr.2012.06.028> (2012).
- Berks, B. C., Palmer, T. & Sargent, F. The Tat protein translocation pathway and its role in microbial physiology. *Adv. Microb. Physiol.* **47**, 187–254 (2003).
- De Buck, E., Lammertyn, E. & Anne, J. The importance of the twin-arginine translocation pathway for bacterial virulence. *Trends Microbiol.* **16**, 442–453 (2008).
- Barkan, A., Miles, D. & Taylor, W. C. Chloroplast gene expression in nuclear, photosynthetic mutants of maize. *EMBO J.* **5**, 1421–1427 (1986).
- Settles, A. M. *et al.* Sec-independent protein translocation by the maize Hcf106 protein. *Science* **278**, 1467–1470 (1997).
- Sargent, F. *et al.* Overlapping functions of components of a bacterial Sec-independent protein export pathway. *EMBO J.* **17**, 3640–3650 (1998).
- Bogsch, E. G. *et al.* An essential component of a novel bacterial protein export system with homologues in plastids and mitochondria. *J. Biol. Chem.* **273**, 18003–18006 (1998).
- Hu, Y., Zhao, E., Li, H., Xia, B. & Jin, C. Solution NMR structure of the TatA component of the twin-arginine protein transport system from gram-positive bacterium *Bacillus subtilis*. *J. Am. Chem. Soc.* **132**, 15942–15944 (2010).
- Berks, B. C. A common export pathway for proteins binding complex redox cofactors? *Mol. Microbiol.* **22**, 393–404 (1996).
- Chaddock, A. M. *et al.* A new-type of signal peptide—central role of a twin-arginine motif in transfer signals for the Δ pH-dependent thylakoidal protein translocase. *EMBO J.* **14**, 2715–2722 (1995).
- Stanley, N. R., Palmer, T. & Berks, B. C. The twin arginine consensus motif of Tat signal peptides is involved in Sec-independent protein targeting in *Escherichia coli*. *J. Biol. Chem.* **275**, 11591–11596 (2000).
- Alami, M. *et al.* Differential interactions between a twin-arginine signal peptide and its translocase in *Escherichia coli*. *Mol. Cell* **12**, 937–946 (2003).
- Gerard, F. & Cline, K. Efficient twin arginine translocation (Tat) pathway transport of a precursor protein covalently anchored to its initial cpTatC binding site. *J. Biol. Chem.* **281**, 6130–6135 (2006).
- Holzappel, E. *et al.* The entire N-terminal half of TatC is involved in twin-arginine precursor binding. *Biochemistry* **46**, 2892–2898 (2007).
- Kreutzenbeck, P. *et al.* *Escherichia coli* twin arginine (Tat) mutant translocases possessing relaxed signal peptide recognition specificities. *J. Biol. Chem.* **282**, 7903–7911 (2007).
- Strauch, E. M. & Georgiou, G. *Escherichia coli* tatC mutations that suppress defective twin-arginine transporter signal peptides. *J. Mol. Biol.* **374**, 283–291 (2007).
- Mori, H. & Cline, K. A twin arginine signal peptide and the pH gradient trigger reversible assembly of the thylakoid Δ pH/Tat translocase. *J. Cell Biol.* **157**, 205–210 (2002).
- Dabney-Smith, C., Mori, H. & Cline, K. Oligomers of Tha4 organize at the thylakoid Tat translocase during protein transport. *J. Biol. Chem.* **281**, 5476–5483 (2006).
- Cline, K. & McCaffery, M. Evidence for a dynamic and transient pathway through the TAT protein transport machinery. *EMBO J.* **26**, 3039–3049 (2007).
- Frobel, J., Rose, P. & Muller, M. Early contacts between substrate proteins and TatA translocase component in twin-arginine translocation. *J. Biol. Chem.* **286**, 43679–43689 (2011).
- Fritsch, M. J., Krehenbrink, M., Tarry, M. J., Berks, B. C. & Palmer, T. Processing by rhomboid protease is required for *Providencia stuartii* TatA to interact with TatC and to form functional homo-oligomeric complexes. *Mol. Microbiol.* **84**, 1108–1123 (2012).
- Chae, P. S. *et al.* Maltose-neopentyl glycol (MNG) amphiphiles for solubilization, stabilization and crystallization of membrane proteins. *Nature Methods* **7**, 1003–1008 (2010).
- Cline, K. & Mori, H. Thylakoid Δ pH-dependent precursor proteins bind to a cpTatC–Hcf106 complex before Tha4-dependent transport. *J. Cell Biol.* **154**, 719–730 (2001).
- Punginelli, C. *et al.* Cysteine scanning mutagenesis and topological mapping of the *Escherichia coli* twin-arginine translocase TatC Component. *J. Bacteriol.* **189**, 5482–5494 (2007).
- Jeong, K. J. *et al.* A periplasmic fluorescent reporter protein and its application in high-throughput membrane protein topology analysis. *J. Mol. Biol.* **341**, 901–909 (2004).
- Behrendt, J., Standar, K., Lindenstrauss, U. & Bruser, T. Topological studies on the twin-arginine translocase component TatC. *FEMS Microbiol. Lett.* **234**, 303–308 (2004).
- Drew, D. *et al.* Rapid topology mapping of *Escherichia coli* inner-membrane proteins by prediction and PhoA/GFP fusion analysis. *Proc. Natl Acad. Sci. USA* **99**, 2690–2695 (2002).
- Gouffi, K., Santini, C. L. & Wu, L. F. Topology determination and functional analysis of the *Escherichia coli* TatC protein. *FEBS Lett.* **525**, 65–70 (2002).
- Kneuper, H. *et al.* Molecular dissection of TatC defines critical regions essential for protein transport and a TatB–TatC contact site. *Mol. Microbiol.* **85**, 945–961 (2012).
- Forrest, L. R., Kramer, R. & Ziegler, C. The structural basis of secondary active transport mechanisms. *Biochim. Biophys. Acta* **1807**, 167–188 (2011).
- Buchanan, G. *et al.* Functional complexity of the twin-arginine translocase TatC component revealed by site-directed mutagenesis. *Mol. Microbiol.* **43**, 1457–1470 (2002).
- Mould, R. M. & Robinson, C. A proton gradient is required for the transport of two luminal oxygen-evolving proteins across the thylakoid membrane. *J. Biol. Chem.* **266**, 12189–12193 (1991).
- Zoufaly, S. *et al.* Mapping precursor-binding site on TatC subunit of twin arginine-specific protein translocase by site-specific photo cross-linking. *J. Biol. Chem.* **287**, 13430–13441 (2012).
- Lausberg, F. *et al.* Genetic evidence for a tight cooperation of TatB and TatC during productive recognition of twin-arginine (Tat) signal peptides in *Escherichia coli*. *PLoS ONE* **7**, e39867 (2012).
- Bolhuis, A., Mathers, J. E., Thomas, J. D., Barrett, C. M. & Robinson, C. TatB and TatC form a functional and structural unit of the twin-arginine translocase from *Escherichia coli*. *J. Biol. Chem.* **276**, 20213–20219 (2001).
- Tarry, M. J. *et al.* Structural analysis of substrate binding by the TatBC component of the twin-arginine protein transport system. *Proc. Natl Acad. Sci. USA* **106**, 13284–13289 (2009).
- Orriss, G. L. *et al.* TatBC, TatB, and TatC form structurally autonomous units within the twin arginine protein transport system of *Escherichia coli*. *FEBS Lett.* **581**, 4091–4097 (2007).
- Maldonado, B., Buchanan, G., Muller, M., Berks, B. C. & Palmer, T. Genetic evidence for a TatC dimer at the core of the *Escherichia coli* twin arginine (Tat) protein translocase. *J. Mol. Microbiol. Biotechnol.* **20**, 168–175 (2011).
- Koch, S., Fritsch, M. J., Buchanan, G. & Palmer, T. *Escherichia coli* TatA and TatB proteins have N-out, C-in topology in intact cells. *J. Biol. Chem.* **287**, 14420–14431 (2012).
- Greene, N. P. *et al.* Cysteine scanning mutagenesis and disulfide mapping studies of the TatA component of the bacterial twin arginine translocase. *J. Biol. Chem.* **282**, 23937–23945 (2007).
- Drew, D., Lerch, M., Kunji, E., Slotboom, D. J. & de Gier, J. W. Optimization of membrane protein overexpression and purification using GFP fusions. *Nature Methods* **3**, 303–313 (2006).
- Chen, V. B. *et al.* MolProbity: all-atom structure validation for macromolecular crystallography. *Acta Crystallogr. D* **66**, 12–21 (2010).
- Ashkenazy, H., Erez, E., Martz, E., Pupko, T. & Ben-Tal, N. ConSurf 2010: calculating evolutionary conservation in sequence and structure of proteins and nucleic acids. *Nucleic Acids Res.* **38**, W529–W533 (2010).

Supplementary Information is available in the online version of the paper.

Acknowledgements We thank D. Byrne, G. Orriss and R. Owens for their contributions to the early stages of this project; R. Keller for advice; and J. Willem de Gier, D. Daley and R. Huber for providing strains and reagents. This work was supported by the Wellcome Trust (studentships to S.E.R., J.E.G. and M.A.M.; grant 083599, P.R.; grant 092970MA, M.S.P.S.), the Swedish Foundation for Strategic Research ('Future research leaders 4' to M.H.), the Swedish Research Council (grant 2010-5061 to M.H.), the E. P. Abrahams Cephalosporin Trust (M.K. and F.R.), the Biotechnology and Biological Sciences Research Council (studentship, M.J.L.; grant BB/E023347/1, S.-M.L.; grant BB/1019855/1, P.J.S.), the Medical Research Council (grant G1001640, F.J.; grant G0900888, S.J.), and the European Research Council (Advanced Grant IMPRESS, J.M. and C.V.R.). Work in S.M.L.'s group is funded by the James Martin 21st Century School Vaccine Design Institute.

Author Contributions The experiments were designed and manuscript written by S.E.R., M.J.T., B.C.B., S.M.L., M.H. and T.P. Experimental work was performed as follows: crystallization trials: S.E.R. and M.J.T.; structure determination: S.E.R., P.R. and S.M.L.; cloning and expression screening: J.E.G., M.J.T., M.J., S.-M.L. and M.J.L.; homogeneity screening: M.J.T., M.J., S.E.R., M.A.M. and S.J.; MD simulations: P.J.S. and M.S.P.S.; disulphide crosslinking: F.J. and T.P.; signal peptide binding and BN-PAGE: S.E.R., M.K. and F.R.; mass spectrometry: J.M. and C.V.R.

Author Information The coordinates and experimental data have been deposited at the Protein Data Bank with accession code 4b4a. Reprints and permissions information is available at www.nature.com/reprints. The authors declare no competing financial interests. Readers are welcome to comment on the online version of the paper. Correspondence and requests for materials should be addressed to B.C.B. (ben.berks@bioch.ox.ac.uk) or S.M.L. (susan.lea@path.ox.ac.uk).

METHODS

Selection of clones, growth conditions and solubilizing detergent. A range of *tatC* genes from thermophilic bacteria and archaea were cloned into plasmid pWaldo-TEV-GFPe⁴⁴ to allow expression in *E. coli* as N-terminal fusions to octahistidine-tagged GFP (TatC–GFP–8His). The resulting fusion proteins contain a TEV protease-cleavable linker between the TatC and GFP domains. The clones were cultured in a variety of background strains and growth conditions and TatC–GFP expression assessed by whole-cell fluorescence^{44,47}. This screen identified *Aquifex aeolicus* TatC as suitable for high-level protein production. The *A. aeolicus* *tatC* gene⁴⁸ contains two possible initiation codons. Although sequence comparisons between TatC proteins from within the phylum Aquificae indicate that the first of these codons is the authentic translation start site, the construct used here starts from the second methionine codon, thereby removing eight poorly conserved amino acids (sequence MSQEKLPE) from the N terminus of the protein. Fluorescence size exclusion chromatography (FSEC)⁴⁹ was used to identify detergents that were able to solubilize the *A. aeolicus* TatC–GFP fusion protein in a monodisperse state. Subsequently size exclusion chromatography-multi-angle laser light scattering (SEC-MALLS) was used to assess whether these detergents were able to maintain TatC in a monodisperse state following proteolytic removal of the GFP domain. Detergents meeting this selection criterion were used to purify *A. aeolicus* TatC for crystallization trials.

Protein purification and crystallization. The *A. aeolicus* TatC–GFP construct was recombinantly expressed in *E. coli* Lemo56(DE3)⁴⁷ cells cultured at 37 °C in Terrific Broth supplemented with 50 µg ml^{−1} kanamycin. When the cells attained OD₆₀₀ = 5.0, 0.1 mM IPTG was added and the cells cultured for a further 16 h at 24 °C. Cells were disrupted by homogenization (Emulsifex C5, Avestin) and membranes recovered by differential centrifugation. Solubilization was carried out at 4 °C for 2 h in 1% w/v lauryl maltose neopentyl glycol (LMNG; Anatrace) in PBS containing 20 mM imidazole. The soluble fraction was loaded on to a 5 ml Ni-NTA column (Qiagen). The column was washed with five column volumes of PBS containing 0.02% LMNG and 25 mM imidazole, then with two column volumes of the same buffer containing 40 mM imidazole, and eluted with the same buffer containing 250 mM imidazole. TatC–GFP-containing fractions were pooled and incubated with 2 mg His-tagged TEV protease, 5 mM sodium citrate pH 6.3, 0.3 mM oxidized glutathione and 3 mM reduced glutathione (final concentrations). This mixture was dialysed in a 10-kDa molecular mass cutoff membrane ('snakeskin tubing', Fisher scientific) against size exclusion (SEC) buffer (20 mM HEPES pH 7.5, 150 mM NaCl, 0.02% w/v LMNG) at 4 °C overnight. Passage over a 5 ml Ni-NTA column removed the His-tagged GFP and His-tagged TEV protease. TatC was concentrated in a centrifugal concentrator device (100 kDa molecular mass cutoff membrane, Millipore) to 5 ml, and loaded on to a Superdex 200 16/60 gel filtration column (GE Healthcare) pre-equilibrated in SEC buffer. Final peak fractions were concentrated to ~8 mg ml^{−1}.

Selenomethionine-substituted TatC was expressed in *E. coli* L56 cells grown in M9 minimal medium, using the feedback inhibition of methionine biosynthesis method⁵⁰. Cells were grown at 37 °C to an OD₆₀₀ = 0.7 and induced as for the native protein. Purification was carried out as for the native protein but the final size exclusion buffer was supplemented with 5 mM β-mercaptoethanol. Full incorporation of selenomethionine was confirmed by mass spectrometry (Supplementary Fig. 1).

Crystallization was carried out using the sitting-drop vapour diffusion method at 21 °C with a drop size of 200 nl. The best crystals were obtained in 0.2 M ammonium sulphate, 0.02 M NaCl, 0.02 M sodium acetate pH 4.0, 33% v/v PEG 200 at a 50:50 ratio of protein:mother liquor and a drop volume of 400 nl. Crystals of the selenomethionine protein were obtained in the same condition. These were flash frozen in liquid nitrogen in the mother liquor, diffracted to 3.5 Å, and belonged to the space group *H*32.

Data collection, structure determination and refinement. Diffraction data were collected at the Diamond light source (Beamline I04-1), at 120 K from four SeMet-labelled crystals (λ = 0.92 Å). The data were processed using xia2⁵¹ and data sets were scaled together using autoSHARP⁵². The first two selenium sites were located using Phenix Hyss⁵³, and the final two positions identified in SHARP LLG gradient maps⁵⁴. The hand was determined by SOLOMON⁵⁵ solvent flattening (CC for observed versus solvent flattened Es was 45% versus 51%). The main chain was traced by hand as a continuous stretch of 220 residues in the experimental map with the SeMet sites allowing unambiguous determination of the chain direction and docking of sequence in the C-terminal portion of the protein. After initial refinement in autoBUSTER⁵⁶, Buccaneer⁵⁷ was used to autobuild a model which had the correct sequence throughout. Further rounds of building using COOT⁵⁸ and refinement in autoBUSTER followed to give a final model for residues 5–229

with R = 25.2% and R_{free} = 28.8%. 92% of residues lie in the favoured regions of the Ramachandran plot and the structure has a Molprobity⁴⁵ score of 3.1 (84th percentile for structures 3.5 Å ± 0.25 Å). The quality of the electron density map is shown in Supplementary Fig. 2. There is one TatC protomer in the asymmetric unit and one molecule of LMNG located on a crystallographic two-fold (occupancy of all LMNG atoms set to 0.5).

The coordinates and experimental data have been deposited at the Protein Data Bank with accession code 4b4a.

Images for publication were generated using PyMol Version 1.5.0.4 (<http://www.pymol.org>; Schrödinger, LLC).

Protein analysis. Isothermal titration calorimetry was carried out using an iTC₂₀₀ isothermal titration calorimeter (Microcal) using synthetic peptides (Geron Ltd) as the titrant. The n-region peptide was amidated on the C terminus. Titrations were carried out at 25 °C using a reference power of 3 cal s^{−1} at a stirrer speed of 1,000 r.p.m. Isotherms were analysed and fitted in SEDPHAT⁵⁹ using a hetero-association model ($A + B \leftrightarrow AB$) with ΔH and K_d as fitting parameters. To allow for inaccuracies in peptide concentrations an inactive peptide fraction was also included as a fitting parameter. Concentrations of TatC were measured by absorption at 280 nm in 6 M guanidinium chloride using an extinction coefficient of 24,870 M^{−1} cm^{−1} calculated from the sequence.

Disulphide-crosslinking experiments were carried out at 24 °C as described previously^{32,42}.

Molecular dynamics simulations and in silico docking. All MD simulations were performed using GROMACS v4.5.4 at 323 K⁶⁰. Coarse-grain MD simulations were run for 1 µs to permit the assembly and equilibration of a dipalmitoylphosphatidylcholine (DPPC) bilayer around the protein^{61,62} using a Martini force field⁶³ (Supplementary Fig. 5). The systems were then converted to atomistic using the CG2AT-align method⁶⁴. The atomistic systems used the Gromos 53a6 force field and were equilibrated for 1 ns with the protein restrained, before 100 ns of unrestrained atomistic MD.

47. Tarry, M., Skaar, K., Heijne, G., Draheim, R. R. & Høgborn, M. Production of human tetraspanin proteins in *Escherichia coli*. *Protein Expr. Purif.* **82**, 373–379 (2012).
48. Deckert, G. *et al.* The complete genome of the hyperthermophilic bacterium *Aquifex aeolicus*. *Nature* **392**, 353–358 (1998).
49. Kawate, T. & Gouaux, E. Fluorescence-detection size-exclusion chromatography for precrystallization screening of integral membrane proteins. *Structure* **14**, 673–681 (2006).
50. Van Duyne, G. D., Standaert, R. F., Karplus, P. A., Schreiber, S. L. & Clardy, J. Atomic structures of the human immunophilin FKBP-12 complexes with FK506 and rapamycin. *J. Mol. Biol.* **229**, 105–124 (1993).
51. Winter, G. xia2: an expert system for macromolecular crystallography data reduction. *J. Appl. Cryst.* **43**, 186–190 (2010).
52. Vonrhein, C., Blanc, E., Roversi, P. & Brice, G. Automated structure solution with autoSHARP. *Methods Mol. Biol.* **364**, 215–230 (2007).
53. Adams, P. D. *et al.* The Phenix software for automated determination of macromolecular structures. *Methods* **55**, 94–106 (2011).
54. Brice, G., Vonrhein, C., Flensburg, C., Schiltz, M. & Paciorek, W. Generation, representation and flow of phase information in structure determination: recent developments in and around SHARP 2.0. *Acta Crystallogr. D* **59**, 2023–2030 (2003).
55. Abrahams, J. P. & Leslie, A. G. Methods used in the structure determination of bovine mitochondrial F₁ ATPase. *Acta Crystallogr. D* **52**, 30–42 (1996).
56. Brice, G. *et al.* BUSTER 2.11.2 (Global Phasing Ltd., 2011).
57. Cowtan, K. The Buccaneer software for automated model building. 1. Tracing protein chains. *Acta Crystallogr. D* **62**, 1002–1011 (2006).
58. Emsley, P., Lohkamp, B., Scott, W. G. & Cowtan, K. Features and development of Coot. *Acta Crystallogr. D* **66**, 486–501 (2010).
59. Houtman, J. C. *et al.* Studying multisite binary and ternary protein interactions by global analysis of isothermal titration calorimetry data in SEDPHAT: application to adaptor protein complexes in cell signaling. *Protein Sci.* **16**, 30–42 (2007).
60. Hess, B., Kutzner, C., van der Spoel, D. & Lindahl, E. GROMACS 4: Algorithms for highly efficient, load-balanced, and scalable molecular simulation. *J. Chem. Theory Comput.* **4**, 435–447 (2008).
61. Monticelli, L., Sorin, E. J., Tieleman, D. P., Pande, V. S. & Colombo, G. Molecular simulation of multistate peptide dynamics: A comparison between microsecond timescale sampling and multiple shorter trajectories. *J. Comput. Chem.* **29**, 1740–1752 (2008).
62. Scott, K. A. *et al.* Coarse-grained MD simulations of membrane protein-bilayer self-assembly. *Structure* **16**, 621–630 (2008).
63. Monticelli, L., Sorin, E. J., Tieleman, D. P., Pande, V. S. & Colombo, G. Molecular simulation of multistate peptide dynamics: a comparison between microsecond timescale sampling and multiple shorter trajectories. *J. Comput. Chem.* **29**, 1740–1752 (2008).
64. Stansfeld, P. J. & Sansom, M. S. P. From coarse grained to atomistic: a serial multiscale approach to membrane protein simulations. *J. Chem. Theory Comput.* **7**, 1157–1166 (2011).

Automated design of ligands to polypharmacological profiles

Jérémy Besnard¹, Gian Filippo Ruda¹, Vincent Setola², Keren Abecassis¹, Ramona M. Rodriguiz³, Xi-Ping Huang², Suzanne Norval¹, Maria F. Sassano⁴, Antony I. Shin³, Lauren A. Webster¹, Frederick R. C. Simeons¹, Laste Stojanovski¹, Annik Prat⁵, Nabil G. Seidah⁵, Daniel B. Constam⁶, G. Richard Bickerton¹, Kevin D. Read¹, William C. Wetsel^{3,7}, Ian H. Gilbert¹, Bryan L. Roth^{2,4} & Andrew L. Hopkins¹

The clinical efficacy and safety of a drug is determined by its activity profile across many proteins in the proteome. However, designing drugs with a specific multi-target profile is both complex and difficult. Therefore methods to design drugs rationally a priori against profiles of several proteins would have immense value in drug discovery. Here we describe a new approach for the automated design of ligands against profiles of multiple drug targets. The method is demonstrated by the evolution of an approved acetylcholinesterase inhibitor drug into brain-penetrable ligands with either specific polypharmacology or exquisite selectivity profiles for G-protein-coupled receptors. Overall, 800 ligand-target predictions of prospectively designed ligands were tested experimentally, of which 75% were confirmed to be correct. We also demonstrate target engagement *in vivo*. The approach can be a useful source of drug leads when multi-target profiles are required to achieve either selectivity over other drug targets or a desired polypharmacology.

The safety and efficacy of a drug is determined not only by its action on an individual protein, but also by its interactions with many proteins in the proteome. The promiscuous interaction of a drug with undesired proteins frequently causes toxicity¹ and adverse effects^{2,3}. Conversely, a single drug target can be therapeutically insufficient, particularly in complex neuropsychiatric conditions, infectious diseases or cancer^{4–6}. Instead, it is frequently necessary for a drug to engage two or more targets simultaneously for therapeutic efficacy⁷. Psychiatric drugs in particular require multiple activities against several targets to modulate therapeutically complex neuropsychiatric domains including perception, cognition and emotion⁴. However, designing drugs with a specific multi-target profile—to achieve either exquisite selectivity over other drug targets or a desired polypharmacology—is a complex and exceedingly difficult task for medicinal chemistry⁸. Accordingly, methods are needed to enable drugs to be designed a priori against several molecular targets simultaneously. Here we describe a solution to the complex problem of designing ligands against multiple drug target profiles by automated design.

From prediction to design

The problem of designing ligands against a multi-target profile involves the parallel optimization of multiple structure–activity relationships within a desired range of physicochemical properties. The prospect of multi-target drug design has been recently aided by the development of computational methods that show success in predicting the molecular targets of drugs^{3,9–13} (Supplementary Fig. 1), although such approaches are not intrinsically design methods.

Drug design can be modelled as an evolutionary process of iterative cycles of exploration and analysis^{14,15}. Adaptive design processes are efficient at solving complex, multi-objective problems. Accordingly, we developed an automated, adaptive design approach to optimize ligands against polypharmacological profiles.

Several *de novo* drug design methods have been proposed previously^{16–21}. However, of those that have been experimentally tested^{22–26}, high affinity ligands have been described only rarely and these are all against a single molecular target objective^{24,26}. In contrast to previous *de novo* approaches, we mimicked the creative process by automated learning of medicinal chemistry design tactics, applying these automated learning approaches to the generation of analogues, and then prioritizing them relative to a set of objectives (Fig. 1a). The development of this approach is described below, starting from ‘off-target’ predictions, progressing to ligand design, and finally to the discovery of novel compounds with predefined multi-target profiles.

Evolution of a drug

James Black proposed that, “the most fruitful basis for the discovery of a new drug is to start with an old drug”²⁷. Accordingly, we tested whether the algorithm could automate the evolution of new biological activities, starting from a known drug. Donepezil (compound 1) is an acetylcholinesterase inhibitor approved for cognitive enhancement in Alzheimer’s disease. Bayesian probabilistic activity models⁹, for 784 molecular targets built from the ChEMBL database²⁸, predicted a moderate likelihood that donepezil possessed D4 dopamine receptor activity and a low chance of D2 dopamine receptor activity (Supplementary Table 1). We found donepezil was a moderately potent D4 inverse agonist (inhibition constant K_i = 614 nM) with minimal D2 activity (Supplementary Figs 2 and 3 and Supplementary Tables 2 and 3). The D4 inverse agonist activity of donepezil is intriguing given analyses demonstrating a significant improvement in memory in the trail making test with this drug²⁹ and findings that D4 antagonists can prevent stress-induced cognitive dysfunction in primates³⁰.

We tested our method by evolving the structure of donepezil with the dual objectives of improving D2 activity and achieving blood–brain

¹Division of Biological Chemistry and Drug Discovery, College of Life Sciences, University of Dundee, Dundee DD1 5EH, UK. ²NIMH Psychoactive Drug Screening Program, Department of Pharmacology, The University of North Carolina Chapel Hill School of Medicine, Chapel Hill, North Carolina 27759, USA. ³Mouse Behavioral and Neuroendocrine Analysis Core Facility, Duke University Medical School, Durham, North Carolina 27710, USA. ⁴Department of Pharmacology and Division of Chemical Biology and Medicinal Chemistry, The University of North Carolina Chapel Hill School of Medicine, Chapel Hill, North Carolina 27759, USA. ⁵Laboratory of Biochemical Neuroendocrinology, Clinical Research Institute of Montreal (IRCM), affiliated with the University of Montreal, Montreal, Quebec, H2W 1R7, Canada. ⁶Ecole Polytechnique Fédérale de Lausanne (EPFL) SV ISREC, Station 19, CH-1015 Lausanne, Switzerland. ⁷Departments of Psychiatry and Behavioral Sciences, Cell Biology, and Neurobiology, Duke University Medical School, Durham, North Carolina 27710, USA.

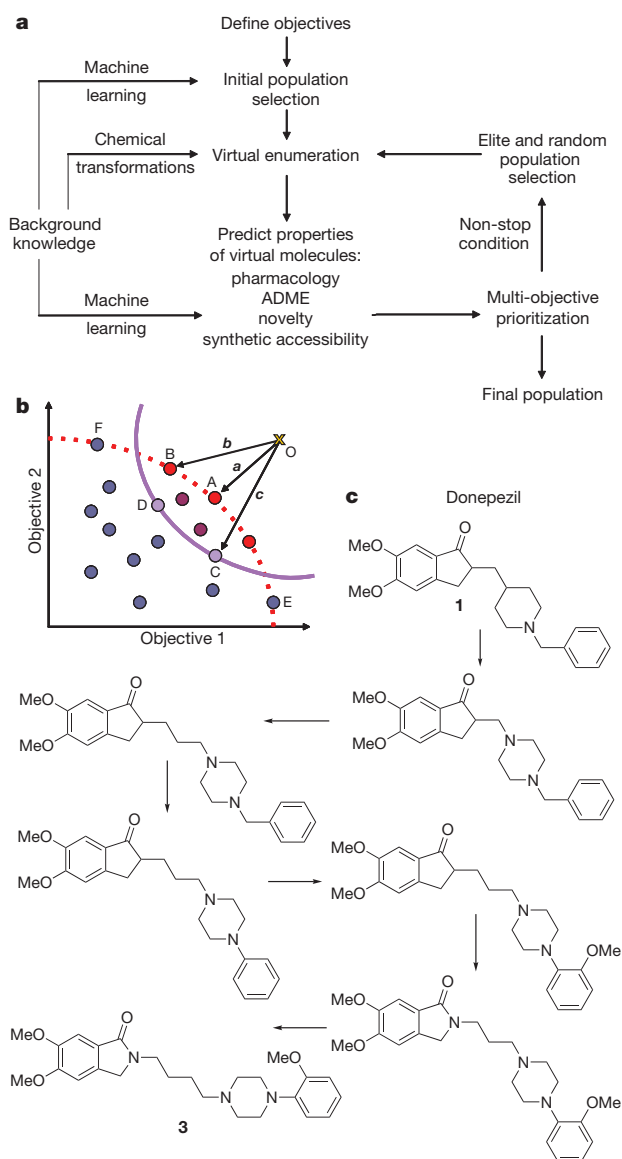


Figure 1 | Adaptive drug design. **a**, Closed loop of automated ligand design algorithm by multi-objective evolutionary optimization. **b**, Multi-objective prioritization by vector scalarization. The multi-target objectives are defined as the coordinates of the ideal achievement point, O (gold cross), and the predicted values of each generated compound (coloured circles) are also defined as coordinates in a multi-dimensional space. The Pareto frontier is displayed as a red dotted line. The multi-objective prioritization is inverse to the magnitude of vectors ($|a| < |b| < |c|$). Compound A is prioritized the highest. Compounds C and D have the same vector length ($|c| = |d|$) and are thus prioritized equally and above the Pareto optimal compounds E and F. **c**, Evolution of donepezil (compound 1) (19% inhibition of D2 receptor at 10 μ M; D2 dopamine Bayesian score = 25) into D2 dopamine inverse agonist compound 3 (96% inhibition of D2 receptor at 10 μ M; D2 dopamine Bayesian score = 92). The Tanimoto similarity between donepezil and compound 3 is only 0.35.

barrier penetration. In our approach the desired multi-objective profile is defined a priori and then expressed as a point in multi-dimensional space termed ‘the ideal achievement point’. In this first example the objectives were simply defined as two target properties and therefore the space has two dimensions. Each dimension is defined by a Bayesian score for the predicted activity and a combined score that describes the absorption, distribution, metabolism and excretion (ADME) properties suitable for blood–brain barrier penetration (D2 score = 100, ADME score = 50). We then generated alternative chemical structures by a set of structural transformations using donepezil as the starting structure. The population was subsequently enumerated by applying a

set of transformations to the parent compound(s) of each generation. In contrast to rules-based or synthetic-reaction-based approaches for generating chemical structures^{16,31–34}, we used a knowledge-based approach by mining the medicinal chemistry literature^{28,35}. By deriving structural transformations from medicinal chemistry, we attempted to mimic the creative design process³⁶ (Supplementary Fig. 4). Activity predictions were calculated for each of the enumerated compounds from all Bayesian models. Scores representing the likelihood of central nervous system (CNS) penetration and good ADME properties were calculated using the program StarDrop and combined into a single value. The predicted properties of the enumerated structures were then expressed as points in multi-dimensional space. The generated structures were subsequently ranked by the distance (in multi-dimensional space) between the predicted properties for each structure and the ideal achievement point³⁷ (Fig. 1b). Compounds were filtered for novelty, Lipinski’s rule of five compliance³⁸ and synthetic accessibility³⁹. The top 10,000 prioritized structures were selected for the next iterative cycle along with 500 random structures from the remaining population. The process was iterated until either a structure close to the objectives was discovered or no further improvements were achieved.

Initially, we evolved a series of isoindoles and prioritized them using our achievement objectives as criteria (Fig. 1c, Supplementary Table 4 and Supplementary Fig. 5). Eight analogues were then synthesized and tested (Fig. 2, Supplementary Figs 2 and 6 and Supplementary Table 5), with all showing substantial D2 receptor affinities (K_i values = 156–1,700 nM, Supplementary Table 3).

The second highest ranking compound (compound 3)—chosen from the final population of evolved structures—exhibited the highest D2 receptor affinity (K_i = 156 nM). Thus, we successfully evolved the negligible D2 receptor binding activity of donepezil into a series of ligands with higher D2 affinities (Fig. 2). Functionally, compound 3 was a dual D2 inverse agonist and D4 agonist (Supplementary Fig. 3). CNS penetration studies showed that compound 3 penetrates the brain as predicted, with an *in vivo* brain–blood ratio (BBR) of 0.5.

Although the evolved compounds were selected for the D2 receptor objective, other predicted activities were not selected against. Accordingly, each of the generated compounds had a predicted polypharmacology profile. In general, this set of isoindole analogues was predicted to exhibit promiscuous profiles, with variable activities predicted for multiple serotonergic, adrenergic and dopaminergic receptor subtypes (Supplementary Tables 1 and 5). These predicted promiscuous profiles were subsequently confirmed (Fig. 2 and Supplementary Tables 2 and 3), and the predicted multi-target profiles displayed excellent agreement with experimentally determined profiles, thereby implying that the approach can be applied to the *de novo* design of multi-target agents.

Reducing anti-target activity

The isoindoles exhibited moderately potent affinities for the α_1 -adrenoceptors (K_i values = 0.9–3,577 nM, mean K_i = 277 nM, Supplementary Table 3 and Supplementary Fig. 2). Because α_1 -adrenoceptor antagonists can induce low blood pressure as a side effect they are considered ‘anti-targets’ to be avoided in drug design⁴⁰. A common drug design optimization problem is to reduce such anti-target activity while maintaining desired on-target activities. We accordingly evolved the eight newly synthesized isoindoles towards a polypharmacological profile (5-HT_{1A} serotonin receptor and D2-, D3- and D4-dopamine receptors) with selectivity over the three α_1 -adrenoceptors anti-targets (α_{1A} , α_{1B} and α_{1D}) while maintaining CNS penetration.

To compare evolutionary strategies, the isoindoles were optimized towards polypharmacology objectives with and without highly predicted α_1 activities filtered-out at each generation (Fig. 3a and Supplementary Fig. 7 and Supplementary Tables 6 and 7). In both optimizations benzolactams were ranked the highest (compounds 11a and 10a respectively) (Fig. 3b and Supplementary Tables 6 and

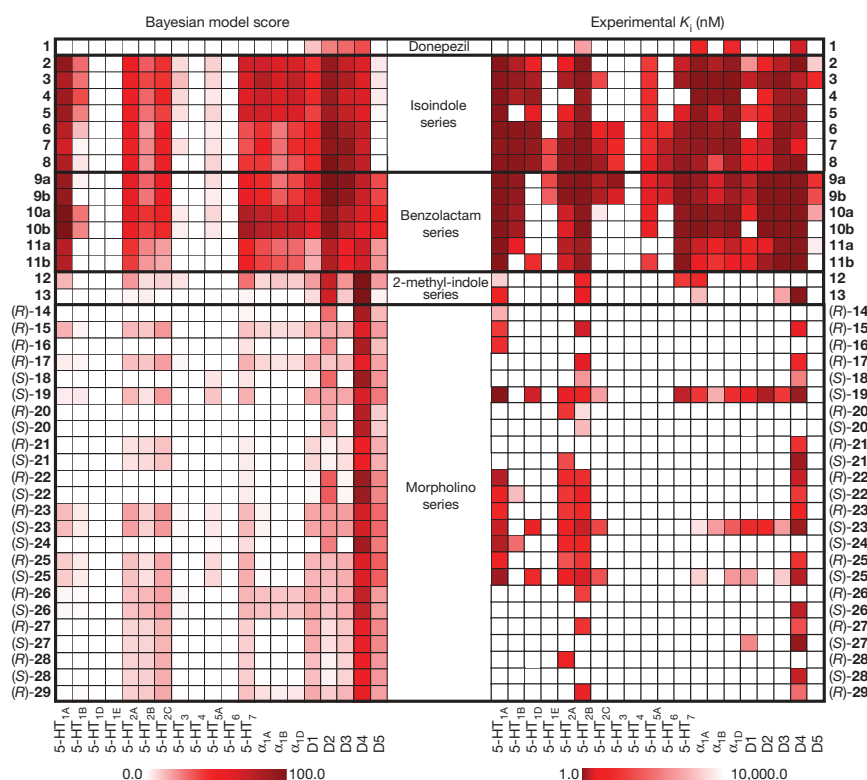


Figure 2 | Polypharmacology profiles of designed ligands. Comparison of the predicted Bayesian and observed polypharmacology profiles for (1) donepezil (compound 1); (2) the isoindole analogues (compounds 2–8)—of the 160 ligand–target associations, 100 were correctly predicted by the Bayesian models ($P = 0.001$; probability of success of 0.63 with 95% confidence intervals of 0.55–0.70); (3) the benzolactam analogues (compounds 9a–11b)—of the 160 ligand–target associations, 107 were correctly predicted ($P = 1.1 \times 10^{-5}$); (4) the 2,3-dihydro-indol-1-yl analogues (compounds 12 and 13); and (5) the morpholino analogues (compounds 14–29)—of the 540 ligand–target associations, 437 were correctly predicted ($P < 2.2 \times 10^{-16}$). The figure is composed of data in Supplementary Tables 1 and 3. In total, of the 800 predictions in the matrix on 39 novel, prospectively designed ligands and donepezil, 599 were experimentally confirmed correct ($P < 2.2 \times 10^{-16}$), with a probability of success of 0.75 (95% confidence interval of 0.72–0.78).

7). Six benzolactam analogues were then synthesized on the basis of both sets of objectives (Supplementary Table 8 and Supplementary Fig. 5). Analogues of the benzo- δ -lactam (3,4,-dihydroisoquinolin-1(2H)-one) (compounds 9a, 10a and 11a) and benzo- ϵ -lactam (2,3,4,5-tetrahydro-1-H-benzo[c]azepin-1-one) (compounds 9b, 10b and 11b) were synthesized for comparison because both ring systems were highly prioritized.

Both the predicted and observed receptor activity profiles for the synthesized benzolactams are shown in Fig. 3b (see also Supplementary Tables 1 and 3 and Supplementary Fig. 2). The 2-pyridine-piperazine analogues (compounds 11a and 11b) have the lowest α_1 predictions and, indeed, exhibited the lowest α_1 affinities (mean $K_i = 1,131$ nM). In agreement with the models, compounds 11a and 11b also have the lowest affinity for all D2-like dopamine receptors of the benzolactams tested. The dichloro-phenylpiperazine analogues (compounds 9a and 9b) exhibited slightly higher α_1 and D2 binding predictions, which were also confirmed experimentally. By contrast, the 2-methoxy phenylpiperazine analogues (compounds 10a and 10b) exhibited potent affinities against the polypharmacology profile of 5-HT_{1A}, D2, D3 and D4 receptors, but also had the highest α_1 predictions and were confirmed as the most potent against the α_1 receptors (mean $K_i = 45.3$ nM) (Fig. 3b). Receptor profiling of the benzolactam series revealed that compared to the isoindoles, from which the compounds were evolved, the benzolactams achieved the objective of an increased polypharmacology profile for 5-HT_{1A}, D2, D3 and D4 receptors compared with the α_1 -adrenoceptors (Fig. 3b). The benzolactams are 11-fold more selective with respect to D2 receptors and 25-fold more selective with respect to the polypharmacology profile than the isoindoles. Notably, the benzolactam compound 9a penetrated the brain, (BBR = 5.9), as predicted.

As the benzolactam series was not present in the ChEMBL database (release 1) used to build the Bayesian models, they constituted a novel chemical series for the system to discover⁴¹. Notably, benzolactam derivatives have recently been independently synthesized and tested as potent D2 and D3 ligands⁴²; however, the broader receptor profiles of the compounds were not evaluated. This observation provides additional verification that the algorithm is capable of generating

and prioritizing novel chemical structures equivalent to those devised by medicinal chemists.

Potency optimization

We next explored selectivity in the context of our multi-target objectives and asked whether we could optimize potent, selective, CNS-penetrant D4 receptor ligands starting from the chemical structure of donepezil. We executed the optimization in two stages; first we optimized for D4 potency and brain penetrability (Fig. 4a), and then for D4 selectivity (Fig. 4b). A series of 2-methylindoline derivatives with predicted high D4 activity was evolved from donepezil after six generations (Fig. 4a and Supplementary Fig. 9). Notably, compounds belonging to a 2,3-dihydro-indol-1-yl chemotype were dominant in the prioritized set (Supplementary Table 9). Compounds 12 and 13, which both belong to the 2,3-dihydro-indol-1-yl class, were then selected for testing (Supplementary Figs 5 and 8). The highest ranking compound, 12, was inactive, whereas compound 13, the third-highest-ranking design out of the final population, was the most potent D4 ligand among all tested compounds (D4 $K_i = 8.9$ nM). Through the process of optimization, compound 13 represents a 69-fold increase in affinity over donepezil. In contrast to the isoindole and benzolactams analogues, compound 13 is predicted to be a highly selective D4 ligand with 95-fold selectivity over 5-HT_{2B} and weak affinities greater than 1 μ M for only five other receptors in our panel of G-protein-coupled receptors (GPCRs) (Fig. 2). Importantly, and as predicted, compound 13 is highly CNS penetrant (BBR = 7.5).

To verify that the predicted properties of selectivity, potency and CNS penetration resulted in D4 receptor activity *in vivo*, we evaluated the effects of compound 13 treatment on behaviour in wild-type and D4 receptor knockout (D4R-KO) mice (Fig. 4c–f), as well as in protein convertase 7 (PC7 encoded by *Pcsk7*) knockout mice (Supplementary Fig. 10a–d) that display a similar D4R-KO phenotype. Although open field locomotor activity declined in vehicle-treated D4R wild-type (D4R-WT) animals (Fig. 4c), it remained high and showed little habituation in D4R-KO mice. Although the treatment with 0.7 mg kg⁻¹ of compound 13 was without significant effect in either genotype, the 1 mg kg⁻¹ dose reduced locomotion at 0–20 min

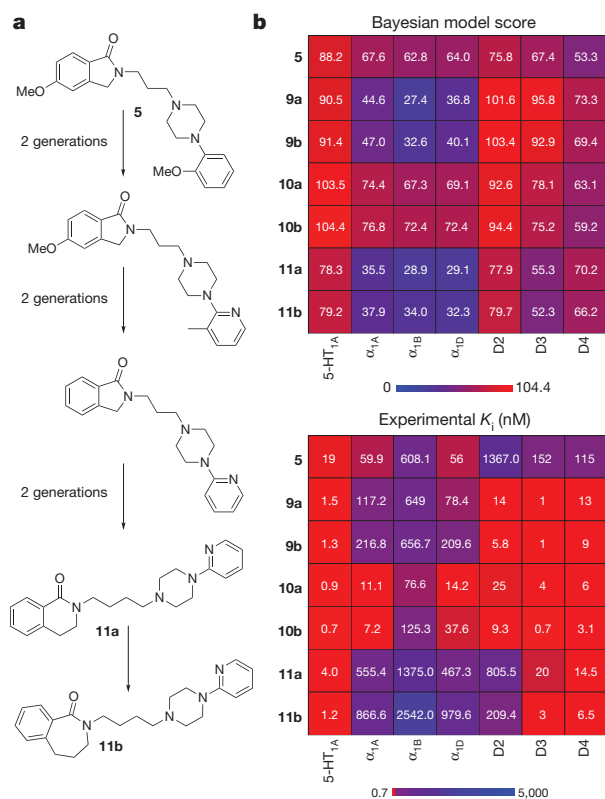


Figure 3 | Reducing α_1 anti-target activity by evolutionary design.

a, Summary of the evolution of the prioritized benzolactam analogues (compounds **11a** and **11b**) from a parent isoindole analogue (compound **5**). The full evolutionary pathway from compound **5** to **11b** is shown in Supplementary Fig. 7. **b**, Comparison of polypharmacology profiles for the Bayesian model score and experimental binding affinities (K_i) of compound **5** and benzolactam analogues (compounds **9a–11b**) for the seven target objectives (α_{1A} , α_{1B} and α_{1D} compared to 5-HT_{1A}, D₂, D₃ and D₄ receptors). On average, the selectivity ratios for the D₂, D₃, D₄ and 5-HT_{1A} receptors for the synthesized benzolactams over the α_1 receptors are 2.8-, 59-, 58- and 312-fold, respectively. In comparison, the average selectivity ratios for D₂, D₃, D₄ and 5-HT_{1A} receptors for the isoindole analogues over the α_1 receptors are 0.27-, 2.1-, 1- and 14-fold, respectively. With respect to the algorithm prioritization for the benzolactam analogues (Supplementary Table 8) against the multi-target objectives, the order of prioritization matches the experimentally determined order for the analogues (dichloro phenylpiperazine > 2-methoxy phenylpiperazine > 2-pyridine piperazine).

in D4R-WT animals. The same dose had no effect in D4R-KO mice. In the centre zone, vehicle-treated D4R-KO mice spent more time in this area at 21–60 min than D4R-WT controls (Fig. 4d). Centre time in D4R-WT animals was enhanced at 0–20 min with both doses of compound **13**; in D4R-KO mice it was attenuated at 41–60 min with the 1 mg kg⁻¹ dose. In the hole-board test, head-poking was increased in vehicle-treated D4R-KO animals compared to D4R-WT controls (Fig. 4e). In D4R-WT mice compound **13** augmented head-pokes in a dose-dependent fashion; only the 1 mg kg⁻¹ dose attenuated head-poking in mutants. In the zero maze, open-area time was increased in vehicle-treated D4R-KO mice relative to D4R-WT controls (Fig. 4f). Treatment of 1 mg kg⁻¹ of compound **13** selectively increased D4R-WT open-area times to similar levels seen with the D4R-KO mice. With regards to PC7 mice, PC7-WT and D4R-WT responses were similar (Supplementary Fig. 8a–d). Although behaviours in PC7-KO vehicle controls essentially phenocopied those in vehicle-treated D4R-KO mice, compound **13** normalized PC7-KO responses to those of PC7-WT controls. By comparison, D4R-KO mice were largely unresponsive to compound **13**—demonstrating high D4R selectivity. Nonetheless, compound **13** did not seem to be absolutely selective because in D4R-KO animals the 1 mg kg⁻¹ dose attenuated head-poking

in the hole-board test, implying some possible off-target actions at increased doses.

Automated invention

Using compound **13**, we further expanded our objective to evolve ligands that were highly selective for D4 dopamine, CNS penetrant and a new chemotype. The evolution of compound **13** against these objectives resulted in the design of new morpholino compounds (Fig. 4b and Supplementary Fig. 11 and Supplementary Tables 10 and 11). Compounds with the new isoindol-1-yl-ethyl-morpholino backbone were prominent in the prioritized final generation population of 10,000 structures (ranked fifth, sixth and ninth of the top 10 compounds in Supplementary Table 10), whereas most known D4 ligands are 1,4-disubstituted aromatic piperidines and piperazines (1,4-DAPs). However 1,4-DAPs are rather promiscuous substructures common in ligands for many biogenic amine GPCRs⁴³. Therefore, the isoindol-1-yl-ethyl-morpholino analogues represent a new D4 chemotype.

A library of 24 morpholino analogues (compounds **14–29**) was then synthesized and profiled against our GPCR panel (Supplementary Table 11 and Supplementary Fig. 5). Individual *R* and *S* morpholino enantiomers were synthesized and assayed separately (chirality designated by prefix). To reduce complexity further, direct analogues with and without the carbonyl oxygen were synthesized (for example, compounds **20** and **21**), as this atom was not predicted to be essential to the overall D4 selectivity profile (Fig. 2).

The assays confirmed the predictions that the new morpholino compounds are generally highly selective for the D4 receptor compared with the other tested receptors (Fig. 2). Seventeen of the compounds had affinities for the D4 dopamine receptor, ranging from K_i = 90 nM (compound (*S*)-**27**) to K_i = 5,526 nM (compound (*S*)-**18**) with eight exhibiting affinities less than 1 μ M for D4 (compounds (*R*)-**15**, (*S*)-**19**, (*S*)-**21**, (*R*)-**22**, (*S*)-**23**, (*S*)-**26**, (*S*)-**27** and (*S*)-**28**). Compounds containing the ethanone linker-group were generally less active than those with the ethyl linker. For compounds with the ethyl linker, the *S* enantiomer was more potent than the *R* enantiomer. Functional assays of an exemplar compound (*R*)-**22** indicated inverse agonism at the D4 receptor (Supplementary Fig. 3).

In agreement with the design objectives, the morpholinos displayed exquisite selectivity for the D4 dopamine receptor. Excluding the dopamine receptors, low positive Bayesian scores were observed for eight of the compounds against 5-HT_{1A} serotonin receptors, 16 of the compounds against the 5-HT_{2A/B/C} serotonin receptors, and almost all had very low scores for 5-HT₇ serotonin receptors. The off-target trends were confirmed when the compounds were profiled (Fig. 2). The morpholino compounds, on average, bound to 3.4 targets (including D4 at K_i < 10 μ M) compared to 15.8 targets for the isoindole and benzolactam compounds. Seven of the active compounds had off-target activities for only 1 of the 20 receptors tested. Compound (*S*)-**26** is the most selective compound with no measured affinity for any other screened receptor. Four compounds possessed both relatively high affinity (D4 K_i < 1 μ M) and two or fewer off-target activities out of the 20 GPCRs profiled ((*S*)-**21**, (*S*)-**26**, (*S*)-**27** and (*S*)-**28**).

The morpholino series thus represents a new class of highly selective, brain-penetrant, D4 dopamine receptor ligands. Compounds (*S*)-**27** (D4 K_i = 90 nM; D1 K_i = 5852 nM; BBR = 2.0) and (*S*)-**21** (D4 K_i = 182 nM, 5-HT_{2A} K_i = 3,545 nM) qualified as lead compounds that fulfilled all of our design objectives of novelty, high affinity for the D4 dopamine receptor, exquisite selectivity and CNS penetration. Clearly the automated design of a new class of ligands with a desired multi-target profile demonstrates that the method is able to generate novel, drug-like lead compounds directly by automated design.

Drug design from knowledge

We focused on the polypharmacology of bioaminergic GPCRs as a convenient test case, owing to the importance of multi-target profiles at these receptors for a variety of neuropsychiatric indications⁴. In

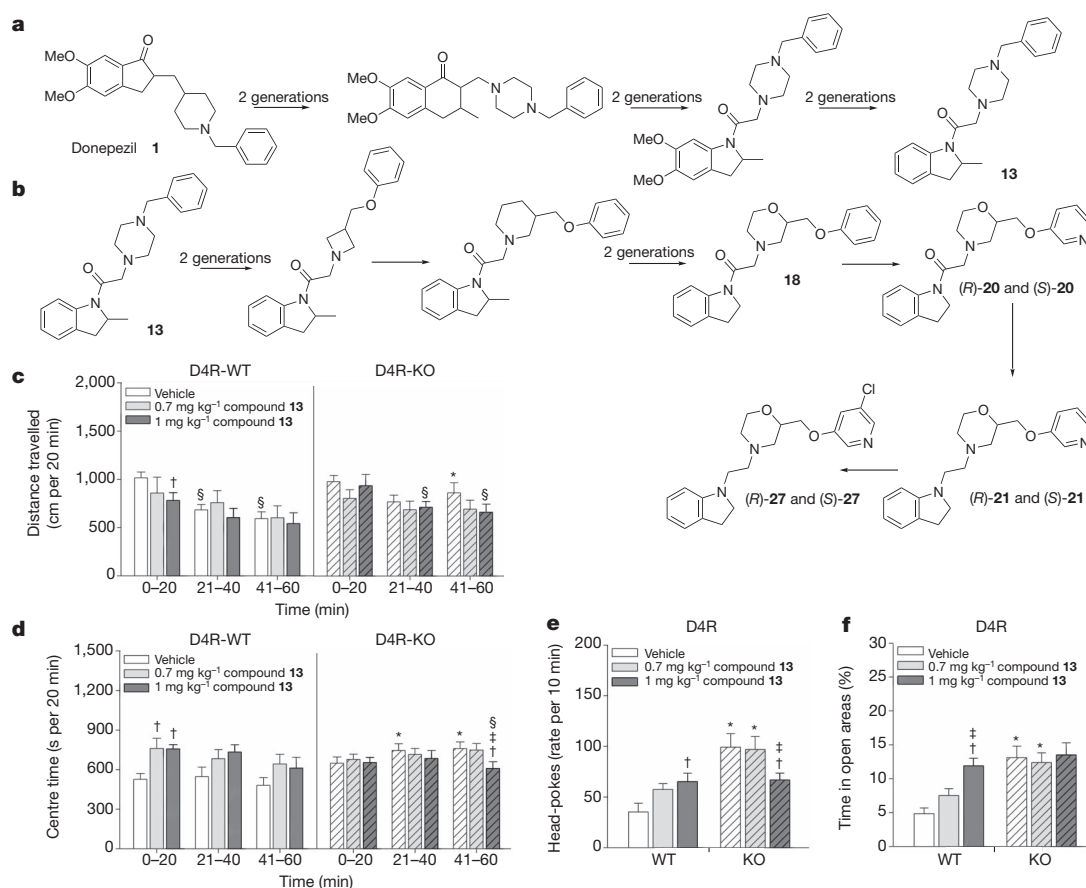


Figure 4 | Evolution of D4 dopamine ligands from donepezil. **a**, Summary of the evolution of donepezil (compound **1**) (D4 dopamine Bayesian score = 26, D4 K_i = 614 nM) into D4 dopamine inverse agonist compound **13** (D4 dopamine Bayesian score = 112, D4 k_i = 8.9 nM). The Tanimoto similarity between donepezil and compound **13** is only 0.26. The full evolutionary pathway from donepezil to compound **13** is shown in Supplementary Fig. 9. **b**, Summary of the evolution of selective novel D4 dopamine ligands. Compound **13** is further evolved by selection for novelty and D4 selectivity into the morpholino analogues **18**, **20** (*R* and *S*), **21** (*R* and *S*) and **27** (*R* and *S*). The full evolutionary pathway from compound **13** to **27** is shown in Supplementary Fig. 11 **c–f**, Behavioural analysis of a novel D4 dopamine ligand in D4 receptor knockout (D4R KO) mice. D4R-WT, D4R-wild type. **c**, Distance travelled in the open field over 60 min. Mice were

given intraperitoneal injection of vehicle or 0.7 or 1 mg kg⁻¹ of compound **13** and tested immediately over 60 min. **d**, Time spent in the centre zone in the open field. **e**, The numbers of head-pokes in the hole-board test. Animals were injected with vehicle or 0.7 or 1 mg kg⁻¹ of compound **13** and tested 30 min later over 10 min. **f**, Percentage of time in the open areas in the zero maze in D4R mice. Animals were administered vehicle or compound **13** and tested 30 min later for 5 min. n = 8–14 mice per treatment/condition.

* P < 0.05, wild-type compared with D4R-KO mice or compared to the D4R-KO mice at the same time-point; † P < 0.05, comparisons within genotype to the vehicle; ‡ P < 0.05, comparisons between 0.7 and 1 mg kg⁻¹ compound **13**; § P < 0.05, compared to the 0–20 min time-point. All error bars are mean ± s.e.m.

principle, the approach is applicable to all drug–target classes, limited only by the requirement for sufficient structure–activity data to create useful models^{9–12}. To extend polypharmacology profiling and hence *de novo* design it will be necessary to develop inference methods to build predictive bioactivity models that integrate all available structure–activity relationships, protein structure and protein sequence information together and combine data from diverse scoring functions into predictive frameworks^{44,45}.

De novo, automated compound design against multi-target profiles provides a powerful new approach for discovering new ligands and drug leads. The method is particularly useful as a new source of leads for polypharmacology profiles.

METHODS SUMMARY

Adaptive optimization. A library of historical chemical structure transformations was derived by mining the ChEMBL database²⁸. Each transformation was systematically applied to every parent compound in each generation. Bayesian activity models^{9,46} were calculated for more than 784 proteins based on the ECFP6 fingerprint representation⁴⁶ of chemical structures of structure–activity data in ChEMBL. Each compound in every generation was scored against the panel of Bayesian models. ADME properties were calculated using StarDrop (Optibrium).

Synthetic accessibility was assessed using a previously published method³⁹ based on the statistical representation of fragments in ChEMBL and molecular complexity. The algorithm was programmed in Pipeline Pilot (version 7.5, Accelrys).

Chemical synthesis. Details of the purchase, synthesis and purification of all compounds are provided in the Supplementary Information.

Experimental testing. The predicted receptor profiles of all the compounds were assessed using standard radioligand binding and functional assay methods at the National Institute of Mental Health Psychoactive Drug Screening Program. The hERG assay was performed as previously described⁴⁷. Metabolic stability was assessed as previously described⁴⁸ and brain penetration was assessed by determining the ratio of tested compound between brain and blood at a set time point following intraperitoneal or intravenous administration. For behavioural studies, compound **13** was dissolved in a 0.1% N,N-dimethylacetamide (DMA) with 15% 2-hydroxypropyl-β-cyclodextrin (Sigma-Aldrich) solution and injected intraperitoneally immediately before placement into the open field or 30 min before the zero-maze or hole-board tests as described^{49,50} using AccuScan (AccuScan Instruments), Noldus Observer XT 9.0 (Noldus Technologies), and Clever Sys TopScan software (Clever Sys), respectively. All behavioural data are presented as means ± s.e.m and were analysed with SPSS 20 (IBM). Details of the *in vivo* experiments are described in the Supplementary Information.

Full Methods and any associated references are available in the online version of the paper.

Received 1 April 2011; accepted 19 October 2012.

- Hughes, J. D. *et al.* Physicochemical drug properties associated with *in vivo* toxicological outcomes. *Bioorg. Med. Chem. Lett.* **18**, 4872–4875 (2008).
- Roth, B. L. Drugs and valvular heart disease. *N. Engl. J. Med.* **356**, 6–9 (2007).
- Campillos, M., Kuhn, M., Gavin, A. C., Jensen, L. J. & Bork, P. Drug target identification using side-effect similarity. *Science* **321**, 263–266 (2008).
- Roth, B. L., Sheffler, D. J. & Kroeze, W. K. Magic shotguns versus magic bullets: selectively non-selective drugs for mood disorders and schizophrenia. *Nature Rev. Drug Discov.* **3**, 353–359 (2004).
- Knight, Z. A., Lin, H. & Shokat, K. M. Targeting the cancer kinome through polypharmacology. *Nature Rev. Cancer* **10**, 130–137 (2010).
- Brötz-Oesterhelt, H. & Brunner, N. A. How many modes of action should an antibiotic have? *Curr. Opin. Pharmacol.* **8**, 564–573 (2008).
- Hopkins, A. L. Network pharmacology: the next paradigm in drug discovery. *Nature Chem. Biol.* **4**, 682–690 (2008).
- Morphy, R. & Rankovic, Z. Designed multiple ligands. An emerging drug discovery paradigm. *J. Med. Chem.* **48**, 6523–6543 (2005).
- Paolini, G. V., Shapland, R. H. B., van Hoorn, W. P., Mason, J. S. & Hopkins, A. L. Global mapping of pharmacological space. *Nature Biotechnol.* **24**, 805–815 (2006).
- Keiser, M. J. *et al.* Relating protein pharmacology by ligand chemistry. *Nature Biotechnol.* **25**, 197–206 (2007).
- Keiser, M. J. *et al.* Predicting new molecular targets for known drugs. *Nature* **462**, 175–181 (2009).
- Vidal, D. & Mestres, J. In silico receptorome screening of antipsychotic drugs. *Mol. Inf.* **29**, 543–551 (2010).
- Lounkine, E. *et al.* Large-scale prediction and testing of drug activity on side-effect targets. *Nature* **486**, 361–367 (2012).
- Schneider, G. & So, S.-S. *Adaptive Systems in Drug Design* (Landes Biosciences, 2002).
- Schneider, G. *et al.* Voyages to the (un)known: adaptive design of bioactive compounds. *Trends Biotechnol.* **27**, 18–26 (2009).
- Schneider, G., Lee, M. L., Stahl, M. & Schneider, P. *De novo* design of molecular architectures by evolutionary assembly of drug-derived building blocks. *J. Comput. Aided Mol. Des.* **14**, 487–494 (2000).
- Gillet, V. J., Willett, P., Fleming, P. J. & Green, D. V. Designing focused libraries using MoSELECT. *J. Mol. Graph. Model.* **20**, 491–498 (2002).
- Brown, N., McKay, B. & Gasteiger, J. The *de novo* design of median molecules within a property range of interest. *J. Comput. Aided Mol. Des.* **18**, 761–771 (2004).
- Nicolaou, C. A., Brown, N. & Pattichis, C. S. Molecular optimization using computational multi-objective methods. *Curr. Opin. Drug Discov. Devel.* **10**, 316–324 (2007).
- Liu, Q., Masek, B., Smith, K. & Smith, J. Tagged fragment method for evolutionary structure-based *de novo* lead generation and optimization. *J. Med. Chem.* **50**, 5392–5402 (2007).
- Dey, F. & Caffisch, A. Fragment-based *de novo* ligand design by multiobjective evolutionary optimization. *J. Chem. Inf. Model.* **48**, 679–690 (2008).
- Vinkers, H. M. *et al.* SYNOPSIS: SYNthesize and OPTimize system in silico. *J. Med. Chem.* **46**, 2765–2773 (2003).
- Heikkilä, T. *et al.* The first *de novo* designed inhibitors of *Plasmodium falciparum* dihydroorotate dehydrogenase. *Bioorg. Med. Chem. Lett.* **16**, 88–92 (2006).
- Roche, O. & Rodríguez Sarmiento, R. M. A new class of histamine H3 receptor antagonists derived from ligand based design. *Bioorg. Med. Chem. Lett.* **17**, 3670–3675 (2007).
- Alig, L. *et al.* Benzodioxoles: novel cannabinoid-1 receptor inverse agonists for the treatment of obesity. *J. Med. Chem.* **51**, 2115–2127 (2008).
- Schneider, G. *et al.* Reaction-driven *de novo* design, synthesis and testing of potential type II kinase inhibitors. *Future Med. Chem.* **3**, 415–424 (2011).
- Wermuth, C. G. Selective optimization of side activities: the SOSA approach. *Drug Discov. Today* **11**, 160–164 (2006).
- Gaulton, A. *et al.* ChEMBL: a large-scale bioactivity database for drug discovery. *Nucleic Acids Res.* **40**, D1100–D1107 (2012).
- Ribeiz, S. R. *et al.* Cholinesterase inhibitors as adjunctive therapy in patients with schizophrenia and schizoaffective disorder: a review and meta-analysis of the literature. *CNS Drugs* **24**, 303–317 (2010).
- Arnsten, A. F., Murphy, B. & Merchant, K. The selective dopamine D4 receptor antagonist, PNU-101387G, prevents stress-induced cognitive deficits in monkeys. *Neuropsychopharmacology* **23**, 405–410 (2000).
- Gillet, V., Johnson, A. P., Mata, P., Sike, S. & Williams, P. SPROUT: a program for structure generation. *J. Comput. Aided Mol. Des.* **7**, 127–153 (1993).
- Stahl, M. *et al.* A validation study on the practical use of automated *de novo* design. *J. Comput. Aided Mol. Des.* **16**, 459–478 (2002).
- Brown, N., McKay, B., Gilardoni, F. & Gasteiger, J. A graph-based genetic algorithm and its application to the multiobjective evolution of median molecules. *J. Chem. Inf. Comput. Sci.* **44**, 1079–1087 (2004).
- Nicolaou, C. A., Apostolakis, J. & Pattichis, C. S. *De novo* drug design using multiobjective evolutionary graphs. *J. Chem. Inf. Model.* **49**, 295–307 (2009).
- Stewart, K. D., Shiroda, M. & James, C. A. DrugGuru: a computer software program for drug design using medicinal chemistry rules. *Bioorg. Med. Chem.* **14**, 7011–7022 (2006).
- Kryssanov, V. V., Tamaki, H. & Kitamura, S. Understanding design fundamentals: how synthesis and analysis drive creativity, resulting in emergence. *Artif. Intell. Eng.* **15**, 329–342 (2001).
- Deb, K., Sundar, J., Udaya Bhaskara Rao, N. & Chaudhuri, S. Reference point based multi-objective optimization using evolutionary algorithms. *Int. J. Comp. Intell. Res.* **2**, 273–286 (2006).
- Lipinski, C. A., Lombardo, F., Dominy, B. W. & Feeney, P. J. Experimental and computational approaches to estimate solubility and permeability in drug discovery and development settings. *Adv. Drug Deliv. Rev.* **23**, 3–25 (1997).
- Ertl, P. & Schuffenhauer, A. Estimation of synthetic accessibility score of drug-like molecules based on molecular complexity and fragment contributions. *J. Cheminform.* **10**, 8 (2009).
- Fanelli, F. & De Benedetti, P. G. in *Antitargets: Prediction and Prevention of Drug Side Effects* (eds Vaz, R. J. & Klabunde, T.) Ch. 8, 155–193 (Wiley-VCH, 2008).
- Bemis, G. W. & Murcko, M. A. The properties of known drugs. 1. molecular frameworks. *J. Med. Chem.* **39**, 2887–2893 (1996).
- Ortega, R. *et al.* Synthesis, binding affinity and SAR of new benzolactam derivatives as dopamine D₃ receptor ligands. *Bioorg. Med. Chem. Lett.* **19**, 1773–1778 (2009).
- Löber, S., Hübner, H., Tschammer, N. & Gmeiner, P. Recent advances in the search for D₃ and D₄ selective drugs: probes, models and candidates. *Trends Pharmacol. Sci.* **32**, 148–157 (2011).
- Martin, R. E., Green, L. G., Guba, W., Kratochwil, N. & Christ, A. Discovery of the first nonpeptidic, small-molecule, highly selective somatostatin receptor subtype 5 antagonists: a chemogenomics approach. *J. Med. Chem.* **50**, 6291–6294 (2007).
- Bender, A. *et al.* Chemogenomic data analysis: prediction of small-molecule targets and the advent of biological fingerprint. *Comb. Chem. High Throughput Screen.* **10**, 719–731 (2007).
- Rogers, D., Brown, R. D. & Hahn, M. Using extended-connectivity fingerprints with Laplacian-modified Bayesian analysis in high-throughput screening follow-up. *J. Biomol. Screen.* **10**, 682–686 (2005).
- Huang, X. P., Mangano, T., Hufeisen, S., Setola, V. & Roth, B. L. Identification of human Ether-à-go-go related gene modulators by three screening platforms in an academic drug-discovery setting. *Assay Drug Dev. Technol.* **8**, 727–742 (2010).
- Ruda, G. F. *et al.* Aryl phosphoramidates of 5-phospho erythronohydroxamic acid, a new class of potent trypanocidal agents. *J. Med. Chem.* **53**, 6071–6078 (2010).
- Pogorelov, V. M., Rodriguiz, R. M., Insko, M. L., Caron, M. G. & Wetzel, W. C. Novelty seeking and stereotypic activation of behavior in mice with disruption of the *Dat1* gene. *Neuropsychopharmacology* **30**, 1818–1831 (2005).
- Porton, B. *et al.* Mice lacking synapsin III show abnormalities in explicit memory and conditioned fear. *Genes Brain Behav.* **9**, 257–268 (2010).

Supplementary Information is available in the online version of the paper.

Acknowledgements This work is supported by SULSA (HR07019), the BBSRC Doctoral Training Programme, the BBSRC Pathfinder (BB/F0F/PF/15/09) and the BBSRC Follow On Fund schemes (BB/J010510/1) (A.L.H.), the University of Dundee's Pump Priming Fund for Translational Medical Research (I.H.G. and A.L.H.) and by grants from the National Institutes of Health (NIH) supporting drug discovery receptor pharmacology (B.L.R.) and the NIH grant MH082441 (W.C.W.). The chemical synthesis and informatics benefits from the infrastructure investments from the Wellcome Trust Strategic Award (WT 083481). We thank J. Overington for StARlite and ChEMBL. We wish to thank D. Murugesan for compound purification and C. Means and T. Rhodes for helping with the open field, hole-board and zero-maze tests. We also wish to thank C. Elms and J. Zhou for their support in the husbandry and generation of the mice used for behavioural testing. We also wish to thank F. Y. Li for customizing the software configuration for the hole-board tests. Some of the equipment used in the behavioural testing was purchased with a grant from the North Carolina Biotechnology Center. B.L.R. also received support from the Michael Hooker Chair of Pharmacology.

Author Contributions A.L.H. devised the method, developed the algorithm and designed the study. J.B. coded the algorithm and undertook the calculations. G.R.B. developed the databases. A.L.H. and J.B. with I.H.G., G.F.R. and K.A. selected the compounds for synthesis. I.H.G., G.F.R. and K.A. designed the synthetic routes and G.F.R. and K.A. undertook the chemical synthesis. L.A.W. purified and analysed several of the compounds. B.L.R. and V.S. designed the empirical tests for the synthesized compound predictions, analysed and interpreted the results and performed the experiments. X.-P.H. performed the 5-HT_{2B} functional assays and the hERG assays. M.F.S. conducted the dopamine D2 and D4 functional assays. K.D.R. designed the drug metabolism and pharmacokinetics studies and analysed the results. S.N., L.S. and F.R.C.S. carried out the DMPK experiments. For the behavioural experiments, D.B.C. created the mice in which the *Pcsk7* gene was disrupted. A.P. and N.G.S. verified the *Pcsk7* deletion in many tissues including brain, and then backcrossed the mice onto a C57BL/6 background. W.C.W. designed the studies; R.M.R. and A.I.S. conducted the experiments and analysed the results; W.C.W., R.M.R., A.I.S., D.B.C., A.P. and N.G.S. interpreted the findings; A.L.H. and B.L.R. wrote the manuscript; I.H.G. wrote the synthetic methods with help from G.F.R., K.A. and L.A.W.; W.C.W. and R.M.R. wrote the behavioural section of the manuscript and J.B., V.S., W.C.W. and R.M.R. prepared the figures. All the authors discussed the results and commented on the manuscript.

Author Information Reprints and permissions information is available at www.nature.com/reprints. The authors declare competing financial interests: details are available in the online version of the paper. Readers are welcome to comment on the online version of the paper. Correspondence and requests for materials should be addressed to A.L.H. (a.hopkins@dundee.ac.uk) or B.L.R. (bryan_roth@med.unc.edu).

METHODS

Data sets. All machine learning and data mining of the medicinal chemistry structure–activity data were conducted on the ChEMBL database (release 1) and a pre-release (StarLite version 31)²⁸. The ChEMBL database contains (release 1) more than 440,000 compounds abstracted in *J. Med. Chem.* and *Bioorg. Med. Chem. Lett.* from 1980 to May 2008. The ChEMBL database is available for download from the EBI.

Chemical transformations. A database of chemical transformations was derived from systematically comparing sets of analogue compounds in ChEMBL²⁸. Sets of analogues with defined structure–activity relationships were identified in ChEMBL²⁸ usually from individual journal articles. The transformations database was seeded with a set of common chemical transformations derived from medicinal chemistry knowledge. The transformations database was then expanded by systematically applying all existing transformations to each of the structures associated with each of the journal articles in ChEMBL. The resulting set of transformed compounds was compared to the published analogues. Analogues that were not present in the transformed set highlighted potential transformations that were missing from the transformation database, and were subsequently added to the database. This iterative mining method attempts to regenerate all the reported structures of every medicinal chemistry publication reported in ChEMBL. The chemical transformations were encoded in RXN format. The procedure was implemented in Pipeline Pilot. The current database contains more than 700 unique structural transformations.

Bayesian models. Predictive polypharmacology profiling was undertaken using Bayesian activity models, based on our previously published approach⁹. The Bayesian method for polypharmacology profiling was chosen as it provided both good performance for noisy data sets and a high speed of calculation⁵¹. High confidence models were built using ChEMBL (release 1). Activity data were filtered to keep only activity end-point points that had half-maximum inhibitory concentration (IC₅₀), half-maximum effective concentration (EC₅₀) or K_i values and where the ChEMBL confidence score was at least seven (protein assignment was direct or a homologue). A compound was considered active when the mean activity value was below 10 μM. All inactive compounds were assigned to the target 'none'. Following this procedure, 133,061 compounds remained with 215,967 activity end-points, which were used for model building. Multiple category Laplacian-modified naive Bayesian models were built with ECFP6 representations⁵² for 784 targets. For each model the data were split in two for the validation step: compounds were clustered and assigned a cluster number. Clusters with an odd number were assigned to the test set, and the clusters with an even number were assigned to the training set. Models were built with the training set, and the test set was scored. The training set was scored using its own model as comparison. Finally, a model was built with all data and scored against itself—the training set and whole set should provide similar validation statistics. Statistics on the performance of the models are described in Supplementary Table 12. The results for the model containing all 785 targets were very similar to the models for the receptor subsets. Two analyses were used to assess the performance of the different models. The first analysis provides an overall score and does not need to specify a cut-off for distinguishing active from inactive compounds. The area under the receiver operating characteristic (ROC) curve provides an indication of the ability of the model to prioritize active compounds over inactive compounds. The ROC curve is the plot of the true positive versus the false positive rate. However, it does not provide information on early enrichment, which was important in studies such as the present one in which only the top-ranking compounds were considered. Therefore the Boltzmann-enhanced discrimination of ROC (BEDROC)⁵³ was used, which solves the early enrichment issue by adding a weight to compounds recognized early. BEDROC was derived from the robust initial enhancement, and the sum of log of ranks test⁵⁴, which provided a statistical test to assess which method performs better than random. The percentage of active compound retrieved in the top 5% is also calculated (recall = 5%). The second analysis required a cut-off to make the distinction between active and inactive, as they varied with the rank of the compounds. For each model, the specificity (true negative rate), sensitivity (true positive rate), false positive rate, false negative rate, precision, F-measure and Matthews correlation coefficient (MCC) were calculated at different cut-off values. The cut-off providing the best MCC score was used, as it was shown to provide better performance⁵⁵ (Supplementary Fig. 12). The quality of the models was assessed using an internal leave-one-out validation: one compound was part of the test set and was scored using the remaining data as the training set. Then the area under the ROC curve was calculated (Supplementary Fig. 13). A cut-off score was calculated to minimize the sum of the percentage misclassified for category members and for category non-members and used to classify compounds in the contingency table.

An all data model for dopamine receptors only was built using data from a pre-release of ChEMBL (StarLite version 31), with similar numbers of compounds

and end-points. The model was built without considering the confidence level of target assignment to gather as much data as possible. This model was used for initial calculation on the evolution of the isoindole series and the 2,3-dihydroindol-1-yl series. The quality of the models was assessed using the same procedures as described earlier. The results from the all data models and the high confidence models were very similar (for example, D2 models R² = 0.998, D4 models R² = 0.984).

Profile prediction probabilities. The cut-off for a good prediction came from the validation steps for the model. From the test set, the cut-off value providing the best MCC value was used. For the 5-HT_{1E} receptor, a cut-off of zero was selected. For each ligand–target association, the probability of success was 0.5 (active or inactive where activity was defined as K_i < 10 μM). To test whether the profile predictions were better than random, an exact binomial test was performed using R (version 2.8.1) (<http://www.r-project.org>), and the cumulative binomial probability was calculated.

Adaptive optimization. The adaptive optimization procedure involves defining a parent population of compounds (P_P), of at least one molecule, and a set of *n* ideal achievement objectives {x_O¹, ..., x_Oⁿ}, where *n* is at least 1. The parent population of compounds for each generation (G) is defined as P_{P(G = n)}, in which *n* = 0 for the initial population. All of the members of the parent population (P_P) are subjected to all possible transformations, to maximize the pool of molecules in the transformed population (P_T). Each member of the transformed population is scored using the calculated predictions and molecular properties and ranked relative to the achievement objectives {x_O¹, ..., x_Oⁿ}. Pareto ranking is a common method for prioritizing multiple criteria¹⁷. The Pareto frontier maps a surface in which all solutions are considered equivalent (non-dominant)—where an increase in one objective leads to a decrease in at least one or more other objectives. However, finding a Pareto optimal solution becomes difficult when many objectives are considered⁵⁶, hence a vector scalarization procedure is used³⁷. Multi-objective prioritization is performed using vector scalarization, by describing the calculated parameters for a compound (A) as a multi-dimensional coordinate. The results are ranked by the magnitude of the vector ||a|| between the multi-dimensional coordinates of predicted values of the chemical structure of a compound (A) and the defined ideal achievement objective point, (O), with the shortest vector length closest to the ideal in multi-dimensional space, being ranked the highest:

$$\|a\| = \sqrt{\sum_{p=1}^n (x_O^p - x_A^p)^2}$$

in which the ideal achievement objective point has the coordinates (x_O¹, ..., x_Oⁿ), and calculated values of the compound A form the coordinates (x_A¹, ..., x_Aⁿ).

For subsequent generations, prioritized individuals with calculated properties and parameters that satisfy defined thresholds are assigned to an elite population (P_E), and those that fail are assigned to a non-elite population (P_N), of which *n* random members form a random population (P_R). For all the calculations performed, P_E has a maximum size of 10,000 and P_R a maximum size of 500. The new parent population (P_{P(G = n + 1)}) is created by merging P_E and P_R (that is, P_{P(G = n + 1)} = P_{E(G = n)} + P_{R(G = n)}). This new population is subjected to another transformation process. The new parent population P_P from each generation is also added to a combined pool of all observed parents (P_{Pall}).

The population of transformed compounds from the last iteration and the pooled parent population are combined and all duplicates and compounds failing structure valency rules are removed to produce a merged population (P_M) of unique members (P_M = P_{Pall} + P_T). Properties and parameters (for example, Bayesian activity models values, physicochemical properties and predicted ADME properties) are calculated for each individual in P_M. Each member population P_M is evaluated against the achievement objectives {x_O¹, ..., x_Oⁿ}, as described above. The entire process is repeated until a stop condition is satisfied.

Novelty is assessed by comparing the generated compound with compounds in ChEMBL, either as an exact match or by comparison of the Murcko framework⁴¹, depending on whether the objectives are defined in terms of new compounds or new chemotypes. Novelty is filtered depending on the goals. ADME properties and CNS penetration are calculated using previously published Gaussian process models^{57,58} as implemented in StarDrop (Optibrium). A synthetic accessibility score, representing historical synthetic knowledge, is calculated using a previously published algorithm³⁹. The synthetic accessibility score combines the observation of fragments in ChEMBL and a complexity penalty. A limitation of the ECFP6-Bayesian prediction method is that fingerprints cannot distinguish stereochemistry if the stereochemistry is not encoded in the training data. In the ChEMBL database only 43% of the chiral compounds with chiral centres have their stereochemistry fully defined, thus it is not possible to distinguish between R

and S enantiomers. To reduce the complexity of synthesis, compounds with two or more chiral centres were filtered from the final population.

Receptor profiling. The detailed experimental protocols for the radioligand and functional receptor assays are available on the NIMH PDSP website (<http://pdsf.med.unc.edu/UNC-CH%20Protocol%20Book.pdf>).

hERG assay. Activity of the potassium channel hERG was assayed by the patch clamp method on a PatchXpress platform and by FluxOR Tl⁺ assays. Assays were performed as previously described⁴⁷.

Metabolic stability assay. Metabolic stability was assessed, generating the *in vitro* intrinsic clearance (Cl_i) following incubation of test compound with mouse hepatic microsomes. The assay was performed as previously described⁴⁸.

Brain penetration measurement. Mice were housed under standard conditions: 12 h:12 h light–dark cycle and food and water available *ad libitum* throughout the study. The Drug Discovery Unit at the University of Dundee is dedicated to the humane care, maintenance and use of research animals and maintains compliance with UK Home Office regulations. All experiments were approved by the local ethical review committee. The ratio of test compound between brain and blood was assessed following intravenous administration to the female NMRI mouse.

Behavioural testing. Adult male and female C57BL/6J, D4R-KO mice (Jackson Laboratory), and PC7-KO mice were used. PC7 mice were backcrossed with C57BL/6J mice for more than ten generations. Animals were maintained in a humidity- and temperature-controlled room under a 14 h:10 h light–dark cycle (lights on at 8:00). All studies were conducted during the light cycle, between 10:00 and 16:00 in the following order: zero maze, open field and hole-board. All tests were separated by at least by 7 days. Animals were assigned to vehicle (0.1% DMA with 15% 2-hydroxypropyl-β-cyclodextrin (Sigma-Aldrich)) or compound **13**-treated groups, and were maintained in these groups throughout the experiments. Water and laboratory chow were supplied *ad libitum*. All experiments were conducted with an approved protocol from the Duke University Institutional Animal Care and Use Committee and according to the NIH Guide for the Care and Use of Laboratory Animals. To overcome the high intrinsic clearance in mouse hepatic microsomes of compound **13** (Cl_i = 13.8 ml min^{−1} g^{−1}), mice were

injected intraperitoneally with vehicle, or 0.7 or 1 mg kg^{−1} of compound **13** and placed immediately into the open field for 60 min as described⁴⁹. Activity was monitored as distance travelled and time spent in the centre zone. In the hole-board and zero-maze tests^{49,50} mice were injected intraperitoneally with vehicle or compound **13** and tested 30 min later. Hole-board test responses were video taped for 10 min using high-resolution low-light cameras (Panasonic) and were scored using the TopScan program (Clever Sys) for the rate of head-pokes into the 16 holes. Zero maze behaviours were video taped over 5 min and were scored by trained observers blinded to the genotype, sex and treatment-condition of the animals using the Observer XT10 program (Noldus Information Technology) for the percentage of time in the open areas. All behavioural data presented as mean ± s.e.m. and were analysed by analysis of variance (ANOVA) and repeated measures ANOVA followed by Bonferroni corrected pair-wise comparisons (IBM SPSS 20). *P* < 0.05 was considered significant.

51. Glick, M., Jenkins, J. L., Nettles, J. H., Hitchings, H. & Davies, J. W. Enrichment of high-throughput screening data with increasing levels of noise using support vector machines, recursive partitioning, and laplacian-modified naive bayesian classifiers. *J. Chem. Inf. Model.* **46**, 193–200 (2006).
52. Rogers, D. & Hahn, M. Extended-connectivity fingerprints. *J. Chem. Inf. Model.* **50**, 742–754 (2010).
53. Truchon, J. F. & Bayly, C. I. Evaluating virtual screening methods: good and bad metrics for the “early recognition” problem. *J. Chem. Inf. Model.* **47**, 488–508 (2007).
54. Zhao, W., Hevener, K. E., White, S. W., Lee, R. E. & Boyett, J. M. A statistical framework to evaluate virtual screening. *BMC Bioinformatics* **10**, 225 (2009).
55. Cannon, E. O., Nigsch, F. & Mitchell, J. B. A novel hybrid ultrafast shape descriptor method for use in virtual screening. *Chem. Cent. J.* **2**, 3 (2008).
56. Corne, D. W. & Knowles, J. D. in *Proc. 9th Annual Conf. Genetic Evolutionary Computation* 773–780 (ACM, 2007).
57. Obrezanova, O., Csanyi, G., Gola, J. M. & Segall, M. D. Gaussian processes: a method for automatic QSAR modelling of ADME properties. *J. Chem. Inf. Model.* **47**, 1847–1857 (2007).
58. Obrezanova, O., Gola, J. M. R., Champness, E. J. & Segall, M. D. Automatic QSAR modeling of ADME properties: blood-brain barrier penetration and aqueous solubility. *J. Comput. Aided Mol. Des.* **22**, 431–440 (2008).

Formation of the widest binary stars from dynamical unfolding of triple systems

Bo Reipurth¹ & Seppo Mikkola²

The formation of very wide binary systems^{1–3}, such as the α Centauri system with Proxima (also known as α Centauri C) separated from α Centauri (which itself is a close binary A/B) by 15,000 astronomical units⁴ (1 AU is the distance from Earth to the Sun), challenges current theories of star formation, because their separation can exceed the typical size of a collapsing cloud core. Various hypotheses have been proposed to overcome this problem, including the suggestion that ultrawide binaries result from the dissolution of a star cluster—when a cluster star gravitationally captures another, distant, cluster star^{5–7}. Recent observations have shown that very wide binaries are frequently members of triple systems^{8,9} and that close binaries often have a distant third companion^{10–12}. Here we report *N*-body simulations of the dynamical evolution of newborn triple systems still embedded in their nascent cloud cores that match observations of very wide systems^{13–15}. We find that although the triple systems are born very compact—and therefore initially are more protected against disruption by passing stars^{16,17}—they can develop extreme hierarchical architectures on timescales of millions of years as one component is dynamically scattered into a very distant orbit. The energy of ejection comes from shrinking the orbits of the other two stars, often making them look from a distance like a single star. Such loosely bound triple systems will therefore appear to be very wide binaries.

Evidence is building that stars often, and possibly always, are formed in small multiple systems^{18,19}. Dynamical interactions between members of such systems lead to close triple encounters in which energy and momentum is exchanged, typically causing the disintegration of the triple system, with the escape of a single component (most frequently the lowest-mass member) and the formation of a stable binary^{20–22}. A bound triple with a hierarchical architecture may also result, but only if it forms in the presence of a gravitational potential can such a triple system achieve long-term stability²³. However, this is

frequently fulfilled for newborn triple systems, since break-up typically occurs in the protostellar phase, when the newborn stars are still deeply embedded in their nascent cloud cores²⁴.

We have used an advanced *N*-body code to run 180,218 simulations of a newborn triple system placed in a gravitational potential²³ (for technical details see Supplementary Information). Figure 1a shows results for the 13,727 stable hierarchical systems that are formed in the 180,218 simulations. The blue dots mark the semimajor axes of the inner binaries, and the red dots indicate the semimajor axes of the outer components relative to the centre of mass of the inner binary. The distant components have semimajor axes that span from hundreds to several thousands of astronomical units, with a small but not negligible number of cases reaching several tens of thousands of astronomical units and beyond.

We run the simulations for 100 million years, and classify the outcome at one million years (1 Myr), 10 Myr and 100 Myr into stable triples, unstable triples and disrupted systems. If the outer orbit is hyperbolic, then the system is disrupted. If not, then the system is (at least temporarily) bound, and a stability criterion is applied²⁵. If the system passes this test, it is classified as stable. If not, it is still bound but internally unstable, and will sooner or later disrupt. Figure 1b shows the semimajor axis distribution for 56,957 bound but unstable triple systems.

The number of systems in each category is merely an estimate, because a rigorous theory of stability is not mathematically possible, given that the three-body problem is non-integrable. Hence we see that the number of stable triples at 1 Myr, 10 Myr and 100 Myr is not completely constant, but declines by a few per cent over time. The number of unstable triples, on the other hand, declines dramatically with age, by a factor of three or more from 1 Myr to 100 Myr (Fig. 2a). At 1 Myr, 39% of systems are bound (stable and unstable), at 10 Myr

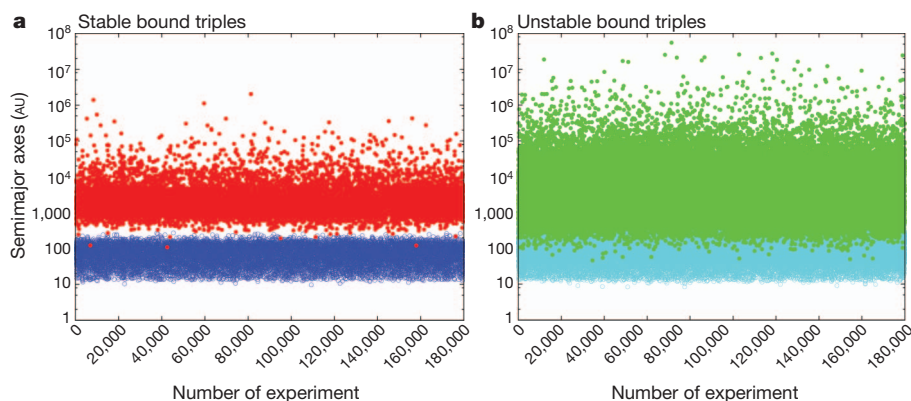


Figure 1 | Semimajor axes of stable and unstable bound triple systems. **a**, The semimajor axes of the outer and inner pairs in stable bound triple systems. Filled blue circles are the inner binaries in stable hierarchical triple systems; filled red circles are the more distant singles in stable hierarchical triple systems. **b**, The semimajor axes of the outer and inner pairs in unstable bound triple systems. Turquoise circles are binaries in unstable bound triple systems;

green circles are singles in unstable bound triple systems. In both panels, the semimajor axes refer to orbital parameters for systems that still remain bound at 1 Myr; at later times many of the unstable systems will have disrupted. For the widest systems, the distant bodies have not yet reached their extreme apastron distances.

¹Institute for Astronomy, University of Hawaii at Manoa, 640 North Aohoku Place, Hawaii 96720, USA. ²Tuorla Observatory, University of Turku, Väisäläntie 20, Piikkiö FI-21500, Finland.

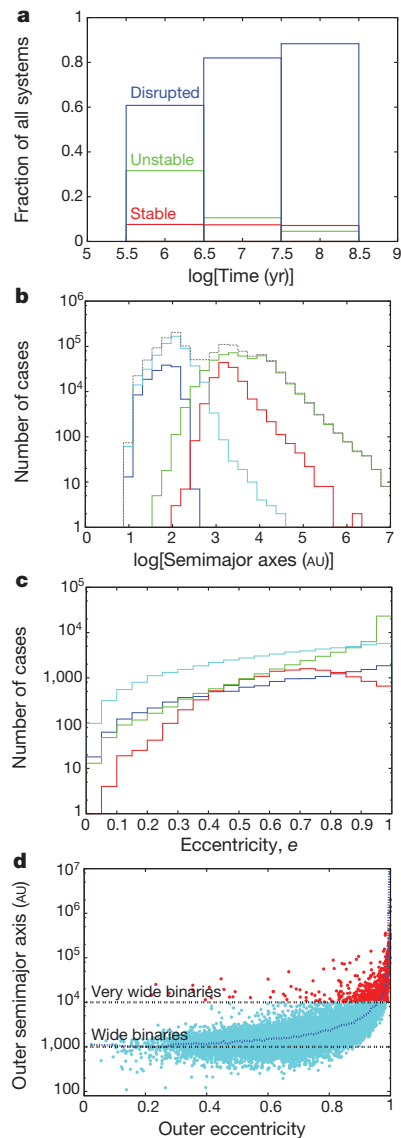


Figure 2 | Statistical properties of stable, unstable, and disrupted triple systems. The colour scheme is the same as in Fig. 1. **a**, Histogram with number of stable hierarchical, unstable hierarchical and disrupted triple systems at 1 Myr, 10 Myr and 100 Myr. The stable systems are essentially constant, whereas many of the unstable systems disrupt. **b**, The distribution of semimajor axes for both inner and outer binaries that are bound at 1 Myr. The grey dashed line shows the sum of all (inner and outer) binaries. **c**, The distribution of eccentricities e for bound inner and outer binaries at 1 Myr. It is evident that highly eccentric systems are common, and the number of triple systems is a growing function of eccentricity for all but the stable outer systems, which peak around $e \approx 0.7$. Systems with very high eccentricity tend to have smaller periastron distances $a(1 - e)$, leading to the possibility of perturbations that, after one or more close periastron passages, eventually lead to break-up. Hence, the decline seen at high eccentricities for bound stable systems (red) is compensated by an increase among the unstable outer systems (green). The eccentricity distribution for the inner binaries will evolve significantly if circumstellar material is still present at birth or owing to Kozai resonance (when the inclination and eccentricity of a perturbed orbit oscillate synchronously). **d**, The distribution of semimajor axes of the outer components in triple systems show a very strong dependence on the eccentricity. On average, wide binaries ($1,000 < a < 10,000$ AU) get increasingly wide as the eccentricity increases. For very wide binaries ($a > 10,000$ AU, marked in red) this correlation becomes even more pronounced. Although very wide binaries can be found with modest eccentricities ($e \approx 0.3$ – 0.4), the majority have eccentricities exceeding 0.9.

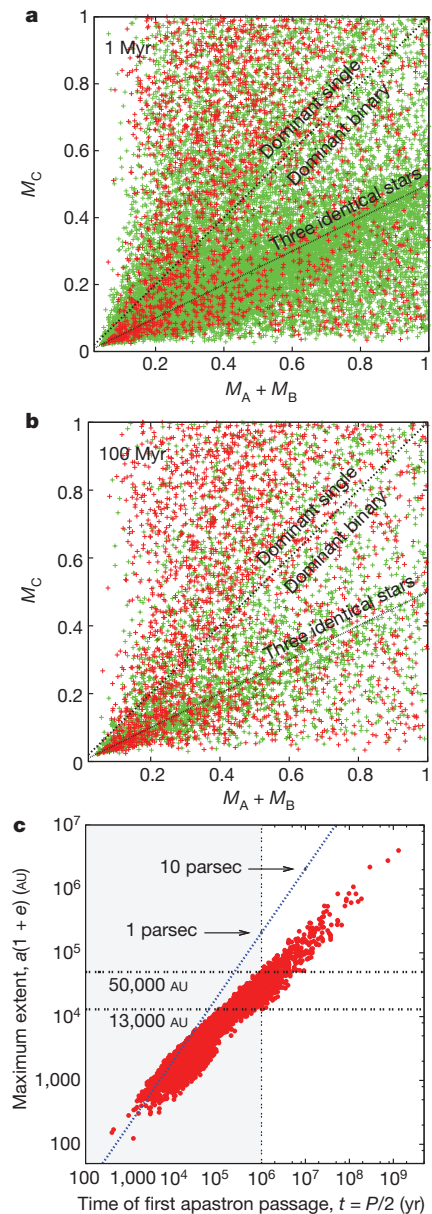


Figure 3 | Stable and unstable hierarchical triple systems at 1 Myr and at 100 Myr, and the maximum extent $a(1 + e)$ of a triple system as a function of time. **a**, The total mass of the close binary ($M_A + M_B$) is plotted against the mass of the distant third body M_C at an age of 1 Myr for all wide systems with outer semimajor axes exceeding 1,000 AU. Systems that are classified as unstable are marked green, and systems that are stable over long timespans are marked red. The figure is divided into two areas, in one half most of the system mass resides in the binary, whereas in the other half the single dominates the system. A line indicates where systems with three identical bodies lie. **b**, As for **a** but for wide systems at an age of 100 Myr. Stable and unstable systems can be found all over the diagram, but with a strong preference for unstable systems to have a dominant binary, while stable unequal systems have a slight preference for a dominant single. At young ages hierarchical triple systems therefore frequently have dominant binaries. **c**, A system with outer period P of 2 Myr will for the first time reach apastron after 1 Myr. All systems in the grey-shaded area have reached apastron at least once within 1 Myr. During that time, no system has reached a separation of more than 50,000 AU. The dotted blue line shows how far the centre of mass of a triple system has moved in a given amount of time assuming a velocity of 1 km s^{-1} . Values are shown for 1 Myr and 10 Myr. The widest systems, which take tens or hundreds of millions of years to unfold, will have moved away from the denser and more perilous environment in which they were born before being fully unfolded.

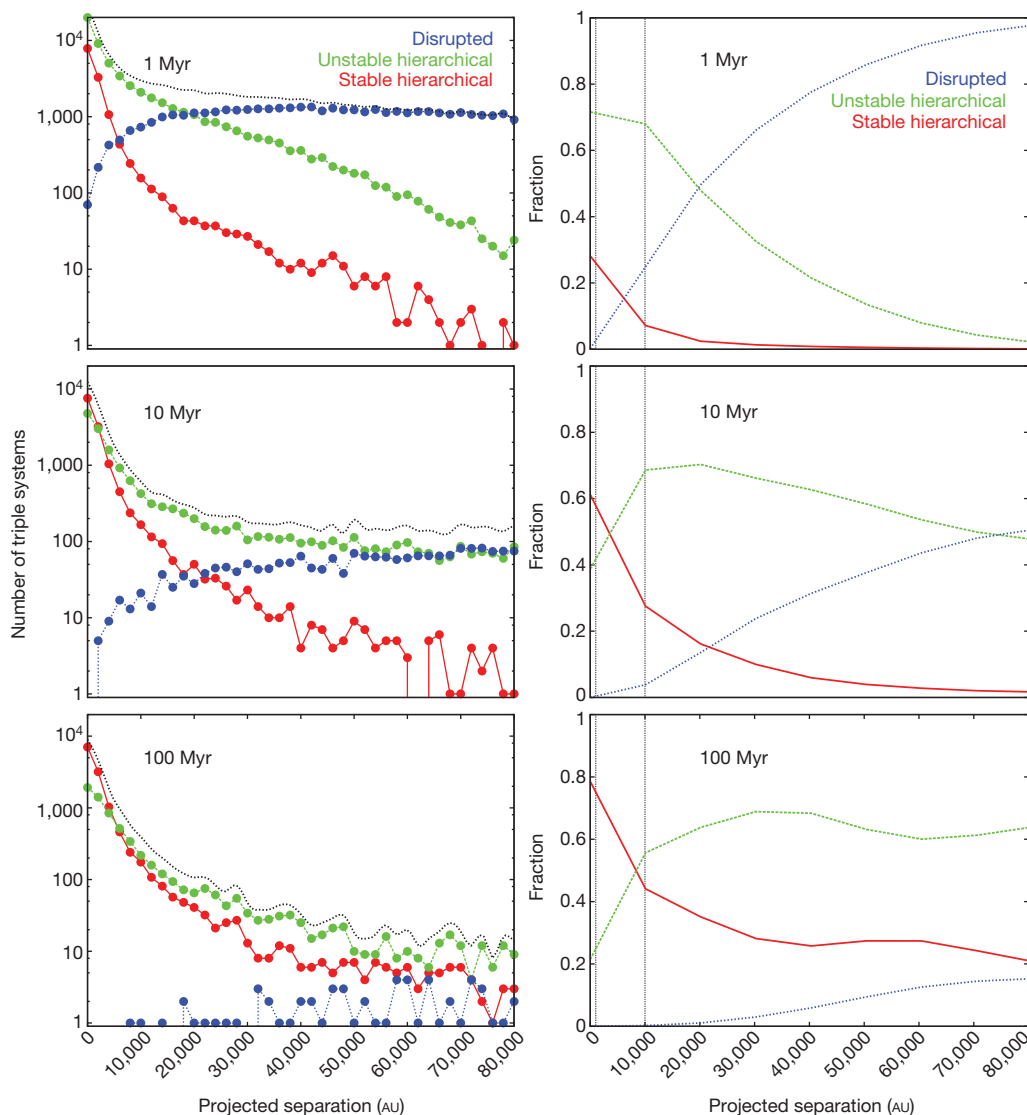


Figure 4 | Frequency of stable, unstable and disrupted triple systems as a function of projected separation. The left panels show the number of bound stable (red), bound unstable (green) and unbound (blue) triple systems as a function of projected separation for three different ages. The black dotted line indicates the sum of all three. This is a snapshot at 1 Myr, 10 Myr and 100 Myr of the random locations in their orbits of the distant third stars relative to the centres of mass of the binaries projected onto the sky for all 180,218 simulations. The right panels show the fraction of bound stable (red), bound unstable (green), and unbound (blue) triple systems relative to the total number of triple systems as a function of projected separation for three different ages. These diagrams allow a statistical determination of the state of an observed triple system. At 1 Myr the bound systems dominate but only out to separations of 0.1 parsec, after which the disrupted pairs strongly dominate. At these early ages, the unstable triples are more common than stable triples by factors of three or more. As time passes, the unstable triples break up and for systems with observed separations of less than 4,000 AU the stable triples slightly outnumber the unstable ones at 10 Myr. At the same time, the disrupted systems (which will appear as common proper motion pairs) are moving apart and become dominant only at separations exceeding 4 parsec. Finally, at 100 Myr, the stable triples dominate out to separations of about 8,000 AU, but for larger separations the very widest binaries are mostly bound but unstable systems, while the disrupted triples play only a minor part at these more advanced ages. The two vertical lines mark separations of 1,000 AU and 10,000 AU.

this number has decreased to 18%, and at 100 Myr it is 12%. This number will continue to decrease until only the stable triple systems remain, which is about 7%. This last number compares well with the 8% of triple systems (the mean of all spectral types) observed in the field²⁶, suggesting that most star-forming events must start as triple systems.

The reason for the difference in distribution of semimajor axes between stable and unstable triple systems (Fig. 1a, b) lies in their orbital parameters. Figure 2b shows the separation distribution function of stable outer (red) and stable inner (blue) and unstable outer (green) and unstable inner (turquoise) systems at an age of 1 Myr. Figure 2c shows the distribution of eccentricities among the bound triple systems. The primary reason that some systems are stable and others unstable is that the stable systems are well separated even at periastron, when the three bodies have their closest approach. In contrast, the unstable systems are much more likely to suffer perturbations at closest approach, ultimately leading to their disruption. This is reflected in the eccentricity of the systems; see Fig. 2 legend for details.

There are three main parameters that control the stability of a triple system: the semimajor axis, the eccentricity e , and the ratio of periastron distance of the outer binary to the apastron distance of the inner binary (periastron and apastron are the points in the orbit when the stars are

closest and most distant, respectively). If the outer periastron distance becomes smaller than roughly 5–10 times the inner apastron distance, then the system will eventually break up. Systems with close inner binaries thus have a larger chance of achieving stability. For the outer binary, the relation between eccentricity and semimajor axis is shown in Fig. 2d. Wide binaries (1,000–10,000 AU) are found with all eccentricities except the very smallest, although there is a clear preference for larger eccentricities. For the very wide binaries ($>10,000$ AU), in contrast, the eccentricities tend to be extreme (red dots in Fig. 2d). The reason they can survive is that their periastron distance $a(1 - e)$ is also large, thanks to their semimajor axes a also being extremely large, although a few are stable even with moderate eccentricity, presumably because they have unusually small inner binaries.

Wide stable and unstable triple systems differ in one important respect. Figure 3a,b shows how total binary mass relates to the mass of the distant third body for systems wider than 1,000 AU at ages of 1 Myr and 100 Myr. A large population exists at 1 Myr with members that are either all three approximately of the same mass, or with the distant third member being of very low mass. This population, however, is largely unstable (green), and so has mostly disappeared after 100 Myr, except for the very low-mass systems. The reason that

systems with a dominant binary and a light single are more unstable than the opposite configuration is probably that massive binaries can more easily alter the orbit of the third body near periastron, eventually leading to disruption. Stable triple systems (red) are much more uniformly distributed across Fig. 3, although with a preference for members of very-low-mass systems to be approximately of the same mass, and a slight preference for systems with dominant singles rather than dominant binaries. Such time-dependent properties of wide triple systems may be a dynamic signature of the triple decay mechanism.

Our simulations do not take into account that there may be further orbital evolution of the inner binary when the decay from the non-hierarchical to the hierarchical configuration occurs during the protostellar phase (as it does for more than 50% of simulations²³). In that case, viscous evolution will cause further in-spiralling of the inner binary, leading to the formation of spectroscopic binaries. Gas-induced orbital decay can ultimately lead to the merger of the binary components in a non-negligible number of cases²⁷. It follows that although wide binaries formed through triple decay initially consist of three stars, during the pre-main sequence phase they may evolve into a true wide binary containing only two stars.

The results presented here refer to the birth population of binaries, at an age of 1 Myr. The orbital parameters of a triple system are established at the moment when a stable hierarchical triple is formed. But since the birth configuration of a triple system is compact, it will take half an orbital period of the outer component before the triple system reaches its first apastron passage and attains its maximum extent $a(1+e)$. We call this the initial unfolding time of the newborn triple system. Many wide systems have not unfolded fully at 1 Myr, and the most extreme wide systems will take tens to hundreds of million years to unfold, and are thus more protected against disruption by passing stars^{16,17} than if triple systems were born with such enormous separations in their crowded natal environments (Fig. 3c). See Supplementary Information for more details.

Non-hierarchical systems that have broken up shortly after birth lead to a close binary and a detached single star that is moving away from the binary. Those with small velocity differences, or with motions mainly along the line of sight, will be observed to linger for a while in the vicinity of each other, mimicking a bound binary. It is of interest to determine what is the fraction of stable bound, unstable bound and unbound triple systems that exist at different projected separations at different ages. Figure 4 shows the number and fraction of systems in each category for 1 Myr, 10 Myr and 100 Myr. As a specific example, the recently discovered very wide ($\sim 12,000$ – $40,000$ AU) triple systems found in 7–10-Myr-old associations^{28,29} have only about a 20% chance of being long-lived systems, a 20% chance of already being disrupted systems, but a 60% chance that they are unstable but still bound systems.

At 100 Myr, 8.5% of the 180,218 simulations have led to bound (stable and unstable) systems with semimajor axes a between 1,000 and 10,000 AU, and 2.1% are bound with $a > 10,000$ AU. That is, more than 10% of the birth population of triple systems end up as wide or very wide, in excellent agreement with observations³⁰. The simulations also broadly reproduce the observed distribution of projected separations^{13–15}; see Supplementary Information for details. The present N -body simulations have thus demonstrated that the widest binaries known can arise naturally as a consequence of three-body dynamics shortly after birth. The subsequent, lengthy unfolding of the widest systems offers increased protection against external disruption by other young stars, and allows such wide systems to be born in both stellar associations as well as the outskirts of dense clusters.

Received 17 June; accepted 5 October 2012.

Published online 5 December 2012.

1. Bahcall, J. N. & Soneira, R. M. The distribution of stars to $V = 16$ th magnitude near the north galactic pole—normalization, clustering properties, and counts in various bands. *Astrophys. J.* **246**, 122–135 (1981).

2. Sesar, B., Ivezić, Z. & Juric, M. Candidate disk wide binaries in the Sloan Digital Sky Survey. *Astrophys. J.* **689**, 1244–1273 (2008).
3. Dhital, S., West, A. A., Stassun, K. G. & Bochanski, J. J. Sloan Low-mass Wide Pairs of Kinematically Equivalent Stars (SLOWPOKES): a catalog of very wide, low-mass pairs. *Astron. J.* **139**, 2566–2586 (2010).
4. Wertheimer, J. G. & Laughlin, G. Are Proxima and α Centauri gravitationally bound? *Astron. J.* **132**, 1995–1997 (2006).
5. Kouwenhoven, M. B. N. *et al.* The formation of very wide binaries during the star cluster dissolution phase. *Mon. Not. R. Astron. Soc.* **404**, 1835–1848 (2010).
6. Moeckel, N. & Clarke, C. J. The formation of permanent soft binaries in dispersing clusters. *Mon. Not. R. Astron. Soc.* **415**, 1179–1187 (2011).
7. Moeckel, N. & Bate, M. R. On the evolution of a star cluster and its multiple stellar systems following gas dispersal. *Mon. Not. R. Astron. Soc.* **404**, 721–737 (2010).
8. Law, N. M., Dhital, S., Kraus, A., Stassun, K. G. & West, A. A. The high-order multiplicity of unusually wide M dwarf binaries: eleven new triple and quadruple systems. *Astrophys. J.* **720**, 1727–1737 (2010).
9. Faherty, J. M. *et al.* The brown dwarf kinematics project. II. Details on nine wide common proper motion very low mass companions to nearby stars. *Astron. J.* **139**, 176–194 (2010).
10. Tokovinin, A., Thomas, S., Sterzik, M. & Udry, S. Tertiary companions to close spectroscopic binaries. *Astron. Astrophys.* **450**, 681–693 (2006).
11. Tokovinin, A. & Smekhov, M. G. Statistics of spectroscopic sub-systems in visual multiple stars. *Astron. Astrophys.* **382**, 118–123 (2002).
12. Allen, P. R., Burgasser, A. J., Faherty, J. K. & Kirkpatrick, J. D. Low-mass tertiary companions to spectroscopic binaries. I. Common proper motion survey for wide companions using 2MASS. *Astron. J.* **144**, 62 (2012).
13. Chanamé, J. & Gould, A. Disk and halo wide binaries from the revised Luyten Catalog: probes of star formation and MACHO dark matter. *Astrophys. J.* **601**, 289–310 (2004).
14. Lépine, S. & Bongiorno, B. New distant companions to known nearby stars. II. Faint companions of Hipparcos stars and the frequency of wide binary systems. *Astron. J.* **133**, 889–905 (2007).
15. Tokovinin, A. & Lépine, S. Wide companions to HIPPARCOS stars within 67 pc of the Sun. *Astron. J.* **144**, 102 (2012).
16. Retterer, J. M. & King, I. R. Wide binaries in the solar neighborhood. *Astrophys. J.* **254**, 214–220 (1982).
17. Weinberg, M. D., Shapiro, S. L. & Wasserman, I. The dynamical fate of wide binaries in the solar neighborhood. *Astrophys. J.* **312**, 367–389 (1987).
18. Goodwin, S. P., Kroupa, P., Goodman, A. & Burkert, A. in *Protostars and Planets V* (eds Reipurth, B., Jewitt, D. & Keil, K.) 133–147 (Univ. of Arizona Press, 2007).
19. D'uchêne, G., Delgado-Donat, E., Haisch, K. E., Loinard, L. & Rodríguez, L. F. in *Protostars and Planets V* (eds Reipurth, B., Jewitt, D. & Keil, K.) 379–394 (Univ. of Arizona Press, 2007).
20. Anosova, J. P. Dynamical evolution of triple systems. *Astrophys. Space Sci.* **124**, 217–241 (1986).
21. Delgado-Donat, E. J., Clarke, C. J., Bate, M. R. & Hodgkin, S. T. On the properties of young multiple stars. *Mon. Not. R. Astron. Soc.* **351**, 617–629 (2004).
22. Valtonen, M. & Mikkola, S. The few-body problem in astrophysics. *Ann. Rev. Astron. Astrophys.* **29**, 9–29 (1991).
23. Reipurth, B., Mikkola, S., Connelley, M. & Valtonen, M. Orphaned protostars. *Astrophys. J.* **725**, L56–L61 (2010).
24. Reipurth, B. Disintegrating multiple systems in early stellar evolution. *Astron. J.* **120**, 3177–3191 (2000).
25. Mardling, R. A. *The Cambridge N-body Lectures* (eds Aarseth, S. J., Tout, C. A. & Mardling, R. A.) 59–96 (Springer, 2008).
26. Tokovinin, A. in *Multiple Stars Across the H-R Diagram* (eds Hubrig, S., Petr-Gotzens, M. & Tokovinin, A.) 38–42 (Springer, 2008).
27. Korntreff, C., Kaczmarek, T. & Pfalzner, S. Towards the field binary population: influence of orbital decay on close binaries. *Astron. Astrophys.* **543**, A126 (2012).
28. Teixeira, R. *et al.* SSSPM J1102–3431 brown dwarf characterization from accurate proper motion and trigonometric parallax. *Astron. Astrophys.* **489**, 825–827 (2008).
29. Kastner, J. H. *et al.* 2M1155–79 (= T Chamaeleontis B): A low-mass, wide-separation companion to the nearby “old” T Tauri Star T Chamaeleontis. *Astrophys. J.* **747**, L23 (2012).
30. Longhitano, M. & Binggeli, B. The stellar correlation function from SDSS. A statistical search for wide binary stars. *Astron. Astrophys.* **509**, A46 (2010).

Supplementary Information is available in the online version of the paper.

Acknowledgements We thank C. J. Clarke, M. B. N. Kouwenhoven and A. Tokovinin for comments. B.R. thanks the European Southern Observatory and Tuorla Observatory for hospitality during the period when this paper was written, and H.-F. Chiang and C. Aspin for providing additional computer facilities. This work was supported by the National Aeronautics and Space Administration through the NASA Astrobiology Institute under Cooperative Agreement number NNA09DA77A issued through the Office of Space Science. This research has made use of the SIMBAD database, operated at Centre de Données astronomiques de Strasbourg, Strasbourg, France, and of NASA's Astrophysics Data System Bibliographic Services.

Author Contributions B.R. conceived the idea, carried out the simulations and data analysis, and wrote the paper. S.M. developed the code and wrote the software tools for analysis.

Author Information Reprints and permissions information is available at www.nature.com/reprints. The authors declare no competing financial interests. Readers are welcome to comment on the online version of the paper. Correspondence and requests for materials should be addressed to B.R. (reipurth@ifa.hawaii.edu).

An unexpectedly low oscillator strength as the origin of the Fe XVII emission problem

S. Bernitt¹, G. V. Brown², J. K. Rudolph^{1,3}, R. Steinbrügge¹, A. Graf², M. Leutenegger^{4,5}, S. W. Epp^{1,6}, S. Eberle¹, K. Kubiček^{1†}, V. Mäkel^{1†}, M. C. Simon⁷, E. Träbert², E. W. Magee², C. Beilmann¹, N. Hell^{2,8}, S. Schippers³, A. Müller³, S. M. Kahn⁹, A. Surzhykov^{10,11}, Z. Harman^{1,12}, C. H. Keitel¹, J. Clementson², F. S. Porter⁴, W. Schlott¹³, J. J. Turner¹³, J. Ullrich^{1†}, P. Beiersdorfer² & J. R. Crespo López-Urrutia¹

Highly charged iron (Fe¹⁶⁺, here referred to as Fe XVII) produces some of the brightest X-ray emission lines from hot astrophysical objects¹, including galaxy clusters and stellar coronae, and it dominates the emission of the Sun at wavelengths near 15 ångströms. The Fe XVII spectrum is, however, poorly fitted by even the best astrophysical models. A particular problem has been that the intensity of the strongest Fe XVII line is generally weaker than predicted^{2,3}. This has affected the interpretation of observations by the Chandra and XMM-Newton orbiting X-ray missions¹, fuelling a continuing controversy over whether this discrepancy is caused by incomplete modelling of the plasma environment in these objects or by shortcomings in the treatment of the underlying atomic physics. Here we report the results of an experiment in which a

target of iron ions was induced to fluoresce by subjecting it to femtosecond X-ray pulses from a free-electron laser⁴; our aim was to isolate a key aspect of the quantum mechanical description of the line emission. Surprisingly, we find a relative oscillator strength that is unexpectedly low, differing by 3.6 σ from the best quantum mechanical calculations. Our measurements suggest that the poor agreement is rooted in the quality of the underlying atomic wavefunctions rather than in insufficient modelling of collisional processes.

Past laboratory measurements using magnetic fusion devices^{5,6} have ruled out some of the astrophysical explanations for the weakness of the strongest Fe XVII line (labelled 3C when first observed in the Sun 40 yr ago⁷; see Fig. 1), including absorption and scattering by a large

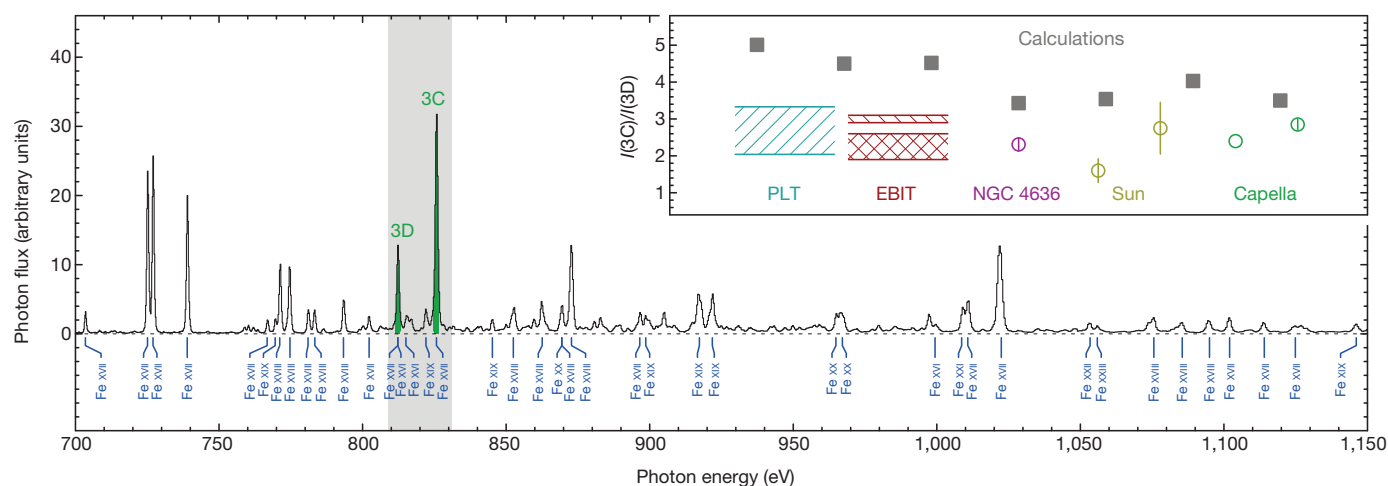


Figure 1 | X-ray spectrum of Capella, and measured as well as calculated values of the 3C/3D intensity ratio. Main panel, the spectrum of Capella (α Aurigae) observed by the Chandra X-ray Observatory²⁵ is dominated by lines from iron ions of different charge, as indicated by the blue labels. Here, the detected photon flux in arbitrary units is plotted versus the photon energy. Fe XVII indicates emission from Fe¹⁶⁺ (that is, iron from which 16 electrons were removed), Fe XVIII refers to emission from Fe¹⁷⁺, and so on. The energy range covered by the present measurement is shaded in grey, corresponding to wavelengths near 15 Å. The Fe XVII lines 3C and 3D are highlighted in green and refer to the $(2p^3)_{1/2}(3d)_{3/2} (J=1) \rightarrow 2p^6 (J=0)$ and $(2p^3)_{3/2}(3d)_{5/2} (J=1) \rightarrow 2p^6 (J=0)$ transitions at 826 eV and 812 eV, respectively. The Fe XVII emission

dominates astrophysical spectra for temperatures between about 2 MK and 8 MK (ref. 1). Inset, illustration of some of the available calculated values^{12,16,21–24} and various astrophysical and laboratory observations. Ranges of measured values from the Princeton Large Torus (PLT) tokamak^{5,6} and from the Livermore electron beam ion trap (EBIT)^{10,26} are shown together with astrophysical values from NGC 4635³, the Sun^{27,28} and Capella^{2,29}. Where available, 1 σ error bars are shown for the astrophysical values. The EBIT range splits into two parts: the upper range (singly hatched) is for measurements where only Fe XVII ions were considered; the lower range (cross hatched) was measured when various amounts of Fe XVI ions were co-mixed with Fe XVII ions. In the latter case, Fe XVI lines blend with line 3D, increasing its apparent line strength.

¹Max-Planck-Institut für Kernphysik, 69117 Heidelberg, Germany. ²Lawrence Livermore National Laboratory, Livermore, California 94550, USA. ³Institut für Atom- und Molekülphysik, Justus-Liebig-Universität Gießen, 35392 Gießen, Germany. ⁴NASA/Goddard Space Flight Center, Greenbelt, Maryland 20771, USA. ⁵Department of Physics, University of Maryland, Baltimore, Maryland 21250, USA. ⁶Max Planck Advanced Study Group, Center for Free Electron Laser Science, 22607 Hamburg, Germany. ⁷TRIUMF, Vancouver, British Columbia V6T 2A3, Canada. ⁸Dr.-Karl-Reimis-Sternwarte Bamberg and Erlangen Centre for Astroparticle Physics, Universität Erlangen-Nürnberg, 96049 Bamberg, Germany. ⁹Kavli Institute for Particle Astrophysics and Cosmology, SLAC National Accelerator Laboratory, Menlo Park, California 94025, USA. ¹⁰Physikalisches Institut, Ruprecht-Karls-Universität Heidelberg, 69120 Heidelberg, Germany. ¹¹GSI Helmholtzzentrum für Schwerionenforschung GmbH, 64291 Darmstadt, Germany. ¹²ExtreMe Matter Institute (EMMI), 64291 Darmstadt, Germany. ¹³Linac Coherent Light Source, SLAC National Accelerator Laboratory, Menlo Park, California 94025, USA. [†]Present addresses: Max-Planck-Institut für biophysikalische Chemie, 37077 Göttingen, Germany (K.K.); RIKEN, Wako, Saitama 351-0198, Japan (V.M.); Physikalisches Institut, 38116 Braunschweig, Germany (J.U.).

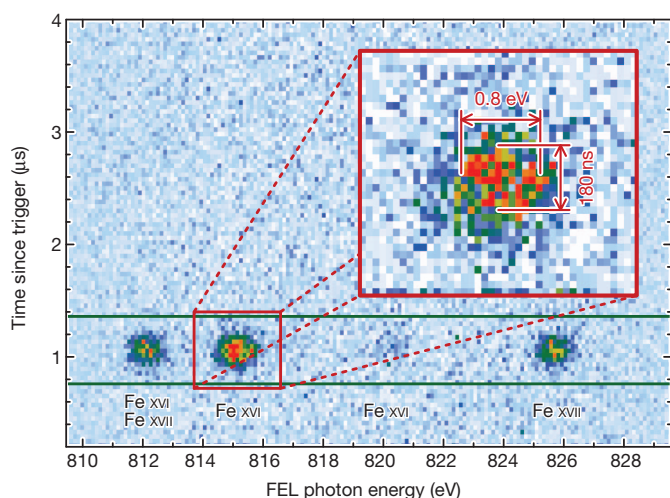


Figure 2 | Time coincidence between the free-electron laser (FEL) pulse and detected X-ray fluorescence. The horizontal axis shows the FEL photon energy, the vertical axis shows the time after a trigger signal, which is provided approximately $1\ \mu\text{s}$ before the FEL fires. The colour code indicates the photon count rate per time and energy, from 0 (white) to 15 (red) in $\text{Hz}\ \mu\text{s}^{-1}\ \text{eV}^{-1}$. The FEL energy was continuously scanned (200 minutes) from approximately 809 eV to 829 eV. Fluorescence is seen from both Fe xvi and Fe xvii, but it is observed only in a small time window following the FEL pulses. The red box (magnified in the inset) shows one of the resonances with the corresponding resolutions in time (180 ns) and photon energy (0.8 eV). The photon energy resolution is determined by the intrinsic energy resolution of the FEL. Because the radiative decay times of the transitions of interest are below a picosecond, all fluorescence photons resulting from a single, femtosecond LCLS pulse are registered as simultaneous by the high-purity Ge detector used to detect the fluorescence X-rays, and the time window is solely determined by the time resolution (180 ns) of the detector. By gating over a 600-ns-wide time region (indicated by the green lines), we included essentially all fluorescence photons, while suppressing the background (produced by the interaction of the target ions with the electron beam from FLASH-EBIT) by a factor of 14,000. The much larger number of photons detected outside this time window was used for background determination with very high statistical significance. The background corrected spectra produced following these procedures are shown in Fig. 3.

column of intervening media^{8,9}. Targeted measurements, which used an electron beam to produce and probe the ions, have furthermore found line blends that can increase the apparent intensity of some of the Fe xvii lines¹⁰. Very importantly, such measurements have produced absolute collisional excitation cross-sections¹¹, which, like the line intensities, have not been reproduced by atomic calculations at the level needed to model astrophysical spectra. Although such laboratory measurements have produced spectra that agree very well with those observed from celestial sources (see Fig. 1 inset), they have not yet pinpointed the fundamental reason why spectral models do not provide the desired agreement with observations.

The consensus among most atomic theorists has been that the remaining problem lies with the calculation of collisional effects, that is, with deficiencies in atomic scattering calculations of the electron-impact excitation cross-section, and special emphasis was therefore placed on correctly including resonances with the help of sophisticated R-matrix methods¹². Numerous resolutions of the problem have been proposed^{13,14}, including the suggestion that kinetic contributions from other levels, which include radiative cascades, collisional depopulation and photon scattering, might need revision depending on the particular plasma conditions¹⁵. Another possibility¹⁶ is that the problem may lie in the incorrect or incomplete description of the mixing between wavefunctions of the same parity and total angular momentum (this mixing can also be viewed as an electron–electron correlation issue). The intensity ratio of the Fe xvii lines 3C and 3D (see Fig. 1) is the key to

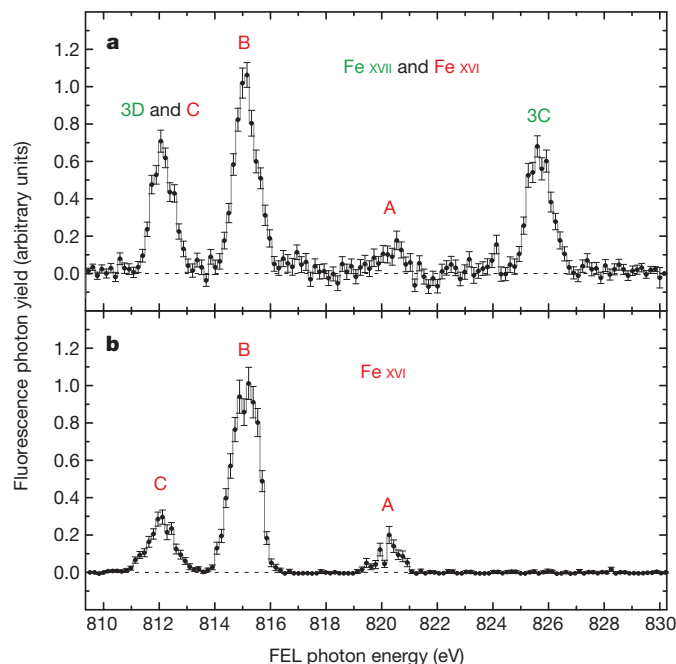


Figure 3 | Measured X-ray fluorescence spectra. **a**, A typical fluorescence spectrum of Fe xvi and Fe xvii when both ion species are among the target ions; **b**, a typical fluorescence spectrum of Fe xvi alone, which is produced in the absence of Fe¹⁶⁺ target ions. Error bars, 1σ uncertainties. Fe xvi lines are labelled A, B and C in red; the Fe xvii lines are labelled in green. Both spectra are normalized to the highest peak (line B). The blend of line 3D from Fe xvii and line C from Fe xvi has to be taken into account when comparing the intensities of 3C and 3D. The plotted fluorescent photon yield has been adjusted for independently monitored variations in the FEL X-ray intensity as a function of FEL energy.

resolving this controversy. Line 3D is forbidden in the Russell–Saunders or LS-coupling approach to constructing wavefunctions. It only exists because of mixing with 3C: the more their upper levels mix, the larger the radiative decay rate and thus the larger the oscillator strength of 3D at the expense of 3C. Because excitation cross-sections vary monotonically with the oscillator strength, as illustrated in Supplementary Information, the increased mixing results in a higher intensity of 3D relative to that of 3C. Mixing, of course, is not restricted to just these two levels, but occurs among all levels with the same parity and total angular momentum. Because there are an infinite number of atomic levels, theory must introduce approximations to this correlation issue when constructing a particular wavefunction.

In a typical plasma, the intensity ratio of lines 3C and 3D not only reflects the mixing among the electronic levels but also depends on the above-mentioned kinetic contributions and on collisional effects, such as electron-impact excitation, resonance excitation, inner-shell ionization and dielectronic recombination, which need to be integrated over the plasma electron distribution function. Hence, the effect of quantum mechanical mixing cannot be cleanly isolated from the plasma environment, which is described by such quantities as the temperature, density, flows, opacity, spatial gradients and temporal variations, so that the question of why the measured ratio does not agree with theory remains obscure and controversial.

X-ray laser spectroscopy¹⁷ provides a new experimental method to resolve this controversy because the excitation and fluorescence of the levels depend only on the atomic wavefunctions and not on electronic collisions. In other words, the intensity of the 3C and 3D lines excited by an X-ray laser is directly proportional to the oscillator strength of each line, providing a direct test of the accuracy of the (mixed) wavefunctions that is totally unaffected by the plasma environment, collisional effects and atomic kinetics. For such a measurement we need a

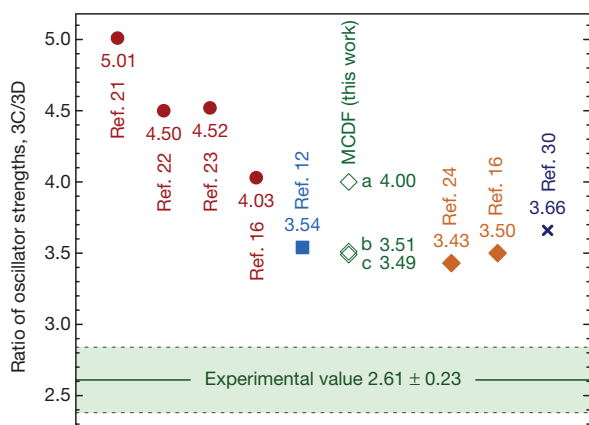


Figure 4 | Predicted and measured intensity ratios of lines 3C and 3D. The experimental value and associated 1σ uncertainty are shown as a green band. The red circles are values produced by wavefunctions used in typical scattering calculations^{16,21–23}. These wavefunctions are not optimized to account for mixing among more than a few electronic levels. The blue square indicates the ratio resulting from wavefunctions employed in a newer scattering calculation that employed more fully converged wavefunctions¹². The green diamonds illustrate the ratios resulting from wavefunctions generated with the MCDF ansatz (see Supplementary Information) at various levels of completeness (that is, convergence) of mixing among the electronic levels: mixing among nearly 800 levels (a); mixing among nearly 90,000 levels (b); and extrapolation to mixing among ‘all’ (infinitely many) levels (c). The filled orange diamonds show the ratios arising from wavefunctions produced in calculations using the MBPT ansatz. This ansatz is designed to optimize the treatment of mixing among electronic levels^{16,24} using perturbative methods. Perturbative calculations were carried out to second order only, but the resulting wavefunctions produce ratios of the oscillator strengths that are already lower than those produced by other methods. Higher-order MBPT calculations do not yet exist. The dark blue cross represents the value listed in National Institute for Standards and Technology (NIST) atomic database³⁰. The assessed uncertainty (rated ‘C+’ (or $\pm 18\%$) and ‘D’ (or $\pm 50\%$) for the relevant Fe XVII lines) associated with the ratio is as large as 50%, which provides overlap with our measurement and enough room for future theoretical improvement using a new quantum mechanical ansatz.

target of Fe¹⁶⁺ and ultrashort, very intense X-ray pulses capable of exciting sufficient numbers of iron ions for detection. The advent of a new kind of ultra-brilliant light source, the free-electron X-ray laser, coupled with a target of trapped, highly charged ions provided by an electron beam ion trap (EBIT)¹⁸, now makes such measurements possible.

The experiment was carried out at the Linac Coherent Light Source (LCLS)⁴ free-electron X-ray laser, where the transportable FLASH-EBIT¹⁹ was installed as an end-station in the Soft X-ray Materials Science (SXR) area²⁰ (see Supplementary Information). Efficient detection of the X-ray-induced fluorescence, which took advantage of the femtosecond time structure of the LCLS photon beam, was the key to a successful measurement (Fig. 2). We performed LCLS photon energy scans at EBIT electron beam energies both above and below the threshold for the production of Fe¹⁶⁺ ions. Using this method, we obtained spectra of Fe XVI and Fe XVII together, as well as Fe XVI alone (Fig. 3), allowing us to take into account blending of Fe XVI and Fe XVII lines.

The linear polarization of the LCLS photon beam causes anisotropic angular emission patterns for the different X-ray transitions. Therefore, the fluorescence detection efficiency is not the same for all the lines but depends on the detection geometry. Fortunately, lines 3C and 3D have identical emission patterns, as discussed in Supplementary Information, precluding a possible source of uncertainty. The photon beam intensity monitor of the SXR beamline did not provide absolute photon fluxes. However, we accurately measured the fluorescence intensity ratio of 3C and 3D as 2.61 ± 0.23 , averaged over two

independent measurement periods (see Supplementary Information and Supplementary Fig. 2), after accounting for the blend of 3D with the Fe XVI line C.

The measured fluorescence ratio can be directly compared to quantum mechanical calculations of the oscillator strengths of lines 3C and 3D, as presented in Fig. 4. Computational limitations typically force scattering calculations to rely on some of the poorest approximations for atomic wavefunctions, in which the mixing of the target wavefunctions may be poorly converged. Indeed, typical scattering calculations^{16,21–23} have been based on wavefunctions that predict ratios of the oscillator strengths between 4.0 and 5.0, as summarized in Fig. 4. Some newer R-matrix scattering calculations¹² have now specifically employed more refined methods to construct wavefunctions, which give a ratio as low as 3.54. Indeed, focused atomic structure calculations designed to produce the best wavefunctions can produce even lower ratios of the oscillator strengths, depending on the quantum mechanical ansatz used. The multiconfiguration Dirac-Fock (MCDF) ansatz (Supplementary Fig. 2) produces a ratio that drops from 4.5, when including mixing among only a reasonable number of wavefunction, to 3.49 when essentially fully converged, that is, when including mixing among a very large number of wavefunctions and thus aiming to approximate the effect of including all levels. The many-body perturbation theory (MBPT) ansatz gives 3.50 or even 3.43 in second order approximation^{16,24} (Fig. 4). The MBPT ansatz might give an even lower ratio, if the calculation were carried out to higher order. However, such a refined MBPT calculation has not yet been done. In other words, our experiment intimates that quantum mechanics has reached a point where the dominant uncertainties lie in the wavefunctions themselves, and a refined MBPT calculation, or yet another different ansatz that includes not only a more complete calculation of correlation effects, but also accounts for quantum electrodynamical terms and the time dependence of atomic dynamics, may be needed to reproduce the experimental value.

Future quantum mechanical calculations may bring the relative oscillator strengths, and thus the ratio of collisional cross-sections associated with them, into closer agreement with our measured value. This would bring the predicted Fe XVII intensity ratios into agreement with those measured in collisional plasmas in the laboratory and observed from X-ray sources in space.

Received 7 May; accepted 27 September 2012.

1. Paerels, F. B. S. & Kahn, S. M. High-resolution X-ray spectroscopy with Chandra and XMM-Newton. *Annu. Rev. Astron. Astrophys.* **41**, 291–342 (2003).
2. Behar, E., Cottam, J. & Kahn, S. M. The Chandra iron-L X-ray line spectrum of Capella. *Astrophys. J.* **548**, 966–975 (2001).
3. Xu, H. *et al.* High-resolution observations of the elliptical galaxy NGC 4636 with the reflection grating spectrometer on board XMM-Newton. *Astrophys. J.* **579**, 600–606 (2002).
4. Emma, P. *et al.* First lasing and operation of an ångström-wavelength free-electron laser. *Nature Photon.* **4**, 641–647 (2010).
5. Beiersdorfer, P. *et al.* Measurement of the 3d→2p resonance to intercombination line-intensity ratio in neonlike Fe XVII, Ge XXIII, and Se XXV. *Phys. Rev. A* **64**, 032705 (2001).
6. Beiersdorfer, P. *et al.* Laboratory measurements of the Fe XVII 2p–3s and 2p–3d transitions and comparison with solar and astrophysical observations. *Astrophys. J.* **610**, 616–623 (2004).
7. Parkinson, J. H. New observations of Fe XVII in the solar X-ray spectrum. *Astron. Astrophys. J.* **557**, L75–L78 (2001).
8. Schmelz, J. T., Saba, J. L. R. & Strong, K. T. Resonance scattering of Fe XVII — a density diagnostic. *Astrophys. J.* **398**, L115–L118 (1992).
9. Waljeski, K. *et al.* The composition of a coronal active region. *Astrophys. J.* **429**, 909–923 (1994).
10. Brown, G. V. *et al.* Diagnostic utility of the relative intensity of 3C to 3D in Fe XVII. *Astrophys. J.* **557**, L75–L78 (2001).
11. Brown, G. V. *et al.* Energy-dependent excitation cross section measurements of the diagnostic lines of Fe XVII. *Phys. Rev. Lett.* **96**, 253201 (2006).
12. Chen, G.-X. Converged Dirac R-matrix calculation of electron impact excitation of Fe XVII. *Phys. Rev. A* **76**, 062708 (2007).
13. Nikulin, V. K. & Trzhaskovskaya, M. B. Comment on “Energy-dependent excitation cross section measurements of the diagnostic lines of Fe XVII”. *Phys. Rev. Lett.* **108**, 139301 (2012).
14. Brown, G. V. & Beiersdorfer, P. Brown and Beiersdorfer reply. *Phys. Rev. Lett.* **108**, 139302 (2012).

15. Fournier, K. B. & Hansen, S. B. Resolution of the long-standing overprediction of the resonance to intercombination line-intensity ratio in mid-Z neonlike ions. *Phys. Rev. A* **71**, 012717 (2005).
16. Gu, M. F. New benchmark of X-ray line emission models of Fe XVII. Preprint at <http://arXiv.org/abs/0905.0519v1> (2009).
17. Epp, S. W. *et al.* Soft X-ray laser spectroscopy on trapped highly charged ions at FLASH. *Phys. Rev. Lett.* **98**, 183001 (2007).
18. Marrs, R. E., Beiersdorfer, P. & Schneider, D. The Electron Beam Ion Trap. *Phys. Today* **47**, 27–34 (1994).
19. Epp, S. W. *et al.* X-ray laser spectroscopy of highly charged ions at FLASH. *J. Phys. At. Mol. Opt. Phys.* **43**, 194008 (2010).
20. Schlotter, W. F. *et al.* The soft X-ray instrument for materials studies at the linac coherent light source X-ray free-electron laser. *Rev. Sci. Instrum.* **83**, 043107 (2012).
21. Bhatia, A. K. Atomic data and spectral line intensities for the neon isoelectronic sequence (Si V through Kr XXVII). *At. Data Nucl. Data Tables* **32**, 435–469 (1985).
22. Bhatia, A. K. & Doschek, G. A. Atomic data and spectral line intensities for Ne-like Fe XVII. *At. Data Nucl. Data Tables* **52**, 1–23 (1992).
23. Cornille, M., Dubau, J. & Jacquemot, S. Radiative and collisional atomic data for neon-like ions. *At. Data Nucl. Data Tables* **58**, 1–66 (1994).
24. Safronova, U. I. *et al.* Electric-dipole, electric-quadrupole, magnetic-dipole, and magnetic-quadrupole transitions in the neon isoelectronic sequence. *Phys. Rev. A* **64**, 012507 (2001).
25. Huenemoerder, D. P. *et al.* TGCat: The Chandra transmission grating data catalog and archive. *Astron. J.* **141**, 129 (2011).
26. Brown, G. V. *et al.* Laboratory measurement and modeling of the Fe XVII X-ray spectrum. *Astrophys. J.* **502**, 1015–1026 (1998).
27. Blake, R. L. *et al.* Spectral and photometric measurements of solar X-ray emission below 60 Å. *Astrophys. J.* **142**, 1–12 (1965).
28. McKenzie, D. L. *et al.* Solar flare X-ray spectra between 7.8 and 23.0 Å. *Astrophys. J.* **241**, 409–416 (1980).
29. Mewe, R. *et al.* CHANDRA-LETGS X-ray observations of Capella. *Astron. Astrophys.* **368**, 888–900 (2001).
30. Ralchenko, Y. *et al.* NIST Atomic Spectra Database (ver. 4.1.0) <http://physics.nist.gov/asd> (National Institute of Standards and Technology; accessed, 27 March 2012).

Supplementary Information is available in the online version of the paper.

Acknowledgements We thank the staff at MPIK, LLNL and SLAC, especially D. Layne (LLNL) who provided technical support. Portions of this research were carried out on the SXR instrument at the LCLS, a division of SLAC National Accelerator Laboratory and an Office of Science user facility operated by Stanford University for the US Department of Energy. The SXR instrument is funded by a consortium whose membership includes the LCLS, Stanford University through the Stanford Institute for Materials Energy Sciences, Lawrence Berkeley National Laboratory, University of Hamburg through the BMBF priority programme, and the Center for Free Electron Laser Science. The present work was performed in part at LLNL under the auspices of the US Department of Energy and supported in part by the Helmholtz Alliance. P.B. performed part of the work reported here while at the Department of Chemistry and the Chemical Physics Program, University of Puerto Rico. A.S. was supported by the Helmholtz association and Z.H. was supported by EMMI. N.H. acknowledges support from BMBF, and E.T., A.M., J.K.R. and S.S. acknowledge support from the Deutsche Forschungsgemeinschaft.

Author Contributions J.R.C.L.-U., P.B. and J.U. conceived the project; G.V.B., A.M. and S.M.K. contributed to the original proposal. S.B., J.K.R., R.S., E.W.M., C.B. and J.R.C.L.-U. prepared the FLASH-EBIT for operation at LCLS. C.B. planned the integration of the FLASH-EBIT at the SXR beamline. S.B., G.V.B., J.K.R., R.S., C.B., A.G., N.H., M.L., S.E., S.W.E., K.K., V.M., M.C.S., S.S., E.T. and J.R.C.L.-U. operated the FLASH-EBIT and detectors. F.S.P. provided technical assistance for the operation of one of the detectors. W.S. and J.J.T. prepared and operated the SXR instruments. A.S., J.C., P.B., Z.H. and C.H.K. performed supporting calculations. R.S. converted raw data for further processing and analysis. S.B. performed the data analysis. S.B., G.V.B., A.G., M.L., S.W.E., S.S., E.T., J.U., P.B. and J.R.C.L.-U. interpreted the results. P.B. wrote the manuscript with input from S.B. and J.R.C.L.-U.; Z.H., C.H.K., S.B., A.S. and P.B. wrote the Supplementary Information. All authors were involved in the discussion of results and commented on the manuscript.

Author Information Reprints and permissions information is available at www.nature.com/reprints. The authors declare no competing financial interests. Readers are welcome to comment on the online version of the paper. Correspondence and requests for materials should be addressed to S.B. (sven.bermitt@mpi-hd.mpg.de).

Mid-infrared frequency comb based on a quantum cascade laser

Andreas Hugi¹, Gustavo Villares¹, Stéphane Blaser², H. C. Liu³ & Jérôme Faist¹

Optical frequency combs¹ act as rulers in the frequency domain and have opened new avenues in many fields such as fundamental time metrology, spectroscopy and frequency synthesis. In particular, spectroscopy by means of optical frequency combs has surpassed the precision and speed of Fourier spectrometers. Such a spectroscopy technique is especially relevant for the mid-infrared range, where the fundamental rotational–vibrational bands of most light molecules are found². Most mid-infrared comb sources are based on down-conversion of near-infrared, mode-locked, ultrafast lasers using nonlinear crystals³. Their use in frequency comb spectroscopy applications has resulted in an unequalled combination of spectral coverage, resolution and sensitivity^{4–7}. Another means of comb generation is pumping an ultrahigh-quality factor microresonator with a continuous-wave laser^{8–10}. However, these combs depend on a chain of optical components, which limits their use. Therefore, to widen the spectroscopic applications of such mid-infrared combs, a more direct and compact generation scheme, using electrical injection, is preferable. Here we present a compact, broadband, semiconductor frequency comb generator that operates in the mid-infrared. We demonstrate that the modes of a continuous-wave, free-running, broadband quantum cascade laser¹¹ are phase-locked. Combining mode proliferation based on four-wave mixing with gain provided by the quantum cascade laser leads to a phase relation similar to that of a frequency-modulated laser. The comb centre carrier wavelength is 7 micrometres. We identify a narrow drive current range with intermode beat linewidths narrower than 10 hertz. We find comb bandwidths of 4.4 per cent with an intermode stability of less than or equal to 200 hertz. The intermode beat can be varied over a frequency range of 65 kilohertz by radio-frequency injection. The large gain bandwidth and independent control over the carrier frequency offset and the mode spacing open the way to broadband, compact, all-solid-state mid-infrared spectrometers.

Unlike the situation in interband semiconductor lasers¹², mode-locked operation of typical high-performance, room-temperature quantum cascade lasers with emission of short single pulses is difficult to achieve because the gain recovery time ($\tau \approx 0.3$ ps) is much shorter than the time required by the pulse to complete one round-trip in the cavity (the round-trip time, $\tau_{rt} = 64$ ps), which defines the mode spacing. Such pulsed operation has so far only been achieved at cryogenic temperatures¹³ over a locking bandwidth of 15 cm^{-1} at 77 K by incorporating an active region that used a diagonal transition with a very long upper-state lifetime¹⁴. Similarly, mode locking of ten modes has also been achieved at cryogenic temperature in terahertz quantum cascade lasers¹⁵. It should be noted, however, that the only requirement for comb operation in spectroscopy applications is the periodicity of the waveform at the round-trip frequency, not the generation of high-intensity pulses. Even though microcavity-based frequency combs have shown ‘true’ comb operation with millihertz stability, their output is sometimes nearly unmodulated in time^{16,17}. In fact, because the intensity of a perfectly frequency-modulated laser is constant, the

power envelope of such a beam would not be perturbed by the fast gain recovery of the quantum cascade laser and the spectrum of such a laser would also be composed of equally spaced and discrete spectral lines. Furthermore, as in radio communication, a frequency-modulated signal may be more robust to noise than an amplitude-modulated signal. In addition, a constant output power can be preferable for linear spectroscopy applications, to avoid additional complexities caused by nonlinear interactions.

Nonlinear effects in quantum cascade lasers, triggering the onset of multimode operation, have been studied in detail¹⁸. As in interband lasers¹⁹, spatial hole burning was found to have a key role in the onset of multimode instabilities. Two counterpropagating waves at frequencies ω_1 and ω_2 create a grating that beats at a frequency $\delta\omega = \omega_1 - \omega_2$, transferring energy between modes separated by that frequency difference. This gain mechanism is phase sensitive. In addition, intersub-band transitions feature strong third-order optical nonlinearities, $\chi^{(3)}$, due to the large optical matrix element between the excited state and the empty lower states^{20–22}, allowing parametric processes due to four-wave mixing. It is important to stress that because these processes are quasi-resonant, the coupling between the modes will occur with a non-trivial phase delay. As shown schematically in Fig. 1a, the result of

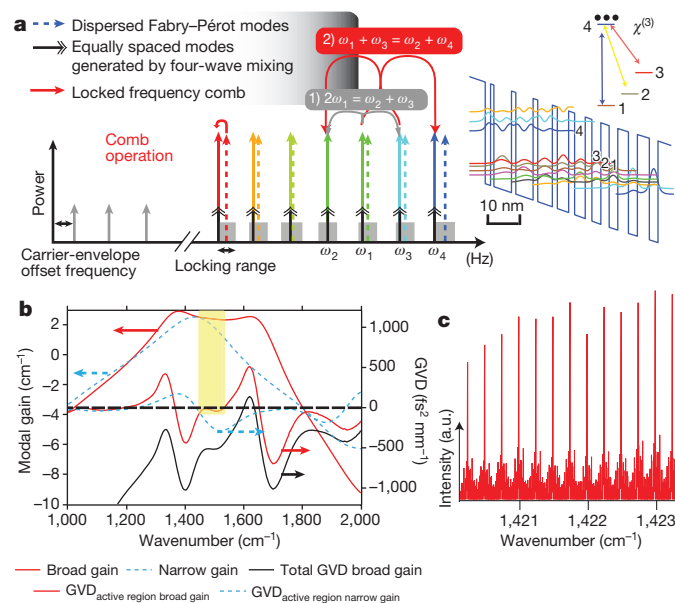


Figure 1 | Optical frequency comb in a quantum cascade laser. **a**, The dispersed Fabry–Pérot resonator modes lock to the equally spaced modes generated by four-wave mixing processes. **b**, Gain and GVD simulations of a narrowband (dotted) and a broadband (solid lines) quantum cascade laser. **c**, Magnified view of the laser spectra at $I = 740$ mA, measured using a high-resolution Fourier transform infrared spectrometer (0.0026 cm^{-1} , 78 MHz). a.u., arbitrary units.

¹Institute for Quantum Electronics, ETH Zurich, 8093 Zurich, Switzerland. ²Alpes Lasers SA, 1–3 Maximilien-de-Meuron, 2001 Neuchâtel, Switzerland. ³Key Laboratory of Artificial Structures and Quantum Control, Department of Physics, Shanghai Jiao Tong University, Shanghai 200240, China.

these nonlinearities will be a proliferation of modes due to degenerate and non-degenerate four-wave mixing processes, in a similar fashion to what occurs in microcavity resonators¹⁰.

The ability to lock longitudinal modes is limited by the material group velocity dispersion (GVD). Our heterogeneous quantum cascade laser is expected to have a much lower GVD in comparison with conventional devices²³. It operates close to the zero-GVD point of our device, a InGaAs/InAlAs heterostructure grown on InP; the low doping of the active region and the waveguide design decrease the contribution from these components. In addition, as shown in Fig. 1b, and in contrast to conventional quantum cascade lasers, the computed GVD has a broad minimum in the centre of the gain curve owing to the 'flat top' shape of the gain curve of the broadband laser.

The broadband quantum cascade laser used in this work was composed of three different substacks and operated at a wavelength of around 7 μm . The laser spectra partly displayed in Fig. 1c were measured using a high-resolution Fourier transform infrared spectrometer and show a single set of longitudinal modes extending over 1.1 μm , with no measurable dispersion within the resolution (0.0026 cm^{-1} , 78 MHz) of the spectrometer over the whole dynamic range (Supplementary Fig. 1). All instabilities related to multiple transverse modes can be completely neglected. A selected set of spectra indicating the power per mode (between 1 μW and 3 mW) is displayed in Supplementary Fig. 2a. The total output power as a function of current at -20°C is shown in Supplementary Fig. 2b. The device switches to multimode operation at $I = 460\text{ mA}$, shortly above threshold ($I_{\text{th}} = 400\text{ mA}$). The spectrum, which is initially spread over $\delta\omega = 40\text{ cm}^{-1}$, broadens progressively to $\delta\omega = 230\text{ cm}^{-1}$ at the maximum current.

To investigate to what extent the modes are coupled, we first measure the intermode beat, that is, the radio-frequency spectrum of the intensity near the round-trip frequency, ν_{rt} , using a fast quantum-well infrared photodetector²⁴. Uncoupled modes (such as those originating from two free-running lasers driven in a similar way to our device) would generate a spectrum with a 5–10-MHz linewidth²⁵. In contrast, as shown in Fig. 2a, such a measurement performed just above the onset of multimode operation shows a linewidth with a full-width at half-maximum of only $\delta\nu = 8.8\text{ Hz}$. For this current, the spectrum is already $\delta\omega = 15\text{ cm}^{-1}$ wide and contains 60 modes. This very narrow intermode beat is observed over the current range $I \approx 460\text{--}480\text{ mA}$. At higher temperatures (13°C), this regime is more dominant and the comb spans up to 60 cm^{-1} (240 modes) with an intermode beat linewidth of $\leq 200\text{ Hz}$. At a current of $\geq 480\text{ mA}$, the intermode beat abruptly becomes wider: $\delta\nu \approx 48\text{ kHz}$. The intensity of the modulation of the laser output is never greater than 2%, indicating a mostly constant amplitude. The abrupt change in intermode beat linewidth is also reflected in the amplitude noise spectra shown in Supplementary Fig. 3. When the current is increased to 500 mA, the spectrum spans $\sim 100\text{ cm}^{-1}$ and the intermode beat widens to $\delta\nu < 250\text{ kHz}$. Above 510 mA, the single narrow intermode beat splits into two distinct broadened peaks spaced by 14 MHz.

The assessment of the coherence properties of a mode-locked laser is usually performed by an autocorrelation measurement on a nonlinear crystal to reveal the time structure of the optical pulse. This technique cannot be used in our case, because we do not expect the respective phases of the longitudinal modes to yield a single optical pulse with high peak intensity, suitable for nonlinear optics. To gain

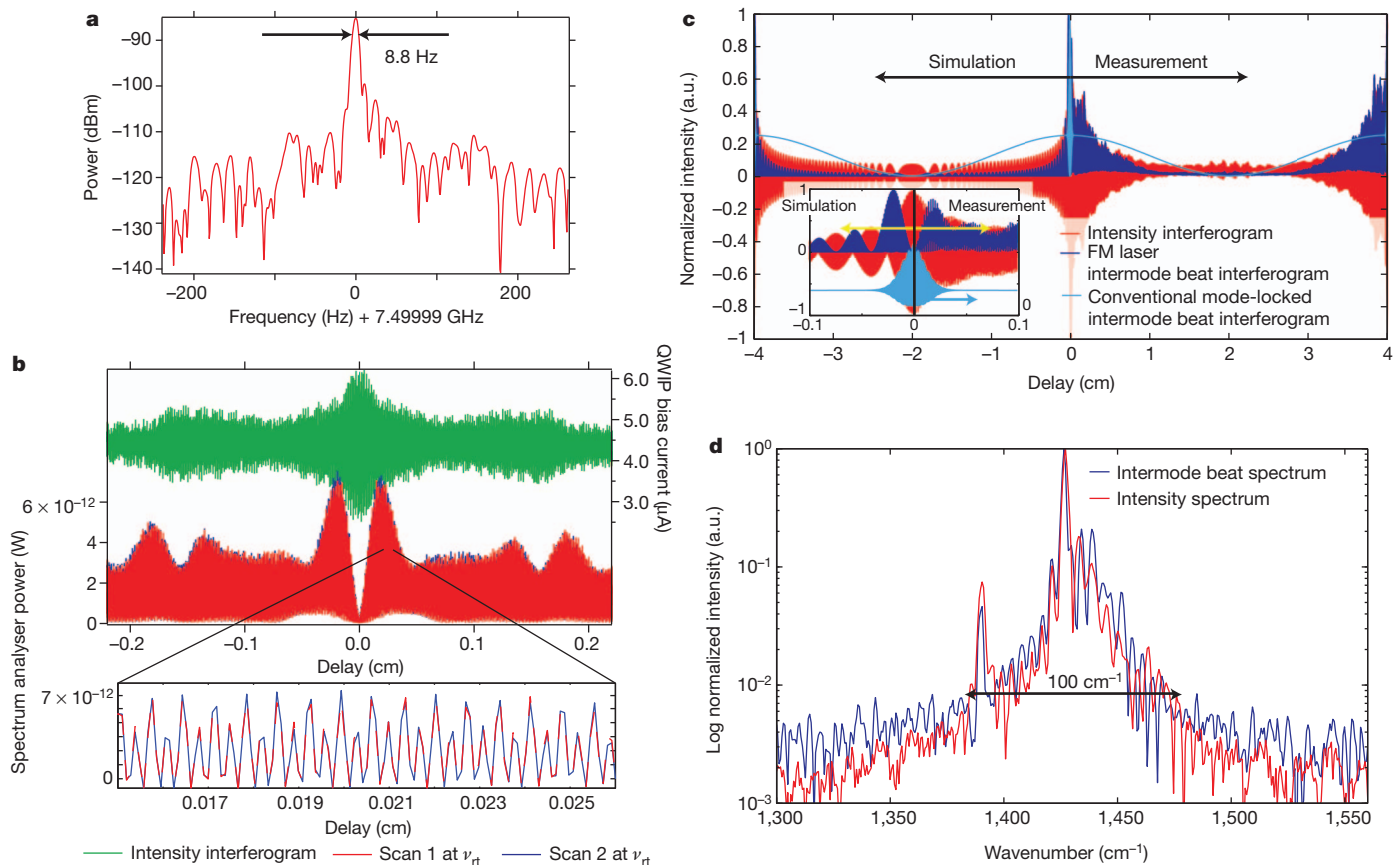


Figure 2 | Intermode beat spectroscopy. **a**, Narrow intermode beat, with a full-width at half-maximum of $<10\text{ Hz}$ at the onset of the multimode emission. The resolution bandwidth of the spectrum analyser is set to 10 Hz. **b**, Intensity interferogram and intermode beat interferograms measured in two successive scans separated by 90 min, at 490 mA. The resolution bandwidth is 100 kHz. QWIP, Quantum-well infrared photodetector. **c**, Comparison of the measured

intermode beat interferogram at 480 mA with two intermode beat interferogram simulations of a perfectly frequency-modulated (FM) signal and a fundamentally mode-locked laser. Inset, magnified view of region at zero delay. **d**, Comparison of the intermode beat spectrum, $\mathcal{J}(\nu_{\text{rt}}, \omega)$, and the intensity spectrum, $\mathcal{J}(0, \omega)$, at an injection current of 500 mA.

insight into the respective phases and coherence properties of the modes, we present here an interferometric technique whereby the autocorrelation of the intermode beat is measured using a Michelson interferometer. The quantity measured is

$$I(\nu, \tau) = |\mathcal{F}(|E(t) + E(t + \tau)|^2)| \quad (1)$$

which is the absolute value of the Fourier component of the intensity at the detector at frequency ν over a chosen resolution bandwidth of the spectrum analyser. Here E denotes the time-dependent amplitude of the electric field and \mathcal{F} stands for the Fourier transform that is applied to the resulting intensity. The normal intensity interferogram measured in a Fourier transform infrared spectrometer is $I(0, \tau)$. In contrast to the intensity interferogram, the intermode beat interferogram, $I(\nu_{\text{rt}}, \tau)$, is a function of both the amplitude and the relative phase of the modes. Furthermore, in analogy with Fourier spectroscopy, the Fourier transform

$$\mathcal{J}(\nu_{\text{rt}}, \omega) = \mathcal{F}(I(\nu_{\text{rt}}, \tau)) \quad (2)$$

will yield the intermode beat spectrum, which roughly indicates the spectral regions contributing to the intermode beat.

Figure 2b shows two successive scans of $I(\nu_{\text{rt}}, \tau)$ acquired with a resolution bandwidth of 100 kHz at the round-trip frequency, measured at 90-min intervals and an injection current of 490 mA. These scans (blue and red) are compared with the zero-frequency component $I(0, \tau)$ (green). Randomly varying phases would generate an intermode beat interferogram roughly proportional to the zero-frequency component around zero time delay (Supplementary Fig. 4). In contrast, the measured $I(\nu_{\text{rt}}, \tau)$ shows long-term stability with a minimum at zero time delay, proving that there is a well-defined phase relation between the modes. The phase relation cannot be easily inferred from the measurement of $I(\nu_{\text{rt}}, \tau)$, however. To help us do so, we compare the measured $I(\nu_{\text{rt}}, \tau)$ to the respective signals predicted for a purely frequency-modulated signal and a conventional mode-locked laser (Fig. 2c; see Supplementary Fig. 5 for a measurement of an intermode beat interferogram of a mode-locked fibre laser). The phases are such that the amplitude modulation of the signal is strongly damped at zero delay ($\tau = 0$), as it would be for a frequency-modulated laser. In general, the comparison emphasizes the frequency modulation characteristics of the output of the laser, as expected from the short lifetime of the excited state. A minimum of the intermode beat is always

observed for $\tau = 0$ over all injected currents, indicating that the device never produces single pulses. To confirm further the frequency-modulated nature of the laser, we put a sheet of polyethylene, which has strong wavelength-dependent absorption, between the laser and the detector. This sheet acts as an optical discriminator that can convert the frequency modulation of the laser output to an amplitude modulation signal. As expected from a frequency-modulated signal, we find that the amplitude of the intermode beat at the detector increases. This amplification factor was measured to be 10–18.

The intermode beat spectrum, $\mathcal{J}(\nu_{\text{rt}}, \omega)$, and the intensity spectrum, $\mathcal{J}(0, \omega)$, are compared in Fig. 2d and show that the entire laser spectrum contributes to the intermode beat. Regardless of the kilohertz intermode beat linewidth, we have a comb-like spectrum because the mode spacing does not fluctuate more than the chosen resolution bandwidth of the spectrum analyser over the whole laser spectrum. The measurement of the whole radio-frequency spectrum around ν_{rt} as a function of τ yields important information about the mechanisms that destabilize the comb. An example of such characteristics is shown in Supplementary Fig. 6a at a high current ($I = 679$ mA) where the intermode beat has two peaks and a wide radio-frequency spectrum. By further increasing the size of the region with low GVD, it should be straightforward to increase the comb bandwidth.

To characterize the comb further, we did a heterodyne beat experiment between a comb line and a single-mode distributed-feedback quantum cascade laser (Supplementary Fig. 7a). The inset of Fig. 3a shows the spectrum of the single-mode quantum cascade laser alongside the comb spectrum that covers 60 cm^{-1} and has an intermode beat linewidth of ≤ 200 Hz. Figure 3a shows the corresponding heterodyne signal. A narrow linewidth of 1.3 MHz is measured, which simply reflects the temperature and current stability of our set-up. The increased phase noise directly translates into a broader linewidth of about 20 MHz in comb-like spectra.

Our measurements show that the low GVD, as well as the existence of nonlinearities, tends to lock the modes together. This locking can also be enhanced through radio-frequency injection. Such injection locking has already been successfully applied to a terahertz quantum cascade laser, enabling the demonstration of pulsed mode-locked operation. In our experiment, a radio-frequency power of 11 dBm is injected close to the round-trip frequency of 7.5 GHz, with an estimated injection loss of -34.5 dB. The direct current is set to 494 mA. While

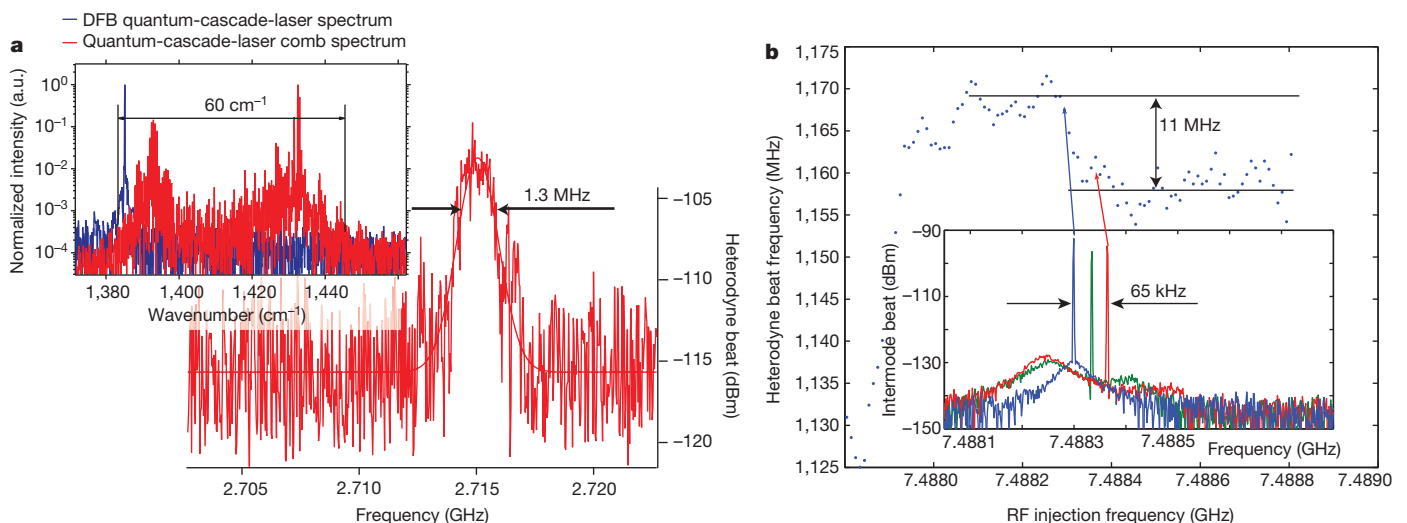


Figure 3 | Linewidth measurement and radio-frequency injection.

a, Heterodyne beat measurement between a single-mode distributed-feedback (DFB) quantum cascade laser and a quantum-cascade-laser comb line. The inset shows the two spectra. The measured heterodyne signal has a linewidth of 1.3 MHz. The resolution bandwidth is 500 kHz and the integration time is 25 ms. **b**, Heterodyne beat measurement of a comb-like line and a stable

single-mode quantum cascade laser while sweeping the radio-frequency (RF) injection frequency around the cavity round-trip frequency. When sweeping across the resonance of the cavity round-trip, the heterodyne signal can be shifted in frequency by 11 MHz. Inset, measured intermode beat at three different characteristic injection frequencies at resonance.

sweeping the radio frequency, we measure the heterodyne beat between one comb-like line and the single-mode quantum cascade laser (Supplementary Fig. 7a). Figure 3b shows the change in the heterodyne beat position and proves that we are able to change the mode spacing actively. The intermode beat with radio-frequency injection around resonance is shown in the inset of Fig. 3b. Unlike previous attempts²⁶, our measurements show the expected collapse of the intermode beat at the round-trip frequency to the resolution of the spectrum analyser. The round-trip frequency can be varied over a range of more than 65 kHz. There are approximately 167 modes between the peak of the laser and the mode that beats with the single-mode quantum cascade laser. Changing the round-trip frequency by 65 kHz should therefore result in a change of $167 \times 65 \text{ kHz} = 10.9 \text{ MHz}$ in the heterodyne beat signal, which agrees with the measured 11 MHz. It should be noted that the carrier frequency offset can be adjusted by the injected direct current (Supplementary Fig. 7b), whereas the mode spacing can be set through the radio-frequency injection. Therefore, it is possible to stabilize quantum-cascade-laser frequency combs fully²⁷. However, as the injected radio-frequency power is increased to 26.6 dBm, the intermode beat interferogram resembles that of a fundamentally mode-locked laser, and, unlike the case for 11 dBm, the intermode beat spectrum shows that only a small fraction (18%) of the modes contribute to the injection-locked intermode beat (Supplementary Fig. 8).

We have presented a mid-infrared quantum-cascade-laser free-running optical frequency comb covering 60 cm^{-1} (308 nm) at a centre wavenumber of $1,430 \text{ cm}^{-1}$ (7 μm). The measured linewidth of the comb lines is $\leq 1.3 \text{ MHz}$ with a narrow intermode beat linewidth of $\leq 200 \text{ Hz}$. At higher currents, we measure comb-like emission spectra that span 100 cm^{-1} and have broader intermode beat linewidths (50–250 kHz). Further measurements using metrological techniques will give deeper insight into this system²⁸. We have shown that the carrier-envelope offset frequency as well as the repetition frequency can be set independently by changing the direct current and through radio-frequency injection. The phase signature of the comb strongly resembles that of a frequency-modulated signal and is stable over time. We identify the locking mechanism responsible for the formation of the frequency comb to be four-wave mixing. Key physical properties of materials used in quantum cascade lasers in frequency combs are therefore strong third-order optical nonlinearities and a low GVD. Further investigation of the GVD and its sign is necessary²⁹. Altogether, this system offers remarkable freedom of design, because it allows control over the electronic transitions, gain flatness, optical nonlinearities and dispersion through band structure engineering. The bandwidth of mid-infrared quantum-cascade-laser frequency combs can be improved through a detailed understanding of the phase-locking mechanism and by appropriately engineering the GVD using waveguide design and facet coatings. The large bandwidth, in combination with independent control over the carrier frequency offset and the mode spacing, opens the way to metrological and sensing applications. Thus, the mid-infrared quantum-cascade-laser frequency comb could become standard technology for broadband, compact, all-solid-state mid-infrared spectrometers.

METHODS SUMMARY

Calculation of the GVD. We include three contributions to the GVD in our calculations. First, the vertical and lateral modal GVDs of the guided mode (GVD_{vert} and GVD_{lat}). GVD_{vert} includes the dispersion of the doped layers due to free-carrier absorption and material dispersion. Second, the GVD due to the gain and loss in the active region. These produce a change in the refractive index, Δn_2 , calculated through Kramers–Kronig relations. The gain is calculated using software based on a density matrix model extended to the whole structure, which also includes second-order gain and loss mechanism between all sub-band pairs³⁰. The total losses are set to 2.5 cm^{-1} . Because the broadband active region is composed of three substacks, each individual stack is simulated again including the loss introduced through cross-absorption. This takes into account the inhomogeneous broadening of these devices. Third, we account for the GVD due to material

dispersion. The total GVD is calculated as a sum of the individual terms weighted by the modal overlap.

Intermode beat spectroscopy set-up. Supplementary Fig. 9 shows the intermode beat spectroscopy set-up. The laser light is collimated through an antireflection-coated ZnSe lens. The light passes through an antireflection-coated quarter-wave plate to reduce the effect of feedback originating from reflections from optical components. The light passes through a Fourier transform infrared spectrometer (Bruker IFS66/S) and is focused through an antireflection-coated ZnSe lens on a $80 \mu\text{m} \times 80 \mu\text{m}$ quantum-well infrared photodetector cooled to the temperature of liquid nitrogen. The Fourier transform infrared spectrometer is run in step-scan mode. At each step, we record the radio-frequency spectrum at the round-trip frequency of the laser. Concurrently, we record the intensity component of the interferogram through the bias current of the photodetector.

Received 25 May; accepted 25 September 2012.

1. Udem, T., Holzwarth, R. & Hänsch, T. W. Optical frequency metrology. *Nature* **416**, 233–237 (2002).
2. Keilmann, F., Gohle, C. & Holzwarth, R. Time-domain mid-infrared frequency-comb spectrometer. *Opt. Lett.* **29**, 1542–1544 (2004).
3. Adler, F. *et al.* Phase-stabilized, 1.5 W frequency comb at 2.8–4.8 μm . *Opt. Lett.* **34**, 1330–1332 (2009).
4. Johnson, T. A. & Diddams, S. A. Mid-infrared upconversion spectroscopy based on a Yb:fiber femtosecond laser. *Appl. Phys. B* **107**, 31–39 (2012).
5. Foltynowicz, A., Ban, T., Maslowski, P., Adler, F. & Ye, J. Quantum-noise-limited optical frequency comb spectroscopy. *Phys. Rev. Lett.* **107**, 233002 (2011).
6. Adler, F., Thorpe, M. J., Cossel, K. C. & Ye, J. Cavity-enhanced direct frequency comb spectroscopy: technology and applications. *Annu. Rev. Anal. Chem.* **3**, 175–205 (2010).
7. Vodopyanov, K. L., Sorokin, E., Sorokina, I. T. & Schunemann, P. G. Mid-IR frequency comb source spanning 4.4–5.4 μm based on subharmonic GaAs optical parametric oscillator. *Opt. Lett.* **36**, 2275–2277 (2011).
8. Del'Haye, P. *et al.* Optical frequency comb generation from a monolithic microresonator. *Nature* **450**, 1214–1217 (2007).
9. Wang, C. Y. *et al.* Mid-infrared optical frequency combs based on crystalline microresonators. Preprint at <http://arxiv.org/abs/1109.2716> (2011).
10. Kippenberg, T. J., Holzwarth, R. & Diddams, S. A. Microresonator-based optical frequency combs. *Science* **332**, 555–559 (2011).
11. Faist, J. *et al.* Quantum cascade laser. *Science* **264**, 553–556 (1994).
12. Derickson, D. J. *et al.* Short pulse generation using multisection mode-locked semiconductor lasers. *IEEE J. Quantum Electron.* **28**, 2186–2202 (1992).
13. Wang, C. Y. *et al.* Mode-locked pulses from mid-infrared quantum cascade lasers. *Opt. Express* **17**, 12929–12943 (2009).
14. Faist, J. *et al.* Laser action by tuning the oscillator strength. *Nature* **387**, 777–782 (1997).
15. Barbieri, S. *et al.* Coherent sampling of active mode-locked terahertz quantum cascade lasers and frequency synthesis. *Nature Photon.* **5**, 306–313 (2011).
16. Del'Haye, P., Arcizet, O., Schliesser, A., Holzwarth, R. & Kippenberg, T. Full stabilization of a microresonator-based optical frequency comb. *Phys. Rev. Lett.* **101**, 053903 (2008).
17. Ferdous, F. *et al.* Spectral line-by-line pulse shaping of on-chip microresonator frequency combs. *Nature Photon.* **5**, 770–776 (2011).
18. Gordon, A. *et al.* Multimode regimes in quantum cascade lasers: from coherent instabilities to spatial hole burning. *Phys. Rev. A* **77**, 053804 (2008).
19. Yamada, M. Theoretical analysis of nonlinear optical phenomena taking into account the beating vibration of the electron density in semiconductor lasers. *J. Appl. Phys.* **66**, 81–89 (1989).
20. Walrod, D., Auyang, S. Y., Wolff, P. A. & Sugimoto, M. Observation of third order optical nonlinearity due to intersubband transitions in AlGaAs/GaAs superlattices. *Appl. Phys. Lett.* **59**, 2932–2934 (1991).
21. Rosencher, E. *et al.* Quantum engineering of optical nonlinearities. *Science* **271**, 168–173 (1996).
22. Banerjee, S. & Shore, K. A. MIR and NIR nonlinear optical processing using intersubband $\chi^{(3)}$ in triple quantum well structures. *Semicond. Sci. Technol.* **18**, 655–660 (2003).
23. Parz, W. *et al.* Intersubband gain-induced dispersion. *Opt. Lett.* **34**, 208–210 (2009).
24. Grant, P. D., Dudek, R., Buchanan, M. & Liu, H. C. Room-temperature heterodyne detection up to 110 GHz with a quantum-well infrared photodetector. *IEEE Photon. Technol. Lett.* **18**, 2218–2220 (2006).
25. Aellen, T. *et al.* Direct measurement of the linewidth enhancement factor by optical heterodyning of an amplitude-modulated quantum cascade laser. *Appl. Phys. Lett.* **89**, 091121 (2006).
26. Soibel, A. *et al.* Active mode locking of broadband quantum cascade lasers. *IEEE J. Quantum Electron.* **40**, 844–851 (2004).
27. Telle, H. *et al.* Carrier-envelope offset phase control: a novel concept for absolute optical frequency measurement and ultrashort pulse generation. *Appl. Phys. B* **69**, 327–332 (1999).
28. Braje, D., Hollberg, L. & Diddams, S. Brillouin-enhanced hyperparametric generation of an optical frequency comb in a monolithic highly nonlinear fiber cavity pumped by a cw laser. *Phys. Rev. Lett.* **102**, 193902 (2009).
29. Herr, T. *et al.* Universal formation dynamics and noise of Kerr-frequency combs in microresonators. *Nature Photon.* **6**, 480–487 (2012).

30. Terazzi, R. & Faist, J. A density matrix model of transport and radiation in quantum cascade lasers. *N. J. Phys.* **12**, 033045 (2010).

Supplementary Information is available in the online version of the paper.

Acknowledgements We thank M. Quack and E. Miloglyadov for their help with the high-resolution Fourier transform infrared spectrometer measurements, U. Keller and V. Wittwer for providing scientific equipment, and J. Khurgin for discussions. This work was financially supported by the Quantum Photonics National Center of Competence in Research of the Swiss National Science Foundation. H.C.L. acknowledges support from the National Major Basic Research Projects (2011CB925603) and the Shanghai Municipal Major Basic Research Project (09DJ1400102).

Author Contributions A.H. carried out the measurements. Simulations and ideas were developed by A.H. and J.F. G.V. contributed to the heterodyne beat measurements as well as the amplitude noise measurements. S.B. provided both quantum cascade lasers. H.C.L. provided the quantum-well infrared photodetector. All the work was done under the supervision of J.F.

Author Information Reprints and permissions information is available at www.nature.com/reprints. The authors declare no competing financial interests. Readers are welcome to comment on the online version of the paper. Correspondence and requests for materials should be addressed to J.F. (jfaist@ethz.ch) or H.C.L. (h.c.liu@sjtu.edu.cn).

Highly efficient organic light-emitting diodes from delayed fluorescence

Hiroki Uoyama¹, Kenichi Goushi^{1,2}, Katsuyuki Shizu¹, Hiroko Nomura¹ & Chihaya Adachi^{1,2}

The inherent flexibility afforded by molecular design has accelerated the development of a wide variety of organic semiconductors over the past two decades. In particular, great advances have been made in the development of materials for organic light-emitting diodes (OLEDs), from early devices based on fluorescent molecules¹ to those using phosphorescent molecules^{2,3}. In OLEDs, electrically injected charge carriers recombine to form singlet and triplet excitons in a 1:3 ratio¹; the use of phosphorescent metal-organic complexes exploits the normally non-radiative triplet excitons and so enhances the overall electroluminescence efficiency^{2,3}. Here we report a class of metal-free organic electroluminescent molecules in which the energy gap between the singlet and triplet excited states is minimized by design⁴, thereby promoting highly efficient spin up-conversion from non-radiative triplet states to radiative singlet states while maintaining high radiative decay rates, of more than 10^6 decays per second. In other words, these molecules harness both singlet and triplet excitons for light emission through fluorescence decay channels, leading to an intrinsic fluorescence efficiency in excess of 90 per cent and a very high external electroluminescence efficiency, of more than 19 per cent, which is comparable to that achieved in high-efficiency phosphorescence-based OLEDs³.

The recombination of holes and electrons can produce light, in a process referred to as electroluminescence. Electroluminescence in organic materials was first discovered in 1953 using a cellulose film doped with acridine orange⁵, and was developed in 1963 using an anthracene single crystal connected to high-field carrier injection electrodes¹. Electrical charge carriers of both polarities were injected into the organic layers, and the subsequent carrier transport and recombination produced blue electroluminescence originating from singlet excitons; that is, fluorescence. According to spin statistics, carrier recombination is expected to produce singlet and triplet excitons in a 1:3 ratio^{6,7}, and this ratio has been examined for many molecular systems^{8–12}. The singlet excitons produced decay rapidly, yielding prompt electroluminescence (fluorescence). Two triplet excitons can combine to form a singlet exciton through triplet–triplet annihilation, which results in delayed electroluminescence (delayed fluorescence). Direct radiative decay of triplet excitons results in phosphorescence, but usually occurs only at very low temperatures in conventional organic aromatic compounds. The first demonstration of phosphorescent electroluminescence using ketocoumarin derivatives in 1990¹³. However, the very faint electroluminescence was observed only at 77 K, and with difficulty, and was assumed to be virtually useless even if included in rare-earth complexes, which should also involve both singlet and triplet excitons in electrical excitation¹⁴. In 1999, efficient electrophosphorescence was first demonstrated using iridium phenylpyridine complexes that achieve an efficient radiative decay rate of $\sim 10^6 \text{ s}^{-1}$ by taking advantage of the strong spin–orbit coupling of iridium². An internal electroluminescence efficiency of almost 100% was achieved³, providing convincing evidence that OLED technology can be useful for display and lighting applications.

In the work reported here, we used a novel pathway to attain the greatest possible electroluminescence efficiency from simple aromatic compounds that exhibit efficient thermally activated delayed fluorescence (TADF) with high photoluminescence efficiency. Figure 1a shows the energy diagram of a conventional organic molecule, depicting singlet (S_1) and triplet (T_1) excited states and a ground state (S_0). It was previously assumed that the S_1 level was considerably higher in energy than the T_1 level, by 0.5–1.0 eV, because of the electron exchange energy between these levels. However, we found that careful design of organic molecules can lead to a small energy gap (ΔE_{ST}) between S_1 and T_1 levels^{4,15}. Correspondingly, a molecule with efficient TADF requires a very small ΔE_{ST} between its S_1 and T_1 excited states, which enhances $T_1 \rightarrow S_1$ reverse intersystem crossing (ISC). Such excited states are attainable by intramolecular charge transfer within systems containing spatially separated donor and acceptor moieties⁴. The critical point of this molecular design is the combination of a small ΔE_{ST} , of $\lesssim 100 \text{ meV}$, with a reasonable radiative decay rate, of $> 10^6 \text{ s}^{-1}$, to overcome competitive non-radiative decay pathways, leading to highly luminescent TADF materials. Because these two properties conflict with each other, the overlap of the highest occupied molecular orbital and the lowest unoccupied molecular orbital needs to be carefully

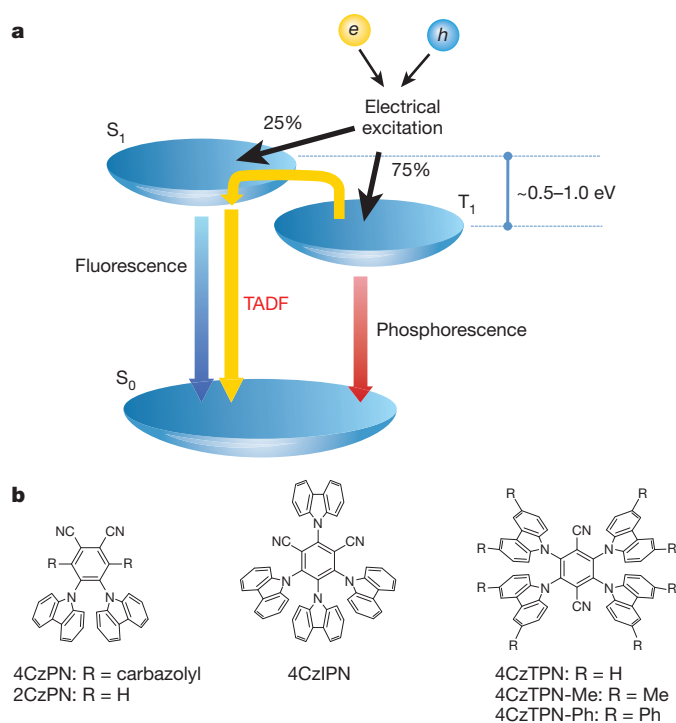


Figure 1 | Energy diagram and molecular structures of CDCBs. **a**, Energy diagram of a conventional organic molecule. **b**, Molecular structures of CDCBs. Me, methyl; Ph, phenyl.

¹Center for Organic Photonics and Electronics Research, Kyushu University, 744 Motooka, Nishi, Fukuoka 819-0395, Japan. ²International Institute for Carbon Neutral Energy Research (WPI-I2CNER), Kyushu University, 744 Motooka, Nishi, Fukuoka 819-0395, Japan.

balanced. Furthermore, to enhance the photoluminescence efficiency of a TADF material, the geometrical change in molecular conformation between its S_0 and S_1 states should be restrained to suppress non-radiative decay. Limited orbital overlap generally results in virtually no emission, as has been shown in benzophenone derivatives. Therefore, it was previously assumed that a high photoluminescence efficiency could never be obtained from molecules with a small ΔE_{ST} . Here we demonstrate that it is possible to realize a high photoluminescence efficiency and a small ΔE_{ST} simultaneously.

We designed a series of highly efficient TADF emitters based on carbazolyl dicyanobenzene (CDCB), with carbazole as a donor and dicyanobenzene as an electron acceptor (Fig. 1b). Because the carbazolyl unit is markedly distorted from the dicyanobenzene plane by steric hindrance, the highest occupied molecular orbital and the lowest unoccupied molecular orbital of these emitters are localized on the donor and acceptor moieties, respectively, leading to a small ΔE_{ST} . Moreover, the dicyanobenzene and carbazolyl groups are important in obtaining a high photoluminescence efficiency and various emission colours, respectively. Dicyanobenzene derivatives are known to alter their chemical bonds in excited states, changing their electronic properties¹⁶. Density functional theory (DFT) calculations predicted that using CDCBs would have the following advantages. The cyano groups suppress both non-radiative deactivation and changes in the geometries of the S_1 and T_1 states of CDCBs, leading to a high quantum efficiency. Conversely, the emission wavelengths of CDCBs should be easy to tune by changing the electron-donating ability of the peripheral groups, which can be altered by changing the number of carbazolyl groups or introduced substituents. Such molecular design should allow us to achieve not only highly efficient TADF but also a wide range of emission colours.

We synthesized CDCBs from commercially available starting materials in a one-step reaction. Palladium or other rare-earth-metal catalysts were not required, making CDCBs cost effective. Nucleophilic aromatic substitution of carbazole anions generated by treatment with NaH and dicyanobenzenes at room temperature (300 K) yielded the CDCBs. All CDCBs were obtained in high yields of >79%, except 4CzPN and 2CzPN, which were obtained in lower yield (38% and 9%, respectively) because of purification problems. CDCBs were fully characterized by NMR and infrared spectroscopy, high-resolution mass spectrometry and elemental analysis (Methods). They had high thermal stability; for example, in thermogravimetric analysis measurements under nitrogen-flow conditions, 4CzIPN began to sublime at around 450 °C before decomposing.

Ultraviolet–visible absorption and photoluminescence spectra of 4CzIPN in toluene are presented in Fig. 2a. 4CzIPN has intense green emission with a maximum at 507 nm and a high photoluminescence quantum yield (Φ) of $94 \pm 2\%$. The Stokes shift of 4CzIPN is very small; generally, the emission produced by intramolecular charge transfer between donor and acceptor units shows a large Stokes shift¹⁷. Under nitrogen-saturated conditions, the delayed component (TADF), which had a lifetime of $\tau \approx 5.1 \pm 0.5 \mu\text{s}$, was more than two orders of magnitude longer than the prompt component, for which $\tau \approx 17.8 \pm 1 \text{ ns}$ (Supplementary Information). To determine whether the T_1 state was involved in luminescence, the transient photoluminescence and photoluminescence quantum yield of 4CzIPN were measured in toluene under an oxygen atmosphere. When oxygen was bubbled through the solution of 4CzIPN in toluene for 10 min, the lifetime of the delayed component became very short ($\tau \approx 91 \pm 3 \text{ ns}$), the prompt component became $\tau \approx 6.9 \pm 0.5 \text{ ns}$ and Φ decreased to 10%. These results suggest that 4CzIPN is a TADF material because the delayed fluorescence was substantially quenched by oxygen⁴.

The geometry of the S_0 state of 4CzIPN in the gas phase was optimized using DFT and the 6-31G(d) basis set¹⁸. Geometry optimizations of the S_1 and T_1 states were carried out using time-dependent DFT. All *ab initio* calculations were performed using Gaussian 09 software¹⁹ without symmetry constraints. For 4CzIPN, generalized

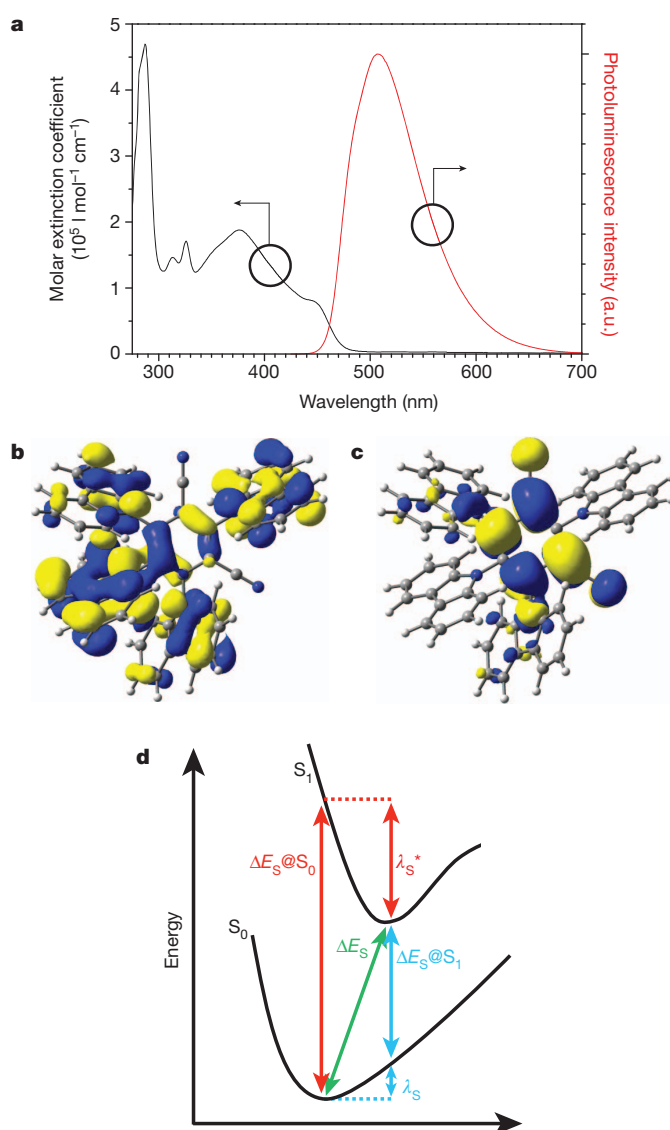


Figure 2 | Photoluminescence characteristics of 4CzIPN. **a**, Ultraviolet–visible absorption and photoluminescence spectra of 4CzIPN in toluene at a concentration of $10^{-5} \text{ mol l}^{-1}$. a.u., arbitrary units. **b**, **c**, Highest occupied NTO (**b**) and lowest unoccupied NTO (**c**) according to the results of time-dependent DFT for the S_1 state of 4CzIPN using the optimized structure of the S_0 state. Colours indicate the different phases of the natural transition orbitals. **d**, Potential energy surfaces, vertical transition energies ($\Delta E_S@S_0$ and $\Delta E_S@S_1$) and relaxation energies (λ_S and λ_S^*) for the S_1 state.

gradient approximation functionals underestimated ΔE_{ST} (the experimental value is 83 meV), whereas long-range corrected functionals overestimated it (Supplementary Information). The M06-2X functional²⁰, a hybrid meta-generalized gradient-approximation functional, yields an intermediate value for ΔE_{ST} and, moreover, by taking into account solvent effects using the polarizable continuum model^{21,22}, predicts an emission wavelength of 460 nm, which is reasonably close to the experimentally obtained photoluminescence peak at 507 nm in toluene solution. In the following discussion, we use the results calculated for M06-2X/6-31G(d). The highest occupied and lowest unoccupied natural transition orbitals²³ (NTOs) based on the results of time-dependent DFT for the S_1 state of 4CzIPN using the optimized structure of the S_0 state are depicted in Fig. 2b and Fig. 2c, respectively. The highest occupied NTO is delocalized over the four carbazolyl moieties, whereas the lowest unoccupied NTO is centred on the dicyanobenzene moiety, suggesting that the S_1 state has charge transfer character; the carbazolyl groups act as electron donors and the

dicyanobenzene group acts as an electron acceptor. Steric hindrance between the carbazolyl and dicyanobenzene moieties causes a large dihedral angle of about 60° between the planes of the carbazolyl and dicyanobenzene groups. Consequently, the highest occupied and lowest unoccupied NTOs are spatially well separated, leading to a small ΔE_{ST} and enhanced $T_1 \rightarrow S_1$ reverse ISC.

As stated above, the Stokes shift of the S_1 state of 4CzIPN is small compared with those for typical charge transfer states, suggesting that the $S_1 \leftarrow S_0$ excitation results in limited relaxation of the molecular geometry. We believe that this small Stokes shift is partly related to the presence of the cyano groups. To investigate the effect of the cyano groups on the geometry relaxation of the S_1 and T_1 states of 4CzIPN, we evaluated vertical transition energies ($\Delta E_{S@S_0}$ and $\Delta E_{S@S_1}$) and relaxation energies (λ_S and λ_S^*) for the S_1 state (Fig. 2d), and compared them with those of the molecule in which the two cyano groups of 4CzIPN are replaced with hydrogen atoms (4CzBz; Supplementary Information). The reorganization energies λ_S for 4CzIPN and 4CzBz were calculated to be 0.27 and 0.83 eV, respectively. This energy is greatly reduced by introducing cyano groups into the electron-accepting unit. Because λ_S represents the degree of geometry relaxation of the S_1 state to the S_0 state, this result suggests that the cyano groups are important in suppressing geometry relaxation in the fluorescent state of 4CzIPN. In addition, λ_S^* is also reduced by the presence of cyano groups. Torsional angles of the carbazolyl groups are calculated to be small in the presence of the cyano groups. This limited torsional flexibility can be a major factor in reducing the non-radiative decay of 4CzIPN. Like that for the S_1 state, the relaxation energy for the T_1 state (λ_T) is markedly reduced by the cyano groups. Thus, it is probable that the cyano groups suppress non-radiative deactivation from the S_1 and T_1 states, leading to the high photoluminescence quantum efficiency of 4CzIPN.

Photoluminescence spectra of the CDCBs in toluene are presented in Fig. 3. The series of CDCBs yielded a wide range of emission colours ranging from sky blue (473 nm) to orange (577 nm). The emission wavelength depends on the electron-donating and -accepting abilities of the peripheral carbazolyl groups and the central dicyanobenzene unit, respectively. Introduction of methyl or phenyl substituents at the 3- and 6- positions of the carbazolyl groups of 4CzTPN induces a shift of the emission maximum to longer wavelengths. Conversely, in the case of 2CzPN, the presence of fewer carbazolyl groups reduces its electron-donating ability and produces a shift of the emission maximum to shorter wavelengths. We measured the photoluminescence quantum yield and transient photoluminescence of CDCBs in toluene under a nitrogen atmosphere, and are summarized in Supplementary Information. For 4CzPN and 4CzTPN Φ is high ($74 \pm 3\%$ and $72 \pm 3\%$, respectively), whereas for 4CzTPN-Me, 4CzTPN-Ph and 2CzPN it is lower ($47 \pm 2\%$, $26 \pm 1\%$ and $47 \pm 2\%$, respectively) because of substituent effects or fewer carbazolyl groups. Because the transient photoluminescence of all CDCBs showed both a nanosecond-scale prompt component and a microsecond-scale delayed component, the CDCBs were confirmed to be TADF materials.

Figure 4a shows the photoluminescence decay curves for emission of 4CzIPN at 100, 200 and 300 K in a 5 ± 1 wt% 4CzIPN:4,4'-bis(carbazol-9-yl)biphenyl (CBP) film. The triplet excitons of 4CzIPN are well confined using a CBP host because the T_1 state of CBP is higher in energy than the S_1 state of 4CzIPN. In addition, the fluorescence of CBP is completely quenched by efficient energy transfer between the guest and host molecules. The intense emission observed around $t = 0$ s corresponds to the prompt component, and the long tail is the delayed fluorescence. The prompt component is assigned to the fluorescence of 4CzIPN. The delayed component is attributed to delayed fluorescence occurring via reverse ISC, that is, TADF, because the photoluminescence spectrum of the delayed fluorescence is identical to that of the prompt fluorescence (Fig. 4b).

Figure 4c shows the temperature dependence of Φ for the prompt and delayed components of the film. The two components were resolved by combining the absolute value of Φ estimated using an

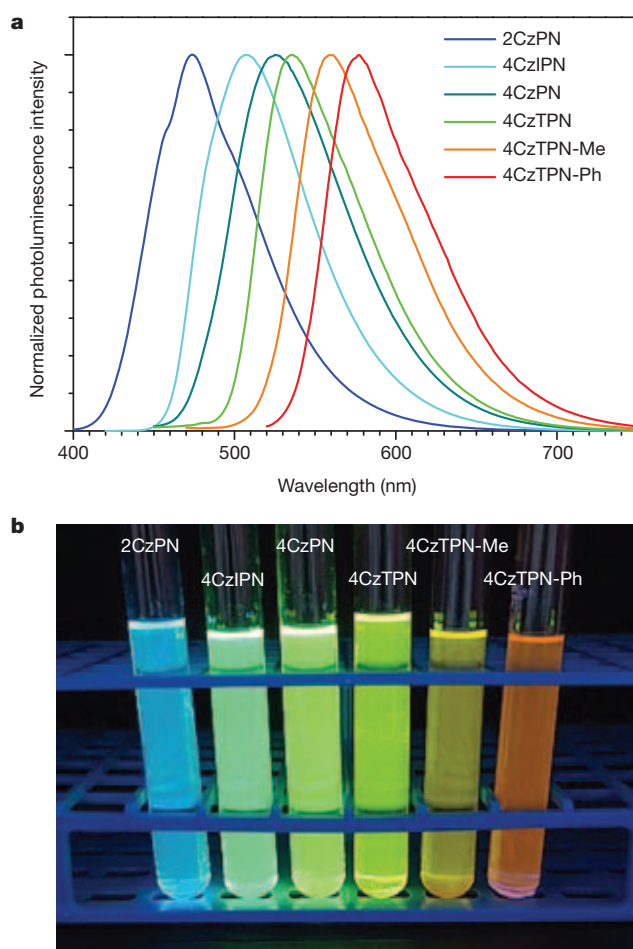


Figure 3 | Photoluminescence of the CDCB series. **a**, Photoluminescence spectra measured in toluene. **b**, Photograph under irradiation at 365 nm.

integrated-sphere photoluminescence measurement system and the temperature dependence of the photoluminescence decay curves (Supplementary Fig. 2). The prompt component increases very slightly as the temperature decreases, indicating the suppression of non-radiative decay from the S_1 state. Conversely, the delayed component decreases monotonically as the temperature decreases because reverse ISC becomes the rate-determining step, similar to the temperature dependence of tin(IV) fluoride/porphyrin complexes, which are typical TADF emitters¹⁴. At room temperature (300 K), a high Φ value, of $83 \pm 2\%$, was observed. To evaluate ΔE_{ST} quantitatively, we estimated the activation energy of the reverse ISC rate constant (k_{RISC}) from $\exp(-\Delta E_{ST}/k_B T)$, where k_B is the Boltzmann constant and T is temperature. This rate constant can be estimated from experimentally determined rate constants and the Φ values of the prompt and delayed components at each temperature using²⁴

$$k_{RISC} = \frac{k_p k_d \Phi_d}{k_{ISC} \Phi_p} \quad (1)$$

where k_p and k_d are the rate constants of the prompt and delayed fluorescence components, respectively; k_{ISC} is the ISC rate constant from S_1 to T_1 states; and Φ_p and Φ_d are the photoluminescence quantum yields of the prompt and delayed components, respectively. In Fig. 4d, the values of k_{RISC} calculated from equation (1), assuming that k_{ISC} was independent of temperature, are plotted against $1/T$ for $T = 200$ – 300 K. From the Arrhenius plot (Fig. 4d), we estimate an activation energy of 83 meV. Therefore, k_{RISC} would be suppressed considerably at low temperatures. However, even at low temperatures, the Φ value of the delayed component is still high, at $>40\%$, implying

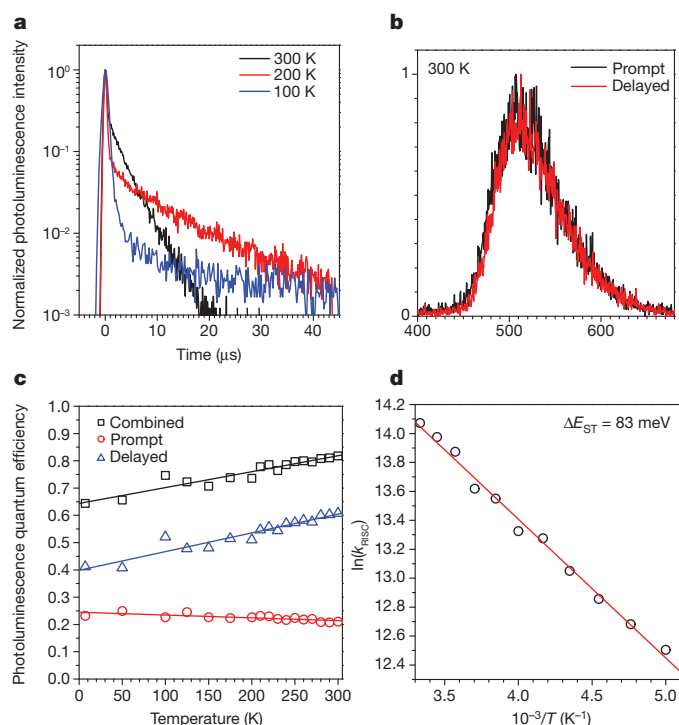


Figure 4 | Temperature dependence of photoluminescence characteristics of a 5 ± 1 wt% 4CzIPN:CBP film. **a**, Photoluminescence decay curves of a 6 wt% 4CzIPN:CBP film at 300 K (black line), 200 K (red line) and 100 K (blue line). The photoluminescence decay curves show integrated 4CzIPN emission. The excitation wavelength of the films was 337 nm. **b**, Photoluminescence spectrum resolved into prompt and delayed components. **c**, Temperature dependence of photoluminescence quantum efficiencies (errors are within 2%) for combined (prompt plus delayed; black squares), prompt (red circles) and delayed (blue triangles) components of 4CzIPN emission for 5 ± 1 wt% 4CzIPN:CBP film. The straight lines are guides for the eye. **d**, Arrhenius plot of the reverse ISC rate from the triplet state to the singlet state of 4CzIPN with k_{ISC} set to $4 \times 10^7 \text{ s}^{-1}$. The straight line (least-squares regression) is used to determine the activation energy. The $\ln(k_{\text{RISC}})$ errors are within 0.2.

that k_{RISC} is higher than the non-radiative rate constant of the T_1 state. It should be noted that for temperatures less than 200 K the decay curves do not agree with the double-exponential decay model, but are described well by a multi-exponential decay model. This can be explained by the widened ΔE_{ST} distribution caused by inhomogeneous molecular environments at lower temperatures.

We then evaluated the performance of OLEDs containing the CDCB derivatives 4CzIPN (green emission), 4CzTPN-Ph (orange emission) and 2CzPN (sky-blue emission) as emitters. Figure 5 shows the external electroluminescence quantum efficiency of OLEDs containing the CDCB derivatives. To achieve high electroluminescence efficiency in these OLEDs, the T_1 state of the CDCB derivatives must be confined using a host material with a higher triplet energy level. Therefore, we used CBP as a host material in the green and orange OLEDs and used 2,8-bis(diphenylphosphoryl)dibenzo[*b,d*]thiophene (PPT) as a host material in the sky-blue OLED. The structures of the OLEDs were composed of multiple layers of indium tin oxide (ITO), 4,4-bis[*N*-(1-naphthyl)-*N*-phenylamino]-biphenyl (α -NPD, 35 nm), 5 ± 1 wt% 4CzIPN or 5 ± 1 wt% 4CzTPN-Ph:CBP (15 nm), TPBi (65 nm), LiF (0.8 nm), Al (70 nm) and ITO (100 nm), α -NPD (40 nm), 1,3-bis(9-carbazolyl)benzene (mCP, 10 nm), 5 ± 1 wt% 2CzPN:PPT (20 nm), PPT (40 nm), LiF and Al. For the green OLED, a very high external electroluminescence quantum efficiency, of $19.3 \pm 1.5\%$, was achieved, which is equivalent to an internal electroluminescence quantum efficiency of 64.3–96.5% assuming a light out-coupling efficiency of 20–30% (refs 25, 26). The orange and sky-blue OLEDs had external electroluminescence quantum efficiencies of

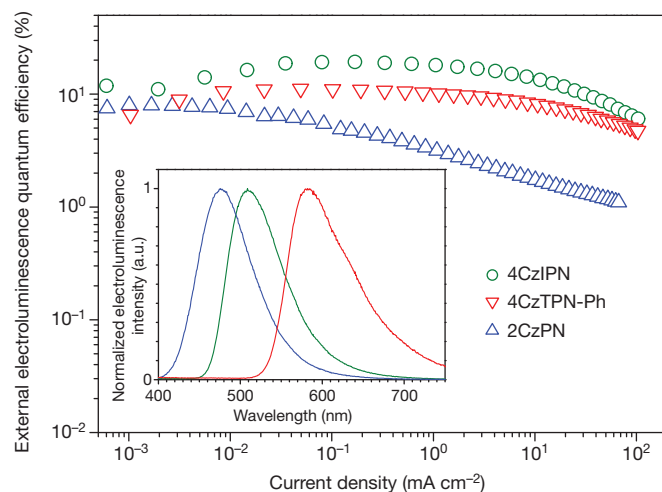


Figure 5 | Performance of OLEDs containing CDCB derivatives. External electroluminescence quantum efficiency as a function of current density for OLEDs containing 4CzIPN (green circles; error within 1.5%), 4CzTPN-Ph (red triangles; error within 1.0%) and 2CzPN (blue triangles; error within 1.0%) as emitters. Inset, electroluminescence spectra of the same OLEDs (coloured accordingly) at a current density of 10 mA cm^{-2} .

$11.2 \pm 1\%$ and $8.0 \pm 1\%$, respectively, which are also higher than those of conventional fluorescence-based OLEDs.

Finally, we consider the mechanism that drives such efficient reverse ISC without heavy metals. It is generally accepted that the introduction of spin–orbit coupling provided by heavy atoms is required for both ISC and reverse ISC to be efficient. Thus, metal complexes containing heavy metals and aromatic compounds with halogens and carbonyls can promote efficient spin conversion. However, our novel molecular design produces highly efficient spin conversion without needing such atoms. This is because the first-order mixing coefficient between singlet and triplet states (λ) is inversely proportional to ΔE_{ST} (ref. 27):

$$\lambda \propto \frac{H_{\text{SO}}}{\Delta E_{\text{ST}}} \quad (2)$$

Here H_{SO} is the spin–orbit interaction. It follows from equation (2) that heavy atoms are not required to achieve efficient spin conversion when a molecule possesses a small ΔE_{ST} and H_{SO} is not vanishingly small. This broadens the scope for the molecular design of TADF materials. A detailed strategy for large λ will be clarified on the basis of correlated quantum-chemical calculations²⁸.

METHODS SUMMARY

Synthesis of carbazolyl dicyanobenzene. The synthesis of CDCB derivatives was performed according to the synthetic method reported previously for pyrrole and fluorobenzene derivatives^{29,30}. CDCBs were synthesized by reaction of a carbazolyl anion with a fluorinated dicyanobenzene at room temperature (300 K) for 10 h under a nitrogen atmosphere. CDCBs were purified by column chromatography on silica gel, by reprecipitation or both. CDCBs were further purified by sublimation before photoluminescence and electroluminescence spectra were measured.

Photoluminescence measurements. Organic films for optical measurements were fabricated by thermal evaporation onto clean quartz and silicon substrates under high vacuum ($\sim 7 \times 10^{-4}$ Pa). The photoluminescence spectra of these films were recorded with a spectrofluorometer (FluoroMax-4, Horiba Jobin Yvon), and the photoluminescence quantum efficiencies were measured using an absolute photoluminescence quantum yield measurement system (C9920-02, Hamamatsu Photonics). The transient photoluminescence characteristics were measured (in terms of photon number) under vacuum using a streak camera (C4334, Hamamatsu Photonics). A nitrogen gas laser with a wavelength of 337 nm and a pulse width of approximately 500 ps (MNL200, Lasertechnik) was used as an excitation source. Low-temperature measurements were made using a cryostat (CRT-006-2000, Iwatani Industrial Gases). InGa alloy was applied as an adhesive to ensure good thermal conductivity between the silicon substrate and sample holder.

OLED fabrication and electroluminescence measurements. The OLED devices were fabricated by thermal evaporation onto clean ITO-coated glass substrates under high vacuum ($\sim 7 \times 10^{-4}$ Pa). Current density/voltage/luminance (J - V - L) characteristics were measured using a semiconductor parameter analyser (E5273A, Agilent) with an optical power meter (1930C, Newport). Electroluminescence spectra of OLEDs were measured (in terms of photon number) using a calibrated multichannel spectrometer (PMA12, Hamamatsu Photonics).

Full Methods and any associated references are available in the online version of the paper.

Received 20 July; accepted 18 October 2012.

- Pope, M., Kallmann, H. P. & Magnante, P. Electroluminescence in organic crystals. *J. Chem. Phys.* **38**, 2042–2043 (1963).
- Baldo, M. A., Lamansky, S., Burrows, P. E., Thompson, M. E. & Forrest, S. R. Very high-efficiency green organic light-emitting devices based on electrophosphorescence. *Appl. Phys. Lett.* **75**, 4–6 (1999).
- Adachi, C., Baldo, M. A., Thompson, M. E. & Forrest, S. R. Nearly 100% internal phosphorescence efficiency in an organic light emitting device. *J. Appl. Phys.* **90**, 5048–5051 (2001).
- Endo, A. *et al.* Efficient up-conversion of triplet excitons into a singlet state and its application to organic light emitting diodes. *Appl. Phys. Lett.* **98**, 083302 (2011).
- Bernanose, A., Comte, M. & Vouaux, P. A new method of emission of light by certain organic compounds. *J. Chim. Phys.* **50**, 64–68 (1953).
- Tsutsui, T. & Saito, S. *Organic Multilayer-Dye Electroluminescent Diodes: Is There Any Difference with Polymer LED?* 127–131 (Kluwer, 1993).
- Rothberg, L. J. & Lovinger, A. J. Status of and prospects for organic electroluminescence. *J. Mater. Res.* **11**, 3174–3187 (1996).
- Wilson, J. S. *et al.* Spin-dependent exciton formation in π -conjugated compounds. *Nature* **413**, 828–831 (2001).
- Segal, M., Baldo, M. A., Holmes, R. J., Forrest, S. R. & Soos, Z. G. Excitonic singlet-triplet ratios in molecular and polymeric organic materials. *Phys. Rev. B* **68**, 075211 (2003).
- Cao, Y., Parker, I. D., Yu, G., Zhang, C. & Heeger, A. J. Improved quantum efficiency for electroluminescence in semiconducting polymers. *Nature* **397**, 414–417 (1999).
- Wohlgenannt, M., Jiang, X. M., Vardeny, Z. V. & Janssen, R. A. J. Conjugation-length dependence of spin-dependant exciton formation rates in π -conjugated oligomers and polymers. *Phys. Rev. Lett.* **88**, 197401 (2002).
- Shuai, Z., Beljonne, D., Silbey, R. J. & Brédas, L. J. Singlet and triplet exciton formation rates in conjugated polymer light-emitting diodes. *Phys. Rev. Lett.* **84**, 131–134 (2000).
- Tsutsui, T., Adachi, C. & Saito, S. in *Photochemical Processes in Organized Molecular Systems* (ed. Honda, K.) 437–450 (Elsevier, 1991).
- Kido, J., Nagai, K. & Ohashi, Y. Electroluminescence in a terbium complex. *Chem. Lett.* **19**, 657–660 (1990).
- Endo, A. *et al.* Thermally activated delayed fluorescence from Sn^{4+} -porphyrin complexes and their application to organic light-emitting diodes: a novel mechanism for electroluminescence. *Adv. Mater.* **21**, 4802–4806 (2009).
- Akai, N., Kudoh, S. & Nakata, M. Lowest excited triplet states of 1,2- and 1,4-dicyanobenzenes by low-temperature matrix-isolation infrared spectroscopy and density-functional-theory calculation. *Chem. Phys. Lett.* **371**, 655–661 (2003).
- Wakamiya, A., Mori, K. & Yamaguchi, S. 3-boryl-2,2'-bithiophene as a versatile core skeleton for full-color highly emissive organic solids. *Angew. Chem. Int. Ed.* **46**, 4273–4276 (2007).
- Hariharan, P. C. & Pople, J. A. The influence of polarization functions on molecular orbital hydrogenation energies. *Theor. Chim. Acta* **28**, 213–222 (1973).
- Frisch, M. J. *et al.* *Gaussian 09, Revision C. 01* <http://www.gaussian.com/index.htm> (2010).
- Zhao, Y. & Truhlar, D. The M06 suite of density functionals for main group thermochemistry, thermochemical kinetics, noncovalent interactions, excited states, and transition elements: two new functionals and systematic testing of four M06-class functionals and 12 other functionals. *Theor. Chem. Acc.* **120**, 215–241 (2008).
- Improta, R., Barone, V., Scalmani, G. & Frisch, M. J. A state-specific polarizable continuum model time dependent density functional method for excited state calculations in solution. *J. Chem. Phys.* **125**, 054103 (2006).
- Improta, R., Scalmani, G., Frisch, M. J. & Barone, V. Toward effective and reliable fluorescence energies in solution by a new state specific polarizable continuum model time dependent density functional theory approach. *J. Chem. Phys.* **127**, 074504 (2007).
- Martin, R. L. Natural transition orbitals. *J. Chem. Phys.* **118**, 4775–4777 (2003).
- Goushi, K., Yoshida, K., Sato, K. & Adachi, C. Organic light-emitting diodes employing efficient reverse intersystem crossing for triplet-to-singlet state conversion. *Nature Photon.* **6**, 253–258 (2012).
- Smith, L. H., Wasey, J. A. E. & Barnes, W. L. Light outcoupling efficiency of top-emitting organic light-emitting diodes. *Appl. Phys. Lett.* **84**, 2986–2988 (2004).
- Tanaka, D. *et al.* Ultra high efficiency green organic light-emitting devices. *Jpn. J. Appl. Phys.* **46**, L10–L12 (2007).
- Turro, N. J. *Modern Molecular Photochemistry* 98–100 (Benjamin Cummings, 1978).
- Beljonne, D., Shuai, Z., Pourtois, G. & Brédas, J. L. Spin-orbit coupling and intersystem crossing in conjugated polymers: a configuration interaction description. *J. Phys. Chem. A* **105**, 3899–3907 (2001).
- Takase, M., Enkelmann, V., Sebastiani, D., Baumgarten, M. & Müllen, K. Annularly fused hexapyrrolohexaazacoronenes: an extended π system with multiple interior nitrogen atoms displays stable oxidation states. *Angew. Chem. Int. Ed.* **46**, 5524–5527 (2007).
- Uno, H. *et al.* Preparation of highly conjugated oligoaza-PAHs based on the oxidative intramolecular coupling of bicyclo[2.2.2]octadiene-fused pyrrole. *Heterocycles* **82**, 791–802 (2010).

Supplementary Information is available in the online version of the paper.

Acknowledgements This work was supported by the Funding Program for World-Leading Innovative R&D on Science and Technology (FIRST) and the International Institute for Carbon Neutral Energy Research (WPI-I2CNER), sponsored by the Japanese Ministry of Education, Culture, Sports, Science and Technology. H.U. acknowledges a Grand-in-Aid for JSPS Fellows. We thank H. Nakanotani, J.-i. Nishide, and H. Miyazaki for their assistance with this research. We also thank K. Tokumaru, H. Sasabe, W. Potschavage and M. Gábor for their assistance with preparation of this manuscript.

Author Contributions H.U. performed the molecular design. H.U. and H.N. performed the synthetic work. K.S. performed the computational experiments. H.U. and K.G. measured the photoluminescence and electroluminescence characteristics of the compounds. All authors wrote the paper. C.A. thought of the TADF concept and supervised the project.

Author Information Reprints and permissions information is available at www.nature.com/reprints. The authors declare no competing financial interests. Readers are welcome to comment on the online version of the paper. Correspondence and requests for materials should be addressed to C.A. (adachi@opera.kyushu-u.ac.jp).

METHODS

Synthesis of carbazolyl dicyanobenzene. NMR spectra were obtained with a Bruker Biospin Avance-III 500 NMR spectrometer at ambient temperature. Because 4CzTPN, 4CzTPN-Me and 4CzTPN-Ph were not sufficiently soluble in common deuterated solvents, their ^{13}C NMR spectra were not obtained. Infrared spectra were measured with a JASCO FT/IR-620 infrared spectrophotometer. High-resolution mass spectrometry (HRMS) by fast atom bombardment was done using a JEOL JMS-700 spectrometer. Matrix-assisted laser desorption/ionization-time of flight (MALDI-TOF) mass spectrometry was done using a BRUKER Autoflex-III. Elemental analysis was performed with a Yanaco MT-5 elemental analyser. All solvents and chemicals were reagent grade, obtained commercially and used without further purification except as noted. Dry tetrahydrofuran (THF) was purchased from Wako Pure Chemical Industries, Ltd. The synthesis of CDCB derivatives was performed according to the synthetic method reported previously for pyrrole and fluorobenzene derivatives^{29,30}. CDCBs were purified by sublimation before photoluminescence and electroluminescence spectra were measured.

We used the following general procedure for the synthesis of tetracarbazolyl dicyanobenzenes. Sixty per cent NaH in oil (0.48 g, 12 mmol) was washed with hexane and then added to a stirred solution of carbazole derivative (10.0 mmol) in dry THF (40 ml) under a nitrogen atmosphere at room temperature. After stirring for 30 min, tetrafluorophthalonitrile, tetrafluoroisophthalonitrile, or tetrafluoroterephthalonitrile (0.400 g, 2.00 mmol) was added. The reaction mixture was stirred at room temperature for 10 h. The reaction was quenched with water (5 ml). The mixture was concentrated under reduced pressure to yield the crude product.

We synthesized 1,2,3,4-tetrakis(carbazol-9-yl)-5,6-dicyanobenzene (4CzPN) according to the general procedure. The crude product was added to water, sonicated for 10 min and then filtered. The residue was purified by column chromatography on silica gel (CHCl_3 :hexane, 2:1 v/v and then CHCl_3 :acetone, 2:1 v/v) and then reprecipitated from CHCl_3 /MeOH to produce 4CzPN as an orange powder (0.602 g, 0.764 mmol, 38%).

The results of our analyses are as follows. Thin-layer chromatography (TLC) (CHCl_3 :hexane, 4:1 v/v): retardation factor (R_F), 0.20. ^1H NMR (500 MHz, $\text{DMSO}-d_6$): δ (p.p.m.) = 7.90 (m, 4H), 7.73 (m, 4H), 7.41 (m, 8H), 7.17–7.12 (m, 8H), 6.76 (m, 4H), 6.62 (m, 4H). ^{13}C NMR (125 MHz, acetone- d_6): δ (p.p.m.) = 141.58, 141.05, 138.75, 137.52, 125.13, 124.03, 123.04, 122.79, 121.06, 120.46, 120.10, 119.29, 119.01, 113.41, 111.17, 111.06. Infrared spectroscopy (KBr): absorption wavelength (cm^{-1}), 2,228, 1,490, 1,457, 1,446, 1,310, 1,223. HRMS (m/z): $[\text{M}+\text{H}]^+$ calculated for $\text{C}_{56}\text{H}_{33}\text{N}_6$, 789.2766; found, 789.2767; analysis (calculated, found for $\text{C}_{56}\text{H}_{32}\text{N}_6$): C (85.26%, 85.16%), H (4.09%, 4.02%), N (10.65%, 10.55%).

We synthesized 1,2,3,5-tetrakis(carbazol-9-yl)-4,6-dicyanobenzene (4CzIPN) according to the general procedure. The crude product was added to water, sonicated for 10 min and then filtered. The residue was purified by column chromatography on silica gel (hexane: CHCl_3 , 5:1 v/v and then acetone: CHCl_3 , 5:1 v/v) and reprecipitated from acetone/ CHCl_3 to produce 4CzIPN as a yellow powder (1.41 g, 1.79 mmol, 90%).

The results of our analyses are as follows. TLC (acetone: CHCl_3 , 5:1 v/v): R_F = 0.25. ^1H NMR (500 MHz, CDCl_3): δ (p.p.m.) = 8.33 (d, J = 7.5 Hz, 2H), 8.06 (d, J = 8.0 Hz, 2H), 7.83 (dd, J = 8.0, 1.5 Hz, 4H), 7.71–7.67 (m, 6H), 7.47 (m, 4H), 7.43 (d, J = 7.5 Hz, 2H), 7.14–7.08 (m, 8H), 6.82 (m, 2H), 6.71 (m, 2H). ^{13}C NMR (125 MHz, acetone- d_6): δ (p.p.m.) = 146.88, 146.20, 141.31, 139.84, 138.82, 137.50, 127.74, 126.41, 125.34, 125.32, 125.03, 124.56, 122.85, 122.32, 121.80, 121.50, 120.98, 120.26, 118.58, 112.99, 111.79, 111.64, 111.36. Infrared spectroscopy (KBr): absorption wavelength (cm^{-1}), 2,233, 1,545, 1,490, 1,479, 1,458, 1,335, 1,309, 1,222. HRMS (m/z): $[\text{M}+\text{H}]^+$ calculated for $\text{C}_{56}\text{H}_{33}\text{N}_6$, 789.2766; found, 789.2781; analysis (calculated, found for $\text{C}_{56}\text{H}_{32}\text{N}_6$): C (85.26%, 85.22%), H (4.09%, 4.03%), N (10.65%, 10.62%).

We synthesized 1,2,4,5-tetrakis(carbazol-9-yl)-3,6-dicyanobenzene (4CzTPN) according to the general procedure. The crude product was added to water, sonicated for 10 min and then filtered. The residue was purified by column chromatography on silica gel (CHCl_3 and then acetone) and reprecipitated from acetone/ CHCl_3 to produce 4CzTPN as an orange powder (1.50 g, 1.90 mmol, 95%).

The results of our analyses are as follows. TLC (acetone): R_F = 0.05. ^1H NMR (500 MHz, $\text{DMSO}-d_6$): δ (p.p.m.) = 7.91 (m, 16H), 7.25 (m, 8H), 7.16 (m, 8H). Infrared spectroscopy (KBr): absorption wavelength (cm^{-1}), 2,235, 1,490, 1,480, 1,455, 1,334, 1,224. HRMS (m/z): $[\text{M}+\text{H}]^+$ calculated for $\text{C}_{56}\text{H}_{33}\text{N}_6$, 789.2766; found, 789.2781; analysis (calculated, found for $\text{C}_{56}\text{H}_{32}\text{N}_6$): C (85.26%, 85.28%), H (4.09%, 4.11%), N (10.65%, 10.61%).

We synthesized 1,4-dicyano-2,3,5,6-tetrakis(3,6-dimethylcarbazol-9-yl)benzene (4CzTPN-Me) according to the general procedure. The crude product was added to MeOH (200 ml) and then filtered. The residue was washed with water and MeOH to produce 4CzTPN-Me as an orange powder (1.72 g, 1.91 mmol, 95%).

The results of our analyses are as follows. TLC (acetone): R_F = 0.05. ^1H NMR (500 MHz, $\text{DMSO}-d_6$): δ (p.p.m.) = 7.81 (d, J = 8.5 Hz, 8H), 7.71 (s, 8H), 7.11 (m, 8H), 2.37 (s, 24H). Infrared spectroscopy (KBr): absorption wavelength (cm^{-1}), 2,241, 1,461, 1,319, 1,281, 1,228. HRMS (m/z): $[\text{M}+\text{H}]^+$ calculated for $\text{C}_{64}\text{H}_{49}\text{N}_6$, 901.4019; found, 901.4027; analysis (calculated, found for $\text{C}_{64}\text{H}_{48}\text{N}_6$): C (85.30%, 85.39%), H (5.37%, 5.36%), N (9.33%, 9.35%).

We synthesized 1,4-dicyano-2,3,5,6-tetrakis(3,6-diphenylcarbazol-9-yl)benzene (4CzTPN-Ph) according to the general procedure. The crude product was added to water, sonicated for 10 min and then filtered. The residue was purified by column chromatography on silica gel (CHCl_3 and then acetone) and reprecipitated from acetone/ CHCl_3 to produce 4CzTPN-Ph as an orange powder (2.20 g, 1.57 mmol, 79%).

The results of our analyses are as follows. TLC (acetone): R_F = 0.05. ^1H NMR (500 MHz, $\text{DMSO}-d_6$): δ (p.p.m.) = 8.37 (d, J = 1.5 Hz, 8H), 8.05 (d, J = 8.5 Hz, 8H), 7.70 (m, 16H), 7.62 (dd, J = 8.5, 1.5 Hz, 8H), 7.45 (m, 16H), 7.36 (m, 8H). Infrared spectroscopy (KBr): absorption wavelength (cm^{-1}), 2,236, 2,228, 1,600, 1,476, 1,456, 1,441, 1,290, 1,226. MALDI-TOF MS (m/z): $[\text{M}]^+$ calculated for $\text{C}_{104}\text{H}_{64}\text{N}_6$, 1396.52; found, 1396.66; analysis (calculated, found for $\text{C}_{104}\text{H}_{64}\text{N}_6$): C (89.37%, 89.26%), H (4.62%, 4.53%), N (6.01%, 5.95%).

To synthesize 1,2-bis(carbazol-9-yl)-4,5-dicyanobenzene (2CzPN), 60% NaH in oil (0.96 g, 24 mmol) was washed with hexane and then added to a stirred solution of carbazole derivative (3.34 g, 20.0 mmol) in dry THF (80 ml) under a nitrogen atmosphere at room temperature. After stirring for 30 min, 4,5-difluorophthalonitrile (1.31 g, 8.00 mmol) was added. The reaction mixture was stirred at room temperature for 10 h. The reaction was quenched with water (20 ml). The mixture was concentrated under reduced pressure. The residue was washed with water, purified by column chromatography on silica gel (CHCl_3 :hexane, 4:1 v/v) and reprecipitated from acetone/hexane to produce 2CzPN as a pale yellow powder (0.310 g, 0.676 mmol, 8.5%).

The results of our analyses are as follows. TLC (CHCl_3 :hexane, 4:1 v/v): R_F = 0.23. ^1H NMR (500 MHz, acetone- d_6): δ (p.p.m.) = 8.73 (s, 2H), 7.79 (m, 4H), 7.38 (m, 4H), 7.13–7.08 (m, 8H). ^{13}C NMR (125 MHz, acetone- d_6): δ (p.p.m.) = 139.86, 139.57, 137.14, 126.76, 124.90, 121.99, 120.96, 116.39, 115.88, 110.74. Infrared spectroscopy (KBr): absorption wavelength (cm^{-1}), 2,236, 1,596, 1,507, 1,478, 1,446, 1,335, 1,221. HRMS (m/z): $[\text{M}]^+$ calculated for $\text{C}_{32}\text{H}_{18}\text{N}_4$, 458.1531; found, 458.1529; analysis (calculated, found for $\text{C}_{32}\text{H}_{18}\text{N}_4$): C (83.82%, 83.81%), H (3.96%, 3.80%), N (12.22%, 12.19%).

Photoluminescence measurements. Organic films for optical measurements were fabricated by thermal evaporation onto clean quartz and silicon substrates under high vacuum ($\sim 7 \times 10^{-4}$ Pa). The photoluminescence spectra of these films were recorded with a spectrofluorometer (FluoroMax-4, Horiba Jobin Yvon), and the photoluminescence quantum efficiencies were measured using an absolute photoluminescence quantum yield measurement system (C9920-02, Hamamatsu Photonics). The transient photoluminescence characteristics were measured (in terms of photon number) under vacuum using a streak camera (C4334, Hamamatsu Photonics). A nitrogen gas laser with a wavelength of 337 nm and a pulse width of approximately 500 ps (MNL200, Lasertechnik) was used as an excitation source. Low-temperature measurements were conducted using a cryostat (CRT-006-2000, Iwatani Industrial Gases). InGa alloy was applied as an adhesive to ensure good thermal conductivity between the silicon substrate and sample holder.

Temperature-dependent photoluminescence characteristics of the prompt and delayed components for a 6 wt% 4CzIPN:CBP film were calculated as follows. Supplementary Fig. 2 shows the temperature-dependent lifetime of the prompt component for a 6 wt% 4CzIPN:CBP film. Assuming that the lifetime of singlet excited states is much longer than those of triplet excited states, the respective rate constants of the prompt and delayed fluorescence components (k_p and k_d), in the presence of mutual ISC between the singlet and triplet states, are given by²⁴

$$k_p = k_r^S + k_{nr}^S + k_{ISC}$$

$$k_d = k_{nr}^T + \left(1 - \frac{k_{ISC}}{k_r^S + k_{nr}^S + k_{ISC}}\right) k_{RISC}$$

where k_r^S and k_{nr}^S are the radiative and non-radiative rate constants of the singlet state, respectively; k_{ISC} is the ISC rate constant from singlet to triplet states; and k_{nr}^T is the non-radiative rate constant of the triplet state. Therefore, the photoluminescence quantum efficiency of the prompt component is given by

$$\Phi_p = \frac{k_r^S}{k_r^S + k_{nr}^S + k_{ISC}} = k_r^S \tau^S$$

where τ^S is the lifetime of the singlet state. By combining the absolute photoluminescence efficiency estimated using an integrated-sphere photoluminescence measurement system and the temperature dependence of the photoluminescence

decay curve at $T = 300$ K, we estimated k_r^S to be $1.27 \times 10^7 \text{ s}^{-1}$. This allowed us to estimate Φ_p from the temperature-dependent lifetime of the prompt component, assuming that k_r^S is independent of temperature. Using the total photoluminescence quantum efficiency estimated from the temperature dependence of the photoluminescence intensity, the photoluminescence quantum efficiency of the delayed component (Φ_d) can also be estimated. Supplementary Table 4 shows the photoluminescence characteristics of a 6 wt% 4CzIPN:CBP film at each temperature. We estimated k_{RISC} using these experimental data.

OLED fabrication and electroluminescence measurements. The OLED devices were fabricated by thermal evaporation onto clean ITO-coated glass substrates under high vacuum ($\sim 7 \times 10^{-4}$ Pa). Current density/voltage/luminance (J - V - L) characteristics were measured using a semiconductor parameter analyser (E5273A, Agilent) with an optical power meter (1930C, Newport). Electroluminescence spectra of OLEDs were measured (in terms of photon number) using a calibrated multichannel spectrometer (PMA12, Hamamatsu Photonics).

Increased future ice discharge from Antarctica owing to higher snowfall

R. Winkelmann^{1,2}, A. Levermann^{1,2}, M. A. Martin^{1,2} & K. Frieler¹

Anthropogenic climate change is likely to cause continuing global sea level rise¹, but some processes within the Earth system may mitigate the magnitude of the projected effect. Regional and global climate models simulate enhanced snowfall over Antarctica, which would provide a direct offset of the future contribution to global sea level rise from cryospheric mass loss^{2,3} and ocean expansion⁴. Uncertainties exist in modelled snowfall⁵, but even larger uncertainties exist in the potential changes of dynamic ice discharge from Antarctica^{1,6} and thus in the ultimate fate of the precipitation-deposited ice mass. Here we show that snowfall and discharge are not independent, but that future ice discharge will increase by up to three times as a result of additional snowfall under global warming. Our results, based on an ice-sheet model⁷ forced by climate simulations through to the end of 2500 (ref. 8), show that the enhanced discharge effect exceeds the effect of surface warming as well as that of basal ice-shelf melting, and is due to the difference in surface elevation change caused by snowfall on grounded versus floating ice. Although different underlying forcings drive ice loss from basal melting versus increased snowfall, similar ice dynamical processes are nonetheless at work in both; therefore results are relatively independent of the specific representation of the transition zone. In an ensemble of simulations designed to capture ice-physics uncertainty, the additional dynamic ice loss along the coastline compensates between 30 and 65 per cent of the ice gain due to enhanced snowfall over the entire continent. This results in a dynamic ice loss of up to 1.25 metres in the year 2500 for the strongest warming scenario. The reported effect thus strongly counters a potential negative contribution to global sea level by the Antarctic Ice Sheet.

During the past decade, the Antarctic Ice Sheet has lost volume at a rate comparable to that of Greenland⁶. The enhanced moisture-carrying capacity of a warming atmosphere, on the other hand, strongly suggests increasing snowfall over Antarctica, as projected by global⁹ and regional climate models⁵. This may lead to a net negative contribution of Antarctica to future sea level, depending on the magnitude of dynamic effects possibly compensating or even overcompensating this ice gain. Because surface melt will remain small even under strong climate change^{2,3}, the major uncertainty in sea-level projections from Antarctica arises from the unknown dynamic contribution. The main mechanisms for dynamic ice loss in future climate scenarios discussed so far are softening of the ice due to surface warming¹⁰, acceleration of ice streams through the reduction or loss of an adjacent ice-shelf¹¹ and an increase in driving stress at the grounding line due to enhanced basal melting at the underside of the shelves caused by a rise in ocean temperature¹², all potentially resulting in higher ice flux across the grounding line (separating the grounded ice sheet from the floating ice shelves) (Fig. 1).

In a perturbed ice-physics ensemble, we estimate a significant additional effect of dynamic ice discharge, which is caused by the projected increase in snowfall itself. As detailed below, this effect makes the largest contribution to future ice loss, as projected by the continental-scale Potsdam Parallel Ice-Sheet Model (PISM-PIK)⁷ with a

consistent representation of the flow in the ice sheet, ice shelves and the transition zone relevant for the fast dynamics¹³. The underlying mechanism is simple and very robust, and consequently the effect is found along almost the entire coastline of Antarctica (Supplementary Fig. 1). It is due to a steepening of the surface gradient near the grounding line and the associated increase in the driving stress acting on the ice flow: additional snowfall increases the surface elevation of grounded ice as well as that of the floating ice shelf. Owing to the floating the resulting change in surface elevation is, however, ten times larger on grounded ice than on the floating shelf for the same amount

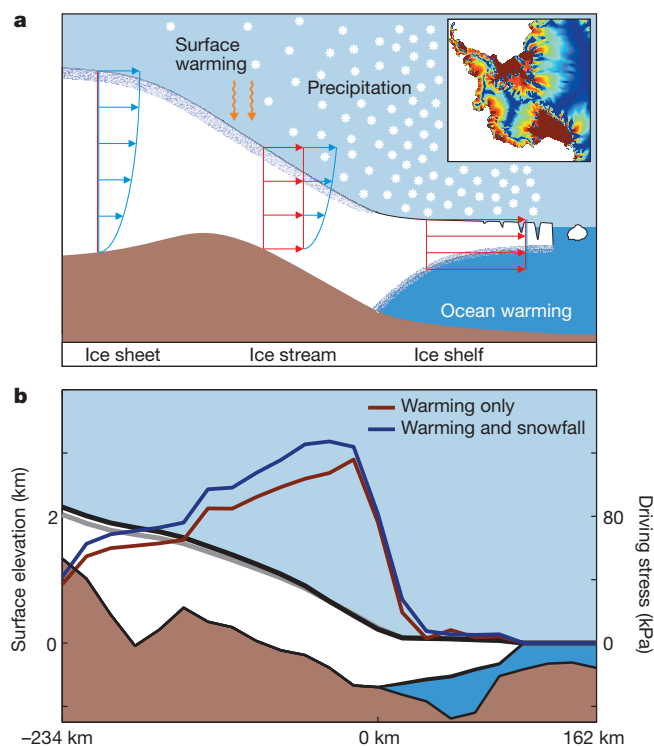


Figure 1 | Main mechanisms of dynamic ice loss. **a**, Conceptual figure illustrating the various forcings acting on the ice sheet. Inset, velocity field of a present-day Antarctic Ice Sheet simulation with PISM-PIK, which models the different flow regimes in sheet, streams and shelves in a consistent manner. The approach allows for the transition from vertical-shearing dominated flow of grounded ice to spreading-dominated flow in ice shelves. The resulting range in ice velocity spans several orders of magnitude and compares well with observational data²⁷. Velocity profiles are illustrated as blue lines for the vertical-shearing-dominated and red lines for the spreading-dominated flow. **b**, Ice contours for the years 2000 (light grey) and 2500 (black) of the ECP 8.5 scenario with enhanced snowfall (for the section depicted in Supplementary Fig. 1b). Enhanced snowfall leads to an increase in surface elevation on the sheet, whereas the elevation of the ice shelf remains almost constant because it floats. The corresponding driving stress with snowfall change (blue) is significantly higher than for the simulation with warming only (red).

¹Potsdam Institute for Climate Impact Research (PIK), 14473 Potsdam, Germany. ²Physics Institute, Potsdam University, 14476 Potsdam, Germany.

of accumulated snow. In the simulations, this increase in surface gradient can be observed in all coastal regions of the Antarctic Ice Sheet; it is also observed when the initial states are forced by snowfall changes projected by regional climate models. It yields an increase in driving stress and hence ice transport across the grounding line (as shown for an exemplary profile of the coastal region of the Amundsen Sea sector in Fig. 1b). As a rule of thumb, the effect is larger than the increase in driving stress induced by enhanced sub-shelf melting as long as the rate of basal melt is less than nine times the snowfall, which is generally the case in all projections presented here (Fig. 2). Under very strong climatic forcing a few regions, such as the catchment area of the Ross Ice Shelf, show a retreat of the grounding line. Here additional snowfall may lead to an increase in the buttressing ability of the ice shelf, countering the effects of enhanced sub-shelf melting and limiting the acceleration of ice flux upstream of the grounding line. In all other regions and under less extreme climatic forcing, snowfall enhances ice loss.

Although projections of Antarctic temperature and snowfall changes are subject to substantial uncertainty⁹, a robust feature of both global and regional model simulations that is relevant for the dynamic effect presented here is the increase in snowfall along the coastal margins⁵. The climate scenarios applied here are based on the Representative Concentration Pathways (RCPs), which span the full range of radiative forcing from 2.6 to 8.5 W m⁻² projected up until the end of the twenty-first century; after this, we used the respective Extended Concentration Pathways (ECPs)¹⁴ until 2500. Using a statistical downscaling method⁸, the corresponding global-mean temperature changes (as obtained from emulations of the full range of CMIP3 atmosphere–ocean general circulation model (AOGCM) responses¹⁵ using MAGICC 6.0¹⁶) were transferred into scenarios for the surface temperature over Antarctica and the ocean temperature near the major ice shelves. The basal-melt rate underneath each of the shelves was computed from the shelf's geometry and the temperature and salinity at its cavity entrance, using a simplified ocean model for the circulation in sub-ice-shelf cavities¹⁷.

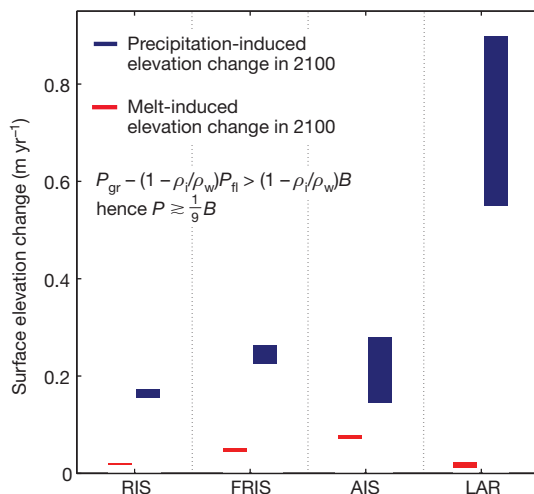


Figure 2 | Comparison of drivers of dynamic ice loss. Given is the model spread (for the perturbed-physics ensemble) of the surface elevation changes at the grounding lines of the Ross (RIS), Filchner-Ronne (FRIS), Amery (AIS) and Larsen (LAR) Ice Shelves in the year 2100 compared to pre-industrial values. Whereas enhanced basal melting induces a surface elevation change of $[1 - (\rho_i/\rho_w)]B$ at the grounding line (shown in red), the surface elevation change due to snowfall (shown in blue) is given by $P_{gr} - [1 - (\rho_i/\rho_w)]P_{\eta}$, where ρ_i and ρ_w are the density of ice and ocean water, respectively, B is the sub-shelf melt rate at the grounding line and P_{gr} and P_{η} denote the snowfall rate upstream and downstream of the grounding line, respectively. Both the sub-shelf melt rate B and the snowfall rate P are given in metres per year. Snowfall-driven ice loss will thus dominate basal-melt driven ice loss if the snowfall rate at the grounding line is larger than approximately one-ninth of the basal melt rate at the grounding line.

Recently observed values for the Ross¹⁸, Filchner¹⁹–Ronne²⁰ and Amery²¹ Ice Shelves as well as the shelf attached to Pine Island Glacier²² are captured by the modelled range for the year 2000. Precipitation changes are parameterized following ref. 23 and account for temperature increase as well as for changes in ice topography. As detailed elsewhere²⁴, we seek to capture the uncertainty that arises from different global climate sensitivity as well as the uncertainty due to ice-model parameters. To this end, each ECP scenario is represented by the median and the upper and lower 33rd percentile of the uncertainty distribution for the Antarctic temperature pathways originating from the inter-AOGCM variations and the uncertainty of the global mean temperature change from MAGICC 6.0. Furthermore, each of these 4×3 (scenarios \times percentiles) simulations was carried out starting from an ensemble of 81 initial states with different ice-parameter settings. All of these initial states closely resemble present-day Antarctica in ice volume and geometry, but differ in ice softness and the friction between ice sheet and

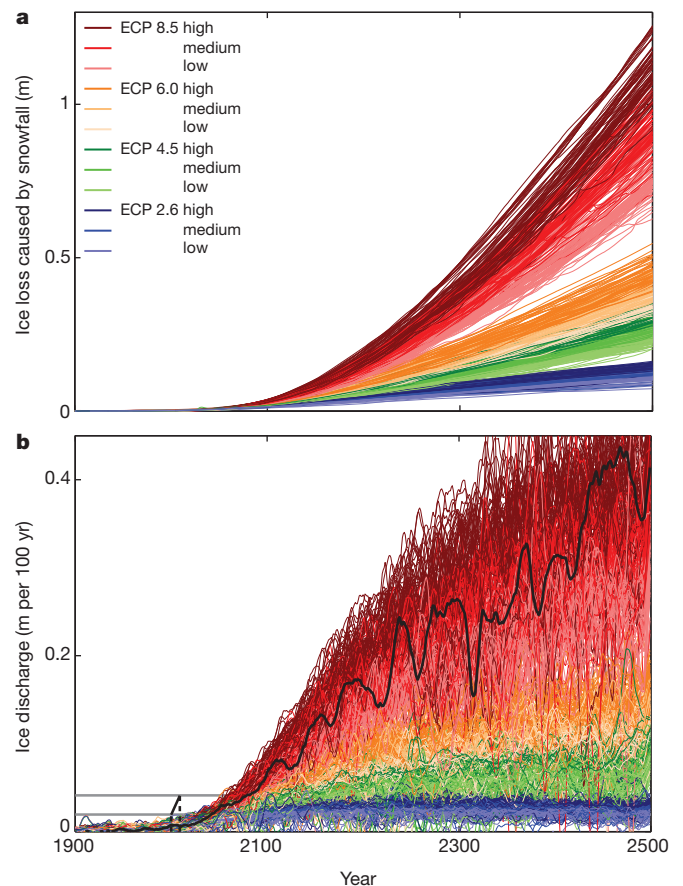


Figure 3 | Time series of snowfall-induced ice loss. **a**, Difference in solid ice loss between full scenario simulations and simulations with warming only, given in metres of sea-level equivalent. The additional ice loss due to enhanced snowfall increases for all scenarios with time. The spread from unknown physics captured in the 81-member ensemble is smaller than the range spanned by the medians for each scenario. **b**, Associated additional solid ice discharge, given in metres of sea-level equivalent per century. The model is in principle capable of reproducing the currently observed solid ice discharge from Antarctica (horizontal grey lines)⁶ of 0.2–0.4 mm yr⁻¹ for the years 2000 to 2009 and the associated acceleration within this time-period (thick black line; dashed lines indicate x -intercepts). These values are, however, reached later within the twenty-first century. As an example, the additional solid ice discharge is marked for one specific ensemble member by a thin black line, illustrating that the currently observed acceleration is within the variability of the additional ice discharge projected for ECP 8.5. The present study does not rely on the exact projection of ice loss from Antarctica but reports the relative importance of enhanced snowfall for the increase in future ice discharge compared to surface and ocean warming.

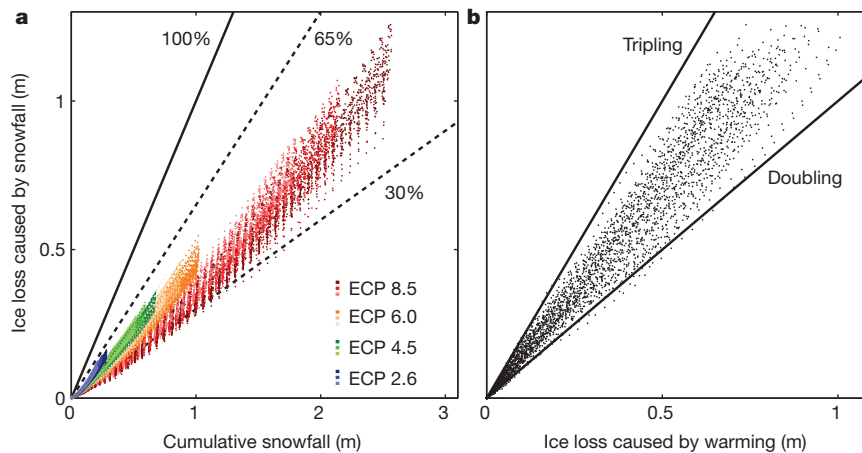


Figure 4 | Snowfall-induced ice loss compared to ice gain from precipitation and ice loss from warming only. All values are given in metres of sea-level equivalent. **a**, The additional ice loss under the ECP scenarios correlates with the cumulative amount of additional snowfall during the simulations. It compensates between 30% and 65% (shown as dashed black lines) of the ice gain due to enhanced snowfall. The percentage depends on the climate scenario—it is highest for the weak ECP 2.6 and lowest for the strong ECP 8.5.

basal topography and therefore in their sensitivity to a change in the climatic boundary conditions. For details of the model and ensemble simulations, see Methods section and ref. 24.

To estimate the influence of snowfall on ice discharge, we conducted simulations with surface and oceanic warming only as well as simulations with additional snowfall using the entire 81-member ensemble. Whereas the median of warming-induced ice loss in the year 2500 ranges from 0.04 m sea-level equivalent for the ECP 2.6 scenario to 0.65 m for the ECP 8.5 scenario, additional snowfall leads to a negative total mass balance in the range from -0.08 m for the ECP 2.6 scenario to -0.56 m sea-level equivalent for the ECP 8.5 scenario. These estimates of future mass loss are likely to be conservative for several reasons: additional mass loss might be caused by dynamic effects such as the marine ice sheet instability as well as the reduction of buttressing due to the retreat or collapse of surrounding ice shelves. It is also noteworthy that the projected snowfall increases represent a best-case scenario for mitigating Antarctica's contribution to sea level rise under continued oceanic and atmospheric warming. In contrast, if snowfall trends remain insignificant, as they have during the past decades²⁵, the sea level contribution of the Antarctic Ice Sheet will be even larger.

The amount of ice flowing across the grounding line in excess of the flux balancing the enhanced snowfall is called dynamic ice loss. For the entire ensemble, the difference in dynamic ice loss between the full scenarios and those with warming only—that is, the snowfall-induced ice discharge—increases throughout the simulations, amounting to 0.07–0.16 m sea-level equivalent for the ECP 2.6 scenario, and 0.63–1.25 m sea-level equivalent for the ECP 8.5 scenario with ensemble means of 0.12 m and 0.92 m, respectively, in the year 2500 (Fig. 3a). PISM-PIK is in principle capable of reproducing a dynamic situation where the ice discharge is of the magnitude and rate currently observed in satellite data⁶, though much later in this century (Fig. 3b). This may be because all scenarios start from an ensemble of equilibrium simulations that may not be the appropriate initialization for a future projection. The results presented here do not rely on this initialization, however; they report the relative importance of snowfall compared to other currently discussed ice-loss processes.

The snowfall-induced ice discharge correlates strongly with the cumulative amount of snowfall, compensating between 30% and 65% of the additional ice volume from the projected increase in precipitation (Fig. 4a). The ratio of this snowfall-induced ice discharge over cumulative snowfall changes predominantly with the warming

For each scenario, the model was forced with the median as well as the upper and lower borders of the likely range of warming: that is, the 50th, the 66th and the 33rd percentile of the spread generated by climate projections. **b**, Dynamic ice loss through snowfall exceeds ice loss through warming. The ice loss from both snowfall and warming amounts to 200% to 300% of the ice loss through warming only.

scenario, ranging, in the year 2500, from 35–50% for the high-emission scenario ECP 8.5, to 48–60% for the weaker ECP 2.6, in which global mean temperature is kept below two degrees with respect to pre-industrial levels¹⁴. The effect is thus highest for low warming scenarios, which might be due to the time-delay of the ice-sheet response to atmospheric forcing. The ice loss caused by the additional snowfall is larger than the ice loss from the combined warming of ice surface and the ocean. It amounts to 100%–200% of the volume change found in the warming-only simulations (Fig. 4b). Here the change in ice softness due to surface warming results in higher ice loss than the warming-induced basal melting, but both effects are significantly smaller than the ice loss caused by additional snowfall (Supplementary Fig. 2).

Our study thus shows that an increase in snowfall over Antarctica under global warming results in additional dynamic ice loss. For future climate scenarios based on the ECPs, this contribution is significantly larger than the dynamic ice loss due to warming only. This is consistent with the fact that the regional rate of snowfall increases the surface gradient across the grounding line nine times stronger than the equivalent rate of basal melt.

METHODS SUMMARY

Simulations were carried out with the Potsdam Parallel Ice Sheet Model, PISM-PIK, as described in ref. 7, extended by an ocean box model¹⁷ that simulates the main overturning circulation in sub-ice shelf cavities. Lack of knowledge about the values of the model input parameters introduces an uncertainty into the projections of future ice discharge. To capture this uncertainty, we perturbed the parameters that are most relevant for the ice flow across the grounding line. These are the two so-called enhancement factors (which determine the ice viscosity in the ice sheet, ice streams and ice shelves) and the pore-water fraction (which influences basal friction). For each parameter configuration, an equilibrium state of the Antarctic Ice Sheet under present-day boundary conditions²⁶ was generated via the spin-up procedure described in ref. 27. We then excluded those initial states whose geometry deviates strongly from present-day observations. In particular, both the sea-level relevant volume of the West Antarctic Ice Sheet and the grounding line position may not differ by more than 10% from their observed values. The remaining 81 representations of the Antarctic Ice Sheet, which span the widest possible range of dynamic sensitivity compatible with these criteria, served as initial states for the simulations discussed here. They were forced by surface and ocean temperature trajectories based on the ECPs that were derived via a statistical downscaling method⁸ from the corresponding global-mean-temperature changes. The dynamic response of the perturbed-physics ensemble to the ECP scenarios is further discussed in ref. 24.

Full Methods and any associated references are available in the online version of the paper.

Received 16 February; accepted 27 September 2012.

- Meehl, G. *et al.* in *Climate Change 2007: The Physical Science Basis* (eds Solomon, S. *et al.*) 747–845 (Cambridge Univ. Press, 2007).
- Huybrechts, P. *et al.* Response of the Greenland and Antarctic ice sheets to multi-millennial greenhouse warming in the Earth system model of intermediate complexity LOVECLIM. *Surv. Geophys.* **32**, 397–416 (2011).
- Vizcaíno, M., Mikolajewicz, U., Jungclauss, J. & Schurgers, G. Climate modification by future ice sheet changes and consequences for ice sheet mass balance. *Clim. Dyn.* **34**, 301–324 (2010).
- Schewe, J., Levermann, A. & Meinshausen, M. Climate change under a scenario near 1.5°C of global warming: monsoon intensification, ocean warming and steric sea level rise. *Earth Syst. Dyn.* **2**, 25–35 (2011).
- Krinner, G., Magand, O., Simmonds, I., Genthon, C. & Dufresne, J. Simulated Antarctic precipitation and surface mass balance at the end of the twentieth and twenty-first centuries. *Clim. Dyn.* **28**, 215–230 (2007).
- Rignot, E., Velicogna, I., van den Broeke, M. R., Monaghan, A. & Lenaerts, J. Acceleration of the contribution of the Greenland and Antarctic ice sheets to sea level rise. *Geophys. Res. Lett.* **38**, L05503, <http://dx.doi.org/10.1029/2011GL046583> (2011).
- Winkelmann, R. *et al.* The Potsdam Parallel Ice Sheet Model (PISM-PIK). Part 1: Model description. *Cryosphere* **5**, 715–726 (2011).
- Frieler, K., Meinshausen, M., Mengel, M., Braun, N. & Hare, W. A scaling approach to probabilistic assessment of regional climate change. *J. Clim.* **25**, 3117–3144 (2012).
- Uotila, P., Lynch, A. H., Cassano, J. J. & Cullather, R. I. Changes in Antarctic net precipitation in the 21st century based on Intergovernmental Panel on Climate Change (IPCC) model scenarios. *J. Geophys. Res.* **112**, D10107, <http://dx.doi.org/10.1029/2006JD007482> (2007).
- Larour, E., Rignot, E., Joughin, I. & Aubrey, D. Rheology of the Ronne Ice Shelf, Antarctica, inferred from satellite radar interferometry data using an inverse control method. *Geophys. Res. Lett.* **32**, L05503, <http://dx.doi.org/10.1029/2004GL021693> (2005).
- Dupont, T. K. & Alley, R. B. Assessment of the importance of ice-shelf buttressing to ice-sheet flow. *Geophys. Res. Lett.* **32**, L04503, <http://dx.doi.org/10.1029/2004GL022024> (2005).
- Rignot, E. & Jacobs, S. S. Rapid bottom melting widespread near Antarctic ice sheet grounding lines. *Science* **296**, 2020–2023 (2002).
- Schoof, C. & Hindmarsh, R. C. A. Thin-film flows with wall slip: an asymptotic analysis of higher order glacier flow models. *Q. J. Mech. Appl. Math.* **63**, 73–114 (2010).
- Meinshausen, M. *et al.* The RCP greenhouse gas concentrations and their extensions from 1765 to 2300. *Clim. Change* **109**, 213–241 (2011).
- Meehl, G. A. *et al.* THE WCRP CMIP3 multimodel dataset: a new era in climate change research. *Bull. Am. Meteorol. Soc.* **88**, 1383–1394 (2007).
- Meinshausen, M., Raper, S. C. B. & Wigley, T. M. L. Emulating IPCC AR4 atmosphere-ocean and carbon cycle models for projecting global-mean, hemispheric and land/ocean temperatures: MAGICC 6.0. *Atmos. Chem. Phys. Discuss.* **8**, 6153–6272 (2008).
- Olbers, D. & Hellmer, H. A box model of circulation and melting in ice shelf caverns. *Ocean Dyn.* **60**, 141–153 (2010).
- Dinniman, M. S., Klinck, J. M. & Smith, W. O. Influence of sea ice cover and icebergs on circulation and water mass formation in a numerical circulation model of the Ross Sea, Antarctica. *J. Geophys. Res.* **112**, C11013, <http://dx.doi.org/10.1029/2006JC004036> (2007).
- Grosfeld, K. *et al.* in *Ocean, Ice and Atmosphere: Interactions at Antarctic Continental Margin* (eds Jacobs, S. S. & Weiss, R.) 83–100 (AGU Antarctic Research Ser. Vol. 75, American Geophysical Union, 1998).
- Joughin, I. & Padman, L. Melting and freezing beneath Filchner-Ronne Ice Shelf, Antarctica. *Geophys. Res. Lett.* **30**, 1477, <http://dx.doi.org/10.1029/2003GL016941> (2003).
- Williams, M. J. M., Grosfeld, K., Warner, R. C., Gerdes, R. & Determann, J. Ocean circulation and ice-ocean interaction beneath the Amery Ice Shelf, Antarctica. *J. Geophys. Res.* **106**, 22383–22400 (2001).
- Payne, A. J. *et al.* Numerical modeling of ocean-ice interactions under Pine Island Bay's ice shelf. *J. Geophys. Res.* **112**, C10019, <http://dx.doi.org/10.1029/2006JC003733> (2007).
- Huybrechts, P. & Wolde, J. D. The dynamic response of the Greenland and Antarctic ice sheets to multiple-century climatic warming. *J. Clim.* **12**, 2169–2188 (1999).
- Winkelmann, R., Levermann, A., Frieler, K. & Martin, M. A. Uncertainty in future solid ice discharge from Antarctica. *Cryosphere Discuss.* **6**, 673–714 (2012).
- Monaghan, A. J. *et al.* Insignificant change in Antarctic snowfall since the International Geophysical Year. *Science* **313**, 827–831 (2006).
- Le Brocq, A. M., Payne, A. J. & Vieli, A. An improved Antarctic dataset for high resolution numerical ice sheet models (ALBMAP v1). *Earth Syst. Sci. Data* **2**, 247–260 (2010).
- Martin, M. A. *et al.* The Potsdam Parallel Ice Sheet Model (PISM-PIK). Part 2: Dynamic equilibrium simulation of the Antarctic Ice Sheet. *Cryosphere* **5**, 727–740 (2011).

Supplementary Information is available in the online version of the paper.

Acknowledgements This study was supported by the German Federal Ministry of Education and Research (BMBF, grant 01LP1171A) and the German Federal Ministry for the Environment, Nature Conservation and Nuclear Safety (BMU, grant 11_IL_093_Global_A_SIDS and LDCs).

Author Contributions R.W. and A.L. designed and performed the research. M.A.M. contributed to the discussion of the results. K.F. provided the climate forcing. R.W. wrote the paper.

Author Information Reprints and permissions information is available at www.nature.com/reprints. The authors declare no competing financial interests. Readers are welcome to comment on the online version of the paper. Correspondence and requests for materials should be addressed to R.W. (ricarda.winkelmann@pik-potsdam.de).

METHODS

Perturbed-physics ensemble. Simulations were carried out with the Potsdam Parallel Ice Sheet Model, PISM-PIK, as described in ref. 7. Lack of knowledge about the values of the model input parameters introduces an uncertainty into the projections of future ice discharge. To capture this uncertainty, we perturbed the parameters that are most relevant for the ice flow across the grounding line. These are the two so-called enhancement factors (which determine the ice viscosity in the ice sheet, ice streams and ice shelves) and the pore-water fraction (which influences basal friction). For each parameter configuration, an equilibrium state of the Antarctic Ice Sheet under present-day boundary conditions²⁶ was generated via the spin-up procedure described in ref. 27. We then excluded those initial states whose geometry deviates strongly from present-day observations. In particular, both the sea-level relevant volume of the West Antarctic Ice Sheet and the grounding-line position may not differ by more than 10% from their observed values. The remaining 81 representations of the Antarctic Ice Sheet, which span the widest possible range of dynamic sensitivity compatible with these criteria, served as initial states for the simulations discussed here.

Climate scenarios. The climate scenarios for our simulations are based on the ECPs¹⁴, which are the extensions of the RCPs^{28,29}. Global mean temperature trajectories were obtained from emulations of the full range of CMIP3 AOGCM responses¹⁵ using MAGICC 6.0¹⁶. The global mean temperature shows a close linear relation to the surface temperature over Antarctica as well as the ocean temperature near the major Antarctic ice shelves. Using the method described in ref. 8, the scaling coefficients were derived and then used to compute the uncertainty distributions for the surface and ocean temperatures under the ECPs. In our simulations of future solid ice discharge, we combined climate and ice-model uncertainty by forcing each of the 81 initial states from the perturbed-physics ensemble with the 33rd, 50th and 66th percentile of the temperature uncertainty distributions. Our results are thus based on a set of 972 simulations. To separate the effect of snowfall on solid ice discharge from the effects of surface warming and enhanced sub-shelf melting, the whole set of simulations was performed for the cases of surface warming only, surface and ocean warming, and surface and ocean

warming including snowfall increase. The dynamic response of the perturbed-physics ensemble to the climate scenarios is further discussed in ref. 24.

Sub-shelf melting. To simulate the main overturning circulation in the sub-ice shelf cavities, which greatly influences the local distribution of basal melting and refreezing, an ocean box model¹⁷ was used. The ocean box model was initialized with recently observed ocean temperatures and salinities¹⁷ near the Ross, Filchner-Ronne and Amery Ice Shelves as well as the shelf attached to Pine Island Glacier, from which we subtracted anomalies of the observational period to 1850 (the first year of the simulations). Sub-shelf melting was then computed from the ocean temperature and salinity provided by the ocean box model as well as changes in ice thickness and thus pressure melting temperature at the underside of the ice shelves. This approach enables the model to capture the wide spread of observed melt rates underneath Antarctic ice shelves¹². Modelled basal melt rates peak near the grounding line, as suggested by observations³⁰.

Blowing snow sublimation and redistribution. Blowing snow sublimation and redistribution might affect the results because it mainly occurs along the coastal margins of Antarctica³¹, where the impact of enhanced snowfall on the ice dynamics is greatest. The increase of relative humidity in the lower atmosphere due to blowing snow leads to an increase in snowfall, especially in the coastal areas where the air is close to saturation³¹. This suggests that the impact on the ice dynamics presented here would be enhanced by blowing snow. However, this is likely to be a higher-order effect because the temporal trends in coastal blowing snow accumulation will be negligible compared to the overall increase in snowfall.

28. van Vuuren, D. *et al.* The representative concentration pathways: an overview. *Clim. Change* **109**, 5–31 (2011).
29. Taylor, K., Stouffer, R. & Meehl, G. An overview of CMIP5 and the experiment design. *Bull. Am. Meteorol. Soc.* **93**, 485–498 (2012).
30. Walker, R. T., Dupont, T. K., Parizek, B. R. & Alley, R. B. Effects of basal-melting distribution on the retreat of ice-shelf grounding lines. *Geophys. Res. Lett.* **35**, L17503, <http://dx.doi.org/10.1029/2008GL034947> (2008).
31. Lenaerts, J. T. M. & van den Broeke, M. R. Modeling drifting snow in Antarctica with a regional climate model: 2. Results. *J. Geophys. Res.* **117**, D05109, <http://dx.doi.org/10.1029/2010JD015419> (2012).

Deep penetration of molten iron into the mantle caused by a morphological instability

Kazuhiko Otsuka¹ & Shun-ichiro Karato¹

The core–mantle boundary of Earth is a region where iron-rich liquids interact with oxides and silicates in the mantle¹. Iron enrichment may occur at the bottom of the mantle, leading to low seismic-wave velocities and high electrical conductivity^{2–5}, but plausible physical processes of iron enrichment have not been suggested. Diffusion-controlled iron enrichment is inefficient because it is too slow⁶, although the diffusion can be fast enough along grain boundaries for some elements⁷. More fundamentally, experimental studies and geophysical observations show that the core is under-saturated with oxygen, implying that the mantle next to the core should be depleted in FeO. Here we show that (Mg,Fe)O in contact with iron-rich liquids leads to a morphological instability, causing blobs of iron-rich liquid to penetrate the oxide. This morphological instability is generated by the chemical potential gradient between two materials when they are not in bulk chemical equilibrium, and should be a common process in Earth's interior. Iron-rich melt could be transported 50 to 100 kilometres away from the core–mantle boundary by this mechanism, providing an explanation for the iron-rich regions in the mantle.

Like the lithosphere near Earth's surface, the core–mantle boundary region (CMB) of Earth (and other planets) is a region where major physical and chemical actions occur¹. Some seismological observations suggest the presence of chemical heterogeneity^{2–4,8}. Also, anomalously high conductance in some regions of the D'' layer is inferred from the observed length-of-day variation^{9,10}. The regional variations in electrical conductivity observed by geomagnetic jerks (sudden changes in Earth's magnetic field) correspond to regions of anomalous seismic properties^{5,11}. Iron enrichment in some regions of the D'' layer is a plausible explanation of these observations.

However, explaining the iron enrichment is difficult for several reasons. In addition to the difficulties with diffusion-controlled models (because diffusion is so slow), the capillary mechanism of infiltration applies only to a penetration of about 100 m into the mantle or less, owing to the influence of gravity¹². Iron-rich core materials may infiltrate into the mantle along the pressure gradient caused by the dynamic topography at the CMB¹³. However, the degree of melt penetration by this mechanism is controlled by the amplitude of dynamic topography, which is in turn controlled by the viscosity of the D'' layer. If we use the viscosity of about 10^{18} Pa s for the D'' layer¹⁴, the extent of iron penetration for this mechanism is less than a metre, too small to cause any appreciable effects.

Here we report the experimental observations of penetration of iron-rich metallic liquid blobs into the single crystals of (Mg,Fe)O through the morphological instability. The penetration depth of iron-rich blobs observed in these experiments far exceeds the penetration depth attributable to a simple diffusion-controlled model or the other mechanisms discussed above (the capillary mechanism and dynamic topography). Hence, this morphological-instability process is more likely to explain the iron enrichment inferred in some regions of the CMB. We describe our experimental observations, interpret the observations in terms of a physical model, and discuss the possible implications of the deep penetration of molten iron-rich blobs for the properties and dynamics of the D'' layer.

We conducted high-pressure and high-temperature experiments using a multi-anvil apparatus in which iron-rich liquid and single crystals of (Mg,Fe)O are in direct contact (see Supplementary Information for details). After annealing, we found that each interface between an (Mg,Fe)O crystal and the molten iron was serrated and the liquid metal had penetrated into the (Mg,Fe)O single crystal to form a layer containing many metal-rich blobs (we call this the metal-rich layer, or MRL) (Fig. 1a). The serrated morphology of the metallic liquid and the (Mg,Fe)O interface is characteristic of the morphological instability. Notably, the morphological instability was not observed at the wall of pure MgO single crystals, indicating that the FeO in (Mg,Fe)O plays an essential part in this.

The chemical composition of matrix (Mg,Fe)O changes gradually over the region of liquid penetration (MRL) such that FeO content increases with the distance from the interface (see Fig. 1b). This means that the chemical equilibrium is established only near the interface, and the bulk of the crystals is out of equilibrium.

The characteristic wavelength of the interface morphology measured along the interface is approximately 1–10 μm (Fig. 2). The least-squares fit with $\lambda = k_m L^m$ (where λ is the instability wavelength, L is the thickness of the MRL and k_m and m are constants) gives $m = 0.5 \pm 0.2$ for Fe–(Mg_{0.45}Fe_{0.55})O and 0.3 ± 0.3 for Fe–(Mg_{0.75}Fe_{0.25})O.

The thickness of the MRL increases with annealing time, whereas their migration velocity decreases with time (Supplementary Information). The least-squares fit with $L = k_n t^n$ (where t is duration of experiments and k_n and n are constants) gives $n = 0.5 \pm 0.2$. Such a relationship is consistent with a model of MRL growth (see below). Consequently, we may define an effective diffusion coefficient corresponding to the extent of melt migration. The effective diffusivity D_{MRL} was calculated using the equation $D_{\text{MRL}} = L^2/t$. Importantly, transcrystalline melt migration is a much more efficient mechanism of chemical transport than the conventional Fe–Mg interdiffusion¹⁵ under most of the conditions investigated.

A morphological instability similar to the one observed in this study has been documented in many systems where two materials sharing one component (FeO in our case) are in contact but chemical equilibrium is attained only near the interface¹⁶. The concentration gradient of the common component provides the driving force for this instability. The characteristic wavelength at which the instability grows fastest is given by¹⁶:

$$\lambda = 2\pi\sqrt{3\Gamma C_{\text{eq}}^{\text{S}}/G} \quad (1)$$

where $\Gamma = \gamma\Omega/RT$ is the capillarity length, C_{eq}^{S} is the equilibrium FeO concentration in solid (Mg,Fe)O and G is the gradient of the FeO concentration (where γ is the liquid–solid interfacial energy, Ω is liquid molar volume and R is the gas constant). Also, the timescale on which the instability grows is given by $\tau \approx \lambda^2/4\pi^2 D$, where D is the Fe–Mg interdiffusion coefficient¹⁶.

The elongated fingers formed at the interface are eventually pinched off (as a result of the surface tension) to produce isolated melt inclusions

¹Yale University, Department of Geology and Geophysics, 210 Whitney Avenue, New Haven, Connecticut 06511, USA.

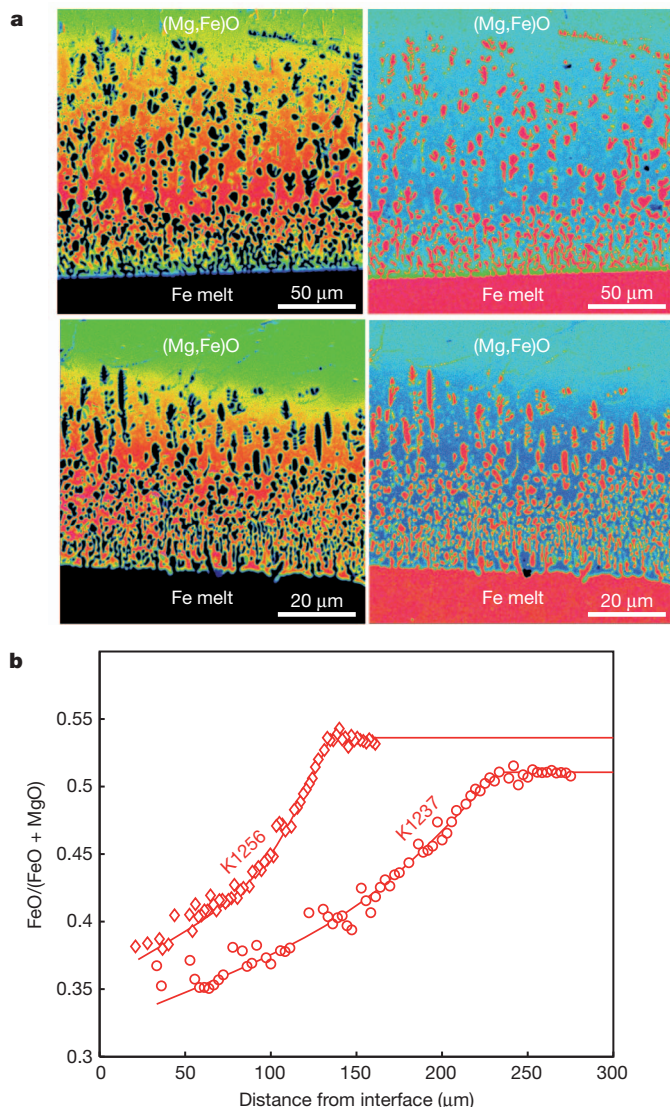


Figure 1 | Distribution of Mg and Fe in the annealed couples of molten Fe and solid (Mg,Fe)O. **a**, Mapping of Mg concentration (left panels) and Fe concentration (right panels) in molten Fe and solid (Mg_{0.45}Fe_{0.55})O annealed at 2,123 K for 60 s (bottom panels, run number K1234), and in molten Fe and solid (Mg_{0.45}Fe_{0.55})O annealed at 2,123 K for 300 s (top panels, run number K1237). In left panels, red corresponds to high Mg concentration and green corresponds to low Mg concentration. In right panels, red corresponds to high Fe concentration and blue corresponds to low Fe concentration. **b**, Typical iron contents—FeO/(FeO + MgO) in molar ratios—in (Mg,Fe)O over the region of transcrystalline migration of iron-rich liquid inclusions as a function of distance from the melt and solid interface.

(blobs) in the (Mg,Fe)O matrix. The isolated blobs will consume FeO from (Mg,Fe)O at the leading edge, while excess FeO will be precipitated at the another edge. In this way, blobs migrate while they re-establish the gradient of FeO that was initially defined by the degree of disequilibrium and the diffusion coefficients of the relevant species. The analysis summarized in the Supplementary Information shows that the gradient in FeO concentration is approximately given by:

$$G \equiv \frac{dC}{dx} \approx \frac{\Delta C}{L} = \frac{C_{\infty}^s - C_{eq}^s}{L}$$

where C is the concentration of FeO, x is the distance measured from the interface, C_{∞}^s is the FeO concentration in (Mg,Fe)O far from the interface, and C_{eq}^s is the FeO concentration in (Mg,Fe)O that will be in equilibrium with the molten iron. Consequently, the growth of the MRL

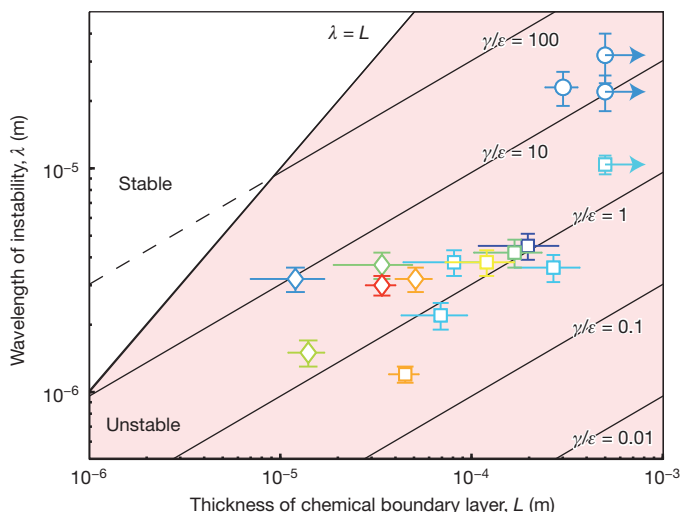


Figure 2 | Instability wavelength λ plotted against thickness of chemical boundary layer L . Squares, Fe-(Mg_{0.45}Fe_{0.55})O in MgO capsule; diamonds, Fe-(Mg_{0.75}Fe_{0.25})O in MgO capsule; and circle, MoO₂-(Mg_{0.75}Fe_{0.25})O in Pt/Mo double capsule. Symbol colour indicates experimental temperature, for example from 1,973 K (dark blue) to 2,473 K (red). Arrows pointing right indicate that only the minimum values of the thickness of the chemical boundary layer are constrained. The stability limit of the interface is given here by $\lambda = L$. In the unstable regime, the relation between instability wavelength and the thickness of the chemical boundary layer was estimated using $\lambda = 2\pi\sqrt{3LF/\epsilon} (\equiv \lambda_{MS})$, where λ_{MS} is the length of the Mullins–Sekerka instability at temperature 2,273 K and pressure 12.5 GPa with the range of γ/ϵ values from 0.01 to 100. Error bars (both horizontal and vertical) indicate one standard deviation.

follows $dL/dt = A\Delta C/L$, where A is a constant that depends on the mechanism of melt blob migration. Therefore the growth of the MRL is described by:

$$L = \sqrt{A\Delta Ct} = \sqrt{D_{MRL}t} \quad (2)$$

where $D_{MRL} (= A\Delta C)$ is the effective diffusion coefficient.

Our experimental observations also show that D_{MRL} is strongly dependent on temperature, and therefore we use the relation $D_{MRL} = A_0\Delta C \exp(-E^*/RT)$ to analyse the data (Fig. 3). We found that the activation energy E^* is significantly smaller than that for the interdiffusion coefficient^{15,17,18} in (Mg,Fe)O, suggesting that processes other than diffusion control the rate of liquid blob migration. One possibility is control by dissolution–precipitation.

The outer core is predominantly composed of iron-rich molten metal with minor amounts of light elements, including oxygen and silicon¹⁹. The inferred amount of minor light elements such as oxygen in the outer core is significantly smaller than their solubility in the outer core at the present-day CMB in equilibrium with the normal mantle composition²⁰. The degree of supersaturation for (Mg,Fe)O at the base of the mantle is estimated to be $\epsilon \approx 10$. Using a plausible value (of the order of 1 J m⁻²) of the interfacial energy, the morphological instability probably occurs at the CMB with a characteristic wavelength of a few centimetres.

To apply our results to the CMB, we need to evaluate the influence of temperature and pressure on the kinetics of MRL growth, because our experiments were conducted at a pressure significantly lower than the CMB pressure²¹ (around 135 GPa) and at lower temperatures than the temperature at the CMB²² (~3,000–4,000 K). We use homologous temperature scaling: $D_{MRL}(T, P) = D_{MRL}(T/T_m(P))$, where $T_m(P)$ is the pressure-dependent melting temperature. For a reasonable value of supersaturation, $\epsilon \left(\equiv \frac{C_{\infty}^s - C_{eq}^s}{C_{eq}^s} \right) = 10$, we estimate that the thickness of the MRL is about 50 km after a billion years, and 100 km after 4 billion years. We conclude that melt penetration by the morphological

instability in (Mg,Fe)O is capable of transporting iron-rich core components over tens of kilometres at the base of the lower mantle, affecting the physical and chemical properties of this region.

The upward migration of iron-rich liquid has implications for several aspects of core–mantle interactions. The penetration of iron-rich blobs to tens of kilometres from the CMB can easily explain large velocity reductions and the high electrical conductance of some regions in the D'' layer. However, the amplitude of velocity anomalies ($\sim 2\text{--}3\%$) and the depth extent of the large low-velocity province^{1,2} ($\sim 200\text{--}300\text{ km}$) may not be consistent with the iron penetration model: the amplitude of velocity reduction is too small and the thickness is too large. Iron penetration may affect physical properties in more localized regions such as a thin layer at the bottom of the large low-velocity province where the concentration of (Mg,Fe)O is large and in small regions with unusually low velocities (see Fig. 4).

Finally, the liquid iron penetrating into the mantle may account for the isotope signatures of the core materials observed in some of the ocean islands²³. However, processes that could produce such a signature in volcanic rocks erupted at the surface are not well understood. The average density of an iron-rich region is too large for large-scale entrainment to occur by mantle convection²⁴. Some small-scale processes, such as flow-induced material segregation²⁵, would be needed to carry core-affected materials to the surface by a plume. Alternatively, some of the heterogeneities in the D'' region could be attributed to the remnant of the magma ocean²⁶ and the pile-up of subducted materials²⁷.

Some issues remain uncertain and hence require further study. First, in this work we studied coupled iron-rich melt and (Mg,Fe)O. At Earth's CMB, not only (Mg,Fe)O but silicate perovskite or silicate post-perovskite also occur. The penetration depth and the volume fraction of metallic blobs in perovskite (and post-perovskite) will be different in these minerals because of the difference in diffusion coefficient of Fe and the properties that control the blob migration (that is, dissolution–precipitation kinetics). Because iron diffusion in perovskite is much slower than in (Mg,Fe)O (ref. 17), either the density of blobs is lower or the MRL is thinner in perovskite than in (Mg,Fe)O. Consequently, the extent to which iron enrichment occurs at the CMB

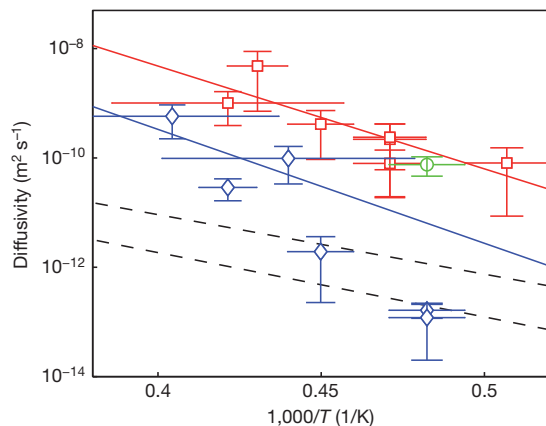


Figure 3 | Effective diffusivity D_{MRL} corresponding to the migration of iron-rich liquid blobs compared with the Fe–Mg interdiffusion coefficient in (Mg,Fe)O. Red squares, Fe–(Mg_{0.45}Fe_{0.55})O in MgO capsule; blue diamonds, Fe–(Mg_{0.75}Fe_{0.25})O in MgO capsule; and green circle, MoO₂–(Mg_{0.75}Fe_{0.25})O in Pt/Mo double capsule. Solid lines indicate the Arrhenius equation $D_{\text{MRL}} = (C_{\infty}^{\text{S}} - C_{\text{eq}}^{\text{S}})A_0 \exp[-(E_{\text{Mg}}X_{\text{Mg}} + E_{\text{Fe}}X_{\text{Fe}})/RT]$ where E is activation energy, and X is the mole fraction, fitted to the data (colours as for data points). Dashed black lines indicate the Fe–Mg interdiffusion coefficients¹⁸ for (Mg_{0.45}Fe_{0.55})O (top line) and (Mg_{0.75}Fe_{0.25})O (bottom line). Vertical error bars indicate one standard deviation. Horizontal error bars indicate the uncertainties in temperature caused by the temperature gradient or by the thermocouple failure (in the latter case, temperature was estimated using the power–temperature calibration).

is probably controlled by the volume fraction of (Mg,Fe)O. When the volume fraction of (Mg,Fe)O exceeds the percolation threshold (about 20%)²⁸, then substantial penetration of molten iron will occur. Consequently, regional variation in the volume fraction of (Mg,Fe)O will control the extent to which iron enrichment occurs at the CMB.

Further studies are needed to investigate the kinetics of metallic liquid penetration in perovskite (and post-perovskite). The CMB in other planets, such as Mercury, is made of olivine and other low-pressure minerals. A dense layer is inferred to exist in the deep mantle of Mercury²⁹ that might be caused by the penetration of iron-rich materials into the mantle. Similar studies of olivine and other low-pressure minerals are also important.

Second, the influence of grain boundaries on liquid blob penetration is unknown. Although iron-rich melt does not completely wet the grain boundaries of silicate minerals in most cases³⁰, complete wetting may occur in (Mg,Fe)O. Gravity will affect the nature of metal penetration if

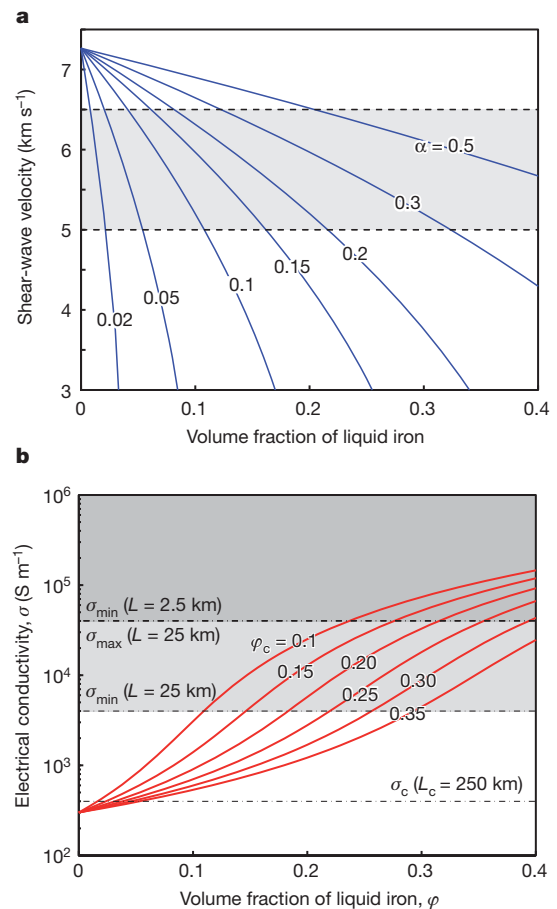


Figure 4 | Influence of liquid iron blobs on geophysically observable properties. **a**, Estimated shear-wave velocity of the silicate/oxide mantle containing the liquid iron. The solid lines are calculated using the oblate spheroid model with aspect ratio α . The shaded region is the range of observed velocities in unusually low-velocity zones. The plausible volume fraction of molten iron is $\sim 0.2\text{--}0.3$ (see Fig. 1a), and with these values, a reduction of seismic wave velocity of $\sim 10\text{--}20\%$ is easily explained with an aspect ratio of 0.2–0.5 (see Fig. 1a). **b**, Electrical conductivity of the silicate/oxide mantle containing the liquid iron. ϕ_c is the volume fraction of iron-rich melt corresponding to the percolation threshold (representative value is about 0.2). σ_{\min} and σ_{\max} are the minimum and maximum conductivities corresponding to an assumed layer thickness L that explain the geophysical observations. Inferred ranges of electrical conductivity of a conductive layer at the base of the mantle depend on the thickness of the metal-rich layer, L . The light- and dark-shaded regions represent conductive layers of thickness 25 km and 2.5 km thick, respectively. Again, geophysically inferred conductivity can be explained by the presence of molten iron with a volume fraction of 0.2–0.3.

the iron-rich melt completely wets the grain boundaries. Further studies of the penetration of metallic liquid blobs into polycrystalline and multi-phase materials will help us to understand core–mantle chemical interactions. Finally, the degree of chemical disequilibrium at the CMB probably reflects the chemical history of the CMB and could be heterogeneous, which would cause the observed lateral heterogeneity in the penetration of molten iron into the mantle.

METHODS SUMMARY

All experiments were performed using the Kawai-type multi-anvil press. The (Mg,Fe)O single crystals with a range of FeO content were synthesized at 1,873 K for around 300 h at 0.1 MPa using a high-temperature controlled-oxygen-fugacity furnace. Single crystals of (Mg,Fe)O were annealed together with molten iron at high pressures and temperatures for a range of time (2 to 3,600 s). After each experiment, the sample was quenched by shutting off the furnace at a given pressure and the distribution of elements (Fe and Mg) in recovered samples was determined using a field-emission-gun electron probe microanalyser (JXA-8530F).

Full Methods and any associated references are available in the online version of the paper.

Received 4 June; accepted 3 October 2012.

- Lay, T., Williams, Q. & Garnero, E. J. The core–mantle boundary layer and deep Earth dynamics. *Nature* **392**, 461–468 (1998).
- Garnero, E. J. A new paradigm for Earth's core–mantle boundary. *Science* **304**, 834–836 (2004).
- Trampert, J., Deschamps, F., Resovsky, J. S. & Yuen, D. A. Probabilistic tomography maps chemical heterogeneities throughout the lower mantle. *Science* **306**, 853–856 (2004).
- Ishii, M. & Tromp, J. Normal mode and free-air gravity constraints on lateral variation in density of Earth's mantle. *Science* **285**, 1231–1236 (1999).
- Nagao, H., Iyemori, T., Higuchi, T. & Araki, T. Lower mantle conductivity anomalies estimated from geomagnetic jerks. *J. Geophys. Res.* **108**, 2254 (2003).
- Stevenson, D. J. Models of the Earth's core. *Science* **214**, 611–619 (1981).
- Hayden, L. A. & Watson, E. B. A diffusion mechanism for core–mantle interaction. *Nature* **450**, 709–711 (2007).
- Masters, G., Laske, G., Bolton, H. & Dziewonski, A. M. in *Earth's Deep Interior* (eds Karato, S. *et al.*) 63–87 (American Geophysical Union, 2000).
- Holme, R. Electromagnetic core–mantle coupling. I. Explaining decadal changes in the length of day. *Geophys. J. Int.* **132**, 176–180 (1998).
- Buffett, B. A. Constraints on magnetic energy and mantle conductivity from the forced nutations of the Earth. *J. Geophys. Res.* **97**, 19581–19597 (1992).
- Ohta, K. *et al.* Electrical conductivities of pyrolytic mantle and MORB materials up to the lowermost mantle conditions. *Earth Planet. Sci. Lett.* **289**, 497–502 (2010).
- Poirier, J.-P. & LeMouél, J.-L. Does infiltration of core material into the lower mantle affect the observed geomagnetic field? *Phys. Earth Planet. Inter.* **73**, 29–37 (1992).
- Kanda, R. V. S. & Stevenson, D. J. Suction mechanism for iron entrainment into the lower mantle. *Geophys. Res. Lett.* **33**, L02310 (2006).
- Nakada, M. & Karato, S. Low viscosity of the bottom of the Earth's mantle inferred from the analysis of Chandler wobble and tidal deformation. *Phys. Earth Planet. Inter.* **192/193**, 68–80 (2012).
- Van Orman, J. A., Fei, Y., Hauri, E. H. & Wang, J. Diffusion in MgO at high pressure: constraints on deformation mechanisms and chemical transport at the core–mantle boundary. *Geophys. Res. Lett.* **30**, doi:10.1029/2002GL016343 (2003).
- Mullins, W. W. & Sekerka, R. F. Stability of a planar interface during solidification of a dilute binary alloy. *J. Appl. Phys.* **35**, 444–451 (1964).
- Holzappel, C., Rubie, D. C., Frost, D. J. & Langenhorst, F. Fe–Mg interdiffusion in (Mg,Fe)SiO₃ perovskite and lower mantle. *Science* **309**, 1707–1710 (2005).
- Yamazaki, D. & Irifune, T. Fe–Mg interdiffusion in magnesiowüstite up to 35 GPa. *Earth Planet. Sci. Lett.* **216**, 301–311 (2003).
- Anderson, O. L. & Isaak, D. G. Another look at the core density deficit of Earth's outer core. *Phys. Earth Planet. Inter.* **131**, 19–27 (2002).
- Frost, D. J. *et al.* Partitioning of oxygen between the Earth's mantle and core. *J. Geophys. Res.* **115**, doi:10.1029/2009JB006302 (2010).
- Dziewonski, A. M. & Anderson, D. L. Preliminary reference Earth model. *Phys. Earth Planet. Inter.* **25**, 297–356 (1981).
- Boehler, R. Temperatures in the Earth's core from melting point measurements of iron at high static pressures. *Nature* **363**, 534–536 (1993).
- Brandon, A. & Walker, R. J. The debate over core–mantle interaction. *Earth Planet. Sci. Lett.* **232**, 211–225 (2005).
- Sleep, N. H. Gradual entrainment of a chemical layer at the base of the mantle by overlying convection. *Geophys. J. R. Astron. Soc.* **95**, 437–447 (1988).
- Leighton, D. & Acrivos, A. The shear-induced migration of particles concentrated suspensions. *J. Fluid Mech.* **181**, 415–439 (1987).
- Labrosse, S., Hernlund, J. W. & Coltice, N. A crystallizing dense magma ocean at the base of the Earth's mantle. *Nature* **450**, 866–869 (2007).
- McNamara, A. K., Garnero, E. & Rost, S. Tracking deep mantle reservoirs with ultra-low velocity zones. *Earth Planet. Sci. Lett.* **299**, 1–9 (2010).
- Stauffer, D. & Aharony, A. *Introduction to Percolation Theory* (Taylor and Francis, 1992).
- Smith, D. E. *et al.* Gravity field and internal structure of Mercury from MESSENGER. *Science* **336**, 214–217 (2012).
- Shannon, M. C. & Agee, C. B. Percolation of core melts at lower mantle conditions. *Science* **280**, 1059–1061 (1998).

Supplementary Information is available in the online version of the paper.

Acknowledgements We are grateful to Z. Du, T. Hiraga, T. Kawazoe, K. Tsuno and T. Yoshino for discussions and J. Eckert, G. Amulele, Z. Du, D. Wang and R. Farla for technical support. We thank M. Zuber, J. Schubert and S. Peale for a discussion on Mercury. B. Buffett provided a useful comment on the magnetic coupling between the core and the mantle. B. Watson provided constructive criticism. This research was financially supported by the National Science Foundation under grant number EAR-0809330.

Author Contributions Experimental studies were conducted by K.O. Theoretical interpretation and geophysical applications were done by both K.O. and S.K. Both authors wrote the paper.

Author Information Reprints and permissions information is available at www.nature.com/reprints. The authors declare no competing financial interests. Readers are welcome to comment on the online version of the paper. Correspondence and requests for materials should be addressed to S.K. (shun-ichiro.karato@yale.edu).

METHODS

Starting materials consisted of single crystals of (Mg,Fe)O and reagent-grade Fe metal or MoO₂ powder. (Mg,Fe)O crystals were synthesized by annealing MgO crystals embedded in the mixtures of MgO and Fe₂O₃ haematite powder in a gas-mixing furnace at temperature of 1,873 K and at an oxygen fugacity of 1 Pa for approximately 300 h as described in ref. 31. The chemical analysis of two sets of recovered samples by a field-emission-gun electron probe micro-analyser (JXA-8530F) showed that the molar Mg/(Mg + Fe) ratio ranged between 0.45 and 0.50 and between 0.75 and 0.80 for each crystal and varied less than 1% over the sample size used for high-pressure, high-temperature experiments. We refer to those compositions as (Mg_{0.45}Fe_{0.55})O and (Mg_{0.75}Fe_{0.25})O, respectively. Those crystals were drilled into cylindrical shapes with thicknesses from 0.5 to 0.8 mm and diameters of 1.1 mm with the cylindrical axis oriented close to the [100] crystallographic direction.

High-pressure and high-temperature experiments were performed using a 1,000-ton Kawai-type multi-anvil apparatus. Tungsten carbide cubes with the truncation edge length of 8 mm or 11 mm were used as second-stage anvils. The octahedral edge-length of the Cr₂O₃-doped MgO pressure medium was either 14 mm or 18 mm for the 14/8 and 18/11 assemblies, respectively. The pressure–load relationship for these cell assemblies were calibrated as described in ref. 32. The cross-section of the cell assembly is shown in Supplementary Fig. 1. For the 14/8 assembly, one single crystal of synthetic ferropericlase was packed with Fe powder in a sample capsule made of single crystals of MgO with inner diameter 1.7 mm and outer diameter 2.6 mm. The sample capsule was directly inserted to a stepped LaCrO₃ furnace. For an 18/11 assembly, one (Mg,Fe)O crystal was packed with MoO₂ powder in an outer Pt and inner Mo double capsule with inner diameter 1.6 mm and outer diameter 2.0 mm. The double capsule was insulated from a stepped graphite furnace by a MgO cylinder. For both assemblies, the cylindrical axis of the sample capsule was vertically aligned with gravity to avoid gravitational rearrangement during annealing. Temperature was monitored with a

W₉₅Re₅–W₇₄Re₂₆ thermocouple with a thermocouple junction placed in contact with one end of the sample capsule without correcting for the effect of pressure on electromotive force. The ceramic parts of the cell assemblies were fired at approximately 1,000 K overnight before assemblage and kept in a vacuum oven at approximately 400 K.

In each experiment, the starting material was brought up to pressure by raising the load at room temperature. Subsequently, temperature was raised by applying current across the furnace at two different heating rates: first at a rate of 50 K min^{−1} up to 1,873 K, close to the eutectic temperature in the Fe–FeO system^{33,34}, and later at a much higher rate, usually 100–200 K min^{−1} (or even higher), up to the target temperature to minimize possible chemical reactions between (Mg,Fe)O and metallic iron during heating. For a 14/8 cell assembly, the resistance of the LaCrO₃ furnace occasionally dropped during heating at around 1,823–1,873 K owing to the leakage of molten Fe from the MgO capsule, which caused very rapid temperature ramp-up at rates of 400–1,000 K min^{−1} in the voltage-controlled heating system. Experimental durations were typically of the order of seconds to hours depending on the speed of melt migration. The samples were then quenched isobarically by shutting off the heating power and subsequently decompressed at room temperature. Experimental conditions are typically pressure 12.5 GPa and temperature 1,973–2,373 K.

31. Otsuka, K., McCammon, C. & Karato, S. Tetrahedral occupancy of ferric iron in (Mg,Fe)O: implications for point defects in the Earth's lower mantle. *Phys. Earth Planet. Inter.* **180**, 179–188 (2010).
32. Otsuka, K. & Karato, S. Control of the water fugacity at high pressures and temperatures: applications to the incorporation mechanisms of water in olivine. *Phys. Earth Planet. Inter.* **189**, 27–33 (2011).
33. Ringwood, A. E. & Hibberson, W. The system Fe–FeO revisited. *Phys. Chem. Miner.* **17**, 313–319 (1990).
34. Seagle, C. T., Heinz, D. L., Campbell, A. J., Prakapenka, V. B. & Wanless, S. T. Melting and thermal expansion in the Fe–FeO system at high pressure. *Earth Planet. Sci. Lett.* **265**, 655–665 (2008).

Nonlinear dendritic integration of sensory and motor input during an active sensing task

Ning-long Xu¹, Mark T. Harnett¹, Stephen R. Williams², Daniel Huber^{1†}, Daniel H. O'Connor^{1†}, Karel Svoboda¹ & Jeffrey C. Magee¹

Active dendrites provide neurons with powerful processing capabilities. However, little is known about the role of neuronal dendrites in behaviourally related circuit computations. Here we report that a novel global dendritic nonlinearity is involved in the integration of sensory and motor information within layer 5 pyramidal neurons during an active sensing behaviour. Layer 5 pyramidal neurons possess elaborate dendritic arborizations that receive functionally distinct inputs, each targeted to spatially separate regions^{1,2}. At the cellular level, coincident input from these segregated pathways initiates regenerative dendritic electrical events that produce bursts of action potential output^{3,4} and circuits featuring this powerful dendritic nonlinearity can implement computations based on input correlation⁵. To examine this *in vivo* we recorded dendritic activity in layer 5 pyramidal neurons in the barrel cortex using two-photon calcium imaging in mice performing an object-localization task. Large-amplitude, global calcium signals were observed throughout the apical tuft dendrites when active touch occurred at particular object locations or whisker angles. Such global calcium signals are produced by dendritic plateau potentials that require both vibrissal sensory input and primary motor cortex activity. These data provide direct evidence of nonlinear dendritic processing of correlated sensory and motor information in the mammalian neocortex during active sensation.

The unique integrative properties of cortical pyramidal neurons enable them to powerfully transform synaptic-input patterns delivered through structured network connectivity⁶. Of particular interest is the ability of pyramidal-neuron dendrites to actively integrate input from spatially segregated and functionally distinct pathways (for example, sensory or motor pathways) when strong temporal correlations exist between these representations^{3–5}. Circuit computations based on active dendritic transformation of different streams of information by pyramidal neurons could underlie a variety of functions that include top-down cortical interactions, associative feature binding and predictive coding^{5–10}. To investigate the role of dendritic integration in behaviourally relevant network computations, we used two-photon microscopy to image dendritic Ca²⁺ signals from distal tuft branches of layer 5 pyramidal neurons of the barrel cortex (S1) labelled with a genetically encoded calcium indicator (GCaMP3)¹¹ through a chronic imaging window while mice performed a task based on vibrissal active touch (Fig. 1a and Methods). Head-fixed mice were trained to move either one row of whiskers or a single whisker to locate an object (Fig. 1a, d, Supplementary Fig. 1 and Methods)¹². In 'go' trials, a vertical pole was presented at one of four positions along the anterior–posterior axis and a correct response was defined as licking for water reward. In 'no-go' trials, the pole was located in a more anterior position and the correct response was to withhold licking. Trained mice touched the pole in the go positions but rarely in the no-go position. Experimental behavioural sessions began after an training period (signal detection statistic (d') > 1.8; Supplementary Fig. 1 and Methods). Whiskers were tracked simultaneously using a high-speed imaging system to quantify whisker-related behavioural variables¹³ (Fig. 1a).

During task performance large-amplitude Ca²⁺ transients were observed in apical tuft dendrites of layer 5 pyramidal neurons (~20–200 μ m below the pial surface; amplitude, $89.9 \pm 42.9\%$ peak $\Delta F/F$; duration, full width at half maximum = 0.48 ± 0.31 s; Fig. 1b, c, Supplementary Fig. 2 and Methods). The dendritic Ca²⁺ signals were primarily observed during the time period when the target pole was present (sampling period; Fig. 1c, d), and less frequently following this period (post-sampling period; Supplementary Fig. 3 and Methods). Quantitative analysis of the whisker–object interactions showed that dendritic Ca²⁺ transients preferentially occurred in trials that contained whisker–object contacts (Fig. 1c–e), with short latency after first touch (40 ± 38 ms, $n = 57$ regions of interest (ROIs) from 4 animals; Fig. 1d). Periods of isolated whisking (non-touch trials) were not associated with detectable tuft Ca²⁺ transients, even though whisking alone is capable of evoking action potentials in layer 5 pyramidal neurons^{14–16}. The touch dependence and short latency from object contact suggest a role for ascending sensory input in the generation of dendritic Ca²⁺ signals. However, passive whisker deflection in anaesthetized mice was ineffective in producing dendritic activation (Supplementary Fig. 4)¹⁷. The above data suggest that active sensation, involving both whisking and object touch, is required for apical tuft dendrite activation.

To examine the spatial extent of behaviourally evoked dendritic Ca²⁺ signals, we imaged multiple apical dendritic branches of a single neuron simultaneously during behavioural sessions (sparse labelling condition, Fig. 2a and Methods). Large Ca²⁺ signals occurred synchronously in all of the imaged branches belonging to the same cell (Fig. 2b, c), such that strong correlations were observed among the branch Ca²⁺ signals (Fig. 2d, f; $R = 0.69 \pm 0.13$ (\pm s.d.), $n = 18$ neurons; Supplementary Fig. 5). However, this was not the case for branches that belonged to different cells (Fig. 2d–f; $R = 0.097 \pm 0.13$, $n = 30$ imaging fields; Supplementary Fig. 5 and Methods). These results indicate that, in contrast to previous experiments using passive sensory stimulation in anaesthetized mice^{17–20} or freely whisking mice²², a salient behavioural event (that is, active touch) produces a strong activation of the entire apical tuft dendrite region. The widespread nature of the Ca²⁺ signals also differs from that expected from more localized NMDA (N-methyl-D-aspartate) spikes²².

To determine the electrophysiological basis of the observed tuft Ca²⁺ signals, we performed *in vivo* targeted whole-cell recordings from apical tuft dendritic branches of layer 5 pyramidal neurons positive for GCaMP3 in the barrel cortex of anaesthetized mice (Fig. 3a, b). We observed electrical events of moderate amplitude (~30 mV) and relatively long durations (~20 ms) during periods of heightened network activity ('unpaired events', 0.26 ± 0.13 Hz; Fig. 3c, d and Supplementary Fig. 6). These unpaired events were not associated with any detectable change in GCaMP3 fluorescence in dendritic regions near the recording pipette (Fig. 3c, d, f). However, prolonged depolarization of the apical tuft dendrite (>15 mV, 500 ms) by current injection converted these electrical events into large-amplitude and long-duration regenerative plateau potentials ('paired events',

¹Howard Hughes Medical Institute, Janelia Farm Research Campus, Ashburn, Virginia 20147, USA. ²Queensland Brain Institute, The University of Queensland, St Lucia, Queensland 4072, Australia.

[†]Present addresses: Department of Basic Neurosciences, University of Geneva, CH-1211 Geneva, Switzerland (D.H.); Department of Neuroscience, Johns Hopkins University School of Medicine, Baltimore, Maryland 21205, USA (D.H.O.).

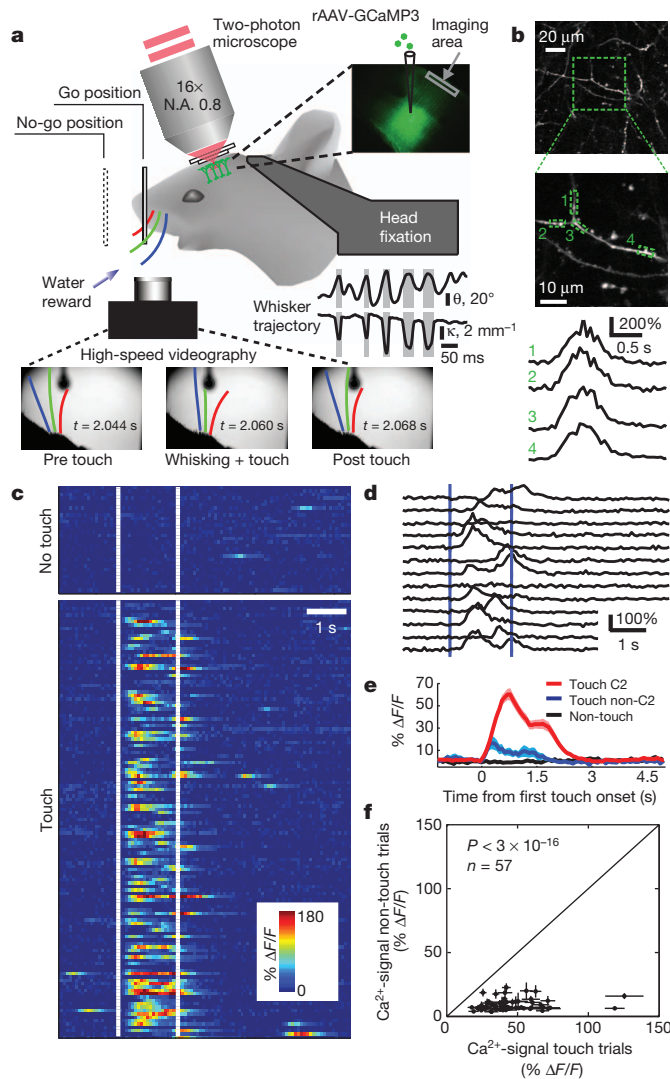


Figure 1 | Active touch evoked large dendritic Ca^{2+} signals in distal tuft branches of layer 5 pyramids. **a**, The experimental set-up; a head-fixed mouse performs a whisker-dependent object-localization task under a microscope. The scanning laser beam (red) is focused on distal dendrites of GCaMP3-labelled neurons (green) through an imaging window. The mouse actively whisks to find the pole and makes a lick response (go) or withholds licking (no-go). Whisker motion was recorded (bottom) and quantified (whisker angle, θ , and curvature change, κ ; grey shows touch). Top left, schematic showing two-photon imaging set-up. Top right, GCaMP3 is expressed in deep layers of barrel cortex. N.A., numerical aperture. **b**, Tuft branches (top and middle panels) and Ca^{2+} signals ($\Delta F/F$; bottom panel) from different sub-regions of a single branch (green dashed boxes). Middle panel is a magnified version of a region of the top panel (outlined by the green box). **c**, Colour raster of Ca^{2+} signals from all trials of a behavioural session sorted into touch (bottom panel) and non-touch trials (top panel). **d**, Touch trials from **c** expanded as traces. Vertical bars in **c** and **d** show sampling period. **e**, Averaged dendritic Ca^{2+} signals aligned to the onset of touch from trials with C2 whisker touch (Touch C2), with touch from whiskers other than C2 (Touch non-C2) and with no touch (Non-touch). **f**, Population data of dendritic Ca^{2+} signals ($\Delta F/F$ amplitude) during whisker sampling time, compared between touch trials and non-touch trials ($n = 57$ dendritic branches, 4 animals). Data in **e** and **f** are mean \pm s.e.m.

2.23 ± 0.55 Hz; Supplementary Fig. 6) that were associated with large dendritic Ca^{2+} signals (Fig. 3 and Supplementary Fig. 6).

Dual dendritic whole-cell recordings from layer 5 pyramidal neurons in acute neocortical slices revealed that apical trunk Ca^{2+} spikes evoked by local current injection decreased in amplitude as they spread back into the tuft dendrites, producing events that were very similar in amplitude, duration and shape to the unpaired events observed *in vivo*

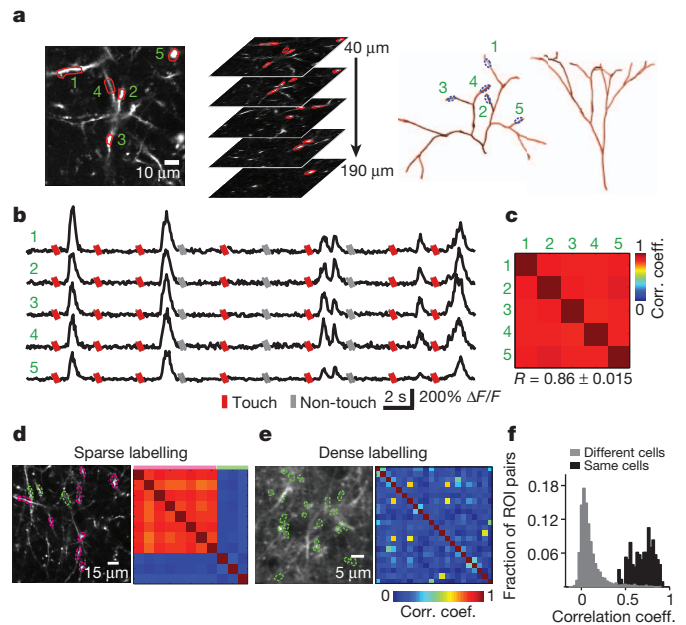


Figure 2 | Global dendritic tuft Ca^{2+} signals during active sensing.

a, Simultaneous Ca^{2+} imaging during behaviour from multiple tuft branches (1–5) of the same cell, identified using three-dimensional reconstruction of imaging stacks. **b**, Ten consecutive trials from the five ROIs indicated in **a**. Signals 0.5 s before to 0.5 s after the sampling period are shown. Vertical bars indicate trial types. **c**, Correlation matrix for the ROIs in **a**. **d**, Ca^{2+} -signal correlation between branches for sparsely labelled imaging fields. ROIs from the same (magenta) and different (green) cells are labelled. **e**, Correlation similar to that in **d**, for a densely labelled imaging field. **f**, Histogram of population data showing distribution of pair-wise correlation for ROIs from multiple cells ($R = 0.097 \pm 0.13$) and for ROIs from single cells ($R = 0.69 \pm 0.13$).

(Fig. 3g and Supplementary Figs 6 and 7). Such unpaired events were not associated with substantial GCaMP-mediated tuft Ca^{2+} signals (Supplementary Fig. 8). Pairing of the back-spread apical trunk Ca^{2+} spikes with simultaneous tuft dendrite depolarization also increased their amplitude and duration to a similar extent to the spikes observed in the *in vivo* recordings (paired events; Fig. 3g and Supplementary Figs 6 and 7). Similar results were obtained when synaptic input was used to produce tuft depolarization (Supplementary Fig. 9).

In addition to increasing the amplitude and duration of individual tuft plateau potentials, the local depolarization also produced multiple or repetitive events during the current-injection period²³ (mean plateau interval: 209 ± 20 ms). Multiple plateau potentials further enhanced the amplitude and duration of the associated tuft Ca^{2+} signals (Supplementary Fig. 6). The time course of the Ca^{2+} signals in the anaesthetized mice covered a similar range to those observed during active sensation (Fig. 3f and Supplementary Fig. 6). Together, these data indicate that tuft dendritic Ca^{2+} signals recorded during active sensation were produced by single or repetitive tuft plateau potentials evoked through an interaction between apical dendrite Ca^{2+} spikes and coincident tuft dendrite depolarization. Importantly, this interaction enhanced the frequency and duration of the apical trunk Ca^{2+} spikes (paired trunk events; Fig. 3g and Supplementary Figs 6, 8 and 9), providing a mechanism by which tuft depolarization can effectively influence action potential output.

What might be the source of apical tuft depolarization during behavioural conditions? It is known that the vibrissal motor cortex (vM1) provides a major excitatory input to layer 1 of barrel cortex^{1,2,24}, and that vM1 neurons code for whisking parameters during active sensing behaviour, with this activity being fed back through vM1 axons to layer 1 of S1 (refs 25–27). We reasoned that the excitatory input from vM1 to the distal dendritic regions of S1 layer 5 pyramidal neurons

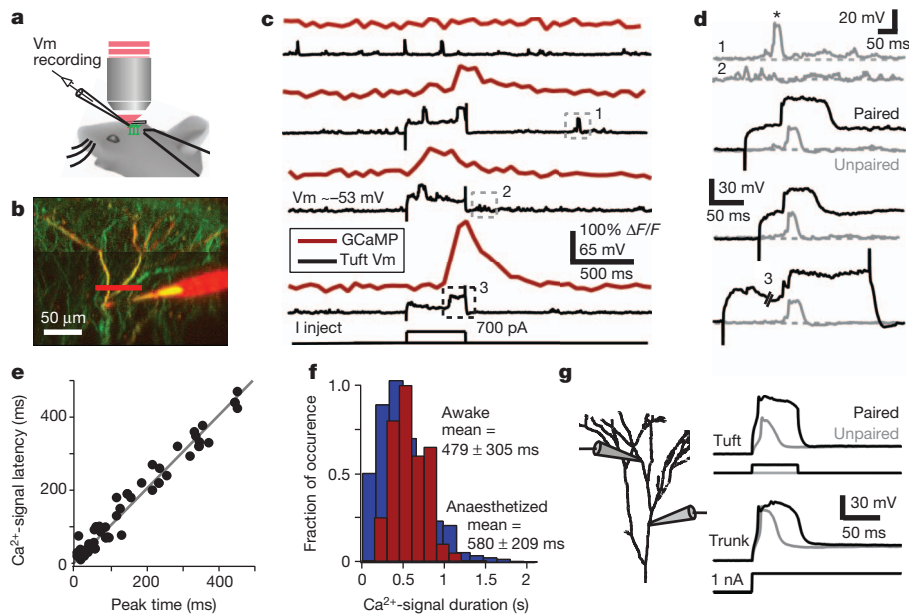


Figure 3 | Dendritic Ca^{2+} signals are produced by tuft plateau potentials. **a**, Schematic of targeted dendritic patch-clamp recording from an anaesthetized mouse *in vivo*. Vm, membrane voltage. **b**, Side projection from a GCaMP3-expressing layer 5 pyramidal neuron. The pipette was filled with Alexa 594. **c**, Ca^{2+} signals (red) and simultaneous intracellular voltage recordings (black). The top records contain only spontaneous dendritic voltage events without dendritic current injection. The three bottom records include 500-ms current injections. I inject, current injection. **d**, Detailed views of the voltage-recording traces in **c** (indicated by the dashed boxes). Top two traces show increased network activity that appears as excitatory postsynaptic potentials (EPSPs) and moderate unpaired events (asterisk). Bottom traces

show that pairing of these spontaneous events (grey traces, unpaired) with tuft depolarization converts them into regenerative plateau potentials (black traces, unpaired). **e**, Tuft plateau potentials are highly correlated in time with Ca^{2+} signals recorded nearby. **f**, Event-duration distributions for plateau-potential-evoked Ca^{2+} signals from anaesthetized mice (red) and for all Ca^{2+} events from awake behaving mice (blue). Occurrence normalized to maximum. **g**, *In vitro* simultaneous dual whole-cell voltage recordings from layer 5 pyramidal neuron tuft and apical trunk dendrites show that unpaired trunk spikes weakly spread into the tuft (grey trace), whereas those paired with local tuft depolarization become regenerative plateau potentials with enhanced amplitudes and durations (black trace).

may interact with ascending sensory input during active touch to produce the observed global distal dendritic nonlinearity. To test this, we silenced vM1 using localized muscimol injection and carried out calcium imaging from the same dendritic branches across several days of behavioural sessions. Dendritic Ca^{2+} signals evoked by active touch during control sessions were largely abolished during sessions when

vM1 was silenced, and recovered in subsequent recording sessions, approximately 24 h after injection (Fig. 4a, b, f and Methods). To control for the specificity of vM1 silencing, we injected the same dose of muscimol to a control site that was the same distance from the imaging window as vM1 (~ 3.2 mm). Imaging from the same dendritic branches showed that whisker touch-evoked dendritic Ca^{2+} signals were still present after muscimol injection to the control site (Fig. 4a, b, g, h).

To determine the effect of vM1 silencing on whisker motion and the strength of sensory drive, we examined both whisking amplitude and the forces on the whiskers (total peak-curvature change ($|\Delta\kappa|$); see Methods) for each experimental condition. We found that vM1 silencing did not reduce the total $|\Delta\kappa|$ compared to the control condition (Fig. 4c), but it greatly diminished dendritic Ca^{2+} signals for the entire range of sensory-input strength (Fig. 4e). Whisking amplitude

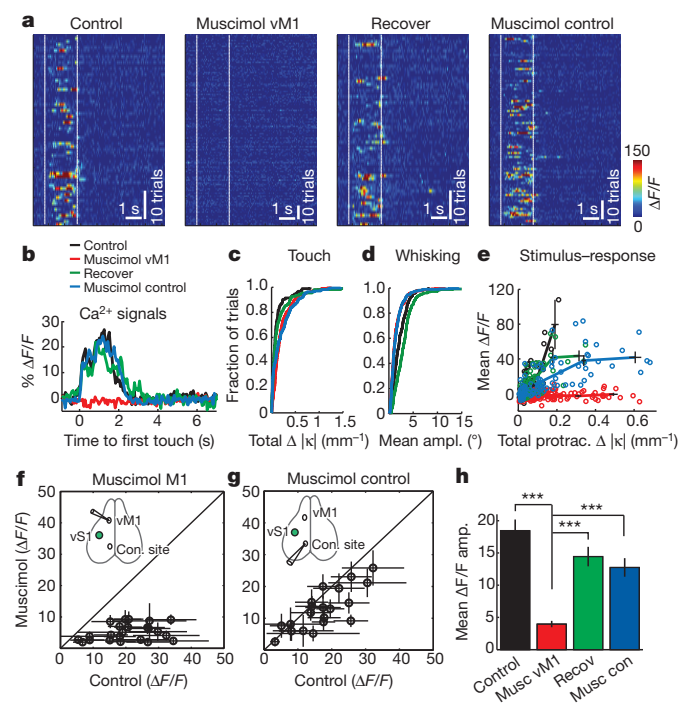


Figure 4 | vM1 silencing abolished touch-evoked dendritic responses.

a, Colour raster of Ca^{2+} signals of touch trials from a dendritic branch imaged across behavioural sessions for four conditions. White vertical lines indicate the sampling time. **b**, Averaged Ca^{2+} signals aligned to the onset of whisker touch from all touch trials under each of the four conditions. **c**, Cumulative distribution of total peak-curvature change (total $|\Delta\kappa|$) for all touch trials under each of the four conditions. **d**, Cumulative distribution of mean whisking amplitude during sampling time for all touch trials under each of the four conditions. **e**, Stimulus-response relationship under each of the four conditions. Mean $\Delta F/F$ during sampling time plotted as a function of total $|\Delta\kappa|$ from protraction touch. Open circles, data from each trial. Solid lines connect binned data points. **f**, Summary of population data comparing Ca^{2+} signals from the same dendritic branches during control sessions and sessions with muscimol injected into vM1 ($n = 23$ branches, 4 animals). **g**, Summary of population data comparing Ca^{2+} signals from the same dendritic branches during control sessions and sessions with muscimol injected into a control site ($n = 20$ branches, 3 animals). **h**, Summary of population data of dendritic Ca^{2+} signals under the four conditions. *** $p < 7 \times 10^{-7}$). Error bars, s.e.m.

during the sampling period was slightly reduced by muscimol injection to either vM1 or the control site (Fig. 4d). However, as dendritic responses were only affected by injection to vM1, this non-specific reduction in whisking amplitude cannot account for the reduced dendritic responses. We also observed that muscimol injection to vM1, but not to the control site, largely eliminated dendritic responses to a second type of whisker stimulation in awake animals (50-ms air puff; Supplementary Figs 4 and 10). These results indicate that distal

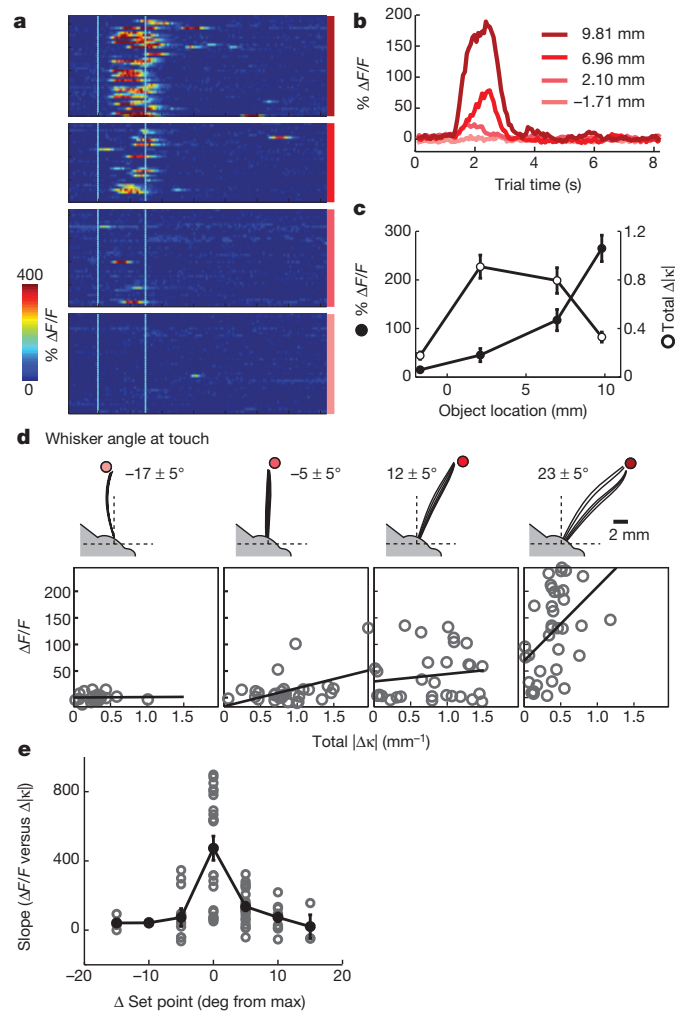


Figure 5 | Whisker-angle dependence and object-location selectivity.

a, Colour raster of dendritic Ca^{2+} signals from an example ROI. Trials are sorted according to object locations (indicated by red vertical bars, as shown in **b**). **b**, Mean $\Delta F/F$ averaged from trials with different object locations. Colours correspond to object locations (measured as the distance from the centre of the whisker pad along the anterior-posterior axis). **c**, Averaged Ca^{2+} signals (filled circles) and total touch induced $|\Delta\kappa|$ (open circles) plotted against object location (object locations as above). **d**, Stimulus-response relationship for dendritic Ca^{2+} signals at different object locations. Top row, projection of five frames of a tracked whisker showing whisker-object contact at different object locations (object locations as above). Whisker images were truncated beyond the object. Whisker set points at touch are indicated. Bottom row, $\Delta F/F$ during sampling time as a function of touch-induced total $|\Delta\kappa|$ for different object locations (whisker angles). Lines are linear regression fits. **e**, The slope of stimulus-response relation (from linear regression as in **d**) from trials binned by whisker set point during touch (bin size = 5°) for population data ($n = 22$ branches from 5 animals with single whisker-object contacts). Whisker set-point bins for all dendritic branches were aligned with the highest slope value set to 0° . The slope value at 0° is significantly higher than that obtained in the same manner from randomly permuted data ($P < 0.0001$; see Methods). Open grey circles indicate data from single dendritic ROIs, filled black circles represent averaging across all ROIs for each set-point bin (mean \pm s.e.m.).

tuft depolarization is required for the behaviourally evoked dendritic activity and that this depolarization is provided by vM1 input to L1. Thus, it seems that distal dendritic plateau potentials are responsible for producing a nonlinear dendritic integration of coordinated sensory and motor information in layer 5 pyramidal neurons during active sensing.

Finally, we observed a pronounced dependence of the dendritic Ca^{2+} signal amplitude on the particular location of the whisker object touch (Fig. 5a, b). This location dependence does not seem to be due to differences in the mean forces generated by whisker touch at the different object locations (Fig. 5c). Furthermore, the relationship between dendritic response and whisker touch was found to vary as a function of the whisker angle during touch (set point: low-pass filtered whisker angle; Methods), even for similar touch force magnitude ranges (Fig. 5d). Grouped data from mice with a single whisker contacting the object at different locations revealed a marked tuning of the stimulus-response slope to particular whisker set-point locations (Fig. 5e). Thus, the variation in dendritic response amplitude at different object locations may be the result of a whisker angle set-point-dependent modulation of the stimulus-response slope or gain. Such an adjustable gain could be produced by whisker set-point-dependent variations in vM1 input to the tuft dendrites of layer 5 pyramidal neurons^{26,27}. These data suggest that a circuit-level computation is implemented in the distal dendrites of layer 5 pyramidal neurons through the integration of correlated sensory and motor information during active touch to produce an object-localization signal.

Our current understanding of dendritic computation during behaviour is limited. Recent recordings from populations of pyramidal-neuron dendrites suggest an active role for dendrites in information processing during the awake state^{21,28}. Here we report that novel long-duration plateau potentials and associated global dendritic Ca^{2+} signals (Figs 2 and 3) are produced in the apical dendrites of individual layer 5 pyramidal neurons when mice perform an active sensing task. The Ca^{2+} -mediated dendritic plateau potentials were probably evoked by correlated perisomatic input from ascending sensory drive (Fig. 1) and layer 1 synaptic inputs from cortico-cortical feedback connections^{1,26} (Fig. 4). This active input processing in pyramidal-neuron dendrites seems to underlie a circuit computation for the tactile localization of salient objects (Fig. 5 and Supplementary Fig. 12). Thus, our results suggest that active nonlinear dendritic integration in layer 5 pyramidal neurons has a central role in the production of a behaviourally related computation in the barrel cortex. Because pyramidal neurons throughout the central nervous system (CNS) are capable of producing related forms of active dendritic integration⁷, the above correlation-based computations may be a common feature of many neuronal circuits^{7-10,29,30}.

METHODS SUMMARY

The GCaMP3 (ref. 11) was expressed using a virus (rAAV-syn-GCaMP3, serotype 2/1, University of Pennsylvania Gene Therapy Program Vector Core), which was injected stereotactically into S1 (20 nl, 750 μm below pia) of adult C57BL/6 male mice (older than postnatal day 60 (P60)) and a circular craniotomy (1.5–2 mm) was made over the left S1. Animals were trained in a head-fixed whisker-based object-localization task. Distal apical dendrites from deep layer neurons were imaged using a custom two-photon microscope during task performance. Images of the whiskers were acquired using a high-speed CMOS camera (EoSense CL, Mikrotrotron) at 500 frames per s.

Full Methods and any associated references are available in the online version of the paper.

Received 12 July 2011; accepted 19 September 2012.

Published online 11 November 2012.

1. Cauller, L. J., Clancy, B. & Connors, B. W. Backward cortical projections to primary somatosensory cortex in rats extend long horizontal axons in layer I. *J. Comp. Neurol.* **390**, 297–310 (1998).
2. Petreanu, L., Mao, T., Sternson, S. M. & Svoboda, K. The subcellular organization of neocortical excitatory connections. *Nature* **457**, 1142–1145 (2009).

3. Larkum, M. E., Zhu, J. J. & Sakmann, B. A new cellular mechanism for coupling inputs arriving at different cortical layers. *Nature* **398**, 338–341 (1999).
4. Williams, S. R. & Stuart, G. J. Dependence of EPSP efficacy on synapse location in neocortical pyramidal neurons. *Science* **295**, 1907–1910 (2002).
5. Takahashi, H. & Magee, J. C. Pathway interactions and synaptic plasticity in the dendritic tuft regions of CA1 pyramidal neurons. *Neuron* **62**, 102–111 (2009).
6. Spruston, N. Pyramidal neurons: dendritic structure and synaptic integration. *Nature Rev. Neurosci.* **9**, 206–221 (2008).
7. Rao, R. P. & Ballard, D. H. Predictive coding in the visual cortex: a functional interpretation of some extra-classical receptive-field effects. *Nature Neurosci.* **2**, 79–87 (1999).
8. Engel, A. K., Fries, P. & Singer, W. Dynamic predictions: oscillations and synchrony in top-down processing. *Nature Rev. Neurosci.* **2**, 704–716 (2001).
9. Shadmehr, R., Smith, M. A. & Krakauer, J. W. Error correction, sensory prediction, and adaptation in motor control. *Annu. Rev. Neurosci.* **33**, 89–108 (2010).
10. Sommer, M. A. & Wurtz, R. H. Brain circuits for the internal monitoring of movements. *Annu. Rev. Neurosci.* **31**, 317–338 (2008).
11. Tian, L. *et al.* Imaging neural activity in worms, flies and mice with improved GCaMP calcium indicators. *Nature Methods* **6**, 875–881 (2009).
12. O'Connor, D. H. *et al.* Vibrissa-based object localization in head-fixed mice. *J. Neurosci.* **30**, 1947–1967 (2010).
13. Clack, N. G. *et al.* Automated tracking of whiskers in videos of head fixed rodents. *PLOS Comput. Biol.* **8**, e1002591 (2012).
14. de Kock, C. P. J. & Sakmann, B. Spiking in primary somatosensory cortex during natural whisking in awake head-restrained rats is cell-type specific. *Proc. Natl Acad. Sci. USA* **106**, 16446–16450 (2009).
15. Curtis, J. C. & Kleinfeld, D. Phase-to-rate transformations encode touch in cortical neurons of a scanning sensorimotor system. *Nature Neurosci.* **12**, 492–501 (2009).
16. O'Connor, D. H., Peron, S. P., Huber, D. & Svoboda, K. Neural activity in barrel cortex underlying vibrissa-based object localization in mice. *Neuron* **67**, 1048–1061 (2010).
17. Helmchen, F., Svoboda, K., Denk, W. & Tank, D. W. *In vivo* dendritic calcium dynamics in deep-layer cortical pyramidal neurons. *Nature Neurosci.* **2**, 989–996 (1999).
18. Jia, H., Rochefort, N. L., Chen, X. & Konnerth, A. Dendritic organization of sensory input to cortical neurons *in vivo*. *Nature* **464**, 1307–1312 (2010).
19. Chen, X., Leischner, U., Rochefort, N. L., Nelken, I. & Konnerth, A. Functional mapping of single spines in cortical neurons *in vivo*. *Nature*, (2011).
20. Varga, Z., Jia, H., Sakmann, B. & Konnerth, A. Dendritic coding of multiple sensory inputs in single cortical neurons *in vivo*. *Proc. Natl Acad. Sci. USA* **108**, 15420–15425 (2011).
21. Gentet, L. J., *et al.* Unique functional properties of somatostatin-expressing GABAergic neurons in mouse barrel cortex. *Nature Neurosci.* **15**, 607–612 (2012).
22. Larkum, M. E., Nevian, T., Sandler, M., Polsky, A. & Schiller, J. Synaptic integration in tuft dendrites of layer 5 pyramidal neurons: a new unifying principle. *Science* **325**, 756–760 (2009).
23. Williams, S. R. Encoding and decoding of dendritic excitation during active states in pyramidal neurons. *J. Neurosci.* **25**, 5894–5902 (2005).
24. Mao, T. *et al.* Long-range neuronal circuits underlying the interaction between sensory and motor cortex. *Neuron* **72**, 111–123 (2011).
25. Huber, D. *et al.* Multiple dynamic representations in the motor cortex during sensorimotor learning. *Nature* **484**, 473–478 (2012).
26. Petreanu, L. *et al.* Activity in motor-sensory projections reveals distributed coding in somatosensation. *Nature* (2012).
27. Hill, D. N., Curtis, J. C., Moore, J. D. & Kleinfeld, D. Primary motor cortex reports efferent control of vibrissa motion on multiple timescales. *Neuron* **72**, 344–356 (2011).
28. Murayama, M. *et al.* Dendritic encoding of sensory stimuli controlled by deep cortical interneurons. *Nature* **457**, 1137–1141 (2009).
29. Kleinfeld, D., Berg, R. W. & O'Connor, S. M. Anatomical loops and their electrical dynamics in relation to whisking by rat. *Somatosens. Mot. Res.* **16**, 69–88 (1999).
30. Dave, A. S. & Margoliash, D. Song replay during sleep and computational rules for sensorimotor vocal learning. *Science* **290**, 812–816 (2000).

Supplementary Information is available in the online version of the paper.

Acknowledgements We thank L. Tian and L. Looger for GCaMP3 constructs; J. Chandrashekar, N. Ryba and C. Zuker for GCaMP3 transgenic mice; W. Denk for comments on the manuscript; N. Clack, G. Myers, T. Zhao, V. Iyer, S. Peron and S. Drukmann for help with software and analysis; and L. Petreanu for help with experimental apparatus. S.R.W. is supported by the Australian research council (FT100100502) and Australian National Health and Medical Research Council (APP1004575).

Author Contributions N.-L.X., K.S. and J.C.M. conceived the project and designed the experiments. N.-L.X. performed all behavioural and chronic imaging experiments, and data analysis. M.T.H. and S.R.W. carried out all *in vitro* experiments. J.C.M. performed *in vivo* dendritic recording experiments. D.H., D.H.O. and K.S. designed behavioural apparatus and whisker data-analysis code. N.-L.X. and J.C.M. wrote the paper with comments from all authors.

Author Information Reprints and permissions information is available at www.nature.com/reprints. The authors declare no competing financial interests. Readers are welcome to comment on the online version of the paper. Correspondence and requests for materials should be addressed to J.C.M. (mageej@janelia.hhmi.org).

METHODS

Chronic imaging window. All procedures were in accordance with protocols approved by the Janelia Farm Research Campus Institutional Animal Care and Use Committee or Queensland Brain Institute Institutional Animal Care and Use Committee. All animals used in awake behaving experiments were adult male (older than P60) C57BL/6J mice (Charles River). During surgery, mice were anaesthetized with isoflurane (~2% by volume in O₂; SurgiVet, Smiths Medical). A craniotomy (~2 mm in diameter) was made over the left barrel cortex. The dura was left intact. Virus-containing solution was slowly injected (20 nl per site, 3 to 4 sites per animal; depth ~700 µm) into the cortex. The injection system was comprised of a pulled glass pipette (broken and bevelled to 25–30 µm (outside diameter); Drummond Scientific, Wiretrol II Capillary Microdispenser) back-filled with mineral oil. A fitted plunger was inserted into the pipette and advanced to displace the contents using a hydraulic manipulator (Narashige, MO-10). Retraction of the plunger was used to load the pipette with virus. The injection pipette was positioned with a Sutter MP-285 manipulator. After injection, the craniotomy was covered with a double-layered glass coverslip^{25,31}, sealed in place with dental acrylic (Jet Repair Acrylic, Lang Dental Manufacturing). The double-layered glass was comprised of a 177–200-µm-thick glass coverslip (diameter ~1.5 mm) attached to a larger glass coverslip (diameter ~5 mm) using ultraviolet cured optical adhesives (Norland Optical Adhesives 61). A titanium head-post with an opening on the left side was attached to the skull with cyanoacrylate glue and dental acrylic to permit head fixation and two-photon imaging over the cranial window. Mice were allowed at least 7 days to recover before water restriction.

Head-fixed mouse behaviour. We designed a head-fixed active object-localization task with multiple target-object locations that require the mice to use active touch to determine the location of a pole, while providing a variety of stimuli to the whiskers (with different object locations). In each trial, the target object (a vertical pole) was presented randomly at either one of multiple 'go' positions or at a single 'no-go' position along the anterior–posterior axis on the right side of the mice (8–9 mm lateralized from the whisker pad). The go position was located within easy reach by whisking, and the location varied from trial to trial on the anterior–posterior axis, within a range of ~18 mm (~5 mm posterior to ~13 mm anterior to the centre of the whisker pad). The no-go position was in an anterior position, but within reach of the whiskers. Mice were trained to report the detection of an object at one of the go positions by licking a water port, and to report an object at the no-go position by withholding licking. Trained mice typically did not touch the object in the anterior no-go location. The trial began with a delay of 0.5–1 s before the pole started to ascend (time of ascent ~0.3 s) into the plane of the whiskers (Fig. 1a). The pole stayed in the whisker field for 1.5–2 s (the 'sampling' period) before starting to descend out of the whisker plane (time of descent ~0.5 s) followed by an 'answer' period (1.5–2 s) during which the mouse responds by licking or withholding licking. Correct no-go responses ('correct rejections') were not rewarded, and incorrect go responses ('misses') were not punished. Licks occurring within the answer period were recorded as go responses. Correct go responses ('hits') were rewarded with a drop of water (~8 µl). The trial was paused for 2 s to give the mouse time to drink. Incorrect no-go responses ('false alarms') led to a 'time-out' period in which the trial was paused for ~2–5 s. Licking during this time-out period triggered additional time-out periods. Licking outside of answer and time-out periods had no consequences.

Behavioural training began after the mice had restricted access to water for at least 7 days (1 ml per day). On days with behavioural sessions, mice generally obtained all water for the day during the session (approximately 1 ml). Food was available ad libitum. The weight and health of the mice were monitored daily. After training, mice learned to respond with licking to whisker-object contact regardless of the position of the pole (Supplementary Fig. 2).

The behavioural apparatus was mounted under a custom two-photon microscope equipped with a high-speed whisker-imaging system, and was controlled by an open-source software system (Z. Mainen and C. Brody) running on MATLAB (Mathworks) communicating with a real-time system (TDT and RTLinux). Imaging sessions started after the mice had completed the initial training and reached a performance criterion of 75% correct responses or $d' > 1.8$ (Supplementary Fig. 2a).

During behaviour, whiskers were illuminated with collimated light using a high-power light-emitting diode (LED) source (960 nm, Roithner) and condenser optics (Thorlabs). Images were acquired through a telecentric lens (×0.36, Edmund Optics) by a high-speed complementary metal-oxide semiconductor (CMOS) camera (EoSense CL, Mikrotrotron) running at 500 frames per s (480 × 352 pixels; resolution, 26 pixels per mm). Image acquisition was controlled by Streampix 3 (Norpix). Synchronization of behavioural trials and two-photon imaging frames was achieved using pulses sent from the real-time behaviour system.

Two-photon calcium imaging from distal dendrites during behaviour. The genetically encoded calcium indicator GCaMP3 (ref. 11) was expressed under the human synapsin 1 promoter after infection with recombinant adeno-associated virus (AAV, serotype 2/1; produced by the University of Pennsylvania Gene Therapy Program Vector Core), which was injected stereotactically to deep layer in barrel cortex. For sparse labelling of layer 5 neurons with GCaMP3, AAV carrying floxed GCaMP3 was co-injected with a diluted AAV carrying Cre recombinase (~1:10,000–1:5,000). This approach reduces the cell density of GCaMP3-expressing neurons without compromising the expression level. Fifteen to twenty days after virus injection, mice began training on the tactile detection task and two-photon imaging sessions began after the criterion of 70% correct responses was reached (5–7 days after the training began). Sessions analysed here occurred between days 25 and 40 post infection.

GCaMP3 was excited at 925 nm (typically 20–40 mW at the back aperture) with a Ti:Sapphire laser (Mai Tai, Spectra Physics) and imaged through a Nikon ×16, 0.8-N.A. objective. Emission light passed through a 565 DCXR dichroic filter (Chroma Technology) and a ET525/70m-2p filter (Chroma Technology) and was detected by a GaAsP photomultiplier tube (10770PB-40, Hamamatsu). Images (512 × 128 pixels) were acquired at ~16 Hz using ScanImage software^{32,33}.

Subregions that contain primarily GCaMP-positive apical dendritic trunks (from layer 5 neurons) at the depth range of 20–400 µm, but not layer 2 or layer 3 somas, were used to image distal dendrite activity. A set of initial trials were usually used to identify imaging fields that show visually identifiable response (corresponding to $\Delta F/F > 10\%$) during the sampling period before a full imaging and behaviour session was initiated. Because of the broad horizontal extension of tuft dendrites, the imaging regions are usually in the proximity of, but not limited to, the barrels corresponding to the present whiskers (determined using intrinsic signal imaging). In our data, 23% of active dendrites show touch responses (we define active dendrites as those that show discernable increase in fluorescence during trials, whether this activity is related to touch or not; see Supplementary Figs 2 and 3). This is an overestimate of the fraction of the total population, as less than 30% (estimated by number of pixels) of all dendrites in a given field of view were active (that is, >70% did not show any detectable change in fluorescence; see Fig. 2e and Supplementary Fig. 2a, b). We did not include in our analysis any fields of view that contained only inactive dendrites (>50% of the examined fields). Thus, although our experiments were not designed to provide an unbiased estimate of the fraction of active dendrites, our sampling strategy suggests ~5% of all layer 5 dendrites showed touch-related Ca²⁺ signals.

In vivo dendritic patch-clamp recording. All animals used in this section of the study were adult male or female (older than P60) GCaMP3-expressing transgenic mice (Thy1, line 10, Charles Zuker, Janelia Farm Research Campus). The animals were surgically prepared as described above for the chronic imaging experiments, except that a half coverslip was used as an optical window and agar (~1%) was applied between the dura–brain surface and the coverslip¹⁷. In addition, a portion of the dura covering the open surface of the neocortex was either surgically removed or partially digested by collagenase treatment (1 mg ml⁻¹ applied to the dura using filter paper for 4 min followed by a 5-min wash with bovine serum albumin (BSA)) before the application of the optical window. Animals were maintained on ~1.5–2% isoflurane saturated with O₂ throughout the surgical and experimental session. The craniotomy was perfused with artificial cerebrospinal fluid (aCSF) (in mM: 125 NaCl, 25 NaHCO₃, 1.25 NaH₂PO₄, 3 KCl, 1.3 CaCl₂, 1.0 MgCl₂, 25 glucose) saturated with 95% O₂ and 5% CO₂. Whole-cell current-clamp recordings were made from tuft dendrites of thick-tufted layer 5 pyramidal neurons using a two-photon targeting method described below and a Dagan BVC-700 amplifier in 'bridge' mode, filtered at 1 kHz and digitized at 50 kHz. Pipettes had an open tip resistance of 7–10 MΩ when filled with (in mM): 134 K-gluconate, 6 KCl, 10 HEPES, 4 NaCl, 0.3 Tris2-GTP, 4 MgATP, 14 phosphocreatine, 0.05 Alexa 594. Pipette capacitance was neutralized just before seal formation and the bridge balance was typically 50–100 MΩ after break-in.

To target the distal dendrites of GCaMP-expressing layer 5 neurons, the anaesthetized mice were mounted to a head-fixation device under a custom two-photon microscope. GCaMP3 was excited at 900 nm (typically ~20 mW at the back aperture) with a Ti:sapphire laser (Chameleon Ultra II, Coherent) and imaged through a Nikon ×16, 0.8-N.A. objective. Emission light passed through a 565 DCXR dichroic filter (Chroma Technology) and a ET525/70m-2p filter (Chroma Technology) and was detected by a GaAsP photomultiplier tube (10770PB-40, Hamamatsu). Images (512 × 128 pixels) were acquired at either 8 or 16 Hz using ScanImage software. Dendrites were selected for recording based on their morphology (large-diameter dendritic trunk and extensive tuft arborization). To ensure the targeting of layer 5 dendrites, the trunk of the dendrite was traced with the two-photon microscope to a depth of at least 400 µm below the cortical surface. The two-photon microscope was used to target the recording pipette (filled with 50 µM Alexa 594) to secondary or tertiary branch points in the apical tuft. Once

in whole-cell mode, resting membrane potential was assessed (range: -55 to -49 mV) and various current steps (from 100 to $1,000$ pA, 500 ms) were injected to evoke plateau potentials or calcium spikes (input resistance = 38 ± 0.3 M Ω ; $n = 6$). During the current injections, Ca^{2+} imaging was performed at ~ 16 Hz over ROIs that contained the recorded dendritic arborization as assessed by red fluorescence emission from the Alexa 594. Unpaired electrical events (events outside current injection periods) were selected for characterization using a threshold-level detection algorithm (threshold = 20 mV above baseline). Unpaired events and plateau potential (threshold = -20 mV) peak time, amplitude and duration, as well as Ca^{2+} -signal latency (interpolated time at which $\Delta F/F$ exceeded noise by 2 s.d.) peak amplitude and duration were automatically determined using a custom detection algorithm (Igor Pro). Event durations are full width at half maximum for Ca^{2+} signals or half width (electrical).

Imaging data analysis. Lateral motion in two-photon images recorded during behaviour was corrected in two steps (Supplementary Fig. 3b). All frames from a behavioural session were first aligned to a target image frame using an efficient cross-correlation-based registration algorithm (single-step discrete fourier transformation (DFT) algorithm)³⁴. The target image was obtained by mean projection of image frames from a trial visually identified to contain still frames. After whole-frame alignment, within-frame motion artefacts were corrected with a line-by-line registration algorithm using the gradient-descent method³⁵.

For the data set from densely labelled dendrites with sparse signals, independent component analysis (ICA) was used to facilitate defining ROIs³⁶. ICA was carried out using a published algorithm, FastICA³⁷, after dimensionality reduction using singular value decomposition on the data matrix from a fraction of trials (typically 50 trials) for each imaging field (each trial contains 128 frames with each frame containing 128×512 pixels). This method generated independent components with hot spots well matching dendritic branch structures that showed transients in sampled trials (Supplementary Fig. 3a, b). The number of independent components was empirically determined such that further increases in their number extracted only noise. ROIs were then manually outlined to include visually distinct hot spots. Because belonging to the same independent component does not necessarily mean belonging to the same dendritic branch or the same cell, multiple ROIs were often defined for the same independent component. This method of ROI selection was corroborated by an alternative approach using time projection of maximum value of pixel intensity above mean, $F_{\text{max}} - F_{\text{mean}}$, where F is the time series of fluorescence intensity from each pixel. For each ROI, $\Delta F/F$ (%) was calculated as $(F - F_0) / F_0 \times 100$, where F_0 is the mode defined from the histogram of F . ROIs with clear spatial cross-talk were visually identified and excluded for analysis. ROIs typically showed two response types, with Ca^{2+} signals occurring either during the whisker sampling epoch (during the presence of the pole; Fig. 1c) or in the post-sampling epoch (after the pole was removed from the whisker field, responses during this period were often less reliable and there was a lack of time locking to tractable behavioural variables; Supplementary Fig. 4).

To estimate the amplitude and duration of individual Ca^{2+} transients during behavioural sessions, we used a simple events-detection approach, and measured the peak $\Delta F/F$ and full width at half maximum of identified Ca^{2+} events. The events detection was based on combined thresholding with both amplitude (>4 standard deviation, estimated using median absolute deviation (MAD)) and rising slope (computed from a span of three frames) of $\Delta F/F$ time series from all trials of a given ROI. Ca^{2+} transients during *in vivo* dendritic patch recording were visually identified, from which the amplitudes and durations were estimated. Ca^{2+} events during behaviour sessions with a full width at half maximum of less than two frames (128 ms) were considered to be noise and were rejected.

For the analysis of active-sensing-related dendritic Ca^{2+} signals (Fig. 1c–e), only ROIs selective to sampling epoch (compared to the post-sampling epoch, $P < 0.05$, Wilcoxon rank-sum test) were used, and ROIs from the same independent components showing strong correlation with each other were treated as redundant, and only one of these was used. For the analysis of signal correlation between branches (Fig. 2a–d and Supplementary Fig. 9), ROIs were included regardless of their trial epoch selectivity, and for a given branch, only one ROI was included. For signal correlation in single cells, ROIs were from sparsely labelled imaging fields in which branches could be traced to single apical trunks, and reconstructed (Fig. 2a) with the custom-written software neuTube³⁸ using imaging stacks (512×512 resolution, $1 \mu\text{m}$ per slice) acquired with a two-photon microscope at the end of each experiment. For signal correlation under densely labelled conditions, branches in a small field of view are likely to originate from many different cells, and ROIs from branches were included regardless of their origin. For the whisker set-point dependence of the stimulus-response relation shown in Fig. 5e, we controlled for potential bias introduced by the alignment of the maximum value to 0° by randomly permuting the data points for each ROI into 4 bins. A paired *t*-test was used to compare the maximum slope values from these randomly permuted data bins with the maximum slope values from the data binned by

set point as in Fig. 5e. The maximum slope value shown in Fig. 5e is significantly different to those obtained from randomly permuted data ($P < 0.0001$).

Details of the method for extracting whisker variables have been described previously^{12,13}. In brief, the whisker angle at the base of the whisker, θ , was extracted from tracked whisker trajectories. A line perpendicular to the midline was defined as $\theta = 0$ and protraction corresponded to increasing angles. Whisking set point is the low-pass (<6 Hz) filtered whisker-angle time series $[\theta(t)]$, capturing mainly temporally averaged whisker positions. The amplitudes of the forces in the follicle are proportional to the curvature of the whisker. We used curvature change ($\Delta\kappa$; Fig. 1a) at a particular location along the whisker ($2\text{--}3$ mm) as a substitute for the mechanical forces acting on the whiskers. Curvature was determined using a second-order polynomial fit to the whisker backbone. Automatic detection of whisker–pole contact was based on thresholding $\Delta\kappa$ with the standard deviation estimated using MAD from frames with a minimal whisker–pole distance for at least three consecutive frames (6 ms; Fig. 1a). The total curvature change during contacts, which was used as a metric for overall touch-evoked sensory drive in a given trial, is computed by summation of the absolute value of peak $\Delta\kappa$ for each contact period. Unless otherwise indicated, data in the text are reported as mean \pm s.d.

Passive whisker stimulation. Compressed air was delivered through a glass pipette pointing towards a single whisker (C2) near the tip. An air puff to the whiskers during the anaesthetized condition is ineffective in evoking any dendritic response (Supplementary Fig. 10). Air puff during the awake condition occasionally evoked dendritic responses. Dendrites often show a distinct response to air puff compared to active touch, with a lower threshold response to active touch (Supplementary Fig. 10d, e). A small fraction (6%) of dendritic branches responded to both air puff and active touch (Supplementary Fig. 10f). To control for the potential spread of air puff to the whisker pad and the animal's face, the whiskers were trimmed at the end of experiments, and the air puff was directed towards the face. The same dendrites that had showed a response to air puff directed at the whiskers did not show any detectable responses to air puff directed at the whisker pad or face (data not shown).

Reversible silencing. To reversibly silence vM1, the GABA (γ -aminobutyric acid) agonist muscimol hydrobromide (Sigma-Aldrich) was dissolved in saline ($5 \mu\text{g} \mu\text{l}^{-1}$), and 60 nl were injected slowly (10 nl per min) to vM1 (1.1 mm lateral to midline and 0.9 mm anterior to Bregma, depth $550\text{--}600 \mu\text{m}$ under the pia) of the ipsilateral side of the S1 imaging window²⁵. For control-site injection, the same dose of muscimol was injected to a control cortical area of the same hemisphere with the distance to the centre of imaging window the same as that for M1 injection (1.1 mm lateral, 3.4 mm posterior to Bregma, depth $550\text{--}600 \mu\text{m}$). The animals were left to recover for 2 h before the behavioural session. To test the possibility that the feedback from motor cortex to S1 is also required for air-puff-evoked dendritic response during the awake condition, dendritic calcium imaging with air-puff stimulation was also conducted on the day of muscimol injection to either M1 or to the control site. M1 silencing led to dropped task performance, but the animal drank normally when water was freely available, suggesting that M1 inactivation did not impair licking function.

In vitro slice preparation and patch-clamp recording. Under control conditions, recordings were made from layer 5B pyramidal neurons visualized in near-coronal brain slices ($300 \mu\text{m}$) of the somatosensory neocortex prepared from Wistar rats ($4\text{--}8$ weeks old). Slices were perfused with a solution of composition (mM): 125 NaCl; 25 NaHCO₃; 3 KCl; 1.25 NaH₂PO₄; 2 (or 1.3) CaCl₂; 1 MgCl₂; 3 Na pyruvic acid and 25 glucose at 35 to 37°C bubbled with 95% O₂ and 5% CO₂. Dual whole-cell recordings were made with identical current-clamp amplifiers (BVC-700A; Dagan Corporation). Pipettes were filled with (mM) 135 K-gluconate; 7 NaCl; 10 HEPES; 2 Na₂-ATP; 0.3 Na-GTP; 2 MgCl₂ and 0.01 Alexa Fluor 568 (Molecular Probes, Eugene) (pH $7.3\text{--}7.4$; KOH) and had open-tip resistance of $8\text{--}12$ MW. Current and voltage signals were low-pass filtered (DC to 10 KHz) and acquired at $30\text{--}50$ KHz. Data were acquired and analysed using AxographX software (AxographX). For each neuron, the apical dendritic recording pipette was positioned as close as possible to the nexus of the apical dendritic trunk (21 ± 9 mm, $n = 13$) and a second pipette positioned at an apical dendritic tuft site under infrared differential interference microscopy. At the termination of each whole-cell recording, the location of recording pipettes and neuronal morphology was examined by fluorescence microscopy and digitally recorded (Retiga EXI, QImaging).

For *in vitro* recordings from GCaMP-expressing layer 5 pyramidal neurons, acute coronal slices containing the barrel and/or somatosensory cortices were prepared from $4\text{--}7$ -week-old male wistar rats (Charles River, OGB-6F experiments) or from $6\text{--}8$ -week-old male wistar rats injected with GCaMP3 virus at $3\text{--}3.5$ weeks of age. Animals were deeply anaesthetized with isoflurane saturated with O₂ and decapitated; the brain was rapidly removed and sectioned at $300 \mu\text{m}$ with a Leica VT1200S vibrating tissue slicer in ice-cold slicing aCSF (in mM:

125 NaCl, 25 NaHCO₃, 1.25 NaH₂PO₄, 3 KCl, 1.0 CaCl₂, 5.0 MgCl₂, 25 glucose, 3 pyruvate, 1 ascorbate) saturated with 95% O₂ and 5% CO₂. Slices recovered at 34 °C for 20–30 min and were subsequently stored at room temperature (20–25 °C) until use. Whole-cell current-clamp recordings were made from thick-tufted layer 5 pyramidal-neuron distal apical trunks or primary tuft dendrites using conventional dot optics with a Dagan BVC-700 amplifier in 'bridge' mode, filtered at 1–5 kHz and digitized at 50 kHz. Experiments were performed at 34–37 °C in aCSF containing (in mM): 125 NaCl, 25 NaHCO₃, 1.25 NaH₂PO₄, 3 KCl, 1.3 CaCl₂, 1.0 MgCl₂, 25 glucose, 3 pyruvate, 1 ascorbate. Pipettes had an open tip resistance of 4–6 MΩ when filled with (in mM): 134 K-gluconate, 6 KCl, 10 HEPES, 4 NaCl, 0.3 TrisGTP, 4 Mg₂ATP, 14 phosphocreatine, 0.05 Alexa 594. After pipette capacitance neutralization and bridge balance (typically between 12 and 24 MΩ after break-in, experiments were terminated if series resistance (Rs) exceeded 40 MΩ) current steps were injected to characterize basic response properties. Dendrites were only accepted for recording if they exhibited prominent h-current sag (H-sag; 40–80%), a resting membrane voltage of more negative than –53 mV, and a short-latency, rapidly rising voltage spike that crossed 0 mV in response to large depolarizing current injection ('plateau potentials' or 'calcium spikes', rheobase of 0.8 to 2.0 nA). All patched dendrites were confirmed to originate from intact somas in layer 5. Synaptic stimulation was carried out in the presence of 2.5 μM GABA_A (SR95531) with a bipolar stimulating electrode placed in layer 1 (~50–100 μm below the pia and ~200–400 μm lateral to the dendritic patch pipette). Each synaptic stimulation experiment imaged at least two separate branches to confirm widespread back-propagation of the plateau potential.

In vitro two-photon imaging and uncaging. Two-photon imaging and uncaging was carried out using a dual galvanometer-based scanning system (Prairie Technologies) coupled with two pulsed, ultra-fast Ti:sapphire lasers (Chameleon Ultra II, Coherent) with their intensity controlled separately by two electro-optical modulators (Conoptics). Alexa 594 was excited at 880 nm to visualize morphology while OGB-6F (100 μM) and GCaMP3 were excited at 92 nm with line-scans through dendrites of interest at high magnification with dwell times of 8–12 μs

at 150–500 Hz. GCaMP3 and OGB-6F signals are expressed as $\Delta F/F$ (%) (calculated as $((F - F_{\text{baseline}}) / F_{\text{baseline}}) \times 100$). Between 3 and 12 individual line-scans were averaged for each condition. Care was taken to collect data only from dendrites that were at least 30 μm (and up to 150 μm) below the surface of the slice that were not prematurely cut off before termination: we consistently observed morphological abnormalities and significantly higher resting $\Delta F/F$ along with substantial plateau-evoked GCaMP or OGB-6F signals in branches that did not meet these criteria (data not shown), presumably owing to the effects of structural damage on their electrotonic architecture. Branches were anatomically defined as incrementing from 0° at the apical trunk. For fast, multi-site glutamate uncaging, 10 mM MNI-glutamate or 1–5 mM RUBI-glutamate (Tocris; dissolved in aCSF) was delivered via pressure ejection through a specially designed puffer pipette to the surface of the slice while focused 720-nm (MNI) or 800-nm (RUBI) laser light was rapidly directed to a sequence of pre-selected points near spine heads (10–20 points over 20–30 μm, 0.2 ms dwell time, 0.1 ms move time).

31. Komiyama, T. *et al.* Learning-related fine-scale specificity imaged in motor cortex circuits of behaving mice. *Nature* **464**, 1182–1186 (2010).
32. Pologruto, T. A., Sabatini, B. L. & Svoboda, K. ScanImage: flexible software for operating laser scanning microscopes. *Biomed. Eng. Online* **2**, 13 (2003).
33. Iyer, V. *et al.* ScanImage for in vivo laser scanning microscopy Program No. 485.2. 2009 Neuroscience Meeting Planner (Society for Neuroscience, 2009).
34. Guizar-Sicairos, M., Thurman, S. T. & Fienup, J. R. Efficient subpixel image registration algorithms. *Opt. Lett.* **33**, 156–158 (2008).
35. Greenberg, D. S. & Kerr, J. N. D. Automated correction of fast motion artifacts for two-photon imaging of awake animals. *J. Neurosci. Methods* **176**, 1–15 (2009).
36. Mukamel, E. A., Nimmerjahn, A. & Schnitzer, M. J. Automated analysis of cellular signals from large-scale calcium imaging data. *Neuron* **63**, 747–760 (2009).
37. Hyvärinen, A. & Oja, E. Independent component analysis: algorithms and applications. *Neural Netw.* **13**, 411–430 (2000).
38. Zhao, T. *et al.* Automated reconstruction of neuronal morphology based on local geometrical and global structural models. *Neuroinformatics* **9**, 247–261 (2011).

Interleukin receptor activates a MYD88–ARNO–ARF6 cascade to disrupt vascular stability

Wei-quan Zhu^{1,2*}, Nyall R. London^{1,2,3*}, Christopher C. Gibson^{2,4*}, Chadwick T. Davis^{2,5}, Zongzhong Tong⁶, Lise K. Sorensen², Dallas S. Shi^{2,5}, Jinping Guo^{1,2,7}, Matthew C. P. Smith^{1,2,3}, Allie H. Grossmann^{2,8}, Kirk R. Thomas^{1,2} & Dean Y. Li^{1,2,3,9,10}

The innate immune response is essential for combating infectious disease. Macrophages and other cells respond to infection by releasing cytokines, such as interleukin-1 β (IL-1 β), which in turn activate a well-described, myeloid-differentiation factor 88 (MYD88)-mediated, nuclear factor- κ B (NF- κ B)-dependent transcriptional pathway that results in inflammatory-cell activation and recruitment^{1–4}. Endothelial cells, which usually serve as a barrier to the movement of inflammatory cells out of the blood and into tissue, are also critical mediators of the inflammatory response^{5,6}. Paradoxically, the cytokines vital to a successful immune defence also have disruptive effects on endothelial cell–cell interactions and can trigger degradation of barrier function and dissociation of tissue architecture^{7–9}. The mechanism of this barrier dissolution and its relationship to the canonical NF- κ B pathway remain poorly defined. Here we show that the direct, immediate and disruptive effects of IL-1 β on endothelial stability in a human *in vitro* cell model are NF- κ B independent and are instead the result of signalling through the small GTPase ADP-ribosylation factor 6 (ARF6) and its activator ARF nucleotide binding site opener (ARNO; also known as CYTH2). Moreover, we show that ARNO binds directly to the adaptor protein MYD88, and thus propose MYD88–ARNO–ARF6 as a proximal IL-1 β signalling pathway distinct from that mediated by NF- κ B. Finally, we show that SecinH3, an inhibitor of ARF guanine nucleotide-exchange factors such as ARNO, enhances vascular stability and significantly improves outcomes in animal models of inflammatory arthritis and acute inflammation.

A defining characteristic of the cytokine-induced inflammatory response is the destabilization of endothelial barriers resulting in vascular permeability^{7–9}. To dissect the pathway(s) involved in this tissue disruption, we treated cultured monolayers of human dermal microvascular endothelial cells (HMVEC-d) with IL-1 β , and detected an increase in endothelial permeability within 15 min (Fig. 1a). The canonical IL-1 β pathway involves ligand-stimulated activation of interleukin-1 receptor (IL-1R), which recruits MYD88 to its cytoplasmic tail¹⁰. The subsequent signalling cascade through IRAK1 results in the phosphorylation of I κ B- α by the I κ B kinase (IKK) complex, leading to translocation of NF- κ B to the nucleus and the eventual transcription of target genes that promote inflammatory-cell responses^{3,4} (Supplementary Fig. 1). To test the involvement of this pathway in IL-1 β -induced vascular permeability, cells were treated with the IKK inhibitor SC-514 (ref. 11). Although SC-514 prevented IL-1 β -induced nuclear localization of NF- κ B, it was unable to rescue either IL-1 β -induced permeability or disruption of vascular endothelial (VE)-cadherin surface localization (Fig. 1b, c and Supplementary Fig. 2a–c). We also wondered whether IL-1 β -induced vascular permeability required other known MYD88-mediated downstream signalling mechanisms,

including ERK1/2, p38 and JNK (also known as MAPK3/MAPK1, MAPK14 and MAPK8, respectively)^{12,13}. Although ERK1/2, p38 and JNK were activated by IL-1 β stimulation of endothelial cells, small-molecule inhibitors of each of these pathways were unable to prevent IL-1 β -induced vascular permeability or IL-1 β -induced disruption of VE-cadherin cell-surface localization (Supplementary Fig. 2d–h). Although specific NF- κ B targets, such as VEGFA, COX-2 (also known as PTGS2) and the COX-2 product prostaglandin E₂ are modulated by IL-1 β , their activation had no effect on IL-1 β -induced endothelial permeability^{3,14,15} (Supplementary Fig. 3a–e). Finally, treatment with actinomycin D or cycloheximide effectively inhibited transcription or translation, respectively, of NF- κ B targets, but did not blunt IL-1 β -induced permeability (Fig. 1d and Supplementary Fig. 3f, g). These data strongly support a role for the immediate and destabilizing effects of IL-1 β on endothelial stability through signalling pathways independent of NF- κ B, transcription and translation.

IL-1 β can disrupt VE-cadherin cell-surface localization by promoting endocytic internalization⁹. We proposed that IL-1 β might use ARF6, a known regulator of adherens protein localization^{16,17}. Indeed, IL-1 β activated ARF6 in HMVEC-d within 1 min, a response accompanied by increased endocytosis of VE-cadherin within 5 min and an increase in monolayer permeability within 15 min (Fig. 1a, e and Supplementary Fig. 4a, b). IL-1 β treatment did not affect total VE-cadherin messenger RNA or protein levels (Supplementary Fig. 4c, d). Adenoviral-mediated overexpression of constitutively active ARF6 (ARF6(Q67L))¹⁸ elicited a dose-dependent increase in endothelial permeability, as well as a disruption of VE-cadherin cell-surface localization (Fig. 1f, g and Supplementary Fig. 4e, f). A similar dose-dependent loss of total VE-cadherin was also observed, probably through internalization and subsequent degradation (Supplementary Fig. 4g). Interestingly, at lower doses of adenovirus at which permeability was still induced, loss of total VE-cadherin was not observed, but a dose-dependent loss of cell-surface VE-cadherin occurred (Fig. 1f–h and Supplementary Fig. 4g). Moreover, short interfering RNA (siRNA) knockdown of *ARF6* enhanced VE-cadherin cell-surface localization and prevented both IL-1 β -induced disruption of VE-cadherin and IL-1 β -induced endothelial permeability (Fig. 1i–k and Supplementary Fig. 4h, i). Collectively, these data link ARF6 as a critical regulator of VE-cadherin trafficking by controlling cell-surface localization and the immediate and disruptive effects of IL-1 β -induced vascular permeability.

The ARF6 activation state is decreased through interaction with GTPase-activating proteins (GAPs) and increased through interaction with guanine nucleotide-exchange factors (GEFs). Consistent with this, treatment of endothelial cells with the ARF-GAP inhibitor QS11 evoked an increase in ARF6–GTP, a decrease in VE-cadherin cell-surface localization and increased permeability (Fig. 2a–d and

¹Department of Medicine, University of Utah, Salt Lake City, Utah 84112, USA. ²Program in Molecular Medicine, University of Utah, Salt Lake City, Utah 84112, USA. ³Department of Oncological Sciences, University of Utah, Salt Lake City, Utah 84112, USA. ⁴Department of Bioengineering, University of Utah, Salt Lake City, Utah 84112, USA. ⁵Department of Human Genetics, University of Utah, Salt Lake City, Utah 84112, USA. ⁶Navigen Inc, Salt Lake City, Utah 84112, USA. ⁷Department of Anatomy, Second Military Medical University, Shanghai 200433, China. ⁸Department of Pathology, University of Utah, Salt Lake City, Utah 84112, USA. ⁹Cardiology Section, VA Salt Lake City Health Care System, Salt Lake City, Utah 84112, USA. ¹⁰The Key Laboratory for Human Disease Gene Study of Sichuan Province, Institute of Laboratory Medicine, Sichuan Academy of Medical Sciences & Sichuan Provincial People's Hospital, Chengdu, Sichuan 610072, China.

*These authors contributed equally to this work.

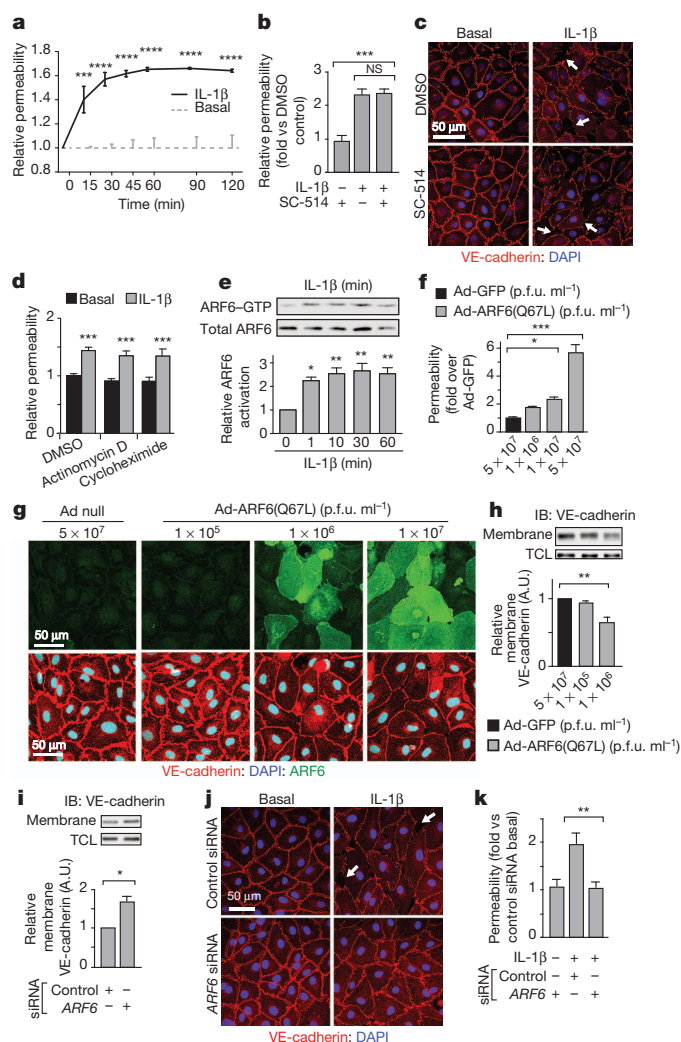


Figure 1 | Immediate effects of IL-1 β are NF- κ B independent and ARF6 dependent. **a–d**, Monolayers of HMVEC-d stimulated with IL-1 β and assayed for permeability to horseradish peroxidase (HRP) over time (**a**), permeability to HRP following 2-h treatment with SC-514 (**b**), immunofluorescent localization of VE-cadherin (**c**) and permeability to HRP after 30-min treatment with actinomycin D or cycloheximide (**d**). **e**, IL-1 β -stimulated HMVEC-d lysates were precipitated with glutathione S-transferase (GST)–GGA3 and immunoblotted for ARF6. **f–i**, HMVEC-d monolayers infected with adenovirus (Ad) containing empty vector (null), green fluorescent protein (GFP) or ARF6(Q67L), showing permeability (**f**) and VE-cadherin localization (**g**) (green denotes ARF6 expression). Membrane fractions from adenoviral-vector-infected (**h**) or ARF6-siRNA-treated (**i**) HMVEC-d were immunoblotted for VE-cadherin. **j**, **k**, ARF6-siRNA-treated HMVEC-d stimulated with IL-1 β , showing VE-cadherin localization (**j**) (arrows denote disrupted VE-cadherin cell-surface localization) and permeability (**k**). A.U., arbitrary unit; DMSO, dimethylsulphoxide; IB, immunoblot; TCL, total cell lysate. *n* \geq 3; error bars denote s.e.m. **P* < 0.05, ***P* < 0.01, ****P* < 0.001, *****P* < 0.0001.

Supplementary Fig. 5a, b)¹⁹. We noted that a class of ARF-GEFs, the cytohesins, is highly expressed in multiple types of endothelial cells (Supplementary Fig. 5c). Accordingly, treatment of HMVEC-d with SecinH3, a cytohesin inhibitor, significantly increased endothelial cell-surface localization of VE-cadherin (Supplementary Fig. 5d–f)²⁰. Notably, SecinH3 inhibited IL-1 β -induced ARF6–GTP, as well as IL-1 β -induced disruption of VE-cadherin cell-surface localization and endothelial permeability (Fig. 2e–g and Supplementary Fig. 5g, h). To determine which GEF might be uniquely involved, we used siRNA to knockdown *CYTH1*, *ARNO* and *CYTH3* (coding for cytohesins 1, 2 and 3, respectively) and *GEP100* (also known as *IQSEC1*) (Supplementary Fig. 6a), and found that only siRNA targeting *ARNO*

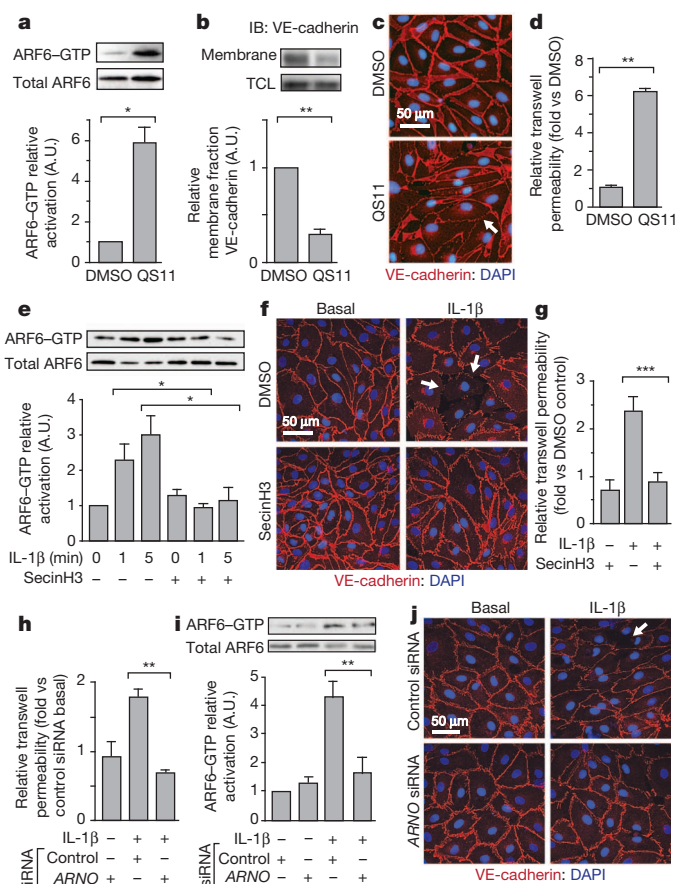


Figure 2 | Inhibition of ARF-GAPs and ARF-GEFs affect ARF6 activation and VE-cadherin localization. **a–d**, HMVEC-d treated with QS11, showing whole-cell lysates precipitated with GST–GGA3 and immunoblotted for ARF6 (**a**), membrane fractions immunoblotted for VE-cadherin (**b**), immunofluorescence for VE-cadherin (red) (**c**) and permeability to HRP (**d**). **e–g**, HMVEC-d treated with IL-1 β and SecinH3, showing immunoblotting for ARF6 (**e**), immunofluorescence for VE-cadherin (**f**) and permeability to HRP (**g**). **h–j**, HMVEC-d treated with anti-ARNO siRNA and stimulated with IL-1 β , showing permeability to HRP (**h**), GST–GGA3 precipitation and ARF6 immunoblotting (**i**) and immunofluorescence of VE-cadherin (**j**). Arrow denotes less cell-surface VE-cadherin. *n* \geq 3; error bars denote s.e.m. **P* < 0.05, ***P* < 0.01, ****P* < 0.001, *****P* < 0.0001.

completely blocked IL-1 β -induced endothelial permeability and phenocopied the knockdown of ARF6 (Fig. 2h and Supplementary Fig. 6b). Furthermore, ARNO siRNA inhibited IL-1 β -induced ARF6–GTP formation, IL-1 β -induced disruption of VE-cadherin cell–cell contacts and IL-1 β -induced internalization of surface VE-cadherin (Fig. 2i, j and Supplementary Fig. 6c, g); all of these effects were rescued by the expression of siRNA-resistant ARNO (Supplementary Fig. 6d–g). In cells treated with ARNO siRNA, viral expression of siRNA-resistant ARNO, but not viral expression of siRNA-resistant ARNO(E156K) (carrying a mutation in the Sec7 domain), rescued the disruption of IL-1 β -induced ARF6–GTP formation and permeability²¹ (Supplementary Fig. 6d, e). These data demonstrate that ARNO is a critical ARF-GEF necessary for IL-1 β -induced activation of ARF6 and subsequent induction of vascular permeability, but does not rule out the role of other GEF family members in similar responses in different cell types or in response to different cytokines.

The signalling components in the NF- κ B pathway downstream of IL-1 β -induced activation of IL-1R are well characterized (Supplementary Fig. 1). Although the inhibition of the NF- κ B pathway at the level of IRAK1 by siRNA did not inhibit IL-1 β -induced ARF6 activation, siRNA knockdown of MYD88 inhibited both IL-1 β -induced permeability and ARF6–GTP activation, suggesting a bifurcation of

IL-1 β -induced signalling at the point of MYD88 (Fig. 3a–c and Supplementary Fig. 7a, b). The proposed bifurcation was further verified by the pharmacological uncoupling of the two pathway arms: although SecinH3 blunted IL-1 β -induced permeability, it did not significantly inhibit IL-1 β -induced NF- κ B nuclear localization or NF- κ B-dependent expression or localization of cell-surface adhesion molecules (Fig. 3d and Supplementary Fig. 7c, d). Furthermore, SecinH3 was unable to inhibit IL-1 β -induced polymorphonuclear leukocyte rolling and adherence under shear stress on an endothelial monolayer (Supplementary Fig. 7e). Mechanistic support for this novel signalling arm was provided by the demonstration of an interaction between MYD88 and ARNO by co-immunoprecipitation in both overexpression and endogenous settings (Fig. 3e, f). Our hypothesis that ARNO is the critical GEF in IL-1 β -induced permeability in endothelial cells was further strengthened by our inability to detect an interaction between MYD88 and other potentially relevant ARF-GEFs including CYTH1, CYTH3 and GEP100 (Supplementary Fig. 7f, g).

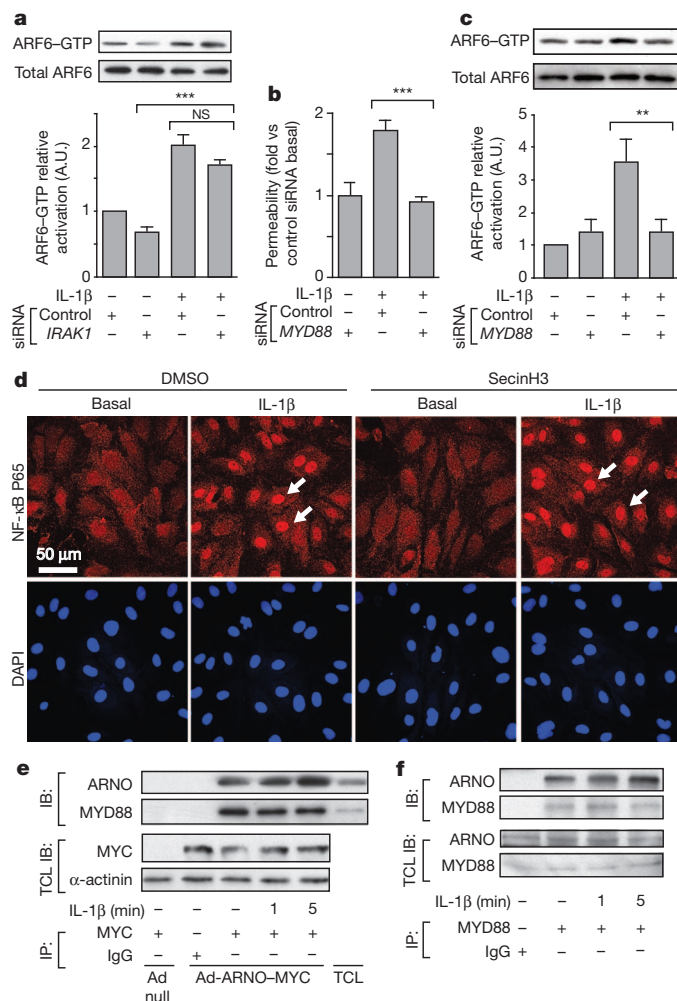


Figure 3 | The immediate IL-1 β -induced permeability pathway diverges at MYD88. **a**, IRAK1-siRNA-treated HMVEC-d, stimulated with IL-1 β , subjected to ARF6-GTP pull-down and immunoblotted for ARF6. **b**, **c**, MYD88-siRNA-treated HMVEC-d stimulated with IL-1 β , showing permeability and ARF6 activation. **d**, NF- κ B p65 (also known as RELA) immunofluorescence in HMVEC-d stimulated with IL-1 β and SecinH3. Arrows denote nuclear localization. **e**, Cell lysates from Ad-ARNO-MYC-infected HMVEC-d immunoprecipitated (IP) with anti-MYC antibodies and immunoblotted with anti-MYD88 antibodies. **f**, Lysates from HMVEC-d immunoprecipitated with anti-MYD88 antibodies and immunoblotted with anti-ARNO antibodies. $n \geq 3$. Error bars denote s.e.m. * $P < 0.05$, ** $P < 0.01$, *** $P < 0.001$.

An effective therapeutic strategy to combat numerous inflammatory conditions is to target pro-inflammatory cytokines proximal to the NF- κ B pathway. However, this strategy can result in undesired pleiotropic effects. We wanted to know whether targeting a single arm in this pathway—the one mediated by ARNO-ARF6—could inhibit acute or chronic inflammation *in vivo* in two animal models of inflammation. The first model we tested was rheumatoid arthritis, a disease characterized by a dysregulated cytokine response causing excessive inflammation and tissue damage and treated therapeutically in humans with the anti-cytokine tumour necrosis factor receptor (TNFR)-Fc fusion protein etanercept (Enbrel)^{22–25}. A standard animal model of arthritis through which a TNFR fusion approach has been proven effective is collagen-induced arthritis (CIA)^{24–26}. Exposure of animals to the cytohesin inhibitor SecinH3 after the onset of CIA reduced vascular permeability in the joints, but had no effect on global cytokine levels at 24 h after treatment initiation (Fig. 4a and Supplementary Fig. 8a, b). In addition, a significant inhibition in the increase in arthritic index, comparable to that achieved by treatment with Enbrel, was observed. The arthritic index is a scoring system determined by the number of digits or joints that are oedematous or erythematous. The significance of our findings was verified by histologic scoring of inflammation, pannus development, cartilage damage and bone damage (Fig. 4c, d). A similar effect of SecinH3 was confirmed in a second model of inflammation, the carrageenan air-pouch model. Six hours after an inflammatory stimulus, a time at which substantial inflammation was induced in the positive control mice, treatment with SecinH3 decreased exudate volume as well as leukocyte concentration in the exudates (Supplementary Fig. 8c, d). Collectively, these data identify MYD88–ARNO–ARF6 as a valid target for inflammatory conditions confirming a relevant role for manipulation of this pathway *in vivo* to modulate inflammatory processes and in the treatment of disease.

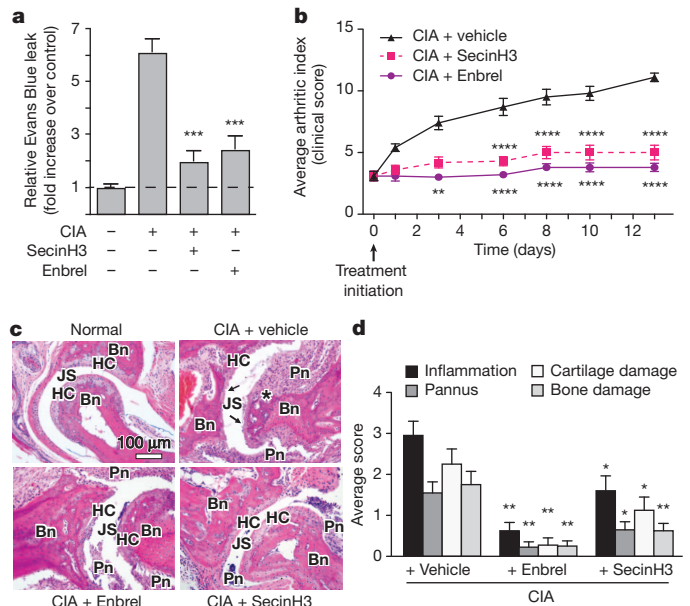


Figure 4 | Inhibition of ARF-GEFs decreases collagen-induced vascular permeability and arthritis in mice. **a**, Arthritis-induced vascular permeability in the joint measured by Evans Blue leak 7 days after treatment initiation in the presence of SecinH3 or Enbrel. $n = 14$ per group. **b**, Chronological arthritic assessment. $n = 10$ per group. Significance values are measured against CIA plus vehicle. **c**, Haematoxylin and eosin staining of sections through joints. Bn, bone; HC, hyaline cartilage; JS, joint space; Pn, inflamed pannus. Asterisk denotes cartilage and bone loss; arrows denote eroded cartilage. **d**, Summary of histological changes of inflammation, pannus, cartilage and bone damage of indicated treatment. Control, $n = 5$; Enbrel and SecinH3, $n = 10$. Error bars denote s.e.m. * $P < 0.05$, ** $P < 0.01$, *** $P < 0.001$, **** $P < 0.0001$ versus disease group.

Chronic inflammation causes tissue destruction through dysregulated cytokine release, inflammatory cell recruitment and vascular permeability; yet each of these mechanisms has critical roles in many physiologic processes, including the immune response^{5,7}. We have identified a novel pathway that uncouples cytokine effects on vascular stability from other critical functions of the canonical NF- κ B transcription program (Supplementary Fig. 1). Our model suggests the potential for inhibition of vascular leak without modulation of immune-cell adhesion or other critical NF- κ B-dependent responses.

The activation of many inflammatory cytokine receptors disrupts cell-cell interactions, precipitating tissue oedema and destruction^{5,7,9,27}. Toll-like receptors and the interleukin receptor also use MYD88, and the mechanism described here may well apply^{3,10}. Interestingly, TNFR1 (also known as TNFRSF1A) does not use MYD88 yet still activates ARF6-GTP after stimulation (Supplementary Fig. 9). Whether ARNO or another ARF-GEF binds directly to TNFR1 or its adaptor protein TRADD is unknown, as is the possibility that ARF-GEF-ARF6-cadherin serves as a common signalling module exploited by multiple cytokines. Although this study focused on the endothelium, the concept of cytokine receptor-ARF-cadherin may also apply to the epithelial barrier, which expresses these constituents and is also compromised by cytokines including IL-1 β ¹⁶.

Inhibition of this novel vascular-stability pathway, which is aimed at enhancing the resilience of the host to the cytokine response, shows effects commensurate to those of class-leading drugs that target cytokines upstream of NF- κ B and seek to blunt the cytokine response of the immune system outright. This approach may be particularly useful in arthritis, as the current medical therapy can render a patient immunocompromised and susceptible to reactivation of infectious disease such as tuberculosis²⁸. Application of these findings to other diseases characterized by excessive acute or chronic inflammatory states, including sepsis, Crohn's disease, ulcerative colitis, scleroderma and psoriasis, should also be considered^{9,29,30}.

METHODS SUMMARY

Transwell permeability. HMVEC-d cells were seeded on 1.0- μ m Costar transwell inserts coated with fibronectin. Cells were grown to confluency and treated with SecinH3 for 3 h or MAPK/NF- κ B/transcription/translation inhibitors for 30 min followed by treatment with 10 ng ml⁻¹ IL-1 β . Alternatively, cells were infected with Ad-GFP or Ad-ARF6(Q67L) for 48 h. siRNA knockdown was performed as described in Supplementary Methods, and cells were treated with IL-1 β 72 h after the second siRNA transfection. Two hours later, HRP was added to the top chamber at a final concentration of 100 μ g ml⁻¹. Medium was removed after 60 min from the lower chamber. For time-course transwell assays and transcription/translation-inhibitor experiments (Fig. 1a, c, d), HRP was added to the insert at the same time as IL-1 β . Transwell inserts were moved to fresh wells after each time point, and the concentration of HRP in the bottom chamber was measured for monolayer permeability. HRP was assessed using media samples obtained from the lower chamber incubated with 0.5 mM of guaiacol and 0.6 mM H₂O₂. Spectrophotometric analysis of absorbance at 490 nm provided a quantitative evaluation of the amount of HRP that crossed the membrane. Data are presented as mean \pm s.e.m. of at least three independent experiments performed in quadruplicate.

A detailed description of all methods is provided in Supplementary Information.

Received 9 December 2011; accepted 19 September 2012.

Published online 11 November 2012.

- Li, Q. & Verma, I. M. NF- κ B regulation in the immune system. *Nature Rev. Immunol.* **2**, 725–734 (2002).
- Collins, T. et al. Transcriptional regulation of endothelial cell adhesion molecules: NF- κ B and cytokine-inducible enhancers. *FASEB J.* **9**, 899–909 (1995).
- Liu, S. F. & Malik, A. B. NF- κ B activation as a pathological mechanism of septic shock and inflammation. *Am. J. Physiol. Lung Cell. Mol. Physiol.* **290**, L622–L645 (2006).
- Rothwarf, D. M. & Karin, M. The NF- κ B activation pathway: a paradigm in information transfer from membrane to nucleus. *Sci. STKE* **1999**, RE1 (1999).
- Pober, J. S. & Sessa, W. C. Evolving functions of endothelial cells in inflammation. *Nature Rev. Immunol.* **7**, 803–815 (2007).
- Muller, W. A. Leukocyte-endothelial cell interactions in the inflammatory response. *Lab. Invest.* **82**, 521–533 (2002).

- Royall, J. A. et al. Tumor necrosis factor and interleukin 1 alpha increase vascular endothelial permeability. *Am. J. Physiol. Lung Cell. Mol. Physiol.* **257**, L399–L410 (1989).
- West, X. Z. et al. Oxidative stress induces angiogenesis by activating TLR2 with novel endogenous ligands. *Nature* **467**, 972–976 (2010).
- London, N. R. et al. Targeting Robo4-dependent Slt1 signaling to survive the cytokine storm in sepsis and influenza. *Sci. Transl. Med.* **2**, 23ra19 (2010).
- Zhu, J. & Mohan, C. Toll-like receptor signaling pathways—therapeutic opportunities. *Mediators Inflamm.* **2010**, 781235 (2010).
- Kishore, N. et al. A selective IKK-2 inhibitor blocks NF- κ B-dependent gene expression in interleukin-1 β -stimulated synovial fibroblasts. *J. Biol. Chem.* **278**, 32861–32871 (2003).
- Matthews, J. S. & O'Neill, L. A. Distinct roles for p42/p44 and p38 mitogen-activated protein kinases in the induction of IL-2 by IL-1. *Cytokine* **11**, 643–655 (1999).
- Martin, M. U. & Wesche, H. Summary and comparison of the signaling mechanisms of the Toll/interleukin-1 receptor family. *Biochim. Biophys. Acta* **1592**, 265–280 (2002).
- Kaltschmidt, B., Linker, R. A., Deng, J. & Kaltschmidt, C. Cyclooxygenase-2 is a neuronal target gene of NF- κ B. *BMC Mol. Biol.* **3**, 16 (2002).
- Funk, C. D. Prostaglandins and leukotrienes: advances in eicosanoid biology. *Science* **294**, 1871–1875 (2001).
- Palacios, F., Price, L., Schweitzer, J., Collard, J. G. & D'Souza-Schorey, C. An essential role for ARF6-regulated membrane traffic in adherens junction turnover and epithelial cell migration. *EMBO J.* **20**, 4973–4986 (2001).
- D'Souza-Schorey, C., Li, G., Colombo, M. I. & Stahl, P. D. A regulatory role for ARF6 in receptor-mediated endocytosis. *Science* **267**, 1175–1178 (1995).
- Riley, K. N., Maldonado, A. E., Tellier, P., D'Souza-Schorey, C. & Herman, I. M. Betacp73-ARF6 interactions modulate cell shape and motility after injury *in vitro*. *Mol. Biol. Cell* **14**, 4155–4161 (2003).
- Zhang, Q. et al. Small-molecule synergist of the Wnt/ β -catenin signaling pathway. *Proc. Natl Acad. Sci. USA* **104**, 7444–7448 (2007).
- Hafner, M. et al. Inhibition of cytohesins by SecinH3 leads to hepatic insulin resistance. *Nature* **444**, 941–944 (2006).
- Béraud-Dufour, S. et al. A glutamic finger in the guanine nucleotide exchange factor ARNO displaces Mg²⁺ and the β -phosphate to destabilize GDP on ARF1. *EMBO J.* **17**, 3651–3659 (1998).
- Arend, W. P. Cytokine imbalance in the pathogenesis of rheumatoid arthritis: the role of interleukin-1 receptor antagonist. *Semin. Arthritis Rheum.* **30**, 1–6 (2001).
- Szekanecz, Z. & Koch, A. E. Vascular involvement in rheumatic diseases: 'vascular rheumatology'. *Arthritis Res. Ther.* **10**, 224 (2008).
- van den Berg, W. B., Joosten, L. A., Helsen, M. & van de Loo, F. A. Amelioration of established murine collagen-induced arthritis with anti-IL-1 treatment. *Clin. Exp. Immunol.* **95**, 237–243 (1994).
- Joosten, L. A., Helsen, M. M., van de Loo, F. A. & van den Berg, W. B. Anticytokine treatment of established type II collagen-induced arthritis in DBA/1 mice. A comparative study using anti-TNF α , anti-IL-1 α/β , and IL-1Ra. *Arthritis Rheum.* **39**, 797–809 (1996).
- Wooley, P. H., Dutcher, J., Widmer, M. B. & Gillis, S. Influence of a recombinant human soluble tumor necrosis factor receptor FC fusion protein on type II collagen-induced arthritis in mice. *J. Immunol.* **151**, 6602–6607 (1993).
- London, N. R., Whitehead, K. J. & Li, D. Y. Endogenous endothelial cell signaling systems maintain vascular stability. *Angiogenesis* **12**, 149–158 (2009).
- Keane, J. et al. Tuberculosis associated with infliximab, a tumor necrosis factor α -neutralizing agent. *N. Engl. J. Med.* **345**, 1098–1104 (2001).
- Lee, W. L. & Slutsky, A. S. Sepsis and endothelial permeability. *N. Engl. J. Med.* **363**, 689–691 (2010).
- Silva, L. C., Ortigosa, L. C. & Benard, G. Anti-TNF- α agents in the treatment of immune-mediated inflammatory diseases: mechanisms of action and pitfalls. *Immunotherapy* **2**, 817–833 (2010).

Supplementary Information is available in the online version of the paper.

Acknowledgements We thank D. Lim and T. Mleynek for graphical assistance, G. Zimmerman and J. Kaplan for reading the manuscript, S. Odelberg for reading the manuscript and statistical analysis, J. Ling for help with immunostaining, R. Campbell and A. Weyrich for providing primary human blood cells, C. Rodesch and the University of Utah Cell Imaging/Fluorescence Facility as well as the University of Utah Flow Cytometry Facility, and M. P. Revelo for help with pathology. D.Y.L. and his laboratory were funded by grants from the National Heart, Lung, and Blood Institute; Burroughs Wellcome Fund; Juvenile Diabetes Research Foundation; NIAID Rocky Mountain Regional Center of Excellence in Biodefense and Emerging Infectious Disease; the American Asthma Foundation; and the Department of Defense. D.Y.L. is the HA and Edna Benning Endowed Professor of Medicine and Cardiology.

Author Contributions W.Z., N.R.L., C.C.G. and D.Y.L. were responsible for project conceptualization, experimental design, data analysis and manuscript preparation. W.Z., C.C.G., C.T.D., Z.T., L.K.S., D.S.S. and J.G. performed and collected data for *in vitro* experiments. N.R.L. collected data for *in vivo* experiments. C.C.G. developed software techniques for immunofluorescence analysis. M.C.P.S. performed flow cytometry experiments. Z.T. and K.R.T. made constructs and adenoviruses. A.H.G. provided histology and pathology expertise. D.Y.L. was responsible for funding the project.

Author Information Reprints and permissions information is available at www.nature.com/reprints. The authors declare competing financial interests: details are available in the online version of the paper. Readers are welcome to comment on the online version of the paper. Correspondence and requests for materials should be addressed to D.Y.L. (dean.li@u2m2.utah.edu).

A soybean cyst nematode resistance gene points to a new mechanism of plant resistance to pathogens

Shiming Liu^{1*}, Pramod K. Kandoth^{2*}, Samantha D. Warren³, Greg Yeckel², Robert Heinz², John Alden², Chunling Yang⁴, Aziz Jamai¹, Tarik El-Mellouki¹, Parijat S. Juvele⁴, John Hill⁴, Thomas J. Baum⁴, Silvia Cianzio⁵, Steven A. Whitham⁴, Dmitry Korkin³, Melissa G. Mitchum² & Khalid Meksem¹

Soybean (*Glycine max* (L.) Merr.) is an important crop that provides a sustainable source of protein and oil worldwide. Soybean cyst nematode (*Heterodera glycines* Ichinohe) is a microscopic roundworm that feeds on the roots of soybean and is a major constraint to soybean production. This nematode causes more than US\$1 billion in yield losses annually in the United States alone¹, making it the most economically important pathogen on soybean. Although planting of resistant cultivars forms the core management strategy for this pathogen, nothing is known about the nature of resistance. Moreover, the increase in virulent populations of this parasite on most known resistance sources necessitates the development of novel approaches for control. Here we report the map-based cloning of a gene at the *Rhg4* (for resistance to *Heterodera glycines* 4) locus, a major quantitative trait locus contributing to resistance to this pathogen. Mutation analysis, gene silencing and transgenic complementation confirm that the gene confers resistance. The gene encodes a serine hydroxymethyltransferase, an enzyme that is ubiquitous in nature and structurally conserved across kingdoms. The enzyme is responsible for interconversion of serine and glycine and is essential for cellular one-carbon metabolism. Alleles of *Rhg4* conferring resistance or susceptibility differ by two genetic polymorphisms that alter a key regulatory property of the enzyme. Our discovery reveals an unprecedented plant resistance mechanism against a pathogen. The mechanistic knowledge of the resistance gene can be readily exploited to improve nematode resistance of soybean, an increasingly important global crop.

The first quantitative trait loci (QTL) for resistance to *Heterodera glycines* (*rhg*) were identified in the early 1960s^{2,3}. Resistance QTL on chromosomes 18 (*rhg1*) and 8 (*Rhg4*) have been consistently mapped in a variety of soybean germplasm and represent the major sources of resistance in soybean cultivars⁴. In the soybean cultivar (cv.) Forrest, resistance to soybean cyst nematode (SCN) requires both *rhg1* and *Rhg4*, with *Rhg4* exhibiting dominant gene action⁵. Roots of plants carrying *Rhg* genes are penetrated by infective juveniles, but feeding cells ultimately degenerate, causing the nematodes to die before reaching adult stages⁶. Genetic variability in *H. glycines* is prevalent, and nematodes that survive on resistant cultivars carry the undefined *ror* (reproduction on a resistant host) alleles⁷, leading to population shifts in the field as a consequence of resistant soybean monoculture⁸. So far, our understanding of resistance to SCN remains limited because the genes underlying resistance QTL have not been cloned^{9,10}.

We report here the positional cloning of the *Rhg4* gene from soybean cv. Forrest (Fig. 1a). For this purpose, three F_{2:6} recombinant inbred line (RIL) populations segregating for SCN resistance were developed. From a total of 355 recombinant lines identified with chromosomal breakpoints at the *Rhg4* locus, two recombinants (ExF74 and ExW5093) were crucial in defining the interval carrying the *Rhg4* gene. Both lines

carry the resistance allele at the *rhg1* locus and are double recombinants for an 8-kilobase (kb) interval carrying the *Rhg4* resistance allele. Two genes, one coding for a serine hydroxymethyltransferase (*SHMT*) and the other a subtilisin-like protease (*SUB1*), were identified in the interval. An alignment of *SUB1* cDNA sequences from Forrest, Essex and Williams 82 cultivars indicates that the two amino acid differences between Forrest and Essex do not correlate with SCN resistance (Supplementary Fig. 1). In addition, no nucleotide differences were identified in the 1,766 base pairs (bp) of sequence 5' of the predicted translational start site for *SUB1* between Forrest and Essex. A comparison between the genomic DNA sequences of *SHMT* from Forrest and Essex identified five nucleotide differences (three single nucleotide polymorphisms (SNPs) and two insertions/deletions (indels)) between the resistant and susceptible alleles (Fig. 1a). Two of the nucleotide differences found between the Forrest and Essex *SHMT* cDNAs result in an amino acid change in the predicted protein sequences (R130P and Y358N) (Fig. 1a). Furthermore, three nucleotide differences were identified in the 2,339 bp of sequence 5' of the predicted start site for *SHMT* between Forrest and Essex (Supplementary Fig. 2a). On the basis of these findings, *SHMT* was characterized further for a role in SCN resistance.

Using TILLING^{11,12}, we identified two Forrest mutants, F6266 and F6756, carrying mutations in the *SHMT* gene on chromosome 8 that lead to missense mutations at amino acid positions 61 (E61K) and 125 (M125I), respectively (Fig. 1b). The M125I mutation is predicted to be deleterious (sorting intolerant from tolerant (SIFT) score = 0.02) to the protein. Both mutants are more susceptible to SCN (Fig. 1c). In the segregating M3 F6756 (M125I) mutant plants, the mutation is directly correlated with the SCN resistance phenotype of individual plants.

To establish a link between *SHMT* alleles and soybean resistance to SCN, we scored 81 soybean lines representing 90% of the sequence diversity in soybean¹³ for SCN female index and then determined their SNP-based *SHMT* haplotype (Supplementary Table 1). The *SHMT* gene was fully sequenced from 28 selected soybean lines (Fig. 2). Eight different *SHMT* haplotypes were identified. Soybean lines with haplotypes H1–H3 carry resistant alleles at *SHMT* and *rhg1* and are resistant to SCN. These include soybean lines PI 548402 (Peking), Forrest, PI 90763, PI 437654 and PI 89772, all of which exhibit 'Peking-type' resistance, which requires both *rhg1* and *Rhg4* (ref. 5).

Further evidence that the *SHMT* gene confers SCN resistance comes from knockdown studies using virus-induced gene silencing (VIGS) and targeted RNA interference (RNAi). We cloned 328 bp of *SHMT* into bean pod mottle virus (BPMV) RNA-2 (ref. 14) and generated infected tissue. Silencing of the *SHMT* gene in the SCN-resistant RIL ExF67 by inoculation with BPMV-*SHMT* results in an increase in susceptibility to SCN compared to ExF67 inoculated with BPMV only (Fig. 3a; $P < 0.0001$). At the time of nematode inoculation,

¹Department of Plant, Soil and Agricultural Systems, Southern Illinois University, Carbondale, Illinois 62901, USA. ²Division of Plant Sciences, Christopher S. Bond Life Sciences Center and Interdisciplinary Plant Group, University of Missouri, Columbia, Missouri 65211, USA. ³Department of Computer Science, Christopher S. Bond Life Sciences Center and Informatics Institute, University of Missouri, Columbia, Missouri 65211, USA. ⁴Department of Plant Pathology and Microbiology, Iowa State University, Ames, Iowa 50011, USA. ⁵Department of Agronomy, Iowa State University, Ames, Iowa 50011, USA.

*These authors contributed equally to this work.

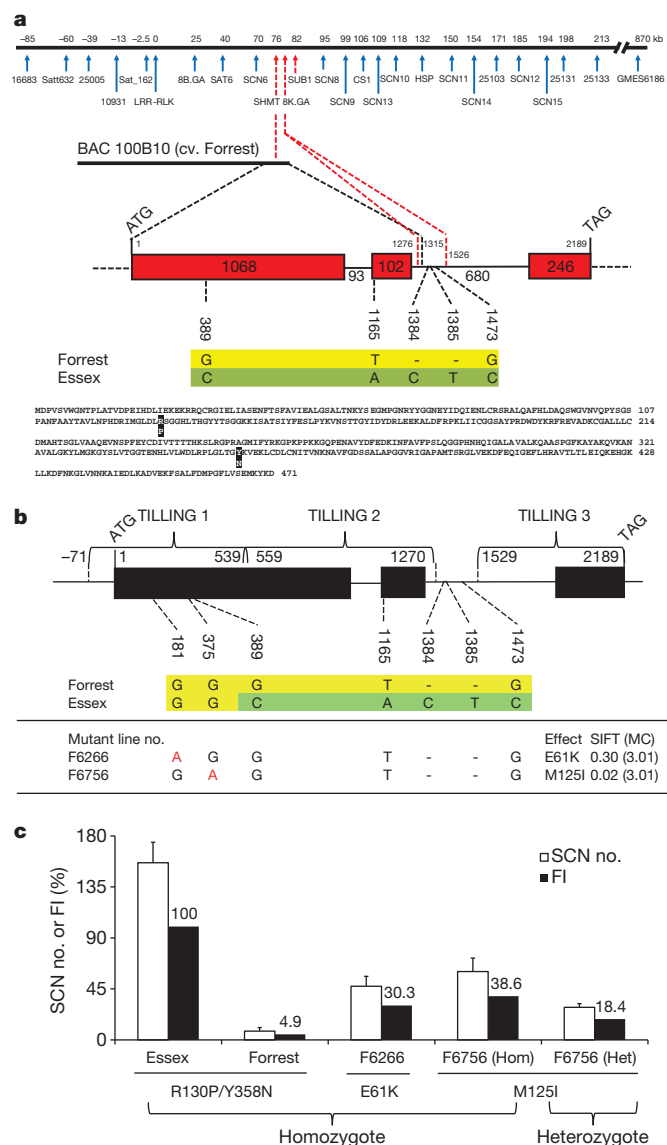


Figure 1 | *Rhg4* positional cloning and functional validation of *SHMT* by TILLING. **a**, Top: high-density genetic map of the *Rhg4* locus showing double recombinants ExF74 and ExW5093 using Williams 82 sequence as reference. Red arrows represent DNA markers with Forrest alleles. BAC clone 100B10 encompasses a partial *SHMT* sequence. Middle: *SHMT* gene model and polymorphisms between Forrest and Essex. Bottom: *SHMT* predicted protein sequence showing amino acid differences (R130P and Y358N) between Forrest and Essex. **b**, Identification of two missense TILLING mutations (E61K and M125I) within the *SHMT*. MC, median sequence conservation. **c**, SCN phenotype of the TILLING mutants. FI, female index. Bars, s.e.m.

SHMT transcript levels were determined by quantitative polymerase chain reaction with reverse transcription (qRT-PCR) to have decreased by an average of 74% in the roots of plants inoculated with BPMV-*SHMT* compared with those inoculated with BPMV only (Fig. 3b). For targeted RNAi, a 338-bp double-stranded RNA (dsRNA) corresponding to *SHMT* was expressed under the control of an SCN-inducible zinc finger transcription factor promoter¹⁵ in soybean hairy roots. Nematode reproduction on hairy roots of the SCN-resistant RIL ExF67 transformed with pZF-SHMTi is greater than on ExF67 hairy roots transformed with pZF-GUSi control (Fig. 3c; $P < 0.01$).

Next we fused 2.3 kb of *SHMT* promoter sequence from Forrest and Essex cultivars with the β -glucuronidase (*GUS*) reporter gene. In uninfected roots, *SHMT* expression is observed within the vasculature of roots (Supplementary Fig. 3). Nematode infection experiments of soybean hairy roots of ExF67 and ExF63 transformed with the Forrest

pSHMT-GUS construct confirm expression of *SHMT* within syncytia of both lines (Fig. 3d–f). The same pattern of *GUS* expression is observed in nematode-infected soybean hairy roots of ExF63 transformed with the Essex pSHMT-GUS construct (Supplementary Fig. 2b). These data verify *SHMT* expression in nematode feeding sites of both resistant and susceptible soybean and indicate that differences in *Rhg4* expression are unlikely to explain the resistance phenotype.

To confirm that *SHMT* is the resistance gene at the *Rhg4* locus, we transformed the SCN-susceptible RIL ExF63 with a 5.1-kb genomic fragment that includes the Forrest *SHMT* gene and the 2.3 kb of sequence upstream of the start and the 0.57 kb downstream of the stop codon (gSHMT). SCN resistance was restored in the complemented, transformed hairy roots (Fig. 3g; $P < 0.0001$), confirming that *SHMT* is the *Rhg4* gene.

To gain insight into the mechanistic basis of resistance, a structural model of *SHMT* was obtained by applying homology modelling. The predicted structure was then used to examine how the variant genotypes may be affecting the structural and functional properties of the enzyme. Forrest P130R and N358Y are co-localized with the tetrahydrofolate (THF)/5,10-methylene tetrahydrofolate (MTHF)/5-formyltetrahydrofolate (FTHF) binding site and are in close proximity to pyridoxal 5'-phosphate (PLP)-serine (PLS), PLP-glycine (PLG), and one of the two glycine binding sites. The position of the E61K mutation overlaps with the PLS and THF/MTHF/FTHF binding sites (Fig. 4a, b, Supplementary Data and Supplementary Video 1). The findings suggest that these residue changes may directly affect the reversible interconversion of serine and THF to glycine and MTHF. On the other hand, the M125I mutation in the Forrest F6756 TILLING mutant is found in an interior β -sheet (Fig. 4a, b), indicating that there may be a different mechanism altering the function of *SHMT* in this mutant, perhaps through the structural instability of the region affected by the TILLING mutation.

We further tested the ability of the Forrest, Essex, F6266 and F6756 *Shmt* proteins to complement an *Escherichia coli* glycine auxotroph¹⁶. Essex *Shmt* fully restores growth, Forrest *Shmt* partially restores growth, and the F6266 and F6756 *Shmt* proteins are unable to restore growth of the mutant (Fig. 4c, d). Although there seems to be a difference in the ability of the Forrest and Essex *Shmt* proteins to complement the *E. coli* glycine auxotroph, this finding establishes that both the Forrest and Essex alleles encode functional *Shmt* enzymes. Consistent with this observation, kinetic studies show different reaction kinetics of the Forrest and Essex *Shmt* proteins. Essex *Shmt* reaction velocity increases with increasing concentrations of THF, peaks, and then declines to a lower rate and remains steady (Fig. 4e). On the other hand, Forrest *Shmt* seems to follow typical Michaelis–Menten kinetics (Fig. 4f and Supplementary Fig. 4). The inhibition of Essex *Shmt* activity at high THF concentrations might have regulatory implications in a cellular environment¹⁷. The residue changes in Forrest *Shmt* seem to change this regulatory property of the enzyme.

Shmt is a ubiquitous enzyme in nature with a key role in one-carbon folate metabolism that is conserved across kingdoms. Although the enzyme has multiple catalytic activities, one of its main roles is to catalyse the reversible conversion of serine and THF to glycine and MTHF to supply one-carbon units for *de novo* purine, thymidylate and methionine synthesis, underlying its importance in DNA synthesis and cellular methylation reactions. Consequently, in humans, mutations in *SHMT* and folate deficiency have been linked to a wide range of disease states^{18–21}.

Transcriptional and metabolic profiling studies of syncytia, the feeding cells formed by cyst nematodes in plant roots, support a high demand on folate one-carbon metabolism for their development and maintenance^{22,23}, perturbations to which could severely compromise their activity. Syncytia induced in plants resistant to SCN degenerate by what has been described as a hypersensitive response, a form of localized programmed cell death (PCD) in plants to ward off invading pathogens. Molecular analysis has identified increased defence-related

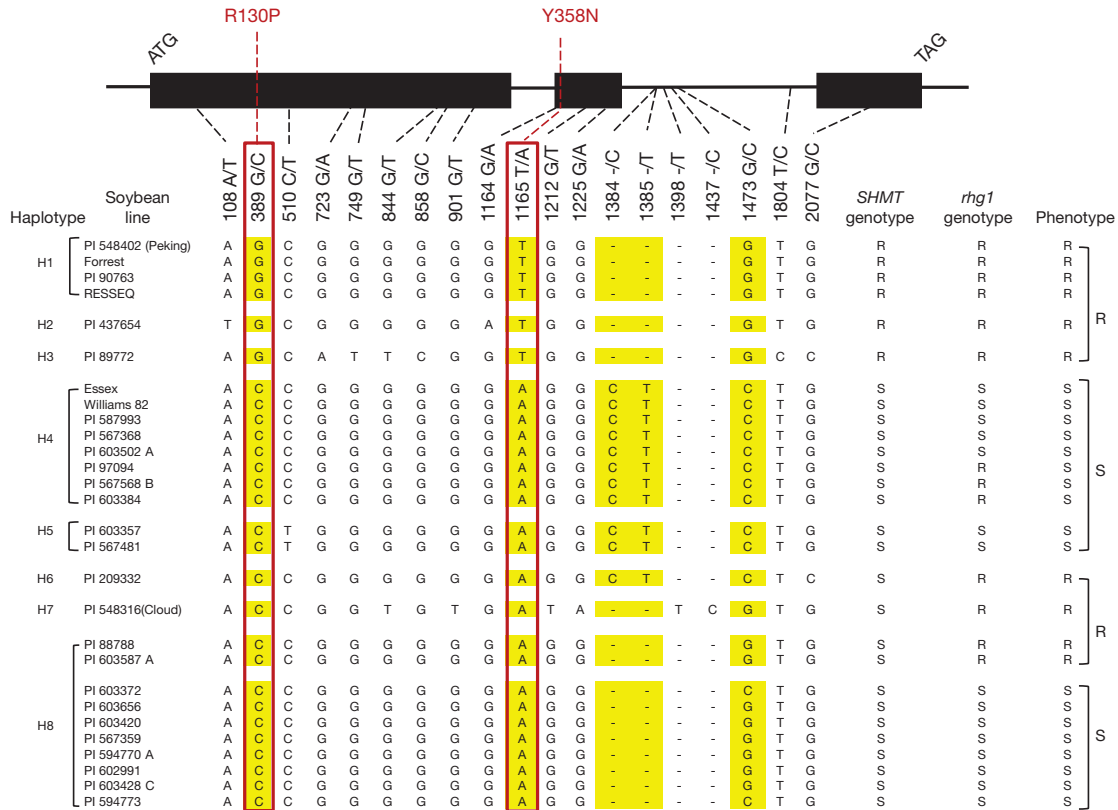


Figure 2 | Haplotypes identified at *SHMT* in 28 soybean lines. The *SHMT* coding region for the 28 lines shown here was sequenced. Lines are classified resistant (R) to SCN if FI $\leq 10\%$ and susceptible (S) if FI $> 10\%$. Polymorphic sites were positioned relative to the first nucleotide of the start codon in Forrest.

Red boxes indicate the G-to-C and T-to-A transitions resulting in the amino acid substitutions R130P and Y358N, respectively, which are correlated with the SCN phenotype.

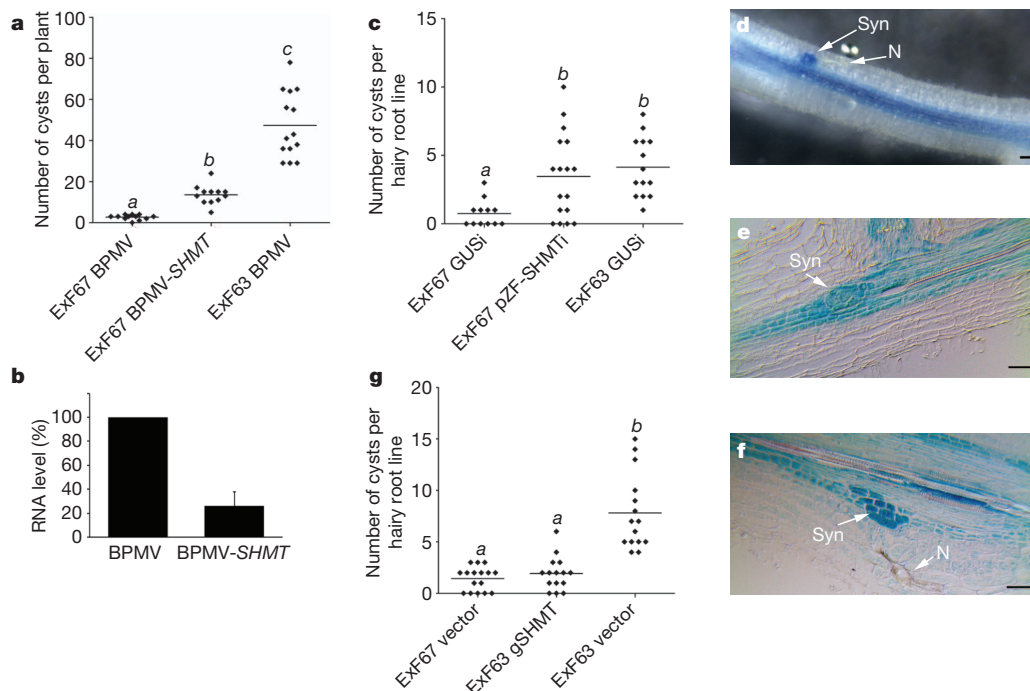


Figure 3 | Functional validation of *SHMT* by VIGS, RNAi and complementation. **a**, Nematode reproduction on SCN-resistant RIL ExF67 inoculated with BPMV or BPMV-*SHMT* ($P < 0.0001$). **b**, qPCR of *SHMT* transcript levels in control and *SHMT*-silenced roots (mean and s.e. of five samples). **c**, Nematode reproduction on ExF67 hairy root lines transformed with a *SHMT* RNAi construct ($P < 0.01$). **d–f**, Forrest *SHMT* promoter-*GUS* analysis in ExF67 (**d**, **e**) and ExF63 (**f**) showing expression in syncytial feeding

cells at 3 days after inoculation with SCN. N, nematode; Syn, syncytium. Scale bars, 50 μm . **g**, SCN reproduction on ExF63 hairy root lines transformed with a 5.1-kb Forrest *SHMT* gene fragment ($P < 0.001$). In graphs, diamonds represent the number of cysts on a single root system or hairy root line and the bars indicate the mean values. At least three independent experiments were performed showing similar results. Data from one experiment are presented. Letters indicate a significant difference at the indicated P value.

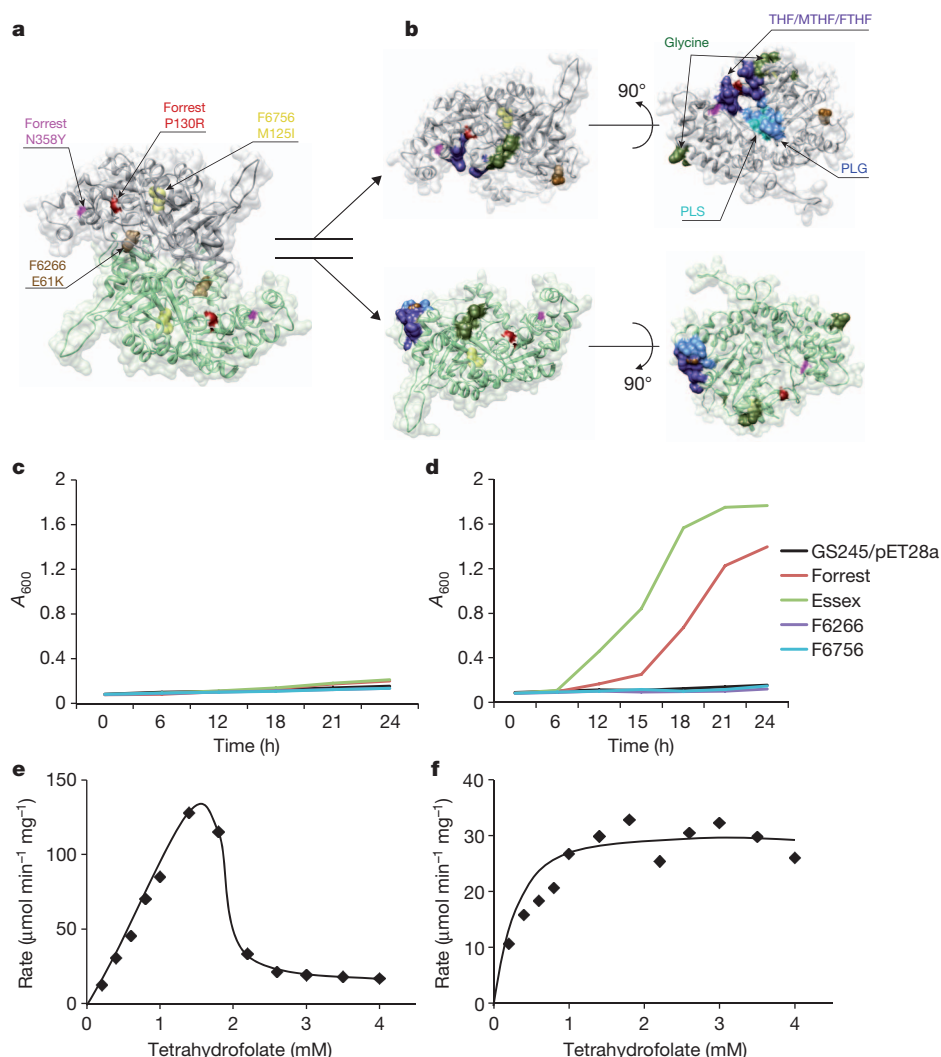


Figure 4 | Modelled structure and biochemical analysis of SHMT.

a, Homology model of the Essex SHMT homodimer. Forrest polymorphisms, P130R and N358Y, are located on the dimer surface; the Forrest F6266 (E61K) mutation is buried in the dimerization interface; the Forrest F6756 (M125I) mutation is located in the core of each monomeric subunit. **b**, Split-open view of the SHMT dimer with the ligand binding sites located at the interface. **c, d**, Complementation of an *E. coli* glycine auxotroph (GS245(DE3)pLysS;

shmt—) by the Essex, Forrest, F6266 and F6756 Shmt proteins. Absorbance at 600 nm (A_{600}) of cultures was measured at different time points as shown, uninduced (**c**) or induced (**d**) with 0.25 mM IPTG. GS245(DE3)pLysS carrying the pET28a vector was used as a control. **e, f**, Enzyme kinetics of Essex (**e**) and Forrest (**f**) Shmt proteins. The graphs were plotted as rate of product formation per min per mg of enzyme at varying concentrations of tetrahydrofolate and 2 mM serine. Graphs shown are representative of three experiments.

gene expression associated with oxidative stress, apoptotic cell death, and the plant hypersensitive response in syncytia formed in resistant plants¹⁵.

Our findings are consistent with the dominant nature of *Rhg4*-mediated resistance and support a model wherein the Forrest Shmt has acquired a new or altered function. Computational analysis predicts that the polymorphisms in Forrest Shmt reside near ligand-binding sites, and our biochemical analyses suggest that these residue changes probably impair a key regulatory property of the enzyme. Any changes in Shmt function can have wide-ranging effects on one-carbon folate metabolism. Alterations to folate homeostasis leading to folate deficiency, which can induce apoptosis in mammalian cells^{24,25}, may trigger hypersensitive-response-like programmed cell death of the developing feeding cells and subsequent death of the nematode. Alternatively, the Forrest Shmt may lead to the production of a nematocidal compound or serve as the target of a nematode-secreted small molecule or effector protein to trigger a resistance signalling pathway. Although the nutritional requirements of plant-parasitic nematodes are not well defined, it is assumed that nematodes, like other animals, acquire folate from their diet. Thus, the nematode's nutritional requirements may also be influencing folate metabolism in developing feeding cells.

Perturbations to the plant's folate pathway may lead to a nutritional deficiency that starves the nematode. Upon nematode death, the loss of stimuli required for maintenance of the feeding cells results in their degeneration. The work described here provides a foundation for future molecular and biochemical studies aimed at achieving a mechanistic understanding of how Shmt functions in resistance to SCN.

METHODS SUMMARY

Three $F_{2:6}$ recombinant inbred line (RIL) populations segregating for resistance to SCN Hg type 0 were developed from crosses of SCN-resistant cv. Forrest (F) with the SCN-susceptible soybean cultivars Williams 82 (W) or Essex (E) and used in mapping studies. Because Forrest resistance to SCN requires both *rhg1* and *Rhg4* (ref. 5), genotyping was conducted using DNA markers flanking both loci to detect informative recombinants at the *Rhg4* locus (Supplementary Table 1). The two $F_{2:6}$ RILs, ExF67 (*rhg1_FRhg1_FRhg4_FRhg4_F*) and ExF63 (*rhg1_FRhg1_FRhg4_ERhg4_E*), used in functional analyses are resistant and susceptible, respectively, to SCN¹⁰. An ethylmethane sulphonate (EMS)-mutagenized M2 population of Forrest containing 1,920 M2 families was used to screen for mutations as previously described¹². VIGS and hairy root assays were carried out as previously described^{10,14}. A 5,103-bp Forrest *SHMT* genomic DNA fragment (GenBank accession number JQ714083) was cloned and sequenced for complementation analysis. Homology

modelling was done using MODELLER-9²⁶. *Escherichia coli* complementation analysis¹⁶ and SHMT assays²⁷ were performed as described.

Full Methods and any associated references are available in the online version of the paper.

Received 4 June; accepted 27 September 2012.

Published online 15 October 2012.

- Koenning, S. R. & Wrather, J. A. Suppression of soybean yield potential in the continental United States from plant diseases estimated from 2006 to 2009. *Plant Health Prog.* <http://dx.doi.org/10.1094/PHP-2010-1122-01-RS> (2010).
- Caldwell, B. E., Brim, C. A. & Ross, J. P. Inheritance of resistance of soybeans to the cyst nematode, *Heterodera glycines*. *Agron. J.* **52**, 635–636 (1960).
- Matson, A. L. & Williams, L. F. Evidence of a fourth gene for resistance to the soybean cyst nematode. *Crop Sci.* **5**, 477 (1965).
- Concibido, V. C., Diers, B. W. & Arellano, P. R. A decade of QTL mapping for cyst nematode resistance in soybean. *Crop Sci.* **44**, 1121–1131 (2004).
- Meksem, K. *et al.* 'Forrest' resistance to the soybean cyst nematode is bigenic: saturation mapping of the *Rhg1* and *Rhg4* loci. *Theor. Appl. Genet.* **103**, 710–717 (2001).
- Endo, B. Y. Histological responses of resistant and susceptible soybean varieties, and backcross progeny to entry development of *Heterodera glycines*. *Phytopathology* **55**, 375–381 (1965).
- Dong, K. & Opperman, C. H. Genetic analysis of parasitism in soybean cyst nematode *Heterodera glycines*. *Genetics* **146**, 1311–1318 (1997).
- Niblack, T. L., Colgrove, A. L., Colgrove, K. & Bond, J. P. Shift in virulence of soybean cyst nematode is associated with use of resistance from PI 88788. Online. *Plant Health Prog.* <http://dx.doi.org/10.1094/PHP-2008-0118-01-RS> (2008).
- Melito, S. *et al.* A nematode demography assay in transgenic roots reveals no significant impacts of the *Rhg1* locus LRR-Kinase on soybean cyst nematode resistance. *BMC Plant Biol.* **10**, 104 (2010).
- Liu, X. *et al.* Soybean cyst nematode resistance in soybean is independent of the *Rhg4* locus LRR-RLK gene. *Func. Integr. Gen.* **11**, 539–549 (2011).
- Cooper, J. L. *et al.* TILLING to detect induced mutations in soybean. *BMC Plant Biol.* **8**, 9 (2008).
- Meksem, K. *et al.* TILLING: A reverse genetics and a functional genomics tool in soybean. In *The handbook of Plant Functional Genomics: Concepts and Protocols* (eds Kahl, G. & Meksem, K.) 251–265 (Wiley, 2008).
- Hyten, D. *et al.* Impacts of genetic bottlenecks on soybean genome diversity. *Proc. Natl Acad. Sci. USA* **103**, 16666–16671 (2007).
- Zhang, C. Q., Bradshaw, J. D., Whitham, S. A. & Hill, J. H. The development of an efficient multipurpose *Bean pod mottle virus* viral vector set for foreign gene expression and RNA silencing. *Plant Physiol.* **153**, 52–65 (2010).
- Kandath, P. K. *et al.* The soybean *Rhg1* locus for resistance to the soybean cyst nematode *Heterodera glycines* regulates expression of a large number of stress- and defense-related genes in degenerating feeding cells. *Plant Physiol.* **155**, 1960–1975 (2011).
- Alfadhli, S. & Rathod, P. K. Gene organization of a *Plasmodium falciparum* serine hydroxymethyltransferase and its functional expression in *Escherichia coli*. *Mol. Biochem. Parasitol.* **110**, 283–291 (2000).
- Reed, M. C., Lieb, A. & Nijhout, H. F. The biological significance of substrate inhibition: A mechanism with diverse functions. *Bioessays* **32**, 422–429 (2010).
- Skibola, C. F. *et al.* Polymorphisms in the thymidylate synthase and serine hydroxymethyltransferase genes and risk of adult acute lymphocytic leukemia. *Blood* **99**, 3786–3791 (2002).
- Lim, U. *et al.* Polymorphisms in cytoplasmic serine hydroxymethyltransferase and methylenetetrahydrofolate reductase affect the risk of cardiovascular disease in men. *J. Nutr.* **135**, 1989–1994 (2005).
- Heil, S. G. *et al.* Is mutated serine hydroxymethyltransferase (SHMT) involved in the etiology of neural tube defects? *Mol. Genet. Metab.* **73**, 164–172 (2001).
- Kim, Y. I. Role of folate in colon cancer development and progression. *J. Nutr.* **133**, 3731S–3739S (2003).
- Ithal, N. *et al.* Developmental transcript profiling of cyst nematode feeding cells in soybean roots. *Mol. Plant Microbe Interact.* **20**, 510–525 (2007).
- Hofmann, J. *et al.* Metabolic profiling reveal local and systemic responses of host plants to nematode parasitism. *Plant J.* **62**, 1058–1071 (2010).
- Novakovic, P., Stempak, J. M., Sohn, K.-J. & Kim, J.-I. Effects of folate deficiency on gene expression in the apoptosis and cancer pathways in colon cancer cells. *Carcinogenesis* **27**, 916–924 (2006).
- Bagnyukova, T. V. *et al.* Induction of oxidative stress and DNA damage in rat brain by a folate/methyl-deficient diet. *Brain Res.* **1237**, 44–51 (2008).
- Sali, A. & Blundell, T. L. Comparative protein modeling by satisfaction of spatial restraints. *J. Mol. Biol.* **234**, 779–815 (1993).
- Zhang, Y., Sun, K. & Roje, S. An HPLC-based fluorometric assay for serine hydroxymethyltransferase. *Anal. Biochem.* **375**, 367–369 (2008).

Supplementary Information is available in the online version of the paper.

Acknowledgements We thank X. Yang for technical assistance with soybean hairy root propagation and M. Kroll for proofreading the manuscript. We thank R. Hussey, W. Gassmann, P. Gresshoff, A. Bendahmane, D. Xu and B. McClure for critical reading of the manuscript. We thank K. Sharma and S. Puthur for use of the HPLC facility and technical help. This work was supported by the Illinois-Missouri Biotechnology Alliance (project 2005-3 to M.G.M. and K.M.), United Soybean Board (project 0253 to K.M., S.C. and M.G.M.; project 3253 to K.M. and S.C.; project 2268 to K.M. and M.G.M.; project 1251 to J.H. and S.A.W.), USDA-NIFA (grant 2006-35300-17195 to K.M.), the National Science Foundation Plant Genome Research Program (grant 0820642 to S.A.W., J.H., M.G.M. and T.J.B.), the National Science Foundation CAREER Program (DBI-0845196 to D.K.), Missouri Soybean Merchandising Council (project 258 to M.G.M.), Illinois Soybean Association, North Central Soybean Research Program, Iowa Soybean Association, and a Department of Education Graduate Assistance in Areas of National Need (GAANN) Fellowship (to S.D.W.).

Author Contributions S.L. and P.K.K. contributed equally as first authors. K.M. and M.G.M. contributed equally as senior authors. S.L. carried out mapping and haplotyping studies. S.L., A.J. and T.E.-M. developed the TILLING population used in this study. S.C. developed two of the RIL populations used in this study. S.L. identified the TILLING mutants and conducted the zygosity analysis. G.Y. and R.H. carried out SCN phenotyping of all RILs, TILLING mutants, and soybean lines. G.Y. collected leaf tissues for RIL and TILLING studies. P.K.K. collected leaf tissues haplotyping analyses. P.K.K. and S.L. confirmed the mutations, cloned the genes, and conducted sequence analyses. P.K.K., C.Y., R.H. and P.S.J. developed and carried out VIGS assays. P.K.K. conducted RNAi experiments. P.K.K. carried out the promoter analysis. P.K.K. and J.A. carried out the complementation analysis. S.D.W. and D.K. performed the computational analysis. P.K.K. performed the biochemical studies. J.H., S.A.W. and T.J.B. provided materials and advice for VIGS analysis. K.M., M.G.M. and D.K. designed the research, and together with S.L., P.K.K. and S.D.W. wrote the manuscript. All authors reviewed and commented on the manuscript.

Author Information All sequences have been deposited in GenBank/EMBL/DBJ under the following accession numbers: Forrest SHMT full-length genomic DNA, JQ714083; Essex SHMT full-length genomic DNA, JQ714084; Forrest SHMT cDNA sequence, JQ714080; Essex SHMT cDNA sequence, JQ714079; Forrest SHMT TILLING mutant F6266 sequence, JQ714081; Forrest SHMT TILLING mutant F6756 sequence, JQ714082; Forrest SUB1 cDNA sequence, JQ762395; Essex SUB1 cDNA sequence, JQ762396; Forrest SUB1 promoter sequence, JQ762397; Essex SUB1 promoter sequence, JQ904711. Reprints and permissions information is available at www.nature.com/reprints. The authors declare no competing financial interests. Readers are welcome to comment on the online version of the paper. Correspondence and requests for materials should be addressed to K.M. (meksemk@siu.edu) or M.G.M. (goellnrm@missouri.edu).

METHODS

Nematode and plant material. The SCN (*Heterodera glycines* Ichinohe) inbred population PA3 (Hg type 0) used in this study was mass-selected on soybean cv. Williams 82 according to standard procedures²⁸ at the University of Missouri. The soybean cultivar Forrest²⁹ is resistant to SCN PA3. The soybean cultivars Essex³⁰ and Williams 82 (ref. 31) are susceptible to SCN PA3. Forrest was used to develop an ethyl methane sulphonate (EMS)-mutagenized M2 population of 1,920 lines for TILLING¹². The two F_{2:6} RILs, ExF67 (*rhg1_Frhg1_FRhg4_FRhg4_F*) and ExF63 (*rhg1_Frhg1_FRhg4_ERhg4_E*), used in this study are resistant and susceptible, respectively, to PA3¹⁰. These two RILs differ at the majority of markers assigned to the *Rhg4* region and seem to be nearly opposite recombination events. The collection of soybean lines used in this study was obtained from the USDA Soybean Germplasm Collection, University of Illinois.

Map-based positional cloning of the *Rhg4* gene. Three genetic populations segregating for resistance to SCN PA3 (Hg type 0) were used for mapping. These included an F_{2:6} RIL population from a cross between Forrest and Essex⁵ (98 individuals) and two large F_{2:6} RIL populations generated from crosses between Forrest and either Essex (1,755 lines) or Williams 82 (2,060 lines), to enrich the chromosomal interval carrying the *Rhg4* gene with recombinants. SCN phenotyping was conducted according to ref. 32.

Because Forrest resistance to SCN requires both *rhg1* and *Rhg4* genes⁵, genotyping was conducted using DNA markers flanking both loci to detect informative recombinants at the *Rhg4* locus (Supplementary Table 2). The SSR markers Satt632, Sat_162 (<http://soybase.org>) and GMES6186 (ref. 33) were used to identify chromosomal breakpoints at the *Rhg4* locus. PCR amplifications were performed using DNA from individuals from each of the three genetic populations. Cycling parameters were as follows: 35 cycles of 94 °C 30 s, 50 °C 30 s and 72 °C 30 s with 7 min of extension at 72 °C. The PCR products were separated on 3–4% metaphor agarose gels. The identified recombinants were subject to a second screening by using the SSR markers Sat_210 and Satt309 (<http://soybase.org>) and SIUC-SAT143 to identify the *rhg1* genotype of each recombinant.

To enrich the chromosomal regions carrying the *Rhg4* locus with DNA markers, the GenBank published sequences AX196297 and AX197417 spanning this region were used to design PCR primers every 5 to 10 kb of the 300 kb carrying the *Rhg4* locus (Supplementary Table 2). DNA from Forrest, Essex and Williams 82 were tested with each primer by using a modified EcoTILLING protocol to find and map polymorphic sequences at the *Rhg4* locus^{10,12}. The identified SNP and indel DNA markers were integrated into the informative recombinants to identify chromosomal breakpoints and the interval that carried the *Rhg4* gene.

The closest DNA markers harbouring the *Rhg4* locus were used to screen three Forrest BAC libraries³⁴. The BAC clone 100B10 was identified, integrated with the developed genetic map, and partially sequenced^{5,10}.

Isolation of the *SHMT* genomic and cDNA sequences. A 5,103-bp Forrest *SHMT* genomic DNA fragment (GenBank accession number JQ714083) was cloned and sequenced. The fragment spans 2,339-bp of sequence 5' of the ATG start site, 2,189 bp of sequence from start to stop including 3 exon and 2 introns, and 0.575 kb of sequence 3' of the stop codon. Because the BAC clone 100B10 contains only a partial *SHMT* gene sequence that includes the 2,339 bp of sequence 5' of the ATG start site and 1,315 bp downstream of the ATG start site (Fig. 1a), we used an internal SacI site at position 108 from the ATG start for a PCR-based cloning approach of the full-length genomic sequence. First, a 2,447-bp fragment, including the 2,339 bp of sequence 5' of the ATG start site and 108 bp of exon 1, was amplified by PCR using both a forward primer designed with an AscI site and a reverse primer spanning the internal SacI site. The fragment was digested and cloned into the CGT35S vector³⁵ by using AscI and SacI. An SbfI site was also introduced into the forward primer internal to AscI for subsequent subcloning for complementation analysis (Supplementary Table 2; see below). The remainder of the *SHMT* gDNA fragment, including the unique internal SacI site, was amplified from Forrest genomic DNA by PCR with a forward primer spanning the internal SacI site and a reverse primer designed with a KpnI site. The fragment was digested and cloned into the SacI and KpnI sites downstream of the 5' fragment in the above CGT35S clone. The reverse primer was designed with an SbfI site internal to KpnI for the purpose of subsequent subcloning for complementation analysis (Supplementary Table 2). The fragments were ligated together using the internal SacI restriction site to generate the 5,103-bp *SHMT* genomic DNA fragment and were sequence-verified for accuracy. Primers designed to the Forrest genomic DNA sequence were used to clone the Essex *SHMT* genomic DNA sequence. PCR primers based on the Forrest and Essex genomic DNA sequences were used to amplify the corresponding cDNA sequences. Genomic DNA was isolated from young leaves using the DNeasy plant mini kit (Qiagen). Total RNA was isolated from roots using the RNeasy plant mini kit (Qiagen), and cDNA was synthesized using a cDNA synthesis kit (Invitrogen).

Mutation screening of *SHMT*. Primers specific for *SHMT* (Supplementary Table 2) were used to screen a population of 1,920 EMS-mutagenized M2 lines from the SCN-resistant cv. Forrest^{11,12}. The gene was divided into three intervals (Fig. 1b), and TILLING was performed as previously described¹². The *SHMT* gene of each mutant was sequenced to characterize the identified allele and its subsequent amino acid changes within the predicted protein sequences. SIFT predictions were performed on identified mutations. SIFT predicts whether an amino acid substitution affects protein function based on sequence homology and the physical properties of amino acids³⁶. SIFT predictions with median sequence conservation (MC) <3.25 are considered confident. Changes with a SIFT score <0.05 are predicted to be damaging to the protein. Both missense mutations identified had MC <3.25 (Fig. 1b), thus the SIFT predictions can be considered confident. **Phenotype and zygosity analyses of *SHMT* TILLING mutants.** Mutant seeds were planted and scored for their SCN female index as described³². DNA from each plant was subjected to TILLING analysis. Wild-type Forrest reference DNA was withheld from the reaction tube before mismatch analyses to detect the zygosity level of the identified mutant.

Haplotyping of soybean lines. A total of 81 soybean lines (plant introductions, landraces, and elite cultivars) representing 90% of the genetic variability in soybean¹³ were scored for their SCN female index. Lines were classified resistant (R) to SCN if the FI was ≤10% and susceptible (S) if the FI was >10%. Soybean lines were genotyped at the *Rhg4* locus by using the DNA markers Sat_162 and SUB1 and at the *rhg1* locus by using the DNA markers 560, 570 and Satt309. The coding region of *SHMT* for 28 lines was sequenced (Fig. 2). Common SNPs and indels were identified and used to determine the different *SHMT* haplotypes.

Virus-induced gene silencing. Bean pod mottle virus (BPMV, genus *Comovirus*) is an effective virus-induced gene silencing (VIGS) vector for soybean. BPMV has a bipartite positive-strand RNA genome consisting of RNA-1 and RNA-2. We used a DNA-based system that places the cDNAs of BPMV genomic RNA-1 and RNA-2 under the control of the cauliflower mosaic virus (CaMV 35S) promoter. Two BPMV VIGS vectors, pBPMV-IA-R1M and pBPMV-IA-D35, were used in this study¹⁴. pBPMV-IA-D35 is a derivative of pBPMV-IA-R2 containing BamHI and KpnI restriction sites between the cistrons encoding movement protein and the large coat protein subunit. Briefly, a 328-bp fragment (spanning base pairs 210–537) of the *SHMT* cDNA sequence (GenBank accession number JQ714080) was amplified from soybean (cv. Forrest) root cDNA by RT-PCR. PCR products were digested with BamHI and KpnI and ligated into pBPMV-IA-D35 digested with the same enzymes to generate pBPMV-IA-SHMT (BPMV-SHMT). Gold particles coated with pBPMV-IA-R1M and pBPMV-IA-SHMT were co-bombarded into soybean leaf tissue as described¹⁴. At 3–4 weeks after inoculation, BPMV-infected leaves were collected, lyophilized, and stored at –20 °C for future experiments. Infected soybean leaf tissues were ground in a mortar and pestle with 0.05 M potassium phosphate buffer (pH 7.0) and used as virus inoculum for VIGS assays.

The SCN-resistant RIL ExF67 was inoculated with pBPMV-IA-SHMT. Control plants were infected with BPMV only. Each treatment consisted of at least 12 plants. Unifoliate leaves of 9-day-old plants were rub-inoculated with virus using carborundum as described¹⁴. Plants were grown in a growth chamber set to the following conditions: 20–21 °C, 16 h light/8 h dark, and 100 μmol m^{–2} s^{–1} light intensity. Twenty-one days after virus inoculation, plants were inoculated with 1,500 SCN eggs and maintained at 20 °C for 35 days. Cysts were isolated from the root systems of individual plants by decanting and sieving and counted under a stereomicroscope. The results were plotted and analysed for statistical significance by an unpaired *t*-test using GraphPad PRISM software. To estimate *SHMT* gene silencing in roots, root tissues were collected at 21 days after virus inoculation (the time of nematode inoculation) from two representative plants inoculated with either pBPMV-IA-SHMT or BPMV only and frozen at –80 °C for RNA isolation and qPCR analysis.

Hairy root RNAi experiments. A 338-bp fragment (spanning base pairs 205–542) of the *SHMT* cDNA sequence was amplified from soybean (cv. Forrest) root cDNA by RT-PCR, cloned into the pDONR/Zeo gateway cloning vector (Invitrogen), and subsequently moved to a gateway RNAi binary vector under the control of the nematode-inducible Glyma15g04570.1 promoter¹⁵ (pZF-RNAi vector) to generate pZF-SHMTi. The pZF-RNAi vector was constructed by introducing gateway cloning sites flanking the FADR intron downstream of pZF promoter in the pAKK vector³⁵, which has a GFP selectable marker *in planta*. Transgenic ExF67 hairy roots transformed with pZF-SHMTi were produced from soybean cotyledons¹⁵. ExF63 and ExF67 hairy roots transformed with pZF-GUSi (the pZF-RNAi vector containing a portion of the *GUS* gene) were used as susceptible and resistant controls, respectively. GFP-positive hairy roots were root-tip propagated three times on media containing antibiotic to clear *Agrobacterium* before nematode inoculation as described previously¹⁵. Briefly, hairy roots (3–4 cm in length) were grown in square Petri plates and infected with approximately 400 sterile infective second-stage nematode juveniles (J2s) 1 cm above the root tip. The plates were

incubated in the dark at room temperature for 30 days. After 30 days, cysts were counted under a stereomicroscope. The experiment was conducted independently three times with a minimum of 12 independent hairy root lines per treatment. The results were plotted and analysed for statistical significance by an unpaired *t*-test using GraphPad PRISM software.

Promoter-GUS analysis. A 2,339-bp fragment corresponding to sequence 5' of the ATG start site of the Forrest *SHMT* gene (GenBank accession number JQ714083) and the same region from the Essex *SHMT* gene (GenBank accession number JQ714084) were amplified by PCR from the BAC clone 100B10 and Essex gDNA, respectively, and cloned into the pYXT1 vector³⁷ to generate transcriptional fusions with the β -glucuronidase (*GUS*) gene. Soybean hairy roots transformed with these constructs were generated and infected with SCN. At 2 and 4 days after inoculation, root pieces excised from the infection zone were stained for GUS activity³⁸. Multiple roots from at least five independent lines were stained for each construct. Root pieces were fixed with 4% v/v paraformaldehyde in phosphate-buffered saline overnight at room temperature, embedded in paraffin, and sectioned longitudinally to a thickness of 10 μ m. The sections were observed using differential interference contrast microscopy on a Vanox (Olympus) microscope and photographed with a CMOS colour digital camera.

Genomic complementation experiments. The 5,103-bp Forrest *SHMT* genomic DNA fragment was subcloned into the SbfI restriction site of the pAKK binary vector, which has a GFP selection for transgenic events. Transgenic hairy roots were produced and infected with SCN as described for RNAi experiments. The SCN-susceptible RIL ExF63 was used for the complementation experiment. Control hairy roots were produced by transforming ExF63 and ExF67 hairy roots with the pAKK binary vector carrying only the *SHMT* promoter sequence. The experiment was conducted independently five times with a minimum of fifteen independent hairy root lines per treatment. The results were plotted and analysed for statistical significance by an unpaired *t*-test using GraphPad PRISM software.

RNA isolation and qPCR analysis. Total RNA was isolated from root tissues using the RNeasy plant mini kit (Qiagen) according to the manufacturer's instructions. Real-time qRT-PCR was conducted as described¹⁵. Samples were normalized relative to soybean ubiquitin and calibrated to the expression in the BPMV control sample.

Computational methods. A two-pronged computational approach was performed to annotate structurally and functionally the identified Shmt protein and to estimate the effects of the mutations on Shmt function. First, a homology model of Shmt was obtained using Essex sequence as a target. Second, the functional sites were mapped onto the surface of Shmt using the structural information of ligand binding by Shmt homologues. The homology analysis of Shmt determined 43 structurally resolved Shmt homologues from a diverse set of bacterial and mammalian species; no structurally resolved plant Shmt proteins were found. Among the group of four homologues with the highest sequence similarities, the mouse SHMT (Protein Data Bank accession 1EJ1) with the largest coverage of the Shmt sequence (sequence identity 57%, template coverage 100%) was selected as a template for homology modelling of Shmt. Homology modelling was done using MODELLER-9²⁶ and the top-ranked model was selected from the set of candidate models using the MODELLER scoring function. To determine the ligand binding sites for pyridoxal 5'-phosphate (PLP)-serine (PLS), PLP-glycine (PLG), and THF/MTHF/FTHF, the obtained model of Shmt was structurally aligned with each of the orthologous Shmt proteins known to interact with the small ligands, and the ligand binding site from each homologue was mapped on to the surface of the Shmt model through the structural alignment (note that the contributing parts of the ligand binding sites are not identical between the two monomers). The residues constituting the glycine binding sites, GBS1 and GBS2, in the Shmt homologues were identified in the literature and then mapped onto the structure of Shmt in a similar way by using the structural alignment of SHMT with its homologue.

E. coli complementation experiment. An *E. coli* GS245 glyA strain³⁹ was obtained from the *E. coli* Genetic Stock Center. The GS245 strain was lysogenized with λ DE3 phage (Novagen) according to manufacturer's protocols and transformed with pLysS plasmid (Novagen) to generate GS245(DE3)pLysS for complementation analysis¹⁶. The cDNA sequences corresponding to Forrest, Essex, F6266 and F6756 Shmt proteins were subcloned at NdeI and HindIII sites of pET28a vector (Novagen) for expression of the recombinant proteins with an N-terminal 6 \times -histidine tag. GS245(DE3)pLysS strains carrying the plasmids were grown in LB medium overnight. The A_{600} value of each culture was measured and an equal absorbance of cells was collected and washed twice in M9 minimal

medium (1 \times M9 salts (Sigma), 10% w/v glucose, 50 mg ml⁻¹ phenylalanine, and 10 mg ml⁻¹ of thiamine) and finally re-suspended in two flasks of M9 minimal medium with required antibiotics for selection. One of the flasks was supplemented with IPTG at 0.25 mM final concentration. The cultures were grown in a shaker incubator (New Brunswick Scientific) at 37 °C and 180 r.p.m. setting. A_{600} values of cultures were measured at 0 h and 6 h and thereafter every 3 h up to 24 h. The A_{600} measurements were plotted versus time of incubation to obtain growth curves.

Shmt purification and kinetic analysis. Shmt proteins were purified from GS245 cultures grown at 30 °C for 4 h after induction with 0.5 mM IPTG at A_{600} of 0.5. His-tagged proteins were purified using His Pur Cobalt Resin (Thermo Scientific) according to manufacturer's instructions. Purified proteins were dialysed against three changes of 50 mM potassium phosphate buffer, pH 7.4, containing 10% v/v glycerol, 10⁻³ M tris(hydroxypropyl)phosphine, and 10⁻⁵ M pyridoxal L-phosphate. Protein concentration was estimated by the Bradford method. Shmt assays were performed as described previously²⁷. Briefly, 50 μ l reactions comprising 2 mM serine, 0.2–4 mM (6R,S)-H₄PteGlu (Tetrahydrofolate, THF) (Schircks Lab), 4 mM tris(hydroxypropyl)phosphine, 0.25 mM PLP, and 6 μ g of enzyme in 50 mM potassium phosphate buffer (pH 7.4) were incubated at 30 °C for 20 min. The reaction was stopped by adding 25 μ l of 0.1 M dithiothreitol (DTT) and 50 μ l of 0.1 M NaBH₄. Each reaction was further incubated for 15 min at 37 °C to drive the reduction of 5,10-methylene tetrahydrofolate (MTHF) to 5-methyltetrahydrofolate to completion. The samples were then boiled for 3 min and centrifuged at 20,000 g to remove precipitated protein. The supernatant from the centrifugation step was supplemented with 25 μ l 0.6 M DTT to prevent product decomposition. A no serine control reaction was performed simultaneously. A 1:10 dilution of this sample was used for HPLC separation and quantification. HPLC injection volume was typically 5 μ l. 5-methyltetrahydrofolate in the final reaction mixture was detected and quantified by HPLC coupled with a fluorescent detector set at 289 nm excitation and 359 nm emission wavelengths (Shimadzu Corp). A Restek Pinnacle II C18 column (5 μ m, 150 \times 4.6 mm, Restek US) was used for HPLC separation. The product separation was done isocratically with a mobile phase consisting of 6% v/v acetonitrile in 30 mM phosphate buffer pH 3.0 (adjusted with phosphoric acid) at 0.7 ml min⁻¹. The level of 5-methyltetrahydrofolate detected was quantified by comparison with standards. For this, a standard calibration curve was created with known amounts of 5,10-methylene tetrahydrofolate reduced to 5-methyltetrahydrofolate using 0.1 M NaBH₄ and 0.1 M DTT and from peak areas of 5-methyltetrahydrofolate eluted. The specific activity of the enzyme at varying concentrations of THF was plotted against THF concentrations to obtain the kinetic curve. Kinetic analysis was repeated three times for each of the enzymes using independent enzyme preparations.

28. Niblack, T. L., Heinz, R. D., Smith, G. S. & Donald, P. A. Distribution, density, and diversity of *Heterodera glycines* in Missouri. *J. Nematol.* **25**, 880–886 (1993).
29. Hartwig, E. F. & Epps, J. M. Registration of 'Forrest' soybeans. *Crop Sci.* **13**, 287 (1973).
30. Smith, T. J. & Camper, H. M. Registration of 'Essex' soybean. *Crop Sci.* **13**, 495 (1973).
31. Bernard, R. L. & Cremeens, C. R. Registration of 'Williams 82' soybean. *Crop Sci.* **28**, 1027–1028 (1988).
32. Brown, S. *et al.* A high-throughput automated technique for counting females of *Heterodera glycines* using a fluorescence-based imaging system. *J. Nematol.* **42**, 201–206 (2010).
33. Hwang, T. Y. *et al.* High density integrated linkage map based on SSR markers in soybean. *DNA Res.* **16**, 213–225 (2009).
34. Meksem, K. *et al.* Two large-inset soybean genomic libraries constructed in a binary vector: Applications in chromosome walking and genome wide physical mapping. *Theor. Appl. Genet.* **101**, 747–755 (2000).
35. Wang, J. *et al.* Dual roles for the variable domain in protein trafficking and host-specific recognition of *Heterodera glycines* CLE effector proteins. *New Phytol.* **187**, 1003–1017 (2010).
36. Kumar, P., Henikoff, S. & Ng, P. C. Predicting the effects of coding non-synonymous variants on protein function using the SIFT algorithm. *Nature Protocols* **4**, 1073–1081 (2009).
37. Xiao, Y.-L. *et al.* Analysis of the cDNAs of hypothetical genes on *Arabidopsis* chromosome 2 reveals numerous transcript variants. *Plant Physiol.* **139**, 1323–1337 (2005).
38. Jefferson, R. A. Assaying chimeric genes in plants: the *GUS* gene fusion system. *Plant Mol. Biol. Rep.* **5**, 387–405 (1987).
39. Stauffer, G. V., Plamann, M. D. & Stauffer, L. T. Construction and expression of hybrid plasmids containing the *Escherichia coli* glyA gene. *Gene* **14**, 63–72 (1981).

An early age increase in vacuolar pH limits mitochondrial function and lifespan in yeast

Adam L. Hughes¹ & Daniel E. Gottschling¹

Mitochondria have a central role in ageing. They are considered to be both a target of the ageing process and a contributor to it¹. Alterations in mitochondrial structure and function are evident during ageing in most eukaryotes², but how this occurs is poorly understood. Here we identify a functional link between the lysosome-like vacuole and mitochondria in *Saccharomyces cerevisiae*, and show that mitochondrial dysfunction in replicatively aged yeast arises from altered vacuolar pH. We found that vacuolar acidity declines during the early asymmetric divisions of a mother cell, and that preventing this decline suppresses mitochondrial dysfunction and extends lifespan. Surprisingly, changes in vacuolar pH do not limit mitochondrial function by disrupting vacuolar protein degradation, but rather by reducing pH-dependent amino acid storage in the vacuolar lumen. We also found that calorie restriction promotes lifespan extension at least in part by increasing vacuolar acidity via conserved nutrient-sensing pathways³. Interestingly, although vacuolar acidity is reduced in aged mother cells, acidic vacuoles are regenerated in newborn daughters, coinciding with daughter cells having a renewed lifespan potential⁴. Overall, our results identify vacuolar pH as a critical regulator of ageing and mitochondrial function, and outline a potentially conserved mechanism by which calorie restriction delays the ageing process. Because the functions of the vacuole are highly conserved throughout evolution⁵, we propose that lysosomal pH may modulate mitochondrial function and lifespan in other eukaryotic cells.

We sought to understand the basis of age-induced mitochondrial dysfunction, using the budding yeast *S. cerevisiae*. Ageing in yeast (replicative ageing) is defined as the number of times an individual cell divides⁴, and aged yeast cells exhibit many of the characteristics of age-induced mitochondrial dysfunction observed in metazoa¹. These include mitochondrial fragmentation, increased levels of mitochondrial reactive oxygen species, and increased loss of mitochondrial DNA in their progeny^{6–9}. We began our inquiry by further characterizing age-associated mitochondrial phenotypes using a genetic system in yeast that enriches for replicatively aged mother cells, the mother enrichment program (MEP)¹⁰. By monitoring an outer mitochondrial membrane protein, Tom70, tagged with green fluorescent protein (Tom70–GFP), we found that mitochondrial dysfunction was prevalent in aged yeast, consistent with results from earlier studies⁶. Mitochondria—which are normally tubular—fragmented and ultimately aggregated in aged cells (Fig. 1a). Mitochondrial fragmentation was present early in the ageing process (86% of cells at 8 divisions), and progressed to large aggregates and small fragments (93% of cells at 17 divisions) that persisted throughout ageing (median lifespan of 28 divisions). We observed similar changes using an inner mitochondrial membrane protein, Tim50–GFP (Supplementary Fig. 2a). Mitochondrial function also declined in aged cells. We measured the mitochondrial membrane potential ($\Delta\Psi$) of aged cells using 3,3'-dihexyloxycarbocyanine iodide (DiOC₆), a $\Delta\Psi$ -dependent mitochondrial fluorescent dye¹¹, and found that 80% of cells had reduced mitochondrial DiOC₆ staining by 7 divisions (Supplementary Fig. 2b). At 18 divisions, $\Delta\Psi$ was even lower and remained low thereafter (100% of cells by 28 divisions). Consistent

with this, $\Delta\Psi$ -dependent import of the mitochondrial matrix chimaeric protein preCox4–mCherry⁹ was also reduced in aged cells (Supplementary Fig. 2c). Collectively, these results indicate that mitochondrial structure and function are progressively altered during the ageing process.

Mitochondrial structure is regulated by 250 identified genes in young cells^{12,13}. We considered whether age-induced mitochondrial dysfunction might be the result of the altered function of processes associated with one or more of these gene products. To explore this

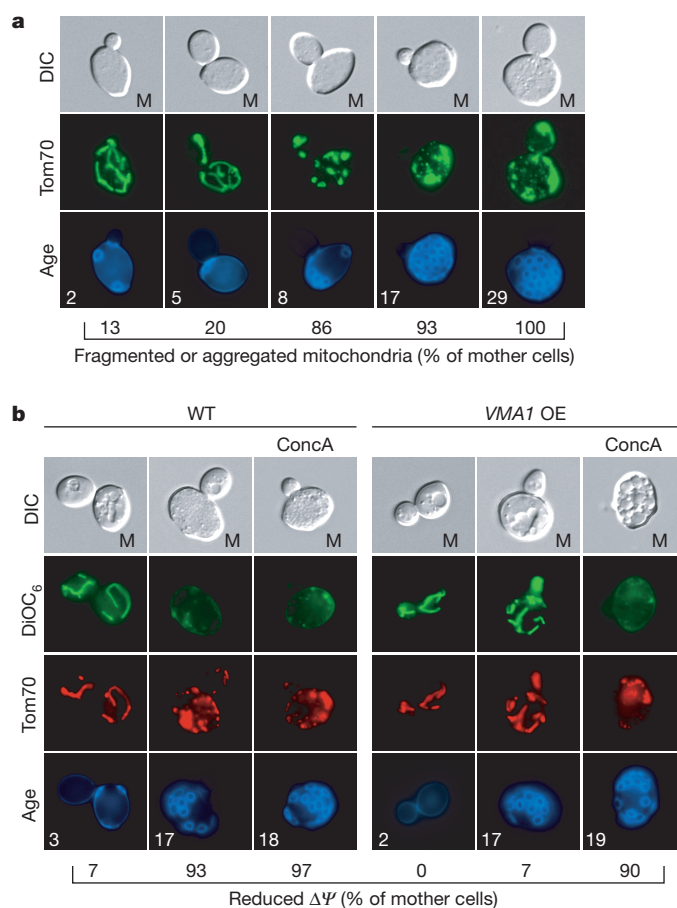


Figure 1 | Age-induced mitochondrial dysfunction is suppressed by VMA1 overexpression. **a**, **b**, Age (divisions) is shown at the bottom of all panels, and represents the exact age for young cells (0–5) and the median age for older cells, as determined by calcofluor staining of bud scars. $n = 30$ for all time points. **a**, Mitochondrial morphology in aged cells expressing the mitochondrial outer membrane protein Tom70–GFP. **b**, Mitochondrial membrane potential as indicated by DiOC₆ staining of aged Tom70–mCherry wild type (WT) and VMA1-overexpressing (OE) cells incubated with or without 500 nM concA for 2 h. Note that DiOC₆ stains the plasma membrane of aged cells.

¹Division of Basic Sciences, Fred Hutchinson Cancer Research Center, Seattle, Washington 98109, USA.

idea, we overexpressed each of the 250 genes in a MEP strain expressing Tom70-GFP, and screened for genes whose overexpression delayed the onset of altered mitochondrial morphology in aged cells. Two suppressors identified in our screen, *VMA1* and *VPH2*, are required for activity of the vacuolar H^+ -ATPase (V-ATPase). The V-ATPase is an evolutionarily conserved protein complex that acidifies the vacuole (the lysosome in metazoa)⁵. Vma1 is the catalytic subunit of the peripheral-membrane-associated V_1 sector of the V-ATPase¹⁴. Vph2 is an endoplasmic-reticulum-localized integral membrane protein required for V-ATPase assembly¹⁵. Overexpression of *VMA1* or *VPH2* from a high-copy promoter suppressed age-induced mitochondrial dysfunction in 93% and 77% of aged cells, respectively (17 or 16 divisions) (Fig. 1b and Supplementary Fig. 3a). Importantly, suppression by *VMA1* or *VPH2* overexpression required V-ATPase activity, as treatment with the specific V-ATPase inhibitor concanamycin A (concaA)¹⁶ blocked their ability to produce normal, tubular mitochondria (Fig. 1b and Supplementary Fig. 3a).

Because overexpressing proteins required for vacuolar acidity prevented age-induced mitochondrial dysfunction, we tested whether vacuolar pH itself was changed in aged cells. Measurement of vacuolar acidity with four different pH-sensitive reporters revealed that the acidity of the vacuole decreased as newborn cells became aged mother cells (Fig. 2a, b and Supplementary Fig. 4a–c). Vacuoles in over 90% of newborn cells were acidic and were stained efficiently with the fluorescent dye quinacrine, which accumulates in acidic environments¹⁷ (Fig. 2a and Supplementary Fig. 4a). However, 87% of cells that had produced daughters had decreased vacuolar acidity, as indicated by little or no quinacrine staining (Fig. 2a and Supplementary Fig. 4a). Kinetic analysis of vacuolar acidity decline using Pho8-SEP/mCherry (a dual fluorescent protein reporter system in which one copy of vacuolar Pho8 is fused to pH-sensitive super ecliptic pHluorin (SEP, which increases in fluorescence with increasing pH)¹⁸ and the other to pH-insensitive mCherry) revealed that vacuolar acidity declined

progressively during approximately the first four mother-cell divisions and then remained low for at least 18 divisions (Fig. 2b). However, acidity did not decline to the level observed in cells lacking V-ATPase function (Fig. 2b), suggesting that the aged cells had not completely lost vacuolar acidity.

Because vacuolar acidity decreases before mitochondrial dysfunction in ageing cells, we wondered whether overexpressing *VMA1* or *VPH2* suppressed mitochondrial dysfunction by preventing vacuolar acidity decline. Indeed, overexpressing *VMA1* or *VPH2* increased vacuolar acidity in $\geq 70\%$ of aged mother cells (~ 18 divisions) (Fig. 2a and Supplementary Fig. 3b). Although it is unclear how *VMA1* overexpression increased vacuolar acidity, overexpressing *VPH2* increased the levels of assembled V-ATPase at the vacuolar membrane (Supplementary Fig. 5).

These results suggest that reduced vacuolar acidity in mother cells leads to the subsequent development of mitochondrial dysfunction. Consistent with this idea, young cells lacking the V-ATPase subunit *VMA2* had reduced $\Delta\Psi$ and mitochondrial morphology similar to aged cells (Supplementary Fig. 6a). Additionally, treatment of young cells with the V-ATPase inhibitor concaA caused mitochondrial depolarization just 30 min after loss of vacuolar acidity (Fig. 2c and Supplementary Fig. 6b). This loss of $\Delta\Psi$ was followed by mitochondrial fragmentation and aggregation that resembled mitochondrial phenotypes present in aged cells. Collectively, these results indicate that vacuolar and mitochondrial function are intimately linked, and suggest that low levels of vacuolar acidity in mother cells cause mitochondrial dysfunction by inducing mitochondrial depolarization that is followed by fragmentation and aggregation.

Because mitochondrial function is a critical regulator of lifespan¹⁹, we suspected that vacuolar pH would be as well. Consistent with this idea, yeast cells lacking V-ATPase activity have drastically shortened lifespans²⁰. We measured the replicative lifespan of wild-type, *VMA1*- and *VPH2*-overexpressing strains and found that overexpressing

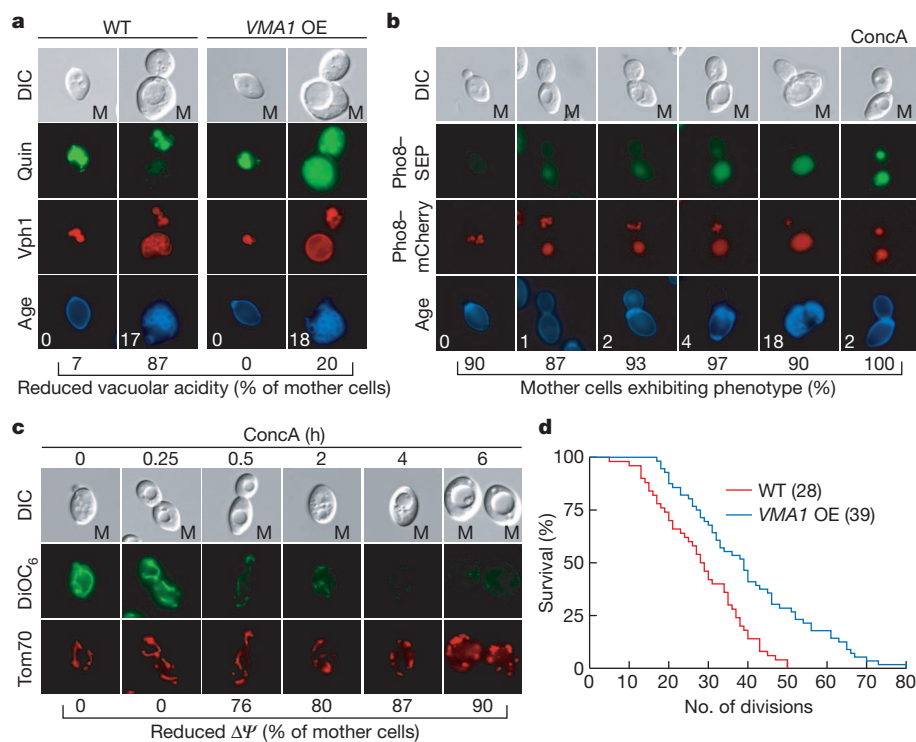


Figure 2 | Vacuolar acidity is reduced in ageing cells and regulates mitochondrial function and lifespan. a–c, Notation is as for Fig. 1a, b. a, b, Vacuolar acidity as indicated by quinacrine (quin; a) staining of aged Vph1-mCherry wild-type (WT) and *VMA1*-overexpressing (OE) cells, and the vacuolar pH reporter Pho8-SEP in cells expressing Pho8-mCherry incubated

with or without 500 nM concaA for 15 min (b). c, DiOC₆ staining of young cells expressing Tom70-mCherry treated with 500 nM concaA for the indicated time. d, Replicative lifespan of wild-type and *VMA1*-overexpressing cells by micromanipulation. Median lifespan is indicated. $P = 0.0002$, Wilcoxon rank-sum test. $n = 50$ for wild-type and 56 for *VMA1*-overexpressing cells.

either gene significantly increased both median and maximal replicative lifespan (Fig. 2d and Supplementary Fig. 3c). These results suggest that vacuolar pH is indeed an important determinant of yeast lifespan.

We then asked how vacuolar pH affects mitochondrial function. The vacuolar proton gradient generated by the V-ATPase is required for efficient protein degradation, and for transport of ions and basic and neutral amino acids into the vacuole for storage⁵. Blocking vacuolar protein degradation in a pH-independent manner by deleting the vacuolar protease *PEP4* (ref. 21) did not alter mitochondrial structure or $\Delta\Psi$ (Supplementary Fig. 7). Therefore, we examined whether reduced import of vacuolar metabolites was responsible for mitochondrial dysfunction under conditions of decreased vacuolar acidity. If reduced import of a particular amino acid or ion into the vacuole led to mitochondrial dysfunction, then overexpressing the transporter required for import of that metabolite into the vacuole might suppress mitochondrial dysfunction in cells with a low vacuolar proton gradient. To test this, we reduced the vacuolar proton gradient by treating cells with low concentrations of concA, and measured mitochondrial $\Delta\Psi$ with DiOC₆ in cells overexpressing individual vacuolar amino acid or ion transporters. Overexpressing most characterized V-ATPase-dependent vacuolar importers^{22–24} had no (*NHX1*, *VBA1*, *VBA3*) or little (*VCX1*, *VBA2*) effect on mitochondrial function. However, overexpressing *AVT1*, a neutral amino acid transporter²⁵, prevented mitochondrial dysfunction in 60% of cells (Supplementary Fig. 8a, b). This suggests that disrupting proton-dependent neutral amino acid storage in the vacuole causes mitochondrial dysfunction.

We also found that *AVT1* was critical in connecting the vacuole and mitochondria during ageing. Overexpressing *AVT1* prevented alterations in mitochondrial structure and $\Delta\Psi$ in 63% of aged cells (19 divisions; Fig. 3a), even though vacuolar acidity was reduced in these cells (17 divisions; Supplementary Fig. 9a). Conversely, deleting *AVT1* accelerated the development of age-induced mitochondrial dysfunction (Fig. 3b) without affecting the kinetics of vacuolar acidity decline

(Supplementary Fig. 9b). Deleting *AVT1* also prevented the suppression of mitochondrial dysfunction by *VMA1* and *VPH2* overexpression without affecting vacuolar acidity (Fig. 3c and Supplementary Fig. 3d). Collectively, these results suggest that reduced vacuolar acidity in aged cells might cause mitochondrial dysfunction by preventing adequate import of neutral amino acids through the vacuolar transporter *Avt1*. Importantly, overexpressing or deleting *AVT1* was sufficient to extend or shorten replicative lifespan, respectively (Fig. 3d). This suggests that changes in vacuolar pH modulate lifespan at least in part through regulation of mitochondrial function. The differences in mitochondrial function and lifespan by *AVT1* overexpression or deletion were not as marked as when vacuolar pH was increased or decreased (compare Fig. 3 to Figs 1 and 2), suggesting that substrates of additional V-ATPase-dependent transporters may contribute to age-induced mitochondrial dysfunction caused by reduced vacuolar acidity.

Calorie restriction extends lifespan in most eukaryotes through conserved nutrient-sensing pathways³. In yeast, calorie restriction is thought to function through at least three nutrient-sensing pathways/kinases: the cAMP-dependent protein kinase A (PKA) pathway, the target of rapamycin (TOR) pathway, and the putative S6 kinase/AKT homologue Sch9 (refs 20, 26). Reduced activity of any of these kinases mimics calorie restriction and extends lifespan. We found that growth in calorie-restricted carbon sources (0.5% glucose, 0.05% glucose and 3% glycerol)^{26,27} increased vacuolar acidity in young cells (Supplementary Fig. 10), and prevented the decline of vacuolar acidity in ageing cells (Fig. 4a). Calorie restriction also suppressed mitochondrial dysfunction in 90% of aged cells (21 divisions) in a V-ATPase-dependent manner (Fig. 4b).

Calorie restriction seems to regulate vacuolar acidity through conserved nutrient-sensing pathways because inhibiting PKA, Sch9 or TOR by the lifespan-extending mutations *gpa2Δ*, *sch9Δ* or *tor1Δ*, also prevented the decline of vacuolar acidity and development of mitochondrial dysfunction in ageing cells (Supplementary Fig. 11a, b)^{20,26}.

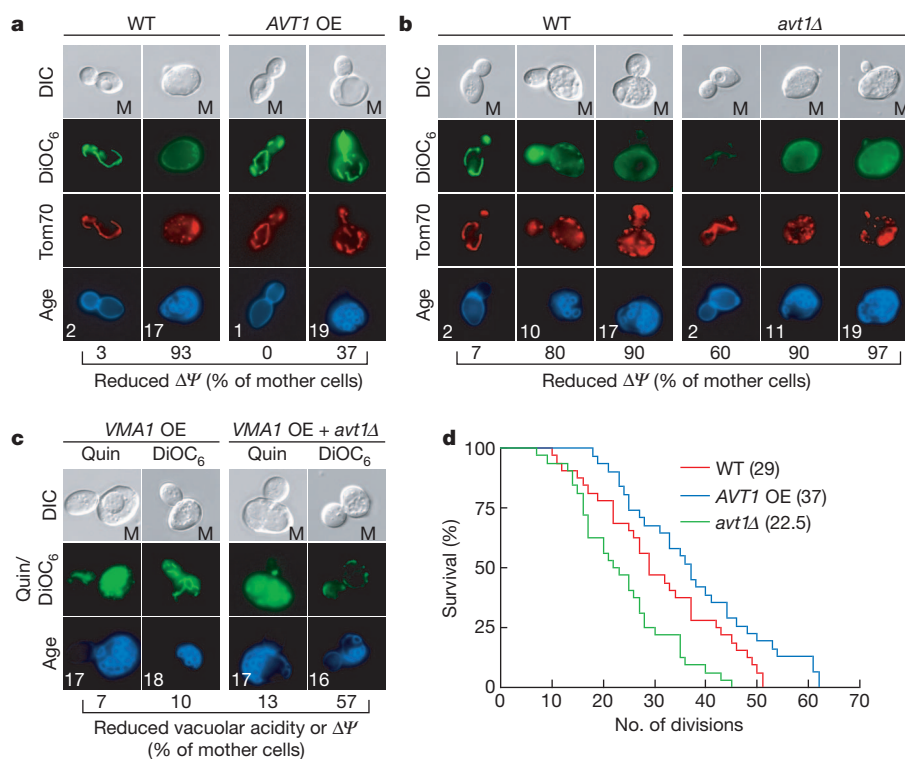


Figure 3 | Reduced vacuolar acidity causes mitochondrial dysfunction by disrupting amino acid homeostasis. **a–c**, Notation is as for Fig. 1a, b. **a**, **b**, DiOC₆ staining of aged Tom70-mCherry wild-type (WT), *AVT1*-overexpressing (OE) (**a**) and *avt1Δ* cells (**b**). **c**, Quinacrine (quin) and DiOC₆ staining of aged wild-type and *avt1Δ* cells overexpressing *VMA1*. **d**, Replicative

lifespan of wild-type, *avt1Δ* and *AVT1*-overexpressing cells by micromanipulation. Median lifespan is indicated. $P = 0.0376$ (wild-type versus *AVT1*-overexpressing cells), $P = 0.0045$ (wild type versus *avt1Δ*), Wilcoxon rank-sum test. $n = 32$ for wild type, 32 for *AVT1*-overexpressing, and 31 for *avt1Δ*.

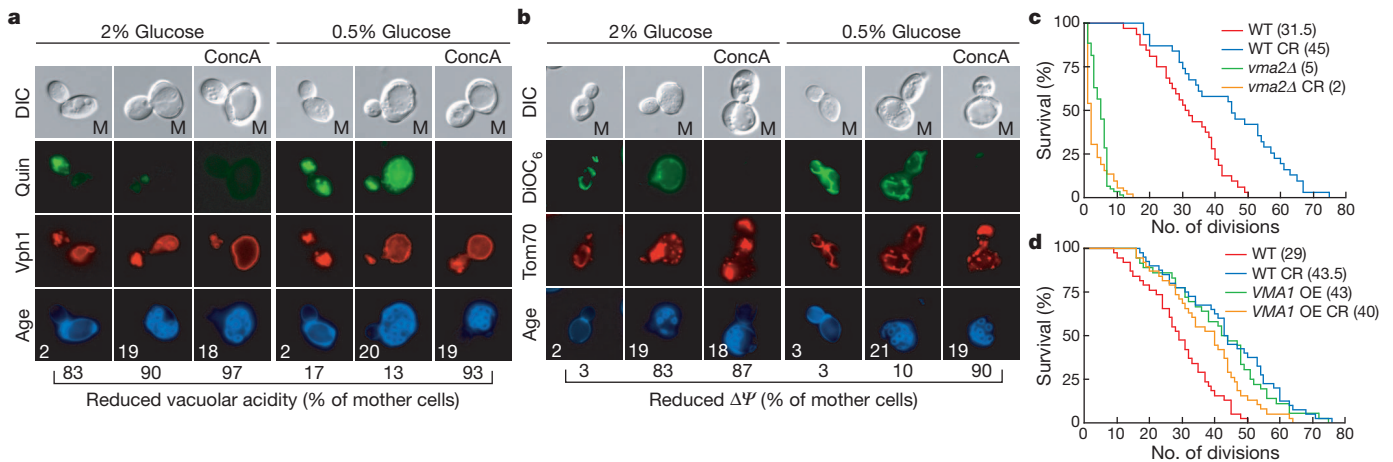


Figure 4 | Calorie restriction extends lifespan by regulating vacuolar acidity. **a, b**, Notation is as for Fig. 1a, b. Quinacrine (**a**) or DiOC₆ (**b**) staining of cells expressing Vph1-mCherry (**a**) or Tom70-mCherry (**b**) aged in 2% or 0.5% glucose with or without 500 nM concA for the final 2 h of ageing. **c, d**, Replicative lifespan of wild-type (WT), *vma2Δ* (**c**) and *VMA1*-overexpressing (OE) cells (**d**) grown with or without calorie restriction (CR; 0.5% glucose). Median lifespan is indicated. **c**, $P < 0.0001$ (wild type versus wild-type calorie restricted), $P = 0.0398$ (*vma2Δ* versus *vma2Δ* calorie restricted), $P < 0.0001$ (wild type versus *vma2Δ*), Wilcoxon rank-sum test.

Consistent with this, constitutively activating the PKA pathway by deleting the Ras GTPase-activating protein *IRA2* (ref. 28), reduced vacuolar acidity and accelerated the development of mitochondrial dysfunction in ageing cells (Supplementary Fig. 11c, d). Deleting *IRA2* also prevented calorie-restriction-mediated enhancement of vacuolar acidity and suppression of mitochondrial dysfunction (Supplementary Fig. 11c, d). Furthermore, we found that lifespan extension by calorie restriction was prevented in a strain lacking V-ATPase activity (Fig. 4c) and, conversely, calorie restriction did not further extend the lifespan of a strain overexpressing *VMA1* (Fig. 4d). Collectively, these results indicate that vacuolar acidity is a target of calorie-restriction-regulated nutrient sensing pathways, and suggest that calorie restriction suppresses age-induced mitochondrial dysfunction and extends lifespan at least in part by preventing the decline in vacuolar acidity in ageing cells.

In budding yeast, cytokinesis is asymmetric with respect to ageing. Although mother cells age, they produce daughter cells with full lifespan potential, suggesting that the cellular events that cause ageing are reset in daughter cells⁴. During our analysis, we discovered a marked distinction in vacuolar pH between mother and daughter cells. Although vacuolar acidity was reduced in mother cells, high acidity was restored in newborn cells, even in daughters of old mothers (Fig. 2a, b and Supplementary Fig. 4a–c). This asymmetry required V-ATPase activity, as it was eliminated in *vma2Δ* cells, which lack V-ATPase activity and have constitutively reduced vacuolar acidity (Supplementary Fig. 4d). Taking all our results together, the acidity of the vacuole seems to be critical for resetting lifespan in new yeast cells, and represents the earliest ‘rejuvenation’ event observed in this organism.

Overall, our results support a model (Supplementary Fig. 1) in which a progressive decline in vacuolar acidity during early mother-cell divisions limits mitochondrial function and lifespan, and provide a potential mechanism by which amino acid and glucose limitation may converge to regulate lifespan. Somewhat surprisingly, our data indicate that at least in yeast, age-induced mitochondrial dysfunction is not the result of a block in vacuolar protein degradation, but is rather due to decreased uptake of neutral amino acids into the vacuolar lumen. How an apparent reduction in neutral amino acid storage leads to a decline in mitochondrial membrane potential remains to be determined, but we speculate that mitochondria-dependent catabolism of

$n = 32$ for wild type, 31 for wild-type calorie restricted, 60 for *vma2Δ*, and 52 for *vma2Δ* calorie restricted. **d**, $P < 0.0001$ (wild type versus wild-type calorie restricted), $P < 0.0001$ (wild type versus *VMA1*-overexpressing), $P = 0.0023$ (wild type versus *VMA1*-overexpressing calorie restricted), $P = 0.52$ (wild-type calorie restricted versus *VMA1*-overexpressing), $P = 0.076$ (*VMA1*-overexpressing versus *VMA1*-overexpressing calorie restricted), Wilcoxon rank-sum test. $n = 38$ for wild type, 40 for wild-type calorie restricted, 36 for *VMA1*-overexpressing, and 38 for *VMA1*-overexpressing calorie restricted.

excess cytoplasmic amino acids (or their derivatives) places a large burden on proton-dependent mitochondrial carrier proteins²⁹ and, in the process, overwhelms mitochondrial $\Delta\Psi$. Other metabolites may also contribute to this vacuolar-mitochondrial cross-talk, and the nature of relevant metabolite(s) will be influenced by the cellular growth environment. Given that V-ATPase-coupled amino acid/ion import⁵ and lifespan extension by reduction of amino acids in food³⁰ are conserved among many organisms, we postulate that our findings in yeast might be applicable to other eukaryotes.

METHODS SUMMARY

A detailed description of all experimental methods including strains, plasmids, cell culture, MEP purification, fluorescent staining, microscopy, lifespan measurement, protein preparation, western blotting and the mitochondrial screen is provided in Methods.

Full Methods and any associated references are available in the online version of the paper.

Received 28 November 2011; accepted 4 October 2012.

Published online 21 November 2012.

- Guarente, L. Mitochondria—a nexus for aging, calorie restriction, and sirtuins? *Cell* **132**, 171–176 (2008).
- Seo, A. Y. *et al.* New insights into the role of mitochondria in aging: mitochondrial dynamics and more. *J. Cell Sci.* **123**, 2533–2542 (2010).
- Bishop, N. A. & Guarente, L. Genetic links between diet and lifespan: shared mechanisms from yeast to humans. *Nature Rev. Genet.* **8**, 835–844 (2007).
- Steinkraus, K. A., Kaeblerlein, M. & Kennedy, B. K. Replicative aging in yeast: the means to the end. *Annu. Rev. Cell Dev. Biol.* **24**, 29–54 (2008).
- Li, S. C. & Kane, P. M. The yeast lysosome-like vacuole: endpoint and crossroads. *Biochim. Biophys. Acta* **1793**, 650–663 (2009).
- Scheekhuber, C. Q. *et al.* Reducing mitochondrial fission results in increased life span and fitness of two fungal ageing models. *Nature Cell Biol.* **9**, 99–105 (2007).
- Lam, Y. T., Aung-Htut, M. T., Lim, Y. L., Yang, H. & Dawes, I. W. Changes in reactive oxygen species begin early during replicative aging of *Saccharomyces cerevisiae* cells. *Free Radic. Biol. Med.* **50**, 963–970 (2011).
- McFaline-Figueroa, J. R. *et al.* Mitochondrial quality control during inheritance is associated with lifespan and mother-daughter age asymmetry in budding yeast. *Aging Cell* **10**, 885–895 (2011).
- Veatch, J. R., McMurray, M. A., Nelson, Z. W. & Gottschling, D. E. Mitochondrial dysfunction leads to nuclear genome instability via an iron-sulfur cluster defect. *Cell* **137**, 1247–1258 (2009).
- Lindstrom, D. L. & Gottschling, D. E. The mother enrichment program: a genetic system for facile replicative life span analysis in *Saccharomyces cerevisiae*. *Genetics* **183**, 413–422 (2009).

11. Pringle, J. R. *et al.* Fluorescence microscopy methods for yeast. *Methods Cell Biol.* **31**, 357–435 (1989).
12. Dimmer, K. S. *et al.* Genetic basis of mitochondrial function and morphology in *Saccharomyces cerevisiae*. *Mol. Biol. Cell* **13**, 847–853 (2002).
13. Altmann, K. & Westermann, B. Role of essential genes in mitochondrial morphogenesis in *Saccharomyces cerevisiae*. *Mol. Biol. Cell* **16**, 5410–5417 (2005).
14. Hirata, R. *et al.* Molecular structure of a gene, *VMA1*, encoding the catalytic subunit of H⁺-translocating adenosine triphosphatase from vacuolar membranes of *Saccharomyces cerevisiae*. *J. Biol. Chem.* **265**, 6726–6733 (1990).
15. Jackson, D. D. & Stevens, T. H. *VMA12* encodes a yeast endoplasmic reticulum protein required for vacuolar H⁺-ATPase assembly. *J. Biol. Chem.* **272**, 25928–25934 (1997).
16. Droese, S. *et al.* Inhibitory effect of modified bafilomycins and concanamycins on P- and V-type adenosinetriphosphatases. *Biochemistry* **32**, 3902–3906 (1993).
17. Weisman, L. S., Bacallao, R. & Wickner, W. Multiple methods of visualizing the yeast vacuole permit evaluation of its morphology and inheritance during the cell cycle. *J. Cell Biol.* **105**, 1539–1547 (1987).
18. Sankaranarayanan, S., De Angelis, D., Rothman, J. E. & Ryan, T. A. The use of pHluorins for optical measurements of presynaptic activity. *Biophys. J.* **79**, 2199–2208 (2000).
19. Lin, S. J. *et al.* Calorie restriction extends *Saccharomyces cerevisiae* lifespan by increasing respiration. *Nature* **418**, 344–348 (2002).
20. Kaeblerlein, M. *et al.* Regulation of yeast replicative life span by TOR and Sch9 in response to nutrients. *Science* **310**, 1193–1196 (2005).
21. Parr, C. L., Keates, R. A., Bryksa, B. C., Ogawa, M. & Yada, R. Y. The structure and function of *Saccharomyces cerevisiae* proteinase A. *Yeast* **24**, 467–480 (2007).
22. Shimazu, M., Sekito, T., Akiyama, K., Ohsumi, Y. & Kakinuma, Y. A family of basic amino acid transporters of the vacuolar membrane from *Saccharomyces cerevisiae*. *J. Biol. Chem.* **280**, 4851–4857 (2005).
23. Miseta, A., Kellermayer, R., Aiello, D. P., Fu, L. & Bedwell, D. M. The vacuolar Ca²⁺/H⁺ exchanger Vcx1p/Hum1p tightly controls cytosolic Ca²⁺ levels in *S. cerevisiae*. *FEBS Lett.* **451**, 132–136 (1999).
24. Nass, R., Cunningham, K. W. & Rao, R. Intracellular sequestration of sodium by a novel Na⁺/H⁺ exchanger in yeast is enhanced by mutations in the plasma membrane H⁺-ATPase. Insights into mechanisms of sodium tolerance. *J. Biol. Chem.* **272**, 26145–26152 (1997).
25. Russnak, R., Konczal, D. & McIntire, S. L. A family of yeast proteins mediating bidirectional vacuolar amino acid transport. *J. Biol. Chem.* **276**, 23849–23857 (2001).
26. Lin, S. J., Defossez, P. A. & Guarente, L. Requirement of NAD and *SIR2* for life-span extension by calorie restriction in *Saccharomyces cerevisiae*. *Science* **289**, 2126–2128 (2000).
27. Kaeblerlein, M., Kirkland, K. T., Fields, S. & Kennedy, B. K. Sir2-independent life span extension by calorie restriction in yeast. *PLoS Biol.* **2**, e296 (2004).
28. Tanaka, K. *et al.* *cerevisiae* genes *IRA1* and *IRA2* encode proteins that may be functionally equivalent to mammalian *ras* GTPase activating protein. *Cell* **60**, 803–807 (1990).
29. Palmieri, F. *et al.* Identification of mitochondrial carriers in *Saccharomyces cerevisiae* by transport assay of reconstituted recombinant proteins. *Biochim. Biophys. Acta* **1757**, 1249–1262 (2006).
30. Piper, M. D., Partridge, L., Raubenheimer, D. & Simpson, S. J. Dietary restriction and aging: a unifying perspective. *Cell Metab.* **14**, 154–160 (2011).

Supplementary Information is available in the online version of the paper.

Acknowledgements We thank L. Pallanck and members of the Gottschling laboratory for reviewing the manuscript; K. Henderson for helpful discussions; G. Miesenböck, D. Lindstrom and J. Hsu for reagents; and L. Dimitrov for technical assistance. This work was supported by National Institutes of Health grants AG037512 and AG023779, and a Glenn Award for Research in Biological Mechanisms of Aging to D.E.G., and by fellowships from the Helen Hay Whitney Foundation and Genetic Approaches to Aging Training Grant (T32 AG000057) to A.L.H.

Author Contributions A.L.H. designed and carried out the experiments. D.E.G. provided experimental guidance and supervision. Both authors discussed the results and implications of the experiments. The paper was written by A.L.H. and edited by D.E.G.

Author Information Reprints and permissions information is available at www.nature.com/reprints. The authors declare no competing financial interests. Readers are welcome to comment on the online version of the paper. Correspondence and requests for materials should be addressed to D.E.G. (dgottsch@fhcrc.org).

METHODS

Strains. Yeast strains are listed in Supplementary Table 1. All strains are derivatives of *S. cerevisiae* S288c (BY) unless otherwise indicated. One-step PCR-mediated gene replacement and epitope tagging were carried out using standard techniques, the previously described template plasmids pRS306, pRS400 KanMX, pKT127 and pBS34 (refs 31, 32), and the newly created template plasmid pKT127-SEP. pBS34 was obtained from the Yeast Resource Center at the University of Washington with permission from R. Tsien³³. Oligonucleotides for gene replacement and tagging are listed in Supplementary Table 2. Strains expressing empty vector, *VMA1*, *VPH2* or *AVT1* from a *GPD* promoter integrated into an empty region of chromosome 1 (199456–199457) were constructed by transformation of parental yeast strains with NotI-digested pAG306-GPD-empty chr 1, pAG306-GPD-VMA1 chr 1, pAG306-GPD-VPH2 chr 1 or pAG306-GPD-AVT1 chr 1, respectively. Strains expressing Vma2-GFP were derived from the yeast GFP collection³⁴.

Plasmids. pAG306-GPD-empty chr 1, pAG306-GPD-VMA1 chr 1, pAG306-GPD-VPH2 chr 1 and pAG306-GPD-AVT1 chr 1 were generated in two steps. First, we created pAG306-GPD-*ccdB* chr 1, a plasmid for high expression of genes from the *GPD* promoter that can be integrated into chromosome 1 (199456–199457) after NotI digestion. We generated pAG306-GPD-*ccdB* chr 1 by ligation of a SmaI-digested fusion PCR product that contained two ~500-base-pair regions of chromosome 1 flanking a NotI site into AatII-digested pAG306-GPD-*ccdB* (Addgene plasmid 14140)³⁵. We generated the fusion PCR product using oligonucleotides ChrI PartB SmaI F and ChrI PartA SmaI R to amplify two templates generated by PCR of yeast genomic DNA using oligonucleotide pairs ChrI PartA NotI F and ChrI PartA SmaI R, and ChrI PartB SmaI F and ChrI PartB NotI R, respectively. Second, we inserted *VMA1*, *VPH2* and *AVT1* into pAG306-GPD-*ccdB* chr 1 from donor Gateway plasmids pDONR221-VMA1 (Harvard Institute of Proteomics (HIP) accession ScCD00023712), pDONR221-VPH2 (HIP accession ScCD00012560) and pDONR221-AVT1 (HIP accession ScCD00012825) using LR clonase according to the manufacturer's instructions (Invitrogen)³⁶. We created pAG306-GPD-empty chr 1 by digestion of pAG306-GPD-*ccdB* chr 1 with HindIII and SpeI to remove the *ccdB* gene, followed by blunt-ended religation of the plasmid after filling in overhangs with T4 DNA polymerase (New England Biolabs).

pKT127-SEP, used for creating in-frame C-terminal chromosomal fusions of a gene of interest with SEP, was created by removing GFP from pKT127 by restriction digestion with PacI/AscI and replacing it with PacI/AscI-digested SEP generated by PCR of template plasmid pGM87 (ref. 18) using oligonucleotides SEP PacI F and SEP AscI R.

Media and cell culture. Cells were grown exponentially for 15 h to a maximum density of 5×10^6 cells ml⁻¹ before the initiation of all experiments. Because nutrients and growth phase affected vacuolar and mitochondrial function, extended log-phase growth was necessary to ensure vacuolar and mitochondrial uniformity across the cell population before the initiation of all experiments. Cells were cultured in YEPD (1% yeast extract, 2% peptone, 2% glucose) unless otherwise indicated. For calorie restriction experiments, cells were cultured in YEP plus the indicated carbon source. Yeast Complete (YC) medium used in the high-copy suppressor screen was previously described³⁷. ConCA (Sigma) was added to cultures at a final concentration of 250 or 500 nM as indicated in figure legends.

Culturing and purification of aged MEP cells. MEP cells were aged and purified for downstream analysis as previously described with slight modifications^{10,38}. Briefly, 2.5×10^7 cells from a 15 h YEPD log-phase culture were washed twice in PBS, pH 7.4, and resuspended in PBS containing 3 mg ml⁻¹ Sulfa-NHS-LC-Biotin (Pierce) at a final concentration of 2.5×10^6 cells ml⁻¹. Cells were incubated for 30 min at room temperature (23 °C) and then washed twice in PBS and once in YEPD. Biotinylated cells were resuspended in 10 ml YEPD at 2.5×10^6 cells ml⁻¹ and recovered with shaking for 2 h at 30 °C. These cells were used to seed cultures at a density of 2×10^4 biotinylated cells per ml in YEPD. β -Oestradiol (Sigma) was added to cultures at a final concentration of 1 μ M to initiate the MEP and cells were cultured at 30 °C for an appropriate time to obtain cells of a desired age (~1 h for median age 2, 12 h for age 8, 24 h for age 16, 48 h for age 28). Cell densities never exceeded 4×10^6 cells ml⁻¹ and cells were washed and resuspended in fresh media every 24 h (12 h for calorie restriction experiments) to prevent nutrient limitation. At each ageing time point, 1×10^8 total cells were harvested for purification, staining, and microscopy analysis.

For live-cell purification, cells were washed twice in PBS, resuspended at a density of 2×10^8 cells ml⁻¹ in 500 μ l of PBS, and incubated for 30 min at room temperature with 25 μ l streptavidin-coated magnetic beads (MicroMACS, Miltenyi Biotec). After incubation, cells were washed twice in PBS, resuspended in 8 ml of PBS, and loaded onto an LS MACS column (Miltenyi Biotec) equilibrated with 5 ml of PBS. After gravity flow-through of unlabelled cells and debris, columns were washed twice with 8 ml of PBS. Columns were then removed from

the magnetic field and aged cells were eluted by gravity flow with 8 ml of PBS. For cell-staining experiments, purified cells were pelleted, resuspended in YEP containing 2% or 0.5% glucose at 2×10^6 cells ml⁻¹, and recovered for 1 h at 30 °C before staining.

For purification of cells after fixation, cells were washed once in PBS and resuspended at 2×10^8 cells ml⁻¹ and fixed in 500 μ l of 4% paraformaldehyde in H₂O for 15 min. Cells were then washed twice in PBS before incubation with streptavidin beads at 4 °C instead of at room temperature. Additionally, 2 mM EDTA was added to PBS in all fixed-cell purification steps to prevent cell clumping.

Labelling and purification of aged non-MEP cells (Supplementary Fig. 2c) was conducted exactly as described for MEP cells except that labelled mother cells were purified after 12 h of log-phase growth, reseeded, and purified a second time after another 12 h of log-phase growth to obtain 18-division-old mother cells. Cells never exceeded a density of 7×10^6 cells ml⁻¹.

Fluorescent staining and microscopy. Quinacrine (Sigma) staining was performed as previously described³⁹. Briefly, 2×10^6 log-phase or purified aged cells were washed once in YEPD plus 100 mM HEPES, pH 7.6, and resuspended in 100 μ l of the same buffered media containing 200 μ M quinacrine. Cells were incubated for 10 min at 30 °C and then 5 min on ice. Cells were pelleted and washed twice with ice-cold 100 mM HEPES, pH 7.6, plus 2% glucose. Cells were resuspended in 100 mM HEPES, pH 7.6, plus 2% glucose for imaging. Before imaging, cells were kept on ice and all images were obtained within 30 min of staining.

For staining with 5-(and-6)-carboxy-2',7'-dichlorofluorescein diacetate¹¹ (CDCFDA) (Invitrogen) or 2',7'-bis (carboxyethyl)-5(6)-carboxyfluorescein⁴⁰ (BCECF-AM) (Invitrogen), 2×10^6 log-phase or purified aged cells were washed once in YEPD plus 100 mM HEPES, pH 7.6, and resuspended in 100 μ l of the same buffered media containing 10 μ M CDCFDA or 50 μ M BCECF. Cells were incubated for 30 min at 30 °C and then washed twice at room temperature with 100 mM HEPES, pH 7.6, plus 2% glucose. Cells were resuspended in 100 mM HEPES, pH 7.6, plus 2% glucose for imaging.

DiOC₆ (Invitrogen) staining was carried out according to manufacturer's instructions. Briefly, 2×10^6 log-phase or purified aged cells were washed once in 10 mM HEPES, pH 7.6, plus 5% glucose and resuspended in 1 ml of the same buffer containing 175 nM DiOC₆. Cells were incubated for 15 min at room temperature and then washed twice with 10 mM HEPES, pH 7.6, plus 5% glucose. Cells were resuspended in 10 mM HEPES, pH 7.6, plus 5% glucose for imaging. Pho8-SEP imaging was also carried out in DiOC₆ imaging buffer after incubation of cells for 20 min in the buffer. In all live-cell experiments, calcofluor (Sigma) staining of bud scars for age determination was carried out by including 5 μ g ml⁻¹ calcofluor in the first post-staining wash step before imaging.

For fluorescence microscopy analysis, cells were visualized under $\times 60$ oil magnification using a Nikon Eclipse E800 with the appropriate filter set: UV-2E/C DAPI for calcofluor; FITC-HYQ for GFP, SEP, quinacrine, CDCFDA, BCECF and DiOC₆; and G-2E/C TRITC for mCherry. Images were acquired with a CoolSNAP HQ² CCD camera (Photometrics) and quantified and processed using MetaMorph version 7.1.1.0 imaging software. Cells that exhibited at least a fourfold reduction in mean fluorescence intensity, compared to young, wild-type cells, were scored as 'reduced' in all figures.

Lifespan measurement by micromanipulation. Replicative lifespan was measured by micromanipulation as previously described, except that cells were grown exponentially in YEPD for 15 h instead of 3 h before lifespan analysis¹⁰.

Membrane protein preparation. 5×10^7 cells were resuspended in 50 μ l B88 buffer (2 mM HEPES, pH 7.2, 150 mM KOAc, 5 mM MgOAc and 250 mM sorbitol) plus protease inhibitors (leupeptin, pepstatin, PMSF and aprotinin) and lysed with glass beads for 10 min in a Multi-Tube Vortexer (VWR) at 4 °C. One-hundred microliters of B88 plus protease inhibitors was added to the sample and the lysate was centrifuged at 500g for 5 min at 4 °C. The supernatant of this spin was centrifuged at 20,000g for 10 min at 4 °C. The membrane pellet was resuspended in 100 μ l of SDS-lysis buffer (10 mM Tris-HCl, pH 6.8, 100 mM NaCl, 1% SDS, 1 mM EDTA and 1 mM EGTA) plus protease inhibitors. The supernatant of the 20,000g spin was used as the cytosolic extract.

Immunoblotting. Membrane and cytosolic extracts were mixed with 0.25 volumes of 5 \times SDS loading buffer (150 mM Tris-HCl, pH 6.8, 15% SDS, 25% glycerol, 0.02% bromophenol blue, 12.5% β -mercaptoethanol) and heated to 37 °C for 15 min. Aliquots of each sample were resolved on 7% polyacrylamide gels and transferred to nitrocellulose membranes (Invitrogen). Membranes were blocked with 5% non-fat dry milk in PBS-T (137 mM NaCl, 2.7 mM KCl, 10 mM Na₂HPO₄, 2 mM KH₂PO₄, 0.05% Tween 20, pH 7.4) and then incubated with primary and HRP-conjugated secondary antibodies (Jackson ImmunoResearch). Blots were washed in PBS-T after each antibody incubation. Bound peroxidase-conjugated antibodies were detected using the SuperSignal West Pico Chemiluminescent substrate (Pierce). Primary antibodies were anti-Vma2 13D11

(Invitrogen), anti-Pgk1 22C5 (Invitrogen), anti-Pho8 1D3 (Invitrogen) and anti-mCherry Living Colours monoclonal (Clontech).

Aged-cell mitochondrial suppressor screen. MEP cells expressing Tom70–GFP were individually transformed in 96-well format with 280 high-copy 2 μ m plasmids from a tiled genomic DNA library⁴¹. Each plasmid contained a unique sequence-verified genomic DNA fragment that expressed at least one of 250 genes previously determined to affect mitochondrial morphology when deleted^{12,13} (some genes were present on more than one plasmid). To identify genes that suppressed age-induced changes in mitochondrial morphology, all 280 plasmid-expressing strains were individually cultured in 5 ml of YEPD at 30 °C for 6 h to a density of 2×10^4 cells ml⁻¹ from overnight-saturated cultures of cells grown in YC-leucine to maintain plasmids. After 6 h in YEPD, β -oestradiol was added to cultures at a final concentration of 1 μ M to initiate the MEP and cells were cultured at 30 °C for an additional 24 h to obtain mother cells with a median age of 16 divisions ($n = 15$). Cells were collected by centrifugation, fixed with 4% paraformaldehyde, stained with calcofluor, and imaged by fluorescence microscopy for mitochondrial morphology as described earlier. Plasmid containing strains in which 40% of aged (median age of 16, $n = 15$) cells exhibited young-cell-like tubular mitochondrial morphology were scored as suppressors of age-induced mitochondrial dysfunction. To confirm potential suppressors, each candidate gene was transferred using LR clonase from pDONR221 Gateway entry plasmids from a previously described collection (HIP) into pAG306-GPD-ccdB chr 1 (ref. 36). Plasmids were integrated into chromosome 1 of a Tom70–GFP-expressing strain after NotI digestion and strains were aged, purified, and examined by fluorescence microscopy as described earlier. Positive integrated suppressors (such as *VMA1* and *VPH2*) were confirmed by their ability to maintain

young-cell-like mitochondrial morphology in at least 70% ($n = 30$) of aged cells (median age of 17).

31. Baker Brachmann, C. *et al.* Designer deletion strains derived from *Saccharomyces cerevisiae* S288C: a useful set of strains and plasmids for PCR-mediated gene disruption and other applications. *Yeast* **14**, 115–132 (1998).
32. Sheff, M. A. & Thorn, K. S. Optimized cassettes for fluorescent protein tagging in *Saccharomyces cerevisiae*. *Yeast* **21**, 661–670 (2004).
33. Shaner, N. C. *et al.* Improved monomeric red, orange and yellow fluorescent proteins derived from *Discosoma* sp. red fluorescent protein. *Nature Biotechnol.* **22**, 1567–1572 (2004).
34. Huh, W.-K. *et al.* Global analysis of protein localization in budding yeast. *Nature* **425**, 686–691 (2003).
35. Alberti, S., Gitler, A. D. & Lindquist, S. A suite of Gateway cloning vectors for high-throughput genetic analysis in *Saccharomyces cerevisiae*. *Yeast* **24**, 913–919 (2007).
36. Hu, Y. *et al.* Approaching a complete repository of sequence-verified protein-encoding clones for *Saccharomyces cerevisiae*. *Genome Res.* **17**, 536–543 (2007).
37. Van Leeuwen, F. & Gottschling, D. E. Assays for gene silencing in yeast. *Methods Enzymol.* **350**, 165–186 (2002).
38. Lindstrom, D. L., Leverich, C. K., Henderson, K. A. & Gottschling, D. E. Replicative age induces mitotic recombination in the ribosomal RNA gene cluster of *Saccharomyces cerevisiae*. *PLoS Genet.* **7**, e1002015 (2011).
39. Morano, K. A. & Klionsky, D. J. Differential effects of compartment deacidification on the targeting of membrane and soluble proteins to the vacuole in yeast. *J. Cell Sci.* **107**, 2813–2824 (1994).
40. Plant, P. J., Manolson, M. F., Grinstein, S. & Demarex, N. Alternative mechanisms of vacuolar acidification in H⁺-ATPase-deficient yeast. *J. Biol. Chem.* **274**, 37270–37279 (1999).
41. Jones, G. M. *et al.* A systematic library for comprehensive overexpression screens in *Saccharomyces cerevisiae*. *Nature Methods* **5**, 239–241 (2008).

Ubiquitin chain conformation regulates recognition and activity of interacting proteins

Yu Ye¹, Georg Blaser², Mathew H. Horrocks², Maria J. Ruedas-Rama³, Shehu Ibrahim², Alexander A. Zhukov², Angel Orte³, David Klenerman², Sophie E. Jackson² & David Komander¹

Mechanisms of protein recognition have been extensively studied for single-domain proteins¹, but are less well characterized for dynamic multidomain systems. Ubiquitin chains represent a biologically important multidomain system that requires recognition by structurally diverse ubiquitin-interacting proteins^{2,3}. Ubiquitin chain conformations in isolation are often different from conformations observed in ubiquitin-interacting protein complexes, indicating either great dynamic flexibility or extensive chain remodelling upon binding. Using single-molecule fluorescence resonance energy transfer, we show that Lys 63-, Lys 48- and Met 1-linked diubiquitin exist in several distinct conformational states in solution. Lys 63- and Met 1-linked diubiquitin adopt extended ‘open’ and more compact ‘closed’ conformations, and ubiquitin-binding domains and deubiquitinases (DUBs) select pre-existing conformations. By contrast, Lys 48-linked diubiquitin adopts predominantly compact conformations. DUBs directly recognize existing conformations, but may also remodel ubiquitin chains to hydrolyse the isopeptide bond. Disruption of the Lys 48–diubiquitin interface changes conformational dynamics and affects DUB activity. Hence, conformational equilibria in ubiquitin chains provide an additional layer of regulation in the ubiquitin system, and distinct conformations observed in differently linked polyubiquitin may contribute to the specificity of ubiquitin-interacting proteins.

Ubiquitin is involved in most aspects of cell biology, as it serves as a post-translational modification of lysine (Lys) residues, regulating many processes including protein degradation, cell signalling, trafficking and the DNA damage response². Most of these functions are mediated by eight structurally and functionally distinct ubiquitin chain types², only two of which have been studied extensively. Lys 48-linked ubiquitin chains target proteins for proteasomal degradation⁴, whereas Lys 63- and Met 1-linked ubiquitin chains have multiple non-degradative roles in cell signalling^{5,6}. Polyubiquitin signals are decoded by ubiquitin-interacting proteins including ubiquitin binding domains³ and DUBs⁷ that bind or hydrolyse ubiquitin chains, respectively. Some ubiquitin-interacting proteins can distinguish between different linkage types, and trigger a specific downstream response to ubiquitination.

The distinct cellular roles of differently linked polyubiquitin have partly been explained by distinct chain conformations. Crystallographic, NMR and small angle X-ray scattering (SAXS) studies have proposed ‘compact’ conformations for Lys 48-linked diubiquitin^{8–10} (Fig. 1a, b). In the prevalent model for Lys 48-linked diubiquitin, ubiquitin moieties interact via a hydrophobic patch on ubiquitin⁸ (Fig. 1a), which is also the most common recognition site for ubiquitin-interacting proteins². NMR relaxation and residual dipolar coupling measurements suggested that this conformation is in equilibrium with a second conformation that partly exposes the hydrophobic patch⁹. A recent crystal structure suggested a third compact conformation with exposed hydrophobic patches on both moieties¹¹ (Fig. 1b). In contrast, Lys 63- and Met 1-linked diubiquitin are thought to adopt ‘open’ conformations with no interactions between ubiquitin moieties, exposing the

hydrophobic patches^{10,12,13} (Fig. 1c, d), although a compact crystal structure of Met 1-linked diubiquitin has been reported recently¹⁴ (Fig. 1d).

Notably, the first crystal structures of ubiquitin and diubiquitin bound to ubiquitin-interacting proteins (reviewed in refs 2, 3, 7) indicate that in some cases known diubiquitin structures are incompatible with binding to ubiquitin-interacting proteins. In particular, DUBs must interact with the isopeptide linkage between ubiquitin moieties, which is not accessible in known models of Lys 48-linked polyubiquitin (Fig. 1a, b). This suggests that compact ubiquitin chain types might undergo remodelling (‘opening’) to be hydrolysed by DUBs. Whether such chain opening is induced by DUB binding, or whether Lys 48-linked diubiquitin pre-exists in open conformations, is unclear.

To understand the principles governing ubiquitin chain recognition, we generated Lys 48-, Lys 63- and Met 1-linked diubiquitin (termed K48NC, K63NC and M1NC, respectively), each containing a fluorescence resonance energy transfer (FRET) compatible dye pair (Alexa488/Alexa647, $R_0 = 5.6$ nm). Linkage-specific assembly reactions and/or selective purification resulted in pure dual-labelled diubiquitin (see Fig. 1e, Supplementary Fig. 1 and Supplementary Methods). Mass-spectrometric and enzymatic analysis, interchanging dye positions, and ensemble measurements of fluorescence lifetime and dye anisotropy confirmed sample quality and dye stability (Supplementary Figs 1 and 2 and Supplementary Methods). Dye photophysics were not significantly altered in labelled diubiquitin (see Supplementary Fig. 2 and Supplementary Methods). All samples showed a FRET signal in ensemble measurements (Fig. 1f).

Distinct ubiquitin chain conformations that underwent FRET were detected at the single molecule level by excitation of the donor fluorophore, with a single laser, and monitoring emission of both donor and acceptor fluorophores. The resulting FRET histograms were fitted to Gaussian functions representing distinct populations of diubiquitin conformations (Fig. 2; see Supplementary Methods). To estimate the proportion of molecules in conformations that gave no detectable FRET (termed ‘non-FRET’), two-colour coincidence detection (TCCD; see Supplementary Methods)¹⁵ was used on the same sample. In TCCD, two lasers are used to excite directly the two fluorophores in the diubiquitin independently, allowing direct quantification of the number of molecules with both donor and acceptor fluorophores. Combined use of TCCD and FRET measurements thus enabled estimation of the proportion of molecules that were in non-FRET conformations (see Supplementary Information).

For K48NC, two distinct FRET populations could be resolved (Fig. 2a): a high-FRET population (FRET efficiency $E \approx 0.69$) representing ~90% of all molecules, and a low-FRET population ($E \approx 0.41$) accounting for the remaining ~10%. We were unable to detect any non-FRET populations in these experiments; however, we cannot rule out the existence of a small population of ‘hidden’¹⁶ non-FRET K48NC species which would be beyond the detection limit (see Supplementary Methods). Hidden protein conformations may modulate enzyme activity but are not easily detected¹⁶.

¹Division of Protein and Nucleic Acids Chemistry, MRC Laboratory of Molecular Biology, Cambridge CB2 0QH, UK. ²Department of Chemistry, University of Cambridge, Cambridge CB2 1EW, UK.

³Department of Physical Chemistry, Faculty of Pharmacy, University of Granada, Campus Cartuja, 18071 Granada, Spain.

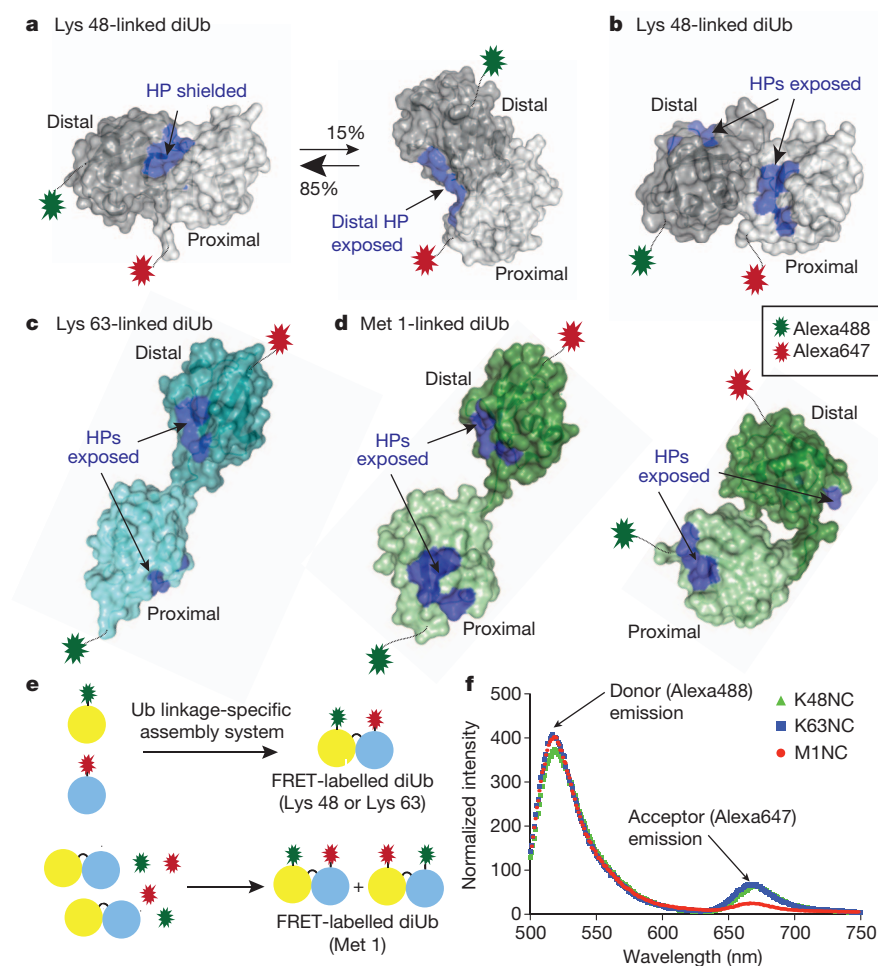


Figure 1 | Ubiquitin chain conformations and ensemble FRET measurements. **a–d**, Distal (dark) and proximal (light) ubiquitin moieties are shown in surface representation with hydrophobic patch (HP) residues (Leu 8, Ile 44, His 68, Val 70) in blue. N- and C-terminal Alexa dye attachment points are indicated. **a**, Lys 48-linked diubiquitin (diUb) derived from crystallographic and NMR analysis. Protein Data Bank (PDB) accession codes 1AAR (left)⁸ and 2PE9 (right)⁹. **b**, Alternative 'compact' Lys 48-linked diubiquitin (PDB 3AU1¹¹). **c**, 'Open' Lys 63-linked diubiquitin (PDB 2JF5¹³). **d**, Met 1-linked diubiquitin from crystallography (PDB 2W9N (left)¹³ and 3AXC (right)¹⁴). **e**, Schematic representation of FRET-labelled diubiquitin assembly. See Supplementary Fig. 1 and Supplementary Methods. **f**, Uncorrected ensemble FRET measurements for diubiquitin used in this study (see Supplementary Methods).

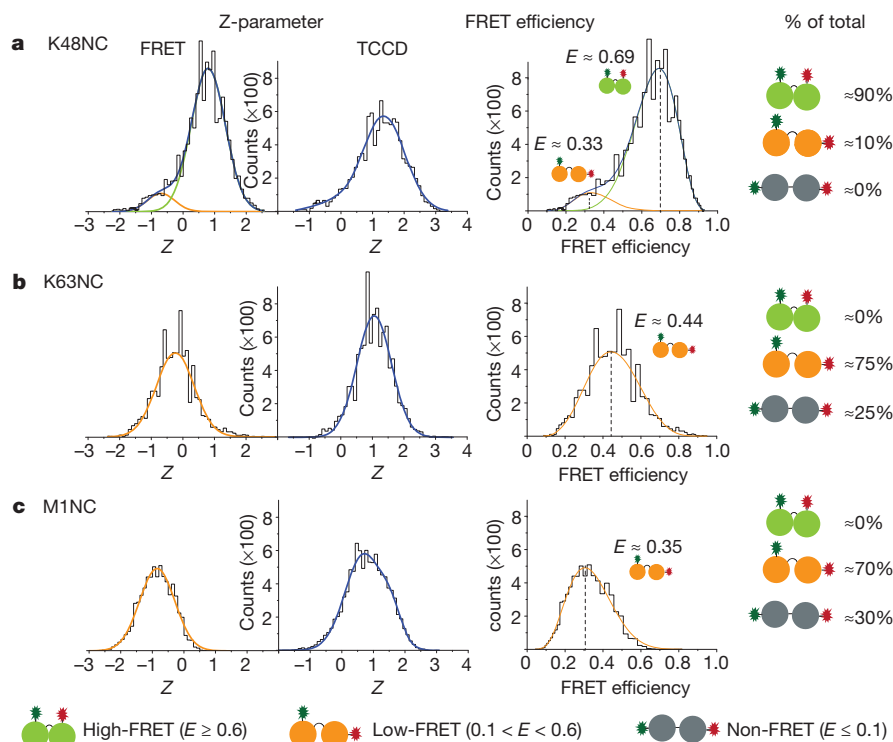


Figure 2 | Single-molecule FRET of K48NC (a), K63NC (b) and M1NC (c). Left: FRET and TCCD signals in histogram counts against the Z-parameter ($\ln(I_A/\gamma I_D)$) for fitting to Gaussian functions, normalized to equal area in TCCD. Gaussian functions (see Supplementary Methods) are shown in green (high-FRET), orange (low-FRET) and blue (cumulative fit). Middle: histograms of FRET species plotted against the FRET efficiency. The curves derived from the Z-parameter Gaussian fits are shown (see Supplementary Methods). Right: estimate of the relative abundance of each population. Non-FRET refers to dual-labelled molecules (detected by TCCD) without FRET emission.

Similar to the results for K48NC, multiple conformations were also observed for K63NC and M1NC, with ~70–75% low-FRET and ~25–30% non-FRET populations (Fig. 2b, c). Models of extended Lys 63- or Met 1-linked diubiquitin (Fig. 1c, d) are compatible with non-FRET populations, whereas the compact crystal structure of Met 1-linked diubiquitin¹⁴ (Fig. 1d) may represent a low-FRET M1NC species. The prevalence of compact Lys 63-linked diubiquitin conformations in FRET is surprising, and has not been observed by other methods^{10,12,13}. This may be due to multiple compact and semi-compact conformations that collectively result in the observed low-FRET populations.

To test whether the observed diubiquitin conformations are relevant for ubiquitin-interacting protein interaction, single-molecule measurements were performed using pM concentrations of K63NC, K48NC or M1NC mixed with ubiquitin-interacting proteins at concentrations exceeding the dissociation constant (K_d) of the interaction (Supplementary Fig. 7). With our methodology we can follow relative changes in the populations upon addition of ubiquitin-interacting proteins, none of which affected dye photophysics (Supplementary Fig. 8). Several ubiquitin-interacting proteins interacted with pre-existing compact conformations of diubiquitin. A Lys 63 linkage-specific antibody increased the FRET population relative to the non-FRET population of K63NC, in agreement with structural work¹⁷ (Fig. 3a, b). Similarly, the ubiquitin-binding UBAN domain of NEMO¹⁸ enriched the low-FRET population of M1NC, consistent with UBAN binding to a compact conformation of linear diubiquitin¹⁸ (Fig. 3c, d).

Access to the isopeptide bond is essential for DUB activity. AMSH-like protein (AMSH-LP; also called STAMBPL1), a Lys 63-specific JAMM family DUB, binds an open Lys 63-linked diubiquitin conformation¹⁹ (Fig. 3e). Indeed, inactivated AMSH²⁰ (AMSHi) depleted

the FRET and increased the non-FRET population of K63NC in single-molecule measurements (Fig. 3e). Structures of ubiquitin-specific protease (USP) DUBs with diubiquitin bound across the active site are unavailable, but monoubiquitin complexes show that the carboxy terminus of a distal ubiquitin is extended⁷ (Fig. 3f), suggesting that USPs also bind open conformations. Indeed, inactivated USP21 (ref. 21; USP21i) enriched non-FRET K63NC conformations in our single-molecule measurements (Fig. 3f). Therefore, whereas the Lys 63 linkage-specific antibody or the UBAN domain of NEMO selects existing compact conformations of K63NC and M1NC, respectively, DUBs select pre-existing open conformations of K63NC (Fig. 3g).

K48NC is in equilibrium between predominantly compact conformations (Fig. 2a). Inactivated OTUB1 (OTUB1i), a Lys 48-specific DUB, enriched the low-FRET and depleted the high-FRET population of K48NC in single-molecule measurements (Fig. 4a, b and Supplementary Fig. 9). This is consistent with recent crystal structures of OTUB1 in complex with E2 and two ubiquitin molecules^{22,23} that revealed a relatively compact conformation of the two ubiquitin moieties when bound to OTUB1 (Fig. 4c).

Notably, titration of K48NC with USP21i resulted in depletion of high-FRET and an increase in low-FRET populations, but also gave rise to a non-FRET population of K48NC (Fig. 4d, e). The appearance of open, non-FRET K48NC species can be rationalized structurally, as USP21 stretches the linkage across the active site to form a catalytically competent conformation (Fig. 3f). However, the increase in low-FRET populations indicates that USP21i binds semi-open conformations directly (Fig. 4d, e). Estimation of binding constants for the low- and non-FRET species indicated a slightly higher affinity of USP21i for the open non-FRET conformation (Supplementary Fig. 9).

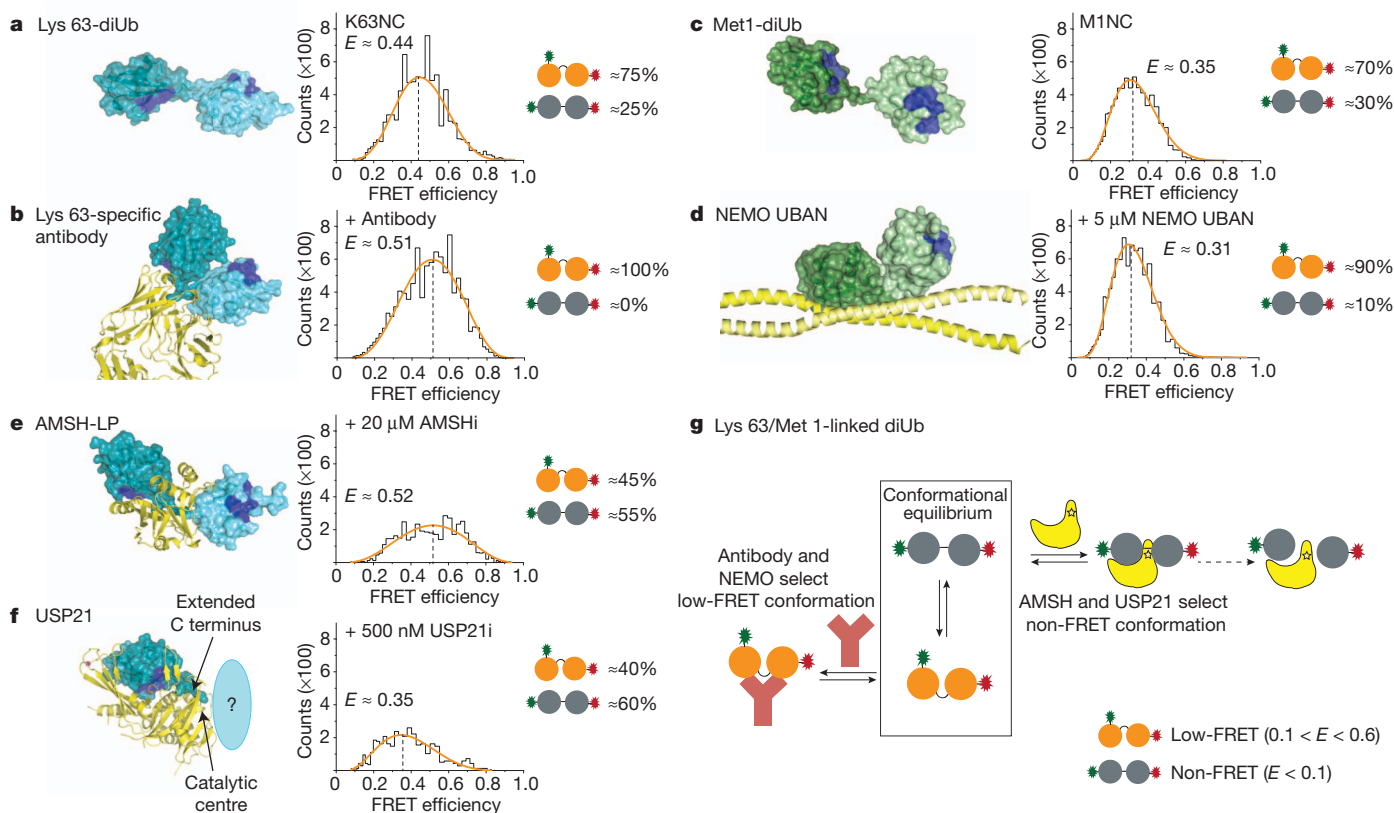


Figure 3 | Ubiquitin-interacting protein binding to Lys 63- and Met 1-linked chains. **a–f**, Structural models (coloured as in Fig. 1a with yellow ubiquitin-interacting protein), FRET efficiency histograms and population estimates are shown. All experiments are normalized to equivalent TCCD areas (see Supplementary Fig. 12 for Z-parameter plots). **a**, Lys 63-linked diubiquitin (PDB 2JF5¹³). **b**, Complex of Lys 63-linked diubiquitin and Lys 63-linkage-

specific antibody (PDB 3DVG¹⁷). **c**, Met 1-linked diubiquitin (PDB 2W9N¹³). **d**, Complex of met 1-linked diubiquitin and NEMO UBAN (PDB 2ZVO¹⁸, only one diubiquitin shown). **e**, Complex of Lys 63-linked diubiquitin and AMSH-LP (PDB 2ZNV¹⁹). **f**, Complex of monomeric ubiquitin with USP21 (PDB 2Y5B²¹, proximal ubiquitin indicated). **g**, Model for Lys 63- and Met 1-linked diubiquitin interaction with binding partners.

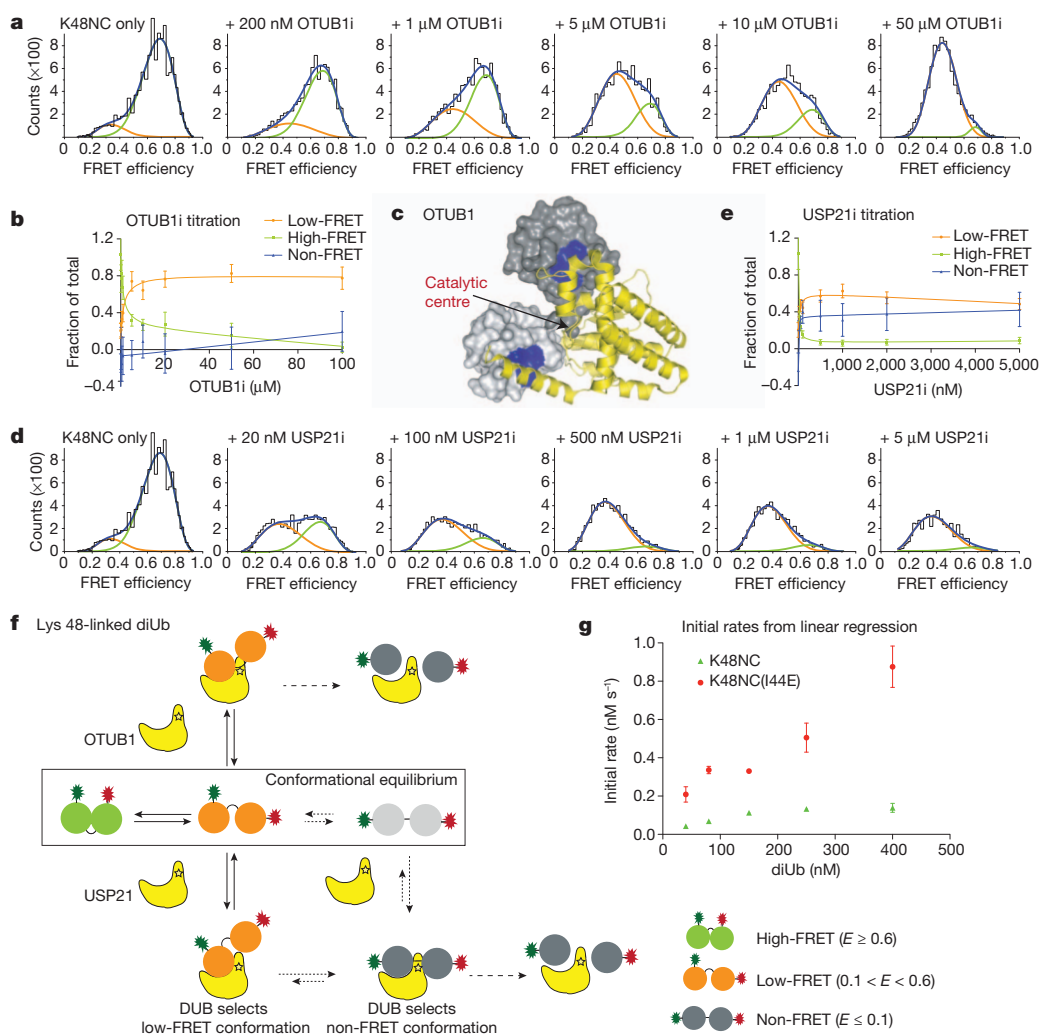


Figure 4 | DUB interaction with Lys48-linked chains. **a**, FRET efficiency histograms of K48NC with increasing OTUB1i concentration. Estimated FRET efficiencies: $E_{\text{high-FRET}} \approx 0.69$, $E_{\text{low-FRET}} \approx 0.45$ (Supplementary Fig. 13 and Supplementary Methods). **b**, Relative changes of K48NC populations from **a**. Errors represent standard deviation in curve fitting. **c**, Structure of OTUB1 (yellow) bound to two ubiquitin molecules (grey) (derived from PDB

4DHZ^{22,23}). **d**, FRET efficiency histograms of K48NC with increasing USP21i concentrations as in **a** ($E_{\text{high-FRET}} \approx 0.71$, $E_{\text{low-FRET}} \approx 0.37$). **e**, Relative changes of K48NC populations derived from **d**, shown as in **b**. **f**, Model for interaction of DUBs with Lys 48-linked chains. **g**, Initial rate analysis of USP21-mediated hydrolysis of K48NC (green) and K48NC(I44E) (red). Errors represent standard deviation of triplicate measurements.

Our data result in two models for DUB interactions with Lys 48-linked ubiquitin chains (Fig. 4f). DUBs such as OTUB1 may directly recognize and hydrolyse low-FRET semi-open conformations of Lys 48-linked diubiquitin. Other enzymes such as USP21 recognize semi-open and open (that is, low-FRET and non-FRET) conformations. Binding of semi-open conformations could lead to remodelling to open conformations that are compatible with catalysis (Fig. 4f). Alternatively, dissociation of low-FRET and re-binding of non-FRET diubiquitin could account for generating a catalytically competent enzyme–substrate complex (Fig. 4f). Both models imply that recognition of Lys 48 linkages is governed initially by conformational selection.

Importantly, our data indicate that the compact, high-FRET population of K48NC is not recognized directly. Access to ubiquitin hydrophobic patches is obstructed in the prevalent compact structure of Lys 48-linked diubiquitin (Fig. 1a and refs 8–10), which would correlate with a high-FRET population. Because all known DUBs bind the hydrophobic patch of ubiquitin⁷, interconversion from compact high-FRET to semi-open low-FRET conformations could be crucial for DUB activity (Fig. 4f). To test this hypothesis, we mutated Ile 44 in the hydrophobic patch of the proximal ubiquitin of K48NC (K48NC(I44E)) to disrupt a hydrophobic-patch-based interface. We observed a reduction in the high- and low-FRET populations and a shift in their peak

positions to lower FRET efficiencies as compared to K48NC (Supplementary Fig. 10), indicating that the mutation changes the conformational equilibria such that open conformations, as well as alternative compact forms of this chain type, may now be populated (for example, Fig. 1b and ref. 11). Importantly, kinetic assessment of USP21-mediated cleavage shows that K48NC(I44E) is hydrolysed significantly faster than wild-type K48NC (Fig. 4g). We propose that ubiquitin chain conformation and dynamics directly affect the rate of DUB hydrolysis.

We show here how FRET/TCCD measurements can be used to probe the complex conformational dynamics of ubiquitin chains in solution, thereby identifying novel conformations not detected using NMR or X-ray crystallography. Our results establish that distinct conformational populations of flexible two-domain ubiquitin chains are recognized by ubiquitin-interacting proteins. In the case of USP21, we suggest that subsequent remodelling may take place to achieve active conformations. Such a combination of ‘conformational selection’ and remodelling would be consistent with the most recent models of macromolecular recognition²⁴, and may further extend these models, as the remodelling step here involves significant translation and presumably rotation of flexibly linked domains with respect to each other. Hence, conformational selection is an important mechanism of

ubiquitin chain recognition. This highlights the importance of understanding the conformational space for the eight different ubiquitin chain types, as this holds the key to linkage-dependent regulation within the ubiquitin system.

Ubiquitin chain recognition further depends on the dynamic inter-conversion of chain conformations. Interfering with conformational dynamics by mutating ubiquitin can directly affect chain hydrolysis by DUBs, providing the first evidence that conformational rearrangements in the chains may govern the speed at which the chains are hydrolysed. An alternative mechanism to interfere with the conformational dynamics is chain length. Lys 48-tetraubiquitin forms a compact structure²⁵ in which all ubiquitin moieties interact with each other through their hydrophobic patches and secondary interaction sites (Supplementary Fig. 11). This probably alters chain dynamics ('breathing' of the chains), which we have shown here to be essential for recognition by DUBs. Consistent with this are recent data showing that some DUBs remove mono- and diubiquitin but not tetraubiquitin or longer polymers from substrates²⁶. It is tempting to speculate that the reported requirement for Lys 48-linked tetraubiquitin to trigger proteasomal degradation²⁷ may have originated partly from improved stability of this length/linkage combination towards DUB action. Therefore, factors affecting ubiquitin chain conformation and dynamics (linkage, length, binding partners) may be key regulators of the ubiquitin system.

METHODS SUMMARY

Diubiquitin molecules were assembled with Alexa488 and Alexa647 fluorophores as detailed in Supplementary Fig. 1. Single-molecule measurements were performed at 20 °C in PBST buffer (150 mM NaCl, 18 mM Na₂HPO₄, 7 mM NaH₂PO₄, 0.01% (v/v) Tween20, pH 7.4). Ubiquitin-interacting proteins were incubated with labelled chains for 5 min. The single-molecule instrument was described previously²⁸. Recording times depended on the amount of FRET-labelled diubiquitin and the signal-to-noise ratio, and were typically between 30 min and 3 h. Both TCCD and FRET data were collected for all measurements, and were analysed using a coincidence criterion. Coincident events in both channels¹⁵ are only selected when the counts in each channel are above its threshold count value, which was selected automatically as described previously²⁹. For experiments in which TCCD data were compared with FRET data, a common threshold was used for the donor channels (determined by maximizing the association quotient in the TCCD experiment), whereas the acceptor channel thresholds were independently determined for FRET and TCCD. This ensured that both the FRET and TCCD measurements of each sample resulted in approximately equal burst rates in the donor channel. Bulk FRET measurements, dye lifetime measurements and periodic acceptor excitation (PAX) experiments were performed as described in Supplementary Methods.

Received 28 September 2011; accepted 25 October 2012.

Published online 2 December 2012.

- Lo Conte, L., Chothia, C. & Janin, J. The atomic structure of protein-protein recognition sites. *J. Mol. Biol.* **285**, 2177–2198 (1999).
- Komander, D. & Rape, M. The ubiquitin code. *Annu. Rev. Biochem.* **81**, 203–229 (2012).
- Husnjak, K. & Dikic, I. Ubiquitin-binding proteins: decoders of ubiquitin-mediated cellular functions. *Annu. Rev. Biochem.* **81**, 291–322 (2012).
- Hershko, A. & Ciechanover, A. The ubiquitin system. *Annu. Rev. Biochem.* **67**, 425–479 (1998).
- Chen, Z. J. & Sun, L. J. Nonproteolytic functions of ubiquitin in cell signaling. *Mol. Cell* **33**, 275–286 (2009).
- Iwai, K. Linear polyubiquitin chains: a new modifier involved in NFκB activation and chronic inflammation, including dermatitis. *Cell Cycle* **10**, 3095–3104 (2011).
- Komander, D., Clague, M. J. & Urbé, S. Breaking the chains: structure and function of the deubiquitinases. *Nature Rev. Mol. Cell Biol.* **10**, 550–563 (2009).

- Cook, W. J., Jeffrey, L. C., Carson, M., Chen, Z. & Pickart, C. M. Structure of a diubiquitin conjugate and a model for interaction with ubiquitin conjugating enzyme (E2). *J. Biol. Chem.* **267**, 16467–16471 (1992).
- Ryabov, Y. & Fushman, D. Interdomain mobility in di-ubiquitin revealed by NMR. *Proteins* **63**, 787–796 (2006).
- Tenno, T. *et al.* Structural basis for distinct roles of Lys63- and Lys48-linked polyubiquitin chains. *Genes Cells* **9**, 865–875 (2004).
- Hirano, T. *et al.* Conformational dynamics of wild-type Lys-48-linked diubiquitin in solution. *J. Biol. Chem.* **286**, 37496–37502 (2011).
- Varadan, R. *et al.* Solution conformation of Lys63-linked di-ubiquitin chain provides clues to functional diversity of polyubiquitin signaling. *J. Biol. Chem.* **279**, 7055–7063 (2004).
- Komander, D. *et al.* Molecular discrimination of structurally equivalent Lys 63-linked and linear polyubiquitin chains. *EMBO Rep.* **10**, 466–473 (2009).
- Rohaim, A., Kawasaki, M., Kato, R., Dikic, I. & Wakatsuki, S. Structure of a compact conformation of linear diubiquitin. *Acta Crystallogr. D* **68**, 102–108 (2012).
- Orte, A., Clarke, R., Balasubramanian, S. & Klenerman, D. Determination of the fraction and stoichiometry of femtomolar levels of biomolecular complexes in an excess of monomer using single-molecule, two-color coincidence detection. *Anal. Chem.* **78**, 7707–7715 (2006).
- Fraser, J. S. *et al.* Hidden alternative structures of proline isomerase essential for catalysis. *Nature* **462**, 669–673 (2009).
- Newton, K. *et al.* Ubiquitin chain editing revealed by polyubiquitin linkage-specific antibodies. *Cell* **134**, 668–678 (2008).
- Rahighi, S. *et al.* Specific recognition of linear ubiquitin chains by NEMO is important for NF-κB activation. *Cell* **136**, 1098–1109 (2009).
- Sato, Y. *et al.* Structural basis for specific cleavage of Lys 63-linked polyubiquitin chains. *Nature* **455**, 358–362 (2008).
- McCullough, J. *et al.* Activation of the endosome-associated ubiquitin isopeptidase AMSH by STAM, a component of the multivesicular body-sorting machinery. *Curr. Biol.* **16**, 160–165 (2006).
- Ye, Y. *et al.* Polyubiquitin binding and cross-reactivity in the USP domain deubiquitinase USP21. *EMBO Rep.* **12**, 350–357 (2011).
- Wiener, R., Zhang, X., Wang, T. & Wolberger, C. The mechanism of OTUB1-mediated inhibition of ubiquitination. *Nature* **483**, 618–622 (2012).
- Juang, Y.-C. *et al.* OTUB1 co-opts Lys48-linked ubiquitin recognition to suppress E2 enzyme function. *Mol. Cell* **45**, 384–397 (2012).
- Boehr, D. D., Nussinov, R. & Wright, P. E. The role of dynamic conformational ensembles in biomolecular recognition. *Nature Chem. Biol.* **5**, 789–796 (2009).
- Eddins, M. J., Varadan, R., Fushman, D., Pickart, C. M. & Wolberger, C. Crystal structure and solution NMR studies of Lys48-linked tetraubiquitin at neutral pH. *J. Mol. Biol.* **367**, 204–211 (2007).
- Schaefer, J. B. & Morgan, D. O. Protein-linked ubiquitin chain structure restricts activity of deubiquitinating enzymes. *J. Biol. Chem.* **286**, 45186–45196 (2011).
- Thrower, J. S., Hoffman, L., Rechsteiner, M. & Pickart, C. M. Recognition of the polyubiquitin proteolytic signal. *EMBO J.* **19**, 94–102 (2000).
- Orte, A., Clarke, R. W. & Klenerman, D. Fluorescence coincidence spectroscopy for single-molecule fluorescence resonance energy-transfer measurements. *Anal. Chem.* **80**, 8389–8397 (2008).
- Clarke, R. W., Orte, A. & Klenerman, D. Optimized threshold selection for single-molecule two-color fluorescence coincidence spectroscopy. *Anal. Chem.* **79**, 2771–2777 (2007).

Supplementary Information is available in the online version of the paper.

Acknowledgements We would like to thank members of the Komander, Jackson and Klenerman laboratories, R. Williams, S. Freund, C. Johnson, S. McLaughlin and A. Fersht for discussions. Work in the Komander laboratory is supported by the Medical Research Council (U105192732) and the EMBO Young Investigator Program. G.B. and S.I. were supported by the BBSRC, the Newton Trust and an EMBO YIP small grant to D.Ko. Work in the Klenerman laboratory is supported by EPSRC.

Author Contributions Y.Y., G.B. and M.H.H. designed and performed the experiments, including single-molecule measurements, and analysed the data. Y.Y. and G.B. generated all proteins used in this study. Y.Y. performed kinetic experiments. M.H.H. and S.I. built the PAX instrument and A.A.Z. programmed the control for PAX measurements. S.I. performed single molecule experiments and contributed to data analysis. M.J.R.-R. and A.O. performed lifetime measurements. D.Kl., S.E.J. and D.Ko. directed the research and analysed the results. All authors contributed to the writing of the manuscript.

Author Information Reprints and permissions information is available at www.nature.com/reprints. The authors declare no competing financial interests. Readers are welcome to comment on the online version of the paper. Correspondence and requests for materials should be addressed to D.Ko. (dk@mrc-lmb.cam.ac.uk), S.E.J. (sej13@cam.ac.uk) or D.Kl. (dk10012@cam.ac.uk).

Activated GTPase movement on an RNA scaffold drives co-translational protein targeting

Kuang Shen¹, Sinan Arslan², David Akopian¹, Taekjip Ha^{2,3} & Shu-ou Shan¹

Approximately one-third of the proteome is initially destined for the eukaryotic endoplasmic reticulum or the bacterial plasma membrane¹. The proper localization of these proteins is mediated by a universally conserved protein-targeting machinery, the signal recognition particle (SRP), which recognizes ribosomes carrying signal sequences^{2–4} and, through interactions with the SRP receptor^{5,6}, delivers them to the protein-translocation machinery on the target membrane⁷. The SRP is an ancient ribonucleoprotein particle containing an essential, elongated SRP RNA for which precise functions have remained elusive. Here we used single-molecule fluorescence microscopy to show that the *Escherichia coli* SRP–SRP receptor GTPase complex, after initial assembly at the tetraloop end of SRP RNA, travels over 100 Å to the distal end of this RNA, where rapid GTP hydrolysis occurs. This movement is negatively regulated by the translating ribosome and, at a later stage, positively regulated by the SecYEG translocon, providing an attractive mechanism for ensuring the productive exchange of the targeting and translocation machineries at the ribosome exit site with high spatial and temporal accuracy. Our results show that large RNAs can act as molecular scaffolds that enable the easy exchange of distinct factors and precise timing of molecular events in a complex cellular process; this concept may be extended to similar phenomena in other ribonucleoprotein complexes.

Co-translational protein targeting faces fundamental challenges in both spatial and temporal coordination. Spatially, both the SRP^{2–4} and SecYEG (known as Sec61 in eukaryotes) translocon⁷ contact the L23 ribosomal protein and the signal sequence, raising puzzling questions about how the translating ribosome is transferred from the targeting to the translocation machinery. Temporally, GTP hydrolysis by the SRP–SRP receptor complex, which drives its irreversible disassembly⁸, must be accurately timed during cargo delivery and unloading to avoid abortive reactions⁹. Such accurate spatial and temporal coordination is required in all protein-targeting pathways, but its underlying molecular mechanism is not understood. Here, single-molecule experiments reveal large-scale rearrangements in the SRP, providing a unifying molecular mechanism to explain how such coordination is achieved during co-translational protein targeting.

The bacterial SRP is comprised of the homologue of an SRP54 protein subunit, Ffh, and a 114-nucleotide SRP RNA¹. Ffh contains two domains connected by a flexible linker: a methionine-rich M domain, which recognizes the signal sequence¹⁰ and binds the SRP RNA¹¹, and a GTPase NG domain that interacts with a homologous NG domain in the SRP receptor, FtsY^{5,6} (Fig. 1a). The SRP RNA is a universally conserved and essential SRP component, but its precise roles are not completely understood. Most previous work^{12–15} focused on the GGAA tetraloop that caps one end of this RNA (Supplementary Fig. 1a), which accelerates the initial SRP–FtsY assembly by electrostatically interacting with FtsY¹³. These findings, however, do not explain why the SRP RNA has a conserved elongated structure¹⁶. Valuable clues come from a recent crystal structure that found the Ffh–FtsY GTPase complex at another docking site near the distal

end of this RNA, where mutations disrupt GTPase activation¹⁷ (Fig. 1a, distal state). This posited an attractive hypothesis in which the Ffh–FtsY GTPase complex, after initial assembly near the tetraloop^{12–15}, can re-localize to the distal site of the SRP RNA ~100 Å away¹⁷. Nevertheless, no functional evidence for the re-localization is available, nor are the importance, timing, mechanism and regulation of such a large-scale movement understood.

To address these questions, we used single-molecule fluorescence resonance energy transfer (smFRET) and total internal reflection fluorescence (TIRF) microscopy to detect conformational dynamics of individual SRPs^{18,19}. Migration of the SRP–FtsY GTPase complex on the SRP RNA was tracked using FRET between a donor (Cy3) attached to the FtsY NG domain and an acceptor (Quasar 670) labelled near the RNA distal end (Fig. 1a). Stable SRP–FtsY complexes, formed with the non-hydrolysable GTP analogue 5'-guanylyl-imidodiphosphate (GMPPNP), displayed rapid transitions among multiple FRET states (Fig. 1b, c). A low FRET state (~0.1; L) was assigned to the proximal state in which the GTPase complex resides near the SRP RNA tetraloop¹³. A high FRET state (~0.8; H) was attained ~20% of the time and assigned to the distal state in which the GTPase complex stably docks at the distal site, as verified below. Cy3 attached to the Ffh NG domain showed similar transitions but with a lower FRET value in the H state (Supplementary Fig. 2a, b), consistent with Ffh being further from the distal site than FtsY¹⁷. These results directly demonstrate dynamic movements of the SRP–FtsY GTPase complex on the SRP RNA that span over 100 Å.

We used hidden Markov modelling (HMM)-based statistical analyses to determine the most likely sequence of FRET transitions²⁰. This revealed an ensemble of additional states with intermediate FRET values (0.3–0.6; M1 and M2) and extremely short lifetimes (Fig. 1b–d and Supplementary Figs 2b–g and 3a–c), representing alternative binding modes of the GTPase complex on the SRP RNA. The transition information was pooled into a transition density plot that describes the number of distinct FRET states, their FRET values, and their transition frequencies (Fig. 1e and Supplementary Fig. 2h). In addition, the kinetics of FRET transitions were obtained from dwell-time analyses (Fig. 1f, g and Supplementary Figs 2i–o and 3d–h). Whereas molecules leaving the L state rapidly transitioned to all the other states, the H state had a longer lifetime than M1 and M2 and was hence more populated (Fig. 1d), indicating more stable docking of the GTPase complex in this state. Fifty-eight per cent of transitions to the H state occurred directly from L, whereas molecules in the intermediate FRET states transitioned primarily back to L (Fig. 1e and Supplementary Fig. 2h). Thus, correct docking at the RNA distal site requires extensive searching that involves frequent trial and error.

To test whether the H state is responsible for GTPase activation, we isolated mutant RNAs that specifically perturb the distal docking site. The 82-nucleotide RNA lacking this site¹⁷ reduced GTPase activation sixfold, whereas a 'super-active' mutant, 99A, enhanced GTP hydrolysis 2.5-fold (Fig. 2a, green bars and Supplementary Figs 1b and 4a). The GTPase activity of these mutants quantitatively correlated with

¹Division of Chemistry and Chemical Engineering, California Institute of Technology, Pasadena, California 91125, USA. ²Department of Physics, Center for the Physics of Living Cells, University of Illinois at Urbana-Champaign, Urbana, Illinois 61801, USA. ³Howard Hughes Medical Institute, Urbana, Illinois 61801, USA.

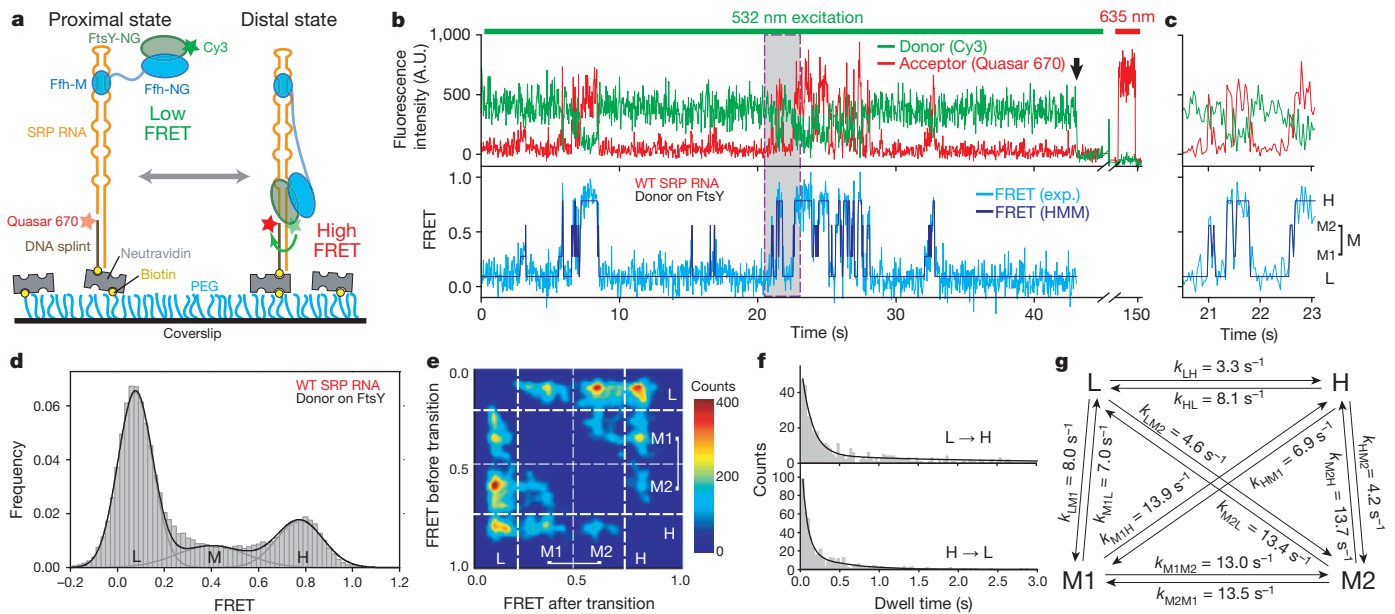


Figure 1 | smFRET-TIRF microscopy reveals dynamic movements of the SRP-FtsY complex on the SRP RNA. **a**, smFRET setup for the SRP-FtsY complex. FtsY Cys 345 is labelled with Cy3. The 5'-end of the DNA splint (2 nucleotides from the 3'-end of SRP RNA) is labelled with Quasar 670. **b**, Fluorescent signals (top) and FRET trajectory (bottom) of the SRP-FtsY complex in GMPPNP. HMM of the FRET trajectory is depicted in navy. The arrow denotes the bleaching of Cy3, after which Quasar 670 was excited using a

635-nm laser to confirm the presence of the complex. A.U., arbitrary units. **c**, Magnification of the grey box in **b** to depict the four FRET states resolved by HMM. **d**, smFRET histogram depicting the distribution of molecules in different states. In M state, the M1 and M2 states are binned together. **e**, Transition density plot for the GTPase movements. **f**, **g**, Analysis of the transition kinetics between L and H states (**f**). Exponential fits of the data gave the transition-rate constants (k) given in **g**.

their efficiency of reaching the H state (Fig. 2a and Supplementary Figs 5 and 6), strongly suggesting that activated GTP hydrolysis occurs at the RNA distal site.

To test the importance of the RNA distal site in protein targeting, we measured the ability of SRP and FtsY to deliver a model substrate, preprolactin (pPL), to endoplasmic reticulum microsomes²¹.

Translocation of pPL results in cleavage of its signal sequence, allowing the targeting and translocation to be efficiency quantified (Supplementary Fig. 4b). Furthermore, the specificity of targeting was tested using pPL variants in which the signal sequence is systematically varied⁹ (Supplementary Fig. 4d). Mutant 82-nucleotide RNA substantially reduced the targeting of correct substrates (wild type, 8L-pPL and 7L-pPL; Fig. 2b, c and Supplementary Fig. 4c, e). By contrast, the super-active 99A RNA targeted these substrates more efficiently than wild-type SRP, without compromising the discrimination against incorrect substrates (Fig. 2b, c and Supplementary Fig. 4c, e). Thus the SRP RNA distal site, although reportedly not essential for cell survival¹¹, does enhance efficient and accurate co-translational protein targeting.

SRP and FtsY undergo an unusual GTPase cycle, driven by multiple conformational rearrangements in their heterodimer that culminate in GTPase activation (Fig. 3a–d, cartoons)^{22–24}. We questioned how these rearrangements within the GTPase complex drive its global movements on the SRP RNA, using conditions that block the GTPase cycle at distinct stages^{22,23}. SRP by itself exhibited no movements on the RNA (Fig. 3a and Supplementary Fig. 7a). Recruitment of FtsY begins with a transient early intermediate, which lacks close contacts between the G domains and hence can be isolated by leaving out GTP analogues^{12,24}. No GTPase movement was observed at this stage either (Fig. 3b and Supplementary Fig. 7b). Subsequently, GTP-dependent rearrangements give a stable closed complex, which lacks optimal positioning of the catalytic loops and can be isolated by a mutation, FtsY(A335W), in the catalytic loop (Fig. 3c, d)^{22,23}. Although GTPase movements were observed in the closed complex, most of them only reached M1 and M2 but did not extensively populate the H state (Fig. 3c–e and Supplementary Fig. 7c, d). Thus, GTP-induced rearrangements within the NG domain complex drive its global movements on the SRP RNA. Moreover, stable GTPase docking at the RNA distal site requires optimal positioning of the catalytic loops, explaining why mutants that block GTPase activation, such as FtsY(A335W), severely impair protein targeting²¹.

If the GTPase complex only transiently reaches the SRP RNA distal site where GTPase activation occurs, previous ensemble measurements⁸ would have considerably underestimated the hydrolysis rate.

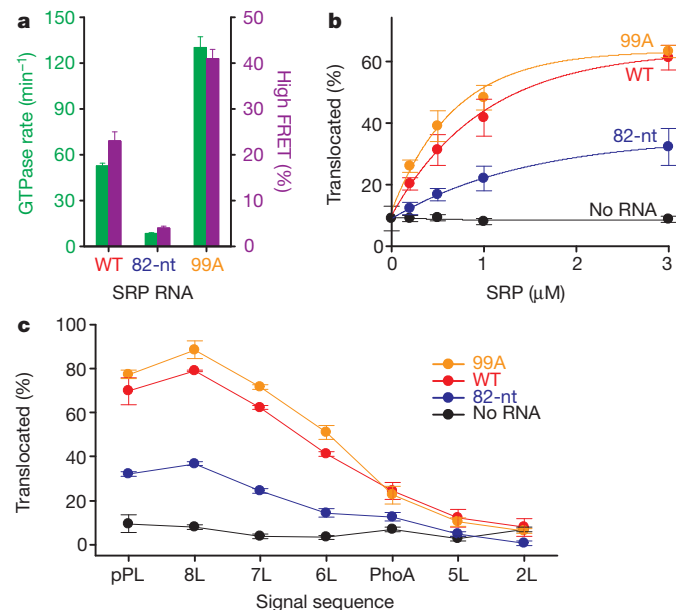


Figure 2 | The distal site of SRP RNA is crucial for GTPase activation and protein targeting. **a**, Correlation between GTPase rate constants in the SRP-FtsY complex (green) and the frequency of reaching the high FRET state (purple) for wild-type, 82-nucleotide (nt) and 99A SRP RNA. Data represent mean \pm s.d. ($n = 5$). **b**, **c**, Co-translational targeting and translocation of pPL (**b**) and its signal sequence variants (**c**) mediated by the wild-type and mutant SRPs. Reactions in the absence of SRP RNA are in black. Data represent mean \pm s.d. ($n = 3$).

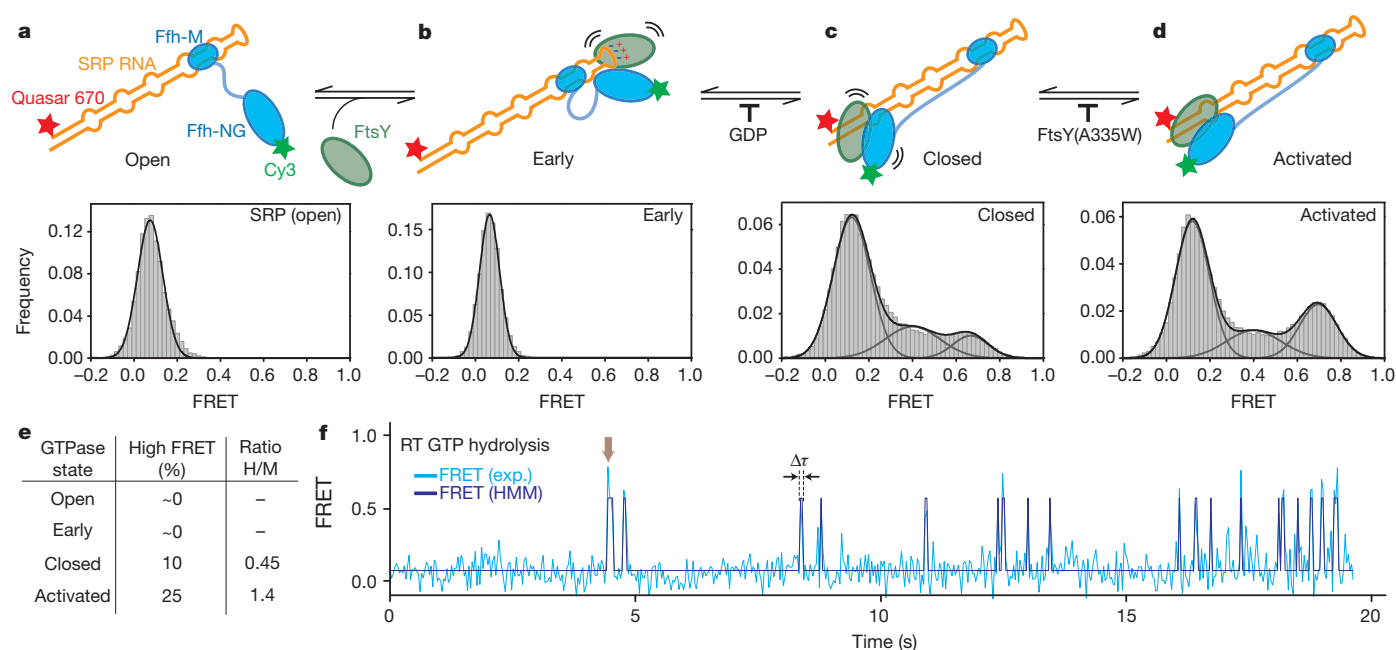


Figure 3 | Conformational rearrangements within the SRP-FtsY GTPase complex drive its movement to the RNA distal site. **a–d**, smFRET histograms of free SRP in the open state (**a**) and of the SRP-FtsY complex in the early (**b**), closed (**c**) and activated (**d**) states. Conditions for isolating each conformational state are described in the text and Methods. **e**, Summary of the

FRET distributions. **f**, A representative smFRET trajectory of the complex incubated in GTP. The arrow denotes a burst of high FRET that results from GTPase docking at the distal site terminated by rapid GTP hydrolysis driving complex disassembly. $\Delta\tau$ denotes the duration of the high FRET burst. RT, real time.

We therefore performed real-time GTPase assays using the smFRET setup. If GTP hydrolysis at the distal site, which drives irreversible SRP-FtsY dissociation, occurred faster than their return to the proximal state, we would observe high FRET 'bursts' with GTP instead of the reversible transitions with GMPPNP. This was indeed observed (Fig. 3f). The duration between these bursts has a rate constant (0.59 s^{-1} ; Supplementary Fig. 8b) expected for rearrangement to the activated complex ($\sim 1\text{ s}^{-1}$)¹² and is similar to the ensemble GTPase rate (0.7 s^{-1})⁸, strongly suggesting that the latter is rate limited by GTPase movement to the RNA distal site. The duration of the high FRET bursts includes GTP hydrolysis and subsequent SRP-FtsY disassembly and exhibits a rate constant of 7.1 s^{-1} (Supplementary Fig. 8a), providing a lower limit for the actual hydrolysis rate and is at least tenfold faster than ensemble measurements⁸.

These results also show that GTP drives almost irreversible movement of the GTPases to the RNA distal site, necessitating accurate control of the timing of this movement. Indeed, ribosome-nascent chain complexes (RNC or cargo) delay GTPase activation in the SRP-FtsY complex^{9,23} (Fig. 4a, wild type). This effect, termed 'pausing', prevents premature GTP hydrolysis and is essential for ensuring the efficiency and specificity of the SRP pathway⁹. We wanted to know whether the RNC negatively regulates the GTPase movement to the SRP RNA distal site. RNC_{FtsQ}, which carries an obligate SRP substrate FtsQ, completely abolished the GTPase movements on the RNA (Fig. 4b and Supplementary Fig. 9a–e). This is specific to the correct cargo, as RNC carrying luciferase, which contains no signal sequence, exerted no effects (Fig. 4c and Supplementary Fig. 9f). Further, GTP hydrolysis in the presence of RNC is no longer affected by mutations in the RNA distal end (Fig. 4a and Supplementary Fig. 10a, b), but is still reduced by a mutation in FtsY active site²² (Supplementary Fig. 10d, e). These results demonstrate that correct cargos stabilize the GTPase complex in the proximal state and prevent its re-localization to the RNA distal site, thus exerting the pausing effect.

On the target membrane, RNC must be transferred from the targeting to the translocation machinery. Both the mechanism of this transfer and its timing have remained long-standing challenges. To test whether the translocon helps to regulate these events, we added the

SecYEG complex to the RNC_{FtsQ}-SRP-FtsY complex (Supplementary Fig. 11a). SecYEG restored the high FRET state (Fig. 4d, e). It also reversed the cargo-induced pausing and restored efficient GTP hydrolysis (Fig. 4a and D.A. and S.-o.S., manuscript in preparation). Neither effect was observed with the detergent *n*-dodecyl- β -D-maltoside (DDM) alone (Supplementary Fig. 11b) nor with mutant 82-nucleotide RNA (Fig. 4f and Supplementary Fig. 10c) or FtsY(A335W) (Supplementary Fig. 11c). Thus, SecYEG drives productive docking of the GTPase complex at the RNA distal site and thus re-activates GTP hydrolysis.

Next we wanted to know how SecYEG restores GTPase movements. Although SecYEG could simply remove the RNC from the SRP-FtsY complex, the following strongly suggests that this is not the case. Compared to the SRP-FtsY complex alone, GTPase movements in the presence of RNC_{FtsQ} and SecYEG displayed a distinct pattern, characterized by fewer transitions to intermediate FRET states, more frequent docking (Fig. 4g, h) and longer dwell times in the H state (Fig. 4d, i). These SecYEG-induced changes were not observed without RNC (Supplementary Fig. 11d, e). To test directly whether RNC remains on the targeting complex, we labelled the RNC with Alexa 647, which was found to co-localize with labelled SRP (Supplementary Fig. 12). These co-localized spots remain after incubation with SecYEG (Supplementary Fig. 12c, d), indicating that RNC was not displaced by SecYEG. These data imply that SecYEG forms a quaternary complex with RNC, SRP and FtsY, which could represent a transient intermediate in the targeting and translocation reaction. These results also suggest that SecYEG drives the GTPase movement through two mechanisms: (1) displacing the GTPase complex from the proximal site, as indicated by the reappearance of the H state even with RNC present (compare Fig. 4d with Supplementary Fig. 9b); and (2) prolonging productive docking at the RNA distal site (Fig. 4i). Finally, non-productive movements to intermediate FRET states are minimized with RNC and SecYEG present (Fig. 4g, h). Considering the size of SRP RNA relative to the ribosome, the RNC possibly masks non-productive GTPase docking sites on the SRP RNA, which could also explain the conserved length of this RNA.

In summary, we demonstrate that the SRP RNA provides a molecular scaffold that mediates large-scale movements of the SRP-FtsY

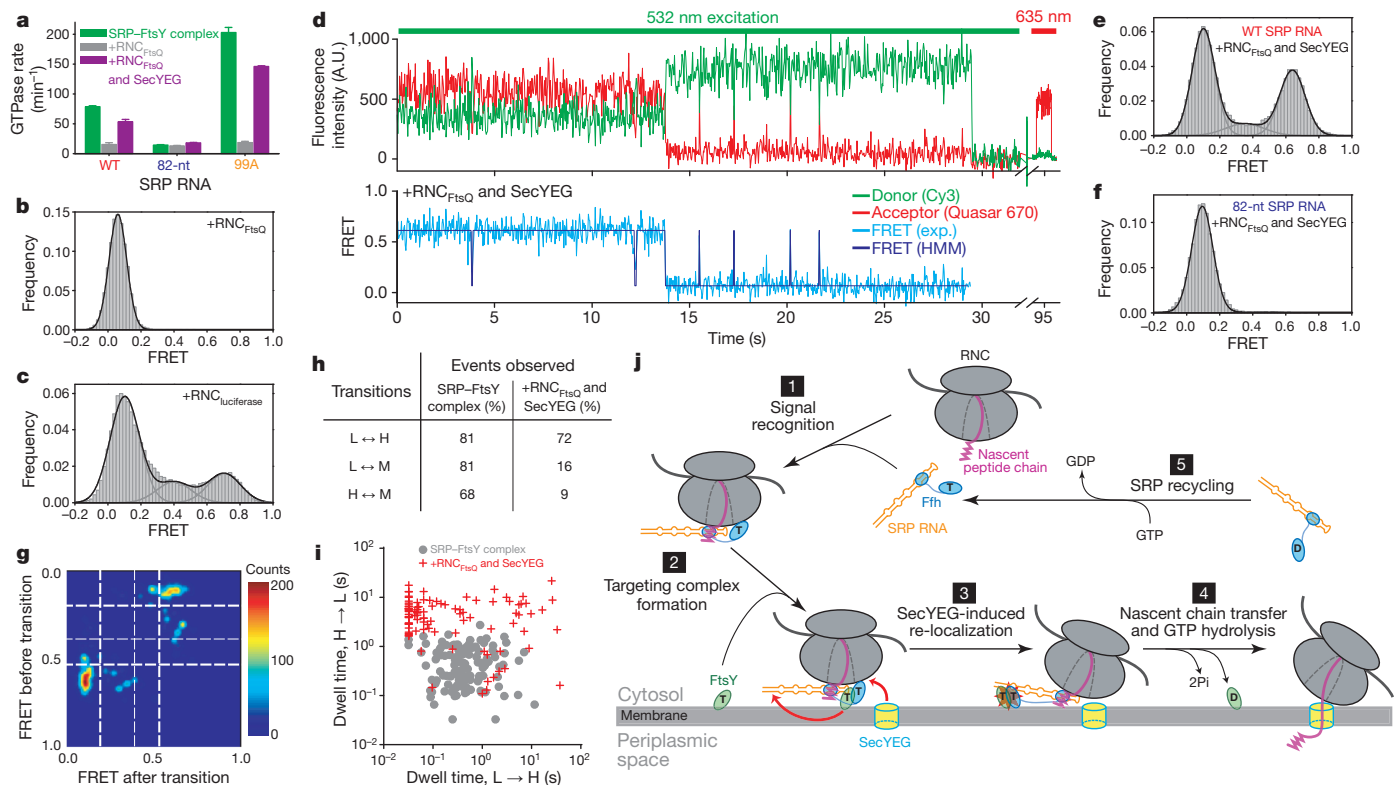


Figure 4 | RNC and SecYEG regulate GTPase movements on the SRP RNA. **a**, Effect of RNC_{FtsQ} (grey) and SecYEG (purple) on the GTPase activity of the SRP-FtsY complex assembled with the wild-type, 82-nucleotide and 99A SRP RNA. Data represent mean \pm s.d. ($n = 3$). **b**, **c**, smFRET histograms of the SRP-FtsY complex bound to RNC_{FtsQ} (**b**) or RNC_{luciferase} (**c**). **d**, Fluorescent signals (top) and FRET trajectory (bottom) of the RNC_{FtsQ}-SRP-FtsY complex in the presence of SecYEG. **e**, **f**, smFRET histograms of the RNC_{FtsQ}-SRP-FtsY complex in the presence of SecYEG, with the wild-type (**e**) or 82-nucleotide

(**f**) SRP RNA. **g**, Transition density plot of GTPase movements in the presence of RNC_{FtsQ} and SecYEG. **h**, Summary of the percentage of molecules that exhibit the specified transitions. In the presence of RNC_{FtsQ} and SecYEG, transitions to intermediate FRET states are almost completely reduced. **i**, Scatter plot of the transition dwell times of individual molecules in the absence (grey circles) and presence of RNC_{FtsQ} and SecYEG (red crosses). **j**, Model for the role of the SRP-RNA-mediated GTPase re-localization in co-translational protein targeting.

complex, which is tightly regulated by the GTPase cycle of SRP and FtsY, the translating ribosome and the SecYEG translocon. Together with previous studies, we propose a molecular model for co-translational protein targeting (Fig. 4j). Upon cargo recognition (step 1), the SRP RNA tetraloop is optimally positioned adjacent to the Ffh NG domain, allowing efficient recruitment of FtsY near the ribosome exit site^{12–15} (step 2). GTP-induced rearrangements in the SRP-FtsY NG-domain complex prime^{23,25} but are insufficient to release this complex for docking at the distal site owing to the pausing effect of RNC. SecYEG is required to drive GTPase re-localization to the SRP RNA distal site (step 3). This vacates the ribosome exit site and allows SecYEG to initiate contacts with L23, thus enabling the coordinated transfer of RNC from the targeting to translocation machinery (step 4). Concomitantly, GTPase docking at the RNA distal site triggers rapid GTP hydrolysis, driving the disassembly and recycling of SRP and FtsY (step 4 and 5). This provides an attractive mechanism to allow the concerted exchange of SRP and SecYEG at the ribosome and the precise timing of GTP hydrolysis, thus minimizing abortive reactions due to premature SRP-FtsY disassembly or non-productive loss of cargo.

Nucleic-acid-mediated protein movement is a widespread phenomenon and has been observed with the spliceosome²⁶, helicases^{27,28} and type I restriction endonucleases^{29,30}. Our results enrich these findings and further suggest that large RNA molecules can provide useful molecular scaffolds to coordinate multiple protein interactions and large-scale protein rearrangements, thus enabling productive exchange of different factors and precise timing of molecular events in a cellular pathway. This may provide general principles for understanding similar phenomena in other ribonucleoprotein particles.

METHODS SUMMARY

Materials. Protein, SRP RNA, messenger RNA, RNC and SecYEG were prepared as described in Methods. Ffh and FtsY were labelled with Cy3 at a unique cysteine residue, Cys 153 and Cys 345, respectively, using maleimide chemistry as described in ref. 12. Labelled DNA splint was purchased from Biosearch Technologies. Translation extracts and salt-washed, trypsin-digested microsomal membranes were prepared as described in ref. 21.

Single-molecule instrumentation and imaging. Olympus IX-81 microscope was modified as described previously in ref. 19. SRP was immobilized by extending the 5'-end of SRP RNA, which hybridizes to a complementary oligonucleotide (DNA splint) 3'-labelled with biotin and thus coupled to PEGylated, streptavidin-coated coverslip surface through biotin-streptavidin interaction. Fluorescent signals were split by DualView (Photometrics) and recorded with an EMCCD camera (Andor). The data were extracted and analysed by scripts written in IDL and MATLAB¹⁹. HMM was carried out using the HaMMY program²⁰, and the transition heat-map was plotted with TDP software²⁰. Details of the instrument setup, sample immobilization, data collection and analyses are described in Methods.

Biochemical assays. Assays for GTPase activity and for co-translational protein targeting and translocation were performed and analysed as described previously in refs 8 and 21, and are summarized in Methods.

Full Methods and any associated references are available in the online version of the paper.

Received 31 July; accepted 26 October 2012.

- Keenan, R. J., Freymann, D. M., Stroud, R. M. & Walter, P. The signal recognition particle. *Annu. Rev. Biochem.* **70**, 755–775 (2001).
- Pool, M. R., Stumm, J., Fulga, T. A., Sinning, I. & Dobberstein, B. Distinct modes of signal recognition particle interaction with the ribosome. *Science* **297**, 1345–1348 (2002).
- Halic, M. et al. Following the signal sequence from ribosomal tunnel exit to signal recognition particle. *Nature* **444**, 507–511 (2006).

4. Schaffitzel, C. *et al.* Structure of the *E. coli* signal recognition particle bound to a translating ribosome. *Nature* **444**, 503–506 (2006).
5. Focia, P. J., Shepotinovskaya, I. V., Seidler, J. A. & Freymann, D. M. Heterodimeric GTPase core of the SRP targeting complex. *Science* **303**, 373–377 (2004).
6. Egea, P. F. *et al.* Substrate twinning activates the signal recognition particle and its receptor. *Nature* **427**, 215–221 (2004).
7. Becker, T. *et al.* Structure of monomeric yeast and mammalian Sec61 complexes interacting with the translating ribosome. *Science* **326**, 1369–1373 (2009).
8. Peluso, P., Shan, S. O., Nock, S., Herschlag, D. & Walter, P. Role of SRP RNA in the GTPase cycles of ffh and FtsY. *Biochemistry* **40**, 15224–15233 (2001).
9. Zhang, X., Rashid, R., Wang, K. & Shan, S. O. Sequential checkpoints govern substrate selection during cotranslational protein targeting. *Science* **328**, 757–760 (2010).
10. Janda, C. Y. *et al.* Recognition of a signal peptide by the signal recognition particle. *Nature* **465**, 507–510 (2010).
11. Batey, R. T., Rambo, R. P., Lucast, L., Rha, B. & Doudna, J. A. Crystal structure of the ribonucleoprotein core of the signal recognition particle. *Science* **287**, 1232–1239 (2000).
12. Zhang, X., Kung, S. & Shan, S. O. Demonstration of a multistep mechanism for assembly of the SRP-SRP receptor complex: implications for the catalytic role of SRP RNA. *J. Mol. Biol.* **381**, 581–593 (2008).
13. Shen, K. & Shan, S. O. Transient tether between the SRP RNA and SRP receptor ensures efficient cargo delivery during cotranslational protein targeting. *Proc. Natl Acad. Sci. USA* **107**, 7698–7703 (2010).
14. Shen, K., Zhang, X. & Shan, S. O. Synergistic actions between the SRP RNA and translating ribosome allow efficient delivery of the correct cargos during cotranslational protein targeting. *RNA* **17**, 892–902 (2011).
15. Estrozi, L. F., Boehringer, D., Shan, S., Ban, N. & Schaffitzel, C. Cryo-EM structure of the *E. coli* translating ribosome in complex with SRP and its receptor. *Nature Struct. Mol. Biol.* **18**, 88–90 (2011).
16. Althoff, S., Selinger, D. & Wise, J. A. Molecular evolution of SRP cycle components: functional implications. *Nucleic Acids Res.* **22**, 1933–1947 (1994).
17. Ataide, S. F. *et al.* The crystal structure of the signal recognition particle in complex with its receptor. *Science* **331**, 881–886 (2011).
18. Ha, T. *et al.* Probing the interaction between two single molecules: fluorescence resonance energy transfer between a single donor and a single acceptor. *Proc. Natl Acad. Sci. USA* **93**, 6264–6268 (1996).
19. Roy, R., Hohng, S. & Ha, T. A practical guide to single-molecule FRET. *Nature Methods* **5**, 507–516 (2008).
20. McKinney, S. A., Joo, C. & Ha, T. Analysis of single-molecule FRET trajectories using hidden Markov modeling. *Biophys. J.* **91**, 1941–1951 (2006).
21. Shan, S. O., Chandrasekar, S. & Walter, P. Conformational changes in the GTPase modules of the signal reception particle and its initiation of protein translocation. *J. Cell Biol.* **178**, 611–620 (2007).
22. Shan, S. O., Stroud, R. M. & Walter, P. Mechanism of association and reciprocal activation of two GTPases. *PLoS Biol.* **2**, e320 (2004).
23. Zhang, X., Schaffitzel, C., Ban, N. & Shan, S. O. Multiple conformational switches in a GTPase complex control co-translational protein targeting. *Proc. Natl Acad. Sci. USA* **106**, 1754–1759 (2009).
24. Zhang, X. *et al.* Direct visualization reveals dynamics of a transient intermediate during protein assembly. *Proc. Natl Acad. Sci. USA* **108**, 6450–6455 (2011).
25. Halic, M. *et al.* Signal recognition particle receptor exposes the ribosomal translocon binding site. *Science* **312**, 745–747 (2006).
26. Hoskins, A. A., Gelles, J. & Moore, M. J. New insights into the spliceosome by single molecule fluorescence microscopy. *Curr. Opin. Chem. Biol.* **15**, 864–870 (2011).
27. Lohman, T. M. & Bjornson, K. P. Mechanisms of helicase-catalyzed DNA unwinding. *Annu. Rev. Biochem.* **65**, 169–214 (1996).
28. Yodh, J. G., Schlierf, M. & Ha, T. Insight into helicase mechanism and function revealed through single-molecule approaches. *Q. Rev. Biophys.* **43**, 185–217 (2010).
29. Yuan, R. Structure and mechanism of multifunctional restriction endonucleases. *Annu. Rev. Biochem.* **50**, 285–315 (1981).
30. Murray, N. E. Type I restriction systems: sophisticated molecular machines (a legacy of Bertani and Weigle). *Microbiol. Mol. Biol. Rev.* **64**, 412–434 (2000).

Supplementary Information is available in the online version of the paper.

Acknowledgements We thank N. Ban and members of the Shan group for comments on the manuscript, C. Richards, L. Cai, T. Zhiyentayev, K. Lee and R. Zhou for help with RNC labelling and the instrument and software setup, and C.L. Guo, S. Kou and H. Lester for discussions. This work is supported by National Institutes of Health (NIH) grant GM078024 to S.-o.S., an NIH instrument supplement to grant GM45162 to D.C. Rees, and Caltech matching fund 350270 for the single-molecule instruments. S.-o.S. was supported by the Beckman Young Investigator award, the David and Lucile Packard Fellowship in Science and Engineering, and the Henry Dreyfus Teacher-Scholar award. T.H. was supported by National Science Foundation Physics Frontiers Centers program (08222613) and NIH grant GM065367.

Author Contributions K.S., S.A., T.H. and S.-o.S. conceived the experiments. K.S. purified and labelled Ffh, FtsY, DNA, RNA and RNC. D.A. purified SecYEG and performed the GTPase assay in Fig. 4a. K.S. and S.A. carried out smFRET measurements under the direction of T.H. K.S. and S.A. analysed the data. K.S. and S.-o.S. wrote the paper with inputs from all other authors.

Author Information Reprints and permissions information is available at www.nature.com/reprints. The authors declare no competing financial interests. Readers are welcome to comment on the online version of the paper. Correspondence and requests for materials should be addressed to S.-o.S. (sshan@caltech.edu).

METHODS

Plasmids. Plasmids for *in vivo* expression of Ffh, full-length FtsY and SRP RNA, and for *in vitro* transcription of FtsQ, luciferase and pPL and its signal sequence variants have been described previously^{8,9,31}. The pEK20 construct for SecYEG expression was a gift from A. Driessen³². Plasmids for mutant SRP RNAs and mutant proteins were constructed using the QuikChange mutagenesis protocol (Stratagene) following manufacturer's instructions. The plasmid for *in vitro* transcription of hammerhead ribozyme-SRP RNA-hepatitis delta virus (HDV) ribozyme was a gift from A. Ferre-D'Amare³³. The hammerhead coding sequence was removed and the 5'-end of SRP RNA was extended using the QuikChange mutagenesis protocol to make *in vitro* transcription constructs for single-molecule RNA (smRNA) constructs.

Protein preparations. Wild-type and single-cysteine mutants of Ffh and FtsY were expressed and purified as described previously⁸. In brief, Ffh expression was induced in logarithmically growing BL21(DE3)pLysE cells with 1 mM isopropyl- β -D-thiogalactoside (IPTG). The soluble fraction from lysed cells was purified by cation-exchange chromatography on SP Sepharose Fast Flow resin (GE Healthcare) using a gradient of 0.25–1 M NaCl, and was further purified by gel-filtration chromatography on the Superose12 column (Amersham Biosciences). His₆-tagged full-length FtsY was expressed in BL21(DE3)pLysS cells by induction with 0.5 mM IPTG in logarithmically growing cells. The soluble fraction from lysed cells was purified by anion-exchange chromatography using Q Sepharose Fast Flow resin (GE Healthcare) with a gradient of 150–500 mM NaCl, followed by affinity purification using nickel-nitrilotriacetic acid (Ni-NTA) resin (Qiagen). For GTPase assays, FtsY was further purified by anion-exchange chromatography on the MonoQ column (Amersham Biosciences) using a gradient of 150–350 mM NaCl. All proteins were exchanged into SRP buffer (50 mM potassium-HEPES, pH 7.5, 150 mM potassium acetate, 2 mM magnesium acetate, 2 mM dithiothreitol, 0.01% Nikkol) before use.

Detergent-solubilized SecYEG was expressed in BL21(DE3) cells with 0.5 mM IPTG and was purified following published procedures^{32,34,35}. Cells were lysed by sonication and the membranes were collected by ultracentrifugation. SecYEG was extracted and purified by cation-exchange chromatography on the SP Sepharose Fast Flow resin (GE Healthcare) followed by affinity purification with Ni-NTA (Qiagen). DDM (Affimetric) was used for purification of solubilized SecYEG, which has been shown to be fully functional in binding RNC (D.A. & S.S., manuscript in preparation)³⁶, in mediating nascent peptide translocation³⁶, and stimulating SecA ATPase activity³⁷.

Fluorescence labelling. Single-cysteine mutants of Ffh and FtsY were labelled with Cy3-maleimide (GE Healthcare) as described in ref. 12. Protein concentration during labelling was 50–100 μ M, and the dye was in tenfold molar excess. Labelling reaction was carried out in buffer A (50 mM potassium-HEPES, pH 7.0, 300 mM NaCl, 2 mM EDTA, 10% glycerol) with gentle shaking at room temperature (22 °C) for 2 h. Unconjugated dyes were removed by gel-filtration chromatography using Sephadex G-25 resin (Sigma). Mass spectrometry confirmed >95% labelling efficiencies. Fluorescence labelling and modifications of the SRP RNA for surface immobilization (Fig. 1a and Supplementary Fig. 1b) did not affect the activity of SRP and FtsY (Supplementary Fig. 1d).

Fluorescent DNA probes for hybridization with the mRNA on RNC were prepared by incubating NH₂-modified DNA oligonucleotides (Integrated DNA Technologies) with a tenfold excess of Alexa Fluor 647 carboxylic acid succinimidyl ester (Invitrogen) for 1 h at 37 °C. Excess dyes were removed by HPLC.

RNA preparation. Wild-type SRP RNA was expressed *in vivo* and purified as described in ref. 8. SRP RNAs for smFRET experiments (smRNA; Supplementary Fig. 1b) were prepared by *in vitro* transcription using T7 polymerase according to the Megascript protocol (Ambion). The 3'-end of the SRP RNA coding sequence was fused to that of an HDV ribozyme (sequence: 5'-GGGCGGCATGGTCCC AGCCTCCTCGTGGCGCGCCTGGGCAACATCCGAGGGGACCGTCCC CTCGGTAATGGCGAATGGGACC-3'). Self cleavage of the HDV ribozyme occurred during *in vitro* transcription to generate a homogeneous 3'-end of the SRP RNA. Purified smRNA was annealed to a complementary DNA splint by the following procedures: (1) heat the TE buffer (10 mM Tris-HCl, pH 7.0, 2 mM EDTA) containing 10 μ M DNA and 20 μ M smRNA for 5 min at 75 °C; (2) gradually cool to 50 °C over a period of 30 min; (3) add 12 mM MgCl₂ to the mixture; and (4) gradually cool to room temperature over a period of 30 min. The annealed DNA-smRNA hybrids were stored at -80 °C.

mRNAs for *in vitro* translation were generated by *in vitro* transcription using T7 (for RNC preparation) or SP6 (for targeting assays) polymerase following the Megascript protocol (Ambion).

Preparation of RNCs. Synchronized RNCs with defined nascent chain length and sequence were prepared as described previously in ref. 31. In brief, mRNAs encoding a Strep₃ tag at the amino terminus, the first 74 amino acids of FtsQ or luciferase, and a SecM translation-stall sequence at the carboxy terminus were translated

by S100 extract as described in ref. 31. RNC from the translation mixture was purified by affinity chromatography using the Strep-Tactin resin (IBA), collected by ultracentrifugation, and re-dissolved in SRP buffer and stored at -80 °C. RNCs used for GTPase assay were further purified by ultracentrifugation and fractionation on a 10–50% sucrose gradient as described in ref. 31.

RNC_{FtsQ} was fluorescently labelled by incubation with fluorescent DNA probes complementary to the mRNA for 3 h at room temperature. Labelled RNC was isolated by ultracentrifugation and re-dissolved in SRP buffer.

Single-molecule instrument. Objective-type TIRF microscope was home-built based on an Olympus IX-81 model as described in ref. 19. Green (532 nm) and red (635 nm) lasers were focused in a \times 100 oil-immersed objective. Scattering light was removed by 560-nm and 660-nm long-pass filters (Chroma) for the green and red lasers, respectively. Cy3 and Quasar 670 signals were split by a dichroic mirror and simultaneously focused onto the iXon 897 camera (Andor) through DV2 Dualview (Photometrics). Data were recorded at 30-ms time resolution.

PEGylated slides and coverslips. PEGylated slides and coverslips were prepared based on an existing protocol¹⁹. In brief, quartz slides and coverslips were treated sequentially with 10% alconox, acetone and 10 M KOH. The surfaces were then burnt with a propane torch to remove autofluorescence. Amino-silication reactions were carried out in methanol with 5% (v/v) acetic acid and 1% (v/v) aminopropylsilane. PEGylation reactions were carried out in 100 mM NaHCO₃ buffer containing 20% (w/v) polyethylene glycol (PEG) and 0.6% (w/v) Biotin-PEG. PEGylated slides and coverslips were stored in vacuum at -20 °C and assembled into flow chambers before use.

Single-molecule assay. To remove aggregates, all protein samples were ultracentrifuged at 100,000 r.p.m. (Optima TLX, Beckman Coulter) for 1 h before use. PEGylated slides and coverslips were assembled to form a flow chamber. Neutravidin (0.2 mg mg⁻¹) was applied to the chamber and incubated for 10 min before flowing in molecules of interest.

SRP complexes were assembled in SRP buffer under the following conditions. SRP-FtsY complex with labelled Ffh: 1 μ M DNA-smRNA hybrid, 2 μ M Ffh-Cy3, 5 μ M FtsY, 100 μ M GMPPNP. SRP-FtsY complex with labelled FtsY: 1 μ M DNA-smRNA hybrid, 2 μ M Ffh, 3 μ M FtsY-Cy3, 100 μ M GMPPNP. RNC-SRP-FtsY complexes: 200 nM DNA-smRNA hybrid, 400 nM Ffh-Cy3, 500 nM RNC_{FtsQ} or 1 μ M RNC_{luciferase}, 1 μ M FtsY, 100 μ M GMPPNP. SecYEG solubilized in 0.02% DDM was added to RNC_{FtsQ}-SRP-FtsY complex at 10 μ M. The samples were then diluted to 50 pM in imaging buffer (SRP buffer supplemented with 0.4% glucose and 1% Gloxy in Trolox), flowed onto the sample chamber and incubated for 5 min before imaging. Movies were recorded at 30-ms intervals for up to 3 min until most fluorescent molecules were photobleached. A red laser was applied at the end of the movie to confirm the presence of immobilized SRP.

Data analysis. Single-molecule data were processed by scripts written in IDL and MATLAB. In brief, fluorescent peaks in the images were identified and traced throughout the trajectory. Traces that showed a single-donor bleaching event were used for data analysis. HMM was calculated using the HaMMY program²⁰. Transition density map was generated by the TDP program²⁰ using the output from HaMMY. FRET histograms were generated using home-written script in MATLAB¹⁹. Transition kinetics between different states was obtained by exponential fits to dwell-time histograms. Two-dimensional scatter plots of the average dwell time of individual molecules during transitions were generated using the home-written script in MATLAB.

GTPase assay. GTPase rate constants were determined using a well-established GTPase assay⁸. In general, reactions contained 100 nM Ffh, 200 nM SRP RNA, 100 μ M GTP (doped with γ -³²P-GTP), varying concentrations of FtsY, and 250 nM RNC_{FtsQ} and 10 μ M SecYEG where applicable. Reactions were quenched with 0.75 M KH₂PO₄, pH 3.3, at different time points, separated by thin layer chromatography and quantified by autoradiography.

Translocation assay. Assays for co-translational protein targeting and translocation were carried out as described in refs 21 and 38. Reactions contained 10 μ l *in vitro* translation mixtures synthesizing ³⁵S-methionine-labelled pPL or pPL signal-sequence variants, to which 200 nM Ffh, 333 nM wild-type or mutant SRP RNA, 300 nM FtsY and 0.5 equiv. per μ l of salt-washed, trypsin-digested microsomal membrane was added to a total volume of 15 μ l. Reactions were analysed by SDS-PAGE followed by autoradiography.

- Schaffitzel, C. & Ban, N. Generation of ribosome nascent chain complexes for structural and functional studies. *J. Struct. Biol.* **158**, 463–471 (2007).
- van der Sluis, E. O., Nouwen, N. & Driessen, A. J. SecY-SecY and SecY-SecG contacts revealed by site-specific crosslinking. *FEBS Lett.* **527**, 159–165 (2002).
- Ferré-D'Amaré, A. R. & Doudna, J. A. Use of *cis*- and *trans*-ribozymes to remove 5' and 3' heterogeneities from milligrams of *in vitro* transcribed RNA. *Nucleic Acids Res.* **24**, 977–978 (1996).
- Dalal, K. & Duong, F. Reconstitution of the SecY translocon in nanodiscs. *Methods Mol. Biol.* **619**, 145–156 (2010).

35. Van den Berg, B. *et al.* X-ray structure of a protein-conducting channel. *Nature* **427**, 36–44 (2004).
36. Mothes, W., Jungnickel, B., Brunner, J. & Rapoport, T. A. Signal sequence recognition in cotranslational translocation by protein components of the endoplasmic reticulum membrane. *J. Cell Biol.* **142**, 355–364 (1998).
37. Duong, F. Binding, activation and dissociation of the dimeric SecA ATPase at the dimeric SecYEG translocase. *EMBO J.* **22**, 4375–4384 (2003).
38. Powers, T. & Walter, P. Co-translational protein targeting catalyzed by the *Escherichia coli* signal recognition particle and its receptor. *EMBO J.* **16**, 4880–4886 (1997).

Centralspindlin links the mitotic spindle to the plasma membrane during cytokinesis

Sergey Lekomtsev¹, Kuan-Chung Su¹, Valerie E. Pye², Ken Blight³, Sriramkumar Sundaramoorthy¹, Tohru Takaki¹, Lucy M. Collinson³, Peter Cherepanov², Nullin Divecha⁴ & Mark Petronczki¹

At the end of cell division, cytokinesis splits the cytoplasm of nascent daughter cells and partitions segregated sister genomes^{1,2}. To coordinate cell division with chromosome segregation, the mitotic spindle controls cytokinetic events at the cell envelope. The spindle midzone stimulates the actomyosin-driven contraction of the cleavage furrow, which proceeds until the formation of a microtubule-rich intercellular bridge with the midbody at its centre. The midbody directs the final membrane abscission reaction^{1,2} and has been proposed to attach the cleavage furrow to the intercellular bridge³. How the mitotic spindle is connected to the plasma membrane during cytokinesis is not understood. Here we identify a plasma membrane tethering activity in the centralspindlin protein complex, a conserved component of the spindle midzone and midbody⁴. We demonstrate that the C1 domain of the centralspindlin subunit MgcRacGAP associates with the plasma membrane by interacting with polyanionic phosphoinositide lipids. Using X-ray crystallography we determine the structure of this atypical C1 domain. Mutations in the hydrophobic cap and in basic residues of the C1 domain of MgcRacGAP prevent association of the protein with the plasma membrane, and abrogate cytokinesis in human and chicken cells. Artificial membrane tethering of centralspindlin restores cell division in the absence of the C1 domain of MgcRacGAP. Although C1 domain function is dispensable for the formation of the midzone and midbody, it promotes contractility and is required for the attachment of the plasma membrane to the midbody, a long-postulated function of this organelle³. Our analysis suggests that centralspindlin links the mitotic spindle to the plasma membrane to secure the final cut during cytokinesis in animal cells.

Despite the importance of the mitotic apparatus for cytokinesis, direct interactions between core midzone or midbody components and the plasma membrane have not been identified so far. A crucial regulator of cytokinesis in animal cells is a conserved heterotetrameric protein complex called centralspindlin⁴. Centralspindlin is composed of two molecules of the kinesin protein MKLP1 and two molecules of the Rho family GTPase-activating protein (GAP) MgcRacGAP^{5,6} (also known as RACGAP1 or CYK4; Supplementary Fig. 1a). Centralspindlin organizes antiparallel arrays of microtubules at the spindle midzone and midbody, controls the activity of the small GTPases RhoA and Rac during furrow ingression^{7–10}, and recruits cytokinetic effector proteins to promote cortical contractility and abscission^{11–16}.

A search for potential membrane-interaction moieties among midzone and midbody components revealed an uncharacterized but evolutionarily conserved C1 domain in the centralspindlin subunit MgcRacGAP (Fig. 1a and Supplementary Fig. 1b). C1 domains can serve as protein- or lipid-binding modules^{17,18}. Using X-ray crystallography, we determined the structure of the C1 domain of human MgcRacGAP and refined it to a resolution of 2.2 Å (Fig. 1b, Supplementary Fig. 2 and Supplementary Table 1; see accession details

below). The crystal structure revealed a characteristic C1 domain fold with two Zn²⁺-coordinating centres and a β -sheet-loop configuration that may act as a ligand-binding interface^{17,18} (Fig. 1b).

To scrutinize the function of MgcRacGAP's C1 domain, we generated monoclonal human HeLa Kyoto cell lines expressing short interfering RNA (siRNA)-resistant and tagged alleles of MgcRacGAP (Fig. 1a, c and Supplementary Fig. 3). Wild-type MgcRacGAP resistant to siRNA (MgcRacGAPr) effectively suppressed the cytokinesis failure caused by depletion of the endogenous counterpart (Fig. 1c). Elimination of the MKLP1-interacting region^{5,6} at the amino terminus of MgcRacGAP (MgcRacGAPr- Δ N) abolished the ability of the transgenic protein to support cell division. Importantly, deletion of the C1 domain (MgcRacGAPr- Δ C1) in MgcRacGAP also completely

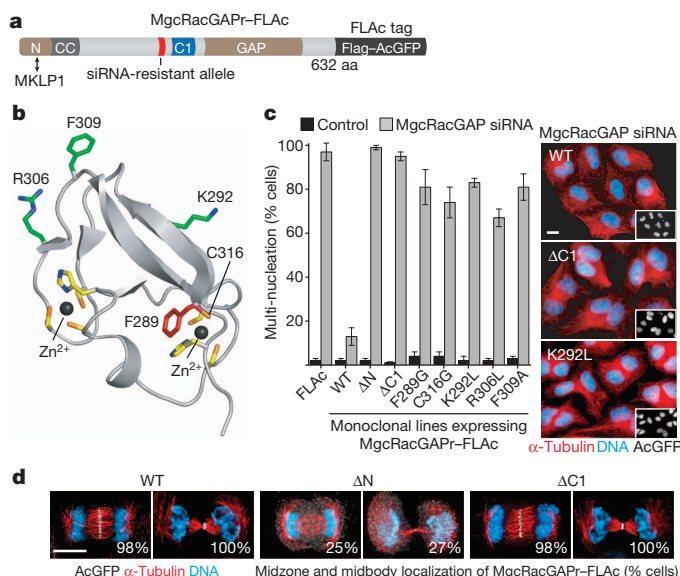


Figure 1 | The C1 domain of MgcRacGAP is required for cytokinesis. **a**, Transgenic MgcRacGAP system. aa, amino acid; AcGFP, *Aequorea coerulescens* green fluorescent protein; C1, cysteine-rich domain; CC, coiled coil; GAP, GTPase-activating protein domain. **b**, Structure of the C1 domain of human MgcRacGAP at 2.2-Å resolution. Side chains of mutated structural core and surface residues are shown in red and green, respectively. Zn²⁺-coordinating residues are shown in yellow. **c**, Monoclonal HeLa Kyoto cell lines expressing the indicated transgenes were transfected with control or MgcRacGAP siRNA duplexes. Multi-nucleation in AcGFP-positive interphase cells 48 h after transfection (graph). Error bars, s.d. of three experiments ($n > 200$ cells each). Immunoblot analysis of cell lines is shown in Supplementary Fig. 3b. **d**, Localization of MgcRacGAPr-FLAc transgenes; endogenous MgcRacGAP depleted in monoclonal MgcRacGAPr-FLAc cell lines ($n > 50$ cells each). Scale bars, 10 μ m.

¹Cell Division and Aneuploidy Laboratory, Cancer Research UK London Research Institute, Clare Hall Laboratories, Blanche Lane, South Mimms, Hertfordshire EN6 3LD, UK. ²Chromatin Structure and Mobile DNA Laboratory, Cancer Research UK London Research Institute, Clare Hall Laboratories, Blanche Lane, South Mimms, Hertfordshire EN6 3LD, UK. ³Electron Microscopy Unit, Cancer Research UK London Research Institute, 44 Lincoln's Inn Fields, London WC2A 3PX, UK. ⁴Inositol Laboratory, Paterson Institute for Cancer Research, The University of Manchester, Wilmslow Road, Withington, Manchester M20 4BX, UK.

abrogated cytokinesis (Fig. 1c). Furthermore, single point mutations in structural core residues (Phe289Gly and Cys316Gly) and conserved surface residues (Lys292Leu, Arg306Leu and Phe309Ala) (Fig. 1b) of MgcRacGAP's C1 domain severely compromised cytokinesis (Fig. 1c). Thus, the C1 domain of MgcRacGAP has a critical role during cell division in human cells.

Biochemical and cellular analyses revealed that MgcRacGAP's C1 domain was dispensable for the assembly of the centralspindlin complex (Supplementary Fig. 4a), the localization of centralspindlin (Fig. 1d and Supplementary Fig. 4b), and the organization of microtubule arrays at the midzone and midbody (Fig. 1d). It was also dispensable for the midzone and midbody localization of known cytokinetic regulators (Supplementary Fig. 4c). In marked contrast, MgcRacGAP- Δ N abolished the formation of the centralspindlin complex and severely impaired the organization of the midzone and midbody (Fig. 1d and Supplementary Fig. 4a, c). Thus, the assembly of the spindle midzone and midbody requires formation of the centralspindlin complex but not MgcRacGAP's C1 domain, suggesting that this domain encodes a novel function of centralspindlin that is essential for cytokinesis.

Based on the ability to interact with diacylglycerol (DAG) and phorbol ester DAG mimetics, C1 domains are divided into two functional groups, typical and atypical¹⁷. Acute treatment with the phorbol ester 12-O-tetradecanoylphorbol-13-acetate (TPA) caused the rapid translocation of the typical C1B domain of human protein kinase C α (PKC α) to the plasma membrane (Fig. 2a). In contrast, the C1 domain of MgcRacGAP remained cytosolic (Fig. 2a and Supplementary Video 1). Consistent with structural considerations (Supplementary Fig. 2c), the C1 domain of MgcRacGAP does not respond to phorbol esters and belongs to the atypical family.

Centralspindlin contains two molecules of MgcRacGAP and can form higher-order clusters^{6,19}. Therefore, we tested the subcellular distribution of tandem MgcRacGAP C1 domains. Fluorescently tagged head-to-tail fusion proteins of two or four C1 domains (C1_{2x} and C1_{4x}) localized to the plasma membrane independently of the actomyosin cortex (Fig. 2b and Supplementary Fig. 5a; see also Methods). Purified glutathione S-transferase (GST)-C1 protein bound to the phosphoinositide lipids phosphatidylinositol-4-phosphate (PtdIns(4)P), phosphatidylinositol-4,5-bisphosphate (PtdIns(4,5)P₂), phosphatidylinositol-3,4,5-trisphosphate (PtdIns(3,4,5)P₃), and to phosphatidic acid *in vitro* (Supplementary Fig. 5b). Ca²⁺ and ionomycin-induced depletion of PtdIns(4)P and PtdIns(4,5)P₂ *in vivo*²⁰ triggered the rapid release of the C1_{2x} protein from the plasma membrane (Fig. 2c). To selectively hydrolyse phosphoinositides at the plasma membrane we used the hybrid lipid phosphatase pseudojanin (PJ)²⁰. Pseudojanin consists of the polyphosphate-5-phosphatase E (INPP5E), which converts PtdIns(4,5)P₂ to PtdIns(4)P, and the *Saccharomyces cerevisiae* Sac1 phosphatase (Sac), which dephosphorylates PtdIns(4)P. Rapamycin-controlled membrane targeting of pseudojanin, but not of its catalytically inactive counterpart (PJ-dead), caused the rapid and complete release of the C1_{2x} protein from the cell envelope (Fig. 2d). Individual elimination of PtdIns(4)P and PtdIns(4,5)P₂ elicited by membrane recruitment of only active Sac or INPP5E, respectively, caused a partial displacement of C1_{2x} from the plasma membrane (Fig. 2d). Together, these results suggest that MgcRacGAP's C1 domain associates with the inner leaflet of the plasma membrane by binding to PtdIns(4)P and PtdIns(4,5)P₂, two polyanionic phosphoinositides that contribute to plasma membrane identity²⁰. Consistent with this conclusion, surface plasmon resonance (SPR) experiments revealed that PtdIns(4)P and PtdIns(4,5)P₂ stimulated the interaction of the purified C1 domain with liposomes *in vitro* (Fig. 2e and Supplementary Fig. 5c).

Importantly, introduction of the C1 domain point mutations that abrogate cytokinesis (Fig. 1) into the tandem C1_{2x} fusion abolished the protein's membrane localization (Fig. 2b). The surface mutation Lys292Leu also eliminated the association of the purified C1 domain with PtdIns(4)P- or PtdIns(4,5)P₂-containing liposomes in SPR

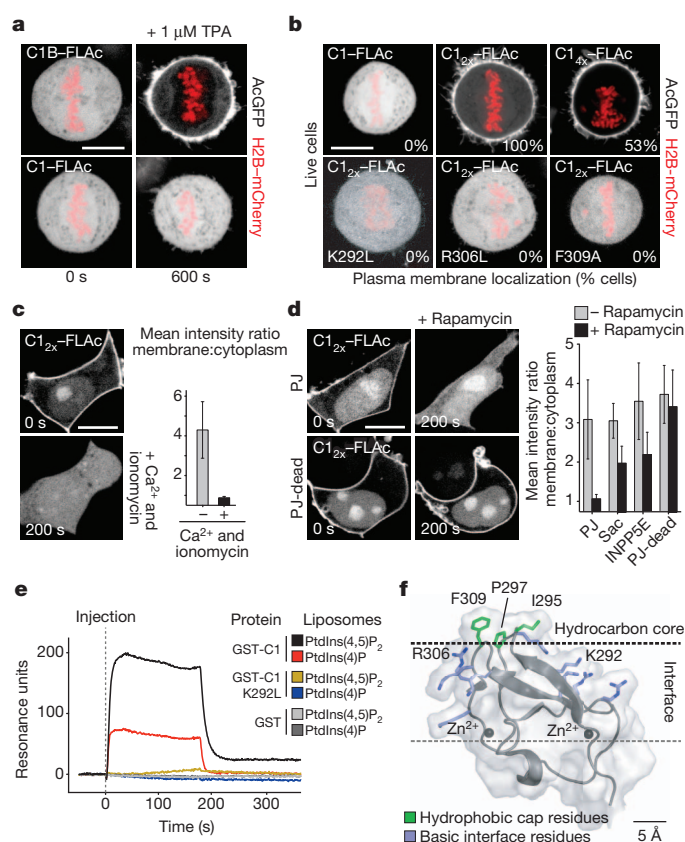


Figure 2 | Plasma membrane association of the C1 domain of MgcRacGAP. **a**, HeLa Kyoto cells expressing the typical C1B domain of human PKC α (C1B-FLAc) or the C1 domain of MgcRacGAP (C1-FLAc) were recorded before (0 s) and 200 s after treatment with 1 μ M TPA. **b**, Analysis of HeLa Kyoto cells expressing the indicated C1-FLAc variants ($n > 30$ cells). **c**, HEK293T cells expressing C1_{2x}-FLAc were recorded before (–) and 200 s after (+) treatment with 1 mM CaCl₂ and 10 μ M ionomycin. Quantification of C1_{2x}-FLAc membrane localization ($n = 15$ cells each). Error bars, s.d. **d**, HEK293T cells co-expressing C1_{2x}-FLAc, Lyn11-FRB-mCherry and one of four monomeric red fluorescent protein (mRFP)-FKBP-tagged lipid phosphatases (pseudojanin (PJ), Sac, INPP5E or the catalytically inactive counterpart of PJ (PJ-dead))²⁰ were recorded before (0 s) and 200 s after treatment with 10 μ M rapamycin. Quantification of C1_{2x}-FLAc membrane localization ($n = 15$ cells each). Error bars, s.d. **e**, Surface plasmon resonance analysis of the binding of purified proteins (250 nM) to phosphatidylethanolamine vesicles containing 5% PtdIns(4)P or PtdIns(4,5)P₂. Binding to phosphatidylethanolamine vesicles was used as a reference. **f**, Model of MgcRacGAP C1 domain–membrane interaction. Scale bars, 10 μ m.

measurements (Fig. 2e). Computational analysis²¹ of MgcRacGAP's C1 domain structure suggests that the protein interacts with a lipid bilayer through a hydrophobic cap that penetrates into the hydrocarbon core (Fig. 2f). This configuration also positions several basic surface residues within the interface region where they could engage with negatively charged lipid heads, such as those of PtdIns(4)P and PtdIns(4,5)P₂. This interpretation is substantiated by the fact that mutations in the hydrophobic cap (Phe309Ala) and in basic residues (Lys292Leu and Arg306Leu) abrogate membrane association of the C1 domain (Fig. 2b, e). The strict correlation between the failure to support cell division and membrane localization in the mutant alleles raised the possibility that plasma membrane binding could be the key function of MgcRacGAP's C1 domain during cytokinesis.

To test this hypothesis, we replaced the atypical C1 domain in MgcRacGAP with the typical C1B domain of human PKC α (MgcRacGAP-C1B) (Fig. 3a). This enabled us to chemically control the membrane association of the hybrid protein by the addition of phorbol esters (Supplementary Fig. 6a, b). After depletion of the

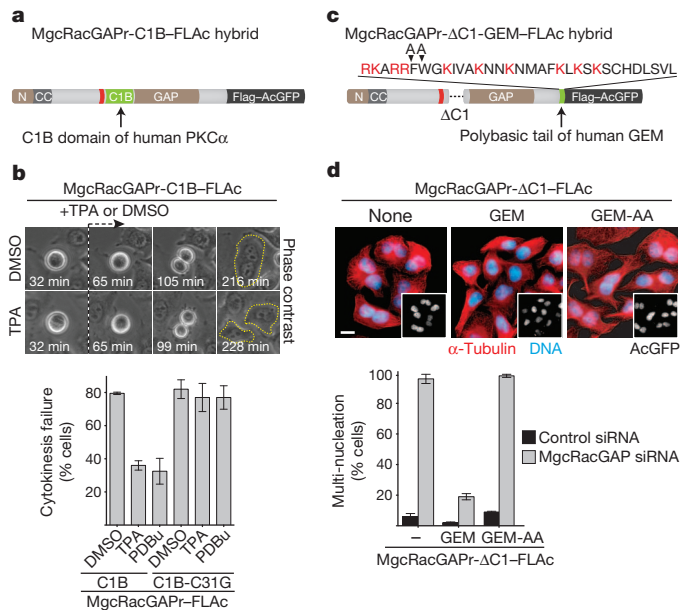


Figure 3 | Artificial plasma membrane tethering of MgcRacGAP restores cytokinesis in the absence of C1 domain function. **a–c**, Domain organization of hybrid proteins (**a**, **c**). Time-lapse series and quantification of cytokinesis failure in cells transfected with MgcRacGAP siRNA (**b**). Dotted arrow, point at which DMSO or TPA was added. Error bars, s.d. of two experiments ($n > 112$ cells each). **d**, Multi-nucleation in AcGFP-positive interphase cells. Images depict MgcRacGAP siRNA-transfected cells. None, protein MgcRacGAPr-ΔC1-FLAc does not contain any GEM fusion. Error bars, s.d. of three experiments ($n > 200$ cells each). Scale bar, 10 μ m.

endogenous MgcRacGAP protein, cells stably expressing MgcRacGAPr-C1B were released from a metaphase arrest and treated with either dimethylsulphoxide (DMSO) or the phorbol esters TPA (2.5 nM) and phorbol-12,13-dibutyrate (30 nM PDBu). Although DMSO-treated cells failed to divide, acute addition of phorbol esters restored successful cytokinesis in more than one-half of the MgcRacGAPr-C1B-hybrid-expressing cells (Fig. 3b). Mutation of a Zn²⁺-coordinating cysteine in the C1B domain (Cys31Gly) abolished the phorbol-ester-dependent membrane translocation and rescue activity of the hybrid protein (Fig. 3b and Supplementary Fig. 6a, b). Next, we inserted the polybasic tail of the human GTPase GEM at the carboxyl terminus of a version of MgcRacGAP that lacks the C1 domain (MgcRacGAPr-ΔC1-GEM) (Fig. 3c). Targeting of the tail of GEM to the plasma membrane involves PtdIns(4,5)P₂ and PtdIns(3,4,5)P₃ lipids²². Insertion of GEM's polybasic sequence restored successful cell division in the absence of MgcRacGAP's C1 domain (Fig. 3d and Supplementary Fig. 6c). Mutation of two hydrophobic residues in GEM's tail to alanine (Phe-Trp to Ala-Ala) abolished both the ectopic membrane association (Supplementary Fig. 6c, d) and the rescue activity of the hybrid protein (Fig. 3d). Insertion of GEM's polybasic tail had no effect on the penetrance of cell-division failure in the MgcRacGAP-ΔN allele that cannot interact with MKLP1 (Supplementary Fig. 7). Thus, artificial tethering of MgcRacGAP to the plasma membrane specifically bypasses the requirement for C1 domain function during cytokinesis. This shows that the atypical C1 domain of MgcRacGAP mediates plasma-membrane tethering of centralspindlin to control cytokinesis.

Complete loss of MgcRacGAP abrogated cleavage-furrow formation and the accumulation of RhoA and the contractile ring component anillin at the equator (Supplementary Fig. 8a–d). Mutations in MgcRacGAP's C1 domain supported full furrow ingression with normal kinetics in the majority of cells but caused furrow retraction and cytokinesis failure within approximately 50 min after anaphase onset (Supplementary Fig. 8a, d, e). In contrast, cells depleted for the abscission regulator CEP55 remained connected for up to 9 h (Supplementary

Fig. 8e). Also, mutation of the catalytic arginine finger in the GAP domain of MgcRacGAP (Arg385Ala) had a far less pronounced effect on the execution of cytokinesis than point mutations within the protein's C1 domain (Supplementary Fig. 9a). These observations suggest that facilitating GTP hydrolysis or cytokinetic abscission do not represent the primary function of centralspindlin's membrane association. Quantification of the intensity of RhoA and anillin revealed a minor reduction in the width of the contractile zone in MgcRacGAP C1 domain mutant alleles, probably accounting for the inability of a fraction of cells to complete furrow ingression (Supplementary Fig. 8a–c). Thus, although membrane tethering of centralspindlin contributes to the stimulation of contractility by the spindle midzone^{8–10,14,15,23}, it becomes critically important for cytokinesis soon after completion of furrowing.

Live-cell imaging in cells complemented with wild-type MgcRacGAP showed that the plasma membrane remained associated with the midbody until abscission (Fig. 4a and Supplementary Video 2) (27 out of 30 cells). MgcRacGAP proteins carrying the C1 domain mutations Lys292Leu or Phe289Gly also accumulated at the midbody after furrow ingression. However, the plasma membrane subsequently detached from the mutant midbody leading to furrow retraction and cytokinesis failure (Fig. 4a and Supplementary Video 2) (19 out of 24 cells). Transmission-electron-microscopy analysis of telophase cells frequently revealed areas of cytoplasmic density between the midbody matrix

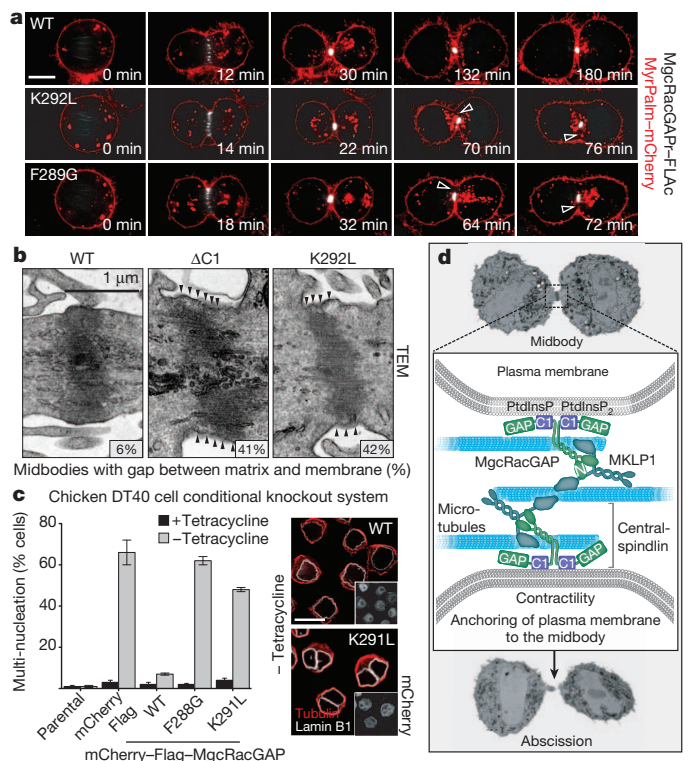


Figure 4 | Persistent association of the plasma membrane with the midbody requires the C1 domain of MgcRacGAP. **a**, Confocal imaging of cell lines stably co-expressing MyrPalm-mCherry and the indicated transgenes. Cells were transfected with MgcRacGAP siRNA. Arrowheads indicate detachment of the plasma membrane from the midbody. **b**, Transmission electron micrographs (TEMs) of cells stably expressing the indicated transgenes. Cells were transfected with MgcRacGAP siRNA. Arrowheads indicate gaps between the midbody matrix and the plasma membrane ($n > 23$ midbodies). **c**, MgcRacGAP knockout DT40 cells expressing a mouse MgcRacGAP rescue transgene from tetracycline-inducible promoter. Constitutively expressed mCherry-Flag-tagged chicken MgcRacGAP transgenes were introduced into the conditional knockout cells. Multi-nucleation in mCherry-positive cells in monoclonal lines. Error bars, s.d. of three experiments ($n > 200$ cells each). **d**, Model showing how centralspindlin could tether microtubules to the plasma membrane. Scale bars, 10 μ m.

and the plasma membrane in MgcRacGAP C1 domain mutant alleles but not wild-type cells (Fig. 4b and Supplementary Fig. 9b). These results suggest that the interaction of MgcRacGAP's C1 domain with the plasma membrane promotes the anchoring of the cell envelope to the midbody.

To extend our observations to another species, we used a conditional knockout system for MgcRacGAP in chicken DT40 lymphocytes²⁴. Mutation of conserved structural (Phe288Gly) and surface (Lys291Leu) residues in the C1 domain of chicken MgcRacGAP lead to severe cytokinesis failure in DT40 cells (Fig. 4c and Supplementary Fig. 9c). Homologous mutations abolished C1 domain membrane binding and cytokinesis in human cells (Figs 1 and 2), suggesting that the link between centralspindlin and the plasma membrane is a conserved and essential feature of cell division in animal cells.

The midbody matrix has been proposed to act as a 'glue' that may hold microtubule bundles and the plasma membrane together³. Experiments in *Drosophila* cells indicated that structures other than those derived from the contractile ring are responsible for anchoring the cleavage furrow to the midbody²⁵. Our data suggest that cooperative binding of centralspindlin's C1 domain to the plasma membrane can provide an essential link between midzone-midbody microtubule arrays and the cell envelope during cytokinesis in animal cells (Fig. 4d). This interaction promotes cortical contractility and the anchoring of the cleavage furrow to the midbody. The centralspindlin-membrane connection is likely to act synergistically with other processes to maintain the long-term stability of the intercellular bridge^{1,2,26–28}. These mechanisms allow the abscission reaction to sever the intercellular bridge long after cleavage-furrow ingression and help to prevent the catastrophic consequences of cytokinesis failure²⁹.

METHODS SUMMARY

Monoclonal cell lines. Flag-AcGFP-tagged (FLAc; AcGFP is a variant of green fluorescent protein cloned from *Aequorea coelestis*) variants of MgcRacGAP were inserted into pIRESpuro3 (Clontech). Plasmids were transfected into HeLa Kyoto cells using FuGENE 6 (Roche). Cells were grown in medium supplemented with 0.4 $\mu\text{g ml}^{-1}$ puromycin (Sigma) to select for and maintain monoclonal transgenic cell lines. For all alleles used here, the results obtained in monoclonal cell lines were validated using independently isolated pools of transgenic cells (data not shown). To generate cell lines co-expressing pIREsneo3-based MyrPalm-mCherry, the medium was further supplemented with 500 $\mu\text{g ml}^{-1}$ G418 (Sigma).

siRNA transfection. The following siRNA duplexes were used at a final concentration of 20 nM: control (Invitrogen Stealth 12935-200), MgcRacGAP (Invitrogen Stealth HSS120934) (5'-GCCAAGAACUGAGACAGACAGUGUG-3'), CEP55 (Invitrogen Stealth HSS182896) (5'-ACGAUUGCUGAACUUGAAAGC AAA-3'). Lipofectamine RNAiMAX (Invitrogen) was used for siRNA transfection. Cells were analysed 48 h after transfection with siRNA duplexes.

Full Methods and any associated references are available in the online version of the paper.

Received 15 May; accepted 9 November 2012.

1. Fededa, J. P. & Gerlich, D. W. Molecular control of animal cell cytokinesis. *Nature Cell Biol.* **14**, 440–447 (2012).
2. Green, R. A., Paluch, E. & Oegema, K. Cytokinesis in animal cells. *Annu. Rev. Cell Dev. Biol.* **28**, 29–58 (2012).
3. Mullins, J. M. & Bieseke, J. J. Terminal phase of cytokinesis in D-98s cells. *J. Cell Biol.* **73**, 672–684 (1977).
4. Glotzer, M. The 3Ms of central spindle assembly: microtubules, motors and MAPs. *Nature Rev. Mol. Cell Biol.* **10**, 9–20 (2009).
5. Mishima, M., Kaitna, S. & Glotzer, M. Central spindle assembly and cytokinesis require a kinesin-like protein/RhoGAP complex with microtubule bundling activity. *Dev. Cell* **2**, 41–54 (2002).
6. Pavicic-Kaltenbrunner, V., Mishima, M. & Glotzer, M. Cooperative assembly of CYK-4/MgcRacGAP and ZEN-4/MKLP1 to form the centralspindlin complex. *Mol. Biol. Cell* **18**, 4992–5003 (2007).

7. Bastos, R. N., Penate, X., Bates, M., Hammond, D. & Barr, F. A. CYK4 inhibits Rac1-dependent PAK1 and ARHGEF7 effector pathways during cytokinesis. *J. Cell Biol.* **198**, 865–880 (2012).
8. Canman, J. C. *et al.* Inhibition of Rac by the GAP activity of centralspindlin is essential for cytokinesis. *Science* **322**, 1543–1546 (2008).
9. Loria, A., Longhini, K. M. & Glotzer, M. The RhoGAP domain of CYK-4 has an essential role in RhoA activation. *Curr. Biol.* **22**, 213–219 (2012).
10. Miller, A. L. & Bement, W. M. Regulation of cytokinesis by Rho GTPase flux. *Nature Cell Biol.* **11**, 71–77 (2009).
11. Carlton, J. G. & Martin-Serrano, J. Parallels between cytokinesis and retroviral budding: a role for the ESCRT machinery. *Science* **316**, 1908–1912 (2007).
12. Simon, G. C. *et al.* Sequential Cyk-4 binding to ECT2 and FIP3 regulates cleavage furrow ingression and abscission during cytokinesis. *EMBO J.* **27**, 1791–1803 (2008).
13. Somers, W. G. & Saint, R. A. RhoGEF and Rho family GTPase-activating protein complex links the contractile ring to cortical microtubules at the onset of cytokinesis. *Dev. Cell* **4**, 29–39 (2003).
14. Su, K. C., Takaki, T. & Petronczki, M. Targeting of the RhoGEF Ect2 to the equatorial membrane controls cleavage furrow formation during cytokinesis. *Dev. Cell* **21**, 1104–1115 (2011).
15. Yüce, O., Piekny, A. & Glotzer, M. An ECT2-centralspindlin complex regulates the localization and function of RhoA. *J. Cell Biol.* **170**, 571–582 (2005).
16. Zhao, W. M., Seki, A. & Fang, G. Cep55, a microtubule-bundling protein, associates with centralspindlin to control the midbody integrity and cell abscission during cytokinesis. *Mol. Biol. Cell* **17**, 3881–3896 (2006).
17. Colón-González, F. & Kazanietz, M. G. C1 domains exposed: from diacylglycerol binding to protein-protein interactions. *Biochim. Biophys. Acta* **1761**, 827–837 (2006).
18. Zhang, G., Kazanietz, M. G., Blumberg, P. M. & Hurley, J. H. Crystal structure of the cys2 activator-binding domain of protein kinase C delta in complex with phorbol ester. *Cell* **81**, 917–924 (1995).
19. Hutterer, A., Glotzer, M. & Mishima, M. Clustering of centralspindlin is essential for its accumulation to the central spindle and the midbody. *Curr. Biol.* **19**, 2043–2049 (2009).
20. Hammond, G. R. *et al.* PI4P and PI(4,5)P2 are essential but independent lipid determinants of membrane identity. *Science* **337**, 727–730 (2012).
21. Lomize, M. A., Pogozheva, I. D., Joo, H., Mosberg, H. I. & Lomize, A. L. OPM database and PPM web server: resources for positioning of proteins in membranes. *Nucleic Acids Res.* **40**, D370–D376 (2012).
22. Heo, W. D. *et al.* PI(3,4,5)P3 and PI(4,5)P2 lipids target proteins with polybasic clusters to the plasma membrane. *Science* **314**, 1458–1461 (2006).
23. Zavortink, M., Contreras, N., Addy, T., Bejsovec, A. & Saint, R. Tum/RacGAP50C provides a critical link between anaphase microtubules and the assembly of the contractile ring in *Drosophila melanogaster*. *J. Cell Sci.* **118**, 5381–5392 (2005).
24. Yamada, T., Hikida, M. & Kurosaki, T. Regulation of cytokinesis by mgcRacGAP in B lymphocytes is independent of GAP activity. *Exp. Cell Res.* **312**, 3517–3525 (2006).
25. Echard, A., Hickson, G. R., Foley, E. & O'Farrell, P. H. Terminal cytokinesis events uncovered after an RNAi screen. *Curr. Biol.* **14**, 1685–1693 (2004).
26. Dambournet, D. *et al.* Rab35 GTPase and OCRL phosphatase remodel lipids and F-actin for successful cytokinesis. *Nature Cell Biol.* **13**, 981–988 (2011).
27. Hu, C. K., Coughlin, M. & Mitchison, T. J. Midbody assembly and its regulation during cytokinesis. *Mol. Biol. Cell* **23**, 1024–1034 (2012).
28. Kechad, A., Jananji, S., Ruella, Y. & Hickson, G. R. Anillin acts as a bifunctional linker coordinating midbody ring biogenesis during cytokinesis. *Curr. Biol.* **22**, 197–203 (2012).
29. Fujiwara, T. *et al.* Cytokinesis failure generating tetraploids promotes tumorigenesis in p53-null cells. *Nature* **437**, 1043–1047 (2005).

Supplementary Information is available in the online version of the paper.

Acknowledgements We would like to thank W. Bement, W. Earnshaw, J. Gannon, D. Gerlich, M. Glotzer, G. Hammond, M. Hikida, H. Hochegger, R. Irvine, M. Kurosaki, B. Larjani, P. Parker, A. Piekny, R. Prekeris, E. Sahai, K. Samejima and M. Symons for reagents and advice. Work in the Petronczki laboratory is supported by Cancer Research UK and the EMBO Young Investigator Programme. S.L. acknowledges support from an EMBO Long-Term Fellowship.

Author Contributions M.P. and S.L. designed the experiments. S.L. conducted all experiments with the following exceptions. The imaging data shown in Fig. 4a were recorded by K.-C. S. The structure of the C1 domain was determined by V.E.P. and P.C. Electron microscopy analysis was carried out with contributions from K.B. and L.M.C. The analysis of MgcRacGAP-R385A was carried out by S.S. Lipid interaction assays were carried out by T.T. and N.D. The manuscript was written by M.P.

Author Information Reprints and permissions information is available at www.nature.com/reprints. The authors declare no competing financial interests. Readers are welcome to comment on the online version of the paper. Correspondence and requests for materials should be addressed to M.P. (mark.petronczki@cancer.org.uk). Coordinates and structure factors for the C1 domain of MgcRacGAP have been deposited at the Protein Data Bank (<http://www.rcsb.org/pdb>) under accession code 4B6D.

METHODS

Protein purification for use in X-ray crystallography. GST-C1 (human MgcRacGAP residues 284 to 338) was expressed in *Escherichia coli* (BL21 (DE3) codon plus RIL) in the presence of 10 μ M ZnCl₂ and purified using Glutathione Sepharose 4 Fast Flow (GE Healthcare). The C1 domain of MgcRacGAP was released from GST by digestion with human rhinovirus 14 3C protease and bound to a 1-ml HiTrap SP Sepharose column (GE Healthcare). The protein, eluted with a linear 50–500-mM NaCl gradient in 25 mM Tris-HCl, pH 7.2 (Supplementary Fig. 2a), was dialysed overnight against 250 mM NaCl, 1 mM DTT (dithiothreitol), 50 μ M ZnCl₂, 25 mM Tris-HCl, pH 7.2, and concentrated to 8–9 mg ml⁻¹ using an Amicon Ultracel-3k device (Millipore).

Crystallization and structure determination. Crystals of MgcRacGAP's C1 domain were grown at 18 °C by vapour diffusion in hanging drops of 1 μ l protein plus 1 μ l reservoir solution containing 1.3 M sodium citrate, pH 7.1, and 0.3 M dimethylethylammonium propane sulfonate (NDSB-195, Hampton Research). Crystals, briefly soaked in 10% glycerol, 1.3 M sodium citrate, pH 7.1, were cryo-cooled by rapid immersion into liquid nitrogen. X-ray diffraction was measured at 100 K on I02 beamline of the Diamond Light Source. A severe intensity modulation present in the data is explained by pseudotranslation (two-thirds of the unit cell were related by a translational non-crystallographic symmetry). To measure intensities of the weak reflections with greater precision, highly redundant data were collected. The intensities, integrated using XDS³⁰ were scaled and merged in Scala³¹. Although the data could be processed assuming space group C22₂ with unit cell dimensions of $a = 36.85$ Å, $b = 107.15$ Å, $c = 133.84$ Å, analysis of Padilla and Yeates L-test plots³² provided strong evidence for twinning. Hence, the data were processed in the lower symmetry group P2₁ (Supplementary Table 1). The free R flags were selected using 5% of the data in Phenix³³, taking into account lattice symmetry. The structure was initially solved by a combination of single-wavelength anomalous dispersion and molecular replacement, using a data set acquired at an X-ray energy of 9.663 keV (wavelength 1.283 Å), corresponding to the K-absorption edge of Zn (Supplementary Table 1). The molecular replacement model was generated using Phenix Scurptor³³ based on the crystal structure of the protein kinase C δ C1 domain (Protein Data Bank (PDB) accession 1PTQ). Positions of Zn atoms were located using SHELXD³⁴, and the substructure was refined in SHARP³⁵. The resulting map, improved by solvent flipping in Solomon³⁶, showed density for six copies of C1 domain per asymmetric unit. Four of the copies were fitted using Molrep³⁷, and the remaining two were fitted manually in Coot³⁸. The structure was refined in Phenix taking into account the pseudomerohedral twin law $h, -k, -h-l$, twin fraction 50%. Experimental phase restraints were used at the initial stages of refinement. Following iterative model improvement in Coot and least squares refinement in Phenix, the model was refined to a resolution of 2.2 Å with an R of 21.03% and R_{free} of 23.55% and good geometry (Supplementary Table 1). Examples of the final weighted $2F_o - F_c$ electron density map are shown in Supplementary Fig. 2b. The coordinates and structure factors have been deposited with the PDB under accession code 4B6D.

Plasmids for expression in human cells. To create pIRESpuo3-FLAc, a single Flag epitope (DYKDDDDK) and AcGFP (AcGFP, *Aequorea coerulescens* green fluorescent protein; Clontech) were inserted into pIRESpuo3 (Clontech) using EcoRI and BamHI. MgcRacGAP variants (NM_013277) were inserted into pIRESpuo3-FLAc using AgeI and EcoRI. To create an siRNA-resistant allele of MgcRacGAP, the sequence AAGAACTGAGACAGACAGT was changed to CCGGACCGAGACCGATTCC by introducing silent mutations. MgcRacGAP variants were created using polymerase chain reaction (PCR) and site-directed mutagenesis. To create MgcRacGAPr-C1B, the residues 287 to 335 of MgcRacGAP were replaced by the C1B domain of human PKC α (amino acids 102 to 151) (provided by P. Parker). To create the MgcRacGAP- Δ C1-GEM, a DNA fragment encoding the 33 C-terminal amino acids of human GEM (RKARRFWGKIVAKNNKMAFKLSKSDHLSVL) was inserted after MgcRacGAP using EcoRI. The sequence MGCIKSKGKDS was inserted at the N terminus of Flag-mCherry to create MyrPalm-Flag-mCherry in pIRESneo3 (Clontech). H2B-mCherry (Addgene plasmid no. 21044)³⁹ and mCherry-UtrCH (Addgene plasmid no. 26740)⁴⁰ transgenes were obtained from Addgene. To create C1-FLAc, MgcRacGAP's C1 domain (MgcRacGAP residues 281 to 341), was inserted into pIRESpuo3-FLAc using AgeI and EcoRI. To create tandem C1_{2x}-FLAc, an additional domain was inserted into pIRESpuo3-C1-FLAc using NheI and AgeI. To create C1_{4x}-FLAc, tandem C1 domains were inserted into pIRESpuo3-C1_{2x}-FLAc using EcoRV and NheI. To create C1B-FLAc, a single C1B domain of human PKC α (PKC α residues 99 to 154) was inserted into pIRESpuo3-FLAc using AgeI and EcoRI. For transient expression experiments in Fig. 2a–d and Supplementary Fig. 6b, HeLa Kyoto and HEK293T cells were transfected using FuGENE HD (Promega) and analysed 24 h to 48 h post transfection.

Monoclonal cell lines. Flag-AcGFP-tagged (FLAc) variants of MgcRacGAP were inserted into pIRESpuo3 (Clontech). Plasmids were transfected into HeLa Kyoto cells using FuGENE 6 (Roche). Cells were grown in medium⁴¹ supplemented with 0.4 μ g ml⁻¹ puromycin (Sigma) to select for and maintain monoclonal transgenic cell lines. For all alleles used here, the results obtained in monoclonal cell lines were validated using independently isolated pools of transgenic cells (data not shown). To generate cell lines co-expressing pIRESneo3-based MyrPalm-mCherry the medium was further supplemented with 500 μ g ml⁻¹ G418 (Sigma).

siRNA transfection. The following siRNA duplexes were used at a final concentration of 20 nM: control (Invitrogen Stealth 12935-200), MgcRacGAP (Invitrogen Stealth HSS120934) (GCCAAGAACUGAGACAGACAGUGUG), CEP55 (Invitrogen Stealth HSS182896) (ACGAAUUGCUGAACUUGAAAGCAAA). Lipofectamine RNAiMAX (Invitrogen) was used for siRNA transfection. Cells were analysed 48 h after transfection with siRNA duplexes.

Immunofluorescence microscopy. Cells were fixed for 16 h in -20 °C methanol, for 15 min at 25 °C in 4% formaldehyde (Fig. 4c and Supplementary Fig. 9c) or for 15 min on ice in 10% trichloroacetic acid (Supplementary Fig. 8b) before being processed for immunofluorescence microscopy as described⁴². Images for Figs 1c, d, 3d and 4c and Supplementary Figs 4b, c, 7 and 9c were acquired on a Zeiss Axio Imager M2 microscope using a Plan-Neofluar $\times 40/1.3$ numerical aperture (NA) oil objective lens (Zeiss) or Plan Apochromat $\times 63/1.4$ NA oil objective lens (Zeiss) equipped with an ORCA-ER camera (Hamamatsu) and controlled by Velocity 6.0.1. software (Improvision). Images in Figs 1d and 4c and Supplementary Fig. 4b, c, 9c are displayed as maximum-intensity projections of deconvolved Z planes that were acquired in 100-nm sections. Images in Figs 1d and 4c and Supplementary Figs 4b, c and 9c were deconvolved using Velocity's iterative restoration function. Images for Supplementary Fig. 8b, c were acquired on an Olympus FV1000D (InvertedMicroscopeIX81) laser confocal scanning microscope using a PlanApoN $\times 60/1.40$ NA Oil Sc objective lens controlled by FV10-ASW software.

Antibodies and dyes. The following primary antibodies were used: mouse monoclonal anti-AcGFP (JL8, Clontech, immunofluorescence microscopy 1:2,000; blot 1:1,000), rabbit anti-AcGFP (Clontech, immunofluorescence microscopy 1:2,000), mouse monoclonal anti- α -tubulin (B512, Sigma, immunofluorescence microscopy 1:10,000, blot 1:30,000), rat monoclonal anti- α -tubulin (MCA78G, AbD Serotec, immunofluorescence microscopy 1:1,000), rabbit anti-anillin (provided by M. Glotzer, immunofluorescence microscopy 1:2,000)⁴³, mouse monoclonal anti-Aurora B (AIM-1, BD Transduction Laboratories, immunofluorescence microscopy 1:500), mouse polyclonal anti-CEP55 (B01P, MaxPab, immunofluorescence microscopy 1:500), rabbit anti-ECT2 (raised against ECT2 amino acids 1 to 421, immunofluorescence microscopy purified serum 1:700)¹⁴, mouse monoclonal anti-GAPDH (6C5, Abcam, blot 1:30,000), rabbit anti-GST (provided by J. Gannon, blot 1:1,000), rabbit anti-lamin B (ab16048, Abcam, immunofluorescence microscopy 1:500), mouse monoclonal anti-mCherry (Clontech, immunofluorescence microscopy 1:1,000; blot 1:300), mouse monoclonal anti-MKLP1 (24, BD Biosciences, blot 1:1,000), rabbit anti-MKLP1 (N-19, Santa Cruz, immunofluorescence microscopy 1:500), mouse monoclonal anti-MgcRacGAP (M01, Abnova, blot 1:50,000), mouse monoclonal anti-PLK1 (F-8, Santa Cruz, immunofluorescence microscopy 1:100), rabbit polyclonal anti-PRC1 (H-70, Santa Cruz, immunofluorescence microscopy 1:500) and mouse monoclonal anti-RhoA (26C4, Santa Cruz, immunofluorescence microscopy 1:75). Secondary antibodies conjugated to Alexa Fluor 488, 568, 594 or 647 (Molecular Probes) were used for immunofluorescence microscopy detection. DNA was stained with 1 μ g ml⁻¹ 4',6-diamidino-2-phenylindole (DAPI; Molecular Probes) and with 0.2 μ g ml⁻¹ Hoechst 33342 (Molecular Probes) in live cells.

Co-immunoprecipitation. Thirty-four hours after transfection with MgcRacGAP siRNA, HeLa Kyoto cells stably expressing MgcRacGAP-FLAc transgenes were arrested in 50 ng ml⁻¹ nocodazole for 14 h. Cells were lysed in buffer containing 20 mM Tris, pH 7.5, 150 mM NaCl, 0.1% Triton X-100, 5 mM MgCl₂ and a protease inhibitor cocktail (Roche). Proteins were collected using anti-Flag M2 antibody-conjugated agarose beads (Sigma) and analysed by immunoblotting.

Live-cell imaging. Before recording of live cells, the medium was changed to phenol-red-free CO₂-independent medium⁴². Images in Supplementary Fig. 8a and Fig. 3b were acquired at 37 °C using a Zeiss Axio Observer Z1 microscope controlled by SimplePCI software (Hamamatsu) and equipped with an Orca 03GO1 camera (Hamamatsu) and a Plan-Apochromat $\times 10/0.45$ NA objective. The images for Supplementary Fig. 6b were acquired on the Axio Observer Z1 system with an EC Plan-Neofluar $\times 40/1.30$ NA oil DICII objective. For Supplementary Video 1, Fig. 2a–d and Supplementary Figs 5a and 6b, d, images were acquired at 37 °C using a Olympus FV1000D (InvertedMicroscopeIX81) laser confocal scanning microscope equipped with a PlanApoN $\times 60/1.40$ NA Oil Sc objective lens and controlled by FV10-ASW software (Olympus). For Fig. 4a and Supplementary Video 2, frames were acquired at 37 °C using a PerkinElmer ERS Spinning disc system equipped with a Nikon TE2000 microscope, Apo TIRF $\times 100/$

1.49 NA (Nikon), a CSU22 spinning disc scanner (Yokogawa), an IEEE1394 Digital CCD C4742-80-12AG camera (Hamamatsu) and controlled by Volocity 5.5.1 software (Perkin Elmer).

Image quantification. For Fig. 2c, d ImageJ software (<http://rsbweb.nih.gov/ij/>) was used to measure mean AcGFP intensities by averaging 6 manually placed circular regions of 9 pixels at the cell periphery and 2 circular regions of 1,000 to 2,000 pixels in the cytoplasm followed by subtraction of the mean background signal outside of the cell. For Supplementary Fig. 8b, c, FV10-ASW software was used to quantify 16-bit images along the periphery of anaphase cells ($n > 10$). To measure the rate of cleavage-furrow ingression (Supplementary Fig. 8d), differential interference contrast (DIC) images of cells were recorded every 30 s. Cleavage-furrow ingression speed was calculated by measuring the cell width at the equatorial plane using ImageJ. Values were normalized to the cell width at metaphase.

Lipid-array binding assay. GST-C1 (human MgcRacGAP residues 284 to 338) fusions were expressed in *E. coli* (BL21) in the presence of 5 μM ZnCl_2 and purified using Glutathione Sepharose 4 Fast Flow (GE Healthcare). Membrane lipid arrays (P-6002, Echelon Biosciences) were incubated with 70 ng ml^{-1} GST-C1 fusion proteins or 50 ng ml^{-1} GST-GRP1-PH domain (G-3901, Echelon Biosciences) in PBS containing 0.1% Tween-20 and 3% BSA for 1 h at 25 °C. After washing, proteins were detected using anti-GST antibodies.

Manipulation of lipids in vivo. HEK293T cells were treated with 1 mM CaCl_2 and 10 μM ionomycin (Sigma) in Opti-MEM (Invitrogen). The rapamycin-controlled membrane targeting system of lipid phosphatases is described in detail in ref. 20. HEK293T cells were transfected with pIRESpuro3-C1_{2x}-FLAc, pmCherry-N1-Lyn11-FRB and one of four different lipid phosphatases (pmRFP-C1-FKBP-PJ, pmRFP-C1-FKBP-PJ-Sac, pmRFP-C1-FKBP-INPP5E or pmRFP-C1-FKBP-PJ-dead) with a ratio of 6:1:1. Rapamycin (10 μM ; Sigma) was applied to cells in Opti-MEM.

Surface plasmon resonance. Surface plasmon resonance (SPR) (Fig. 2e) was carried out using the Bio-Rad Protein Interaction Array System ProteOn XPR36. Phosphatidylethanolamine (95%) in chloroform was mixed with 1- α -phosphatidyl-1,2-dipalmitoyl-phosphoinositides PtdIns(4)P or PtdIns(4,5)P₂ (5%) as indicated. Chloroform mixtures were dried, resuspended in 10 mM Tris, pH 7.4, and sonicated into solution. Equal levels of sonicated lipid solutions were loaded, as determined by changes in SPR response units, onto a GLM sensor chip (Bio-Rad) derivatized with undecylamine to act as a vesicle capture tether. Recombinant purified GST-tagged proteins (Supplementary Fig. 5c) were diluted in PBS to a concentration of 250 nM and analyte injections were carried out at a flow rate of 50 $\mu\text{l min}^{-1}$ and with a sensor-chip temperature of 25 °C. Resonance units for SPR signals are presented after subtraction of the resonance units observed in the phosphatidylethanolamine-only vesicle-reference channel.

Prediction of C1 domain-membrane interaction. The interaction of MgcRacGAP's C1 domain and a lipid bilayer was predicted using the atomic coordinates of the C1 domain (PDB accession 4B6D) and the Positioning of Integral and Peripheral Proteins in Membranes (PPM) server²¹.

Phorbol ester treatment. For the experiment shown in Fig. 3a, b cells were transfected with MgcRacGAP siRNA and arrested in metaphase using the proteasomal inhibitor MG132 (10 μM ; Sigma) for 2 h, then synchronously released into anaphase as described⁴¹. Sixty-five minutes after release from MG132, cells were treated with 2.5 nM TPA (Sigma) or 30 nM PDBu (Sigma).

Electron microscopy. Cells expressing FLAc-tagged variants of human MgcRacGAP were plated on 13-mm cover glasses (Gerhard Menzel, Thermo Scientific) coated with 0.01% poly-L-lysine solution (SigmaAldrich). After transfection with MgcRacGAP, siRNA cells were synchronized at anaphase as described⁴¹.

Cells were fixed 100 min after release from metaphase in 1.5% glutaraldehyde and 2% paraformaldehyde in 0.1 M phosphate buffer, pH 7.4, for 45 min. The samples were post-fixed in reduced osmium tetroxide, stained with tannic acid, dehydrated step-wise to 100% ethanol and embedded in epon. Ultrathin sections of 80 nm were cut, post-stained with lead citrate and viewed in a Tecnai Spirit Biotwin 120 keV transmission electron microscope (FEI Company). Images were captured using an Orius CCD (Gatan) with Digital Micrograph software (Gatan).

DT40 cell methods. Chicken MgcRacGAP (XM_424490) was amplified from total DT40 RNA (provided by H. Hocheegger) using the OneStep RT-PCR Kit (QIAGEN). Point mutations were introduced using site directed mutagenesis. Chicken MgcRacGAP variants were inserted into pmCherry-Flag using AgeI and EcoRI sites. Parental and targeted DT40 cells²⁴ (provided by M. Hikida and M. Kurosaki) were grown in RPMI1640 (Invitrogen) supplemented with 50 μM 2-mercaptoethanol (Sigma), 10% fetal bovine serum (Sigma), 1% chicken serum (Sigma), 2 mM L-glutamine and antibiotics (Invitrogen) at 37 °C in 5% CO₂. The medium was supplemented with 100 ng ml^{-1} tetracycline (Sigma) to maintain expression of the Flag-tagged mouse MgcRacGAP rescue gene in the conditional knockout cell line²⁴. pmCherry-Flag-based plasmids were introduced into DT40 cells using a Bio-Rad Gene Pulser Xcell Electroporation system (settings: 300 V, 950 μF). Puromycin resistance was introduced by co-electroporating cell with the plasmid pLoxPuro⁴⁴. pmCherry-Flag-based plasmids and pLoxPuro plasmid were linearized before electroporation by EagI and PvuI, respectively. To select for and maintain monoclonal cell lines expressing pmCherry-Flag transgenes the medium was supplemented with 0.3 $\mu\text{g ml}^{-1}$ puromycin (Sigma). Cells were analysed 48 h after removal of tetracycline.

30. Kabsch, W. XDS. *Acta Crystallogr. D* **66**, 125–132 (2010).
31. Evans, P. Scaling and assessment of data quality. *Acta Crystallogr. D* **62**, 72–82 (2006).
32. Padilla, J. E. & Yeates, T. O. A statistic for local intensity differences: robustness to anisotropy and pseudo-centering and utility for detecting twinning. *Acta Crystallogr. D* **59**, 1124–1130 (2003).
33. Adams, P. D. et al. PHENIX: a comprehensive Python-based system for macromolecular structure solution. *Acta Crystallogr. D* **66**, 213–221 (2010).
34. Sheldrick, G. M. Experimental phasing with SHELXC/D/E: combining chain tracing with density modification. *Acta Crystallogr. D* **66**, 479–485 (2010).
35. Brodersen, D. E. et al. Applications of single-wavelength anomalous dispersion at high and atomic resolution. *Acta Crystallogr. D* **56**, 431–441 (2000).
36. Abrahams, J. P. & Leslie, A. G. Methods used in the structure determination of bovine mitochondrial F1 ATPase. *Acta Crystallogr. D* **52**, 30–42 (1996).
37. Vagin, A. & Teplyakov, A. Molecular replacement with MOLREP. *Acta Crystallogr. D* **66**, 22–25 (2010).
38. Emsley, P. & Cowtan, K. Coot: model-building tools for molecular graphics. *Acta Crystallogr. D* **60**, 2126–2132 (2004).
39. Steigemann, P. et al. Aurora B-mediated abscission checkpoint protects against tetraploidization. *Cell* **136**, 473–484 (2009).
40. Burkel, B. M., von Dassow, G. & Bement, W. M. Versatile fluorescent probes for actin filaments based on the actin-binding domain of utrophin. *Cell Motil. Cytoskeleton* **64**, 822–832 (2007).
41. Petronczki, M., Glotzer, M., Kraut, N. & Peters, J. M. Polo-like kinase 1 triggers the initiation of cytokinesis in human cells by promoting recruitment of the RhoGEF Ect2 to the central spindle. *Dev. Cell* **12**, 713–725 (2007).
42. Lénárt, P. et al. The small-molecule inhibitor BI 2536 reveals novel insights into mitotic roles of polo-like kinase 1. *Curr. Biol.* **17**, 304–315 (2007).
43. Piekny, A. J. & Glotzer, M. Anillin is a scaffold protein that links RhoA, actin, and myosin during cytokinesis. *Curr. Biol.* **18**, 30–36 (2008).
44. Arakawa, H., Lodygin, D. & Buerstedde, J. M. Mutant loxP vectors for selectable marker recycle and conditional knock-outs. *BMC Biotechnol.* **1**, 7 (2001).

Regulation of ISWI involves inhibitory modules antagonized by nucleosomal epitopes

Cedric R. Clapier¹ & Bradley R. Cairns¹

Chromatin-remodelling complexes (CRCs) mobilize nucleosomes to mediate the access of DNA-binding factors to their sites *in vivo*. These CRCs contain a catalytic subunit that bears an ATPase/DNA-translocase domain and flanking regions that bind nucleosomal epitopes¹. A central question is whether and how these flanking regions regulate ATP hydrolysis or the coupling of hydrolysis to DNA translocation, to affect nucleosome-sliding efficiency. ISWI-family CRCs contain the protein ISWI², which uses its ATPase/DNA-translocase domain to pump DNA around the histone octamer to enable sliding^{3–7}. ISWI is positively regulated by two ‘activating’ nucleosomal epitopes: the ‘basic patch’ on the histone H4 tail, and extranucleosomal (linker) DNA^{8–13}. Previous work defined the HAND-SANT-SLIDE (HSS) domain at the ISWI carboxy terminus that binds linker DNA, needed for ISWI activity^{14,15}. Here we define two new, conserved and separate regulatory regions on *Drosophila* ISWI, termed AutoN and NegC, which negatively regulate ATP hydrolysis (AutoN) or the coupling of ATP hydrolysis to productive DNA translocation (NegC). The two aforementioned nucleosomal epitopes promote remodelling indirectly by preventing the negative regulation of AutoN and NegC. Notably, mutation or removal of AutoN and NegC enables marked nucleosome sliding without the H4 basic patch or extranucleosomal DNA, or the HSS domain, conferring on ISWI the biochemical attributes normally associated with SWI/SNF-family ATPases. Thus, the ISWI ATPase catalytic core is an intrinsically active DNA translocase that conducts nucleosome sliding, onto which selective ‘inhibition-of-inhibition’ modules are placed, to help ensure that remodelling occurs only in the presence of proper nucleosomal epitopes. This supports a general concept for the specialization of chromatin-remodelling ATPases, in which specific regulatory modules adapt an ancient active DNA translocase to conduct particular tasks only on the appropriate chromatin landscape.

ISWI is the catalytic subunit of a set of CRCs, with orthologues in all eukaryotes¹ (Fig. 1). To define how ISWI is intrinsically regulated, we undertook an extensive structure–function analysis of the *Drosophila* ISWI ATPase, and its regulation by the histone H4 tail and extranucleosomal DNA. In the amino terminus of ISWI, we recognized a region similar to the ‘basic patch’¹⁰ of the histone H4 tail (Fig. 1a) that is conserved in eukaryotes (Fig. 1b). To test function, we replaced either (R91A or R93A) or both (2RA) arginine residues with alanines. Nucleosome sliding by wild-type ISWI normally requires nucleosomes with intact H4 tails^{8,9} and the presence of extranucleosomal DNA^{11,12}; however, wild-type ISWI ATPase activity can be elicited by combining DNA and H4 tail peptide bearing the basic patch (Fig. 1c)¹⁰. Notably, the ISWI(2RA) derivative showed ~threefold higher ATPase activity than wild-type ISWI and was independent of H4 epitopes (Fig. 1c). For extended nucleosomes (200 base pairs (bp)), synthetic centrally positioned sequence (601), loss of either the basic patch (Ala 17, Ala 19) or the H4 tail (globular H4 (g4)) markedly diminished (fivefold) wild-type ISWI activity, whereas ISWI(2RA) was only modestly attenuated, retaining ~63% activity and ~ninefold higher activity than wild-type ISWI (Fig. 1d). Notably, ISWI(R91A) and ISWI(R93A) resemble

moderate and weak gain-of-function derivatives, respectively; as their ATPase activities increase, their dependence on the H4 tail decreases (Supplementary Fig. 1). Thus, ISWI(2RA) greatly activates ATPase activity, and renders the enzyme largely independent of the H4 tail, defining an N-terminal autoinhibitory region (AutoN) with similarity to the H4 tail.

Remodeller ATPases are SF2-family¹⁶ DNA translocases that couple DNA translocation to ATP hydrolysis^{3–7,17–19}, wherein the two RecA-like

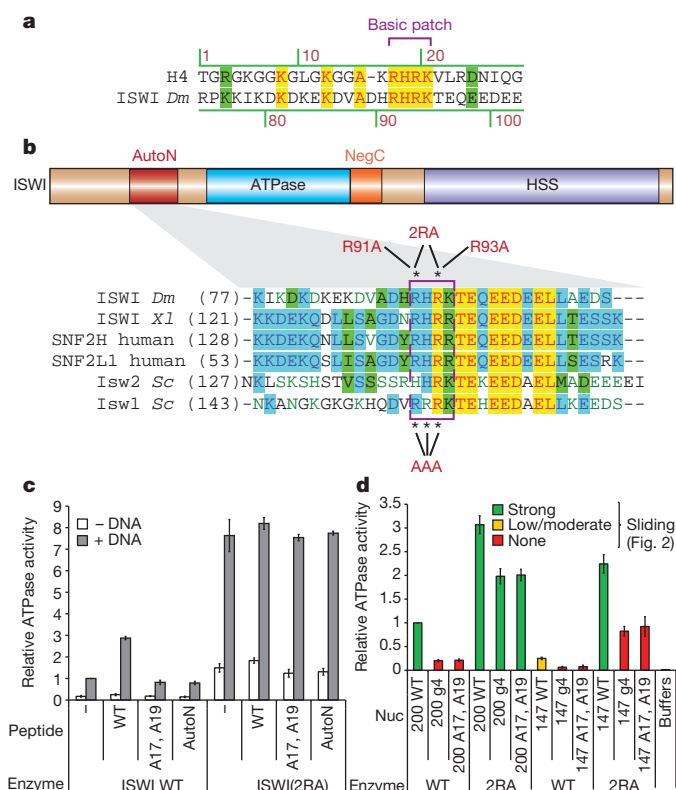


Figure 1 | AutoN resembles the histone H4 tail basic patch and restricts ISWI ATPase activity. **a**, Alignment of *Drosophila* ISWI and the histone H4 N terminus, with the basic patch depicted. **b**, ISWI protein and domains/regions, including ATPase, HSS and new functional regions (AutoN and NegC), with zoom of AutoN alignments for ISWI orthologues in *Drosophila* (Dm), *Xenopus* (Xl), human and *S. cerevisiae* (Sc). The human orthologues SNF2H and SNF2L1 are also known as SMARCA5 and SMARCA1, respectively. **c**, Mutation of AutoN (2RA) hyperactivates ISWI ATPase activity and bypasses H4 tail stimulation by peptides. Values are mean of ≥ 3 experiments, normalized to wild-type ISWI with DNA. Error bars denote \pm s.e.m. **d**, AutoN (2RA) mutation stimulates ISWI ATPase activity with mononucleosomes (nuc): native (WT), H4 tail-less/globular (g4), or containing basic-patch mutations (Ala 17, Ala 19). Numbers (147, 200) denote length (in bp) of DNA fragment. Colour code reflects nucleosome-sliding activity (in Fig. 2c, d). Values are mean of ≥ 3 experiments, normalized to wild-type ISWI. Error bars denote \pm s.e.m.

¹Howard Hughes Medical Institute and Department of Oncological Sciences, Huntsman Cancer Institute, University of Utah School of Medicine, 2000 Circle of Hope, Salt Lake City, Utah 84112, USA.

protein lobes of the ATPase domain sequentially grip and release the DNA backbone, typically moving a small number of base pairs per ATP hydrolysis^{20,21}. 'Coupling' refers to how efficiently ATP hydrolysis results in productive DNA translocation. Uncoupling by mutation is well documented^{22,23}, but of unknown relevance for regulation. The key question is whether and how coupling is regulated by nucleosomal epitopes. To monitor coupling, we used a 'tethered translocation' system, which uses plasmid supercoiling to quantify DNA translocation by ISWI (Supplementary Fig. 2). Notably, DNA translocation by wild-type ISWI was greatly enhanced by H4 tail peptide, whereas ISWI(2RA) showed robust DNA translocation without peptide (Fig. 2a), consistent with our ATPase results (Fig. 1c, d).

Nucleosome sliding was monitored by achieving an equilibrium between end- and centre-positioned octamers, from an initial centre-positioned population (Fig. 2b). ISWI(2RA) yielded an end↔centre equilibrium much faster than wild-type ISWI; ISWI(2RA) shifted in 30 s the amount shifted in 30 min by wild-type ISWI (Fig. 2b). Wild-type ISWI required the full H4 tail for *in vitro* sliding (shown previously)⁸, and here we establish the importance of the basic patch (Fig. 2c, top panels). Notably, ISWI(2RA) partially bypassed mutations in the H4 basic patch, enabling sliding, but only weakly bypassed the full H4 tail (Fig. 2c, bottom panels). This suggested an additional H4 epitope (beyond the basic patch) needed for coupling high ATPase activity to efficient sliding, and an extensive set of experiments involving peptides and nucleosomes bearing mutations in the H4 tail revealed a major contribution from H4 lysine 12 (H4K12) in promoting coupling (Supplementary Fig. 3).

We next examined core nucleosomes (147bp, 601 sequence). Supporting previous work¹¹, wild-type ISWI activity required both extranucleosomal DNA and H4 tail epitopes (Figs 1d and 2d). Interestingly, with ISWI(2RA), both ATPase and sliding remained efficient on core nucleosomes (Figs 1d and 2d), establishing independence from extranucleosomal DNA. However, omitting the H4 tail greatly reduced sliding but not ATPase activity with ISWI(2RA) (Figs 1d and 2d). Taken together, AutoN functions as an autoinhibitory region that, when mutated (in ISWI(2RA)), largely bypasses the H4 tail for ATPase stimulation, but retains reliance on the H4 tail to 'couple' that ATP hydrolysis to productive DNA translocation. One simple model is that AutoN binds to and holds the ATPase domain in an inactive conformation, with the H4 tail competing for part of that surface; the binding of the H4 tail displaces AutoN and enables a conformational change that activates ISWI ATPase activity, an effect mimicked by the ISWI(2RA) mutation. Here, the ATPase activity of our derivative series (2RA>R91A>R93A) was the reciprocal of H4 tail stimulation (Supplementary Fig. 1), consistent with competition/antagonism for a region on ISWI involving the H4 tail and AutoN. Consistent with this model, a peptide from the AutoN region of wild-type ISWI (Lys 76–Glu 98) does not activate ISWI (Fig. 1c).

Previous work defined a HSS domain present in the C terminus of ISWI (and the related yeast Chd1 protein) that binds extranucleosomal DNA, needed for ISWI and Chd1 remodelling activity^{14,15,24}. However, our results with AutoN prompted a search for an analogous unknown region that prevents ATPase action unless the HSS is bound to extranucleosomal DNA. Multiple approaches (alignments, protease mapping, structural modelling) yielded a candidate region (covering residues 617 to 648) immediately following the second of the two RecA-like ATPase lobes, which we term NegC (Fig. 3a, b). A structural model using Phyre² (ref. 25; Fig. 3b) revealed NegC as a 'C-terminal bridge' traversing from ATPase lobe 2 back to the ATPase lobe 1, crossing the key functional ATPase cleft. Furthermore, this structural model of NegC is consistent with crosslinking experiments of ISWI²⁶, and a recent crystal structure of Chd1 (ref. 27). Notably, NegC is conserved only in remodellers that bear an HSS domain and are regulated by extranucleosomal DNA (ISWI and Chd1, not SWI/SNF), although NegC function is entirely unknown.

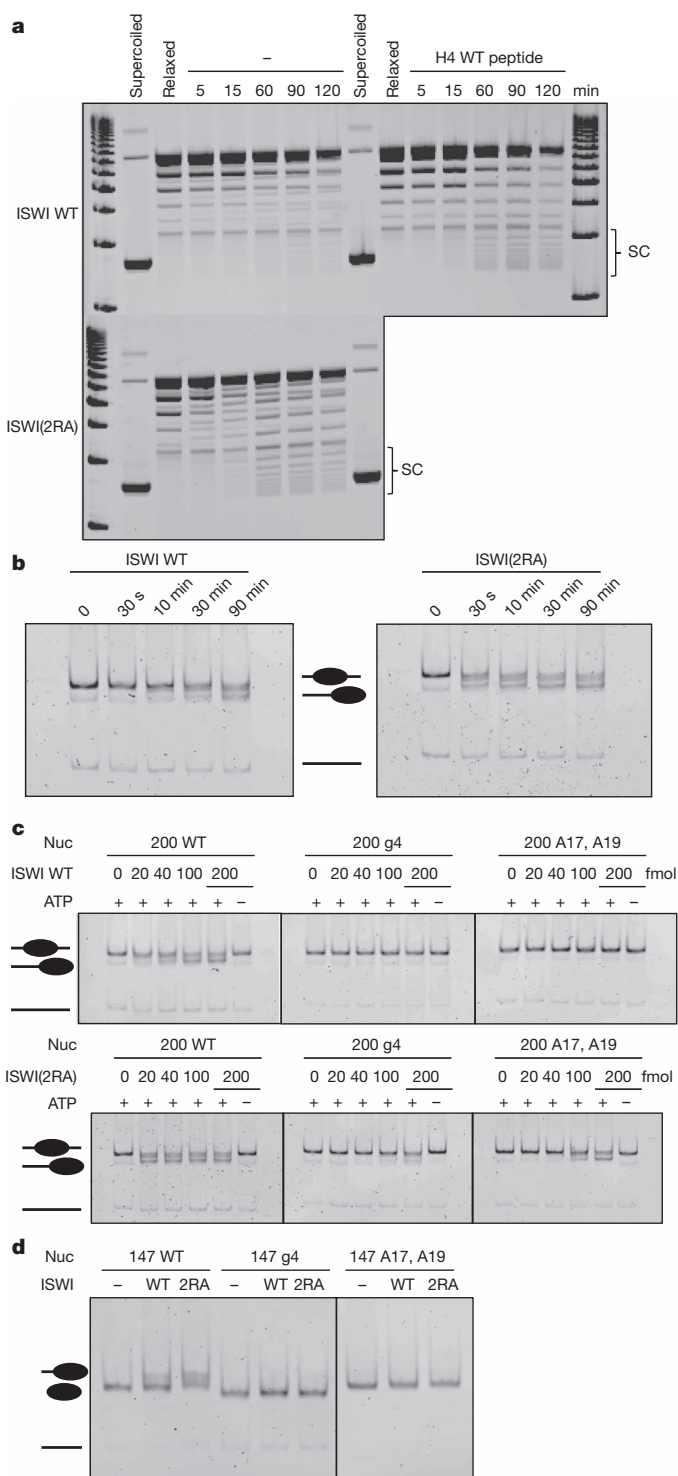


Figure 2 | AutoN mutation (ISWI(2RA)) increases DNA translocation and nucleosome sliding. **a**, Comparative DNA-translocation activity (see Supplementary Fig. 2) of ISWI derivatives. Translocation generates supercoiled topoisomers (SC). **b**, **c**, Comparative sliding of extended nucleosomes by ISWI derivatives, as a time course (**b**), and their reliance on H4 tail epitopes, in titration series (**c**). **d**, Comparative sliding activity on core nucleosomes reveals a reliance on H4 tail epitopes. For **b** and **d**, enzyme:substrate molar ratio is 1:2.

To test NegC function, we isolated three ISWI C-terminal truncation derivatives: Δ C697 (omitting the HSS), Δ C648 (further deletion) and Δ C617 (omitting NegC), as well as combinations with AutoN mutations. First, omitting C-terminal regions from wild-type ISWI did not render them stimutable by naked DNA (Fig. 3c). By

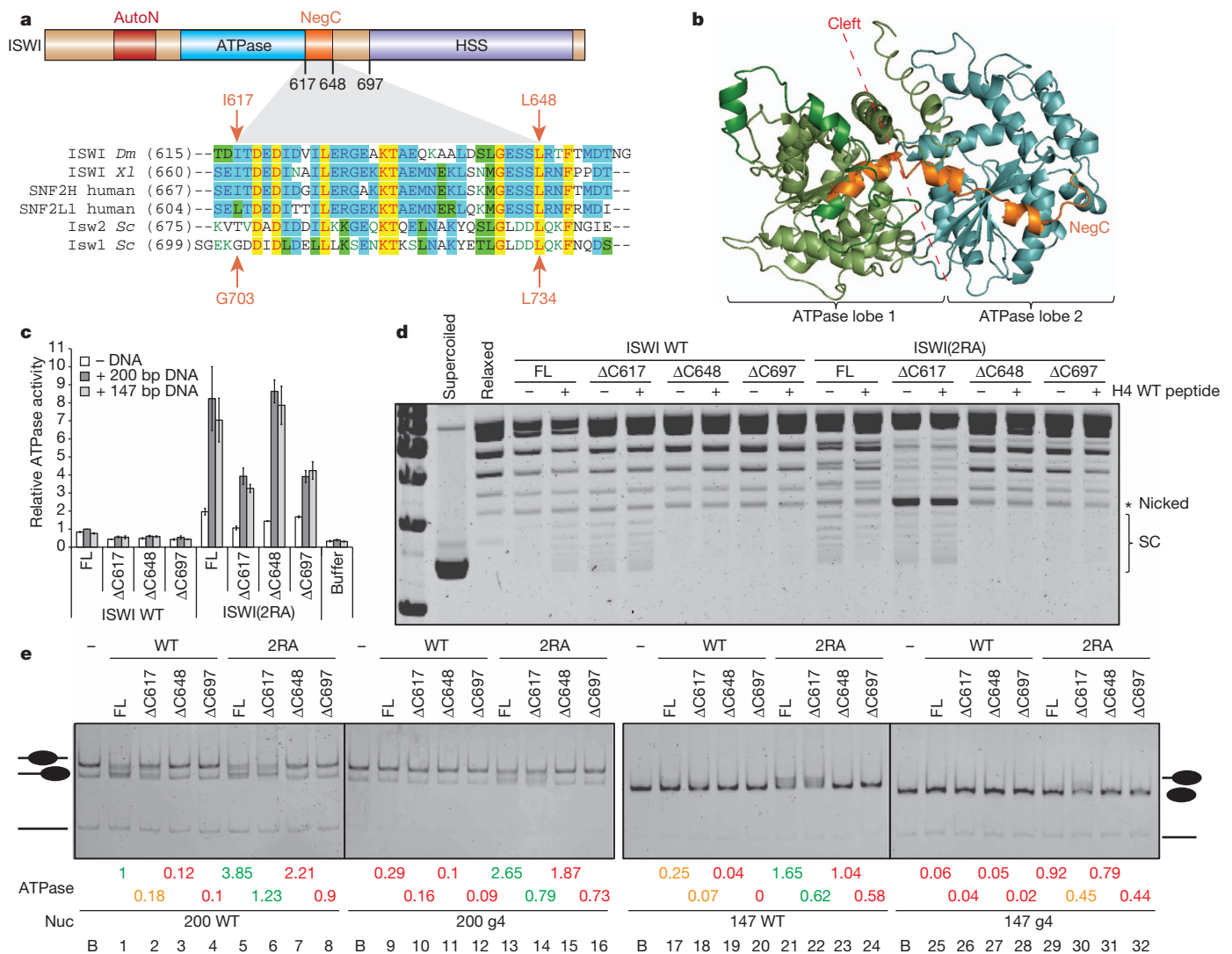


Figure 3 | NegC inhibits the coupling of ATP hydrolysis to DNA translocation, and nucleosome sliding. **a**, NegC conservation, revealed in zoomed alignment of ISWI orthologues. **b**, Modellization of ISWI(ΔC697) showing NegC (orange) traversing the cleft (red dashed line) from ATPase lobe 2 (blue) to ATPase lobe 1 (green). Model generated using Phyre²; depicted with PyMol³⁰. **c**, The AutoN (2RA) mutation elicits robust DNA-dependent ATPase activity independent of the HSS. Values represent mean of three experiments,

contrast, both full-length ISWI(2RA) and ISWI(2RA/ΔC) derivatives were highly stimulated by DNA (Fig. 3c), showing that the ATPase domain itself has an intrinsic DNA-dependent ATPase activity, which is held in check by the AutoN region. Notably, removal of the HSS domain (ΔC697 or ΔC648) prevented DNA translocation (Fig. 3d) while retaining high ATPase activity (Fig. 3c, for ISWI(2RA)), demonstrating a lack of coupling. Notably, further truncation to ΔC617 (ISWI(2RA/ΔC617)) restored DNA translocation (Fig. 3d), establishing that NegC negatively regulates the coupling of ATP hydrolysis to DNA translocation.

We then tested these ISWI(ΔC) derivatives with core or extended nucleosomes that either contain or lack the H4 tail (Fig. 3e). As expected¹⁴, omitting the HSS domain in ISWI(ΔC697) (or ISWI(ΔC648)) greatly reduced sliding of extended nucleosomes (lanes 3, 4, 19, 20). Surprisingly, ISWI(2RA/ΔC697) and ISWI(2RA/ΔC648) displayed high ATPase activity, but completely failed to slide either core (lanes 23, 24) or extended (lanes 7, 8) nucleosomes, mirroring the uncoupling of ATPase activity and DNA translocation above (Fig. 3c, d). Remarkably, and in-keeping with our tethered translocation

normalized to wild-type ISWI, with 200-bp DNA fragment. Error bars denote \pm s.e.m. **d**, Deletion of NegC through truncation restores DNA translocation. **e**, Impact of NegC region on sliding activities of core and extended nucleosomes (and H4 tail-less versions). ATPase activities (values, coloured by impact on sliding: high (green), moderate/low (orange), absent (red)). Enzyme:substrate molar ratio is 1:2. B, buffer. FL, full length.

results, further removal of NegC (ΔC617) restored sliding activity, without an accompanying increase in ATPase activity. Restoration was moderate with ISWI(ΔC617) (lane 2) and efficient with ISWI(2RA/ΔC617) (lane 6) on extended nucleosomes. Similarly, with core nucleosomes, sliding was low but detectable with ISWI(ΔC617) (lane 18), and efficient with ISWI(2RA/ΔC617) (lane 22). Thus, NegC is a new region that negatively regulates sliding through ATPase/translocation uncoupling. NegC is entirely separate from, and opposite in function to, characterized regions in other ATPases that promote sliding^{23,28}.

We then addressed how ISWI integrates the presence of nucleosomal epitopes. For wild-type ISWI, omission of extranucleosomal DNA (lane 17) greatly impaired sliding, whereas omission of the H4 tail (lane 9, or omitting both, lane 25) prevented sliding. With ISWI(2RA), loss of both the H4 tail and extranucleosomal DNA prevented sliding (lane 29), even though ATPase activity was high; comparable to wild-type ISWI on extended nucleosomes (lane 1). However, ISWI(2RA) could slide extended nucleosomes lacking the H4 tail (lane 13), or core nucleosomes bearing H4 tails (lane 21). Thus,

both the H4 tail and extranucleosomal DNA contribute to coupling. Importantly, whereas ISWI(2RA/ Δ C697) and ISWI(2RA/ Δ C648) are unable to slide nucleosomes lacking the H4 tail (g4; lanes 15, 16, 31, 32), removal of NegC (ISWI(2RA/ Δ C617)) restored relatively efficient sliding of extended g4 nucleosomes (lane 14), and moderate sliding of core g4 nucleosomes (lane 30). Furthermore, removal of NegC from ISWI(2RA) restores sliding ability with nucleosomes bearing amino-acid substitutions in both H4K12 and the basic patch (Supplementary Fig. 4). Thus, with ISWI(2RA), NegC omission enables sliding of nucleosomes without a basic patch or extranucleosomal DNA (Fig. 3e, lanes 6, 14, 22, 30); properties that normally define SWI/SNF-family remodellers.

To examine the effects of AutoN and NegC *in vivo*, we expressed (in *Saccharomyces cerevisiae*) mutations/truncations in Isw1 equivalent to those from our ISWI biochemistry (see Figs 1b and 3a) and tested complementation (Supplementary Fig. 5) or dominant phenotypes (using a sensitized *rsc7 Δ* (also known as *NPL6*) background, synthetically lethal with a wide range of chromatin mutants²⁹). Interestingly, expression of an Isw1 derivative lacking both AutoN and NegC regulation prevented growth (Fig. 4a), consistent with rogue chromatin-misregulation activity (although loss of proper regulation by Isw1-associated proteins may also contribute).

Taken together, our work provides several conceptual advances that affect both ISWI regulation and mechanism (Fig. 4b). Regarding regulation, the prior model involved 'positive' regulation of ISWI by the H4 basic patch and by extranucleosomal DNA. Here, we replace that conception with an inhibition-of-inhibition model, whereby these two

nucleosomal epitopes function to relieve an intrinsic autoinhibition conferred by two new negative regulatory domains, AutoN and NegC. Notably, whereas AutoN functions primarily to inhibit ATPase activity, NegC functions to inhibit ATPase coupling to DNA translocation, with structural models for NegC supporting this function. By this model, interaction of the HSS domain with extranucleosomal DNA does not activate the ATPase per se, it relieves NegC and restores ATPase coupling. Regarding mechanism, a key current model involves the HSS pushing extranucleosomal DNA into the nucleosome, providing the initial mechanical power stroke to form a translocated DNA loop on the surface of the nucleosome. However, as we observe efficient DNA translocation and nucleosome sliding following deletion of the HSS (when combined with NegC omission), the primary function of the HSS is not mechanical, but rather to regulate DNA translocation by antagonizing NegC, ensuring that coupling occurs only when extranucleosomal DNA is of sufficient length.

METHODS SUMMARY

ISWI protein derivatives were produced as N-terminal fusions to proteins coding for trigger factor and the Tet repressor DNA-binding domain (TF-TetR-ISWI), which heterodimerizes with an unfused TetR to enable *tetO* binding for DNA-translocation assays. Proteins were expressed in *Escherichia coli* BL21CodonPlus(DE3)RIL, and were purified to homogeneity as monodisperse derivatives. Chemically synthesized H4 tail peptides encompass residues Lys 8 to Asp 24 and AutoN peptide includes ISWI residues Lys 76 to Glu 98.

The ATPase assays were performed at 26 °C using a colorimetric assay based on the formation of a complex between inorganic phosphate and molybdate-malachite green. Reactions were an addition/omission series involving ISWI (10 pmol), pBluescript plasmid (500 ng), peptide (50 μ M), DNA fragments (500 fmol) or nucleosomes (500 fmol), as indicated.

Mononucleosomes used purified recombinant *Drosophila* histones expressed in *E. coli* BL21-CodonPlus(DE3)RIL, assembled with 147-bp or 200-bp DNA fragments (isolated from a plasmid by restriction digests, and containing the 601 strong-positioning sequence) by a salt-dialysis linear gradient. For the 200-bp fragment, the 601 sequence was centrally located.

The DNA-translocation assays measured plasmid supercoils generated by a single ISWI protein anchored through its TetR fusion to a previously relaxed (by *E. coli* topoisomerase I) plasmid DNA containing a single *tetO* operator sequence (Supplementary Fig. 2). Deproteinized samples were loaded on a 1.3% agarose gel, subsequently stained in ethidium bromide, and scanned on a Typhoon Trio (Amersham, GE).

The nucleosome-sliding assays were performed at 26 °C using a 1:2 enzyme: substrate molar ratio, except in the titration series. The reactions were stopped by adding competitor pBluescript plasmid DNA, and loaded on a 4.5% (37.5:1) native polyacrylamide gel, subsequently stained in ethidium bromide, and scanned on a Typhoon Trio.

Full Methods and any associated references are available in the online version of the paper.

Received 18 January; accepted 27 September 2012.

Published online 11 November 2012.

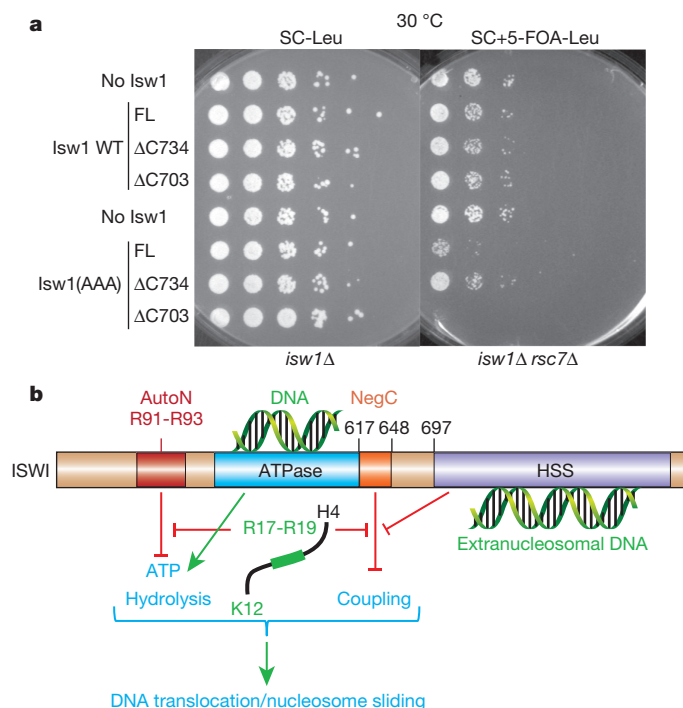


Figure 4 | Expression of ISWI derivatives *in vivo*, and regulation model for ISWI. **a**, Isw1 lacking AutoN and NegC regulation greatly impairs growth of a *S. cerevisiae* strain sensitized for chromatin misregulation (*rsc7 Δ*). Isw1 derivatives expressed in an *isw1 Δ rsc7 Δ* strain bearing a *URA3*-marked *RSC7⁺* plasmid; growth on 5-FOA media enforces the loss of the plasmid, imposing an *rsc7 Δ* genotype. SC-Leu, synthetic complete growth medium lacking leucine. **b**, Logic of ISWI ATPase regulation. The ISWI ATPase activity is positively regulated by DNA in the ATPase cleft. ISWI is also negatively regulated by two intrinsic domains: AutoN and NegC. AutoN inhibits the ATP-hydrolysis rate, and is relieved by the basic patch (R17-R19) of the H4 tail, whereas NegC inhibits ATPase coupling to DNA translocation, and is relieved by the HSS domain binding to sufficient extranucleosomal DNA, defining the 'inhibition of inhibition' mode of ISWI regulation (note: an additional lysine (H4K12) also promotes coupling.)

- Clapier, C. R. & Cairns, B. R. The biology of chromatin remodeling complexes. *Annu. Rev. Biochem.* **78**, 273–304 (2009).
- Corona, D. F. & Tamkun, J. W. Multiple roles for ISWI in transcription, chromosome organization and DNA replication. *Biochim. Biophys. Acta* **1677**, 113–119 (2004).
- Saha, A., Wittmeyer, J. & Cairns, B. R. Chromatin remodeling by RSC involves ATP-dependent DNA translocation. *Genes Dev.* **16**, 2120–2134 (2002).
- Whitehouse, I., Stockdale, C., Flaus, A., Szczelkun, M. D. & Owen-Hughes, T. Evidence for DNA translocation by the ISWI chromatin-remodeling enzyme. *Mol. Cell. Biol.* **23**, 1935–1945 (2003).
- Zofall, M., Persinger, J., Kassabov, S. R. & Bartholomew, B. Chromatin remodeling by ISW2 and SWI/SNF requires DNA translocation inside the nucleosome. *Nature Struct. Mol. Biol.* **13**, 339–346 (2006).
- Strohner, R. et al. A 'loop recapture' mechanism for ACF-dependent nucleosome remodeling. *Nature Struct. Mol. Biol.* **12**, 683–690 (2005).
- Saha, A., Wittmeyer, J. & Cairns, B. R. Chromatin remodeling through directional DNA translocation from an internal nucleosomal site. *Nature Struct. Mol. Biol.* **12**, 747–755 (2005).
- Clapier, C. R., Langst, G., Corona, D. F., Becker, P. B. & Nightingale, K. P. Critical role for the histone H4 N terminus in nucleosome remodeling by ISWI. *Mol. Cell. Biol.* **21**, 875–883 (2001).

9. Hamiche, A., Kang, J. G., Dennis, C., Xiao, H. & Wu, C. Histone tails modulate nucleosome mobility and regulate ATP-dependent nucleosome sliding by NURF. *Proc. Natl Acad. Sci. USA* **98**, 14316–14321 (2001).
10. Clapier, C. R., Nightingale, K. P. & Becker, P. B. A critical epitope for substrate recognition by the nucleosome remodeling ATPase ISWI. *Nucleic Acids Res.* **30**, 649–655 (2002).
11. Dang, W., Kagalwala, M. N. & Bartholomew, B. Regulation of ISW2 by concerted action of histone H4 tail and extranucleosomal DNA. *Mol. Cell. Biol.* **26**, 7388–7396 (2006).
12. Schwanbeck, R., Xiao, H. & Wu, C. Spatial contacts and nucleosome step movements induced by the NURF chromatin remodeling complex. *J. Biol. Chem.* **279**, 39933–39941 (2004).
13. Fazio, T. G., Gelbart, M. E. & Tsukiyama, T. Two distinct mechanisms of chromatin interaction by the Isw2 chromatin remodeling complex *in vivo*. *Mol. Cell. Biol.* **25**, 9165–9174 (2005).
14. Grüne, T. *et al.* Crystal structure and functional analysis of a nucleosome recognition module of the remodeling factor ISWI. *Mol. Cell* **12**, 449–460 (2003).
15. Yamada, K. *et al.* Structure and mechanism of the chromatin remodelling factor ISWIa. *Nature* **472**, 448–453 (2011).
16. Flaus, A., Martin, D. M., Barton, G. J. & Owen-Hughes, T. Identification of multiple distinct Snf2 subfamilies with conserved structural motifs. *Nucleic Acids Res.* **34**, 2887–2905 (2006).
17. Fitzgerald, D. J. *et al.* Reaction cycle of the yeast Isw2 chromatin remodeling complex. *EMBO J.* **23**, 3836–3843 (2004).
18. Lorch, Y., Maier-Davis, B. & Kornberg, R. D. Mechanism of chromatin remodeling. *Proc. Natl Acad. Sci. USA* **107**, 3458–3462 (2010).
19. Fyodorov, D. V. & Kadonaga, J. T. Dynamics of ATP-dependent chromatin assembly by ACF. *Nature* **418**, 896–900 (2002).
20. Sirinakis, G. *et al.* The RSC chromatin remodelling ATPase translocates DNA with high force and small step size. *EMBO J.* **30**, 2364–2372 (2011).
21. Blosser, T. R., Yang, J. G., Stone, M. D., Narlikar, G. J. & Zhuang, X. Dynamics of nucleosome remodelling by individual ACF complexes. *Nature* **462**, 1022–1027 (2009).
22. Singleton, M. R., Dillingham, M. S. & Wigley, D. B. Structure and mechanism of helicases and nucleic acid translocases. *Annu. Rev. Biochem.* **76**, 23–50 (2007).
23. Patel, A., McKnight, J. N., Genzor, P. & Bowman, G. D. Identification of residues in chromodomain helicase DNA-binding protein 1 (Chd1) required for coupling ATP hydrolysis to nucleosome sliding. *J. Biol. Chem.* **286**, 43984–43993 (2011).
24. Ryan, D. P., Sundaramoorthy, R., Martin, D., Singh, V. & Owen-Hughes, T. The DNA-binding domain of the Chd1 chromatin-remodelling enzyme contains SANT and SLIDE domains. *EMBO J.* **30**, 2596–2609 (2011).
25. Kelley, L. A. & Sternberg, M. J. Protein structure prediction on the Web: a case study using the Phyre server. *Nature Protocols* **4**, 363–371 (2009).
26. Forné, I., Ludwigsen, J., Imhof, A., Becker, P. B. & Mueller-Planitz, F. Probing the conformation of the ISWI ATPase domain with genetically encoded photoreactive crosslinkers and mass spectrometry. *Mol. Cell. Proteom.* **11**, M111.012088 (2012).
27. Hauk, G., McKnight, J. N., Nodelman, I. M. & Bowman, G. D. The chromodomains of the Chd1 chromatin remodeler regulate DNA access to the ATPase motor. *Mol. Cell* **39**, 711–723 (2010).
28. Sen, P., Ghosh, S., Pugh, B. F. & Bartholomew, B. A new, highly conserved domain in Swi2/Snf2 is required for SWI/SNF remodeling. *Nucleic Acids Res.* **39**, 9155–9166 (2011).
29. Wilson, B., Erdjument-Bromage, H., Tempst, P. & Cairns, B. R. The RSC chromatin remodeling complex bears an essential fungal-specific protein module with broad functional roles. *Genetics* **172**, 795–809 (2006).
30. Schrodinger, L. L. C. *The PyMOL Molecular Graphics System, Version 0.99rc6* (2010).

Supplementary Information is available in the online version of the paper.

Acknowledgements We thank S. Tan for pST55-16 × NCP601a and G. Längst for pUC12 × 601. We thank C. Müller for experience gained by C. Clapier on structural aspects of ISWI protein. We thank T. Owen-Hughes for the *S. cerevisiae* strain TOH1358, T. Tsukiyama for the initial ISWI-containing plasmid, P. Gawu for technical assistance and B. Schackmann for DNA sequencing and peptide synthesis. This work was supported by National Institutes of Health grant GM60415 (supplies), Howard Hughes Medical Institute (support of C.R.C. and B.R.C.), and CA042014 (University of Utah core facilities).

Author Contributions B.R.C. and C.R.C.: experimental design. C.R.C.: experiments and figures. B.R.C. and C.R.C. wrote the paper.

Author Information Reprints and permissions information is available at www.nature.com/reprints. The authors declare no competing financial interests. Readers are welcome to comment on the online version of the paper. Correspondence and requests for materials should be addressed to B.R.C. (brad.cairns@hci.utah.edu) or C.R.C. (cedric.clapier@hci.utah.edu).

METHODS

Reagents. ISWI protein derivatives were expressed in *Escherichia coli* BL21CodonPlus(DE3)RIL, upon 0.5 mM isopropyl- β -D-thiogalactoside induction at $D_{600\text{ nm}}$ ~0.5 for 24 h at 15 °C, as complexes from two vectors: one—pCDFDuet-1—bears a gene coding for TetR-(His)₇, and the other—pCold TF (Takara) lacking the His tag—is a gene fusion containing TF-3C cleavage site-TetR-ISWI-Flag. A sequence of eight amino acids (GGQGGQGG) was inserted between the genes coding for TetR and ISWI. The properly assembled complex contains a heterodimer of TetR obtained by two successive affinity purifications. The bacterial-cell extracts were first mixed with nickel-nitrilotriacetic acid agarose resin (Qiagen), capturing the complex and the unwanted TetR homodimer. The sample eluted from the resin was then purified using the Flag tag and anti-Flag M2 affinity gel and eluted with 3 \times Flag peptide (Sigma) to obtain the desired complex. Then, trigger factor was cleaved from the complex using human rhinovirus 3C protease (Novagen) using 1 unit of protease per 0.1 mg of complex by incubating 16 h at 4 °C, in the presence of 10 mM β -mercaptoethanol and 0.5 mM EDTA. Finally, the purification of the complex was achieved by a gel-filtration step on two S200GL 10/300 (Amersham, GE) in series. Obtained complexes were homogen and monodisperse.

Chemically synthesized H4 tail peptides encompass residues Lys 8 to Asp 24; AutoN peptide includes ISWI residues Lys 76 to Glu 98.

Mononucleosomes were produced from single recombinant *Drosophila* histones expressed in *E. coli* BL21CodonPlus(DE3)RIL, purified as inclusion bodies, and assembled in octamers by salt-dialysis, essentially as described in ref. 31. The 200- and 147-bp DNA fragments containing the 601 positioning sequence³² were respectively produced from plasmids pUC12 \times 601 (digested by *Ava*I) and pST55-16 \times NCP601a (digested by *EcoRV*). For the 200-bp fragment, the 601 sequence was centrally located. The DNA fragments were purified from the backbone using preparative electrophoresis (PrepCell, Bio-Rad) 4.5% (37.5:1) native polyacrylamide gel running at 400 V constant in 0.5 \times TBE (Tris-borate 45 mM, pH 8, with 1 mM EDTA), with TE (Tris 10 mM, 1 mM EDTA) as elution buffer. Mononucleosome assemblies were performed by titration reactions, as 50- μ l reaction containing 40 pmol of DNA fragment in 2 M KCl mixed with a variable amount of histone octamers covering the equimolar ratio, with a linear salt-gradient dialysis applied from 2 M to 50 mM KCl, essentially as described in ref. 31, using an Econo-Pump (Bio-Rad) and Slide-A-Lyser Mini dialysis units with a 7,000 molecular weight cutoff (Thermo Scientific).

ATPase assay. Measurement of ATP hydrolysis was based on the formation of a complex between inorganic phosphate and molybdate-malachite green. ATPase assays were performed in 10 mM HEPES buffer, pH 7.3, 20 mM potassium acetate, 5 mM MgCl₂, 0.5 mM dithiothreitol, 0.1 mg ml⁻¹ BSA and 5% glycerol, in the presence of 1 mM ATP. After 30-min incubation at 26 °C with 500 r.p.m. shaking in a Thermomixer (Eppendorf), 800 μ l of MGAM reagent (3 volumes of MG = 0.045% (w/v) malachite green in 0.1 N HCl, mixed with 1 volume of AM = 4.2% (w/v) ammonium molybdate in 4N HCl) were added, followed 1 min later by 100 μ l of 34% (w/v) Na₃citrate. Measures were performed at $D_{650\text{ nm}}$ 10 min later. In the plasmid DNA and peptide experiments, 10 pmol of ISWI was used with or without 500 ng of pBluescript plasmid and/or 50 μ M peptide. In the mononucleosome or DNA-fragment experiments, 10 pmol of ISWI was in the presence of 500 fmol of nucleosome or DNA fragment, respectively.

DNA-translocation assay. The 20- μ l reaction contained 10 pmol ISWI, with or without 15 μ M peptide, in the presence of 250 ng of previously relaxed plasmid, 1 mM ATP, 2.5 U of topoisomerase I (NEB) in NEB1 \times buffer, 1 mg ml⁻¹ BSA. Experiments were performed at 30 °C for 2 h (or shorter during time course), followed by heat inactivation at 65 °C for 20 min. De-proteinization was performed by adding 2 μ l of proteinase K at 10 mg ml⁻¹ and 1 μ l SDS 20% and incubated at 50 °C for 1 h. Reactions were subsequently precipitated in ethanol, prior to loading on a 1.3% agarose gel run for 3 h at 130 V. Gels were stained for 20 min in a 1 μ g ml⁻¹ ethidium bromide solution, and scanned on a Typhoon Trio (Amersham, GE). Time-course experiments are performed using a starting reaction corresponding to a scale-up of amounts above, proportional to the number of desired aliquots.

Sliding assay. 100 fmol (or variable for titration) ISWI was incubated in 10 mM Tris buffer, pH 7.4, 50 mM KCl, 3 mM MgCl₂, 0.1 mg ml⁻¹ BSA, 1 mM ATP, in the presence of 200 fmol of mononucleosome for 90 min at 26 °C, with shaking at 500 r.p.m. in a Thermomixer (Eppendorf). 10- μ l reactions were stopped by adding 200 ng competitor DNA (pBluescript plasmid) and incubated for an additional 30 min as previously. Reactions were loaded using glycerol 10% on a 4.5% (37.5:1) native polyacrylamide gel and run in 0.4 \times TBE for 55 min at 110 V constant. Gel was stained for 10 min in a 1 μ g ml⁻¹ ethidium bromide solution, and scanned on a Typhoon Trio (Amersham, GE). Time-course experiments were performed using a starting reaction corresponding to a scale-up of amounts above, proportional to the number of desired aliquots.

In vivo yeast experiments. Plasmids expressing Isw1 derivatives were generated by marker conversion to *LEU2* (from *S. cerevisiae*) of pRS416-Isw1 (ref. 33), followed by site-directed mutagenesis (via PCR) generating AAA mutations and Δ C truncations. Final constructs were verified by sequencing.

Complementation assay: the growth of *S. cerevisiae* strain TOH1358 lacking *CHD1* and *ISW1* genes is temperature sensitive³⁴. Complementation experiments were performed by transforming the strain with plasmids expressing various derivatives of Isw1 under control of the endogenous promoter, performing tenfold spot dilutions, and observing the rescue of the growth ability at high temperature. Plate medium is SC-Leu.

Testing the dominant-negative phenotype: here, we used a sensitized genetic background strain YBC 2233, lacking *ISW1* and *RSC7*. The strain was transformed with plasmids expressing separate Isw1 derivatives under control of the endogenous *ISW1* promoter, selecting for colonies on SC-Leu. Growth ability (in spot dilution format) was tested at 30 °C on SC-Leu plates, which either lacked or contained 5-FOA (which enforces the loss of a *URA3*-marked plasmid bearing *RSC7*).

- Dyer, P. N. *et al.* Reconstitution of nucleosome core particles from recombinant histones and DNA. *Methods Enzymol.* **375**, 23–44 (2004).
- Lowary, P. T. & Widom, J. New DNA sequence rules for high affinity binding to histone octamer and sequence-directed nucleosome positioning. *J. Mol. Biol.* **276**, 19–42 (1998).
- Tsukiyama, T., Palmer, J., Landel, C. C., Shiloach, J. & Wu, C. Characterization of the imitation switch subfamily of ATP-dependent chromatin-remodeling factors in *Saccharomyces cerevisiae*. *Genes Dev.* **13**, 686–697 (1999).
- Gkikopoulos, T. *et al.* A role for Snf2-related nucleosome-spacing enzymes in genome-wide nucleosome organization. *Science* **333**, 1758–1760 (2011).

The TEL patch of telomere protein TPP1 mediates telomerase recruitment and processivity

Jayakrishnan Nandakumar^{1,2}, Caitlin F. Bell^{1,2†*}, Ina Weidenfeld^{1,3*}, Arthur J. Zaug^{1,2}, Leslie A. Leinwand^{1,3} & Thomas R. Cech^{1,2,3}

Human chromosome ends are capped by shelterin, a protein complex that protects the natural ends from being recognized as sites of DNA damage and also regulates the telomere-replicating enzyme, telomerase^{1–3}. Shelterin includes the heterodimeric POT1–TPP1 protein, which binds the telomeric single-stranded DNA tail^{4–9}. TPP1 has been implicated both in recruiting telomerase to telomeres and in stimulating telomerase processivity (the addition of multiple DNA repeats after a single primer-binding event)^{9–14}. Determining the mechanisms of these activities has been difficult, especially because genetic perturbations also tend to affect the essential chromosome end-protection function of TPP1 (refs 15–17). Here we identify separation-of-function mutants of human TPP1 that retain full telomere-capping function *in vitro* and *in vivo*, yet are defective in binding human telomerase. The seven separation-of-function mutations map to a patch of amino acids on the surface of TPP1, the TEL patch, that both recruits telomerase to telomeres and promotes high-processivity DNA synthesis, indicating that these two activities are manifestations of the same molecular interaction. Given that the interaction between telomerase and TPP1 is required for telomerase function *in vivo*, the TEL patch of TPP1 provides a new target for anticancer drug development.

Genetic analysis of TPP1 regulation of telomerase is complicated by the potential of TPP1 mutations to uncap telomeres, which can give unnatural telomerase hyperextension or induce a DNA-damage response. Our search for separation-of-function mutants of TPP1 that would affect only its telomerase interactions was conducted on the TPP1 OB domain (TPP1(OB)), which is separate from its POT1 single-stranded DNA (ssDNA)-interaction domain (Fig. 1a) and previously implicated in telomerase interaction^{13,14}. We engineered 12 single amino-acid mutants and two double mutants of TPP1(OB), choosing residues that are both conserved among mammalian TPP1 proteins and reside on the protein surface⁹ (Supplementary Fig. 1a, b). All mutant and wild-type proteins were expressed recombinantly in *Escherichia coli* and purified (Supplementary Fig. 1c; see Methods).

The POT1–TPP1 heterodimer has a higher affinity for telomeric ssDNA than does POT1 alone⁹, which is consistent with the role of this complex in protecting single-stranded telomeric DNA from the DNA-damage response machinery¹⁵. Quantitative DNA-binding experiments demonstrated that all the mutant proteins, like wild-type TPP1, were able to enhance POT1–DNA affinity (Fig. 1b and Supplementary Fig. 2a). Furthermore, all TPP1 mutants formed stable POT1–TPP1–ssDNA ternary complexes in electrophoretic mobility shift assays (Supplementary Fig. 2b). These results suggest that the TPP1(OB) surface mutations do not disrupt the overall structure or the DNA-end protection function of TPP1.

Addition of purified POT1–TPP1 to telomerase enzyme activity assays enhances telomerase processivity 2–3-fold *in vitro*⁹. We developed a new direct telomerase assay in which TERT, TR, TPP1 and POT1 were recombinantly co-expressed in human cells. Lysates

from these cells were used in direct telomerase activity assays involving extension of primer a5 (TTAGGGTTAGCGTTAGGG; the underlined G-to-C mutation ensured positioning of the POT1–TPP1 complex at the 5' portion of the DNA primer, thereby providing a homogenous substrate for telomerase extension⁹). The 14 TPP1 mutants varied substantially in their stimulation of processivity; some such as S106A, S111A and R175V, resulted in long extension products indicative of high processivity, similar to wild-type TPP1, but others, such as E169A/E171A and L212A, resulted in low-processivity patterns similar to that with no TPP1 added (Fig. 1c). Quantification of data (Fig. 1d) showed that several TPP1 mutants gave significantly decreased processivity ($P < 0.005$). Western blot analysis showed that TERT, POT1 and TPP1 proteins were expressed at similar levels across all transfections (Fig. 1e). Note that processivity, unlike activity, is not influenced by enzyme concentration.

As an independent test of processivity, lysates from HEK 293T cells transiently overexpressing telomerase were supplemented with purified POT1 and TPP1 proteins before the telomerase assay, as described previously^{9,11,18} (Supplementary Fig. 3; see also alternative quantification of processivity in Supplementary Fig. 4). This traditional assay gave results in agreement with the new co-transfection method. We also analysed the 14 TPP1 mutants using a primer with a purely telomeric sequence and a different sequence permutation (GGTTAGGGTTAGGGTTAG); we obtained essentially the same results as with primer a5 (Supplementary Fig. 5), verifying that the TPP1 mutant phenotype was not primer specific. All three assays identified the same separation-of-function mutants of TPP1 (L104A, D166A/E168A, E169A/E171A, R180A, L183A and L212A), with E215A and R208V being intermediate and the other mutants having wild-type activity. Further dissection of the two double mutants into four single mutants revealed that E168, E169 and E171, but not D166, were important for telomerase stimulation (Supplementary Fig. 3). Most of the TPP1 mutants that were defective in processivity also gave a statistically significant decrease in activity (Supplementary Fig. 3b). In agreement with previous results⁹, the stimulation of activity (and its dependence on specific TPP1 residues) was observed even in the absence of added POT1 protein (Supplementary Fig. 6).

The effects of TPP1 mutations might be explained by disruption of a TPP1–telomerase interaction. To test this directly, we developed a co-immunoprecipitation assay involving co-transfection of Flag–TPP1 and untagged telomerase (TERT plus TR) in HeLa-EM2-11ht cells. Inspection and quantification by immunoblot of proteins co-precipitated with anti-Flag beads shows that TERT, but not actin, was associated with Flag–TPP1 (Fig. 2a, compare lanes 1 and 2). More TERT protein was co-precipitated with Flag–TPP1 when POT1, the *in vivo* binding partner of TPP1, was also present (compare lanes 2 and 4). Addition of primer a5 (a ligand for POT1–TPP1 and a substrate for telomerase) to lysates containing Flag–POT1 and Flag–TPP1 before immunoprecipitation increased the TPP1–telomerase interaction by

¹University of Colorado BioFrontiers Institute, Boulder, Colorado 80309, USA. ²Howard Hughes Medical Institute and Department of Chemistry and Biochemistry, University of Colorado, Boulder, Colorado 80309, USA. ³Department of Molecular, Cellular, and Developmental Biology, University of Colorado, Boulder, Colorado 80309, USA. †Present address: Vanderbilt School of Medicine, M.D. program, 215 Light Hall, Nashville, Tennessee 37232, USA.

*These authors contributed equally to this work.

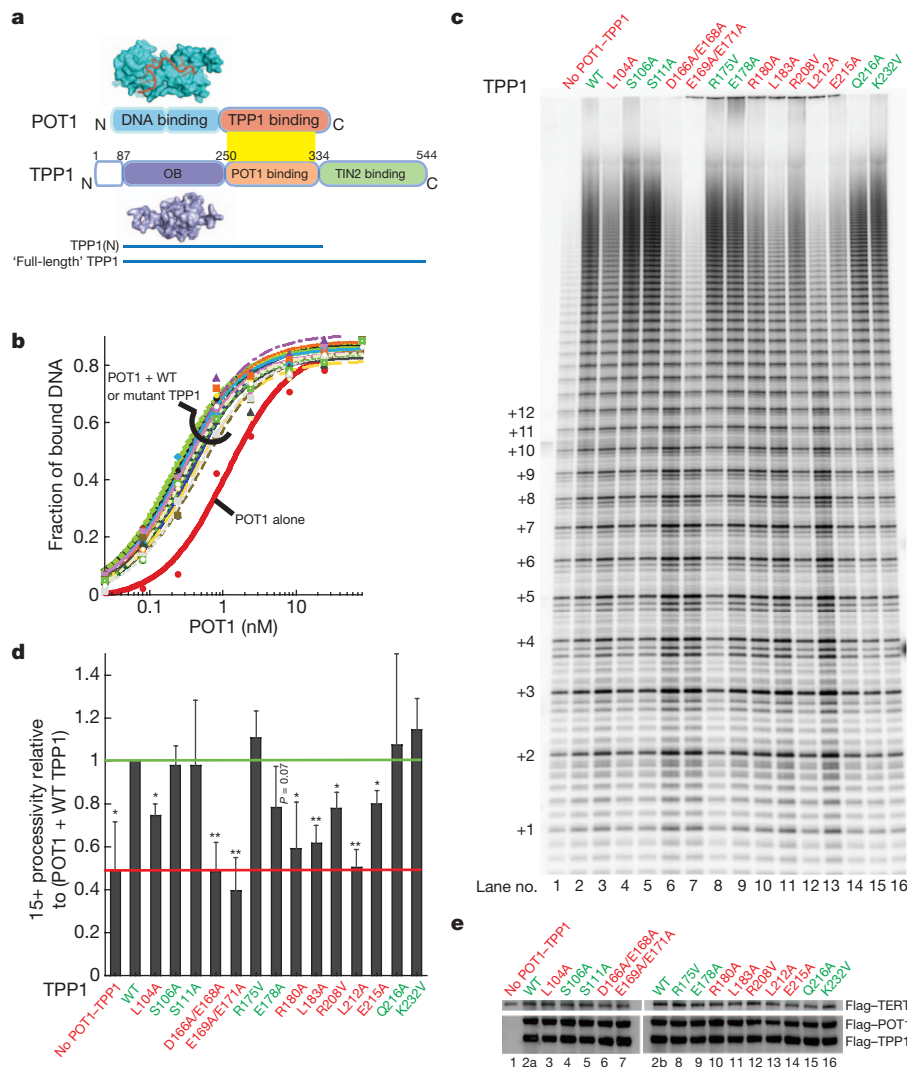


Figure 1 | Separation-of-function mutants of TPP1 affect telomerase processivity without affecting telomere complex formation. **a**, Domain architecture of POT1–TPP1 shown alongside the crystal structures of the DNA-binding domain of POT1 (cyan surface) bound to DNA (red ribbon; Protein Data Bank (PDB) accession 1XJV) and the TPP1(OB) domain (PDB accession 2I46). **b**, DNA binding curves from filter-binding of mixtures containing trace amounts of ^{32}P -labelled ssDNA (GGTTAGGGTTAG), 200 nM TPP1, and varying concentrations of POT1. See Supplementary Fig. 2a for dissociation constant (K_d) values. WT, wild type. **c**, Direct telomerase activity assay with primer a5 of lysates from cells co-transfected with a TR plasmid and Flag-tagged POT1, TPP1 and TERT plasmids. ‘No POT1–TPP1’

~2.5-fold compared to the basal interaction in the absence of POT1 and a5 DNA (compare lanes 2 and 6). The enhanced interaction between telomerase and POT1–TPP1 is unlikely to be occurring indirectly via bridging of TPP1 and telomerase by POT1–DNA, because Flag–POT1 did not pull down telomerase even in the presence of a5 DNA (lane 5).

The interaction between TPP1 and telomerase was reduced when either TR or TERT was omitted from co-transfections (Supplementary Fig. 7a, b). These results indicate that TPP1 interacts with telomerase optimally in the context of the fully assembled RNP. The TEN (telomerase essential N-terminal) domain of TERT has been implicated in a functional interaction with POT1–TPP1¹⁹ and in binding to TPP1(OB)²⁰. However, deletion of the TEN domain or mutating G100V (ref. 19) did not abolish telomerase binding (Supplementary Fig. 7c and ref. 21). These data indicate that the observed immunoprecipitation of telomerase with TPP1 involves contacts both within and outside the TEN domain of TERT, which is consistent with the implication of

indicates transfection without POT1 and TPP1. The number of telomeric repeats added to primer are indicated along the left. **d**, Processive extension (>15 repeats/total) with TPP1 mutants relative to that with wild-type TPP1 (green line) obtained from three independent sets of experiments (as in panel c); error bars indicate s.d. Stimulation of processivity is assessed relative to the ‘no POT1–TPP1’ negative control (red line). Two-tailed student’s *t*-test with respect to R175V: **P* < 0.02, ***P* < 0.005. Red labels indicate significantly defective; green labels indicate not significantly defective. **e**, Immunoblot of lysates used in panel c probed with anti-Flag antibody–HRP conjugate shows uniform expression.

C-terminal TERT residues in TPP1(OB)-mediated recruitment of telomerase to telomeres²⁰.

When the TPP1 mutants were tested for binding telomerase (Fig. 2b, c), there was strong correlation with the telomerase stimulation results. Five of the six mutants that showed a defect in telomerase stimulation *in vitro* also showed defects in telomerase association in the presence of POT1 and DNA primer, and the intermediate mutant E215A was also defective in binding. An exception was mutant L104A, which showed wild-type levels of associated telomerase.

When the separation-of-function mutations that fail to stimulate processivity and also interfere with telomerase binding are mapped on the surface of the TPP1(OB) structure, the seven critical amino acids (E168, E169, E171, R180, L183, L212 and E215) cluster to reveal a patch on the protein surface (orange in Fig. 2d). We name this conserved surface the TEL patch (TPP1 glutamate (E) and leucine (L)-rich patch). The fact that the TEL patch promotes both processivity and

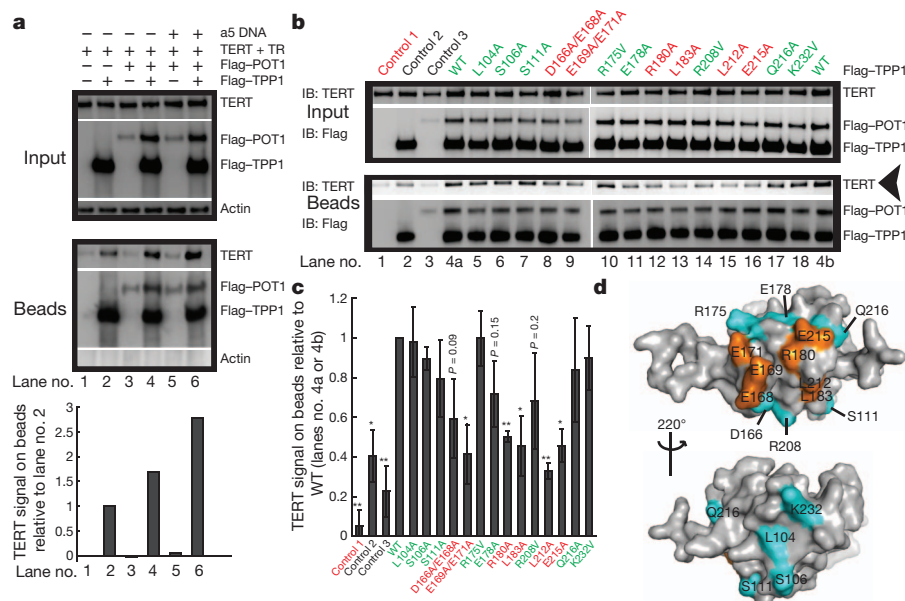


Figure 2 | TPP1 mutations that disrupt telomerase stimulation also disrupt telomerase binding. **a**, Pull down of transiently expressed Flag-TPP1, Flag-POT1 and associated untagged TERT from HeLa-EM2-11ht lysates on anti-Flag conjugated beads. 'Input' indicates immunoblot of soluble cellular lysates before incubation with beads; 'beads' indicates immunoblot of proteins retained on antibody beads after 2 h incubation at 4 °C and washing. The TERT signal was plotted after correction for loading differences (using the actin signal). **b**, Comparison of TERT pull down by Flag-TPP1 mutants in the presence of Flag-POT1 and primer a5. Control 1, Flag-POT1/TPP1 and

primer a5 omitted; control 2, Flag-TPP1 (WT) present, Flag-POT1 and primer omitted; control 3, Flag-POT1 and primer present, Flag-TPP1 omitted. **c**, The mean TERT signal on beads obtained from quantification of three independent sets of experiments of which panel **b** is representative; error bars indicate s.d. Two-tailed Student's *t*-test with respect to R175V: **P* < 0.05, ***P* < 0.01. The red label indicates significantly defective; green label indicates not significantly defective. **d**, Structure showing the TEL patch (amino acids in orange), the surface of the OB domain of TPP1 that mediates telomerase association and stimulation. Other amino acids mutated in this study are shown in cyan.

telomerase binding fulfils a prediction of a previous model for telomerase processivity¹¹. The 'back face' of TPP1(OB) (bottom view of Fig. 2d) contains amino acids not involved in binding telomerase.

Previously, knockdown of TPP1 in human HTC75 cells resulted in telomere lengthening⁷, whereas skin keratinocytes from *Tpp1*^{Δ/Δ}*K5-cre* newborn mice displayed telomere shortening¹². However, loss of both end-protection and telomerase-regulatory functions of TPP1 complicates interpretation of such studies. To test how the TPP1–telomerase interaction influences telomere maintenance under conditions where chromosome end protection is unperturbed, we constructed stable cell lines containing a single-copy gene cassette with a bidirectional tetracycline-inducible promoter (Ptet-bi, Fig. 3a). The promoter expresses both a short hairpin RNA (shRNA; shTPP1) to knockdown endogenous TPP1 (Fig. 3b, c and Supplementary Fig. 8a–c) and a shRNA-resistant version of Flag-TPP1 (Flag-TPP1* or wild type*; Fig. 3d and Supplementary Fig. 8a, d). E169A/E171A*, R175V* and L212A* cell lines express shRNA-resistant versions of the various mutant TPP1 proteins (asterisks indicate shRNA-resistant mRNAs). We also constructed a similar set of cell lines in which various TPP1 proteins were ectopically expressed without knocking down the endogenous TPP1 (Supplementary Figs 9a, b and 10a, b).

Overexpression of TPP1 as described above (~25-fold; data not shown) could potentially sequester shelterin components from telomeres, leading to the appearance of telomere-dysfunction-induced foci (TIFs)¹³. However, expression of the TPP1 mutants resulted in the same low levels of TIFs as wild type (Supplementary Fig. 11). These data are consistent with the unaltered POT1–DNA binding properties of the TPP1(OB) mutants (Fig. 1b) and with a previous study showing that deletion of the entire TPP1(OB) domain fails to elicit chromosome end-deprotection¹⁴.

The stable cell lines expressing wild-type and control (R175V) Flag-TPP1 showed a robust increase in telomere length over 81 population doublings (~40 bp per population doubling) in a doxycycline-dependent (Flag-TPP1 expression-dependent) manner, whereas the telomeres of

the untransfected cell line were stable (Fig. 3e, f and Supplementary Figs 9c, d and 10c, d). In contrast, the telomeres of cell lines expressing E169A/E171A and L212A did not change in length over 81 population doublings. This result is in full agreement with our data showing that E169A/E171A and L212A have a greatly diminished ability to stimulate telomerase (Fig. 1) and to associate with telomerase (Fig. 2), but that R175V behaves like the wild-type protein. We conclude that TPP1 increases telomerase action *in vivo* and that the TEL patch of TPP1 is necessary for this effect.

We tested whether the inability of the E169A/E171A and L212A mutants to stimulate telomere lengthening was due to their inability to recruit telomerase to telomeres. The cell lines stably co-expressing shTPP1 and TPP1* (wild type*, E169A/E171A*, R175V*, or L212A*) were transfected with expression plasmids encoding TERT and TR and analysed by co-immunofluorescence (co-IF) and immunofluorescence–fluorescence *in situ* hybridization (IF–FISH). As expected, wild-type and all mutant Flag-TPP1 proteins localized to telomeres (Supplementary Fig. 12). Telomerase was efficiently recruited to telomeres containing wild-type and R175V proteins, as indicated by the co-localization of TR and Flag-TPP1 (Fig. 4a, b). By the same criterion, the E169A/E171A* and L212A* cell lines showed reduced levels of telomerase recruitment to telomeres. Instead, the TR foci in E169A/E171A* and L212A* cells resided in Cajal bodies (marked by coilin; Fig. 4c), indicating that the corresponding TPP1 mutations prevent telomerase in Cajal bodies from being delivered to telomeres. TEL patch mutations also reduced recruitment of endogenous TR to telomeres (Supplementary Fig. 13).

We conclude that a small patch of amino acids on the surface of the chromosome-end-binding protein TPP1, the TEL patch, binds telomerase to enable both its recruitment to telomeres and its high-processivity extension of telomeric DNA. While this manuscript was under review, two groups independently reported the involvement of portions of the TEL patch in telomerase association²¹ and telomerase recruitment²⁰.

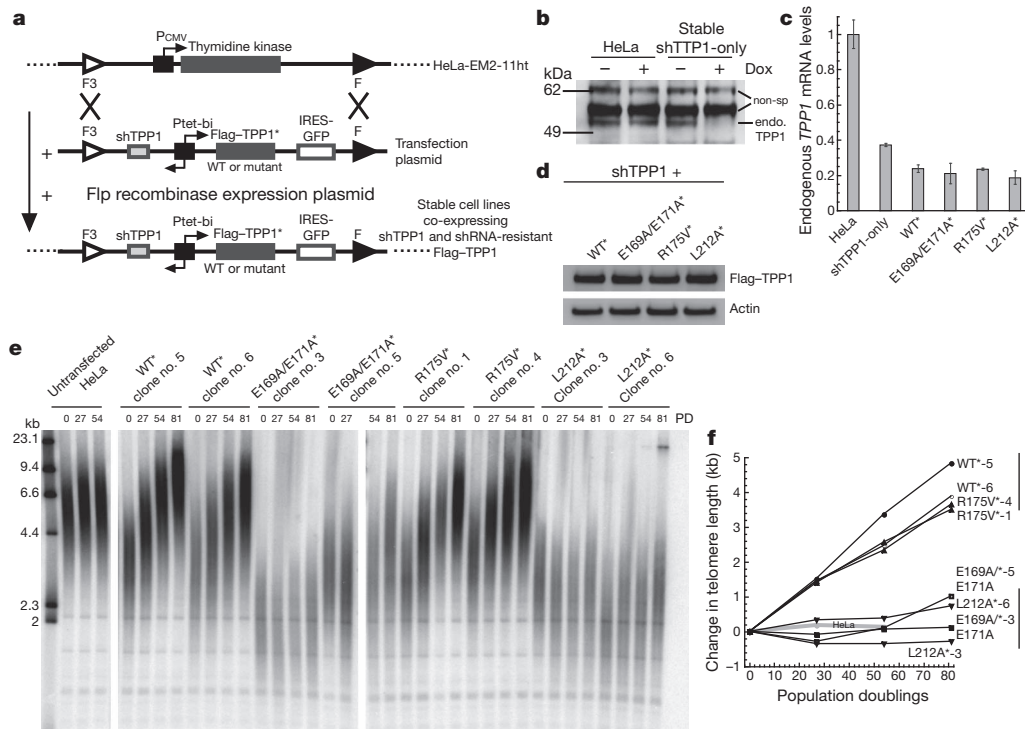


Figure 3 | TPP1 TEL-patch mutants fail to stimulate telomere lengthening in human cells. **a**, Engineering HeLa-EM2-11ht stable cell lines containing single-copy integration of bidirectional Tet-inducible shTPP1 and shRNA-resistant Flag-TPP1* (wild type or mutants) genes. **b**, A stable cell line encoding shTPP1 (no exogenous Flag-TPP1) shows doxycycline-dependent knockdown of endogenous TPP1 protein. Nonspecific bands serve as loading controls. **c**, Quantitative RT-PCR showing knockdown of endogenous *TPP1* mRNA in the indicated cell lines \pm s.d. ($n = 3$). **d**, Western blot showing similar protein levels of shRNA-resistant Flag-TPP1 in the indicated cell lines also

expressing shTPP1. **e**, Telomeric restriction fragment (TRF) Southern blot of DNA from HeLa-EM2-11ht (untransfected HeLa) and stable cell lines expressing shTPP1 and the indicated TPP1 constructs at the indicated population doublings (PD). DNA length standards are indicated along the left. **f**, Change in mean telomere length for data shown in panel **e** was plotted against population doublings. The vertical bars at the right indicate the distinct ranges of telomere length attained by wild-type* and R175V* versus E169A/E171A* and L212A* cells after 81 population doublings.

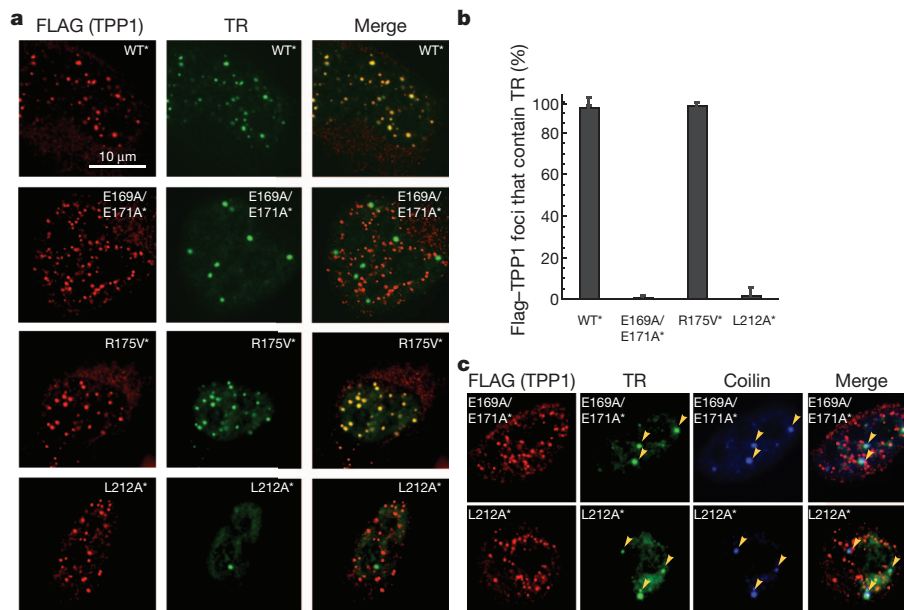


Figure 4 | Failure to stimulate telomere lengthening correlates with inability to recruit telomerase to telomeres. **a**, Fluorescence *in situ* hybridization (FISH) detects TR (green) and immunofluorescence (IF) detects the indicated Flag-TPP1 proteins (red). In the merge panels, yellow spots indicate recruitment of telomerase to telomeres. **b**, Quantification of telomerase recruitment data of which panel **a** is representative. The average percentage of

Flag-TPP1 foci containing TR (y axis) and standard deviations (error bars) of 15 fields of view (40–120 cells total) were plotted for the indicated stable cell lines. **c**, IF-FISH experiment showing that telomerase (TR in green) in E169A/E171A* and L212A* cells fails to be recruited to telomeres (Flag-TPP1 in red) and instead remains localized in Cajal bodies (coilin in blue).

In the simplest model, the TEL patch binds telomerase directly. If there were a bridging molecule, it would probably be an abundant cellular component, because TPP1–telomerase binding is robust under conditions of TPP1 and telomerase overexpression, where any telomerase-specific factors would be substoichiometric. There is precedence for such a bridging molecule in *Schizosaccharomyces pombe*, where Ccq1 physically connects Tpz1 (the *S. pombe* TPP1) to telomerase^{22–24}. However, there is no identifiable homologue of Ccq1 in humans (see Supplementary Discussion for comparison with telomerase recruitment in budding yeast).

The substantial reduction of telomerase recruitment by subtle mutations in the TEL patch of TPP1 indicates the potential for novel strategies to inhibit telomerase for cancer therapy. By targeting the TEL patch, instead of telomerase itself, a compound could potentially inhibit telomerase action only at telomeres without interfering with other hTERT functions^{25,26}. Furthermore, such an inhibitor should not perturb genomic stability in normal cells lacking telomerase, because the TEL patch is physically and functionally separate from the portion of TPP1 engaged in chromosome end-protection.

METHODS SUMMARY

All experiments involving recombinant TPP1 expressed in bacteria⁹ used TPP1(N) (amino acids 87–334), which recapitulates all *in vitro* functions of the full-length human protein⁹. Experiments involving TPP1 expressed in human cells used full-length TPP1 that we define as starting from amino acid Met 87 (refs 9, 14) (Fig. 1a). Telomerase was obtained from HEK 293T cells transfected with human TERT and TR plasmids¹⁸ or from HeLa-EM2-11ht cells transfected with Flag-TERT, TR, Flag-POT1 and Flag-TPP1 plasmids. Cell lines were engineered by integrating gene cassettes containing Tet-inducible *TPP1* genes into a unique targeting site in the genome of the HeLa-EM2-11ht cell line (Tet Systems Holdings GmbH & Co. KG) using Flp recombinase-mediated cassette exchange. Where indicated, the integration cassette contained a bi-directional Tet-inducible promoter driving both shTPP1 and shRNA-resistant *TPP1* genes in opposite directions. FISH and IF experiments were performed by modifying existing protocols²⁷ (<http://delangelab.rockefeller.edu/protocols.html>).

Full Methods and any associated references are available in the online version of the paper.

Received 24 May; accepted 4 October 2012.

Published online 24 October 2012.

1. Palm, W. & de Lange, T. How shelterin protects mammalian telomeres. *Annu. Rev. Genet.* **42**, 301–334 (2008).
2. Greider, C. W. & Blackburn, E. H. A telomeric sequence in the RNA of Tetrahymena telomerase required for telomere repeat synthesis. *Nature* **337**, 331–337 (1989).
3. Lingner, J. *et al.* Reverse transcriptase motifs in the catalytic subunit of telomerase. *Science* **276**, 561–567 (1997).
4. Baumann, P. & Cech, T. R. Pot1, the putative telomere end-binding protein in fission yeast and humans. *Science* **292**, 1171–1175 (2001).
5. Houghtaling, B. R., Cuttonaro, L., Chang, W. & Smith, S. A dynamic molecular link between the telomere length regulator TRF1 and the chromosome end protector TRF2. *Curr. Biol.* **14**, 1621–1631 (2004).
6. Liu, D. *et al.* POT1 interacts with POT1 and regulates its localization to telomeres. *Nature Cell Biol.* **6**, 673–680 (2004).
7. Ye, J. Z. *et al.* POT1-interacting protein PIP1: a telomere length regulator that recruits POT1 to the TIN2/TRF1 complex. *Genes Dev.* **18**, 1649–1654 (2004).
8. Lei, M., Podell, E. R. & Cech, T. R. Structure of human POT1 bound to telomeric single-stranded DNA provides a model for chromosome end-protection. *Nature Struct. Mol. Biol.* **11**, 1223–1229 (2004).

9. Wang, F. *et al.* The POT1–TPP1 telomere complex is a telomerase processivity factor. *Nature* **445**, 506–510 (2007).
10. Lue, N. F. Adding to the ends: what makes telomerase processive and how important is it? *Bioessays* **26**, 955–962 (2004).
11. Latrick, C. M. & Cech, T. R. POT1–TPP1 enhances telomerase processivity by slowing primer dissociation and aiding translocation. *EMBO J.* **29**, 924–933 (2010).
12. Tejera, A. M. *et al.* TPP1 is required for TERT recruitment, telomere elongation during nuclear reprogramming, and normal skin development in mice. *Dev. Cell* **18**, 775–789 (2010).
13. Abreu, E. *et al.* TIN2-tethered TPP1 recruits human telomerase to telomeres *in vivo*. *Mol. Cell. Biol.* **30**, 2971–2982 (2010).
14. Xin, H. *et al.* TPP1 is a homologue of ciliate TEBP- β and interacts with POT1 to recruit telomerase. *Nature* **445**, 559–562 (2007).
15. Denchi, E. L. & de Lange, T. Protection of telomeres through independent control of ATM and ATR by TRF2 and POT1. *Nature* **448**, 1068–1071 (2007).
16. Guo, X. *et al.* Dysfunctional telomeres activate an ATM-ATR-dependent DNA damage response to suppress tumorigenesis. *EMBO J.* **26**, 4709–4719 (2007).
17. Hockemeyer, D. *et al.* Telomere protection by mammalian Pot1 requires interaction with Tpp1. *Nature Struct. Mol. Biol.* **14**, 754–761 (2007).
18. Cristofari, G. & Lingner, J. Telomere length homeostasis requires that telomerase levels are limiting. *EMBO J.* **25**, 565–574 (2006).
19. Zaug, A. J., Podell, E. R., Nandakumar, J. & Cech, T. R. Functional interaction between telomere protein TPP1 and telomerase. *Genes Dev.* **24**, 613–622 (2010).
20. Zhong, F. L. *et al.* TPP1 OB-fold domain controls telomere maintenance by recruiting telomerase to chromosome ends. *Cell* **150**, 481–494 (2012).
21. Sexton, A. N., Youmans, D. T. & Collins, K. Specificity requirements for human telomere protein interaction with telomerase holoenzyme. *J. Biol. Chem.* <http://dx.doi.org/10.1074/jbc.M112.394767> (2012).
22. Miyoshi, T., Kanoh, J., Saito, M. & Ishikawa, F. Fission yeast Pot1–Tpp1 protects telomeres and regulates telomere length. *Science* **320**, 1341–1344 (2008).
23. Moser, B. A., Chang, Y. T., Kosti, J. & Nakamura, T. M. Tel1^{ATM} and Rad3^{ATR} kinases promote Ccq1–Est1 interaction to maintain telomeres in fission yeast. *Nature Struct. Mol. Biol.* **18**, 1408–1413 (2011).
24. Yamazaki, H., Tarumoto, Y. & Ishikawa, F. Tel1^{ATM} and Rad3^{ATR} phosphorylate the telomere protein Ccq1 to recruit telomerase and elongate telomeres in fission yeast. *Genes Dev.* **26**, 241–246 (2012).
25. Park, J. I. *et al.* Telomerase modulates Wnt signalling by association with target gene chromatin. *Nature* **460**, 66–72 (2009).
26. Majerská, J., Sykorová, E. & Fajkus, J. Non-telomeric activities of telomerase. *Mol. Biosyst.* **7**, 1013–1023 (2011).
27. Abreu, E., Terns, R. M. & Terns, M. P. Visualization of human telomerase localization by fluorescence microscopy techniques. *Methods Mol. Biol.* **735**, 125–137 (2011).

Supplementary Information is available in the online version of the paper.

Acknowledgements We thank T. de Lange, M. Terns and S. Langer for suggestions and sharing protocols; T. Nahreini for maintenance of the departmental tissue culture facility; J. Friedman and G. Voeltz for help with confocal microscopy; and A. Berman, S. Borah and M. Nakashima for critical reading of the manuscript. T.R.C. is an investigator of the Howard Hughes Medical Institute (HHMI). J.N. was an HHMI fellow of the Helen Hay Whitney Foundation during a major part of this study and is supported by the National Cancer Institute of the National Institutes of Health under award number K99CA167644. This work was supported in part by US National Institutes of Health grant R01GM29090 to L.A.L. and R01GM099705 to T.R.C.

Author Contributions J.N. and T.R.C. conceived the project and designed experiments with help from I.W. and L.A.L. on biological aspects. C.F.B. with help from J.N. and A.J.Z. conducted protein purifications, DNA-binding assays and telomerase assays. J.N. and I.W. constructed the stable HeLa cell lines. J.N. performed all remaining experiments including molecular cloning, cell culture, co-IP, TRF analysis and IF–FISH. J.N. and T.R.C. wrote the paper.

Author Information Reprints and permissions information is available at www.nature.com/reprints. The authors declare competing financial interests: details are available in the online version of the paper. Readers are welcome to comment on the online version of the paper. Correspondence and requests for materials should be addressed to T.R.C. (thomas.cech@colorado.edu).

METHODS

All experiments involving recombinant TPP1 expressed in bacteria⁹ used TPP1(N) (amino acids 87–334), which recapitulates all *in vitro* functions of the full-length human protein⁹. Experiments involving TPP1 expressed in human cells used full-length TPP1 that we define as starting from amino acid Met 87 (refs 9, 14) (Fig. 1a).

Oligonucleotides. Synthetic oligonucleotides used in gel-shift, filter-binding and telomerase activity assays were purchased from Integrated DNA Technologies and resuspended in 10 mM Tris-Cl (pH 8.0) to obtain 50 μ M stocks that were stored at -20°C and diluted to required concentrations immediately before use.

Plasmid constructs for cell-based assays. Mammalian cell expression plasmids encoding human TERT (pTERT-cDNA6/Myc-His C¹⁸) and human TR (pTR-Bluescript II SK(+)¹⁸) were a gift from J. Lingner. The pd1gfpPtetmiR and pTet-BI4 vectors, and HeLa-EM2-11ht cell line were obtained from Tet Systems Holdings GmbH & Co. KG upon signing a materials transfer agreement. The pTet-BI4 vector, which contains a bidirectional tetracycline-inducible promoter (Ptet-bi), allows for doxycycline (dox)-dependent expression (Tet-on) of genes in the HeLa-EM2-11ht cell line, which constitutively expresses the reverse tetracycline-controlled transactivator gene²⁸. The pIRES2-EGFP Rac2 plasmid²⁹ that was used to PCR-amplify IRES-GFP was a gift from G. Johnson.

shRNA and shRNA-resistant constructs of TPP1. The target sequence for shRNAs illustrated in Supplementary Fig. 8 are as follows: shRNA-A, 5'-CGT TGCATCCGCTGGGTGT-3'; shRNA-B, 5'-TGGAGTTCAAGGAGTTTGT-3'; shRNA-C, 5'-GACTTAGATGTTTCAGAAAA-3'¹³. shTPP1, shown in Fig. 3, contains two repeats each of shRNA-B and shRNA-C arranged in tandem. shRNA-resistant mutations were introduced by site-directed mutagenesis using the following primers (and their reverse complements): shRNA-A resistant, 5'-GGA AACCCGGGCCCCcTtCaCCCGCTcGgAGtGcCCGTGGGGATG-3'; shRNA-B resistant, 5'-CCCCAGAAACCTAGCCTcGAaTTtAAGGAaTtCGTcGGGTTG CCCTGCAAG-3'; shRNA-C resistant, 5'-GGGTGCTGGTTCGAACCAAG AtcTtGATGtCaAaAGAGCTCTATGACTGCCTTGAGG-3'; where lower-case indicates silent mutations introduced in the TPP1 gene to make the mRNA resistant to the indicated shRNA. In addition to possessing the duplex RNA sequence for silencing, all shRNA constructs also contained critical sequence elements derived from microRNA mR-30 for increasing the efficiency of RNA silencing³⁰.

Immunoblotting. Standard immunoblot protocols were used with the following antibodies at specified dilutions: mouse monoclonal anti-Flag M2-HRP conjugate (Sigma; A8592; 1:10,000), rabbit monoclonal TERT (C-term) antibody (Epitomics; 1531-1; 1:500), mouse monoclonal anti- β -actin antibody (Sigma; A5441; 1:10,000), and mouse monoclonal TPP1 antibody (Abnova; H00065057-M02; 1:1,000). Secondary horseradish peroxidase-conjugated goat antibodies against rabbit IgG (Santa Cruz Biotechnology; 1:10,000) or donkey antibodies against mouse IgG (Jackson ImmunoResearch; 1:10,000) were used to reveal the primary antibodies using chemiluminescence detection by ECL plus reagents (GE Healthcare Lifesciences). The data were visualized and quantified using a FluorChem HD2 (Alpha Innotech) imaging system.

Molecular cloning. C-terminally 3 \times -Flag-tagged human TPP1 and C-terminally 3 \times -Flag-tagged human POT1 genes were amplified from human TPP1 cDNA (Open Biosystems; Thermo Scientific) and POT1 cDNA (pET-Smt3-POT1; unpublished results), respectively, using forward primers containing a NotI site upstream of the start codon and reverse primers that contained: a stop codon-to-serine mutation, a DNA sequence coding for a 3 \times -Flag tag, and a terminal SalI site at the 5' end. For transient transfection experiments, the PCR fragments were restriction digested and cloned upstream of the IRES-GFP in the pTet-IRES-eGFP-BI4 vector (obtained by cloning a PCR-amplified and restriction digested IRES-eGFP fragment into pTet-BI4) to furnish p3 \times -Flag-TPP1-BI4 and p3 \times -Flag-POT1-BI4 plasmids. Using this construct, TPP1 and GFP proteins are synthesized as separate polypeptides in the cell. For stable transfection purposes, the TPP1-IRES-GFP fragment was subcloned from the p3 \times -Flag-TPP1-BI4 vector to the pd1gfpPtetmiR vector (replacing the existing d1GFP gene in the vector) that contains the F/F3 FLP recombination sites flanking the multiple cloning site to yield p3 \times -Flag-TPP1-F3 constructs that were subsequently used for stable transfection. p3 \times -Flag-TERT-cDNA6/Myc-HisC, which contains an N-terminal 3 \times -Flag tag immediately upstream from the TERT start codon, was obtained via site-directed mutagenesis of pTERT-cDNA6/Myc-HisC¹⁸. For stable co-transfections with shTPP1 and shTPP1-resistant TPP1, the bi-directionality of the pTet promoters of pTet-IRES-eGFP-BI4 and pd1gfpPtetmiR was exploited. Whereas the TPP1 constructs were cloned as mentioned above, the shTPP1 was cloned between the SpeI/NheI sites of the second multiple cloning site downstream of the second pTet element. The shTPP1-resistant mutations were made by site-directed mutagenesis (as detailed below).

Site-directed mutagenesis. Missense mutations were introduced into the TPP1 gene using fully complementary mutagenic primers (QuickChange site-directed

mutagenesis kit from Agilent Technologies). For the generation of TPP1(N) mutants for overexpression in bacteria, the pET-Smt3-TPP1(N) plasmid⁹ was used as the template in the PCR, whereas for expression in the HeLa-EM2-11ht cell line, p3 \times -Flag-TPP1-BI4 was used as the template in the PCR. The TPP1 genes in the mutant plasmids were sequenced completely to verify the presence of the intended mutation(s) and exclude the acquisition of unwanted changes during PCR amplification and cloning.

Protein purification. Purified mutant and wild-type Smt3-TPP1(N) fusion proteins were obtained from soluble lysates of isopropyl β -D-thiogalactopyranoside-induced BL21(DE3) cells after nickel-agarose chromatography, treatment with Ulp1 protease to cleave the Smt3 tag¹ and size-exclusion chromatography⁹. Purified recombinant human POT1 protein was obtained from baculovirus-infected insect cells as described previously⁸.

Gel-shift and filter-binding assays. Electrophoretic mobility shift assays and filter-binding assays of POT1-TPP1-oligonucleotide complexes were performed exactly as described previously³².

Cell culture. All human cells were cultured at 37 $^{\circ}\text{C}$ with 5% CO₂. HEK 293T cells were cultured in growth medium containing Dulbecco's modified Eagle medium (DMEM) supplemented with 10% fetal bovine serum (FBS), 2 mM glutamax (Life Technologies), 100 units ml⁻¹ penicillin, and 100 μ g ml⁻¹ streptomycin. HeLa-EM2-11ht and stable cell lines derived from it were propagated in growth medium containing DMEM, 10% FBS, 2 mM glutamax, 1 mM sodium pyruvate, 100 units ml⁻¹ penicillin and 100 μ g ml⁻¹ streptomycin. Doxycycline was added to a final concentration of 200 ng ml⁻¹ for induction of pTet-driven genes.

Telomerase preparations. Telomerase preparations from HEK 293T cell extracts (super-telomerase) were obtained from transient transfection of TERT and TR using a published protocol¹⁸. For telomerase preparations from HeLa-EM2-11ht cells, 300,000 cells per well of a 6-well plate were seeded and transfected 42 h later using Lipofectamine 2000 (Invitrogen) and indicated plasmid DNA using the manufacturer's recommendation. 1 μ g p3 \times -Flag-TERT-cDNA6/Myc-HisC and 3 μ g pTR-Bluescript II SK(+)¹⁸ were added per transfection. For transfections involving POT1 or TPP1, 1 μ g of p3 \times -Flag-POT1-BI4 or p3 \times -Flag-TPP1-BI4 was added per transfection. In control transfections where POT1 and TPP1 were omitted, pTet-BI4²⁸ (empty vector) was included. Medium was removed after 5 h and exchanged with fresh medium containing 200 ng ml⁻¹ doxycycline to induce TPP1 and/or POT1 expression from the tetracycline-driven promoter. After 48 h of transfection, the cells were trypsinized, washed with phosphate buffered saline (PBS), re-suspended in 100 μ l CHAPS lysis buffer¹¹ containing 1 μ l of RNasin plus (Promega), mixed with rocking on a nutator at 4 $^{\circ}\text{C}$ for 20 min, and centrifuged (13,600 r.p.m., 10 min) to remove cell debris. Aliquots of the soluble cell lysates were flash frozen in liquid nitrogen and stored at -80°C .

Telomerase activity assays. Telomerase reactions were carried out as 20 μ l reactions containing: 50 mM Tris-Cl (pH 8.0), 30 mM KCl, 1 mM MgCl₂, 1 mM spermidine, 5 mM β -mercaptoethanol, the indicated concentration of primer a5 or b⁹, 500 μ M dATP, 500 μ M dTTP, 2.92 μ M unlabelled dGTP, 0.33 μ M radiolabelled dGTP (3,000 Ci mmol⁻¹), and 3 μ l of super-telomerase cell extract (or telomerase from HeLa-EM2-11ht cell extracts) at 30 $^{\circ}\text{C}$ for 30 min. Reactions were stopped with buffer containing 100 μ l of 3.6 M ammonium acetate, 20 μ g of glycogen and a 5' end-labelled (7.5 c.p.m. μ l⁻¹) 18mer oligonucleotide loading control, and precipitated with ethanol. The pellets were re-suspended in 10 μ l H₂O and 10 μ l of loading buffer (95% formamide, 5% H₂O, loading dye), heated at 95 $^{\circ}\text{C}$ for 10 min, and loaded onto a 10% acrylamide, 7 M urea, 1 \times TBE sequencing gel. Gels were run at 90 W for 1.75 h, dried, exposed to an image plate and imaged on a phosphorimager (Typhoon Trio). The data were analysed using Imagequant TL software and telomerase activities quantified as described previously¹¹. Processivity calculations were performed as described previously¹¹ (Supplementary Fig. 4) although it was not possible to include the higher molecular weight products on the gel in these calculations due to severe band overlap. To include the contributions of these upper bands (which are the result of the highly processive action of telomerase; data not shown) in processivity measurements, we defined a '15+' relative processivity term as the fraction of the total activity present in bands resulting from 15 (number chosen arbitrarily to define the lower limit of high processivity) or more telomeric repeats added by telomerase (Fig. 1d and Supplementary Fig. 3c), noting that the '15+' method does not correct for the greater number of G nucleotides (three per repeat) in the upper bands compared to lower bands.

Co-immunoprecipitation experiments. The protocol was adapted from a previously published protocol⁷. HeLa-EM2-11ht cells were seeded and transfected as stated above for telomerase preparations. After 24 h of transfection, cells were washed with PBS, dislodged with a cell-scraper using 400 μ l ice-cold lysis buffer (50 mM Tris-Cl (pH 7.4), 20% glycerol, 1 mM EDTA, 150 mM NaCl, 0.5% Triton X-100, 0.02% SDS, 1 mM dithiothreitol, 2 mM phenylmethylsulphonyl fluoride, complete protease inhibitor cocktail (Roche)) and kept on ice. After 5 min, 20 μ l of 5 M NaCl was added and mixed. After another 5 min on ice, 420 μ l of ice-cold

water was added and mixed before immediate centrifugation (13,600 r.p.m., 10 min). Supernatants were collected and used directly for immunoprecipitation. Lysate (40 μ l) added to 40 μ l of 4 \times LDS sample loading buffer (Invitrogen) was kept aside for analysis of 'input' samples. Anti-Flag/M2 affinity gel beads (50 μ l; Sigma) pre-incubated with 100 mg ml⁻¹ of bovine serum albumin in PBS were added to lysate prepared from each well of a 6-well plate. Mixtures were mixed with rocking on a nutator for 2 h at 4 °C. Beads were washed three times with 1:1 diluted lysis buffer and proteins were eluted with 180 μ l 1:1 diluted 4 \times LDS sample loading buffer (Invitrogen) for analysis of 'beads' samples. All 'input' (10 μ l) and 'beads' (15 μ l) samples were heated at 90 °C for 12–14 min and analysed by SDS-PAGE and immunoblotting.

Stable cell line generation using HeLa-EM2-11ht cells and p3 \times -Flag-TPP1-F3 plasmids. Detailed protocols for stable transfection of HeLa-EM2-11ht cells are reported elsewhere³³. HeLa-EM2-11ht cells were co-transfected in a 6-well format using either Lipofectamine 2000 (Life Technologies) or TransIT (Mirus) using the manufacturer's protocol with 1 μ g each of the p3 \times -Flag-TPP1-F3 (containing wild type, E169A/E171A, R175V, or L212A mutants for experiments in Supplementary Fig. 9, and containing shTPP1 and shTPP1-resistant wild type, E169A/E171A, R175V, or L212A mutants for experiments in Fig. 3), and 1 μ g of a plasmid expressing Flp recombinase and conferring puromycin resistance. Twelve hours post-transfection, transfected cells were selected for 36 h using 5 μ g ml⁻¹ puromycin. Subsequently, fresh medium lacking puromycin but including 50–100 μ M ganciclovir (Sigma-Aldrich) was added and negative selection was conducted for 10 days. Next, 12 individual clones were picked from each transfection and expanded. To verify the identity of the clone and distinguish it from false-positive clones that survived selection, a small aliquot of cells was induced overnight with 200 ng ml⁻¹ doxycycline and observed under a fluorescence microscope (Supplementary Fig. 10a). Positive clones were selected based on green fluorescence arising from their IRES-GFP locus downstream of the *Flag-TPP1* gene (Fig. 3a) and also confirmed using flow cytometry (Supplementary Fig. 10b). The typical efficiency of cloning (positive clones/total survivors) using this protocol was between 8% and 50%. Positive clones were expanded until they grew to confluency in 10-cm culture dishes and induced with 200 ng ml⁻¹ doxycycline for studying the effect of TPP1 mutations in cells.

Telomere length analysis. Genomic DNA was isolated from confluent 10-cm culture dishes of the original HeLa-EM2-11ht cells and Flag-TPP1 expressing stable cell lines using the GenElute kit (Sigma). Genomic DNA (1.5 μ g) was restriction digested with frequent cutters *HinfI* and *RsaI* overnight at 37 °C. The DNA digests were run on a 0.8% Agarose-1 \times TBE gel at 50 V for a total of 1,100 V-hours. A 5' ³²P-labelled (with T4 PNK; NEB) λ DNA-HindIII digest ladder (10,000 c.p.m.) was run as a marker on a separate lane on the gel. Next morning, the gel was shaken in 0.25 M HCl for 15 min followed by two rounds (15 min each) of shaking in solution containing 0.5 M NaOH and 1.5 M NaCl. Next, the gel was shaken in solution containing 0.5 M Tris-Cl and 1.5 M NaCl (pH 7.5) for 30 min. The gel was blotted on the positively charged Hybond N+ (GE) membrane in 10 \times SSC buffer (1.5 M NaCl, 0.15 M sodium citrate at pH 7.2) overnight by capillary blotting. Next morning, the membrane was irradiated with UV (260 nm; set at 1,200 μ J \times 100 energy) and prehybridized in 15 ml Rapid-hyb (GE) for 30 min at 50 °C in a hybridization oven with rotation. 5' ³²P-labelled (with T4 PNK; NEB) telomeric probe of sequence (TTAGGG)_n was added (20,000,000 c.p.m.) and hybridization was continued for 1 h at 50 °C. The hybridization solution was discarded and the membrane was rinsed three times with buffer containing 0.1 \times SSC and 0.1% SDS. The membrane was washed three times in this buffer at 50 °C, wrapped in Saran-wrap, exposed to a phosphorimager screen for 24–72 h, and analysed using the Imagequant TL software. The gel was calibrated using the known molecular weights of the λ DNA-HindIII ladder and the mean telomere length for each lane was plotted as a function of population doubling for each cell line. A linear regression (MS Excel) was used to calculate the rate of telomere elongation.

Quantitative RT-PCR. Total RNA was purified from the indicated cell lines using TRIzol reagent (Life Technologies). Total cDNA was prepared from total RNA using the High Capacity cDNA reverse transcription kit (Applied Biosystems). A fragment of the cDNA from endogenous *TPP1* mRNA spanning a part of the 5' UTR (absent in Flag-tagged constructs) and continuing into the ORF was amplified, and qPCR was performed with the iQ SYBR green Supermix (Biorad) using the LightCycler 480 (Roche) equipment.

Immunofluorescence (IF) and fluorescence *in situ* hybridization (FISH). For IF and FISH experiments, protocols were adapted from those described previously in the literature²⁷ and online sources (<http://delangelab.rockefeller.edu/protocols.html>). For TIF analysis using co-immunofluorescence (co-IF), 10,000 cells of HeLa-EM2-11ht-derived stable cell lines were seeded on coverslips in a 12-well

culture plate containing growth medium adjusted to 200 ng ml⁻¹ doxycycline. After 96 h, medium was removed and all subsequent steps were performed at room temperature. Cells were washed once with PBS and fixed with 3% or 4% formaldehyde in PBS for 8 min. The fixative was removed and the cells washed three times with PBS. The cells were permeabilized with PBS containing 0.1% Triton X-100 (PBS-T) for 5 min and blocked in PBS-T containing nuclease-free 3% BSA for 30 min. Cells were incubated with mouse monoclonal anti-TRF2 (Imgenex; IMG-124A; 1:500) and rabbit polyclonal anti-53BP1 (Novus Biologicals; NB100-304; 1:1,000 dilution) in PBS-T containing nuclease-free 3% BSA for 1 h. The cells were then washed three times in PBS (5 min each), and incubated with Alexa Fluor 568-conjugated anti-mouse IgG (Life Technologies) and Alexa Fluor 647-conjugated anti-rabbit IgG (Life Technologies) diluted 1:500 in PBS-T containing nuclease-free 3% BSA for 30 min in the dark. The cells were then washed three times in PBS and the excess PBS was removed by blotting. The coverslips were mounted on microscope slides using Vectashield mounting medium with DAPI (Vector Laboratories), sealed using transparent nail polish and stored at 4 °C or -20 °C until the time of imaging. Detection of Flag-TPP1 and RAP1 by co-IF was done essentially as above, but with mouse monoclonal anti-Flag M2 (Sigma; F1804; 1:500) and rabbit polyclonal anti-RAP1 (Novus Biologicals; NB100-292; 1:500) primary antibodies.

For combined immunofluorescence-fluorescence *in situ* hybridization (IF-FISH) experiments, the IF was performed before FISH. Briefly, IF was performed as described above using the appropriate primary and secondary antibodies. After the final PBS wash, the cells were fixed again in 4% formaldehyde in PBS for 10 min at room temperature. The cells were washed twice with PBS and dehydrated by successive 5-min incubations in 70%, 95% and 100% ethanol. The ethanol was removed and the coverslips allowed to dry for 2 min. The cells were rehydrated in 50% formamide in 2 \times SSC for 5 min. The coverslips were placed (with cells facing down) on a drop (~40 μ l) of pre-hybridization solution containing 100 mg ml⁻¹ dextran sulphate, 0.125 mg ml⁻¹ *E. coli* tRNA, 1 mg ml⁻¹ nuclease-free BSA, 0.5 mg ml⁻¹ salmon sperm DNA, 1 mM vanadyl ribonucleoside complexes, and 50% formamide in 2 \times SSC for 1 h at 37 °C in a humidified chamber. Hybridization solution was made by adding a mixture of three Cy5-conjugated TR probes²⁷ (30 ng of each probe per coverslip) to the pre-hybridization solution and the cells were hybridized in this solution overnight at 37 °C in a dark humidified chamber. Next morning, the cells were washed twice in 50% formamide in 2 \times SSC and twice in PBS, and the coverslips were then mounted on microscope slides using ProLong Gold Antifade Reagent (Life Technologies). After 24 h at room temperature in the dark, the coverslips were sealed using transparent nail polish and stored at 4 °C or -20 °C until the time of imaging. In addition to antibodies mentioned above, rabbit polyclonal anti-coilin (Santa Cruz; sc-32860; 1:100) and Alexa Fluor 405-conjugated anti-mouse (and anti-rabbit) IgG antibodies (Life Technologies; 1:500) were used to stain and image Flag-TPP1 and Cajal bodies.

Microscopy. Imaging was performed using a Nikon TE2000-U inverted fluorescence microscope equipped with Photometrics Cascade II EM-CCD camera and Yokogawa Spinning disc Confocal (CSU-Xm2) (Nikon Instruments, Inc.) and a 60 \times oil objective. Images were acquired using Metamorph software. Linear image adjustments were made when necessary using ImageJ and Adobe Photoshop and applied to all images in a given channel. The colours depicted in the figures do not necessarily correspond to the emission of the fluorescent labels, but are used to facilitate visualization/analysis of 'merged' signals from two or more channels. Representative cells are shown in all microscopy figure panels. Quantification of co-localizations was done manually and plots of numbers of co-localizations per cell (one focal plane) show data obtained from 15 or more fields of cells (40–120 cells in total) for each sample set processed in parallel on the same day.

28. Weidenfeld, I. *et al.* Inducible expression of coding and inhibitory RNAs from retargetable genomic loci. *Nucleic Acids Res.* **37**, e50 (2009).
29. Abell, A. N. *et al.* Rac2^{D57N}, a dominant inhibitory Rac2 mutant that inhibits p38 kinase signaling and prevents surface ruffling in bone-marrow-derived macrophages. *J. Cell Sci.* **117**, 243–255 (2004).
30. Berger, S. M. *et al.* Quantitative analysis of conditional gene inactivation using rationally designed, tetracycline-controlled miRNAs. *Nucleic Acids Res.* **38**, e168 (2010).
31. Mossessova, E. & Lima, C. D. Ulp1-SUMO crystal structure and genetic analysis reveal several interactions and a regulatory element essential for cell growth in yeast. *Mol. Cell* **5**, 865–876 (2000).
32. Nandakumar, J., Podell, E. R. & Cech, T. R. How telomeric protein POT1 avoids RNA to achieve specificity for single-stranded DNA. *Proc. Natl Acad. Sci. USA* **107**, 651–656 (2010).
33. Weidenfeld, I. Inducible microRNA-mediated knockdown of the endogenous human lamin A/C gene. *Methods Mol. Biol.* **815**, 289–305 (2012).

ADDENDUM

doi:10.1038/nature11735

Addendum: The Cancer Cell Line Encyclopedia enables predictive modelling of anticancer drug sensitivity

Jordi Barretina, Giordano Caponigro, Nicolas Stransky, Kavitha Venkatesan, Adam A. Margolin, Sungjoon Kim, Christopher J. Wilson, Joseph Lehár, Gregory V. Kryukov, Dmitriy Sonkin, Anupama Reddy, Manway Liu, Lauren Murray, Michael F. Berger, John E. Monahan, Paula Morais, Jodi Meltzer, Adam Korejwa, Judit Jané-Valbuena, Filipa A. Mapa, Joseph Thibault, Eva Bric-Furlong, Pichai Raman, Aaron Shipway, Ingo H. Engels, Jill Cheng, Guoying K. Yu, Jianjun Yu, Peter Aspesi Jr, Melanie de Silva, Kalpana Jagtap, Michael D. Jones, Li Wang, Charles Hatton, Emanuele Palescandolo, Supriya Gupta, Scott Mahan, Carrie Sougnez, Robert C. Onofrio, Ted Liefeld, Laura MacConaill, Wendy Winckler, Michael Reich, Nanxin Li, Jill P. Mesirov, Stacey B. Gabriel, Gad Getz, Kristin Ardlie, Vivien Chan, Vic E. Myer, Barbara L. Weber, Jeff Porter, Markus Warmuth, Peter Finan, Jennifer L. Harris, Matthew Meyerson, Todd R. Golub, Michael P. Morrissey, William R. Sellers, Robert Schlegel & Levi A. Garraway

Nature **483**, 603–607 (2012); doi:10.1038/nature11003

In the Supplementary Information of this Letter, the use of distinct data normalization and directionality methods for pharmacological response calculations caused minor inconsistencies. We have therefore updated Supplementary Table 11 and some of the Supplementary Figures to resolve any confusion (see the Supplementary Information to this Addendum). We also wish to describe the relevant drug sensitivity normalization and response score calculations more completely.

Two versions of the drug response data were generated. First, raw activity values were calculated at each dose as $A = 100(T/U - 1)$, in

which T represents the Cell Titer Glo (CTG) level measured for the compound-treated well, and U is the median level of the untreated wells across the plate. This raw A is 0% with no drug and 100% for fully active compounds, when no CTG is detected. Second, the data were adjusted to a plate surface pattern and normalized to the MG132 positive control, as described in the Supplementary Methods. This normalized A is also 0% with no drug, but 100% corresponds to the median MG132 response on that plate. Although normalized drug responses were used to determine EC_{50} , IC_{50} and A_{max} values, we used the raw drug responses for calculating the activity area (AA). This distinction is now clear in the corrected Supplementary Table 11 (the two AA measures, derived from raw or normalized data, correlate closely: $r = 0.98$).

The activity is the sum of differences between the measured A_i at concentration i and $A = 0$, excluding positive A values: $AA = \sum i\{0 - \min(0, A_i/100)\}$. This AA has a value of 0 with no drug, and +8 for a compound inhibiting at $A = 100\%$ at all eight drug concentrations, as illustrated in Fig. 2b of the original Letter. We hope that this definition eliminates any confusion that may have existed in the original Supplementary Methods (page 13) and enables others to reproduce our AA results starting from the raw drug sensitivity data. As a further means of clarification, we have added three columns to Supplementary Table 11 showing the raw (non-normalized) response data necessary to calculate AA, MG132 activity, and AA derived from normalized response data.

In addition, although all computational analyses used the above AA formula, a few Supplementary Figures (Supplementary Figs 6, 11, 9 and 14b) used a scale showing $8 - AA$. This value was used for display purposes, so that low values corresponded to sensitive cell lines and the visualization remained consistent with other sensitivity metrics (IC_{50} , A_{max}). This specification was noted in Supplementary Fig. 8 but had been inadvertently cut off the Supplementary Fig. 9 legend. We have therefore updated the Supplementary Fig. 9 legend to clarify where an inverted scale was used, and updated the scale of Supplementary Figs 6, 11 and 14b to reflect our definition of AA (noted above).

These changes do not affect the analyses, results or scientific conclusions presented in the paper. The authors are indebted to B. Yadav, who alerted them to these inconsistencies.

Supplementary Information is available in the online version of the Addendum.

TWO MICROSCOPES ARE BETTER THAN ONE

Using two different kinds of imaging can give scientists a powerful combination of high specificity and detailed structural information.

CARL ZEISS MICROSCOPY



This image of a butterfly wing was constructed using two types of microscopy: a confocal image of the reflective eyespots shows scales (green) and wing (red); scanning electron microscopy reveals the different structure of non-reflective scales (upper left).

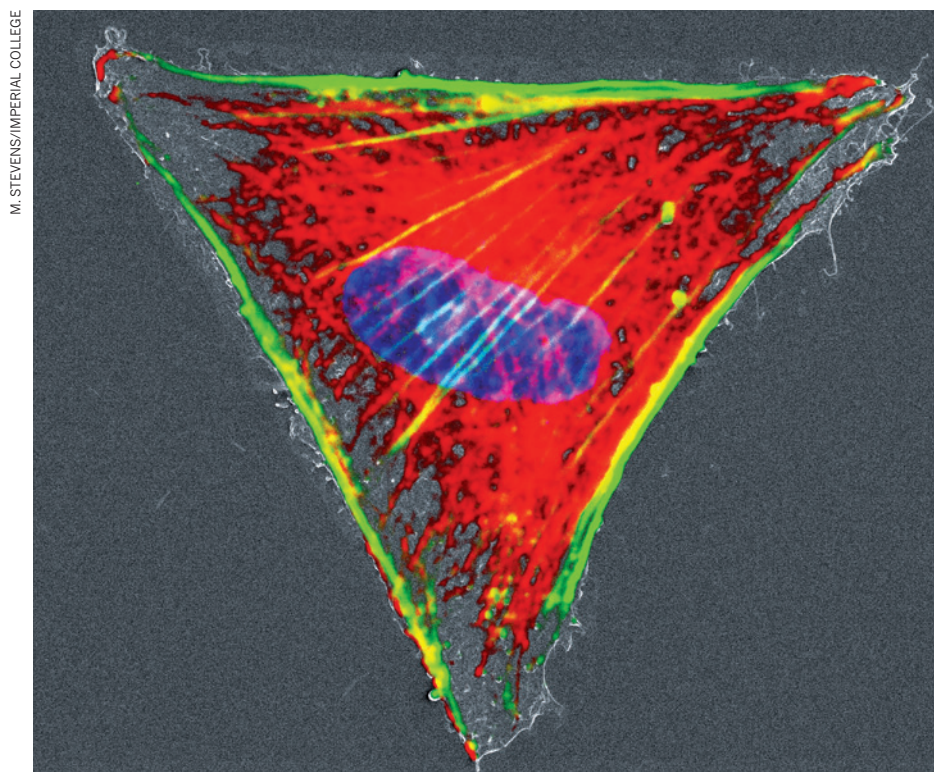
BY CAITLIN SMITH

There are many types of microscopy, each providing a unique set of benefits. Light microscopy of cells that express fluorescently labelled molecules, for example, lets scientists observe the movements of specific molecules or protein complexes in live cells in real time, or in fixed samples. Scanning electron microscopy (EM) reveals tiny details of the cell surface, and transmission

EM shows the detailed cytoarchitecture of sections through fixed tissue. Other aspects of the structure of cells and tissues can be explored using techniques such as ion microscopy, total internal reflection microscopy, atomic force microscopy and super-resolution microscopy. Each type provides different information, but using two sorts of microscopy simultaneously provides even more — and molecular tools have been developed to link them together. Researchers testing the waters of this

‘correlative microscopy’ are beginning to discover its challenges and rewards.

Correlated light–electron microscopy, for example, provides both the specificity and real-time observation of light microscopy with fluorescent labelling and the better structural resolution of EM. But such correlative microscopy has historically been tricky to use. Scientists who tried it might have needed to switch to EM halfway through an experiment, which meant moving the sample from one ►



Composite image created from correlated light-ion microscopy showing a fibroblast stained to show tubulin (red), actin (green) and the nucleus (blue).

► microscope to another that may be located in a different lab, or even in another building. Not only would this journey take time, but delicate samples could be damaged by the motion, or by changes in temperature or humidity.

A second obstacle is the need to ‘find back’, which means searching the thin section prepared for EM to relocate the region observed under the light microscope. To help them find the sample, scientists could create fiducial markers, which act as landmarks to pinpoint the area of interest — they could be marks etched onto the sample dish, for example. But even then, the process is not straightforward, and correlative microscopy has faced a slow uptake.

Instrument manufacturers have developed several solutions to address these problems. In the summer of 2010, Carl Zeiss, based in Jena, Germany, released the Shuttle & Find. This consists of a sample holder, enabling tissue sections to be transported safely, and a software module that connects to both microscopes and uses a coordinate system to find the region of interest. According to Kirk Czymmek, director of North American labs at Carl Zeiss Microscopy in Thornwood, New York, this approach offers a way of “relocating the region of interest in

different microscope systems within a matter of minutes — a task that until now had taken hours, and sometimes even days”.

Another way to make finding back easier is to use thicker tissue sections in EM. Cell biologist Judith Klumperman, director of the Cell Microscopy Center at the Utrecht University Medical Center in the Netherlands, says that she uses correlative light-electron microscopy to characterize “distinct endosome populations by their dynamics, interactions, subcellular localization, cargo, protein composition and ultrastructural morphology”. After observing the dynamics of fluorescently labelled lysosomal proteins with a light microscope, for example, her group uses EM to study their structural details. “When using thin 80–100-nanometre sections, these structures will appear in only one or two EM sections of the 20 to 40 that are generally obtained from one cell,” says Klumperman. “With three-dimensional electron tomography, we can use 300–400-nanometre sections, which increases the chance of finding back the region of interest”.

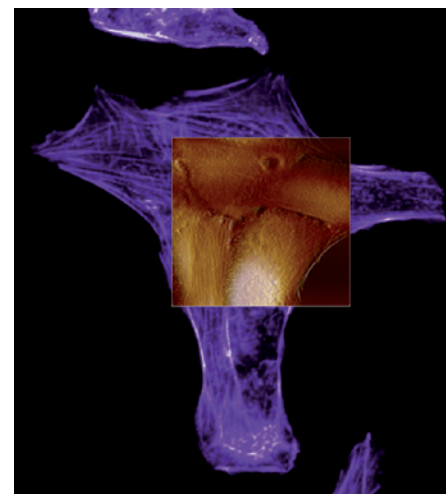
There is no need to switch between microscopes if one instrument integrates both fluorescence and electron microscopy. Furthermore, using the same stage reduces the chance of damaging the specimen and makes it easier to find back the region of interest. Zeiss’s Merlin, for example, has all these features and also offers the option of an integrated atomic force microscope (see

‘Multimodal microscopy’) in the vacuum chamber of its scanning EM. A range of similar correlative microscopes is produced by FEI based in Hillsboro, Oregon.

The ClairScope, produced by Japanese company JEOL, based in Tokyo, has a different solution to the same problems. It has an inverted scanning EM below the culture dish, which can be viewed at atmospheric pressure, and an optical microscope above it. A window coated with a silicon nitride film allows electrons to be projected from underneath while maintaining a vacuum between the EM and the sample dish. This set-up allows researchers to perform concurrent imaging of a sample in solution by both microscopes, says Donna Guarrera, assistant director in the SEM Division at JEOL USA. “There is no running from the optical microscope lab, then preparing the sample to be vacuum-compatible for SEM imaging.”

Despite recent improvements, technical difficulties still limit what scientists can accomplish with correlated light and electron microscopy. Jeffrey Caplan, associate director of the University of Delaware’s bioimaging centre, finds that the speed of fixation is holding him back — he would like to study live-cell dynamics and then immobilize the cells rapidly for EM imaging. “Current cryo-fixation methods take about 10 seconds to a couple of minutes,” he says, “but we would like a tool that can stop movement of dynamic structures in less than one second if possible.” This would make it easier to study dynamic events such as vesicle docking and trafficking, cytoskeletal remodelling and calcium signalling¹.

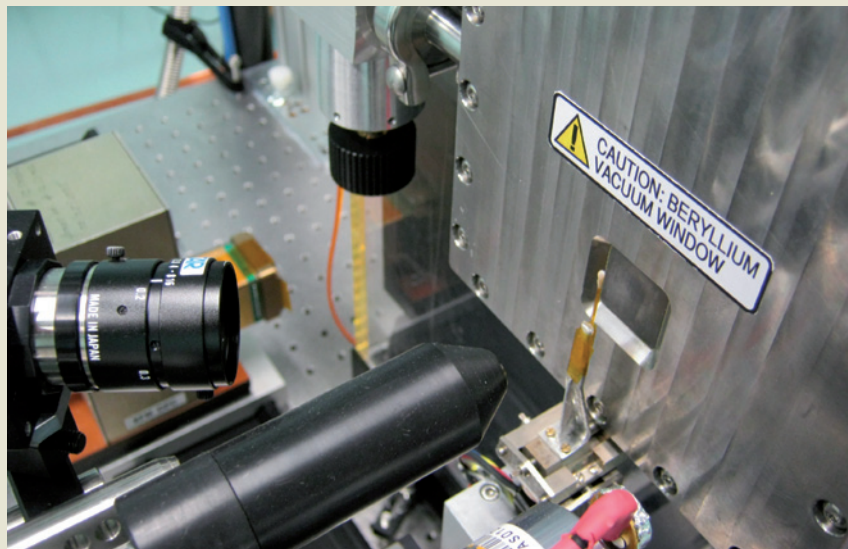
Immunogold labelling has historically been the gold standard for identifying subcellular structures in EM. However, the sheer bulk of gold-labelled antibodies can interfere with the identification of targets with single-molecule precision. Caplan’s group is now developing



Correlated epifluorescence (purple) and atomic force microscopy (brown) images of live osteocarcinoma cells stained for actin.

“There is no need to switch between microscopes if one instrument integrates both forms of microscopy.”

Multimodal microscopy



The Australian Synchrotron's beamline allows fine measurements in multimodal microscopy.

Correlative microscopy is becoming more widespread as fresh opportunities to correlate different types of imaging data arise. “Rather than just correlative imaging, the goal is to combine a whole suite of characterization methods into something that might better be described as multimodal microscopy,” says Andrew Peele, director of science at the Australian Synchrotron in Clayton, a suburb of Melbourne, Australia. The synchrotron is a circular particle accelerator, about the size of a football field, where strong magnetic fields force high-energy electrons to travel round its tunnels. The intense beams of light it generates, usually optimized in the X-ray region, can be used for imaging experiments that may include X-ray fluorescence, X-ray diffraction, light microscopy, electron microscopy, tomography or infrared microscopy, says Peele.

Despite all these options, multimodal imaging is not straightforward. “One

of the challenges we face is comparing information across widely different techniques,” says Peele, “especially those with quite different resolutions”, such as fluorescence data and high-resolution diffraction data.

Other labs are using multimodal imaging, too. Molly Stevens, a biomedical materials professor at Imperial College London, hopes her research using correlative microscopy will advance our understanding of cells and their environments, perhaps leading to applications such as the design of biomaterials and scaffolds for tissue engineering. Her group is currently developing a protocol for correlating images from electron and ion microscopy, and following it with fluorescence imaging. “Then we will be able to correlate topographical information, ultrastructures of cells and specific biochemical changes using fluorescently tagged proteins,” she says. **C.S.**

an alternative to immunogold labelling for electron and super-resolution microscopy “to ensure that single-molecule localizations are accurately mapped onto the EM image”, he says.

LIGHT-ION MICROSCOPY

One drawback of correlative light–electron microscopy is the fixed order of tasks: fluorescence microscopy must be carried out before EM, rather than after it, because the electron beam can destroy the fluorescence signal. It is therefore not possible to verify fluorescence microscopy results after EM. Scanning ion

microscopy may provide the answer.

Biomedical materials professor Molly Stevens and her colleagues at Imperial College London recently described correlated light–ion microscopy (CLIM), in which fluorescence microscopy is correlated with ion microscopy². Ion microscopy is similar to EM except that a beam of ions is used to scan the sample, instead of electrons. After imaging the fluorescent signal, Stevens and her colleagues fixed the sample and performed ion microscopy by scanning it with a beam of gallium ions. “I believe that helium ions might also work,” says Sergio Bertazzo, a postdoctoral researcher

in Stevens’ lab. “One concern we have is that helium ions might penetrate much more into the sample, damaging the fluorescence signal.” Because the gallium ions did not damage it, the scientists could go back and forth between the two microscopy techniques. They could revisit the fluorescence in the sample after assessing its three-dimensional structure with scanning ion microscopy — several times for the same sample, in fact.

“We have used this to study how cells interact with environments such as biomaterials, scaffolds for tissue engineering, and 2D micropatterned surfaces”, which guide cell growth in specified geometries, Stevens says.

Her group has also combined ion microscopy with total internal reflection fluorescence microscopy, a technique that can boost the resolving power to single-molecule resolution near the edges of the cell. The resulting sub-micrometre scale resolution allowed Stevens’ group to see a migrating fibroblast in an intermediate step of the migration process, with one edge mobilized for travel and the opposite edge still firmly adhering to the substrate².

FLUORESCENCE-ATOMIC FORCE MICROSCOPY

In another approach called atomic force microscopy (AFM), the sample is scanned by the tip of a sensitive cantilever probe, providing high-resolution, three-dimensional, structural information. Unlike electron microscopy, AFM can deliver three-dimensional images of live cells without requiring imaging agents such as fluorophores, and it can detect single molecules with nanometre resolution.

There is a practical reason why microscopy companies sometimes correlate AFM and light microscopy. “AFM can only visualize a very small area at a time, so you are essentially hunting around blind without correlation with light microscopy,” says Ben Ohler, product manager for research atomic force microscopes at Bruker, based in Billerica, Massachusetts. “Some basic correlation is simply a requirement to participate in the market.”

Nicholas Geisse, a bio-applications scientist at Asylum Research in Santa Barbara, California, which specializes in AFM, thinks that AFM needs to have faster imaging to keep up with millisecond-scale fluorescence microscopy measurements. Asylum’s Cypher AFM was designed for faster scanning and data acquisition, he says. “Many of Cypher’s technical advancements, including the use of small cantilevers, have enabled high-speed scanning.”

Bruker’s latest instruments are also designed with speed in mind, says Ohler. “Where AFM images have typically taken minutes per image, Dimension FastScan Bio now acquires images in seconds, or even several images per second,” he says. He believes that such technology can lead to AFM measurements of dynamic biological events.

A research group in Italy is also heading in that direction. Physicist Alberto Diaspro, director of the nanophysics department at the Italian Institute of Technology in Genoa, is correlating AFM with super-resolution stimulated emission depletion (STED) microscopy to develop tools for topographical imaging, nanomechanical imaging, and measurements of cell stiffness³. In STED, researchers intentionally deactivate some fluorophores in part of the sample, which enhances the resolution in that area. Diaspro is optimistic that combining correlative-microscopy techniques with STED's nanoscale resolution will reveal valuable information about cellular nanostructures. The rapid image acquisition possible with STED also holds promise for measuring fast events, such as intracellular vesicle dynamics during secretion or neurotransmitter release, or cytoskeletal remodeling during cell motility.

FLUORESCENT BRIDGES

Researchers have long searched for a molecule that can bridge fluorescence and electron microscopy — a fluorescent molecule that also stains in EM images, for example. The ideal tool would be a genetically encodable molecular tag, small enough to penetrate fixed tissues better than awkward gold-labelled antibodies, but fluorescent and capable of delivering good contrast in EM. Two groups at the National Center for Microscopy and Imaging Research at the University of California, San Diego, are investigating a variety of molecules for use in more than one type of microscopy. Mark Ellisman, the centre's director, and biochemist Roger Tsien, who shared the 2008 Nobel Prize in Chemistry for developing the widely used green fluorescent protein (GFP) tag, often collaborate in what Ellisman calls “molecular painting” in the search for a reliable, genetically encodable tag to label proteins in EM. “We were looking for the GFP of electron microscopy,” says Ellisman.

Last year, researchers from both groups revealed a molecular tool they had engineered called mini singlet oxygen generator (mini-SOG), which is derived from a plant photoreceptor⁴. Singlet oxygen generator molecules are easy to see because they fluoresce in light microscopy and can be stained by diaminobenzidine for EM⁵. The group expressed proteins labelled with miniSOG to demonstrate its utility as a genetically encoded tag for protein targets in EM. “MiniSOG is an extremely good singlet oxygen generator, so we believe this one will get to single-molecule sensitivity,” says Ellisman. “We're working on that now.”

Meanwhile, miniSOG is already proving useful. Using a combination of microscopy techniques, molecular biologist Clodagh O'Shea and her colleagues at the Salk Institute for Biological Studies in La Jolla, California, are studying the puzzling observation that small viral oncoproteins seem to hijack



Clodagh O'Shea and her team use a variety of techniques to investigate viral oncoproteins.

cellular machinery to stimulate both viral and pathological cellular replication. According to O'Shea, her group wondered: “how do small viral oncoproteins win?” The group imaged infected cells by using miniSOG to label the adenovirus oncoprotein E4-ORF3 (ref. 6). Serial block-face scanning EM gave them reconstructed, three-dimensional views of infected cells. “The scanning electron microscope slices an infected cell from top to bottom in tiny 60-nm blocks,” says O'Shea. The group also used electron tomography to make hundreds of 0.5-nm-thick computational slices through cells, and used specialized software to recreate cells from the computed slices. “Three-dimensional reconstructions show that E4-ORF3 assembles into a remarkable network of cables that weaves through the nucleus,” she says. The images showed that the weave

“We have been looking for the green fluorescent protein of electron microscopy.”

A cousin of miniSOG is also on the horizon. Ellisman and former postdoc Alice Ting, now at the Massachusetts Institute of Technology in Cambridge, collaborated to create an enzyme called APEX that has enhanced singlet oxygen generator activity⁷. Ellisman stresses the importance of genetically encoded tags for miniSOG and APEX. “Both are molecules we can introduce genetically, and both will result in contrast in EM,” he says.

Researchers continue to push the limits of correlative microscopy. “We are currently developing a methodology that combines CLIM with super-high-resolution fluorescence microscopy,” says Stevens. “If successful, it will

offer a new way of studying molecular interactions.” Meanwhile, Ellisman and his colleagues are working on expressing two genetically encoded miniSOGs that have different colours. “This is what we call multicolour EM,” he says. “The idea is that you would be able to do your dynamic light microscopy, then correlate a high-resolution subvolume down to the molecular scale. It's a hard project, but we know we'll succeed.”

Bridging light and electron microscopy with genetically encodable fluorescent tags may one day be as routine as labelling with GFP is today. High-throughput methods applied to tissue sections may make super-resolution microscopy faster and easier. When that happens, two — or perhaps more — microscopes will definitely be better than one. ■

Caitlin Smith is a freelance science writer based in Portland, Oregon.

1. Caplan, J., Neither, M., Taylor, R. M. & Czymbek, K. J. *Curr. Opin. Struct. Biol.* **21**, 686–693 (2011).
2. Bertazzo, S., von Erlach, T., Goldoni, S., Candarhaglu, P. L. & Stevens, M. M. *Nanoscale* **4**, 2851–2854 (2012).
3. Harke, B., Chacko, J. V., Haschke, H., Canale, C. & Diaspro, A. *Opt. Nanoscopy* **1**, 3 (2012).
4. Shu, X. *et al. PLoS Biol.* **9**, e1001041 (2011).
5. Maranto, A. R. *Science* **217**, 953–955 (1982).
6. Ou, H. D. *et al. Cell* **151**, 304–319 (2012).
7. Martell, J. D. *et al. Nature Biotechnol.* **30**, 1143–1148 (2012).

CORRECTION

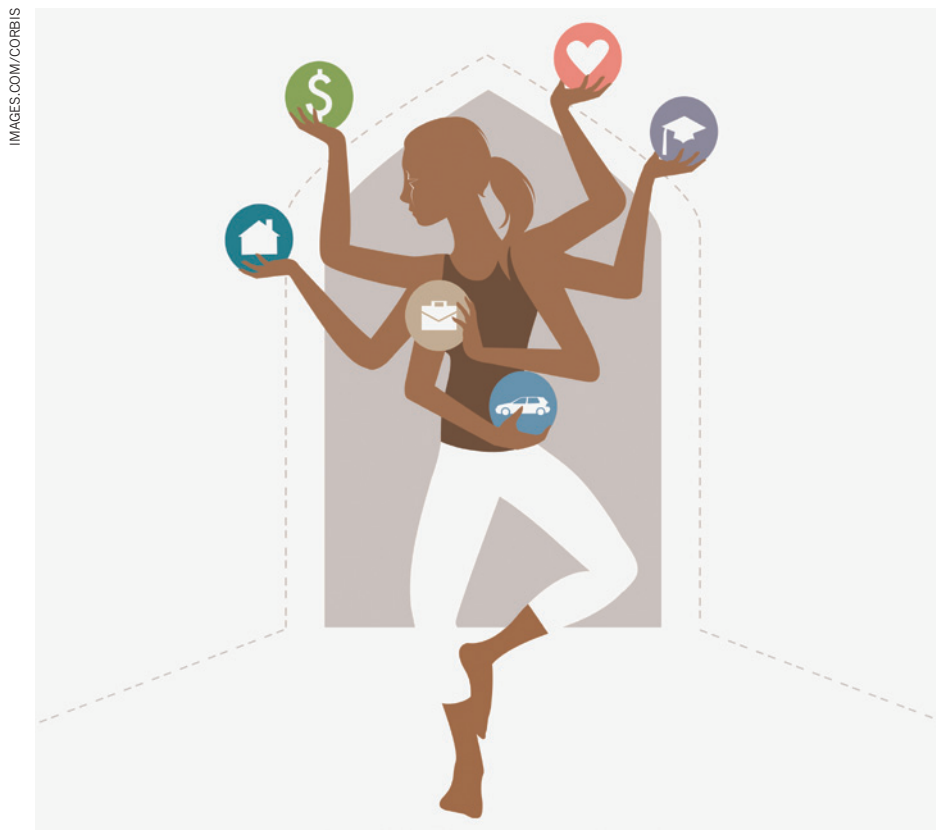
The Technology Feature ‘Reading the second genomic code’ (*Nature* **491**, 143–147; 2012) wrongly stated that Constellation and Genentech are collaborating to develop inhibitors of BET proteins and EZH2 chromatin-writers. Although they are working together on inhibitor development, the targets are not those mentioned.

CAREERS

TURNING POINT Physiologist relinquishes major grant to return to former post **p.301**

UNITED STATES Programme sends research fellows abroad for collaboration **p.301**

NATUREJOBS For the latest career listings and advice www.naturejobs.com



LAB LIFE

Balancing act

Many researchers struggle to take time off from the lab. But scientists should try to improve their work–life balance.

BY QUIRIN SCHIERMEIER

As a PhD student and later a postdoc at the University of California, Berkeley, Axel Meyer almost had to force himself to have a life outside the laboratory. Wanting to experience the arts, he worked the odd evening as an usher at Zellerbach Hall, Berkeley's on-campus performance theatre. If time allowed, he would also play in the university's field-hockey team. But on most days, his leisure activity was limited to riding his motorcycle to campus early in the morning and back home late at night.

Working long hours and at weekends was

common in Berkeley's zoology department, from which Meyer received his PhD in 1988. As an evolutionary-biology postdoc, Meyer says, 80-hour working weeks were the rule rather than the exception.

"You might think we were brainwashed to work so much, and in a positive sense I guess we were," says Meyer, now chair of zoology and evolutionary biology at the University of Konstanz in Germany. But, he adds, the research was so exciting and he felt so privileged to be part of his supervisor's group that it never crossed his mind that he might be working too hard.

Still, for many early-career researchers the

joy of doing science is tarnished by heavy workloads and excessive demands. Personal interests — and maybe even a family life — are often sacrificed for the sake of producing the papers and grants that pave the way to permanent jobs in academia. And yet a healthy work–life balance can be more fruitful than endless hours in the lab or in front of the laptop. Scientists — and their work — can benefit from setting aside time for hobbies, travel or just about anything else that does not directly intersect with lab activities.

A HARD DAY'S NIGHT

The working habits of scientists are poorly monitored, but an analysis of download patterns of scientific literature across all fields suggests that many researchers work after hours or at weekends (X. W. Wang *et al. J. Informetr.* **6**, 655–660; 2012). Using a tool devised by Springer publishing, the researchers tracked when people downloaded papers from the publisher across five weekdays and four weekend days in April 2012. Working late into the night is particularly widespread among scientists in the United States, whereas Chinese researchers work many hours on the weekend, they found (see 'Literature searches around the clock').

"Scientists are generally under great pressure, and most young scientists are spending much more time working than they initially expected when they were undergraduate students," says co-author Shenmeng Xu, a master's student at the Dalian University of Technology in China.

At Chinese universities, she says, even master's and PhD students are expected to dedicate some 60 hours a week to their studies. Constantly working overtime is exhausting, physically and mentally, and limits students' social life. "I do some swimming for exercise," she says. "But other than that I can't afford any entertainment and I can go home no more often than twice a year to see my parents. I like what I'm doing but I do wish I could have a more balanced life."

Demands on scientists have greatly increased as research has become more data-intensive in the past few decades, says Julie Overbaugh, an HIV researcher at the Fred Hutchinson Cancer Research Center in Seattle, Washington. Generating and sifting through large amounts of data takes time, and using specialized equipment — which is often shared between groups of researchers — can mean reserving time slots and thus working at odd hours. Striking a healthy balance between work and a personal life is difficult, she says, but more important ►

► than many hard-working young scientists and their supervisors will admit.

“Prioritizing the things that are most important for you is key, as is evaluating whether you are using your time wisely,” says Overbaugh. “If you feel you’re missing out on things that are really important for you — family, friends or hobbies — something is wrong.”

TAKE A BREAK

For Daniel Mietchen, a biophysicist and web-tool developer who earned his PhD in 2006 from Saarland University in Saarbrücken, Germany, that important something outside science is playing in a band. A singer in a traditional Central Asian song and dance group, he took pains to organize his doctoral research on mapping brain structure with nuclear magnetic resonance imaging so as to allow him sufficient time for rehearsals and gigs with his Berlin-based music collective. He even managed to persuade his supervisor to grant him four weeks of educational leave in 2004 to improve his Uzbek language skills in Samarkand. “I’d strongly recommend that anyone complement their research work with at least one non-scientific activity that you really enjoy,” he says. “As for me, I get my best ideas in unfamiliar surroundings, often while travelling, but rarely in the lab.”

Fearing disapproval from colleagues and superiors, few early-career scientists treat themselves to such out-of-office time. But time off should be part of any sensible research schedule, says Sabine Lerch, an independent soft-skills instructor who frequently coaches German PhD students on time management.

Young scientists, she adds, should rid themselves of “imaginary demands” such as working extra hours in the lab. “You will achieve more in one productive day than on a series of days in poor mental and physical condition,” she says. “Students tend to think about recreation last when they structure their research work — if they structure their time at all — but everybody needs breaks.” Lerch suggests that

scientists keep at least one weekend day clear of any professional duties and set aside time on work days for exercise and hobbies.

Even short breaks from intense work help recharge creativity, agrees Overbaugh. In science, she says, success is not necessarily a function of the amount of time spent in the lab or at the computer. Scientists are more likely to produce new ideas and insights when they are not under deadline pressure, she suggests.

Time-management guidance from advisers can be invaluable. When HIV researcher Jennifer Kerubo Maroa first arrived in Seattle from Kenya to do a PhD at the Hutchinson Center, her supervisor, Overbaugh, told her more than once that getting herself and her family settled was more important than the lab. “At first, I didn’t quite believe her, but I eventually accepted she was being truthful with her advice,” says Kerubo Maroa. “When I arrived in the United States I thought all that counts is work. Knowing that I could leave whenever I needed to take care of my family’s needs in turn allowed me to organize a balanced schedule between the lab and my kids.”

“Of course there were many times after she got settled that she worked very hard on her science,” says Overbaugh. “But she also made sure to keep her family life in balance.” Kerubo Maroa has since received the distinguished student award from Hutchinson, produced a couple of papers, and accepted an offer of a postdoc position at the KwaZulu-Natal Research Institute for Tuberculosis and HIV in Durban, South Africa, a collaboration between the US Howard Hughes Medical Institute and the University of KwaZulu-Natal.

At the Hutchinson Center, students can get advice on work and work-life balance from mentoring committees that include three senior faculty members from across the spectrum of age, ethnicity and career level. The

committees are there to guide early-career researchers informally, as well as to formally evaluate PhD students’ annual progress.

POINT OUT PRIORITIES

If supervisors are not understanding about time pressures, making a specific plan can obviate conflicts. Lerch advises students to make a project plan, laying out what is to be done and by when, and to revisit it regularly. She suggests that they then make a shorter-term plan with more specific goals. If a supervisor asks for extra tasks, the student can point out what other aims, already planned, will have to fall by the wayside. And scientists should try not to take on too much, says Lerch — they should not be afraid to say no to taking on administrative tasks and other advisory roles.

Such measures — in conjunction with the support of trusted colleagues, friends and career coaches — can help to mitigate the stress created by demanding supervisors. In extreme cases, if there are misconduct issues or breaches of employment law, scientists should seek advice from an ombudsman or PhD organization, such as the European Council of Doctoral Candidates and Junior Researchers (Eurodoc) in Brussels.

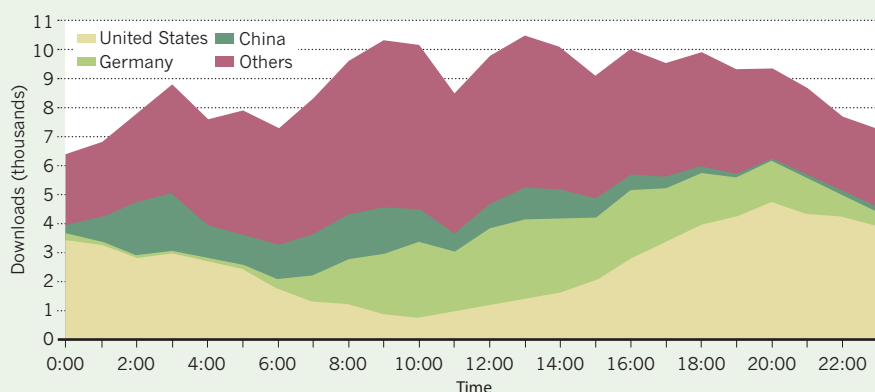
Even with scientists’ best efforts, progress is difficult. Many countries have been hit by the financial crisis, for example, forcing young scientists to fight even harder for jobs and funding — which means more demands on their time. “Across hard-hit southern Europe, most of those who do still have work are now doing a double job, including full-time teaching and full-time research, for one salary,” says Eurodoc president Slobodan Radičev, a doctoral candidate in industrial engineering at the University of Novi Sad in Serbia. Few young researchers, he adds, have anything resembling a healthy work-life balance. For Radičev himself, this balance is a pipe dream. Although his studies are in Serbia, he spends much of his time in Italy, where his wife has a science job. He says that his situation only works because his supervisor is sympathetic — and because flights are cheap. But when jobs are in short supply, it is tempting to prioritize career obligations over personal challenges.

However, not everyone agrees that working long hours is a bad thing. Meyer tries to convey to his students and postdocs the inexhaustible thrill that he experienced during his hard-working Berkeley years. Meyer is demanding, even elitist. He hopes that all his lab members will want to become researchers or professors, and sets high standards for his group. Those who really love what they do should not lament the long hours, he opines. “I can’t force anyone to work more than they want,” he says. “But it does hurt me when I come in to my lab on a weekend and find only a couple of people at work.” ■

Quirin Schiermeier is Nature’s Germany correspondent.

LITERATURE SEARCHES AROUND THE CLOCK

The number of research papers downloaded each hour on 12 April 2012 varied by country.



Reprinted from X. W. Wang et al. Exploring scientists' working timetable: Do scientists often work overtime? *J. Informetr.* 6, 655–660, 2012 with permission from Elsevier.

TURNING POINT

Patrik Rorsman

Physiologist Patrik Rorsman accepted a prestigious 7-year, Can\$10-million (US\$10-million) grant to serve as the Canadian Excellence in Research Chair in Diabetes at the University of Alberta in Edmonton. But last autumn, after seven months in the post, he returned to the University of Oxford, UK, forgoing the generous funding.

What persuaded you to accept the Canadian Excellence in Research Chair?

I'm a bit of a gypsy as a scientist. I had made two other big moves before settling at Oxford. So when Alberta approached me with significant funding and plans to spend millions expanding their facilities, I was easily seduced. A former postdoc and valued colleague of mine, Patrick McDonald, is now a research star there, and the prospect of working with him again was appealing. Alberta has access to human pancreatic islet cells, which are the focus of my work. And my children would be finishing school in the United Kingdom in a few years, so my family and I thought it was a good time to move.

Describe the challenges you faced at the University of Alberta.

I had no complaints about the university or the faculty; our problems were more related to human resources. My wife, who had been promised a job in university administration, had problems negotiating holiday time — which was important to her, given that our children were to stay in the United Kingdom. Ultimately, she did not accept a position. And although my staff members were told that their immigration would be fast-tracked, several people were experiencing difficulties.

Was it a difficult decision to return to Oxford?

Yes, for several reasons: my salary was significantly higher in Canada, for example. But I enjoy being on the same continent as my wife, and she didn't want to sacrifice her career. It is unfortunate that she and the university couldn't come to an agreement. It would have been a great experience and opportunity. And, because I am Swedish, I was looking forward to being near mountains and snow. Part of me regrets that it didn't work out.

Did you create a safety net at Oxford in case it didn't work out in Canada?

Not deliberately, but a few factors left the door open. I had decided to take a year of leave from Oxford so that my family could stay in our UK home for the first year that I



was in Canada. And although I had never intended to come back, I had submitted a grant application to the Wellcome Trust biomedical research foundation before I left, as a goodwill gesture to Oxford, and ended up getting it.

Do you plan to continue collaborating with colleagues at Alberta?

I certainly hope we will continue working together in future. For example, one of my postdocs, Matthias Braun, with whom I've published almost 30 papers, came to Alberta with me, and decided to stay.

Would you encourage other nations to start a research-chair programme like Canada's?

Yes. But it takes a lot of courage, because it involves federal dollars and there will always be opposition from people who want to see the money used in other ways. But if you feel that the science needs an influx of new ideas and people, this is the programme you need. It will help to get some really good people — you need significant funding to draw international talent.

What advice would you give to people considering offers from foreign universities?

It depends on who you are and your domestic situation, but I encourage colleagues to take advantage of this perk of our profession — the thrill of living and working in a different place. One of the big problems in science is that there is too little mobility between countries. But it is important to make sure that you negotiate the most favourable terms possible. It is such an upheaval to move from one country to another. ■

INTERVIEW BY VIRGINIA GEWIN

SWEDEN

Basic-research boost

One of Sweden's largest private research funders has awarded the first 30 grants in its early-career fellowship programme. The Wallenberg Academy Fellows initiative of the Knut and Alice Wallenberg Foundation in Stockholm aims to "kick-start" Swedish science, especially basic research, says Göran Sandberg, the foundation's executive director. "Sweden is still performing well, but we need young people to focus on science," he says. At least 250 fellows across all disciplines will be funded. Researchers in and outside Sweden are nominated by Swedish universities, which will hire them as faculty members if they are selected. Grantees receive 7.5 million kronor (US\$1.1 million) over 5 years, with the potential for a 5-year renewal. Applications for the next round are due by 1 March.

UNITED KINGDOM

Visa policy warning

A fall in the number of students entering the United Kingdom could cause problems for graduate courses in science, technology, engineering and maths (STEM), warns Universities UK (UUK) in London, which represents more than 130 institutions. According to the Office for National Statistics, 8.2% fewer international students arrived in the country in the year to March 2012 than in the previous year. The UUK says that the drop may be linked to changes that make visas harder to get. Jo Attwooll, a policy adviser for the UUK, notes that UK graduate STEM classes have tended to include a lot of non-European students. "Immigration policy could affect the number of students taking these courses and thus their viability," she says.

UNITED STATES

Graduates can go abroad

The US National Science Foundation (NSF) has expanded an international collaboration initiative for its graduate fellows. Fellows may now apply to spend 3–12 months at an institution in Norway, Finland, Denmark, Sweden, Japan, South Korea, Singapore or France, with a living allowance from the host nation and travel subsidized by the NSF. "In this era of science with more international collaboration and interdisciplinary work, we want to encourage our graduate students to step into those environments," says Maria Zacharias, a spokeswoman for the NSF. Applications must be in by 1 February; awardees will be told in April.

AN UNINTENDED FUTURE

The next great threat.

BY TRISTAN SCOTT

“There’s another one! That’s five fish-eyes. I win.” The croaking voice of old Mr Duvelle mocked his equally seasoned friend as they looked out of the window of the geriatric ward. He was referring to a man outside whose eyes had regressed into an earlier form, resembling the ‘pin-hole’ eyes of some fish.

Mr Higgins lifted his cane with a liver-spotted hand, and stabbed at a hairy fellow who was shuffling down the street on his knuckles. “Ah darn-it,” he wheezed through his oxygen mask, “another monkey-boy and I would have won. Five seconds too late.”

“Five decades too late,” Sullivan thought to himself as he overheard the two men’s conversation from a few feet away. He too looked out at the extensive array of genetic regressions that passed by: a woman with a tail, a man without an opposable thumb. If these kinds of aberrations were the worst of it, it would not have been so disastrous, but at least half of the regressions were lethal, and that number got worse with each generation.

“It was a simpler time,” Mr Duvelle continued to Mr Higgins’s affirming grunts. “All we had was that whole climate-change fiasco.”

“And look how we fixed that!” Mr Higgins chimed in. “But kids these days, they don’t know a thing about banding together for a common cause. Now they have this ... induced ... what do they call it again?”

“Huh?” the partially deaf Mr Duvelle leaned closer, straining to hear his friend.

He pointed a gaunt hand at the people outside and shouted: “What do they call this again?”

“Malform.”

They nodded together as Mr Higgins mumbled, “Yes, induced malform evolution.”

“My granddaughter, I don’t even know if we are related,” said Pastor Kane, a man who had aged well, with only fine lines on his dark skin. “She is not of my blood!” He continued to preach to his small congregation of three elderly women across the room, who were fanning themselves. “We thought we knew what we were doing! And for all our improving, look at us now.”

“What was the difference again?” asked Mr Duvelle loudly. “That reporter, what did she say the difference for a new species was? You know, the pretty one with the nice teeth.”

“0.004%,” Mr Higgins said before he took another deep gasp of oxygen.

“That’s it. 0.004%.” Mr Duvelle’s head bobbed on his thin neck like a vulture. “That’s the difference between a Neanderthal and us. The difference between us and them.”

If only the difference was that small, Sullivan silently wished to himself. It is closer



to 1% in really bad cases. Those ones aren’t human any more.

He stared out of the window at a world he did not recognize. It had become a fad after companies commercialized equipment that could easily replace genes, especially the ones that nature never gave you: a year-round tan, blue eyes, a better metabolism. The technology was originally intended to cure diseases, and cure them it did, but eventually it filtered down to be used for what the popular media called ‘genetic tattoos’.

It had seemed harmless at first, but over time, much like the slow, silent accumulation of greenhouse gases, it built. A change to a gene here, a deletion there, a little bit left in then passed on to the next generation, then more changes added to that. The changes were cumulative and, before they knew it, the visible signs started appearing.

‘Smog,’ it was called.

Genetic pollution.

“We should not

have been meddling,” the pastor announced again. “And now — can it be fixed?”

Sullivan wasn’t sure if it could, once you have mixed water and jelly, it is hard to separate them. Now it was as if they had mixed hundreds of flavours together and had left them to set for far too long. Natural genes had become dependent on the artificial ones. If they removed the one, the other would be affected. It was incredibly difficult, if not impossible, to tease apart the extensive networks that had become so intricately linked. He scooped up a bit of jelly from his tray and sucked it into his toothless mouth.

“Time to take a sample, Doctor Sullivan,” said a young nurse with pseudo-gills along her neck.

He lifted up his sleeve and exposed a thin arm riddled with tiny puncture scars. The nurse placed a thin, silver canister on his arm and with a clipping sound another lump of tissue was excised. She put a plaster on the wound, and then left to prepare the sample. His arms looked no different from those of everyone else in the ward. All of them had hundreds of star-shaped scars, an indication of as many failed experiments.

“Lord knows we are the last of the pure ones,” the pastor preached, and the three women sounded ‘Amen’s’ to his sermon. “We are the unedited!” He cast an outstretched finger to the window. “And we are their salvation!”

Sullivan had heard enough. He stood up slowly and reinserted his dentures. The stinging of his arm was a piercing reminder of the work he had yet to achieve, as he shuffled through the hospital. He donned his lab coat, which felt as heavy as the guilt that would not let him rest. He looked up at his old award — the engraved image of Alfred Nobel seemed purposefully turned away, as if shunning him. It was, however, for the same reason that he had received the award, that humanity now faced its next, great threat.

He took a dispirited look at the sample taken from him, and gazed along the rows of tubes containing a hundred others. It was a vain hope, but somehow he had to figure out an answer: how do you backtrack up the evolutionary tree? ■

Tristan Scott is a PhD student at the University of the Witwatersrand in the field of therapeutic RNA interference. His first fiction novel, Vertical City, has been accepted for publication.

➤ **NATURE.COM**
Follow Futures:
@NatureFutures
go.nature.com/mtoodm